



Основана в 1724 году

**RUSSIAN ACADEMY OF SCIENCES
SCIENTIFIC COUNCIL FOR DIRECT ENERGY CONVERSION
SCIENTIFIC COUNCIL FOR FLUID MECHANICS
SCIENTIFIC COUNCIL FOR LOW TEMPERATURE PLASMA PHYSICS**

THE 9TH INTERNATIONAL WORKSHOP ON MAGNETO-PLASMA AERODYNAMICS

**MOSCOW
APRIL 13-15, 2010**

**Organized by Institute of High Temperatures of RAS
In co-operation and sponsorship by:**



RAS



RFBR

UDK 533.6.011:(533.95:537.84)

Proceedings the 9th Workshop on Magneto-Plasma Aerodynamics.
Ed. V.A.Bityurin, Moscow, JIHT RAS, 2010, pp.**308**

© Joint Institute of High Temperature of Russian Academy of Sciences, 2010
ISBN 5-201-09557-7

Program Committee

Aleksandrov A.F. (Russia)
Alferov V.I. (Russia)
Batenin V.M. (Russia)
Bazhenova T.V. (Russia)
Bityurin V.A. – Chairman (Russia)
Bobashev S.V. (Russia)
Borghi C. (Italy)
Chernyi G.G. (Russia)
Ishikawa M. (Japan)
Giordano D. (The Netherlands)
Khodataev K.V. (Russia)
Laux C. (France)
Lineberry J. (USA)
Macheret S. (USA)
Miles R. (USA)
Tishkoff J. (USA)
Vatazhin A.B. (Russia)

Local Committee

Bityurin V. A
Bocharova E. A.
Klimov A. I.
Kolesnichenko Yu. F.
Kuznetsova T. N.
Leonov S. B.
Sukhov V. N.
Semenova T. M.
Son E.E.

Contents

SESSION 1. Plasma Aerodynamics – 1

Key Experiments in Plasma- Aerodynamics Today	13
<i>Klimov A.I.</i>	
Jet Noise Control by Nozzle Surface HF DBD Actuators.....	21
<i>Kopiev V., Ostrikov N., Zaitsev M., Belyaev I., Bityurin V., Klimov A., Moralev I., Godin S.</i>	
Turbulent Boundary Layer Control by Spanwise Travelling Waves Created by DBD Plasma Actuators	23
<i>Richard Whalley and Kwing-So Choi</i>	
Effect of Source on the Evolution of Cylindrical Vortex	35
<i>Shugaev F.V., Petrova T.A.</i>	
Study of a Longitudinal Capacity Coupled HF Discharge in a Swirl Airflow	40
<i>Moralev I.A., Boytsov A.Yu., Klimov A.I.</i>	
Properties of DC Discharge Near Surface in Supersonic Gas Flow at Low Gas Pressure	46
<i>Schweigert I.V.</i>	
Sliding Surface Distributed Nanosecond Discharge in the Laminar and in the Turbulent Boundary Layer	51
<i>Znamenskaya I. and Mursenkova I.V.</i>	

SESSION 2. Plasma Aerodynamics – 2

<i>Peculiarities of Flow Past Bodies in the Presence of Steady and Pulsing Toroidal-Type Upstream Energy Deposition. (Invited)</i>	54
<i>Georgievsky P.Yu., Levin V.A.</i>	
<i>Thermal Chocking of a Cylindrical or Spherical Mass Source</i>	59
<i>Kogan M.N., Kucherov A.N.</i>	
<i>Specific Features of Supersonic Streamlining for Asymmetrical Energy Supply Into External Flow</i>	70
<i>Azarova O., Kolesnichenko Yu.</i>	
<i>The Influence of an Electric Discharge on the Flow Pattern of a Supersonic Impacting Jet</i>	84
<i>Fomin V.M., Lomanovich K.A., and Postnikov B.V.</i>	
<i>Investigation of Vortex Flow Induced by Dielectric Barrier Discharge in Quiescent Air</i>	88
<i>Golub V.V., Saveliev A.S., Sechenov V.A., Son E.E.</i>	
<i>To a Theory of Gas Discharge with Complex Kinetics in Free Space</i>	93
<i>Bychkov V.L., Dvinin S.A.</i>	
<i>Numerical Simulation of Supersonic Flow in Convergent-Divergent Duct with Discharge Supply</i>	100
<i>Firsov A.A., Leonov S.B., Miller A.B.</i>	
<i>Nonsteady-State Behavior of a “Gliding Arc” in Air Flow</i>	103
<i>Korolev Yu.D., Frants O.B., Landl N.V., Geyman V.G., Enenko A.A.</i>	
<i>Investigation of a High-Frequency Discharge Parametres Influence on the Processes of Plasmoids Formation and Dynamics in a Gas Flow</i>	105
<i>Pashchina A.S., Nikolaeva V.I., Sidorenko M.K., Prudchenko V.A.</i>	

SESSION 3. Plasma Assisted Ignition and Combustion – 1

Plasma-Assisted Mechanism of Cool Flame Appearance. (Invited).....112
Bityurin V.A., Filimonova E.A.

**Numerical Study of Stages of Ignition of Ethylene-Air Mixture by Plasma
Initiation. (Invited).....115**
Deminsky M.A., Kochetov I.V., Napartovich A.P., Leonov S.B.

**Processes Responsible for Near-the-Axis Ignition of Methane-Oxygen Mixture by
Means of Ring-Shaped Electric Discharge.....125**
Barkhudarov E.M., Berezhetskaya N.K., Kop'ev V.A., Kossyi I.A., Levin V.A., Manuilovich I.S., Markov V.V.,
Popov N.A., Taktakishvili M.I. and Temchin S.M.

Ultra-Lean Flames Stabilization by High-Voltage Nanosecond Pulsed Discharge.....134
A Nikipelov, Il Popov, Giuseppe Correale, A. Rakitin, A. Starikovskii

SESSION 4. Plasma Assisted Ignition and Combustion – 2

<i>The Effect of Nonequilibrium Excitation on Hydrogen-Oxygen Mixtures Ignition. (Invited)</i>	141
<i>Popov N.A.</i>	
<i>Liquid Hydrocarbon Films Ignition in the Air Stream with the Help of the Microwave Discharge Created in a Programmable Pulse Mode</i>	156
<i>V.M.Shibkov, V.A.Bityurin, A.A.Karachev, R.S.Konstantinovskii, P.V.Kopyl, L.V.Shibkova</i>	
<i>Low-Energy Electron Attachment and Detachment in Vibrationally Excited Oxygen and Air</i>	164
<i>Aleksandrov N.L., Anokhin E.M.</i>	
<i>Modeling of Toluene Conversion in Non-Thermal Non-Equilibrium Nitrogen Plasma</i>	172
<i>Deminsky M.A., Kochetov V.I., Trushkin A.N., Umanskii S.Ya.</i>	
<i>Detonation Initiation Through a Gradient Mechanism with Application of Nonequilibrium Nanosecond Discharge</i>	179
<i>Rakitin A, Starikovskii A.</i>	
<i>Submicrosecond Discharge in Nonhomogeneous Media and in High-speed Flow</i>	186
<i>Firsov A. A., Isaenkov Y. I., Leonov S. B., Shurupov M. A., Yarantsev D. A.</i>	
<i>The Formation of Positively Charged Plasma Structure in Nanosecond Discharge with Slot Cathode</i>	193
<i>Ashurbekov N.A., Iminov K.O., Kobzev O.V., Kobzeva V.S.</i>	

SESSION 5. MHD – 1

Remarks on Ground-Based MHD Experiments. (Invited).....195

Bityurin V.A., Bocharov A.N., Popov N.A.

Investigation of the Flow Around a Wedge by Air with $M = 6$ at the Local MHD-Action On The Free Stream.....205

Podzin V.E., Fomichev V.P., Shevchenko A.B., Yadrenkin M.A.

Electrogasdynamic and Magnetohydrodynamic Control of Body Supersonic Streamline.....208

Erofeev A.V., Lapushkina T.A., Poniaev S.A.

Research of the Phenomenon of the Current Crisis in the Channel of the Plasma Accelerator with the Continuous Electrodes within the Framework of the Two-Fluid MHD-Model.....216

Kozlov A.N.

SESSION 6. Shock Waves/Related Problem

Study of Shock Wave Impact on Gas Inhomogeneity Produced by Pulse Gas Discharge..... 224
Fokeev V.P., Grin Yu.I.

Features of Converging Shock Wave Behavior Influenced by Medium Thermodynamic Non-Ideality227
Konyukhov A.V., Likhachev A.P., Fortov V.E.

Shock Wave Propagation un the Stationary Dusted Plasma of the Glow Discharge in the Different Gases232
Baryshnikov A.S., Basargin I.V., Chistyakova M.V.

Speed Limits at Propagation of Shock Wave in Multicomponent Dispersive Medium.....238
Serov Yu.L.

On Specifics of Inertial Electrostatic Confinement Fusion at Miniature Vacuum Discharge.....245
Kurilenkov Yu. K., Tarakanov V.P., Karpukhin V.T. and Valyano G.E.

POSTER SESSION

Plasma-Assisted Reaction of Heterogeneous Al-H₂O Mixture in High-Speed Swirl Flow	260
<i>Klimov A.I., Bityurin V.A., Grigorenko A.V., Efimov A.V., Kutuzov D.S., Tolkunov B.N., Tsymbal A.A., Polyakov L.B.</i>	
Influence of Gasdynamic Processes on Structure and Breakdown Levels of MW Discharge Initiated by Laser Spark.....	266
<i>Afnas'ev S., Brovkin V. and Kolesnichenko Yu.</i>	
Methods of Definition of Gas Stream Parameters at Not-Designed Mode of Nuzzle Operation.....	270
<i>Karachev A.A., Kopyl P.V., Shibkov V.M., Shibkova L.V.</i>	
Evaluation of Radiation Losses in Al-H₂ MHD Generator Tract.....	276
<i>Bityurin V.A., Galaktionov A.V., Kolpakov A.V.</i>	
Flow Control around Wing Model by HF DBD Discharge Study of the Influence of Surface Capacitive HF Discharge on a Lateral Flow Around the Circular Cylinder.....	281
<i>Moralev I., Bityurin V., Kasansky P., Klimov A., Chertov D.</i>	
Flow Control Around Cylinder by Surface Capacity Coupled HF Discharge.....	287
<i>Moralev I.A., Bityurin V.A., Kazansky P.N., Klimov A.I., Chertov D.N.</i>	
MHD Power Extraction in Re-Entry Flight. Bityurin V.A., Bocharov A.N.	292
<i>Bityurin V.A., Bocharov A.N.</i>	
Physical-Chemical Kinetics of Aluminum Oxidation by Steam	295
<i>Dobrovol'skaya A.S.</i>	
Electrical Discharge Interaction with Gas Medium in External Magnetic Field and Its Influence on Flow Structure and Mixing.....	295
<i>Klementyeva I.B., Bityurin V.A., Bocharov A.N.</i>	
The Simple Scaling for a Microfusion Flying Machines (MFFM) and the Variety Mobile Systems.....	304
<i>Belokogne V.A.</i>	
Index of Autors.....	305

KEY EXPERIMENTS IN PLASMA-AERODYNAMICS TODAY

Klimov A.I.

Joint Institute of High Temperature RAS
Izhorskaya 13 bld.2, Moscow, 125417, Russia

Plasma aerodynamics (PA) was intensively developed during last 30 years. Remind that the first plasma- ballistic experiments were carried out by scientist joint team from Ioffe's Institute (St.-Petersburg) and Radio Engineering Institute (Moscow) in the frame of National State Research Program in 1978. Interaction of a moving projectile with weakly ionized non-equilibrium plasma was studied in this experiment. The diploma on scientific discovery [1] was obtained after investigation of this task. This work stimulated appearance of new science branch named plasma aerodynamics (PA). Many experimental and theoretical studies were carried out in the field of PA in Russia and foreign countries during last 30 years. New important experimental results and theoretical ones were obtained in this time period. So, it is necessary to analyze of these obtained results to formulate the new key tasks and the strategy directives for its future PA development. These conclusions and key tasks help us to realize of plasma technology implementation in aviation.

PA's achievements are well-known today. The following experimental results are reliable and important [1-30]:

1. Drag decrease by plasma up to 80%.
2. Lift increase by plasma formation up to 40% and higher.
3. Flight control by plasma.
4. Flow control by local plasmoid created by pulse repetitive electric discharge.
5. Boundary layer control and flow separation control by surface plasma formations.
6. Shock wave dispersion and its propagation in non-equilibrium weakly ionized plasma. Sonic boom reduction by plasma.
7. Acoustic wave dispersion and its amplification in non-equilibrium weakly ionized plasma. Jet noise reduction by plasma formations.
8. Heat flux control and flow control by magneto-hydrodynamic methods at hypersonic airflow velocity.
9. And others.



Figure 1. Flight vehicle with fast plasma actuators. Drag decrease by plasma formation.

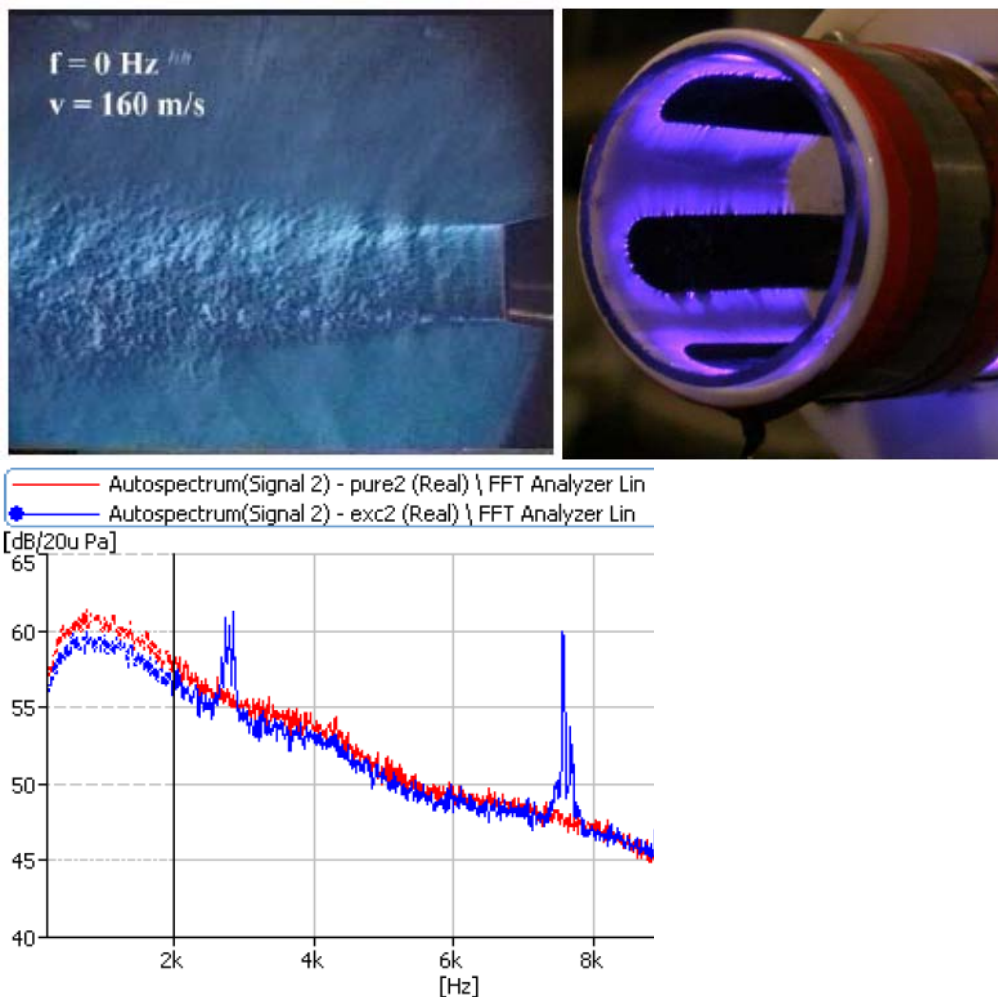


Figure 2. Jet noise control by HF plasma actuator (top). Noise spectra of unexcited jet (red) and excited jet by HF plasma actuator at frequency $F = 10.350 \text{ kHz}$

According our opinion the item #4 is very important for possible implementation of the plasma technologies in *hypersonic aviation* namely. Really, the typical time of plasma formation creation near moving body by fast *power electronic devices* is very small about of $10^{-6} - 10^{-9} \text{ s}$. So, plasma actuator can operate with very high frequency up to $F = 10^1 - 10^6 \text{ Hz}$.

However there are many technical difficulties to use of plasma technologies in aviation today. The first of them connected with expensive plasma formation creation near a real airplane. Another one is connected with high value of electric power needed for flow control realization by plasma. For example, it is necessary to use onboard plasma generator with a mean electrical power about 1-10MW to decrease of fighter's drag up to 30-40%. But available onboard electric power of a modern fighter is about 30-60kW only. So, it is necessary to increase *plasma efficiency* and *its effectiveness*

considerably for the possible plasma technology implementation in aviation today.

The following Strategy Program of PA development is proposed in this work:

1. Realization of a local flow control near vehicle by plasma formation at resonant regimes of plasma- airflow interaction (for example, Strouhal's number $St \sim 0.3 \div 1$; ionization wave velocity is closed to airflow velocity; and others) in the sensitive zones (such as flow separation zone, swirl flow, plasma precursor before bow shock wave and others) only, [2], Fig.2.
2. Using a positive (or negative) feedback between plasma formation and airflow disturbed by it. For example, jet noise reduction is based on this method namely [3], fig.3.

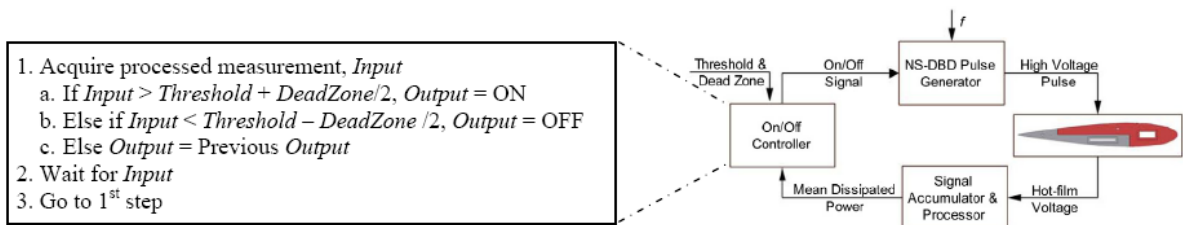


Figure3. The on/off control scheme with control feedback of airflow around airfoil model

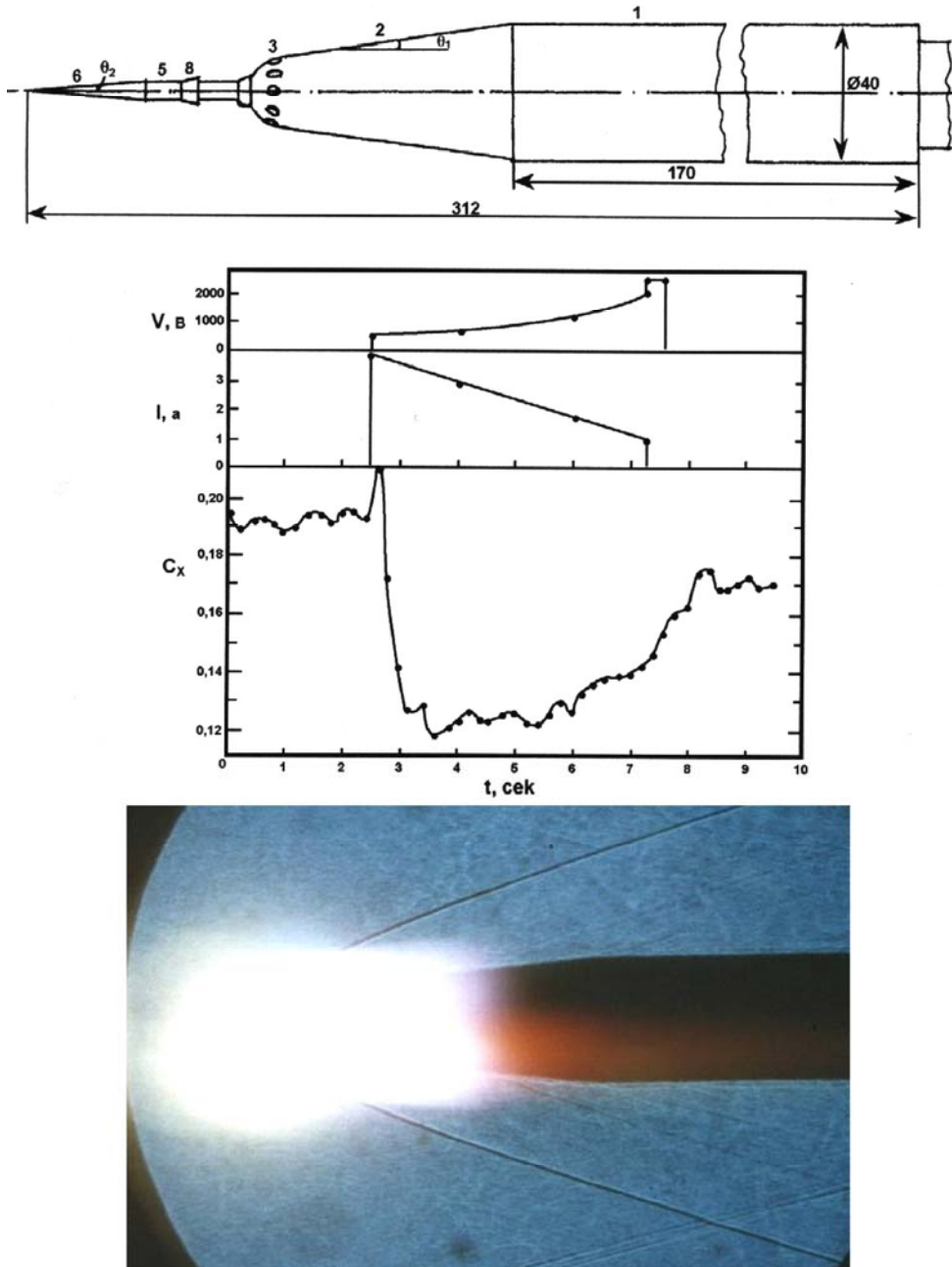


Figure 4. Plasma-aerodynamic hysteresis. DC discharge created in the head part of the model N. Airflow Mach number $M \sim 4$, $P_{st} \sim 40$ Torr

3. Plasma –gas dynamic hysteresis is revealed in the works [4, 5], fig.5. This hysteresis is

connected with vortex reconstruction near body at a large attack angle. Note that this result is very important for minimization of

mean power input in plasma and optimization of plasma actuators design.

4. Electric power extraction from plasma flow by three electrode (3E) configuration is discussed in the works [7,8,17,18]. Creation of onboard

plasma-gas dynamic convertor is possible by this electrode's configuration. Well-known electrostatic Van der Graph's generator is the prototype of this new device. Another possibility of extraction of electric power from



Figure 5. Possible control of conical vortex parameters near plane by plasma formation at large attack angle. 1- HF plasmoid, 2-conical vortex

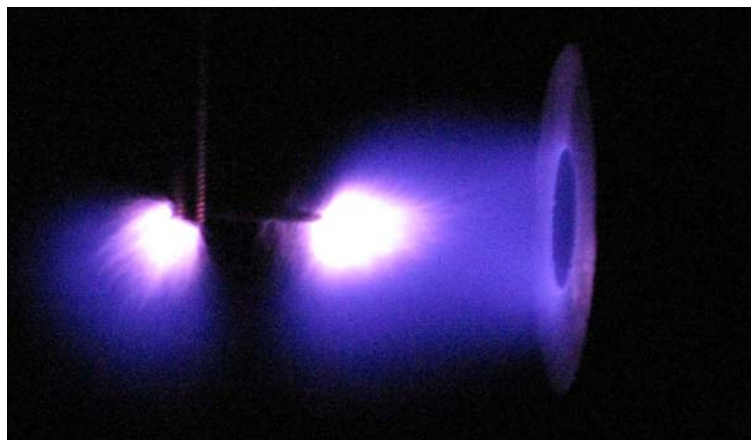
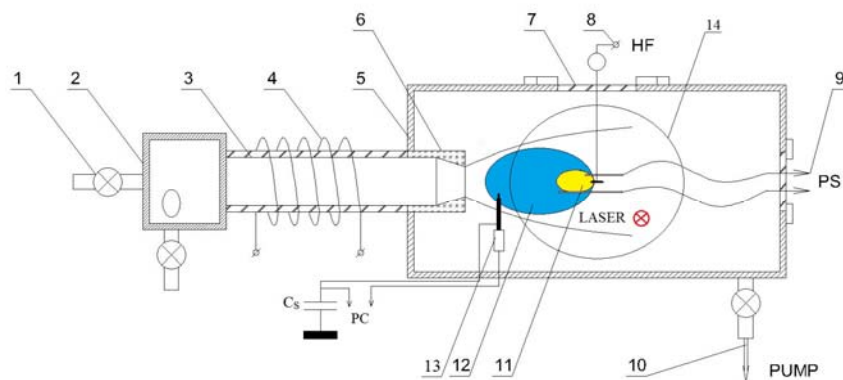


Figure 6. Prototype of plasma-aerodynamic convertor. DS power supply created by HF plasma in supersonic airflow at $M=1.5$. Scheme of plasma aerodynamic experiment in wind tunnel (top), charged HF plasmoid in airflow (down)

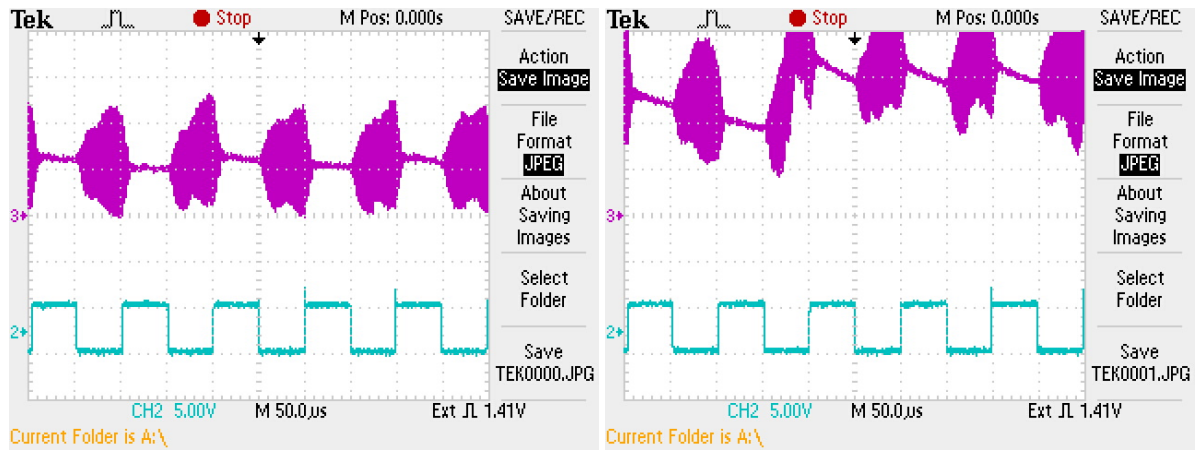


Figure 7. Typical HF plasmoid's electric potential at different experimental conditions.
 Left.- longitudinal charged HF plasmoid with blue halo at $P_{st} \sim 300\text{Torr}$, $M \sim 0.5$
 Right.- longitudinal charged HF plasmoid with blue halo at $P_{st} \sim 300\text{Torr}$, $M \sim 1.5$

- plasma flow is discussed in [5] and connected with different ion drift of AC discharge in high-speed airflow. Plasma-aerodynamic rectifier was realized in the experiment described supply in our work [5]. Now this ion properties in high speed airflow helps us to create DC power supply in FH plasma in supersonic airflow at $M \sim 1.5$ also, [4], fig. 6,7.
5. Implementation of a plasma-chemical long-lived *charged* plasmoid for airflow control. This method helps us to minimize of power input in plasma also.
 6. Flow control by a local external plasma-assisted combustion formation created near vehicle's surface is discussed in the work [9, 10].
 7. Analysis of the experimental results obtained in the field of the PA helps us formulate the following main key task in this field: - *Vortex-plasma interaction* [11-13]. There are preliminary experimental results on vortex control by non-equilibrium plasma (vortex amplification and its destruction by plasma), [13]. Study of this task is very important for the different aviation applications today. For example, the results obtained during this study fulfilment may be used to control of wing's lift force, flow separation, base drag and others by plasma formation, fig.5. However detail experimental study of plasma-vortex interaction is absent now.
 8. Implementation of a resonant power pumping of plasmoid near airplane by an external long-distant power transmitter (radar, radio

antenna, laser beam and others) arranged in ground surface, sea water and space (Avramenko-Kapitsa-Tesla's method).

There is a number of research Programs based on external power pumping of the plasmoid created near vehicle, namely:

- Russian Program "Trust" proposed by academician Avramenko R. Powerful MW radiation created by spaced radars is used for flight control of different moving bodies in atmosphere.
- US Project "Light Vehicle" under the direction of Dr. Mirabo L, [14]. Combined Laser-MW powerful pumping of the plasmoid is used in this Work. There is analogical Research Project in Japan (Prof. Sacho),
- US Project "MW Rocket". Focused powerful MW radiation is used inside rocket's nozzle for hydrogen jet heating,
- Remind that the first Project on creation of MW weapon was proposed and realized in part by N.Tesla, fig.8, [15]. He tried to use MW radiation to create of a stable plasmoid near a vehicle. Note that this task was studied in plasma-ballistic experiment also, [1], fig.8b. One can see cylindrical projectile with secondary Tesla's coil in this figure. Primary coil was arranged inside ballistic set up. Two HF plasmoids were created near moving projectile.

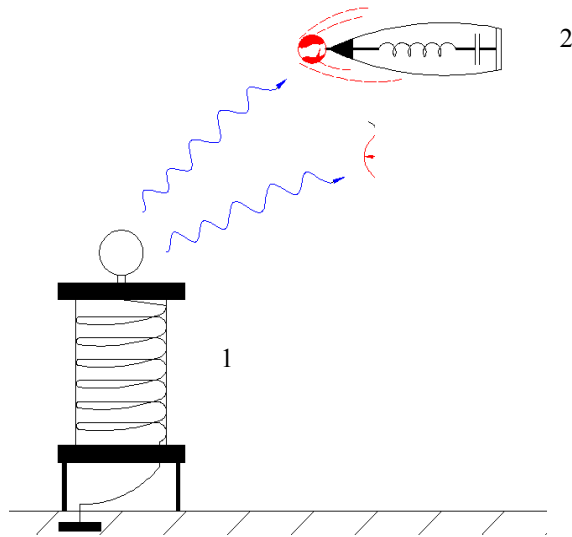


Figure 8a. Scheme of EM pumping of a plasmoid by Tesla's coil generator. 1- HF Tesla's coil generator, 2-vehicle with HF plasmoid created near its head part

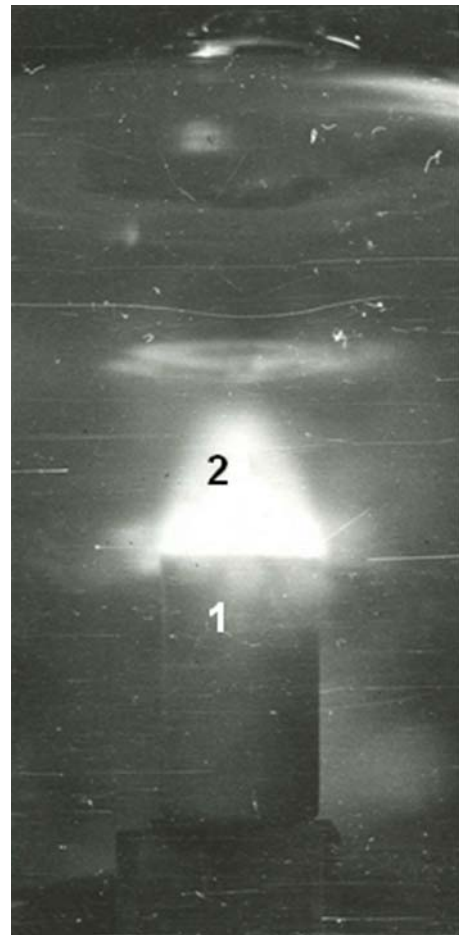
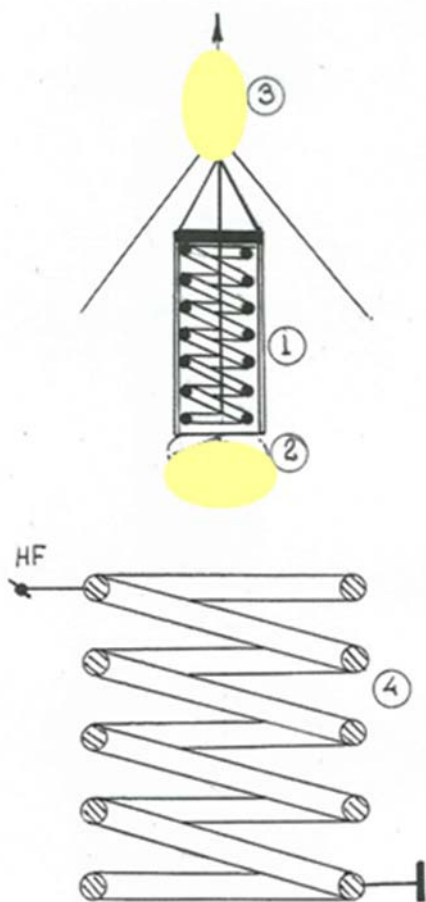


Figure 8b. Scheme of EM pumping of a plasmoid created near a projectile by Tesla's coil generator and its testing. 1- projectile with HF Tesla's coil; 2, 3- HF plasmoid created near its head part and its base, 4- primary coil

References

1. Avramenko R., Klimov A., Mishin G., et al., Diploma on Scientific Discovery №007, 25 March 1988, USSR State Committee
2. Bityurin V., Klimov A., Kopiev V., et al., Jet Noise Control by Nozzle Surface HF DBD Actuator, AIAA Paper 2011-0911, P.5
3. Adamovich I., Samimy M., et al., Flow Separation Control over an Airfoil with Nanosecond Pulse Driven DBD Plasma Actuator, AIAA Paper 2011-487, P.25
4. Klimov A., Moralev I., et al., ISTC Report #3794P, Delivery 11, Oct. 2010, P.20
5. Ershov A.P., Klimov A.I., Timofeev I.B. et al., Flow Around Body and Characteristics of AC/DC Discharges in Plasma Aerodynamic Experiment. Proc. 2nd WIG Workshop. Norfolk. April 24-25. 1998, P.59.
6. Гридин А.Ю., Ефимов Б.Г., Забродин А.В., Климов А.И. и др., Расчетно-экспериментальное исследование сверхзвукового обтекания затупленного тела с иглой при наличии электрического разряда в его головной части. Препринт ИПМ № 19, 1995, С.31
7. Biturin V., Klimov A., Charged Plasma Formation in High Speed Airflow, 2007, Proc. WSMFA-06, M., IVTAN, P.15
8. Byturin V., Bocharov A., Klimov A., et al., Analysis of Non-Thermal Plasma Aerodynamics Effects, 44th AIAA Aerospace Sciences Meeting & Exhibit. AIAA 2006-1209, 9-12 January 2006, Reno, NV, p.8
9. Klimov A., Bityurin V., et al., Non-Premixed Plasma-Assisted Combustion in High-Speed Vortex Airflow, Proc. 4th Workshop on TCP in PA, St.-Petersburg, 2006, P.7
10. Klimov A., Byturin V., Kuznetsov A., Sukovatkin N., Vystavkin N., Van Wie D.M., Plasma-Assisted Combustion, 33rd AIAA Plasma dynamics and Lasers Conference, 11-14 June 2002, Maui, Hawaii, P.10
11. Zheltovodov A., Knight D., Pimenov E., Research of Shock Wave-Induced Vortex Breakdown Control by Energy Deposition, Proc. EUCASS, Moscow, 2005, P.7
12. Maslov A., Fomichev B., Malmuth N., et al., Plasma Control of Separated Flow Assymetry on a Cone at High Angles of Attack, AIAA Paper 2004-843, P.8
13. Klimov A., Bityurin V., Moralev I., et al., Study of a Longitudinal Plasmoid Created by Capacity Coupled HF Discharge in Vortex Airflow, AIAA Paper 2009-1046, 47th AIAA Aerospace Sciences Meeting & Exhibit, 5-9 Jan 2009, Orlando, FL, P.14
14. Mirabo L., AIAA Paper 1001-98, 1998
15. N.Tesla, D.Childress, Fantastic Invention of Nicola Tesla, Adventures Unlimited Press, Illinois, 1993, P.349
16. Beaulieu W., Byturin V., Klimov A., et al., Plasma Aerodynamic WT Tests with 1/6 Scale Model. Proc. of the Workshop on Magneto-Plasma- Aerodynamics in aerospace applications, Moscow, March 24-25, 1999, IVTAN, p.44
17. Byturin V., Bocharov A., Klimov A., et al., Analysis of Non-Thermal Plasma Aerodynamics Effects, 44th AIAA Aerospace Sciences Meeting & Exhibit. AIAA 2006-1209, 9-12 January 2006, Reno, NV, p.8
18. Bityurin V., Bocharov A., et al., Numerical Simulation of the Discharge in Supersonic Flow Around a Sphere, AIAA 2007-0223 Paper, 45th AIAA Aerospace Sciences Meeting & Exhibit, 8-11 January 2007, Reno, NV, p.14
19. Liu C., Roth J., Atmospheric Glow Discharge Plasma for Aerodynamic Boundary Layer Control, Paper 1P-26, Proc. 21st IEEE Int. Conf. On Plasma Sci.,
20. Ross J.R., Dai X., Optimization of the Aerodynamic Plasma actuator as an Electrohydrodynamic Electrical Device, 44th AIAA Aerospace Sciences Meeting and Exhibit, 9-12 Jan 2006, Reno, NV, AIAA 2006-1203 Paper, P.28
21. Ross J.R., Wilkinson S., et al., Flow Re-Attachment and Acceleration by Paraelectric and Peristaltic EHD Effects , 41th AIAA Aerospace Sciences Meeting and Exhibit, 6-9 Jan 2003, Reno, NV, AIAA 2003-531 Paper, P.28
22. Shin J., Raja L., Generation of Plasma induced Flow Actuation by DC Glow-like Discharge in Supersonic Flow, 44th AIAA Aerospace Sciences Meeting & Exhibit. AIAA 2006-169, 9-12 January 2006, Reno, NV, p.10
23. Shin J., Raja L., Characteristics of a Plasma Actuator in Mach 3 Flow, AIAA 2007-788 Paper, 45th AIAA Aerospace Sciences Meeting & Exhibit, 8-11 January 2007, Reno, NV, p.11
24. Moreua E., Touchard G., et al., Airflow Electric Fluid Dynamic Actuator, 38th AIAA Laser and Plasma Dynamics Conference, 27-28 June 2007, Miami, FL, AIAA 2007-4622, P.30
25. Corke T., McLaughlin T., et al., Scaling Effects of an Aerodynamic Plasma Actuator, 45th AIAA Aerospace Sciences Meeting and Exhibit, 8-11 Jan 2007, Reno, NV, AIAA 2007-635 Paper, P.28
26. Opaitis D., Macheret S., Shneider M., et al., Experimental Investigation of DBD Plasma Actuators Driven by Repetitive High Voltage Nanosecond Pulses with DC or Low-Frequency Sinusoidal Bias, 38th Plasmadynamics and

- Lasers Conference, 25-28 June 2007, Miami, FL, AIAA 2007-4532 Paper, P.21
27. Opaits D., Macheret S., Shneider M., Opaits D., Macheret S., Shneider M., et.al., Experimental Investigation of DBD Plasma Actuators Driven by Repetitive High Voltage Nanosecond Pulses with DC or Low-Frequency Sinusoidal Bias, 38th Plasmadynamics and Lasers Conference, 25-28 June 2007, Miami, FL, AIAA 2007-4532 Paper, P.13
 28. Abe T., Takizawa Yu., et.al., Optical Observation of Discharge Plasma Structure in DBD Plasma Actuator, 38th Plasmadynamics and Lasers Conference, 25-28 June 2007, Miami, FL, AIAA 2007-4376 Paper, P.11
 29. Abe T., Takizawa Yu., et.al., A Parametric Experimental Study for Momentum Transfer by Plasma Actuator, 45th AIAA Aerospace Sciences Meeting and Exhibit, 8-11 Jan 2007, Reno, NV, AIAA 2007-187 Paper, P.11
 30. Johnson G., Scott S., et.al., Plasma-Aerodynamic Boundary Layer Interaction Studies, 32nd Plasmadynamics and Lasers Conference, 11-14 June 2007, Anaheim, CA, AIAA 2001-3052 Paper, P.11

JET NOISE CONTROL BY NOZZLE SURFACE CHF D ACTUATOR

V. Kopiev, N.Ostrikov, M.Zaitsev, Vl.Kopiev, I.Belyaev*
V. Bityurin, A.Klimov, I. Moralev, S.Godin**

*TsAGI, **JIHT RAS

Active jet noise control by DBD actuators is studied in a number of the works today [1, 2]. New plasma actuator based on surface capacity coupled HF discharge (CHFD) is used in this work to decrease jet noise. Organization of streamline vorticity inside a nozzle by using surface CHF D actuator is shown in fig.1. Dielectric nozzle (Nilon-6 or ceramics) with surface HF electrodes is designed, manufactured and tested in TsAGI's facility, fig.2. It is obtained that this surface plasma actuator created by CHF D can induce an electric wind with the typical velocity up to 4m/s in the normal direction to the nozzle surface near inner nozzle surface. It is revealed that jet excitation by a plasma actuator at $St \sim 0.5$ results in the broadband amplification of jet noise up to 5dB. Interaction of surface HF plasma created by pulse repetitive discharge with a high-speed jet ($V \sim 100\text{m/s}$) is close to the Vlasov- Ginevsky's effect in Aeroacoustics in many aspects. It is means that jet excitation by intensive high frequency sound waves created by

pulse repetitive CHF D can reduce of broad band jet noise [3]. This study shows that a new CHF D plasma actuator has effect on acoustic characteristics of turbulent high-speed jet. This work is realized in the framework FP7 of research Project OPENAIR.

1. Samimy, M., Kim, J.-H., Kastner, J., Adamovich, I., and Utkin, Y., \Active control of high-speed and high- Reynolds-number jets using plasma actuators," Journal of Fluid Mechanics, Vol. 578, 2007, pp. 305{330.
2. Samimy, M., Kim, J.-H., Kastner, J., Adamovich, I., and Utkin, Y., \Active control of a Mach 0.9 jet for noise mitigation using plasma actuators," AIAA Journal, Vol. 45, No. 4, 2007, pp. 890{901.
3. А. Гиневский, Власов А., Акустическое управление турбулентными струями, М. Физматлит, 2001, С.239

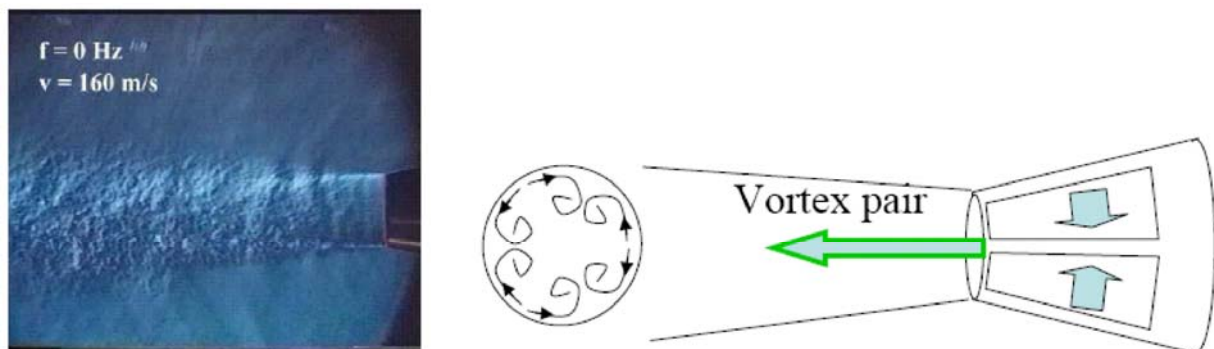


Fig.1. Scheme of HF electrode arranged in a subsonic nozzle and shadow picture of a subsonic jet near nozzle ($P_{st}=1 \text{ Bar}$, $V_j=160\text{m/s}$)



Fig.2. Subsonic nozzle with operating CHFD actuator ($P_{st}=1$ Bar, $V_j\sim 100$ m/s)

TURBULENT BOUNDARY LAYER CONTROL BY SPANWISE TRAVELLING WAVES CREATED BY DBD PLASMA ACTUATORS

Richard Whalley and Kwing-So Choi

Address: L4-135, Faculty of Engineering, University of Nottingham, University Park, Nottingham, NG7 2RD, UK

eaxrw@nottingham.ac.uk

Abstract Dielectric barrier discharge (DBD) plasma is used to create 4-phase spanwise travelling wave excitations for turbulent boundary layer control in uni- and bi-directional forcing configurations. Each forcing configuration generates a spanwise travelling wave, effectively spreading the low-speed fluid in the spanwise direction to reduce skin-friction drag. It was observed that the interactions of starting vortices on the initiation of DBD plasma are also important in the spanwise fluid transfer. More than half the boundary-layer thickness was affected by the spanwise travelling wave excitation, causing intriguing changes in the turbulent boundary layer structure.

1. Introduction

DBD plasma actuators consist of an upper and lower electrode separated by a thin dielectric material, Figure 1a). On application of several kilovolts of AC power at kilohertz frequency between these electrodes, local ionization takes place around the upper electrode. This couples momentum to the surrounding fluid to induce a jet flow¹, which is caused by the movement of plasma ions to and from the dielectric surface. The charge build up on the dielectric surface opposes the charge of the exposed electrode, quenching the emission of the plasma discharge and stopping the plasma from collapsing into an arc. In other words, DBD plasma actuation is a self-limiting process². During each AC cycle the plasma consists of glow and corona-like discharges. The glow discharges are qualified as micro-discharges or streamers³ of large amplitude, short duration current pulses which

are separated by low current, longer duration corona-like discharges^{4,6}. It is thought that the corona-like discharge phases have a dominant contribution to the total body force exerted by the plasma since their durations are much longer and act over a larger volume.

Numerical simulations of plasma actuation in inert gases^{4,7}, document that the predominant force is on the positive-going portion of the forcing cycle, the backward stroke. Whereas recent experimental results^{8,9} suggest that the predominant force is on the negative-going portion of the forcing cycle, the forward stroke. Enloe *et al*⁸ used a Michelson interferometer to measure the oscillatory motion of a second order mechanical system driven by a plasma actuator to show that the majority, 97%, of the momentum coupling occurs during the negative-going portion of the forcing cycle. Qualitatively, the same result was found by Kim *et al*⁹ who phase locked PIV measurements

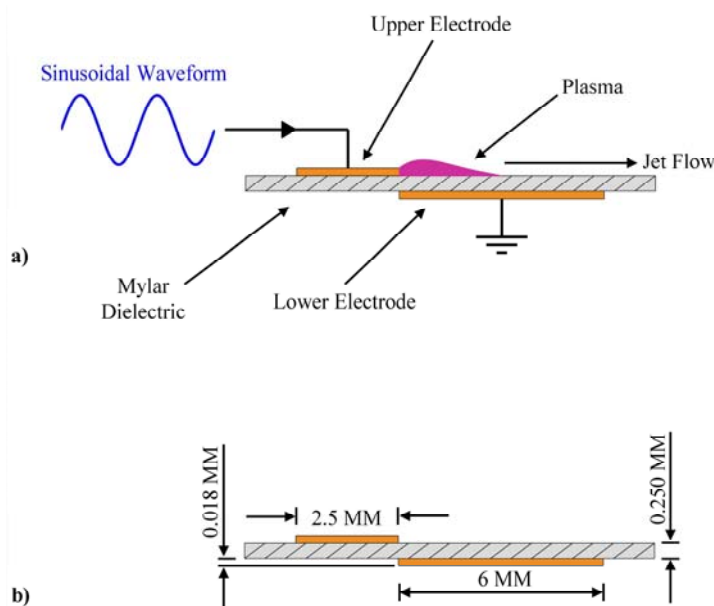


Figure 1. DBD plasma actuator. a) Asymmetric configuration, b) Actuator dimensions.

with the plasma forcing cycle. It is thought that the reason for the difference in results between the numerical and experimental studies is the omission of negative ions in the inert gas modelling. It is well known that plasma discharges in oxygen, hence air, produces both positive and negative ions which could offer the reason for the major force contributor being found in the negative half cycle experimentally^{8, 9}. Recently Boeuf *et al*⁵ and Likhanskii *et al*¹⁰ modelled the DBD plasma actuator in air, identifying the key role of the negative ions which were absent in previous DBD plasma models. They found that the integrated tangential force was downstream of the plasma actuator for both the forward and backward stroke of plasma forcing.

For some time glow discharge plasmas have been used in microelectronic fabrication, ozone generation, gas laser excitation^{11, 12} and for hypersonic velocity measurements through plasma anemometry¹³. Moreover, DBD plasma has already been successfully applied for lift enhancement and separation control of aerofoils¹⁴⁻¹⁷, circular cylinder flow control¹⁸⁻²⁰, acoustic noise attenuation^{21, 22} and turbulent skin-friction reduction^{23, 24}. An extensive review of airflow control by non-thermal plasma actuators can be found in Moreau²⁵.

It has been well established that the near wall region of the turbulent boundary layer²⁶ is comprised of coherent motions. Low speed streaks collected on the upwash side of quasi-streamwise vortices break-up and cause ejection events, violent expulsion of low speed fluid into the outer region of the boundary layer. The downwash side causes sweep events, the inrush of high speed fluid into the wall. This turbulence production process is usually referred to as bursting and is responsible for the majority of the turbulence production in the boundary layer. It has been shown²⁷ that sweep events are the major contributor to skin-friction in the turbulent boundary layer. As a result, drag reduction mechanisms²⁸ attempt to disrupt the bursting cycle by displacing the low speed streaks inside the viscous sublayer in order to weaken the near wall structures. This leads to a reduction in skin-friction drag by lowering momentum transfer to the wall. Skin-friction reduction was successfully implemented with DBD plasma by Jukes *et al.*^{23, 24}. Here, a spanwise flow oscillation created by oscillatory plasma forcing used two sets of asymmetric plasma actuators flush mounted over a flat plate inside a turbulent boundary layer, $Re_\tau = 380$. A skin-friction reduction on the order of 45% was achieved. On initiation of DBD plasma starting vortices were created^{29, 30}. It was postulated that in addition to the drag reduction mechanism of spanwise flow oscillation³¹, the starting vortices could be interacting with the quasi-streamwise vortices in the near wall region of the boundary

layer, further disrupting the turbulence production cycle and weakening near wall events.

Du *et al.*³² conducted direct numerical simulations of a wall bounded turbulent flow and found that turbulence production could be suppressed with the application of a spanwise travelling wave. The spanwise travelling wave was applied with a Lorentz force which was maximum at the wall and decayed exponentially. The maximum skin-friction reduction was on the order of 30% which was obtained by applying periods of $T^+ = Tu_\tau^2/\nu = 25, 50$ or 100 depending on the penetration depth and amplitude of the Lorentz force. They proposed that if a product of force amplitude, I , period T^+ and penetration depth, Δ equals unity, $I \times T^+ \times \Delta = 1$, a skin-friction drag reduction of 30% should be obtained. This implies that spanwise travelling waves have favourable energetics over similar flow control methods, like spanwise flow oscillation where increasing forcing amplitudes are needed to achieve higher skin-friction reduction. However, not all combinations of (I, T^+) were valid. Low amplitudes of forcing with large periods, $I = 0.25, T^+ = 200$, led to drag increase as the travelling wave motion, the phase speed, was too low. This implies that a correct range of forcing period needs to be found with the correct forcing amplitude to produce a spanwise travelling wave capable of skin-friction reduction. Furthermore, penetration depths, $\Delta^+ > 10$, outside the viscous sub layer, were seen to increase skin-friction.

Xu & Choi³³ studied experimentally a spanwise travelling wave with Lorentz forcing in a turbulent boundary layer and obtained a skin-friction reduction on the order of 30% with forcing periods of $T^+ = 42$ and 82 when the near wall fluid was displaced more than 115 wall units in the spanwise direction. This spanwise spatial scale is on the order of spacing between low speed streaks and provides a constraint for the minimum wavelength needed for skin-friction reduction, $\lambda^+/2 > 115$. Xu & Choi³³ also performed flow visualisations of the near wall region during travelling wave excitation and found that the near wall streaky structures, the low speed streaks were substantially altered. This phenomenon was also observed by Du *et al.*³² who saw the annihilation of the low speed streaks and a large ribbon of low speed fluid being propagated in the spanwise direction during forcing. The mechanism for the skin-friction reduction was thought to be due to the stabilisation of near wall streaks and the turbulence regeneration cycle.

Furthermore, numerical simulations of a travelling wave by a flexible wall have been studied by Zhao *et al.*³⁴ with a forcing period of $T^+ = 50$, where a skin-friction drag reduction of 30% was achieved. They believed that the main mechanism for the drag reduction is the change in boundary

vorticity flux due to the flexible wall's acceleration that causes a thin Stokes's Layer of concentrated streamwise vorticity, which suppresses quasi-streamwise vortices from the viscous sublayer and causes a regularised skin-friction pattern at the wall. Itoh *et al.*³⁵ studied experimentally a flexible wall in a turbulent boundary layer of 8 m/s. The spanwise travelling wave was actuated with a 10 μm thick polythene sheet forced by a loud speaker at 100 Hz, $f_d^+ = 0.01$, where a skin-friction drag reduction of 7.5% was achieved.

In this paper we present an experimental study using hot-wire anemometry and Particle Image Velocimetry (PIV) of spanwise travelling waves generated with DBD plasma for skin-friction reduction inside the turbulent boundary layer. As DBD plasma is a surface based technique it makes an ideal candidate for turbulent boundary layer control with spanwise travelling wave excitation. However Lorentz and plasma forcing are fundamentally different. Lorentz forcing has an exponentially decaying velocity profile, maximum at the wall whereas DBD plasma forcing forms laminar wall jets³⁰ and the production of starting vortices. From the reviewed literature, we expect to see a skin-friction drag on the order of 30% with

the spanwise travelling waves created by DBD plasma.

2. Experimental Setup

The plasma actuator sheet used in the spanwise travelling wave experiments consists of a 250 μm Mylar dielectric, with 24 copper electrodes, 18 μm in thickness in asymmetric configurations powered by a set of high voltage sinusoidal RF inputs, Figure 1. The upper and lower electrodes are 2.5 mm and 6 mm in width respectively and have an active length of 338 mm. The actuator sheet is insulated with a thin coat of lacquer on its underside and bonded to a 10 mm Perspex substrate to ensure plasma formation on the upper surface only. The Mylar has a dielectric constant of $\epsilon = 3.1$, with the actuator designs fabricated by photo-chemically etching a double sided copper laminate of Mylar.

The 4-phase, spanwise travelling-waves actuator sheets have two different forcing configurations. Figure 2a) shows a schematic representation of the bi-directional forcing. Here, travelling waves of the wavelength $\lambda = 56$ mm are created by two electrodes, by forcing fluid in

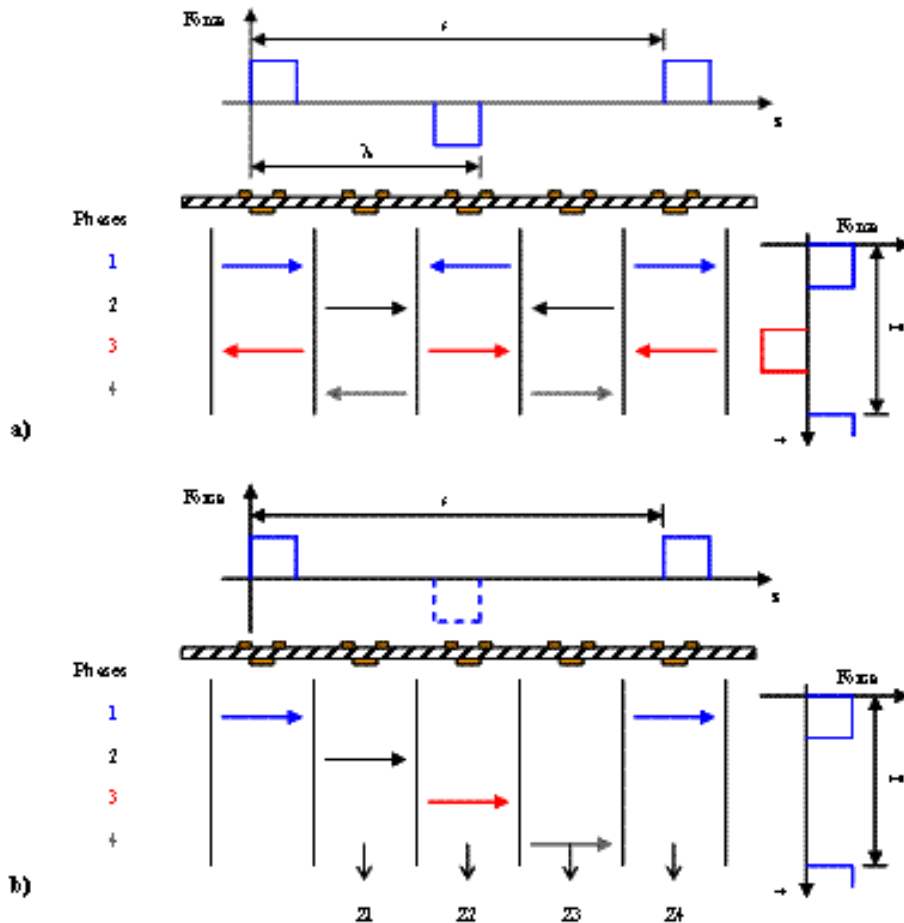


Figure 2. Schematic representation of 4-phase travelling wave excitations. a) Bi-directional forcing, b) Uni-directional forcing.

opposite directions in each phase. Each 4-phase cycle covers the spanwise length of $s = 100$ mm over the actuator sheet 300 mm wide. Figure 2b) represents the uni-directional forcing, where the travelling waves are forced in one direction only. The spatial and temporal scales used in the experiments are based on the conditions studied by Xu & Choi³³ where a 30% reduction in turbulent skin-friction drag was obtained using Lorentz forcing.

Experiments in quiescent air are conducted inside a 1.5 m long, 508 x 508 mm² octagonal chamber in a wind tunnel. Measurements of the flow field are performed using a time-resolved PIV system. This consists of a pulsed copper vapour laser and the Photron Fastcam SA-3 high speed camera. Glycerine droplets of 1 μ m are used to seed the air inside the chamber. The laser sheet is aligned with the actuator mid-span illuminating the z-y plane, where the co-ordinate system has the origin at the end of the upper electrode on the dielectric surface where the plasma actuation initiates. Image pairs are taken at a frame rate of 1 kHz with the time delay between frames being typically 200-400 μ s. Each image is exposed with a 30 ns laser pulse. PIV processing is performed using ILa software where velocity vectors are computed on a 32x32 pixel interrogation area with 50% overlap using a cross-correlation technique to an accuracy of 3-5%³⁶. Image calibration is performed using a calibration target to an accuracy of 0.2% with a typical conversion of 100 μ m/pixel. This gives a spatial resolution of 1.6 mm in the velocity measurements. We create a single travelling wave over a distance $s = 100$ mm, powering the 8 central electrodes with 8 plasma power supplies. Throughout the experiments the sinusoidal voltage input to the plasma power supplies is varied from 6.3-7 kV_{p-p} at a fixed frequency of 25 kHz, which is monitored using a Tektronix TDS2024 200MHz oscilloscope. The time period T is varied from 124-208 ms with an 8 channel BNC 575 series Pulse generator.

Turbulent boundary layer measurements are conducted using a low speed, closed loop wind tunnel. The wind tunnel has a cross section of 508x508 mm². The turbulent boundary layer is developed over a 3 m long flat plate, fabricated from polished MDF of 20 mm thickness with a super elliptic leading edge and a trailing edge flap. The flat plate is positioned in the upper section of the wind tunnel with a turbulent trip placed 100 mm downstream from the leading edge. Measurements are taken a further 2.3 m downstream from the trip where the turbulent boundary layer is fully developed. The free stream velocity was $U_\infty = 1.7$ m/s, which gave the boundary layer thickness of $\delta \sim 90$ mm. The Reynolds number based on the friction velocity was $Re_\tau \sim 450$, where the momentum thickness was $Re_\theta \sim 1100$. The pressure gradient

across the test section is nearly zero and the free stream turbulence intensity is 0.24%.

Flow diagnostics are made by constant temperature, hot-wire anemometry using Dantec 56C17 CTA bridges and 56N20 signal conditioners. Measurements of the streamwise velocity are taken with Dantec 55P15 probes which have a 5 μ m diameter and length of 1.25 mm. One probe is used to obtain the boundary layer profile. Another probe is kept stationary in the free stream of the wind tunnel to monitor the free stream velocity. Each probe is operated with an overheat ratio of 1.8 and calibrated in-situ. Ambient temperature drift during experiments is monitored using a LM35 Precision Temperature Sensor and the hot-wire data compensated accordingly. Hot-wire signals are low pass filtered at 300 Hz and a gain of 5 applied before data acquisition. The entire CTA main frame is enclosed in a copper Faraday cage to minimise the noise effects during the application of DBD plasma. Data is collected using an IoTech 488/8s ADC and stored on a PC. The signals are sampled at 1 kHz with duration of 90 seconds without plasma, and 60 seconds with plasma at each measurement location. The plasma is actuated in 3 second bursts with a 60 second pause at the end of each acquisition to minimise thermal damage to the electrode sheets. A 3-axis traverse mechanism is used to position the boundary layer probe. This has a spatial resolution of 1.25 μ m in the wall normal direction and 2.5 μ m in the streamwise and spanwise directions. For each boundary layer profile 127 data points are taken, where about 75 of these are located within the viscous sublayer ($y^+ < 7$). Each boundary-layer profile measurement lasts about 9.5 hours. Both uni- and bi-directional forcing in the turbulent boundary layer are examined by taking data at four spanwise locations, Figure 2. Throughout the boundary layer experiments the sinusoidal voltage input to the plasma power supplies is varied from 6.3-7 kV_{p-p} at a fixed frequency of 25 kHz requiring up to 12 power supplies. The time period T is varied from 124-208 ms ($50 < T^+ < 90$).

3. Results and Discussion

Instantaneous PIV images of a spanwise travelling wave with bi-directional forcing in quiescent air are shown in Figure 3 through velocity magnitude and vorticity plots. In each of these figures there are 4 images, one taken at the end of each phase. The location of the plasma actuators and the direction of the DBD plasma jets are indicated under each image, where the DBD plasma is actuated with 7 kV_{p-p} at 25 kHz for 52 ms per phase, $T = 208$ ms. The travelling wave direction is from left to right. On actuation of DBD plasma a starting vortex is created. This vortex develops, moving along and away from the wall as seen in

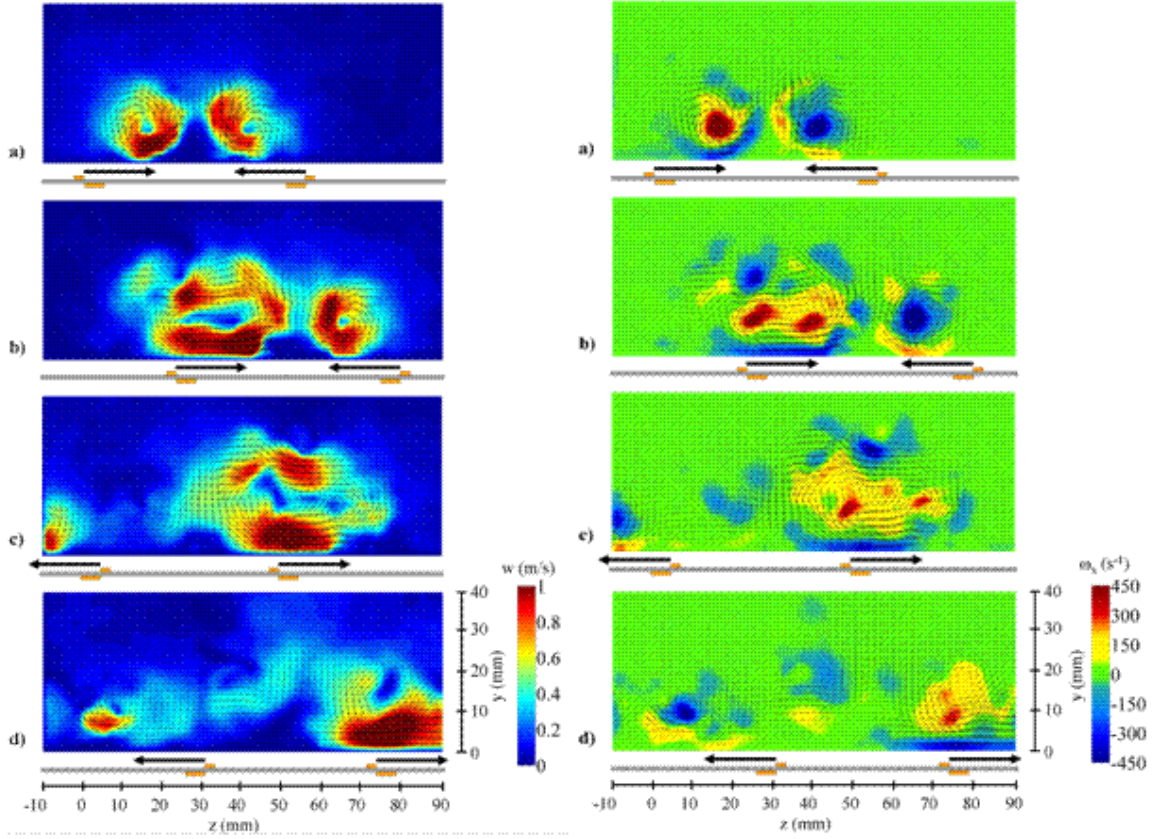


Figure 3. PIV velocity magnitude (Left had column) and Vorticity (Right hand column) with bi-directional forcing. $E = 7$ kV_{p-p} , $f = 25$ kHz, $T = 208$ ms. a) Phase 1, $t = 54$ ms, b) Phase 2, $t = 106$ ms, c) Phase 3, $t = 158$ ms, d) Phase 4, $t = 210$ ms.

Figure 3a). The vortices have an asymmetric velocity distribution with a maximum velocity on the order of 1 m/s under the core and have effectively collected fluid in a region close to the phase 2 actuator. The strong sense of vorticity indicates the core locations at 10 mm from the wall, with the secondary vorticities generated due to the no-slip boundary condition. The secondary vorticities are seen wrapped around the primary rollers, aiding vortex movement away from the wall³⁷. Figure 3b) clearly shows the first movement of the travelling wave motion at the end of phase 2. A large stretch of high speed fluid on the order of 1 m/s encapsulated within the first 10 mm of the wall can be seen emanating away from the second actuation region in the positive z-direction. This is part of the high speed fluid on the underside of the starting vortex that has been entrained into the plasma region by actuation of the second phase. This region of the fluid is then pushed forwards in the positive z-direction during this phase of actuation. Figure 3c) and 3d) show the end of phases 3 and 4. The stretches of high speed fluid have moved further in the positive z-direction through a combination of fluid entrainment and momentum addition from each actuation of the

travelling wave excitation. As this region of high speed fluid is being transported along the wall in the positive z-direction there is also a highly vortical flow structure developing throughout the phases. Secondary vorticity is being generated at the wall which is being moved in the direction of the travelling wave. This is in qualitative agreement to Lorentz forcing in the turbulent boundary observed by Du et al.³² Other vortical systems are also generated on top, behind and in front of the travelling wave, showing a complex system of vortical interaction during the initiation of DBD plasma.

The change in mean velocity inside the turbulent boundary layer with uni- and bi-directional forcing at four spanwise locations is shown in Figures 4 and 5, where the DBD plasma is actuated with 7 kV_{p-p} at 25 kHz with $T^+ \sim 90$ ($T = 208$ ms). It can be seen that the turbulent boundary layer can be modified up to $y/\delta \sim 0.3$ ($y^+ \sim 150$) with uni-directional forcing and $y/\delta \sim 0.6$ ($y^+ \sim 300$) for bi-directional forcing. Both forcing configurations lead to an increase in mean velocity up to the lower part of the logarithmic region. There is also a velocity deficit in the logarithmic region for each forcing type. Uni-directional forcing sees a

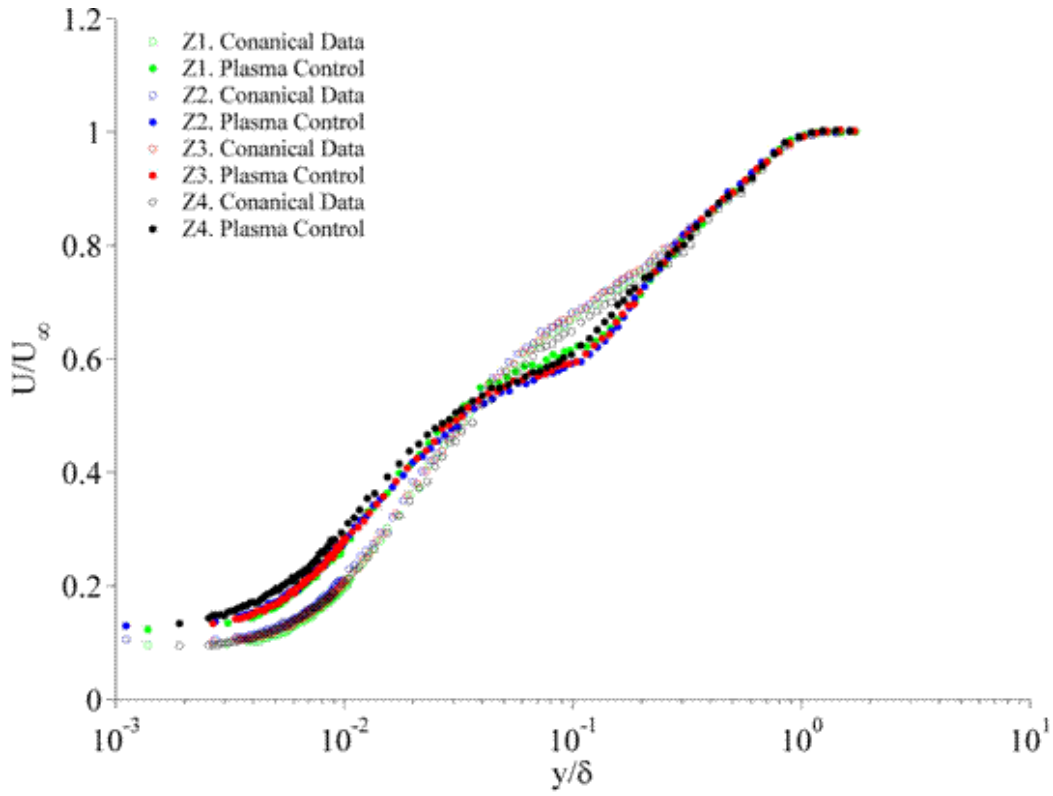


Figure 4. Mean velocity profile of a turbulent boundary layer with uni-directional forcing, 7 kV_{p-p} , 25 kHz , $T = 208 \text{ ms}$.

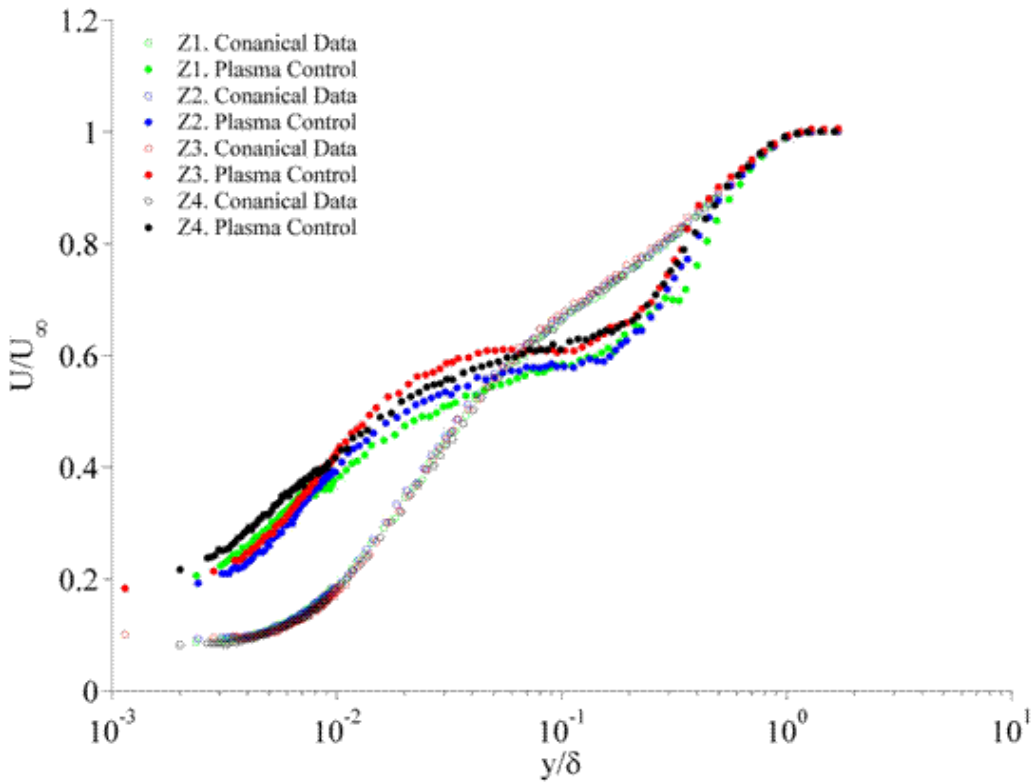


Figure 5. Mean velocity profile of a turbulent boundary layer with bi-directional forcing, 7 kV_{p-p} , 25 kHz , $T = 208 \text{ ms}$.

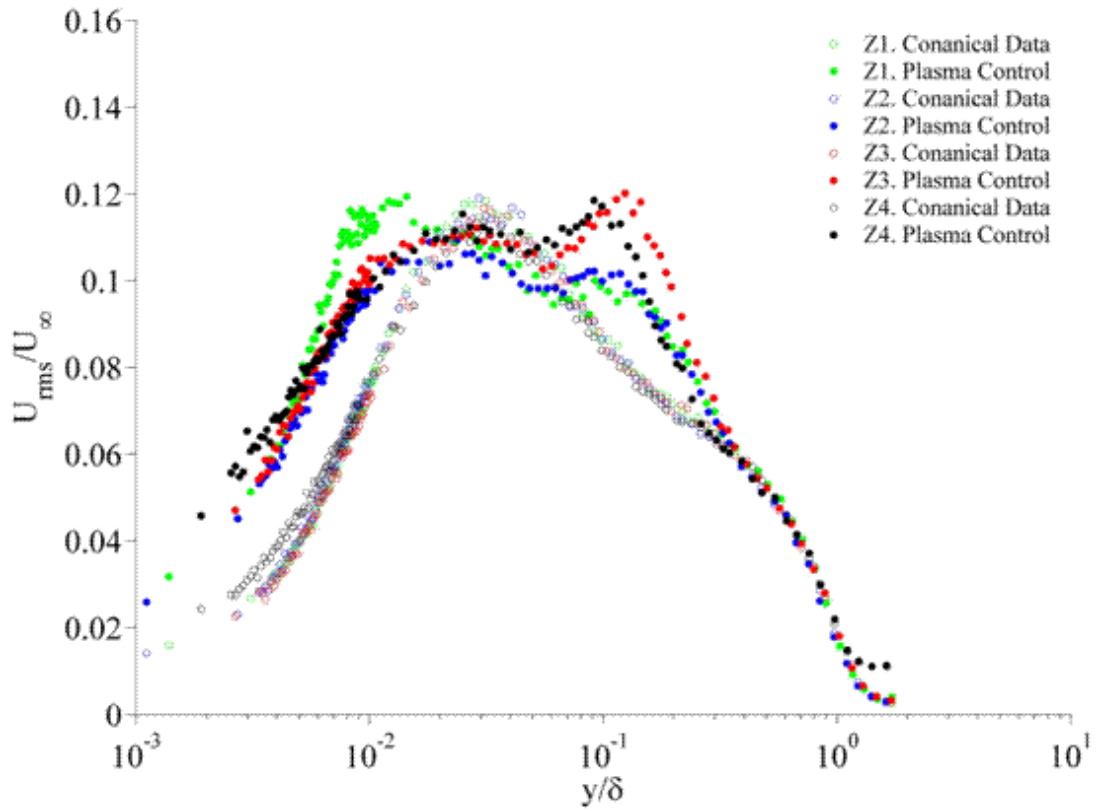


Figure 6. Turbulence intensity profile of a turbulent boundary layer with uni-directional forcing, 7 kV_{p-p} , 25 kHz , $T = 208 \text{ ms}$.

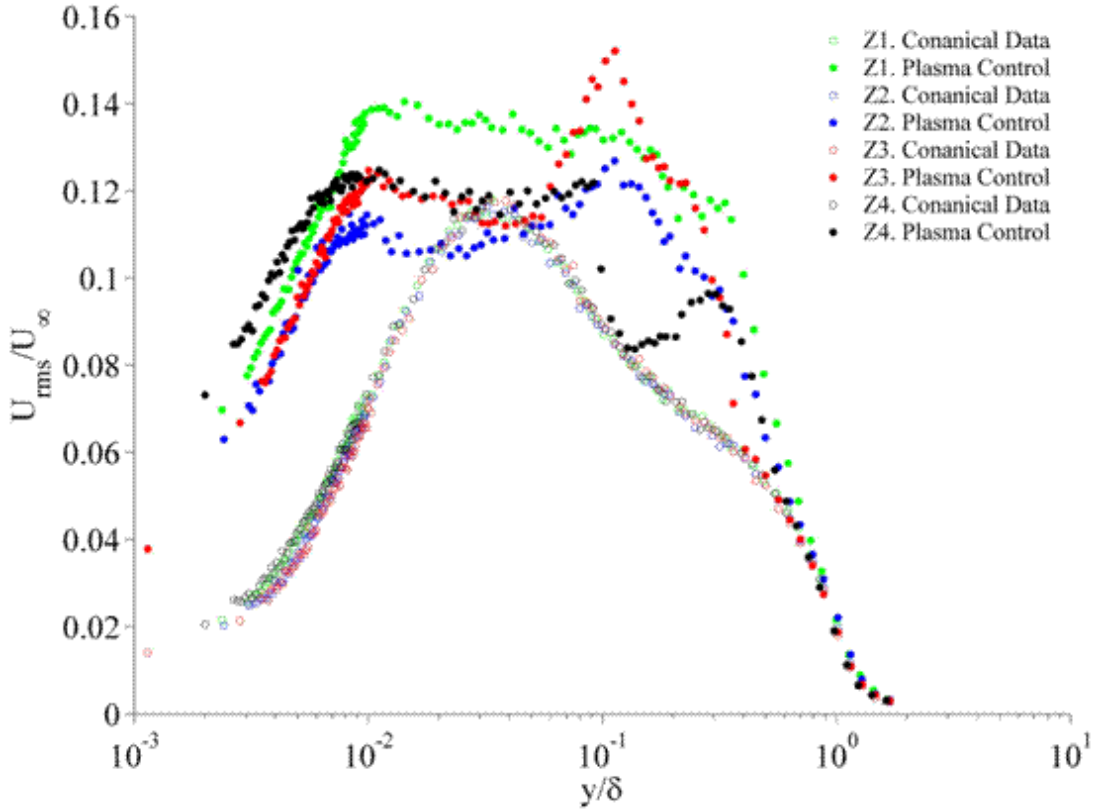


Figure 7. Turbulence intensity profile of a turbulent boundary layer with bi-directional forcing, 7 kV_{p-p} , 25 kHz , $T = 208 \text{ ms}$.

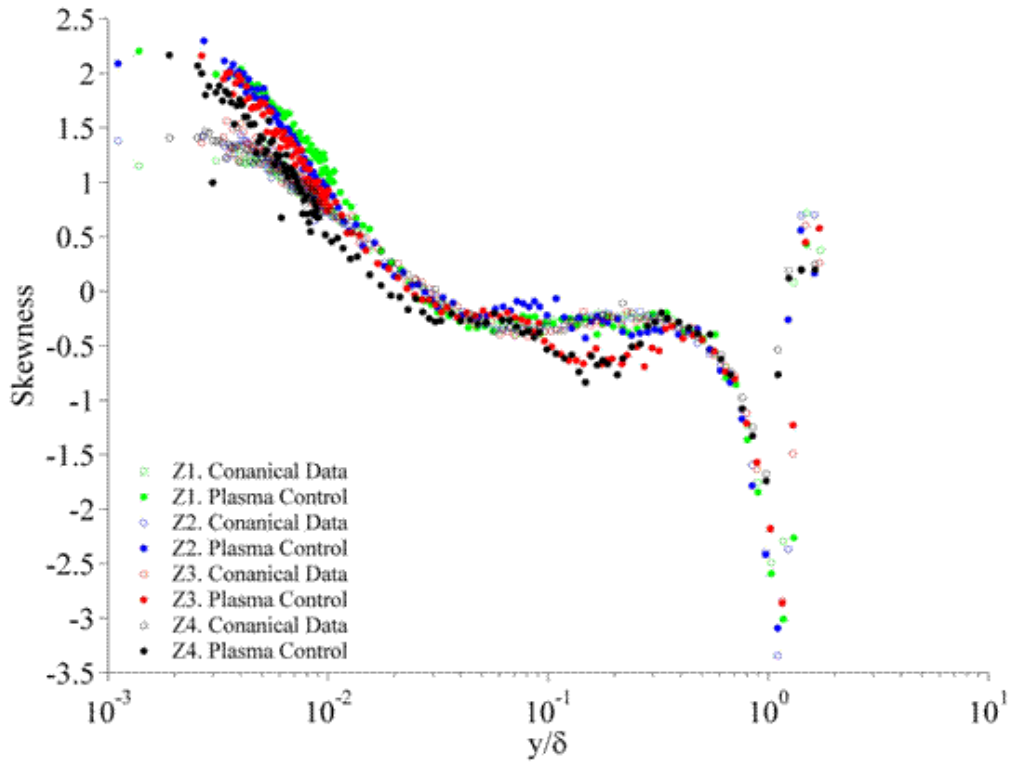


Figure 8. Skewness profile of a turbulent boundary layer with uni-directional forcing, 7 kV_{p-p}, 25 kHz, T = 208 ms.

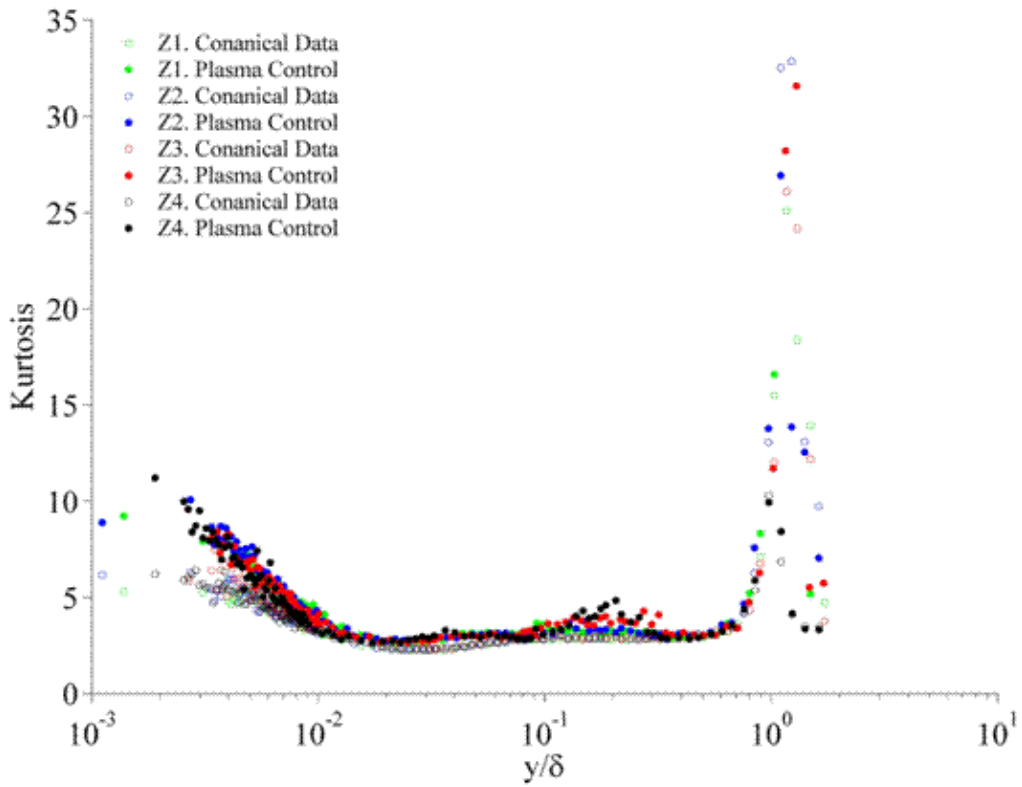


Figure 9. Kurtosis profile of a turbulent boundary layer with uni-directional forcing, 7 kV_{p-p}, 25 kHz, T = 208 ms.

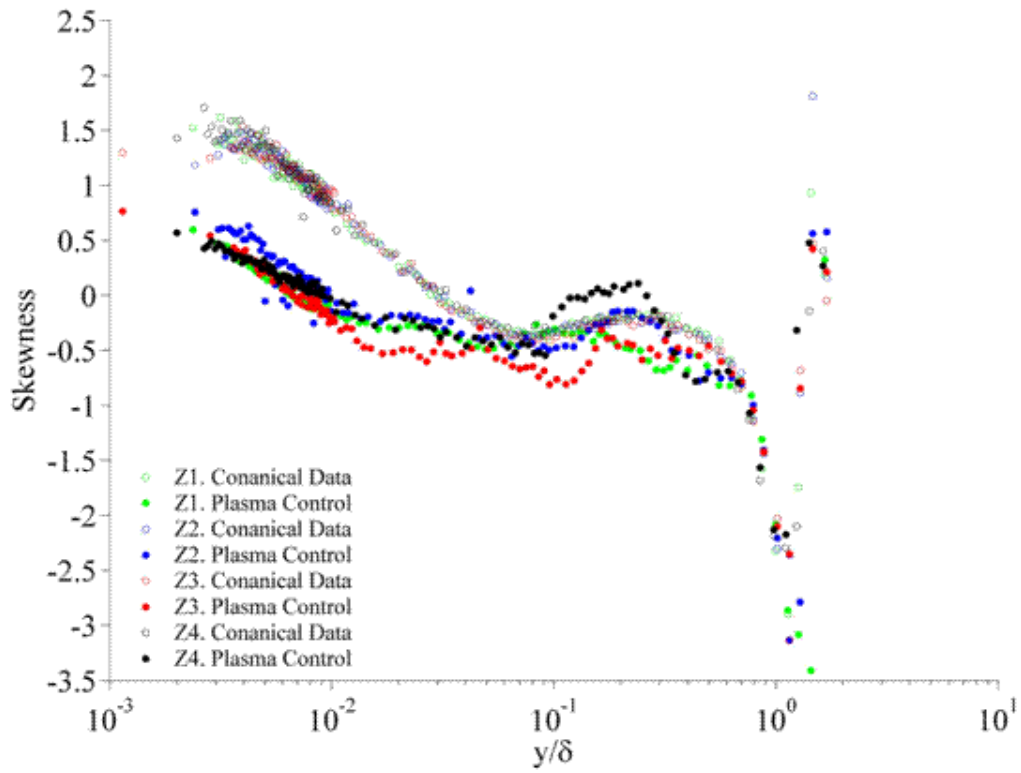


Figure 10. Skewness profile of a turbulent boundary layer with bi-directional forcing, 7 kV_{p-p} , 25 kHz , $T = 208 \text{ ms}$.

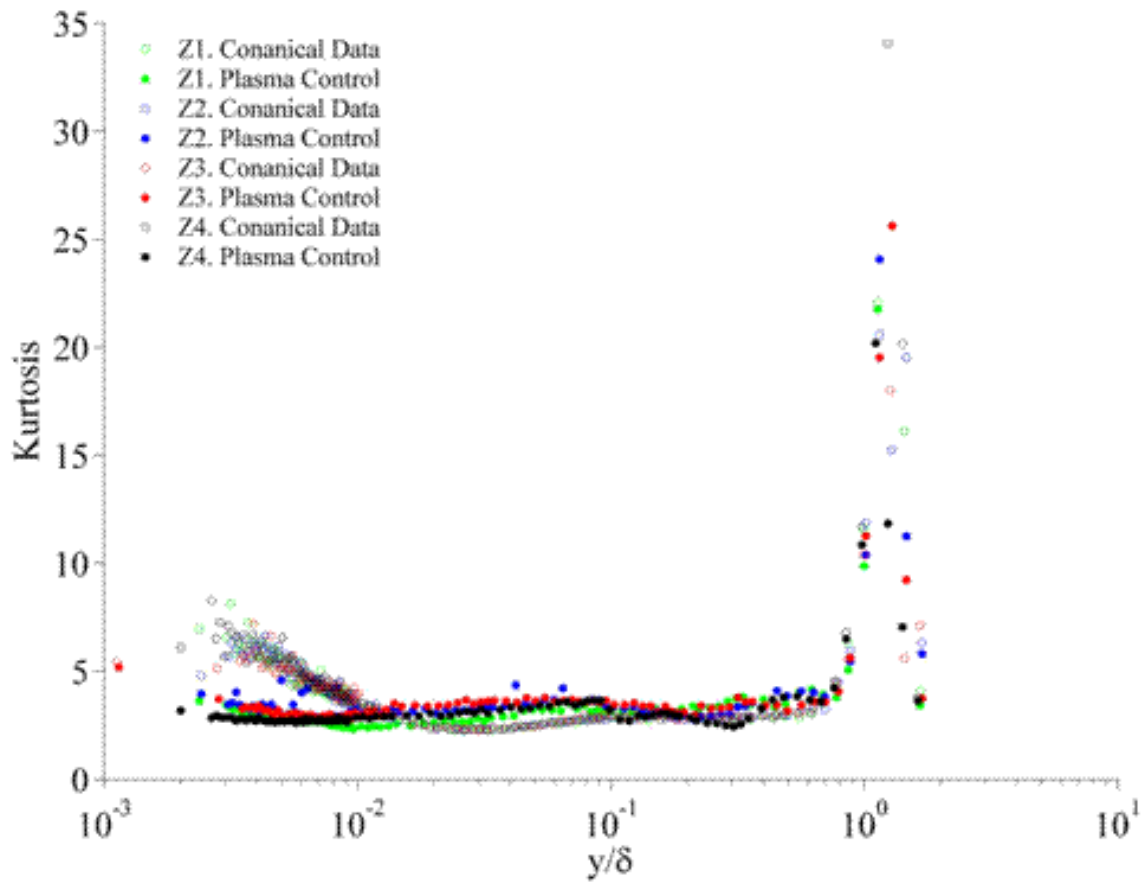


Figure 11. Kurtosis profile of a turbulent boundary layer with bi-directional forcing, 7 kV_{p-p} , 25 kHz , $T = 208 \text{ ms}$.

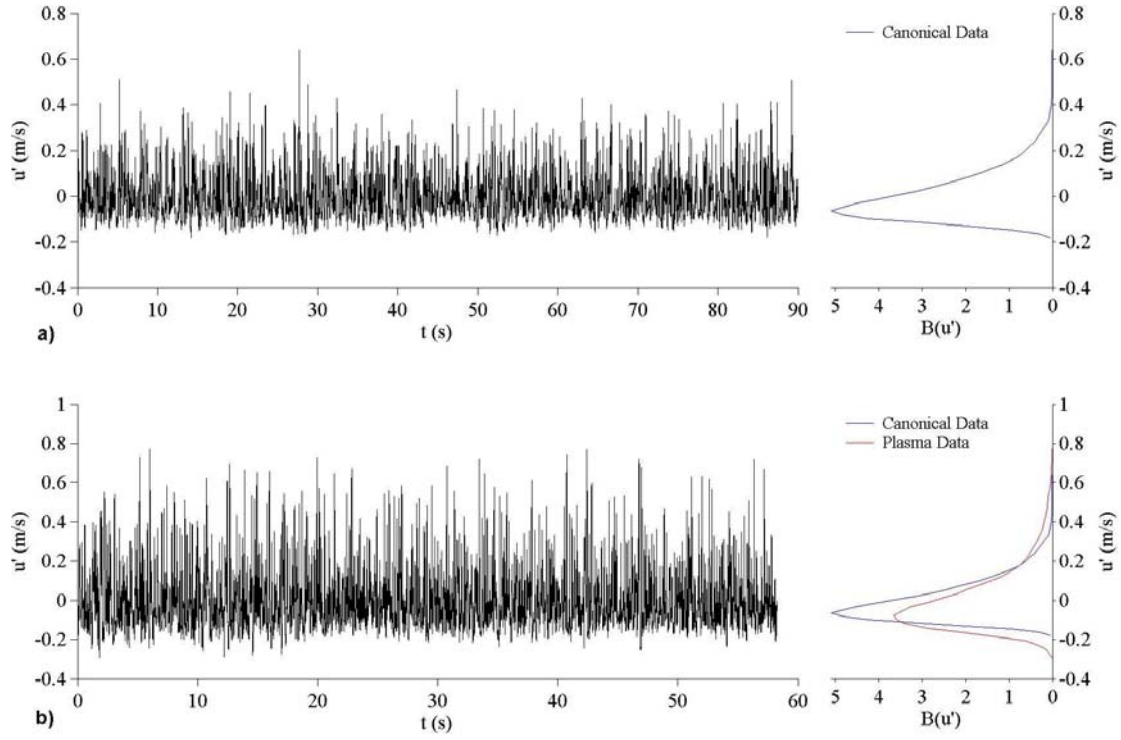


Figure 12. Uni-directional forcing time series without DBD plasma a) and with DBD plasma b) at $y/\delta \sim 0.007$ at the Z2 location. 7 kV_{p-p} , 25 kHz , $T = 208 \text{ ms}$.

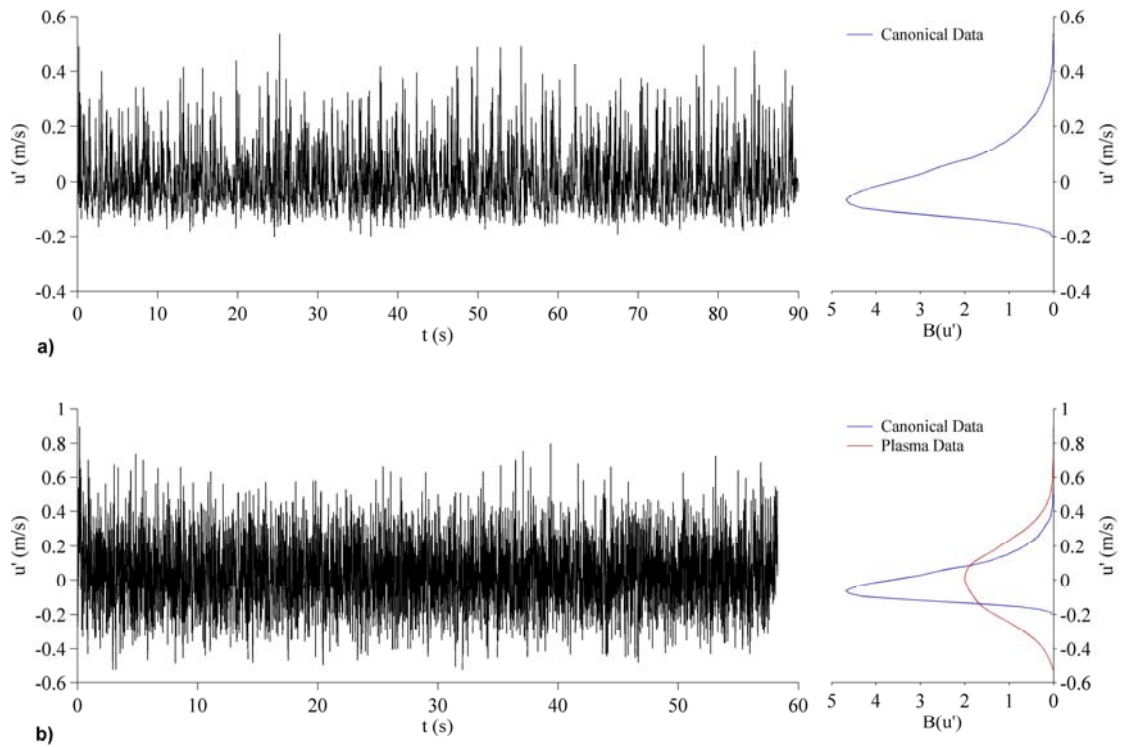


Figure 13. Bi-directional forcing time series without DBD plasma a) and with DBD plasma b) at $y/\delta \sim 0.007$ at the Z2 location. 7 kV_{p-p} , 25 kHz , $T = 208 \text{ ms}$.

reduction in velocity spanning from $y/\delta \sim 0.04 - 0.25$ ($y^+ \sim 25 - 115$) by a factor of ~ 0.9 , while bi-directional forcing sees the velocity reduction spanning from $y/\delta \sim 0.05 - 0.6$ ($y^+ \sim 20 - 300$) by a factor of ~ 0.8 . The change in structure of the boundary layer with the two forcing types shown in these two figures looks qualitatively similar. Turbulence intensity profiles for both forcing configurations are shown in Figures 6 and Figure 7. The turbulence intensity with both forcing configurations is larger than its canonical counterpart for the majority of the boundary layer thickness. Some spread of data over the four spanwise locations may be due to the spanwise travelling wave being generated from discrete actuators. In both figures we see two peaks in intensity, at $y/\delta \sim 0.01$ ($y^+ \sim 5$) and $y/\delta \sim 0.1$ ($y^+ \sim 50$). At $y/\delta > 0.4$ and $y/\delta > 0.6$ for uni- and bi-directional forcing the spanwise travelling waves cease to have an effect on the turbulence intensity profile. These locations are approximately the upper limit of the span of the velocity reduction seen in the mean velocity profiles, Figures 4 and 5. Skewness and kurtosis profiles for uni-directional forcing are shown in Figures 9 and 10, showing a clear increase in both skewness and kurtosis inside the viscous sublayer, $y/\delta < 0.01$ ($y^+ < 5$). However, both the kurtosis and the skewness for bi-directional forcing are reduced for $y/\delta < 0.01$ ($y^+ < 5$) as shown in Figures 10 and 11, respectively. This shows that there is a change in near wall structure of the turbulent boundary layer due to different forcing configuration. The fluctuating velocity time series and corresponding probability density functions for uni- and bi-directional forcing at the Z2 location at $y/\delta \sim 0.007$ ($y^+ \sim 3.5$) are shown in Figures 12 and 13, respectively. When DBD plasma is applied in uni-directional forcing, the time series spikes more evidently with larger positive fluctuations, Figure 12. This increased the skewness and kurtosis by a factor of ~ 1.25 , which is clearly demonstrated by the change in the pdf's shown at the side of each signal. On the contrary, bi-directional forcing clearly shows a reduction in both skewness and kurtosis, Figure 13. This is made clear by the drastic changes in the pdf shown alongside the signal. Here the skewness is reduced by a factor ~ 0.9 and kurtosis by a factor ~ 0.3 . It's interesting to note that bi-directional forcing applied with Lorentz forcing experimentally³³ and numerically³² have achieved skin-friction reduction on the order of 30% and typically drag reducing flows see an increase in skewness and kurtosis in the near wall region.³⁸ However, generating a spanwise travelling with bi-directional forcing using DBD plasma appears to cause a reduction in skewness and kurtosis. Furthermore, Du *et al.*³² showed in their numerical simulations that creating a spanwise travelling wave with uni-directional forcing can increase skin-friction. Generating a uni-

directional travelling wave with DBD plasma causes increases in both skewness and kurtosis, exhibiting properties of a drag reducing flow.

Currently cold-wire and cross-wire measurements are underway to establish the thermal effects and spanwise velocity created in the turbulent boundary layer with uni- and bi-directional forcing. It is thought that DBD plasma excitation in the form of spanwise travelling waves should yield a 30% reduction in turbulent skin-friction. The analysis of near wall gradients at different spanwise locations is close to completion which should hopefully lead to conclusive evidence as to whether DBD plasma in the form of a spanwise travelling wave excitation can yield turbulent skin-friction reduction.

References

- ¹ C. L. Enloe, T. E. McLaughlin, R. D. VanDyken, K. D. Kachner, E. J. Jumper and T.C. Corke, "Mechanisms and Responses of a Single Dielectric Barrier Plasma Actuator: Plasma Morphology," *AIAA J.* **42**, 589-594 (2004).
- ² C. L. Enloe, T. E. McLaughlin, R. D. VanDyken, K. D. Kachner, E. J. Jumper, T.C. Corke, M. Post and O. Haddad, "Mechanisms and Responses of a Single Dielectric Barrier Plasma Actuator: Geometrics Effects," *AIAA J.* **42**, 595-604 (2004).
- ³ V. I. Gibalov and G. J. Pietsch, "The development of dielectric barrier discharges in gas gaps and on surfaces," *J. Phys. D.* **33**, 2618-2636 (2000).
- ⁴ J. P. Boeuf and L. C. Pitchford, "Electrohydrodynamic force and aerodynamic flow acceleration in surface dielectric barrier discharge," *J. Appl. Phys.* **97**, 103307 (2005).
- ⁵ J. P. Boeuf, Y. Lagmich, Th. Callegari and L. C. Pitchford, "EHD Force in Dielectric Barrier Discharges Parametric Study and Influence of Negative Ions," *AIAA Paper No. 2007-183* (2007).
- ⁶ J. P. Boeuf, Y. Lagmich, Th. Callegari and L. C. Pitchford, "Electrohydrodynamic force in dielectric barrier discharge plasma actuators," *J. Phys. D.* **40**, 652-662 (2007).
- ⁷ B. Jayaraman, Y-C. Cho and W. Shyy, "Modeling of dielectric barrier discharge plasma actuator," *J. Appl. Phys.* **103**, 053304 (2008).
- ⁸ C. L. Enloe, M. G. McHarg and T. E. McLaughlin, "Time-Correlated force production measurements of the dielectric barrier discharge plasma aerodynamic actuator," *J. Appl. Phys.* **103**, 073302 (2008).
- ⁹ W. Kim, H. Do, M. G. Mungal and M. A. Cappelli, "On the role of oxygen in dielectric barrier discharge actuation of aerodynamic flows," *Appl. Phys. Lett.* **91**, 181501 (2007).

- ¹⁰ A. V. Likhanskii, M. N. Shneider, S. O. Macheret and R. B. Miles, "Modeling of dielectric barrier discharge plasma actuator in air," *J. Appl. Phys.* **103**, 053305 (2008).
- ¹¹ J. R. Roth, "Industrial Plasma Engineering. Vol 1: Principles," Inst. Of Physics Publishing, Bristol, England, UK (1995).
- ¹² J. R. Roth, "Industrial Plasma Engineering. Vol 2: Applications to Non-thermal Processing," Inst. Of Physics Publishing, Bristol, England, UK (2001).
- ¹³ E. H. Matlis, T. C. Corke and S. P. Gogineni, "A.C. Plasma Anemometer for Hypersonic Mach Number Experiments," *IEEE*, **12-1**, 245-256 (2005).
- ¹⁴ M. L. Post and T. C. Corke, "Separation Control on High Angle of Attack Airfoil Using Plasma Actuators," AIAA Paper No. 2003-1024 (2003).
- ¹⁵ T. C. Corke and C. He, "Plasma Flaps and Slats: An Application of Weakly-Ionized Plasma Actuators," AIAA Paper No. 2004-2127 (2004).
- ¹⁶ T. C. Corke and M. L. Post, "Overview of Plasma Flow Control: Concepts, Optimization, and Applications," AIAA Paper No. 2005-0563 (2005).
- ¹⁷ M. P. Patel, T. T. Ng, S. Vasudevan, T. C. Corke, M. L. Post, T. E. McLaughlin and C. F. Suchomel, "Scaling Effects of an Aerodynamic Plasma Actuator," *Journal of Aircraft*. **45**, 223-236 (2008).
- ¹⁸ T. N. Jukes and K-S Choi, "Flow control around a circular cylinder using pulsed dielectric barrier discharge surface plasma," *Phys. Fluids* **21**, 084103 (2009).
- ¹⁹ T. E. McLaughlin, M. D. Munska, J. P. Vaeth, T. E. Dauwalter, J. R. Goode and S. G. Siegel, "Plasma-based actuators for cylinder wake vortex control," AIAA Paper No. 2004-2129, July 2004.
- ²⁰ M. D. Munska and T. E. McLaughlin, "Circular cylinder flow control using surface plasma actuators," AIAA Paper No. 2003-1028, January 2003.
- ²¹ F. O. Thomas, A. Kozlov and T. C. Corke, "Plasma actuators for cylinder flow control and noise reduction," *AIAA. J.* **46**, 1921 (2008).
- ²² X. Huang and X. Zhang, "Streamwise and spanwise plasma actuators for flow-induced cavity noise control," *Phys. Fluids*. **20**, 037101 (2008).
- ²³ T. N. Jukes, K-S Choi, G. A. Johnson and S. J. Scott, "Turbulent boundary layer control for drag reduction using surface plasma," AIAA Paper No. 2004-2216, June 2004.
- ²⁴ T. N. Jukes, K-S Choi, G. A. Johnson and S. J. Scott, "Turbulent drag reduction by surface plasma through spanwise flow oscillation," AIAA Paper No. 2004-2216, June 2004.
- ²⁵ E. Moreau, "Airflow Control by non-thermal plasma actuators," *J. Phys. D: Appl. Phys.* **40** (2007).
- ²⁶ S. K. Robinson, "Coherent motions in the turbulent boundary layer," *Annu. Rev. Fluid Mech.* **23**, 601 (1993).
- ²⁷ P. Orlandi and J. Jiménez, "On the generation of turbulent wall friction," *Phys. Fluids* **6**, 634 (1994).
- ²⁸ G. E. Karniadakis and K-S Choi, "Mechanisms on transverse motions in turbulent wall flows," *Annu. Rev. Fluid. Mech.* **35** (2003).
- ²⁹ T. N. Jukes, K-S Choi, T. Segawa and H. Yoshida, "Jet flow induced by a surface plasma actuator," *Proc. Inst. Mech. Eng., Part I: J. Syst. Control Eng.* **222**, 347 (2008).
- ³⁰ T. N. Jukes, K-S Choi, G. A. Johnson and S. J. Scott, "Characterisation of surface plasma-induced wall flows through velocity and temperature measurement," *AIAA J.* **44**, 764 (2006).
- ³¹ K-S Choi and R. B. Clayton, "The mechanism of turbulent drag reduction with wall oscillation," *Int. J. Heat Fluid Flow* **22** (2001).
- ³² Y. Du, Y. Symeonidis and G. E. Karniadakis, "Drag reduction in wall-bounded turbulence via a transverse travelling wave," *J. Fluid. Mech.* **457** (2002).
- ³³ P. Xu and K-S Choi, "Boundary Layer Control for Drag Reduction by Lorentz Forcing," *Proceedings of the IUTAM Symposium on Flow Control and MEMS* (2006).
- ³⁴ H. Zhoa, J-Z Wu and J-S Luo, "Turbulent drag reduction by travelling wave of flexible wall," *Fluid Dynamics Research*, **34** (2004).
- ³⁵ M. Itoh, S. Tamano, K. Yokota and S. Taniguchi, "Drag reduction in a turbulent boundary layer on a flexible sheet undergoing a spanwise travelling wave motion," *Journal of Turbulence*, **7**, No. 27 (2006).
- ³⁶ J. Westerweel, "Fundamental of digital particle image velocimetry," *Meas. Sci. Technol.* **8** (1997).
- ³⁷ J. J. Allen and M. S. Chong, "Vortex formation in front of a piston moving through a cylinder," *J. Fluid. Mech.* **416** (2000).
- ³⁸ K-S Choi, "Near-wall structure of the turbulent boundary layer with spanwise-wall oscillation," *Phys. Fluids* **14**, 7 (2002).

EFFECT OF A HEAT SOURCE ON THE EVOLUTION OF A CYLINDRICAL VORTEX

F. V. Shugaev, T. A. Petrova

Faculty of Physics, M.V. Lomonosov Moscow State University, 119991, Moscow, GSP-1, Vorobyovy Hills,
Moscow, Russia,
shugaev@phys.msu.ru, +7-495-939-2816 (office), +7-495-932-8820 (fax)

Abstract. The non-linear system of the Navier-Stokes equations with a source-like term on the right-hand side in the energy equation is used in order to model the influence of heat flux on the evolution of a decaying cylindrical vortex. It is found that the heat flux diminishes the intensity of the vortex. The problem is considered in a semi-infinite space ($z \geq 0$). The boundary condition $v=0$ is set on the plane $z=0$.

Introduction

Effect of a heat flux on the vortical flow was experimentally investigated by Hide [1]. In his experiments, a cylindrical vessel contained water was rotated about its axis, and was heated near its border and cooled near its center. Under certain conditions an irregular flow pattern appeared, and changed its shape in an irregular manner.

We studied theoretically the effect of a point thermal source on a decaying cylindrical vortex in gas. The boundary value problem is shown in Fig. 1.

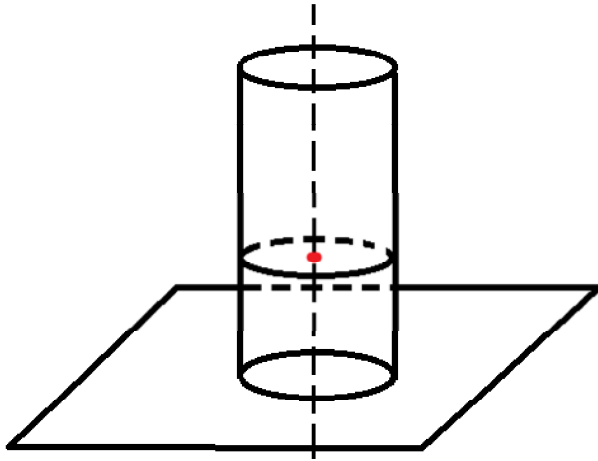


Fig. 1 The boundary value problem.

We studied the problem using the system of the Navier-Stokes equations.

A new method of solving the Navier-Stokes equations is proposed recently[2]. It is based on the fundamental solution of linear parabolic systems. The distinctive feature of the method is that no finite-difference schemes are used. The method has no restrictions to values of Reynolds numbers.

Thus the solutions used are intrinsic to the Navier-Stokes equations.

Method for solving the Navier-Stokes Equations

The full system of the unsteady Navier-Stokes equations can be written in the form (using the Lagrangian variables)

$$\begin{aligned} \frac{\partial \Omega_i}{\partial t} &= \nu \Delta \Omega_i + f_{li}, \\ \frac{\partial \Omega_i}{\partial t} &= \nu \Delta \Omega_i + f_{li}, \\ \frac{\partial s}{\partial t} &= \frac{4}{3} \nu \Delta s + \frac{1+h}{\gamma} \Delta w - \frac{1}{\gamma} \Delta h + f_2, \\ \frac{\partial h}{\partial t} &= \frac{\gamma}{Pr} \eta \Delta h - (\gamma - 1)s + f_3 + F, \end{aligned} \quad (1)$$

$$f_{li} = f_{li}(\vec{u}, t, \psi_j, \partial \psi_j / \partial u^m),$$

$$f_l = f_l(\vec{u}, t, \psi_j, \partial \psi_j / \partial u^m),$$

$$\vec{\Omega} = \text{rot } \vec{v}, w = -\ln \rho, s = \text{div } \vec{v}, h = T - 1,$$

$$\nu = \mu / \rho, \eta = \lambda / \rho, \psi_1 = w, \psi_2 = s, \psi_3 = h,$$

$$i = 1, 2, 3; l = 2, 3; m = 1, 2, 3.$$

Here F is a thermal source:

$$F = 0.5 \sin(\omega_0 t) \delta(\vec{x} - \vec{x}_0),$$

$$\vec{x}_0 = \{0, 0, z_0\}$$

Here ρ, T, μ, λ are density, temperature, viscosity, thermal conductivity, respectively; Δ is the Laplace operator, Pr is the Prandtl number, γ is

the adiabatic exponent. The symbols $f1, f2, f3$ denote nonlinear members (with regards to the first derivatives). Appropriate expressions have been given earlier [2].

The system (1) is written in dimensionless form, the characteristic length being ν_0/c_0 , the characteristic time being ν_0/c_0^2 , $\nu_0 = \mu_0/\rho_0$, where c is the sound velocity, the subscript "0" refers to the initial state.

The system (1) is a parabolic one [3]. The proposed method of solution consists in reducing it into the system of integral equations of the Volterra type and in subsequent use of iterative procedure. The procedure can be divided into two parts. First of all we find an approximate solution, the so-called parametrix [4, 5]. Then we construct the fundamental solution. While considering the first part, we do not take into account the last terms in the right-hand side of Eqs. (1). The last terms in the right-hand side are taken into account while constructing the fundamental solution. As mentioned, the iterative procedure is used [4,5]. The solution of the linearized system is taken as the first iteration. Suppose that the (n-1)th iteration is known. Then the coefficients referring to the Laplace operators are known. Thus we have linear equations with variable coefficients. Furthermore, we suppose that the coefficients depend on t solely, the coordinates being considered as parameters.

The Fourier transform of the system of equations under consideration with $\tilde{f}_i=0$ is

$$\begin{aligned} \frac{d\tilde{\Omega}_i^{(n+1)}}{dt} &= -k^2\nu^{(n)}(\tilde{y}, t)\tilde{\Omega}_i^{(n+1)}, \\ \frac{d\tilde{w}^{(n+1)}}{dt} &= \tilde{s}^{(n+1)}, \\ \frac{d\tilde{s}^{(n+1)}}{dt} &= -\frac{4}{3}k^2\nu^{(n)}(\tilde{y}, t)\tilde{s}^{(n+1)} - \\ &\quad -\frac{1+h^{(n)}(\tilde{y}, t)}{\gamma}k^2\tilde{w}^{(n+1)} + \frac{k^2}{\gamma}\tilde{h}^{(n+1)}, \\ \frac{d\tilde{h}}{dt} &= -\frac{\gamma}{Pr}k^2\tilde{\eta}^{(n)}(\tilde{y}, t)\tilde{h}^{(n+1)} - (\gamma - 1)\tilde{s}^{(n+1)}. \end{aligned}$$

Thus we have a system of linear ordinary differential equations with variable coefficients. They can be solved, for example, using the technique proposed by Goursat [6].

Results

We fulfilled computations for three values of the source frequency and for two distances l from the heat source :

$$\omega_0 = 0.05; 0.2; 0.4, \quad l = 0.54; 2.83$$

We have $\Omega_s = \Omega_0 + \Omega_d$.

Here the subscripts $0, s, d$ refer to the undisturbed value, the total one and to the disturbed part, respectively. The quantity Ω_d is always negative, except a small neighborhood near zero. So heat source decreases vorticity. The decrease is equal to several per cent and more.

Figs. 2-4 show the evolution of the vortex when there is no source. Figs. 5-7 present the effect of the thermal source (temporal evolution of the quantity Ω_d).

Conclusion

The numerical procedure is set forth that enables to analyze vortical structures and the effect of heat flux. It is found that the intensity of the cylindrical vortex diminishes due to the influence of the thermal source. The proposed method can be applied for further investigation of the effect of heat flux on vortical structures.

References

1. Hide, R., An experimental study of thermal convection in a rotating fluid, *Phil. Trans. Roy. Soc. London*, 250, 441-447 (1958).
2. F.V. Shugaev, E.N. Terentiev, L.S. Shtemenko, O.I. Dokukina, O.A. Ignateva. "On the problem of beam focusing in turbulent atmosphere", in *Optics in Atmospheric Propagation and Adaptive Systems VIII*, ed. by Karin Stein, Anton Kohnle, Proc. SPIE Vol. 6747, 67470K (2007).
3. O.A. Ladyzhenskaya, N. N. Uraltseva "Boundary value problem for linear and quasilinear equations and systems of parabolic type", *Izvestia AN USSR, Ser. Mat.*, 27(1), 161-240, (1963).
4. Friedman, A., *Partial Differential Equations of Parabolic Type*, Prentice Hall, New York (1964).
5. Eidelman S. D., *Parabolic systems*, Nauka, Moscow (1964).
6. Goursat, E., *Cours D'Analyse Mathématique, t.III, Equations Intégrales*, Gauthier-Villars, Paris, (1929).

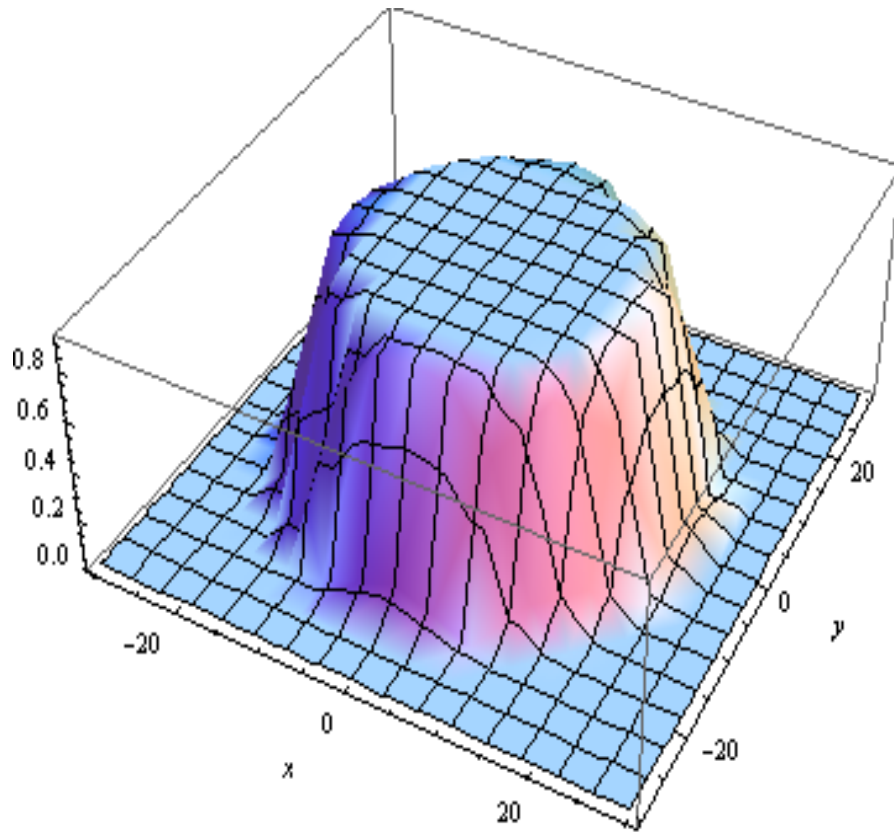


Fig. 2. Vorticity distribution (no heat source), $t=1; z=4$.

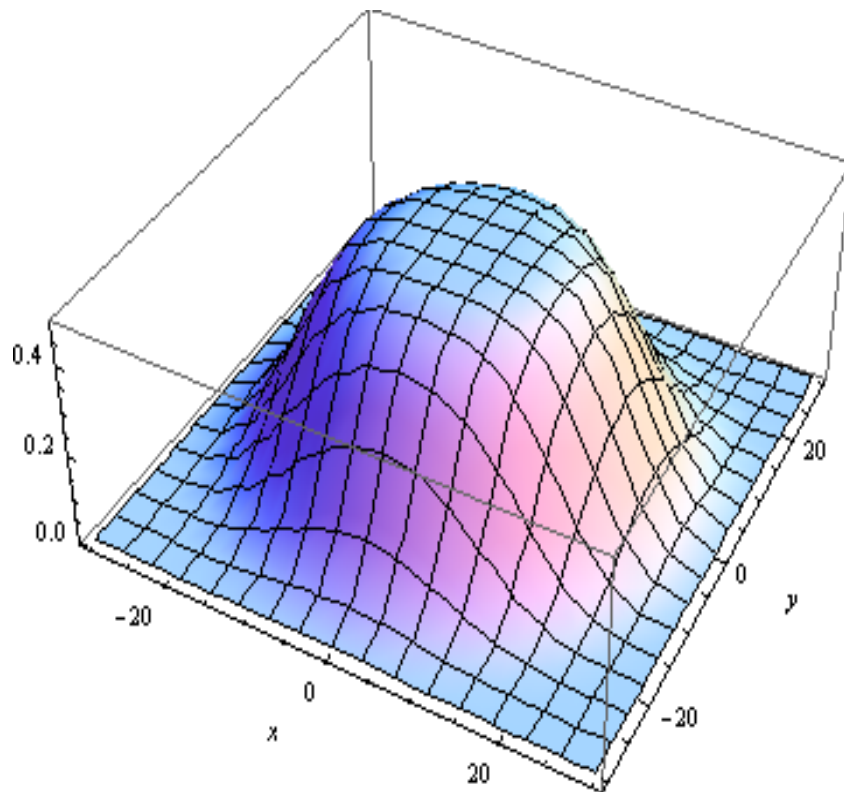


Fig. 3. Vorticity distribution (no heat source), $t=10; z=4$.

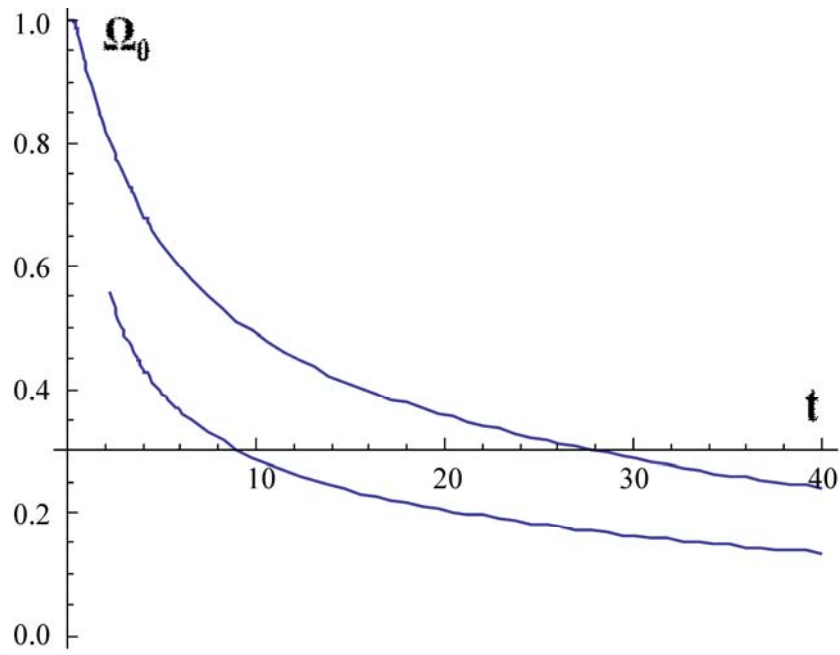


Fig. 4. Evolution of the vortex in a fixed point (no source)
 1 - $r=0.5, z=2.2$; 2 - $r=2, z=4$.

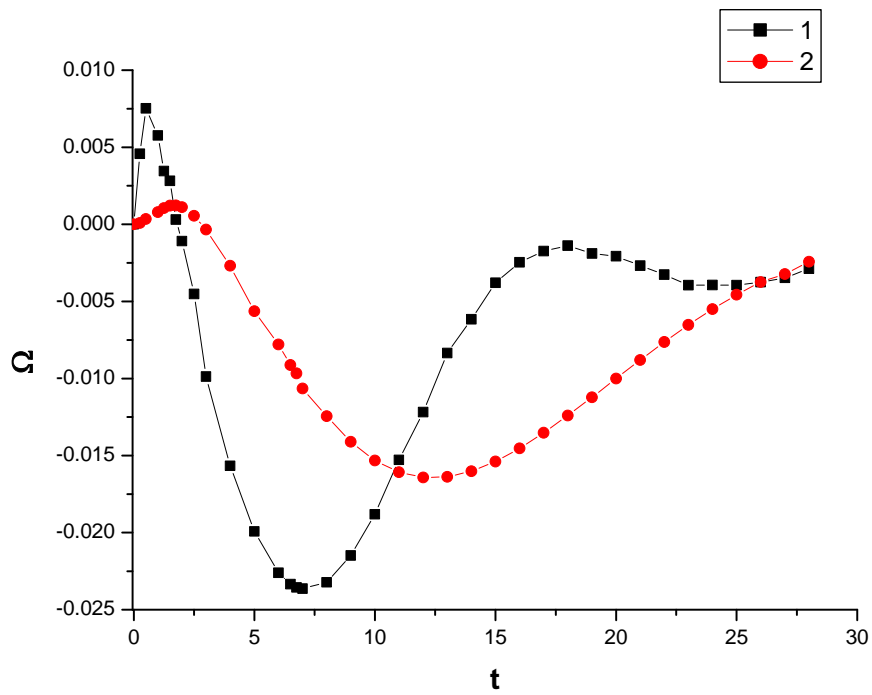


Fig. 5. 1- $r=0.5; z=2.2; \omega_0=0.4; qt=0.5$
 2- $r=2; z=4; \omega_0=0.2; qt=0.5$

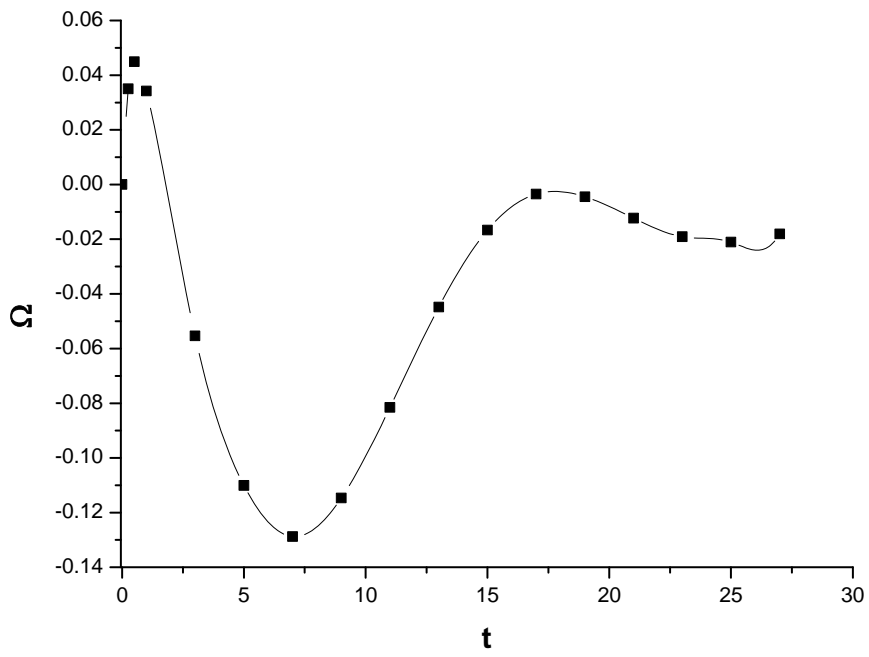


Fig.6. $r=0.5$; $z=2.2$; $\omega_0=0.4$; $qt=3$.

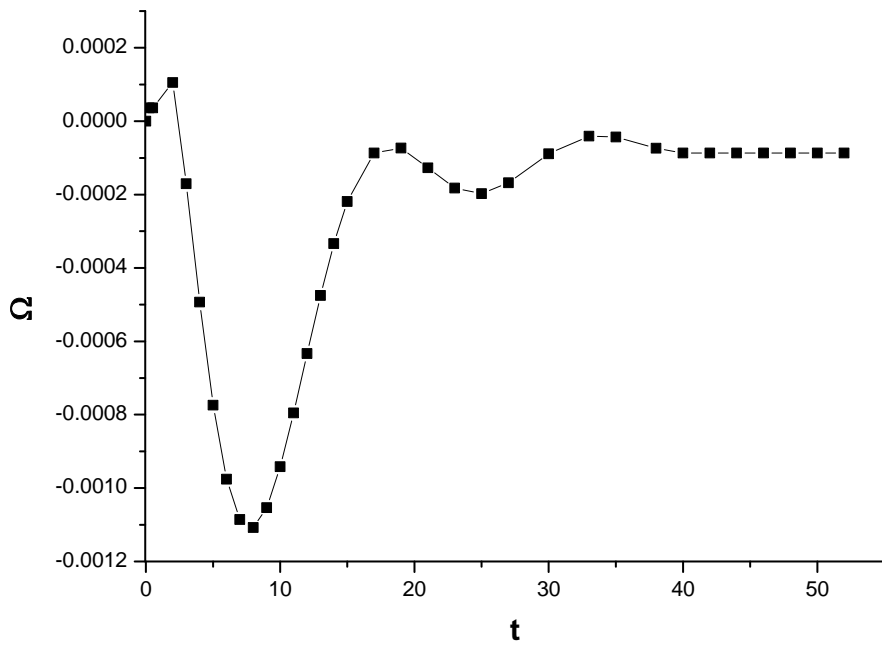


Fig.7. $r=2$; $z=4$; $\omega_0=0.05$; $qt=0.5$.

STUDY OF A LONGITUDINAL CAPACITY COUPLED HF DISCHARGE IN A SWIRL AIRFLOW

Moralev I.A., Boytsov A.Yu., Klimov A.I.

Joint Institute for High Temperatures RAS, Moscow

HF discharge with a frequency 320kHz in a swirling flow is studied at atmospheric pressure and discharge current <500mAmp. HF plasma parameters are defined. The measured value of reduced electrical field in this HF discharge is about $E/N = 10 \div 15$ Td. The gas temperature near vortex axis is about of $T_g = 1500 \div 2000$ K. The electron density is about of $N_e \leq 10^{12} \text{cm}^{-3}$. The gas temperature profiles in the vortex filament are measured at HF plasma on. Distributions of the HF voltage and phase shift along HF filament are obtained.

A propagation and evolution of HF filament created by pulsed repetitive HF power pumping is studied by optical interferometer. It is revealed that plasma formation consists of two parts: filament and RF sparks ("streamers") localized near its head in this non-stationary regime. The similar structure is obtained for the transient regimes [2] of HF discharge at a latest stage of the process. The temperature distributions in HF filament and a separate HF spark are obtained by optical interferometer.

It is revealed that preliminary gas flow heating leads to a single HF filament creation from multi spark discharge.

Nomenclature

LP = longitudinal vortex plasmoid

HF = high frequency

HFD = high frequency discharge

F_{HF} = HF frequency

F_M = modulation frequency of CHFD

T_i = pulse duration

I_{HF} = HF electric discharge current

V_{HF} = HF electric discharge voltage

N_{HF} = pulse power input in plasma

M = Mach number

V_{ax} = axial component of the velocity

V_t = tangential component of the velocity

P_{st} = static pressure

T_g = gas temperature

T_R = rotation temperature

T_V = vibration temperature

1. Introduction

A problem concerning interaction of vortex structures with a non-equilibrium plasma of different electrical discharges is important for plasma aerodynamics itself and for a number of technical applications: parameters control of boundary layer, separated vortex region, trailing vortices.

Several results of numerical study of compressible linear vortex filaments with local energy release regions are concerned in works [1-5].

Theoretical and numerical results on the dynamics and structure of the column-like vortex in a non-equilibrium excited gas are presented in [6]. It is shown, that stimulated relaxation processes in a non-equilibrium gas (in [6] condensation processes were considered) may lead to changes of the vorticity in the vortex core.

Turbulizer vortical wake evolution in a non-equilibrium flow in the discharge chamber of the gas laser is studied in [7]. In [8] the same

authors argued the evolution of the 2D vortex at different media relaxation rates after its instantaneous excitation.

In [9] theoretical study was focused on the evolution of the the vortex flow with a non-equilibrium plasma of the DC glow discharge. Authors assert, that the main vorticity component in the flow can increase or decrease, depending on the electrical field direction.

A practical task of vortex parameters modification assumes interaction with the discharge at some distance from the plane surface. Therefore, HF and MW discharges seems promising in this case. In several publications, this interaction was considered for particular cases. In [10], linear vortex interaction with a shock wave in the presence of local heat release source was numerically studied at $M \sim 2-5$. Several works were devoted to modification of the vortex structure behind the bow shock by MW filaments. However, relaxation processes and effects of space charge were not studied yet.

Specific gas dynamics of the vortex structure also significantly affects the discharge properties. Arc discharge stabilization on the axis on the swirling flow in plasmatrons is widely known. Properties of the HF single-electrode discharge in the swirling airflow at atmospheric pressure are the main goal of this work.

Some previous results on this subject were published earlier [11,12]. It was revealed, that in the vortex airflow at nearly constant pressure discharge can exist in two main regimes – multifilament HF corona and stable flare (longitudinal plasmoid). Form of the discharge depends on the flow properties, namely on axial and tangential velocity ratio.

2. Experimental setup

Scheme of the experimental setup VT-1 is shown on the fig. 1. Swirling flow was created via

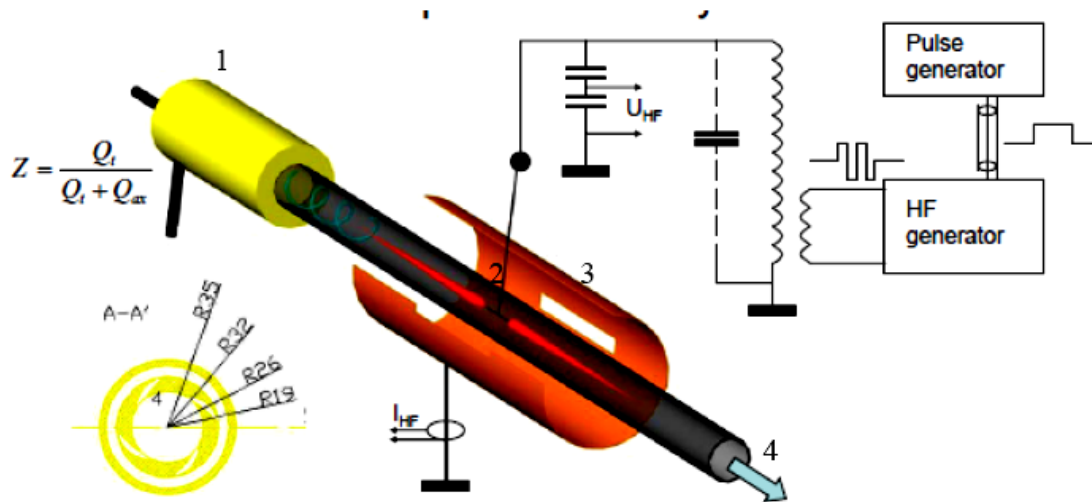


Fig.1. Experimental set up SWT-2. 1-vortex generator, 2- HF electrode, 3-ground electrode, 4-to vacuum chamber.

vortex generator 1, at that swirl rate can be changed by changing the ratio of flowrates Q_1 and Q_2 through straight and tangential gas inlets. Test chamber of the setup is manufactures of the quartz tube 2 36mm in diameter and 40cm in length. Tube's other end is opened either to the room air or to the vacuum chamber 6 (volume 0,8 m³).

Single-electrode longitudinal capacity-coupled discharge was created by a "RF-switch" generator. Plasma cord in a vortex flow was created on the electrode 3 – tungsten needle 2mm in diameter. Current loop is closed by displacement currents through the grounded parts of the setup or through the metallic shield 4. Discharge is ignited and hold by the resonant Tesla transformer. Pulse modulation of the HF power is made by external signal generator.

Typical HF discharge parameters: HF power – less than 10kW, HF-frequency – 450 kHz, modulation frequency – less than 5kHz, pulse duration – more than 80us.

Discharge voltage was measured with Tektronix P6014A HV probe, discharge current was measured in the lead between metal shield and ground with Tektronix AC current shunt. Stray current between the needle and shield was digitally subtracted from total one. Electrical power input was calculated by digital multiplication of current and voltage signals via TDS 2014B oscilloscope with ~10% error.

Diagnostic instrumentation of the experimental setup VT-1 includes pressure sensors, thermocouples, special rotating pressure probe for velocity measurements in a swirling flow [13], optical spectrometers DFS-1 (resolution – 0.01 nm) and Avaspec (resolution – 0.2 nm, 200 – 800 nm), optical interferometer with a He – Ne laser, capacitive HV HF voltage probe and Tektronix current shunt P6021.

For atmospheric pressure in the output chamber flow typical parameters are: top azimuth velocity – 30 m/s, top axial velocity – 15 m/s. Maximal pressure drop measured is 1,2 kPa, maximal tangential vvelocity is achieved on the radius of 10 mm. Typical distributions of pressure and velocity components in the swirling flow across the channel cross-section are presented elsewhere [12].

3. Results and discussion

A. Discharge parameters

Plasma parameters were measured by optical spectroscopy method. Optical spectra of the discharge was recorded by Andor 4200E CCD camera, connected to the imaging DFS spectrometer. Total spectral resolution of the system appeared to be 0.05 nm.

Data were acquired with 1 mm resolution along the spectrometer slit in 25mm separated cross-sections of the discharge with ~1s integration time.

Main features, obtained in the spectra of discharge column are A-X transition of hydroxyl and 2⁺ system of nitrogen molecules. One should note that OH emission is mainly obtained in the near-core regions of the discharge.

The *experimental conditions* were the followings:

- Mach number $M < 0.1$
- Static pressure $P_{st} \sim 1 \text{ Bar}$
- Testing gas air
- Axial velocity V_x module 10 m/s
- Tangential velocity V_t $V_t < 30 \text{ m/s}$
- Mean HF power $N_{HF} = 240 \text{ W}$
- HF current amplitude $I_d \sim 168 \text{ mA}$
- HF frequency $F_{HF} \sim 0,32 \text{ MHz}$
- Operation regime continuous
- Typical plasmoid's length $\sim 200 \text{ mm}$

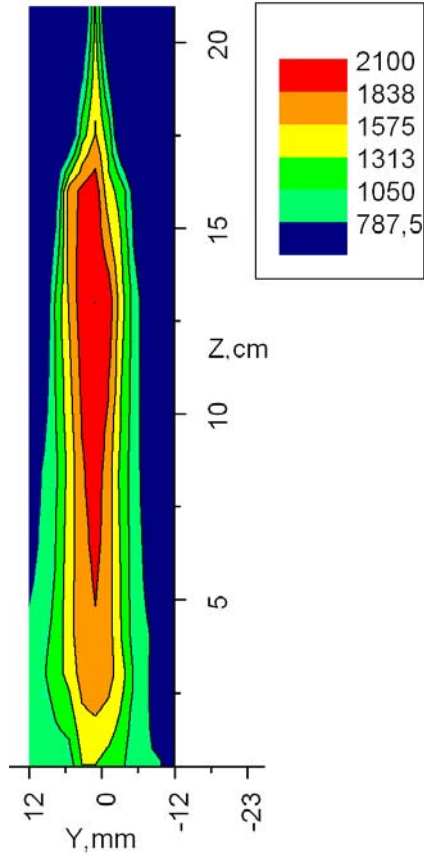


Fig. 2. The typical gas temperature spatial distribution in HF plasmoid. $V_r \sim 20 \text{ m/s}$, $I_{HF} = 168 \text{ mA}$, $\langle P_{HF} \rangle = 240 \text{ W}$

Rotation temperature T_R of the excited nitrogen molecules is defined by processing of the N_2^+ band spectra. Simulated spectra of molecular nitrogen band $\Delta v = -1$ ($\lambda = 345 \div 360 \text{ nm}$) are obtained by the program “SPECAR” [14]. Accuracy of the method is about $\delta T_R \sim \pm(100 \div 200 \text{ K})$. This accuracy depends on spectrum’s noise. It is well-known that rotation temperature of excited nitrogen is close to the translation temperature of gas in these conditions.

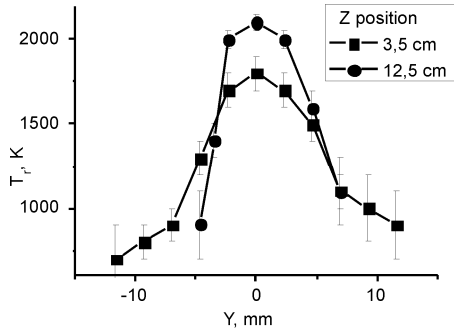


Fig.3. The typical radial gas temperature distribution at different cross-sections of the longitudinal plasmoid created by CHFD in swirl flow. $V_r \sim 20 \text{ m/s}$, $I_{HF} = 168 \text{ mA}$, $\langle P_{HF} \rangle = 240 \text{ W}$

The typical space temperature distribution inside a longitudinal plasmoid is shown in the fig. 2. Following features of temperature field can be distinguished:

- Temperature increases from $T_g \sim 1000 \text{ K}$ near electrode up to 2000 K at the coordinate $Z = 20 \div 50 \text{ mm}$. It does not change in the space interval $\delta Z = 20 \div 150 \text{ mm}$. There is a temperature drop with the typical temperature gradient about of 120 K/cm at the $Z > 150 \text{ mm}$.
- Diameter of hot gas region is increased near HF electrode tip. Its maximal value is of about 20 mm
- Maximal gas temperature is located near cross section $Z \sim 120 \text{ mm}$
- The typical radial temperature distributions of HF plasmoid at the different cross sections are shown in the fig. 3.

It is obtained that measured vibration temperature of excited nitrogen molecules T_V in vortex plasmoid is about $T_V \sim 3000 \div 4000 \text{ K}$. It slightly depends on plasmoid’s radius and its length. So, *plasma with a maximal non-equilibrium level* $\eta = T_V/T_R$ is created in a distant “cold” area around hot HF plasmoid’s kernel and *plasma with a minimal non-equilibrium level* is created in its hot area near vortex axis.

B. Electric field distribution

Distribution of the HF field amplitude along the discharge channel was measured by capacitive probe. The latter was made of a 5 mm diameter ball, connected to the P6014A HV probe. Probe could be transferred along the discharge cell. Probe head and HF cord constitute a voltage divider with $\sim 1:5$ coefficient. One can therefore calculate voltage distribution along the cord from probe signal amplitude at different points on Z axis.

Typical U_{HF} and ϕ distributions are shown on fig.4. One can see that amplitude reduces to the values $\sim 0.3 \text{ kV}$, and phase shift changes from 0 to $\pi/2$ as the probe is transferred to the discharge tip. Voltage seems to reduce rather linearly than exponentially. Typical distance, for which phase achieves value of $1 \text{ rad} = 0.31\pi$, appears to be 12 cm . This gives as an estimate of attenuation coefficient $\beta \sim 8.3 \times 10^{-2} \text{ cm}^{-1}$. HF field amplitude on the cord axis can be estimated to be $E_{HF||} = 500 \text{ V/cm}$. Taking into account temperature measurements (see part A), we get the reduced field value $E_{||}/N \sim 12\text{-}15 \text{ Td}$. Finally, typical plasma conductivity can be estimated as $\sigma = 3 \times 10^4 \text{ Ohm}^{-1} \text{ cm}^{-1}$. Electron density can be calculated as $n_e = 3.5 \times 10^3 \sigma v_m$, with $v_m = 3.9 \times 10^5 \text{ s}^{-1} \text{ Torr}^{-1}$ [15]. This estimation gives $n_e \sim 10^{12} \text{ cm}^{-3}$.

Radial field value can be estimated from as $E_r = U/r = 5\text{-}10 \text{ kV/cm}$. In this estimation, discharge was treated as ideal conductor with 1 cm radius, voltage amplitude is taken to be 18 kV . In the

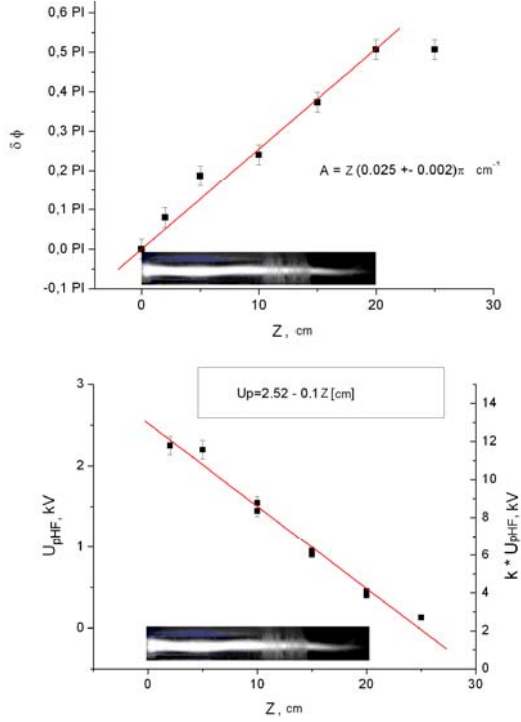


Fig.4. Amplitude (a) and phase (b) of the HF voltage along the discharge. $I_{HF} \sim 220$ mA.

discharge shell $T_g \sim 600$ K, and reduced field value in she discharge shell can be estimated as $E/N \sim 50$ - 70 Td.

Discharge can also be treated as a line with distributed parameters [16-18]. From the geometrical properties of the discharge, line capacity may be estimated as $C = 24/\lg(R/r) = 0.24$ pF/cm, resistance – $R \sim E/I = 2.3$ kOhm/cm, where $r = 1$ cm and $R = 10$ cm – discharge and outer shield radii. In such a line, typical attenuation length should be ~ 72 cm. Obtained discrepancy of the estimation results with experiment should refer to neglecting of the real distribution of line parameters along the discharge.

C. Discharge evolution in time

In our previous work [12], discharge propagation along the vortex axis was studied by means of high-speed videocamera. Main results obtained from these experiments were the following:

- a complex structure of the discharge head was revealed. At fact, discharge consists of a cord-like plasma formation (LP), justified along the vortex axis, and a multi-filament HF corona discharge on the top of it,
- the head of LP propagates towards the air swirler with the typical velocity of 10 m/s.

However, the reason of the two discharge forms existence remained unclear.

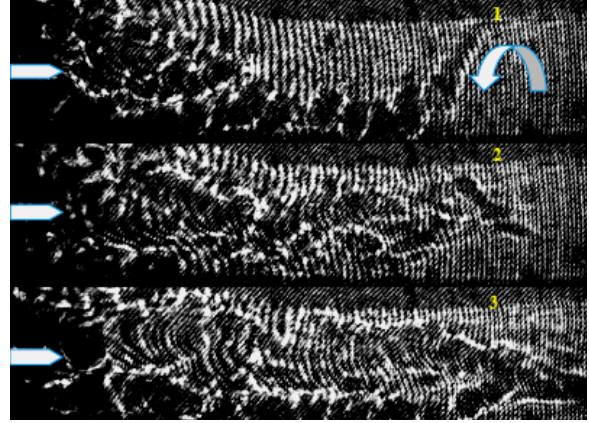


Fig. 5. Interferograms of a longitudinal HF discharge in a swirl flow. Odd frame numbers correspond to pulsed HF power on, even – correspond to pulsed HF power off. $F_m = 150$ Hz, $\tau = 2.5$ ms, $f = 350$ kHz $Q_{ax} = 0$ G/s, $Q_t = 5$ G/s, $t_{exp} = 40$ us.

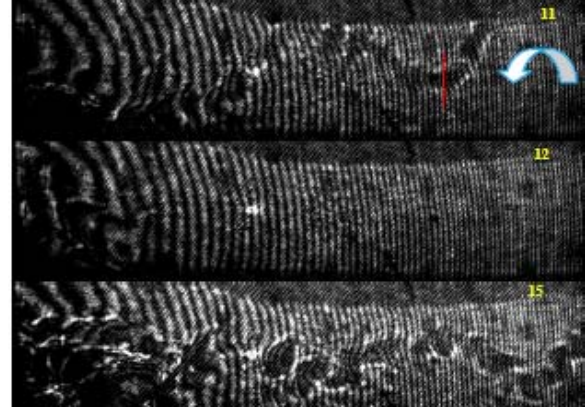


Fig. 6. Interferograms of a longitudinal HF discharge in a swirl Flow. Odd frame numbers- HF power on, even- pause time period. $F_m = 150$ Hz, $\tau = 2.5$ ms, $f = 350$ kHz $Q_{ax} = 5$ G/s, $Q_t = 5$ G/s, $t_{exp} = 40$ us.

In the current work, we have studied the temperature distribution of the pulsed-periodic discharge by an optical interferometer, combined with a high speed camera as an acquisition system.

Two different regimes of LP creation are studied at maximal axial mass flow rate ($Q_{ax} = Q_t = 5$ G/s) and minimal axial mass flow rate ($Q_{ax} = 0$, $Q_t = 5$ G/s). First regime corresponds to LP creation and the second one corresponds to HF plasma filament corona creation (or transient regime). The typical interferograms corresponding to these cases are shown in fig.5,6. One can see that there is secondary discharge propagate inside the hot cavern, created by previous pulses.

It is revealed that LP propagates towards a swirl generator with a velocity of 5-10 m/s.. Mean temperature of this LP is about ~ 600 K – 1000 K in the pause between RF pulses. Stable hot cavern with diameter ~ 1.2 cm and length about 15 cm is

created at latest stages of HF generator operation and mean power input in plasma $N_p \sim 700W$. Therefore, discharge "head" velocity measured from high speed visualization corresponds to the typical velocity of the stable low density cavern, created by discharge on the axis of the vortex. Additionally in the case of discharge propagation towards the swirler, this velocity corresponds to axial speed on the flow axis. However, latter relation can be occurrent since heat release in the discharge might change the flow structure in the vortex.

Discharge propagation seems to proceed as follows. Discharge initially appears on the electrode tip in the form of a multifilament RF corona. First pulses heat the gas in the vicinity of the electrode, that leads to density decrease in this region on ms timescales. Due to temperature rise, detachment of electrons from O_2 molecules partly reduce electrons losses due to attachment processes. Consequently, further discharges propagate through the media with significant initial conductivity, that is thought to be the main reason of HF corona-to-flare transition. Also, a density nonuniformity leads to the increase of E/N in the preheated region, that should also affect discharge propagation process.

4. Conclusions

- Plasma-vortex interaction is studied in the atmospheric conditions and azimuthal velocities up to 20 m/s and discharge currents up to 500 mAmp.
- Single electrode HF longitudinal discharge parameters for these conditions are: $T_r < 2,5$ kK, $T_e > T_v > 3,5$ kK, $E/N = 12-17$ Td, $n_e \sim 10^{12} \text{ cm}^{-3}$. Cord voltage-current characteristic is a decreasing one.
- Discharge propagation along the vortex axis is studied by high speed interferometer and video camera. "Cord-like" discharge propagation velocities are of the order of convective ones – 6-10 m/s. The complex structure of the discharge head is revealed.
- Transition between the different forms of discharge is studied as a function of flow parameters, initial flow temperature, power input to the discharge. Main reason for discharge transition seems to be the overheating of the vortex core region.

5. References

1. A.V. Kazakov, "Stability of a viscous subsonic swirl flow," *Fluid Dynamics*, vol. 33, May. 1998, pp. 338-345.
2. A.V. Kazakov, "Stability of an axisymmetric swirled flow in a supersonic cocurrent stream for volume energy supply in the viscous vortex core," *Fluid Dynamics*, vol. 40, Jan. 2005, pp. 62-70.
3. A.V. Kazakov, "Effect of volume energy supply on swirled flows in a subsonic cocurrent stream," *Fluid Dynamics*, vol. 33, Nov. 1998, pp. 850-855.
4. A.V. Kazakov and A.P. Kuryachii, "Stability of a compressible swirling flow in a circular pipe," *Fluid Dynamics*, vol. 34, Jan. 1999, pp. 29-34.
5. A.V. Kazakov, "Effect of Volume Energy Supply on the Stability of a Subsonic Vortex Flow," *Fluid Dynamics*, vol. 38, 2003, pp. 552-560.
6. I.P. Zavershinski, A.I. Klimov, N.E. Molevich, and D.P. Porfiriev, "Renkin vortex evolution in a gas with heat source," *Pisma Zh. Techn. Fiz.*, vol. 35, 2009, pp. 106-110.
7. A.I. Osipov, A.V. Uvarov, and N.A. Vinnichenko, "Influence of the initial vibrationally nonequilibrium state of a medium on the structure of von Karman vortex street," *Physics of Fluids*, vol. 18, Oct. 2006, p. 105106.
8. N.A. Vinnichenko, A.V. Uvarov, and A.I. Osipov, "Modification of a Single Vortex in a Medium With Internal Heat," *The third international workshop "Nonequilibrium processes in combustion and plasma based technologies", 2008, Minsk*, pp. 75-78.
9. V.S. Soukhomlinov, V.A. Sheverev, and M.V. Otigen, "Evolution of a vortex in glow discharge plasma," *Physics of Fluids*, vol. 17, 2005, pp. 1-4.
10. E.A. Pimonov, A.A. Zheltovodov, and K. D.D., "Research of Shock Wave-Induced Vortex breakdown Control by Energy Deposition," *European conference for aerospace sciences (EUCASS) 2005*, p. № 2.02.03.
11. A.I. Klimov, V.A. Bityurin, B.N. Tolkunov, I.A. Moralev, M.V. Plotnikova, and K.B. Minko, "Study of a Longitudinal Plasmoid Created by Capacity Coupled HF Discharge in Vortex Airflow," *New Horizons*, 2009, pp. 1-14.
12. I.A. Moralev, A.I. Klimov, D.S. Preobrazhensky, B.N. Tolkunov, and K. V.A., "HF Discharge Interaction with a Swirling Flow in a Tube," *WSMPA Moscow, 31 march - 02 april 2009*, pp. 267-271.
13. A.I. Klimov, I.A. Moralev, K.B. Minko, and M.V. Plotnikova, "Diagnostic instrumentation for measurements of the discharge-vortical flow interaction paramers," *3d School on Magnetoplasma aerodynamics, Moscow, 8-10 april 2008*, pp. 191-196.
14. C.O. Laux, "Radiation and Nonequilibrium Collisional-Radiative Models," von Karman Institute Lecture Series 2002-07, Physico-Chemical Modeling of High Enthalpy and Plasma Flows, eds. D. Fletcher, J.-M. Charbonnier, G.S.R. Sarma, and T. Magin, Rhode-Saint-Genise, Bel."

15. Y.P. Raizer, *Gas Discharge Physics*, Springer-Verlag, Berlin, 1991.
16. I.A. Tihomirov, V.A. Vlasov, and Y.Y. Lutzenko, "HF flare discharge electrodynamics [in russian]," *Izv. Tonsk Politechnical Univ.*, vol. 306, 2003, pp. 21-29.
17. H. Nowakowska, Z. Zakrzewski, and M. Moisan, "Propagation characteristics of electromagnetic waves along a dense plasma filament," *Journal of Physics D: Applied Physics*, vol. 34, 2001, pp. 1474-1478.
18. M.A. Aronov and V.P. Larionov, eds., *Electrical Insulation of high-frequency high-voltage devices [in russian]*, "Znak", Moscow, 1994.

PROPERTIES OF DC DISCHARGE NEAR SURFACE IN SUPERSONIC GAS FLOW AT LOW GAS PRESSURE

I.V. Schweigert

Institute of Theoretical and Applied Mechanics,
Novosibirsk 630090, Russia
ischweig@yahoo.com

Abstract. Kinetic particle-in-cell simulations are performed to examine the characteristics of the surface glow discharge in a supersonic nitrogen flow. The gas pressure is varied between 100 and 500 mTorr; the applied voltage, between 500 and 1000 V. The analysis focuses on the effect of boundary conditions at the dielectric barrier surrounding the electrodes on the electron energy distribution function. The potential on the dielectric is found by using a local balance condition for the electron and ion currents to the surface. The results of self-consistent simulations show that a negative potential on the dielectric substantially reduces the rate of high-energy electron loss from the bulk plasma and thus significantly changes the ionization rate, as well as plasma parameters and configuration.

Electrical discharges of various types are widely used to control the properties of gas flows around subsonic and supersonic vehicles. To understand the discharge modes in the upper atmosphere, where the gas pressure is relatively low, kinetic plasma simulations are required. When the voltage across a low pressure gas discharge is on the order of kilovolts, the plasma is characterized by nonlocal electron and ion energy distributions. This explains why both energy and momentum transfer from electrons and ions to neutrals must be simulated by kinetic modeling. Current simulations of the discharge plasma effects on gas flows around gas flows are based on fluid models [1–3]. However, this approach requires separate computations of the electron and ion distribution functions, and the resulting overall solution to the problem is not self-consistent. Furthermore, the boundary conditions at the dielectric surface are extremely difficult to determine in the framework of a fluid model [3]. Just as any surface exposed to a plasma, the dielectric layer surrounding the electrodes is negatively charged, because electrons have a higher mobility than ions. The charge density on the dielectric surface is determined by local balance between electron and ion fluxes. Because of steep electric field gradients near the surface and at the electrode edges, the barrier potential varies over the dielectric surface. This potential can significantly change the plasma properties and configuration by reducing the rate of high energy electron loss to the surface. In this study, the Particle-in-cell Monte Carlo collision (PIC–MCC) method [4] is used to examine the characteristics of a coplanar direct current (DC) discharge in supersonic flow at gas pressures of $P = 100$ and 500 mTorr and cathode voltages of $U = -500$ and -1000 V. The discharge geometry is illustrated by Figure 1. The simulations presented below take into account the secondary electrons produced by

ion impact on the surface. The paper focuses on discharge plasma characteristics at low pressures and dependence of the electron distribution function on the boundary conditions for dielectric surface potential.

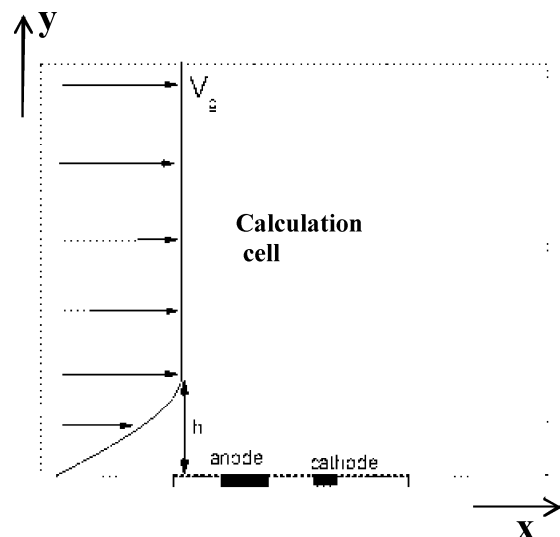


Fig. 1. Calculation cell. Bold line segments represent cathode and anode. Flow direction can be from left to right or from left to right.

The system of equations used in the present model to describe DC discharge in a gas flow includes kinetic equations for electrons and ions (three dimensional in velocity space and two dimensional in space) and the Poisson equation. The electron and ion energy distribution functions, $f_e(r, v)$ and $f_i(r, v)$, are found by solving the Boltzmann equations. The Poisson equation potential distribution is supplemented by the boundary conditions $\phi = 0$ at the anode, $\phi = U_c$ at the cathode, $\partial E_y / \partial y = 0$ at the upper boundary of the computational domain, and $\partial E_x / \partial x = 0$ at its lateral boundaries. The boundary condition for the

potential on the dielectric surface at is determined by a local balance condition for the electron and ion fluxes to the surface.

Equation system is solved self-consistently performing PIC–MCC simulations of DC glow discharge in nitrogen [4]. The electron kinetics model includes elastic scattering of electrons by molecules, rotational and vibrational excitations, excitation of metastable states, and ionization. The emission of secondary electrons produced by ion impact on the cathode is also taken into account by introducing a secondary emission coefficient γ . The gas velocity profile is modeled as

$$v_g(y) = 0.5 v_{\max} \left(1 + \sin \left(\pi \left(\frac{y}{y_s} - 0.5 \right) \right) \right),$$

$$y < y_s,$$

$$v_g(y) = v_{\max}, \quad y > y_s,$$

where $v_{\max} = 10$ cm/s is the maximum gas velocity and $y_s = 1.5$ cm is the corresponding ordinate. The effects of gas velocity on ion motion, scattering by gas molecules, and ion production by electron impact are taken into account. An analysis of plasma effects on local flow characteristics based on self-consistent computations of DC discharge and gas flow parameters will be performed in a future study.

Now, consider the plasma parameters obtained by solving the equations self-consistently by PIC–MCC simulation for a model gas. Two regimes were simulated: (a) $P = 100$ mTorr, $U = -1000$ V, $\gamma = 0.1$; (b) $P = 500$ mTorr, $U = -500$ V, $\gamma = 0.05$. The computational domain geometry, including electrodes, is illustrated by Fig. 1. The anode is placed at $10.0 \text{ cm} < x < 12.5 \text{ cm}$, and cathode is at $14.5 \text{ cm} < x < 16.0 \text{ cm}$ for $P = 100$ mTorr. For higher gas pressure of $P = 500$ mTorr the anode is placed at $2.0 \text{ cm} < x < 3.5 \text{ cm}$, and the cathode is at $5.5 \text{ cm} < x < 7.0 \text{ cm}$. We consider the cases when the gas flow directed from both direction and found that DC discharge glows when the flow direction is from right to left.

The electron and ion number density distributions obtained for $P = 100$ mTorr are represented as bontour plots normalized to 10^9 cm^{-3} in Figs. 2 and 3, respectively. The bulk plasma region extends over 15 and 6 cm along the x and y axes, respectively. The plasma density drops by a factor of 30 from center to periphery. The plasma is almost entirely quasineutral, except for a near surface region. The plasma density maximum is downstream from the cathode sheath toward the anode. The cathode sheath is clearly seen in Fig. 2 because of the absence of low energy electrons. The corresponding electron energy distribution is illustrated by Fig. 4. In the quasineutral region, secondary electrons are thermalized and confined

by an electrostatic potential. The electron energy varies from 3.0 to 1.5 eV between the center and periphery of the bulk plasma. As the secondary electrons emitted from the cathode are accelerated by the strong field of the cathode sheath, their mean energy reaches 300 to 400 eV.

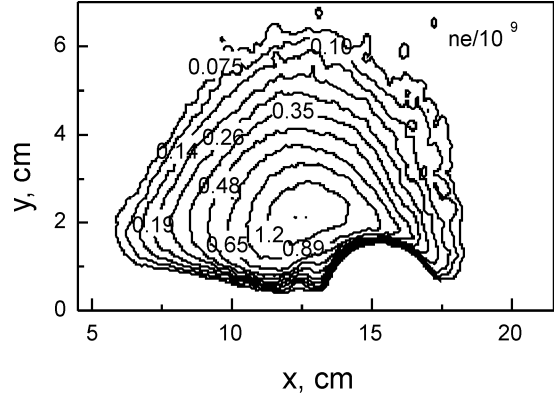


Fig.2. Electron density distribution at a pressure of 100 mTorr: $ne_{\max} = 3 \times 10^9 \text{ cm}^{-3}$; $ne_{\min} = 10^8 \text{ cm}^{-3}$.

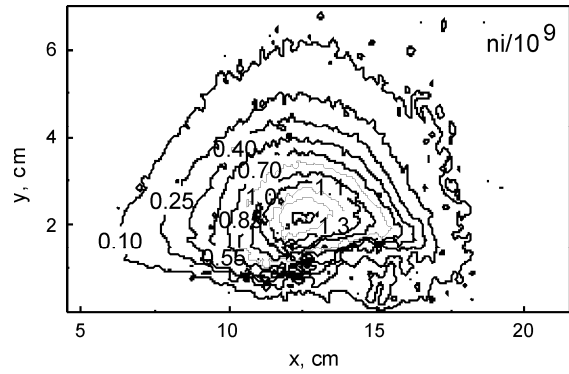


Fig.3. Electron density distribution at a pressure

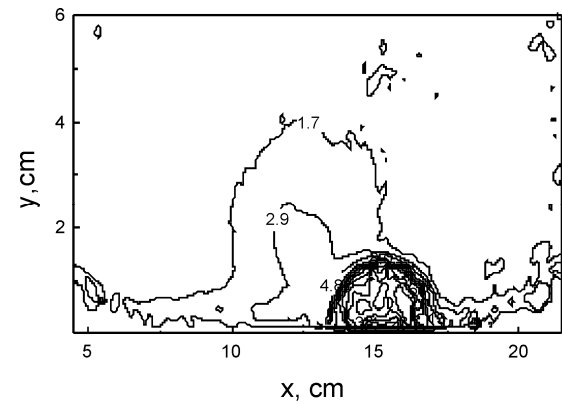


Fig. 4. Electron energy distribution at a pressure of 100 mTorr.

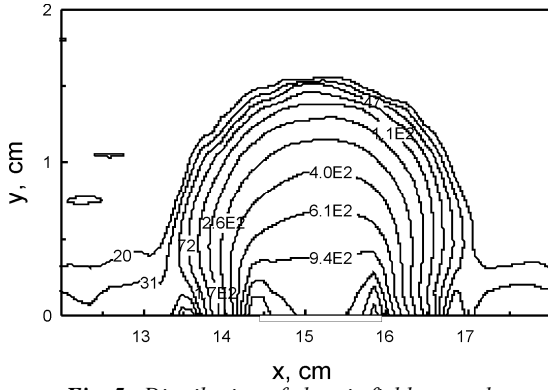


Fig. 5. Distribution of electric field strength
 $E = (E_x^2 + E_y^2)^{1/2}$
 near the cathode at a pressure of 100 mTorr.

Figure 5 shows a contour plot of the electric field $E = (E_x^2 + E_y^2)^{1/2}$ near the cathode. The steepest field gradients are observed at the edges of the cathode.

The electric field strength at the dielectric surface between the electrodes is $E = 51$ cm. According to simulations, the cathode sheath occupies a region of width $l_y = 1.6$ cm separated from the cathode edges by a distance of $l_x = 1.0$ cm. Figure 6 shows the profiles of electric field strength, mean electron energy, and electron and ion number densities at $x = 15.3$ cm, which corresponds to the cathode center. It is clear that the field strength decreases almost linearly from the cathode to the quasineutral region, while the mean electron energy monotonically increases over approximately 0.8 cm. This interval corresponds to the electron energy relaxation length $\lambda = 1/\sigma_{tot} N$, where σ_{tot} is the total cross section for electron impact excitation of N₂ triplet states and ionization of molecular nitrogen, and N is the gas number density. The plasma number density increases in the quasi-neutral region, while the mean electron energy decreases to 2 eV. The ion number density is 3×10^8 cm⁻³ in the cathode sheath and reaches $(1-3) \times 10^9$ cm⁻³ in the quasi-neutral region. When $P = 500$ mTorr and $U = -500$ V, the plasma number density is higher by an order of magnitude, while the cathode sheath is narrower ($l_y = 0.7$ cm), than that at $P = 100$ mTorr. The electron number density distribution at $P = 500$ mTorr is illustrated by the contour plot in Fig. 7. Because of a higher rate of resonant charge transfer between ions and nitrogen molecules, both the shift of the plasma density maximum and the distortion of the cathode sheath are more pronounced than those at $P = 100$ mTorr.

For both gas pressures it is seen that the dielectric barrier surrounding the electrodes has a visible negative potential. This increases the potential barrier for electrons with energy close to

the ionization threshold of N₂ (15.6eV), reducing the rate of highenergy electron loss to the surface and increasing the ionization rate and number density in the bulk plasma.

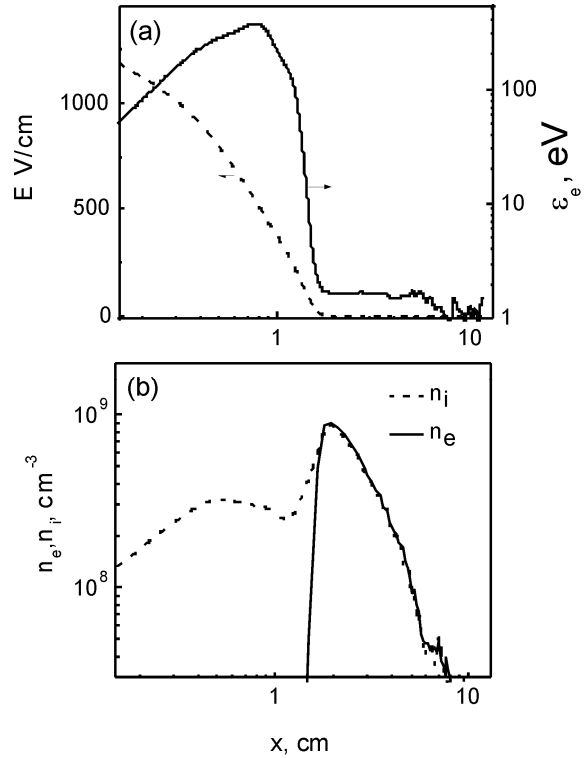


Fig. 6. Distribution along the y axis of (a) electric field strength, mean electron energy, and (b) electron and ion number densities at $x = 15.3$ cm (cathode center) and $P = 100$ mTorr.

Figure 8 shows the distribution of the dielectric surface potential obtained for $P = 500$ mTorr. At this pressure, the plasma density is higher by an order of magnitude and the dielectric surface potential is much higher than those at $P = 100$ mTorr.

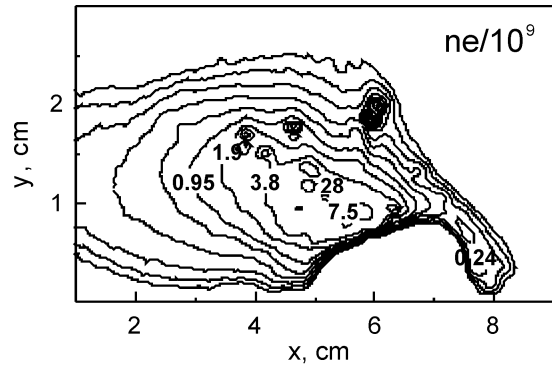


Fig. 7. Electron number density distribution at a pressure of 500 mTorr: $n_{e,max} = 2.6 \times 10^{10}$ cm⁻³; $n_{e,min} = 2.6 \times 10^7$ cm⁻³

The results of kinetic simulations demonstrate the nonlocality of electron energy distribution function (EEDF) as a function of electric field strength even at relatively high gas pressures, such as 500 mTorr. The peak values of mean electron energy and ionization rate are reached at the boundary of the cathode sheath. At lower gas pressures, such as 100 mTorr, ionization mainly occurs outside the cathode sheath. Figures 9 show the ionization rates at $P = 100$ mTorr; the cathode sheath boundary is represented by a dotted line. When the dielectric surface potential is zero at $P = 500$ mTorr, the ionization rate is approximately half that in the case of a self-consistent potential illustrated by Fig. 10.

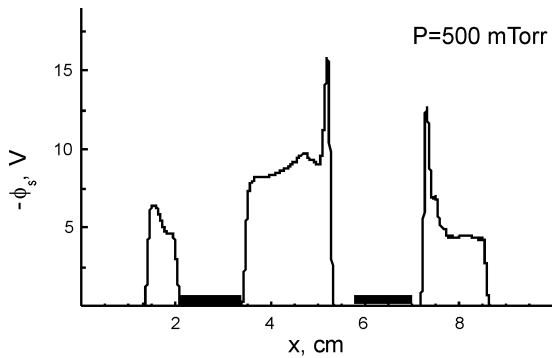


Fig. 8. Potential distributions over the dielectric surface at a pressure of 500 mTorr, $U = -500$ V, and $\gamma = 0.05$.

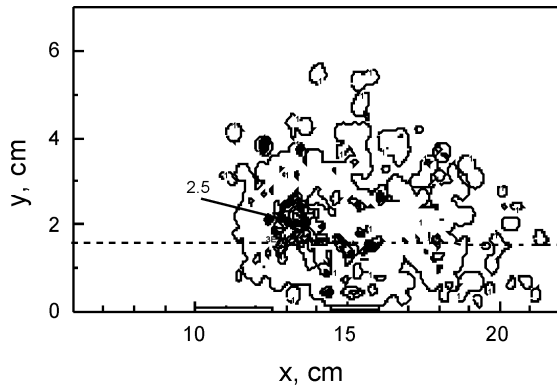


Fig. 9. Electron impact ionization rate v_i normalized to $10^{15} \text{ cm}^{-3} \text{ s}^{-1}$ at $P = 100$ mTorr: $v_{i\text{max}} = 2.5 \times 10^{10} \text{ cm}^{-3} \text{ s}^{-1}$; $v_{i\text{min}} = 10^{12} \text{ cm}^{-3} \text{ s}^{-1}$

Fig. 9. Electron impact ionization rate v_i normalized to $10^{15} \text{ cm}^{-3} \text{ s}^{-1}$ at $P = 100$ mTorr: $v_{i\text{max}} = 2.5 \times 10^{10} \text{ cm}^{-3} \text{ s}^{-1}$; $v_{i\text{min}} = 10^{12} \text{ cm}^{-3} \text{ s}^{-1}$. The results of kinetic simulations demonstrate the nonlocality of electron energy distribution function (EEDF) as a function of electric field strength even at relatively high gas pressures, such as 500 mTorr. The peak values of mean electron energy and ionization rate are reached at the boundary of the cathode sheath. At lower gas pressures, such as potentials. It is obvious that the fraction of high

energy electrons capable of ionizing is larger in the case of a self-consistent ϕ_s . As the surface is approached, the low-energy fraction decreases while the high-energy fraction increases, resulting in a relatively high ionization rate near the dielectric.

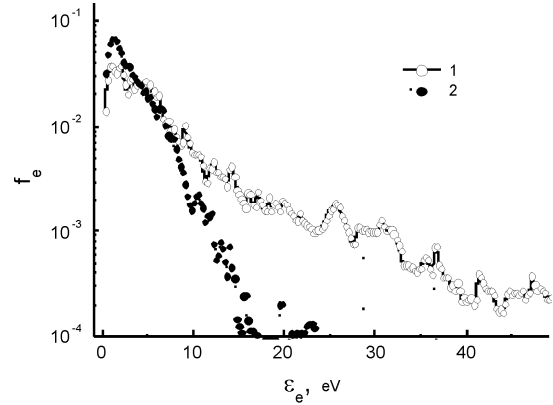


Fig. 10. Electron energy distribution function at $x = 5.3 \text{ cm}$, $y = 0.3 \text{ cm}$ for (1) self-consistent surface potential ϕ_s and (2) $\phi_s = 0$; $P = 500$ mTorr.

The boundary conditions at the dielectric surface strongly affect the electron energy distribution. Figure 10 compares the EEDFs at the point $x = 5.3 \text{ cm}$, $y = 0.3 \text{ cm}$ obtained for self-consistent and zero surface

In conclusions two dimensional kinetic particle in cell simulations are performed to examine the characteristics of dielectric barrier glow discharge at low pressures ($P = 100$ and 500 mTorr). The gas velocity profile is modeled by a function describing a supersonic flow boundary layer. The simulations demonstrate that production of secondary electrons by ion impact on the electrode surface determines both ionization rate and plasma density. The electron energy distribution exhibits nonlocal behavior as function of electric field strength, and ionization occurs outside the cathode sheath. The potential induced on the dielectric surface by fluxes from the bulk plasma is computed. It is shown that the electron energy distribution function at the dielectric surface is determined by the surface potential. An additional negative potential barrier substantially reduces the rate of high-energy electron loss and increases the ionization rate both in the quasi neutral region and near the surface.

ACKNOWLEDGMENTS

This work was supported by the Siberian Division of the Russian Academy of Sciences, interdisciplinary integration project no. 113, 2009.

References

1. A. Klimov, V. Bitiurin, I. Moralev, B. Tolkunov, and K. Zhirnov, in Proceedings of the 46th AIAA Aerospace Sciences Meeting and Exhibit, Reno, NV, United States, 2008 (American Institute of Aeronautics and Astronautics, Reno, 2008), 2008,1411.
2. V. R. Soloviev and V. M. Krivsov, J. Phys. D: Appl. Phys. 42, 125 208 (2009).
3. S. T. Surzhikov, Physical Mechanics of Gas Discharges (Bauman Moscow State Technical University, Moscow, Russia, 2006).
4. C. K. Birdsall and A. B. Langdon, Plasma Physics via Computer Simulation (McGraw-Hill, New York, 1985).
5. Yu. P. Raizer, Gas Discharge Physics (Nauka, Moscow, 1987; Springer, Berlin, 1991).

SLIDING SURFACE DISTRIBUTED NANOSECOND DISCHARGE IN THE LAMINAR AND IN THE TURBULENT BOUNDARY LAYER

Znamenskaya I. and Mursenkova I.V.

M.V. Lomonosov Moscow State University, Faculty of Physics;
znamen@phys.msu.ru, murs_i@mail.ru

Energy deposition into the boundary layer of high-speed gas flow can be used to control the flow around the surface by the influence on the separation zone, the area of laminar-turbulent transition, the area of the interference of the boundary layer with a shock wave [1, 2]. Pulse energy deposition into the boundary layer can be realized effectively using the surface-distributed high-current discharge of nanosecond duration, i.e. the plasma sheet [2]. The analysis of shock dynamics from the area of the discharge showed that this type of discharge provides a high-energy influence on gas flow including supersonic flow with shock wave [3]. The sliding surface discharge having duration of about 200 ns and an area of 30×1 mm² was initiated at the channel walls of the shock tube in a supersonic air flow behind the plane shock wave (flow Mach number was up to 1.5, the pressure of 150-400 Torr). The duration of homogeneous flow behind the shock wave was 600-250 μ s, its length was about 30 cm. The transversal discharge was initiated in the laminar and turbulent areas of the boundary layer (laminar-turbulent transition occurs at a distance of 10-15 cm from the shock front). The discharge current reached 1000 A when a voltage was of 25 kV.

The energy contribution into gas occurs instantly in time t_{dis} at initiation of plasma sheet in comparison with characteristic gasdynamics time t_{fl} . Research of molecular kinetics for this type of electric discharge has shown that sufficient part of discharge electric energy is converted directly in

translational degrees of freedom. Thus the quick discharge energy input produces sound disturbances and even shock waves in gas. The Damkohler number applied for the process of that type (flow characteristic time t_{fl} versus time of gas ionization t_{dis}) is very big ($10 \cdot 10^3$). Initiation of a nanosecond discharge greatly influence the structure of gas-dynamic flow. Because of the quick input of energy into the thin near surface gas layer, shock waves arise. The disturbances arise it time t_{fl} - after flow luminescence interval t_{dis} and can not influence plasma glow image. They were visualized by shadow method for both laminar and turbulent regions for the boundary layer. During registration of discharge radiation structure of the near surface

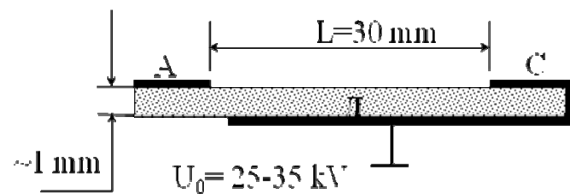


Fig. 1.

flow does not change, because it has significantly less duration than the characteristic gasdynamics time in the shock tube. This enables to visualize "instantaneously" the structure of the surface flow by plasma sheet radiation. It is shown that the type

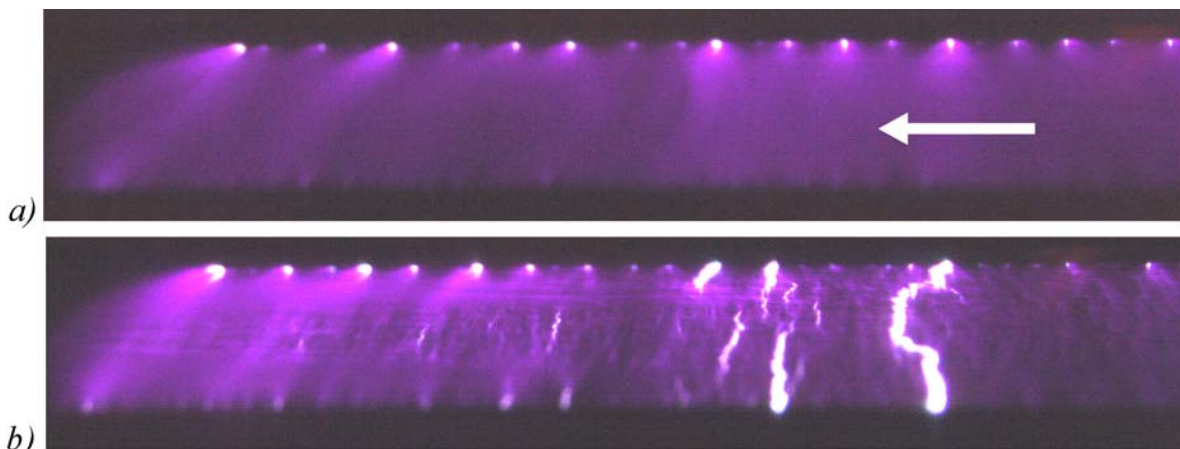


Fig. 2. Gas discharge plasma radiation in the supersonic flow boundary layer: a) in the laminar area, b) in the turbulent area. The arrow shows the flow direction.

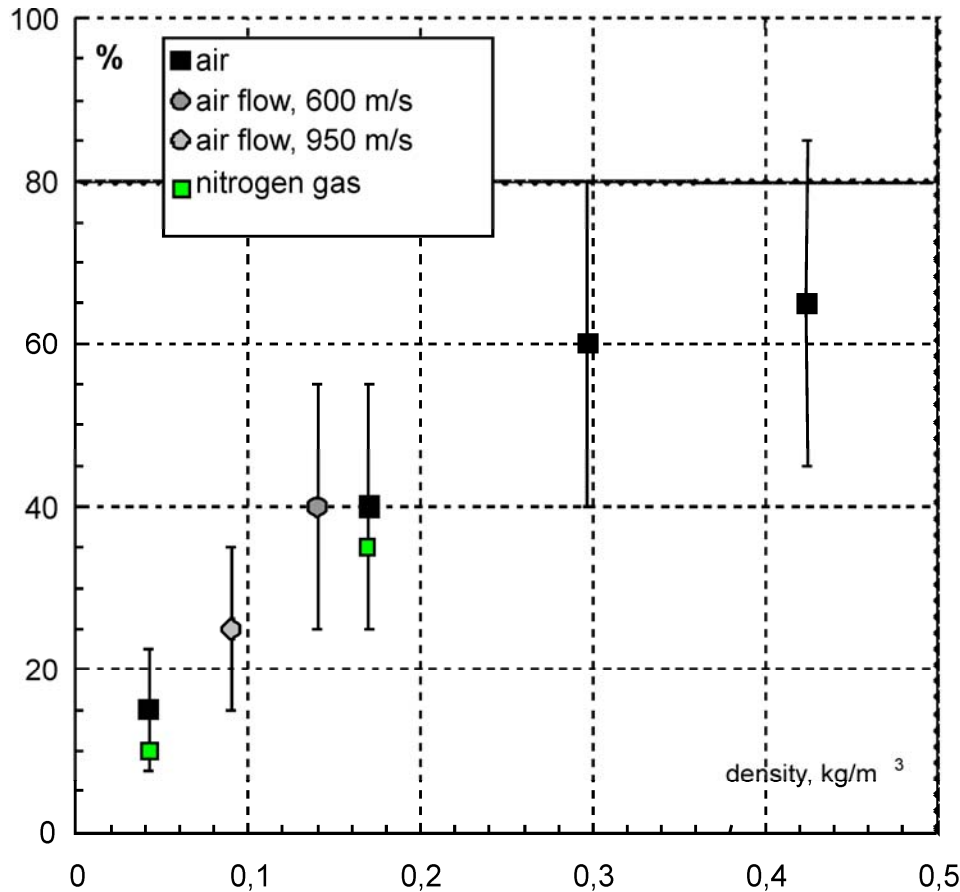


Fig. 3. Rate of electric energy, converted to heat during discharge current time.

of the boundary layer influences the character of development of discharge channels across a flow. Basic plasma instabilities do not have time to develop over the discharge time (less than 1 μ s). It distinguishes the plasma sheet from slower discharges. Image analysis of the integral discharge radiation images showed that behind the shock front (in the area of laminar boundary layer) discharge plasma radiation diffusely homogenous and smooth, without visible breaks of radiation. In the turbulent area of the boundary layer the discharge radiation becomes inhomogeneous with the separate curved plasma channels. The turbulent gas flow is ionized with the formation of plasma structures; their scale corresponds with the scale of flow turbulence.

It was shown that the energy input into the area of the boundary layer of gas is comparable with the enthalpy of the gas behind the shock wave. The energy input reached 70-110% of enthalpy during the discharge both in the laminar and the turbulent layer. The thickness of the plasma sheet (the region of energy release) in a flow of about 0,5 mm, i.e. scale of the thickness of the boundary layer. Change of the type of the boundary layer does not influence considerably the magnitude and uniformity of the energy contribution into the flow in the investigated range of parameters. The

applicability of the fast homogeneous energy transfer model to analyze the influence of discharge on the flow is reflected in the identity of the dynamics of shock waves from the discharge area for both types of boundary layer. Turbulence of boundary layer does not significantly affect the uniformity of energy deposition. Inverse problem was solved and fitting method was used in order to find rate of electric energy, converted to heat during discharge current time versus gas density. As the mathematical model for flow simulation, the system of two-dimensional time-dependent Navier-Stokes equations were taken [3] with the corresponding boundary conditions. Inverse dynamic problem was solved: in comparing CFD and shadow images, the gas dynamic configurations of the shock wave produced by surface discharge were analyzed. On Fig.2 rate of electric energy, converted to heat during discharge current time versus gas density is shown. Rate of electric energy, converted to heat increases from 15% up to 60-65% at increasing of density 0.05-0.45 kg/m³. It should be connected with changing of kinetic processes in plasma of sliding surface discharge at changing of E/N . At E/N increasing (and gas density decreasing) rate of ionization, dissociating and electron energy excitation processes rises.

Thus, the quantitative research of the shock waves dynamics from the area of the discharge showed that this type of discharge – transversal distributed sliding surface discharge provides a high-energy pulse influence on both the laminar and the turbulent boundary layer.

This work was supported by the grant RFBR 08-08-00903-a.

References

1. Larin O.B., Levin V.A. Boundary Layer Separation in a Laminar Supersonic Flow with Energy Supply Source. // *Pis'ma v Zhurnal Tekhnicheskoi Fiziki*, 2008. Vol. 34. No. 5. P.1-6.
2. Znamenskaya I.A., Latfullin D.F., Mursenkova I.V. The Surface Transverse Distributed Nanosecond Discharge in the Supersonic Boundary Layer. // *Doklady Akademii Nauk*, 2009. Vol. 427. No. 1. P.32-34.
3. Ivanov I., Kryukov I., Orlov D., Znamenskaya I. Investigations of shock wave interaction with nanosecond surface discharge // *Experiments in Fluids*, 2010, Vol 48, Is.4, P. 607-613.
4. Bazhenova T.V., Znamenskaya I.A., Lutsky A.E., Mursenkova I.V. An investigation of surface energy input to gas during initiation of a nanosecond distributed surface discharge. *High Temperature*. 2007. T. 45. № 4. C. 523-530.

PECULIARITIES OF FLOW PAST BODIES IN THE PRESENCE OF STEADY AND PULSING TOROIDAL-TYPE UPSTREAM ENERGY DEPOSITION

P.Yu. Georgievsky

Institute for Mechanics of Moscow State University,
1 Michurinsky prospect, Moscow 119192, Russia, georgi@imec.msu.ru

V.A. Levin

Institute for Automation and Control Processes of Russian Academy of Sciences,
5 Radio street, Vladivostok 690041, Russia, levin@iacp.dvo.ru

Comparative numerical investigation of a supersonic flow past blunt and streamlined bodies in the presence of steady and pulsing toroidal-type upstream energy deposition was carried out. Depending on the geometry of the energy deposition region and the body, different regimes were observed. The conditions for equivalence of steady and pulse-periodic modes of the energy deposition are determined and the consequences of these conditions disturbance were estimated.

Previously the possibility of control of flows past blunt and streamlined bodies by the energy deposition in a small region, located upstream, was demonstrated [1]. The interaction of a thin high temperature wake, which appears downstream an energy deposition region, with a shock layer ahead of bodies was mentioned as a reason for front separation zones formation. In this case the efficiency of wave drag reduction could be infinitely high because a static pressure inside a front separation zone is determined by a dynamic pressure value inside the temperature wake but not by the temperature wake thickness [2]. However a serious conceivable problem was volume and shift instabilities of front separation zones, which were observed during numerical simulations for small energy deposition regions. Some methods were proposed to avoid these instabilities [3].

The idea to use the energy deposition in a toroidal-type region for wave drag reduction was formulated in [4]. The supersonic flows for different energy deposition regions geometry (ellipsoidal and toroidal-type) located upstream of blunt bodies were examined in [5]. The effect of Mach reflection of converging hanging shock wave near the symmetry axes was mentioned as a key factor for restructuring of flow regimes.

In the present paper comparative numerical investigation of a supersonic flow both past blunt and streamlined bodies in the presence of steady and pulsing toroidal-type upstream energy deposition was carried out. Depending on the geometry of the energy deposition region and the body, different regimes were observed. The conditions for equivalence of steady and pulse-periodic modes of the energy deposition are determined and the consequences of these conditions disturbance were estimated.

1. Formulation of the problem

The Euler equations were used for numerical simulation of unsteady inviscid flow in the presence

of the localized energy deposition (here the equations are presented in vector form):

$$\frac{\partial \rho}{\partial t} + \operatorname{div} \rho \mathbf{V} = 0; \quad \frac{d\mathbf{V}}{dt} + \frac{1}{\rho} \operatorname{grad} p = 0;$$

$$\frac{\partial e}{\partial t} + \operatorname{div} (e + p) \mathbf{V} = \rho Q; \quad e = \frac{p}{\gamma - 1} + \frac{\rho}{2} \mathbf{V}^2$$

Here p is pressure, ρ – density, \mathbf{V} – velocity vector, e – the total energy of a volume gas unit. Axially symmetrical flows were examined, but depending on the problem specific cylindrical r, z or spherical R, θ coordinates were used. The energy deposition was assumed to be the predetermined function of coordinates and time – that is the essence of the “energy source” mathematical model. The power input per a mass unit Q for cylindrical coordinates z, r is determined by the relationship:

$$Q(r, z, t) = Q_0 f(t) \exp \left(- \left(\frac{r - r_0}{\Delta r(t)} \right)^2 - \left(\frac{z - z_0}{\Delta z(t)} \right)^2 \right) \quad (1)$$

Here Q_0 – intensity, $\Delta r, \Delta z$ – radiuses of “effective” section, r_0, z_0 – location (for toroidal region – $r_0 > 0$). The space distribution for the power input is of Gaussian type, so that $Q > 0$ for each point in the calculation domain. But it is not a problem for a numerical simulation because of exponential decreasing of the power input with the distance from the energy source center.

For steady energy deposition regime the power input was “switched on” in the undisturbed supersonic flow (for all cases under the consideration – $M_\infty = 2, \gamma = 1.4$):

$$f(t) = \begin{cases} 0, & t < 0 \\ 1, & t \geq 0 \end{cases} \quad (2)$$

Pulse-periodic unsteady regimes with rectangular pulses of the period duration T and the pulse duration τ were examined:

$$f(t) = \begin{cases} T/\tau, & 0 \leq \text{mod}(t, T) \leq \tau \\ 0, & \tau < \text{mod}(t, T) < T \end{cases} \quad (3)$$

The total power input W is determined not only by the energy source parameters but also by the density distribution and therefore could be found only during the numerical simulation process:

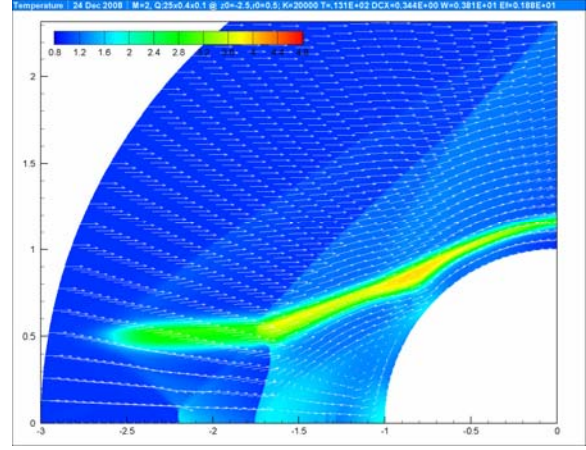
$$W(t) = 2\pi \iint \rho Q r dr dz . \quad (4)$$

All values are dimensionless. Scales for different physical parameters could be combined from the basic scales: p_∞, ρ_∞ – the static pressure and the density of the undisturbed upstream flow and l_∞ – some linear scale (typically the radius of bodies mid-section). For example, the scale for the velocity is $(p_\infty/\rho_\infty)^{1/2}$, the scale for the time – $l_\infty (p_\infty/\rho_\infty)^{-1/2}$, the scale for the power input per mass unit Q – $(p_\infty/\rho_\infty)^{3/2} l_\infty^{-1}$, the scale for the total power input W – $p_\infty l_\infty^2 (p_\infty/\rho_\infty)^{1/2}$ etc.

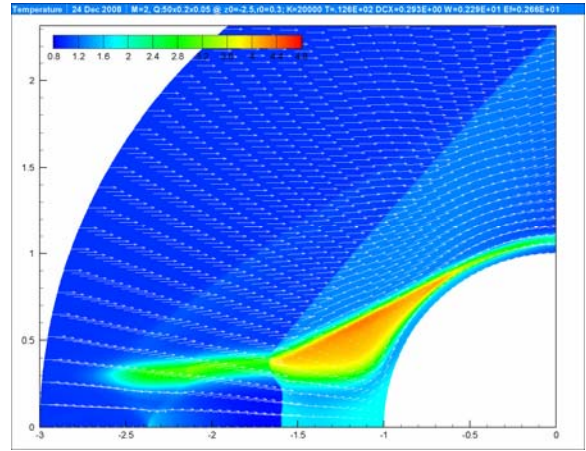
The wave drag coefficient c_x was determined as an integral of the extra pressure over the body surface with respect to the normal vector direction. The efficiency coefficient η could be defined as a ratio of the saved power to the total power input W (S_B – the body midsection):

$$c_x = \frac{2}{\gamma M_\infty^2 S_B} \int (p-1) 2\pi r dr, \quad \eta = \frac{\gamma^{3/2} M_\infty^3 S_B \Delta c_x}{2W} \quad (5)$$

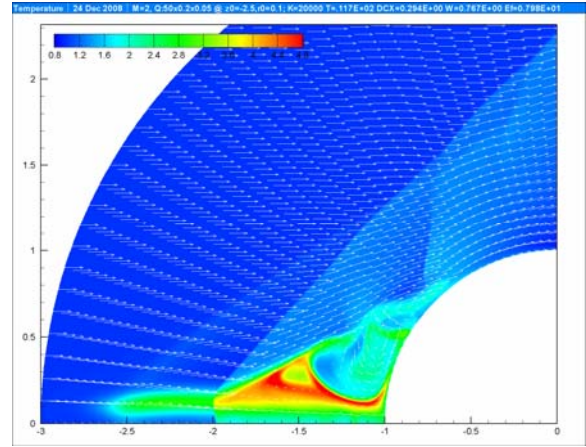
The explicit MacCormack finite difference method [6] of the second order accuracy with coordinates and time was used for the numerical simulation. Discontinuities (shock waves and tangential surfaces) were not allocated specially but calculated using regular algorithm. Special procedures were applied to ensure the impermeability conditions on the body surface and the condition of the free outlet – on the outgoing surface. On the incoming surface the flow was uniform. The time marching procedure was used to establish steady solutions or to examine unsteady processes. Courant–Friedrichs–Lewy stability condition was used to determine the time step. Spherical coordinates were used for blunt bodies and cylindrical coordinates – for streamlined bodies. Mesh resolution typically was 400x360 points for spherical coordinates R, θ and 400x800 for cylindrical coordinates r, z .



a) $Q_0 = 50, \Delta z = 0.2, \Delta r = 0.05, z_0 = -2.5, r_0 = 0.5$
 $c_x = 0.44, \Delta c_x = 44\%, W = 3.8, \eta = 1.9$



b) $Q_0 = 50, \Delta z = 0.2, \Delta r = 0.05, z_0 = -2.5, r_0 = 0.3$
 $c_x = 0.50, \Delta c_x = 37\%, W = 2.3, \eta = 2.7$



c) $Q_0 = 50, \Delta z = 0.2, \Delta r = 0.05, z_0 = -2.5, r_0 = 0.1$
 $c_x = 0.50, \Delta c_x = 37\%, W = 0.77, \eta = 8.0$

Fig. 1 The supersonic flow past sphere in the presence of the toroidal-type energy deposition: formation of front separation zone (a), temperature wake “explosion” (b), pulsing separation zone (c).

2. Regimes of steady flows for toroidal-type energy deposition

The supersonic flow past sphere (initial wave drag coefficient $c_x^0 = 0.78$) in the presence of upstream toroidal-type energy deposition was examined. Depending on the geometrical parameters of the region different regimes were observed during numerical experiments (Fig. 1). For the situation when the toroid radius is large enough ($r_0 = 0.5$) – Mach reflection of the converging hanging shock wave near the symmetry axes was realized (Fig. 1a). Because of the total pressure defect near the symmetry axes downstream the Mach stem the front separation zone ahead of the sphere surface appears. For smaller radius ($r_0 = 0.3$) when the Mach stem is small the sudden enlargement of the high temperature wake during its interaction with the bow shock ahead of the sphere – “wake explosion”, was observed (Fig. 1b). For the small radius ($r_0 = 0.1$) the unsteady pulsing front separation region of special type (with central high enthalpy stream) was formed (Fig. 1c).

Thus new stable regimes for the supersonic flow past blunt bodies in the presence of upstream toroidal-type energy deposition regions were determined: the regime of front separation zone formation (Fig. 1a) and the regime of “wake explosion” (Fig. 1b). It is essential that these regimes are characterized by the appearance of tube-type high enthalpy cold stream, which becomes an isolator for the body surface from the high temperature wake, spreading inside a shock layer.

For all cases under the consideration the wave drag reduction was considerable (35% – 45%). The efficiency depends on the toroid radius – the larger is the radius, the less is the efficiency (the coefficient was varied from $\eta = 2$ to $\eta = 8$).

The supersonic flow past streamlined ogival-type bodies was also examined. The surface of the body was formed by rotating of the circle arc around the symmetry axes. The initial wave drag coefficient was $c_x^0 = 0.37$ – much less than the one for blunt bodies. Previously the formation of front separation zones for streamlined bodies because of the interaction of a shock layer with subsonic temperature wake, which was appeared downstream ellipsoidal energy deposition region, was observed [1,2].

The formation of front separation zones was not observed for supersonic flows past streamlined bodies with upstream toroidal-type energy deposition regions. The flow over body was regular (with attached shock wave at body apex) regardless of the toroid radius (Fig. 2). The appearing of complicated shock wave structures – “double Mach reflection” (Fig. 2a) or “single Mach reflection” (Fig. 2b) during the interaction of the temperature wake with the shock layer was typical.

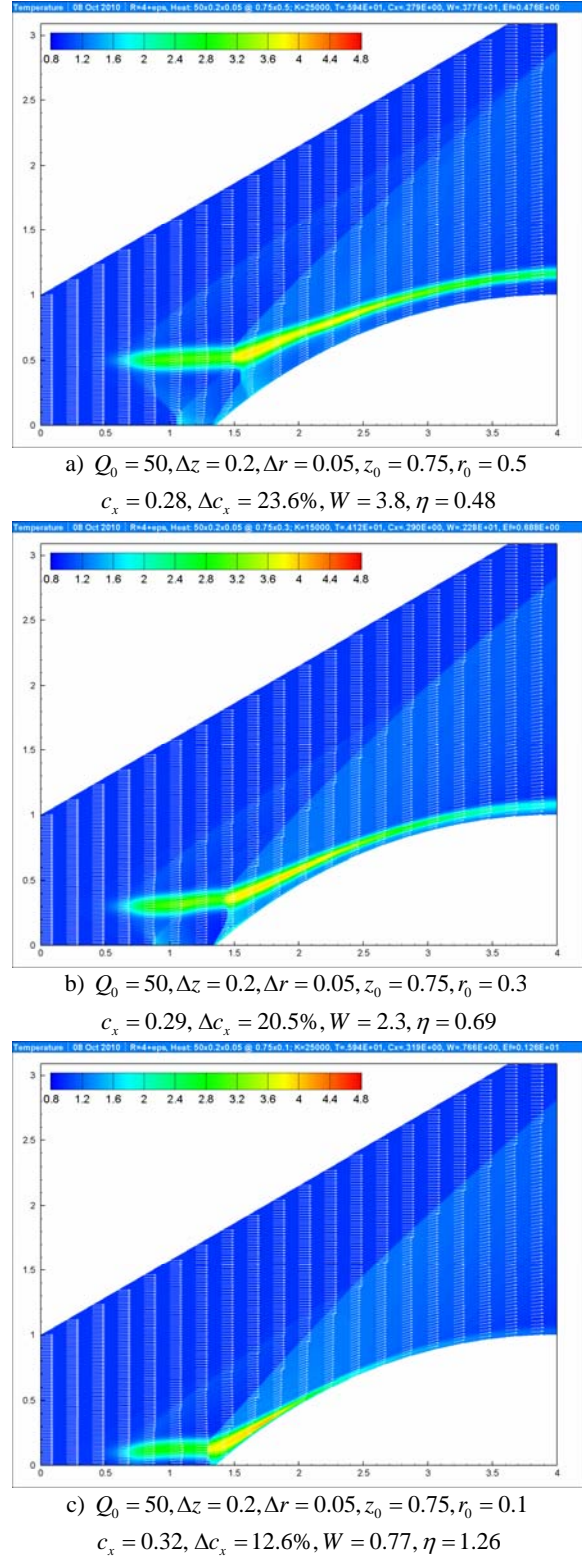


Fig. 2 The supersonic flow past streamlined body in the presence of toroidal-type energy deposition: double Mach reflection (a), single Mach reflection (b), regular interaction (c).

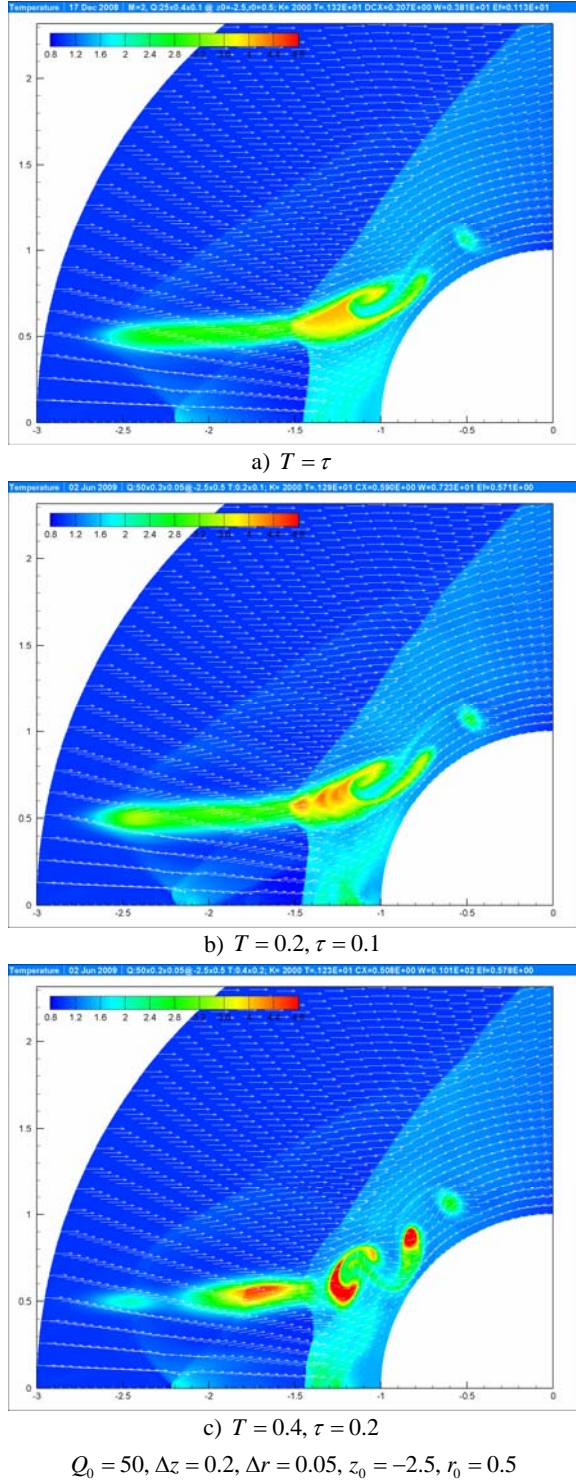


Fig. 3 Vortex generation for early stage of an interaction of a growing high temperature cloud with a shock layer ahead of a sphere for steady (a), quasi-stationary (b) and essentially pulsing (c) regimes of energy input.

As before for blunt bodies the stability of gas-dynamic structures and the appearance of isolating tube-type high enthalpy cold stream should be mentioned as the positive factor. The negative factor is low efficiency for wave drag reduction. When de-

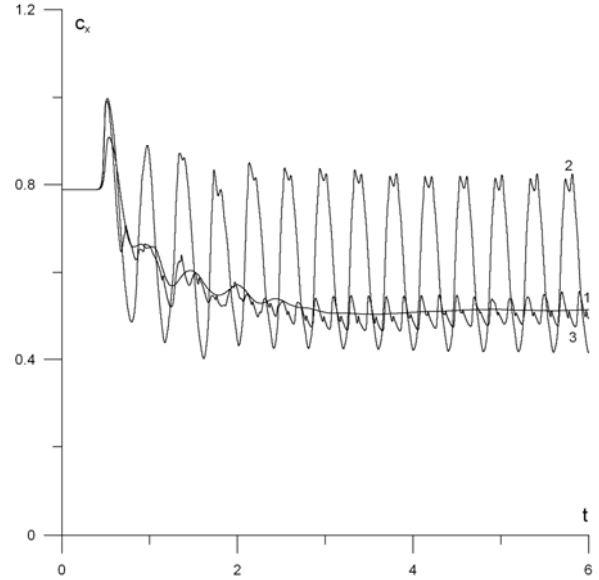


Fig. 4 Dynamics of wave drag reduction with time for steady (1), essentially pulsing (2) and quasi-stationary regimes (3) of toroidal-type energy deposition.

creasing the toroid radius from $r_0 = 0.5$ to $r_0 = 0.1$ the wave drag reduction decreases from 24% to 12% whereas the efficiency coefficient increases from $\eta = 0.5$ up to $\eta = 1.25$.

3. Pulse-periodic regimes of toroidal-type energy deposition

Numerical investigation of supersonic flow past blunt bodies in the presence of a steady and pulse-periodic toroidal-type upstream energy deposition was carried out. Pulse-periodic unsteady regimes (3) with rectangular pulses of the period duration T and the pulse duration $\tau = T/2$ were examined.

The sufficient condition for the quasi-stationary regime realization is the continuity of a temperature wake, which appears downstream the energy deposition region. So the simplest estimation for the critical period duration T^* could be delivered as follows. A drift of a temperature cloud by an ambient flow during the time between pulses should be smaller than the length of the energy deposition region:

$$\sqrt{\gamma} M_\infty (T^* - \tau) \leq 2\Delta z \quad (6)$$

The appearance of vortices for an early stage of an interaction of a growing high temperature cloud with a shock layer ahead of a body is typical both for steady and pulse-periodic (quasi-stationary and essentially pulsing) energy deposition regimes (Fig. 3). The reason for this effect is the interaction of the tube-type temperature wake, which is formed down-

stream the energy deposition toroidal region, with the bow shock wave ahead of the body. Flow structures for quasi-stationary mode (b) are very close to the steady ones (a).

Flow structures for essentially unsteady mode (c) differ from steady (a) and quasi-steady (b) analogs – every pulse generate vortex inside the shock layer. The generation of vortex structures during a whole calculation time is typical for essentially pulsing regimes, when the conditions for quasi-stationary regime realization were not satisfied.

The dynamics of wave drag coefficient c_x with time t for steady, essentially unsteady and quasi-stationary time modes are presented in Fig. 4. The quasi-stationary mode function (3) repeats steady mode function (1) within some small oscillations. So the transitional dynamics during the numerical time-marching estimation process for quasi-stationary and steady regimes are equivalent. The amplitude pulsations for the essentially unsteady mode (2) are very large and pick values are even higher than the initial wave drag level.

So the equivalence of steady and pulse-periodic regimes of the energy deposition in toroidal region is the necessary condition for effective wave drag reduction – the pulse period should be shorter than critical to secure quasi-stationary regime of the energy deposition. For period longer than critical essentially unsteady mode is realized, vortex generation in the shock layer is taking place and pulsations of wave drag are inadmissibly large. The critical period duration is proportional to the elongation of the energy deposition region.

Conclusions

Comparative numerical investigation of a supersonic flow past blunt and streamlined bodies in the presence of steady and pulsing toroidal-type upstream energy deposition was carried out. Depending on the geometry of the energy deposition region and the body, different regimes were observed. The wave drag reduction was considerable and effective for blunt bodies but ineffective for streamlined bodies. The positive effect is the stability of gasdynamic structures and the appearance of tube-type high enthalpy cold stream, which becomes an isolator for the body surface from the high temperature wake. The conditions for equivalence of steady and pulse-

periodic modes of the energy deposition are determined. To realize quasi-stationary regimes the period duration should be less than critical value, which is proportional to the elongation of the energy deposition region. The realization of quasi-stationary regimes of an energy deposition is the important condition for effective wave drag reduction.

Acknowledgments

These investigations were financially supported by Russian Foundation for Basic Researches (grant 08-01-00033), Ministry of Education and Sciences of Russian Federation (grant NSh-8424.2010.1) and Russian Academy of Sciences (as a Part of Special Program for Support of Fundamental Researches).

References

1. Georgievskii P.Yu., Levin V.A. Control of the Flow past Bodies Using Localized Energy Addition to the Supersonic Oncoming Flow // *Fluid Dynamics*. 2003. Vol. 38. No. 5. P. 154–167.
2. P.Yu. Georgievsky, V.A. Levin, R.R. Gadelev, O.G. Sutyurin Control of Front Separation Regions for Supersonic Flows over Blunt and Streamlined Bodies by Upstream Energy Deposition // *Proc. 7th International Workshop on Magneto-Plasma Aerodynamics* / Ed. V.A. Bityurin, 2007. P. 79–86.
3. Georgievsky P.Yu., Levin V.A., Sutyurin O.G. Stability Problem for Front Separation Regions Formation by the Localized Energy Deposition Upstream of the Body // *Proc. 3rd School-Seminar on Magneto-Plasma Aerodynamics* / Ed. V.A. Bityurin, 2008. P. 115–182 (in Russian).
4. Yuriev A., Pirogov S., Savischenko N., Ryizhov E. Hypersonic Flow over a Body with a Torus-Shaped Energy Addition Region Ahead of It // *AIAA Paper 2001–3054*, 2001.
5. Georgievsky P.Yu., Levin V.A. Regimes of Flow over Bodies for Upstream Energy Deposition of Various Geometrical Configurations // *Proc. 8th International Workshop on Magneto-Plasma Aerodynamics* / Ed. V.A. Bityurin, 2009. 5p.
6. McCormack R.W. The Effect of Viscosity in Hypervelocity Impact Cratering // *AIAA Paper 1969–354*, 1969, 7 p.

THERMAL CHOKING OF A CYLINDRICAL OR SPHERICAL MASS SOURCE

Kogan M.N., Kucherov A.N.

Central Aerohydrodynamic Institute n.a. N.E. Zhukovsky,
140180 Zhukovsky, Moscow region, Russia

e-mail: mkogan@aerocentr.msk.su, ank@aerocentr.msk.su, Fax: (495) 7776332

The flow choking by heat addition in a finite fixed layer (thermal crisis) in the flow field of a cylindrical or a spherical mass source is investigated. Choking is defined by the value of Mach number equal to unity at the back section of the energy addition layer or at the section that is very close to the back section. Distinction from the thermal crisis in the one-dimensional uniform gas flow is under consideration. It is shown that situations exist when Mach number takes its extremal value, which is close to unity, at some section inside the heat addition region, then after initial growth it diminishes, and after initial decrease it increases. Examples of thermal crisis are given for different energy release laws, for the source and the sink, to the stagnation region and to vacuum. Asymptotic solutions near such peculiar sections with the changing Mach number derivation sign are investigated. Common regularities are outlined for relative values of energy parameters and coordinates of the peculiar section in the case of heat addition per unit mass and per unit volume, for the source to the stagnation region and to vacuum, for cylindrical and spherical sources, at variations of energy addition region location. Evaluation is made for the influence of circulation in the cylindrical mass vortex-source on flow choking by energy addition.

1. Introduction

In reference [1] identities and distinctions of stationary flows with heat sources for three-, two-, and one-dimensional cases are examined. The threshold of shock wave formation is investigated, and the regime of continuous (without shock waves) transition through the sonic speed is studied [2]. The dependencies of the mentioned phenomena on similarity numbers E , Q (energy parameter E for heat addition per unit volume, or Q - per unit mass), adiabatic index γ , and on perpendicular-longitudinal sizes of the heat source are studied. The phenomenon of flow choking (thermal crisis) for the one-dimensional stationary stream is noted [3,4]. A principal physical difference is shown between the one-dimensional case and the two- or three-dimensional ones [1].

At cylindrical or spherical sources [5-8] we can also prescribe the heat addition $g(r)$ per unit mass or per unit volume in some layer of thickness d . Energy sources may be chemical reactions, electrical discharge, [9-11], laser radiation [12-14].

As the analysis shows stationary flows (cylindrical or spherical source/sink), that depend on one coordinate have characteristic distinctions [15]. The distinction is the greater number of possible variants: flow to vacuum, to stagnation region, from stagnation zone, from the space of a rarified gas (from vacuum). The Mach number of the flow can vary not only due to heat addition but due to space divergence/convergence also. The investigation of E - and Q - variants of the energy increase process aimed at achieving Mach number values equal to unity at the back section of the energy addition region $r_{cr}=r_2$ or $r_{cr}=r_1$, showed that situations exist, in

which, when energy parameters E , Q slightly differ from their critical values, the Mach number is very close to unity near the critical section $r^* < r_2$ at some coordinate r_Δ , being close to r^* , and simultaneously the Mach number derivation becomes equal to zero $dM(r_\Delta)/dr=0$. In this section the value of M_Δ is extremal and in subsequent sections the Mach number varies in the opposite direction as compared with Mach number variations before the section $r=r_\Delta$. Strictly speaking by mathematics the Mach number is as close to unity as possible but not equal to unity. The sections r_Δ and r^* are indistinguishable by physics. The subsonic flow accelerating before the section r_Δ starts decelerating, and the supersonic flow decelerating before $r < r_\Delta$ starts accelerating. The thermal crisis realizes at the section r^* and is impossible in the back section r_2 . This characteristic feature of the thermal crisis in the flow field of a cylindrical or spherical source seems to be essential both in theoretical and in applied aspects. For example, one can economize energy by eliminating a part of the energy addition region (r^* , r_2), if the aim of the heat addition is to realize the thermal crisis, to achieve the value of Mach number equal to unity $M=1$.

2. Statement of the Problem

The conservation equations of gas mass, momentum, energy in physical variables are:

$$\frac{1}{\rho} \frac{d\rho}{dr} + \frac{1}{u} \frac{du}{dr} + \frac{n}{r} = 0 \quad (1)$$

$$\rho u \frac{du}{dr} + \frac{dp}{dr} = 0 \quad (2)$$

$$u \frac{dp}{dr} - u \frac{\mathcal{P}}{\rho} \frac{d\rho}{dr} = (\gamma - 1)g(r) =$$

$$= (\gamma - 1)f(r) \times \begin{cases} g_0 \\ q_0 \rho(r) \end{cases} \quad (3)$$

Here ρ is the density, p is the pressure, u is the gas velocity, $n=1,2$ for the cylindrical or spherical source accordingly; g_0, q_0 are characteristic intensities of heat addition per unit volume W/m^3 or per unit mass W/kg .

Without energy addition $g(r)=0$, conservation equations (1)-(3) give the integral of source mass flow m_0 , the isentropic condition $p/\rho^\gamma = \text{const}$ and the integral of total gas enthalpy H_0 (J/kg):

$$2^n \pi r^n \rho u = m_0, \quad \frac{p}{p_0} = \left(\frac{\rho}{\rho_0} \right)^\gamma, \quad (4)$$

$$H = \frac{\mathcal{P}}{(\gamma - 1)\rho} + \frac{u^2}{2} = \frac{u_0^2}{2} \equiv \frac{\mathcal{P}_0}{(\gamma - 1)\rho_0}$$

Substituting $u(\rho(r)), p(\rho(r))$ in the total enthalpy conservation equation, we find an implicit solution $r(\rho)$ and therefore functions $u(r), p(r)$:

$$r = \left(\frac{m_0^2}{2^{2n} \pi^2 u_0^2 \rho^2 \left(1 - (\rho/\rho_0)^\gamma \right)} \right)^{1/2n} \quad (5)$$

Let us nondimensionalize the equations and define similarity numbers. We take values p_0, ρ_0, u_0 as characteristic gasdynamic values, that are the maximal pressure, density and velocity without heat addition ($u \rightarrow 0, p \rightarrow p_0, \rho \rightarrow \rho_0$ at $r \rightarrow \infty$, the flow stream to the stagnation region; $p \rightarrow 0, \rho \rightarrow 0, u \rightarrow u_0 = [2\gamma p_0/(\gamma - 1)\rho_0]^{1/2}$ at $r \rightarrow \infty$, flow stream to vacuum) and the minimal radius r_0 , where the Mach number $M(r_0)=1$ [6-8].

Further we denote values $u/u_0, p/p_0, \rho/\rho_0, r/r_0$ as u, p, ρ, r . We rewrite nondimensional equations (1-3) in the following form:

$$\frac{1}{\rho} \frac{d\rho}{dr} + \frac{1}{u} \frac{du}{dr} + \frac{n}{r} = 0, \quad (6)$$

$$r^n \rho u = m, \quad (7)$$

$$\rho u \frac{du}{dr} + \frac{\gamma - 1}{2\gamma} \frac{dp}{dr} = 0, \quad (8)$$

$$\frac{1}{p} \frac{dp}{dr} - \frac{\gamma}{\rho} \frac{d\rho}{dr} = \frac{f(r)}{up} \times \begin{cases} E \\ Q\rho(r) \end{cases}, \quad (9)$$

$$\frac{p(r)}{\rho(r)} + u^2(r) = \varphi(r) \quad (10)$$

Here (7), (10) are the integrals of mass and energy conservation equations, E, Q are the energy parameters (the main similarity numbers of the problem), moreover

$$m = \frac{m_0}{2^n \pi r_0^n \rho_0 u_0} = \left(\frac{2}{\gamma + 1} \right)^{1/(\gamma - 1)} \left(\frac{\gamma - 1}{\gamma + 1} \right)^{1/2}, \quad (11)$$

$$\varphi(r) = 1 + \frac{1}{\gamma m} \times \begin{cases} EF(r) \\ QF_\rho(r) \end{cases}, \quad (12)$$

$$E = \frac{(\gamma - 1)g_0 r_0}{u_0 p_0}, \quad (13)$$

$$Q = \frac{(\gamma - 1)\rho_0 q_0 r_0}{u_0 p_0}, \quad (14)$$

where the dimensionless mass flow value m is found using the condition $dr/d\rho=0$ of the minimal radius, and functions $F(r), F_\rho(r)$ are integrals:

$$F(r) = \int_{r_1}^r r^n f dr, \quad F_\rho(r) = \int_{r_1}^r r^n \rho f dr \quad (15)$$

The function $f(r)$ is normalized, so that the integral by space of f is equal to the total source power W_0 :

$$W_0 = g_0 r_0^{n+1} 2^n \pi \int_{r_1}^{r_2} f r^n dr = g_0 r_0^{n+1} = q_0 \rho_0 r_0^{n+1},$$

$$2^n \pi \int_{r_1}^{r_2} f r^n dr = 1 \quad (16)$$

We took the value q_0 equal to $q_0 = g_0/\rho_0$. Due to the fact that in the Q -variant (heat addition prescribed per unit mass) the intensity function of heat source $f(r)$ under the symbol of integral is multiplied by the density value ρ , which is less than unity, the total energy added to gas W_{add} is less than W_0 :

$$W_{add} = q_0 \rho_0 r_0^{n+1} 2^n \pi \int_{r_1}^{r_2} \rho f r^n dr < g_0 r_0^{n+1} = W_0$$

3. Examples

Let us consider specific laws of heat addition. Uniform heat addition:

$$f = C = \frac{n+1}{2^n \pi \{r_2^{n+1} - r_1^{n+1}\}}, \quad (17)$$

$$F(r) = C \frac{r^{n+1} - r_1^{n+1}}{n+1}, \quad F_\rho(r) = \int_{r_1}^r \rho f r^n dr$$

Linear law with intensity increase:

$$f = C_{LA}(r - r_1), \quad C_{LA} = \frac{1}{2^n \pi} \times \frac{1}{\left\{ \frac{r_2^{n+2} - r_1^{n+2}}{n+2} - r_1 \frac{r_2^{n+1} - r_1^{n+1}}{n+1} \right\}}, \quad (18)$$

$$F = C_{LA} \left\{ \frac{r^{n+2} - r_1^{n+2}}{n+2} - r_1 \frac{r^{n+1} - r_1^{n+1}}{n+1} \right\}$$

$$F_\rho(r) = \int_{r_1}^r \rho f r^n dr$$

Linear law with intensity decrease:

$$f = C_{LB}(r_2 - r), \quad C_{LB} = \frac{1}{2^n \pi} \times \frac{1}{\left\{ r_2 \frac{r_2^{n+1} - r_1^{n+1}}{n+1} - \frac{r_2^{n+2} - r_1^{n+2}}{n+2} \right\}}, \quad (19)$$

$$F(r) = C_{LB} \left\{ r_2 \frac{r^{n+1} - r_1^{n+1}}{n+1} - \frac{r^{n+2} - r_1^{n+2}}{n+2} \right\}$$

$$F_\rho(r) = \int_{r_1}^r \rho f r^n dr$$

Dome (quadric) law of heat release:

$$f = C_k(r - r_1)(r_2 - r), \quad (20)$$

$$C_k = 2^{-n} \pi^{-1} \times \left\{ -\frac{r_2^{n+3} - r_1^{n+3}}{n+3} + (r_1 + r_2) \frac{r_2^{n+2} - r_1^{n+2}}{n+2} - r_1 r_2 \frac{r_2^{n+1} - r_1^{n+1}}{n+1} \right\}^{-1},$$

$$F(r) = C_k \left\{ -\frac{r^{n+3} - r_1^{n+3}}{n+3} + (r_1 + r_2) \frac{r^{n+2} - r_1^{n+2}}{n+2} - r_1 r_2 \frac{r^{n+1} - r_1^{n+1}}{n+1} \right\}$$

In Figure 1 dependencies of the Mach number on the coordinate are shown at the uniform heat addition for the Q -variant in the interval $[r_1=2, r_2=3]$ at the flow field of the spherical mass source $n=2$. Curve 1 corresponds to the case of the stream to vacuum, 2 – to the stagnation region, 3 – from the stagnation region, 4 – from the space of the rarefied gas (from vacuum).

Curve 2 corresponds to the case, in which $M=1$ is achieved inside the energy release zone at the critical coordinate $r_* \approx 2.78$, curve 2a contains the point $r_\Delta \approx r_*$, at which the Mach number derivation $dM(r_\Delta)/dr=0$ and after which the value M goes away from unity. Note that strict values of Q_* , r_* , Q_Δ , r_Δ depend on the step of the finite-difference scheme (or an equivalent one). Here the error of several percent is tolerable. So, Figure 1 shows the case being described in Introduction and representing the main essential distinctions as compared to the one-dimensional uniform flow with heat addition. In the spherical mass source at interval $[r_*, r_2]$ even under energy addition the values of Mach number go away from unity.

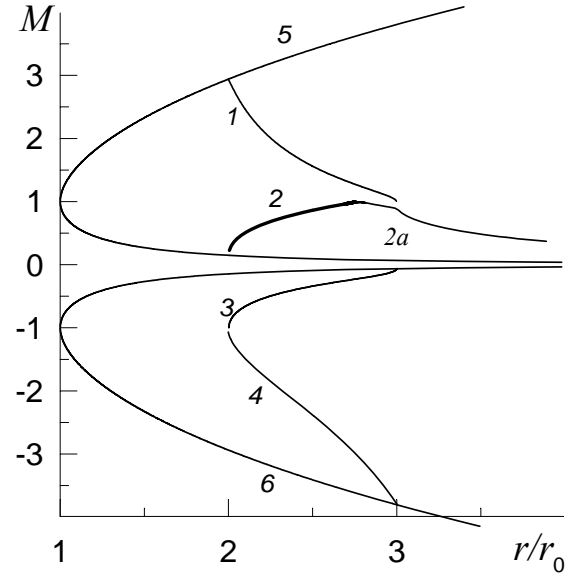


Figure 1. Mach number as function of coordinate $M(r)$ at uniform heat addition $f(r)=C$ in the interval $[2,3]$. Spherical mass source ($n=2$): 1 – to vacuum, $Q_{cr}=91.7$; 2 – to stagnation region, $Q_*=2824$, $r_* \approx 2.78$; 2a – $Q_\Delta=2823.5 < Q_*$; 3 – from stagnation region, $Q_{cr}=469$; 4 – from vacuum, $Q_{cr}=27$; 5 and 6 – without heat addition. Adiabatic index $\gamma=1.4$ (air).

Note that as compared to the one-dimensional flow with the energy addition prescribed in the interval (layer), the number of possible variants grows from two (E and Q -variants) to sixteen: 1) flow to vacuum, 2) to stagnation zone, 3) sink from stagnation space, 4) sink from rarefied gas space (from vacuum) [16, 15]. Energy expense

(by the value of similarity number E and Q) increases in passing from one variant to another in the following order: 4, 1, 3, 2. For cylindrical and spherical cases, for E and Q -variants the hierarchy is identical. Thermal choking was defined by the $M=1$ at the back section of the energy release region, at $r_{cr}=r_2=4$ for the source and at $r_{cr}=r_1=3$ for the sink (where $M(r_{cr})=1$ at $E=E_{cr}$ or $Q=Q_{cr}$; critical values E_{cr}, Q_{cr} are similarity numbers at the thermal crisis).

In calculating we took the system of equations (6)-(10) in the form [17]:

$$\frac{dp}{dr} = \frac{\frac{\gamma p n m^2}{r^{2n+1}} - \frac{\rho m}{r^n} f(r) \left\{ \begin{matrix} E \\ \rho Q \end{matrix} \right\}}{\frac{\gamma-1}{2} \rho p (1-M^2)}, \quad (21)$$

$$\frac{d\rho}{dr} = \frac{\frac{\rho n m^2}{r^{2n+1}} - \frac{(\gamma-1)\rho^3 r^n}{2\gamma m} f(r) \left\{ \begin{matrix} E \\ \rho Q \end{matrix} \right\}}{\frac{\gamma-1}{2} \rho p (1-M^2)},$$

$$M^2(r) = \frac{2}{\gamma-1} \frac{u^2 \rho}{p}, \quad u(r) = \frac{m}{r^n \rho}$$

This statement shows that in the limit $M \rightarrow 1$ there is a peculiarity. The system of equations (6)-(10) can be also written in the form of a single equation, for example, for $M(r)$ (equations for $u(r)$, $\rho(r)$ or $p(r)$ see in Reference [15]):

$$\frac{M^2-1}{M} \frac{dM}{dr} = -\frac{1+\gamma M^2}{2\gamma p} f(r) \left\{ \begin{matrix} E \\ \rho(r)Q \end{matrix} \right\} + \left(1 + \frac{\gamma-1}{2} M^2\right) \frac{n}{r}, \quad (22)$$

$$\text{where } u(r) = \sqrt{\varphi(r)} \left(1 + \frac{2}{(\gamma-1)M^2}\right)^{-1/2},$$

$$\rho = \frac{m}{r^n u(r)}, \quad p = \frac{2m u(r)}{(\gamma-1)r^n M^2(r)} \quad (23)$$

The first member in the right part of equation (22) describes Mach number variations due to heat addition: heat addition decelerates the gas flow at $M>1$, and accelerates it at $M<1$. The second member describes the spatial flow divergence/convergence: on moving to vacuum the spatial expanse accelerates the supersonic flow, but with the stream to stagnation zone it decelerates the gas flow. Therefore, in the case of the source the spatial expansion opposes Mach number variation due to heat addition.

In the case of the sink from the stagnation space ($M<1$) both heat addition and space convergence accelerate the gas flow. In the case of the

sink from the rarefied gas zone ($M>1$) space divergence and heat addition decelerate the gas flow.

Thus for the source there might be situations, in which energy addition is compensated by space expansion well before the gas exits from the heat addition zone. At some section $r_\Delta (<r_*)$ for the energy parameter value $E_\Delta (<E_*)$ or $Q_\Delta (<Q_*)$ we get $dM(r_\Delta)/dr=0$. After that section the values of Mach number begin to go away from unity.

No similar situations are possible for sink.

In Figure 2 the following functions of the coordinate r_1 are presented: critical coordinate r_* (curve 1) and critical value of the energy parameter Q_* (4) for the case of the source to the stagnation space. As the energy release zone arrives close to the minimal radius, the difference between coordinate r_* and back coordinate r_2 becomes comparable with the characteristic (minimal) radius.

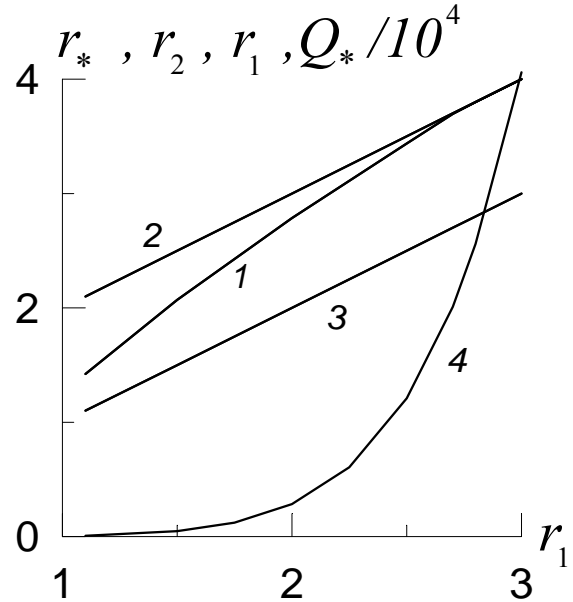


Figure 2. Spherical source flow to the stagnation zone, $n=2$, $\gamma=1.4$, uniform heat addition $f=C=3/[4\pi(r_2^3-r_1^3)]$ in interval $[r_1, r_2=r_1+1]$. Values r_* (curve 1) and Q_* (4) as function of initial coordinate r_1 , 2 – coordinate r_2 , 3 – r_1 .

In Figure 3 the energy $Q_* F_{p*}$ added to the gas from the initial to the critical section is shown as a function of the initial coordinate r_1 of the heat release zone (curve 1). For the E – variant the added energy $E_{cr} F(r_2)/4\pi$ is higher throughout the whole range (curve 2). At $r_1=1.5$ for the E – variant the supplied energy is more than twice that for the Q – variant. Note that at $r_1=1.2$ and the energy parameter equal to $E=25$ the Mach number inside the energy addition zone is practically constant $M \approx 0.453$ (with the error less than 1%).

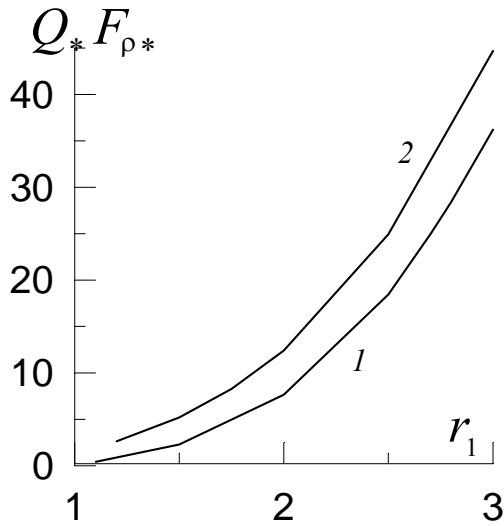


Figure 3. Power supplied to gas $Q^*F_{\rho^*}=W_{add}/(4\pi r_0^2 u_0 p_0/(\gamma-1))$ as function of coordinate r_1 , curve 1; added power $E_{cr}F(r_2)=W_0/(4\pi r_0^2 u_0 p_0/(\gamma-1))=E_{cr}/4\pi$ - curve 2. Spherical source, $n=2$. Uniform heat addition, $\gamma=1.4$.

For the case of the uniform law of heat addition in the flow field of the source, that streams to vacuum, in Figure 3 [15] it is shown that a slow energy addition to the extended region $d=r_2-r_1=3$ ($r_1=1.5$, $r_2=4.5$) will require more energy to choke flow of a cylindrical mass source $E_{cr^*}=2.125$ as compared to the variant of intense heat release in the narrow interval $d=1$ ($r_1=3.5$, $r_2=4.5$), $E_{cr^*}=1.449$.

For the flow to the stagnation space and the narrow zone of heat addition $d=1$, $r_1=3$, $r_2=4$ the sufficient energy is $E_{cr^*}=18.8$, and for the wider zone $d=2.5$, $r_1=1.5$, $r_2=4$ - the sufficient energy is $E_{cr^*}=13.4$, i.e. the sufficient energy is lower for the wide zone of heat addition. Therefore in the considered examples it is preferable to decelerate the flow (which streams to vacuum) in the narrow interval of heat addition, but to accelerate it (to the stagnation zone) in the wide one.

Equation (22) differs from the respective one in [1], which describes Mach number changes at the axis ($r=0$) for two- and three-dimensional flows. In the present paper the situation is different by physics. Stream lines in the considered cylindrical or spherical sources may only be straight rays radiated from a single center with different angles, moreover the values of all independent variables are governed by the single coordinate r .

For two- and three-dimensional variants [1] streamlines may be curved. In the case of cylindrical or spherical mass sources the curvature of streamlines is zero at the sections r_{cr} and r^* .

The calculations of variants with the linear law of heat addition increasing along r by formula

(18) show no sections r^* (see Reference [15], table 2,a).

In Figure 4 for E - variants of cylindrical source the critical section coordinates r^* (Figure 4,a) and the critical energy parameters E^* (figure 4,b) are presented as functions of the initial coordinate r_1 of the energy supply zone for the case of flow to vacuum (curves 1) and to the stagnation space (2). In the second case the dependence $E^*(r_1)$ is convex, weak, and in the first one it is concave and stronger.

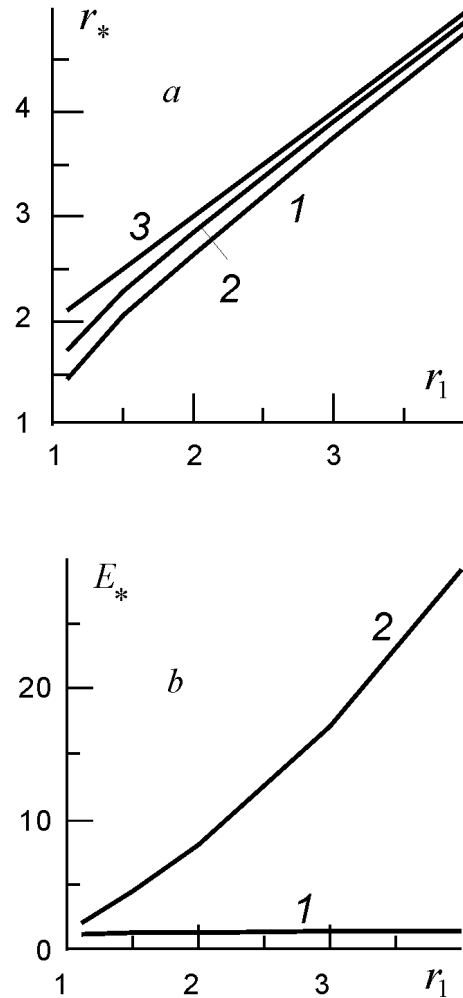


Figure 4. Cylindrical source to vacuum, $n=1$ (curves 1) and to the stagnation space (2), E - variants, heat addition by linear law (19):

- a - critical coordinate r^* versus initial coordinate r_1 , curves 3 - $r_2=r_1+1$;
- b - critical energy parameter E^* versus coordinate r_1 .

In Figure 5 dependencies of the critical coordinate $r^*(r_1)$, critical energy parameter $E^*(r_1)$ and Mach number $M(r)$ are shown for the E - variant of the cylindrical source to vacuum with heat release in unit layer $r_2=r_1+1$. The initial coordinate r_1 of energy addition zone varies

throughout the range $r_1 = 1.1-4$. The dependence (curve) $E_*(r_1)$ is convex.

The results obtained for the laws (19), (20) allow us to conclude that for $f(r_2)=0$ the critical section $r_* < r_2$ always exists.

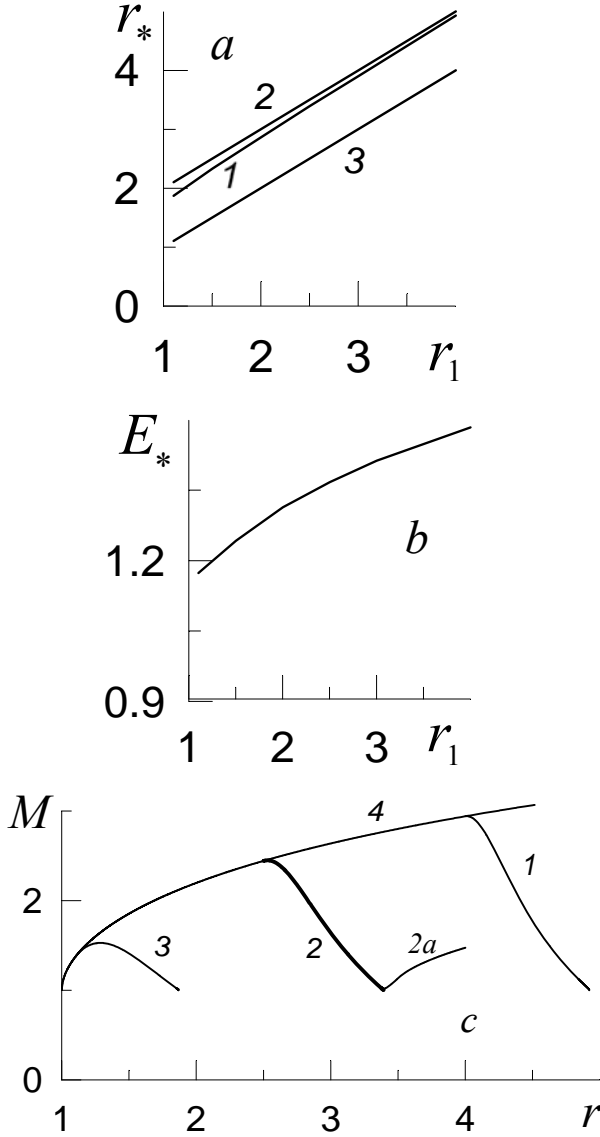


Figure 5. Cylindrical source ($n=1$), flow to vacuum, heat addition law (20), dome:

a – critical coordinate r_* (curve 1), back section r_2 (2), initial coordinate r_1 (3) as functions of r_1 ;
b – critical energy parameter E_* versus r_1 ;
c – Mach number $M(r)$;
 at $r_* = 4.922$, $E_* = 1.484$, $r_1 = 4$ (curve 1),
 $r_* = 3.392$, $r_1 = 2.5$, $E_* = 1.367$ (2), $E_\Delta = 1.366$ (2a);
 $r_* = 1.863$, $E_* = 1.174$, $r_1 = 1.1$ (3);
 without heat addition, $E = 0$ (4).

4. Asymptotic Solution Near a Peculiar Point

Let us build up asymptotic expansions of gasdynamic values under consideration near sections r_* . At the point $r=r_*$, in which the Mach

number equals unity $M=M_*=1$ and in the vicinity of which the first Mach number derivation $dM/dr \approx 0$, one can write using equations (7), (10), (21) the following expressions for density ρ_* , velocity u_* , pressure p_* :

$$r_*^n \rho_* u_* = m, \quad M_*^2 = 1 = \frac{2}{\gamma - 1} \frac{\rho_* u_*^2}{p_*},$$

$$\frac{p_*}{\rho_*} + u_*^2 = \varphi_*, \quad \varphi_* = 1 + \frac{1}{\gamma m} \times \begin{cases} E_* F_* \\ Q_* F_{\rho_*} \end{cases},$$

$$\rho_* = \frac{m}{r_*^n} \sqrt{\frac{\gamma + 1}{(\gamma - 1)\varphi_*}}, \quad u_* = \sqrt{\frac{(\gamma - 1)\varphi_*}{\gamma + 1}},$$

$$p_* = \frac{2m}{r_*^n} \sqrt{\frac{\varphi_*}{(\gamma - 1)(\gamma + 1)}} \quad (24)$$

The examples presented in [15] and in Figure 6 show that we have a peculiar point of “saddle” type [18].

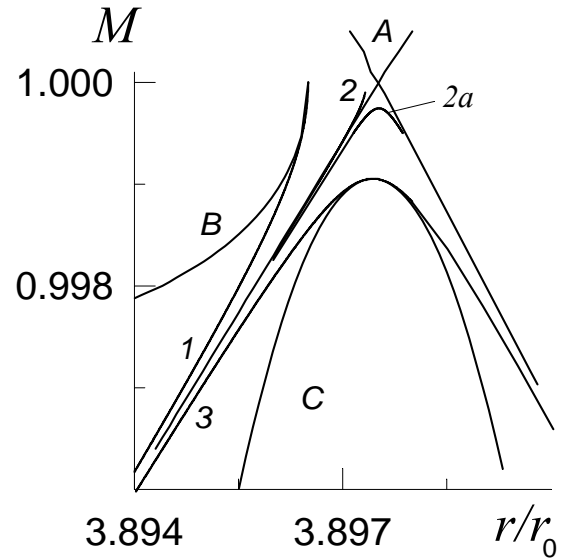


Figure 6. Mach number M in the neighbourhood of critical coordinate $r_* \approx 3.89752$ (with critical energy parameter $E_* \approx 17.1294793$) inside heat addition layer [$r_1=3, r_2=4$] by law (19) in cylindrical source $n=1$ to stagnation space: 1 – $M(r_\Delta)=1$, $r_\Delta < r_*$, $dM/dr \rightarrow \infty$ (flow choking); 2 – $M(r_\Delta \rightarrow r_*)=1$, $E_\Delta = 17.1294795$ (strictly by mathematics it is the limit of curve 1), 2a – $M \rightarrow 1$, $M(r_\Delta) < 1$, $E_\Delta = 17.1294791$ (“limit” of curve 3), 3 – $M(r_\Delta)=1-\Delta < 1$, $r_\Delta \neq r_*$, $dM(r_\Delta)/dr=0$ (subsonic flow); curves B, A, C (dashed lines) are analytical approximations of variants 1, 2, 3, correspondingly.

The asymptotes passing through the critical point r_* can be described by the following expressions, using an auxiliary value $x=r-r_*$:

$$\rho = \rho_* (1 + x a_{2*} + x^2 a_{4*} + \dots),$$

$$u = u_* (1 + x b_{2*} + x^2 b_{4*} + \dots),$$

$$p = p_* (1 + x d_{2*} + x^2 d_{4*} + \dots),$$

$$M = 1 + x\alpha_{2*} + x^2\alpha_{4*} + \dots \quad (25)$$

The coefficients a_{i*} , α_{i*} , b_{i*} , d_{i*} of gasdynamic values expressions were defined by substituting expansions (25) to equations (6), (8), (9) and (22), these coefficients are presented in [15] in Appendix A as functions of n and γ . In Figure 6 asymptotes of Mach number $M(r)$ are presented by dotted lines A .

If the energy parameter E_δ (or Q_δ) is greater than its critical value by small quantity $(E_\delta - E^*)/E^* = (\delta/r^*)C_E \ll 1$ (where C_E is constant, moreover at $C_E=0$ it is necessary to take the next in order term $(\delta/r^*)^2 C_{E2}$), then Mach number assumes unity at some point $r_\delta < r^*$ (such that $0 < \delta/r^* = (r^* - r_\delta)/r^* \ll 1$). In close proximity to the peculiar point r_δ , which precedes the section r^* , it is necessary to search asymptotic expansions by degrees of value $z = |r - r_\delta|^{1/2}$:

$$\begin{aligned} \rho &= \rho_\delta (1 + za_1 + z^2 a_2 + \dots), \\ u &= u_\delta (1 + zb_1 + z^2 b_2 + \dots), \\ p &= p_\delta (1 + zd_1 + z^2 d_2 + \dots), \\ M &= 1 + z\alpha_1 + z^2 \alpha_2 + \dots \end{aligned} \quad (26)$$

$$\begin{aligned} \rho_\delta &= \frac{m}{r_\delta^n u_\delta}, \quad \varphi_\delta = 1 + \frac{1}{\gamma m} \times \begin{cases} E_\delta F_\delta \\ Q_\delta F_{\rho\delta} \end{cases}, \\ u_\delta &= \sqrt{\frac{\gamma-1}{\gamma+1}} \varphi_\delta, \quad p_\delta = \frac{2mu_\delta}{(\gamma-1)r_\delta^n} \end{aligned} \quad (27)$$

Substituting expansions (26) to the equations (6), (8), (9) and (22), we find the coefficients a_i , b_i , d_i , α_i (see [15], Appendix B). The order of value of the coefficients α_1 , a_1 , b_1 , d_1 is $\delta^{1/2}$, the coefficients α_2 , a_2 , b_2 , d_2 are of the order of unity, and coefficients α_3 , a_3 , b_3 , d_3 are of order $\sim \delta^{-1/2}$. The first two terms of asymptotic expansions (26) with the found coefficients in the neighbourhood of the point r_δ satisfactorily approximate the numerical solution (see dotted line B in Figure 6).

Let us consider the behaviour of the solution in the neighbourhood of the point $r_\Delta \neq r^*$ (at the energy parameter value $E_\Delta < E^*$, $Q_\Delta < Q^*$), in which the Mach number is not equal to unity $M = M_\Delta = 1 + \Delta \neq 1$ and the Mach number derivation equals zero $dM(r_\Delta)/dr = 0$. The differences between the values r_Δ and r^* , values E_Δ and E^* , Q_Δ and Q^* are small, so that $\delta_\Delta/r^* = |r_\Delta - r^*|/r^* \ll 1$, the energy parameter equals $E_\Delta = E^*(1 + (\delta_\Delta/r^*)C_E)$, $Q_\Delta = Q^*(1 + (\delta_\Delta/r^*)C_Q)$, where C_E and C_Q are constants of the order of unity.

Asymptotic expansions by degrees of $x = r - r_\Delta$ are to be searched for in the form of series:

$$\begin{aligned} \rho &= \rho_\Delta (1 + xa_{23} + x^2 a_{43} + \dots), \\ u &= u_\Delta (1 + xb_{23} + x^2 b_{43} + \dots), \\ p &= p_\Delta (1 + xd_{23} + x^2 d_{43} + \dots), \\ M &= M_\Delta (1 + x\alpha_{23} + x^2 \alpha_{43} + \dots) \end{aligned} \quad (28)$$

$$\rho_\Delta = \frac{m}{r_\Delta^n u_\Delta}, \quad u_\Delta = \sqrt{1 + \frac{\varphi_\Delta}{2M_\Delta^2(\gamma-1)}}, \quad (29)$$

$$\varphi_\Delta = 1 + \frac{\begin{cases} E_\Delta F_\Delta \\ Q_\Delta F_{\rho\Delta} \end{cases}}{\gamma m}, \quad p_\Delta = \frac{2mu_\Delta}{(\gamma-1)M_\Delta^2 r_\Delta^n}$$

The coefficients of expansions α_{i3} , a_{i3} , b_{i3} , d_{i3} are presented in Appendix C in [15]. The coefficient α_{23} is equal to zero due to the zeroth first derivation of the Mach number $dM(r_\Delta)/dr = 0$. And the coefficients a_{23} , b_{23} , d_{23} are the values of order of unity. The coefficients α_{43} , a_{43} , b_{43} , d_{43} , being peculiar, are of order of $1/\delta_\Delta$. Expansions (28) give a satisfactory approximation of the numerical solution at $|x| < |\delta_\Delta|$ (see Figure 6, curve 3), but at some values $|x| > |\delta_\Delta|$ the distinction from the numerical solution is essential.

Let us analyse the example of heat addition per unit volume (E - variant) by the linear law with zero value at the final back section $f(r) = C_{LB}(r_2 - r)$ for the cylindrical source $n=1$ to the stagnation zone, see Figure 6.

Figure 6 shows numerical solutions 1, 2, 3 and analytical approximations (dotted lines B , A , C) in the neighbourhood of the peculiar point $r^* \approx 3.89752$ (at the energy parameter value equal to $E^* \approx 17.1294793$): at the peculiar point $r_\delta < r^*$, curve 1 – energy parameter $E_\delta > E^*$ (dotted line B is the approximation by formula (26), at $M=1$ we have flow choking) and at the coordinate $r_\Delta (\neq r^*)$, curve 3 – energy parameter equal to $E_\Delta < E^*$ (dotted line C is the approximation by formula (28), curve 2a is very close to the limit A , and everywhere the Mach number is less than unity $M < 1$; curve 2 is valid only up to the cross section of asymptotes A , flow choking at $M=1$). Values r^* , G^* , r_δ , G_δ , u_δ , p_δ , ρ_δ , r_Δ , G_Δ , u_Δ , p_Δ , ρ_Δ , M_Δ were taken directly from the procedure of numerical solution calculation.

By physics the limit variant A with flow choking is not realizable, as it is in the numerical procedure. In Figure 6 this variant is presented by curve 2 as the limit of variant 1. Curve 2a can approach the asymptote A from the curve 3 as close

as possible, but the flow is subsonic everywhere, $M < 1$. Curve 2a has break at the peculiar point r_Δ (which is very close to r_*). In concordance the coefficient α_{2*} can take two values, that differ in sign in the corresponding formula [15]. For the series of curves 1 the part of the analytical curve A up to the crosssection point of two analytical asymptotic curves is real. The flow can not be transformed in a continuous way through the speed of sound for the cylindrical or spherical source (sink) with a prescribed distributed heat addition, as well as for the case without heat addition. Therein lies the essence of the phenomenon of thermal crisis.

Similar examples are presented in [15]. Note that, all other factors being the same, the critical section in the cylindrical source is always placed closer to the back section r_2 as compared to the spherical source.

A comparison of E - and Q -variants of the flow to the stagnation space gives us the following result: the section r_* is closer to the back section r_2 for the E -variant (and for the Q -variant in the case of flow to vacuum).

At the varying initial coordinate r_1 and the fixed unit extent $d=1$ of heat addition zone and all other conditions being the same the peculiar coordinate r_* approaches the coordinate r_2 when coordinate r_1 increases. Strictly speaking the terms "initial" and "back section" correspond to the case of the source, but, as we noted above, there are no critical sections r_* in the case of sink.

5. Circulation Influence on the Thermal Crisis in a Cylindrical Mass Source

Let us consider a cylindrical mass source with circulation Γ_0 , m^2/c . The conservation equation of radial momentum component (8) will change and the conservation equation of azimuth momentum component is to be added to the mass (6) and energy (9) conservation equations [6-8]:

$$\rho u \frac{du}{dr} + \frac{\gamma-1}{2\gamma} \frac{dp}{dr} - \frac{\rho v^2}{r} = 0, \quad \frac{dv}{dr} = -\frac{v}{r}, \quad v = \frac{\Gamma}{r} \quad (30)$$

Here the azimuth velocity component v is divided by u_0 , the circulation Γ_0 is divided by the characteristic value $\Gamma = \Gamma_0 / 2\pi u_0 r_0$, where $u_0 = [2\gamma p_0 / (\gamma-1)\rho_0]^{1/2}$ is the maximal speed, $r_0 = m_0 / 2\pi \rho_0 u_0 m$ is the minimal radius, we described them at the beginning. The mass conservation integral is the same, but the energy conservation integral (10) takes the following form:

$$\frac{p(r)}{\rho(r)} + u^2(r) + v^2(r) = \varphi(r) \quad (31)$$

Without heat addition we have a solution:

$$r^2 = \frac{m^2 / \rho^2 + \Gamma^2}{1 - \rho^{\gamma-1}}, \quad u = \frac{m}{r\rho}, \quad v = \frac{\Gamma}{r}, \quad p = \rho^\gamma \quad (32)$$

It follows from the condition of the minimal radius $dr/d\rho=0$ that:

$$\rho(1) = \left[\frac{2}{\gamma+1} (1 - \Gamma^2) \right]^{1/(\gamma-1)} \quad (33)$$

The solution $r(\rho)$, taken at the minimal radius, gives the relation between similarity numbers m and Γ :

$$1 - \Gamma^2 = \frac{\gamma+1}{2} \left(\frac{2m^2}{\gamma-1} \right)^{\frac{\gamma-1}{\gamma+1}}, \quad (34)$$

$$m = \sqrt{\frac{\gamma-1}{2}} \left[\frac{2}{\gamma+1} (1 - \Gamma^2) \right]^{\frac{\gamma+1}{2(\gamma-1)}}$$

The variation ranges of values m and Γ are:

$$\Gamma = 0 \div 1, \quad m = 0 \div \sqrt{\frac{\gamma-1}{\gamma+1}} \left(\frac{2}{\gamma+1} \right)^{\frac{1}{\gamma-1}}$$

Figure 7 presents the relations between m and Γ at the adiabatic index values $\gamma=1.1-1.4-5/3$. Therefore it is possible to characterize the circulation and the mass flow by the single similarity number $G=\Gamma/m$, which varies within the range from zero to infinity $G=0 \div \infty$.

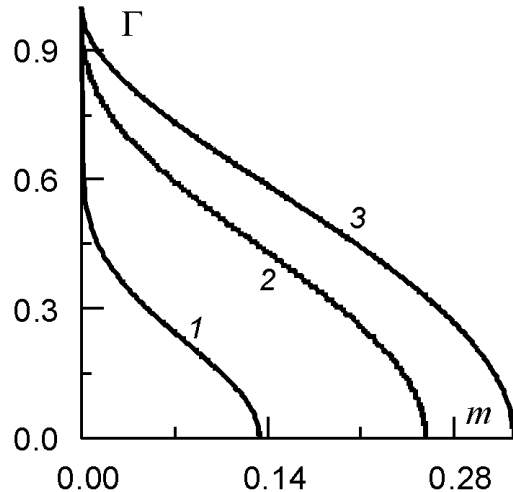


Figure 7. Relations of circulation Γ with mass flow m : 1 – adiabatic index is $\gamma=1.1$, 2 – 1.4, 3 – 5/3.

For the heat addition in the vortex-source flow field of the system of equations may be assumed in the following form [17]:

$$\frac{dp}{dr} = \frac{\frac{\gamma p(m^2 + \rho^2 \Gamma^2)}{r^3} - \frac{\rho m}{r} f(r) \left\{ \frac{E}{\rho Q} \right\}}{\frac{\gamma-1}{2} \rho p (1 - M_r^2)}, \quad (35)$$

$$\frac{d\rho}{dr} = \frac{\frac{\rho(m^2 + \rho^2 \Gamma^2)}{r^3} - \frac{(\gamma-1)\rho^3 r}{2\gamma m} f(r) \left\{ \frac{E}{\rho Q} \right\}}{\frac{\gamma-1}{2} \rho p (1 - M_r^2)},$$

$$M_r^2(r) = \frac{2}{\gamma-1} \frac{u^2 \rho}{p}, u(r) = \frac{m}{r\rho}, v = \frac{\Gamma}{r}$$

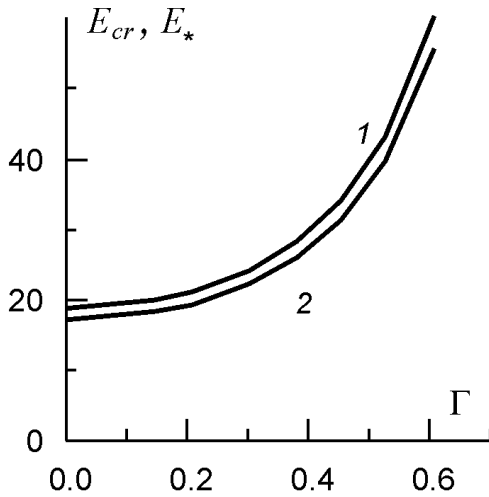


Figure 8. Critical values of energy parameters E_{cr} , E_* as a function of circulation Γ . Vortex-source to the stagnation zone. Uniform heat addition (17) – curve 1, linear law with decreasing (19) – 2; $\gamma=1.4$, $r_1=3$, $r_2=4$.

Fig. 8 shows an abrupt increase of the critical energy parameters values E_{cr} , E_* due to the growing circulation $\Gamma=0-1$ (with the simultaneous diminishing of the mass flow $m=m_{max}-m_{max}/2-0=0.2588-0.1294-0$, at $\gamma=1.4$) for the cases of uniform (curve 1, E_{cr}) and linear with decreasing (2, E_*) laws of heat addition. An extremely fast growth can be seen at the circulation approaching to the maximal value $\Gamma \rightarrow 1$ (and the mass flow approaching zero $m \rightarrow 0$). For the dependence $E_{cr}(\Gamma)$, curve 2, flow choking is realized at the back coordinate $r=r_2=4$, and for the relation $E_*(\Gamma)$, curve 1, it occurred at the critical coordinate $r_* < r_2$. The coordinate r_* varies weakly $r_*=3.897-3.906$. Curves 1 and 2 are very close each to other.

In Figure 9 critical energy parameter values E_* are presented as a function of the adiabatic index γ in the case of heat addition law (19) at the maximal mass flow (curve 1, circulation is $\Gamma=0$) and at

the mass flow equal to one-half the maximal one $m_{max}/2$ (the circulation Γ and parameter $G=\Gamma/m$ are $\Gamma=0.2527-0.454-0.541$, $G=3.77-3.51-3.345$ at the adiabatic index equal to $\gamma=1.1-1.4-1.667$). Therefore at the circulation growing up to the value 0.6 (Figure 8, $\gamma=1.4$) the critical energy parameter value E_{cr} , E_* increases by three times. At the adiabatic index γ growing from 1.1 (multi-atomic gas) up to 1.667 (5/3, single – atomic gas) the critical energy parameter value E_* increases from 7.55, 13.8 to 24.08, 43.93 (at the mass flow $m=m_{max}$, $m_{max}/2$), i.e. more than by three times. At the adiabatic index γ variations from 1.1 up to 1.4 (air) the critical energy parameter value E_* increases more than twice. The critical coordinate r_* increases weakly, less than 1%.

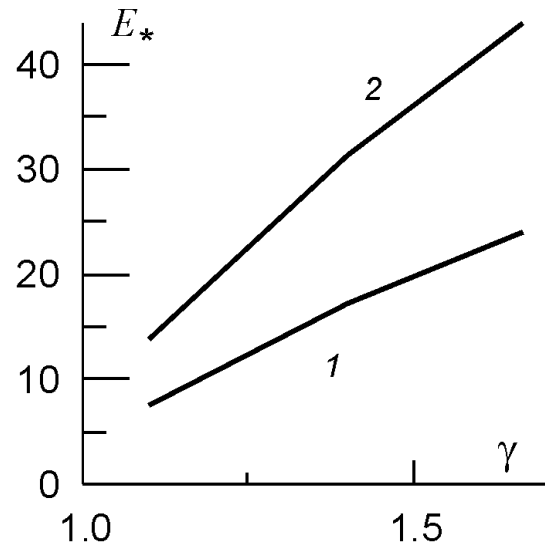


Fig. 9. Critical energy parameter E_* as a function of adiabatic index γ : curve 1 - $m=m_{max}$, 2 - $m=m_{max}/2$ (vortex-source). Linear law of heat addition with decreasing (19), $r_1=3$, $r_2=4$.

6. Transition Through Sonic Speed

Near the minimal radius section, for example at $r_1=1.1$, the azimuth velocity $v=\Gamma/r$ is sufficiently large, and the total flow velocity $V=\sqrt{(u^2+v^2)}$ at the beginning is less than sound speed c_s , the total Mach number is less than unity $M=V/c_s < 1$ (Fig. 10, curves 2, 1, section $r_1 \approx 1.5$), then in the neighbourhood of the critical section r_* the Mach number exceeds unity. In this case the radial velocity component u is lower than sound speed c_s and the corresponding radial Mach number $M_r = u/c_s$ is within unity everywhere. A body placed in the flow field of such a vortex-source with heat addition will result in shock waves.

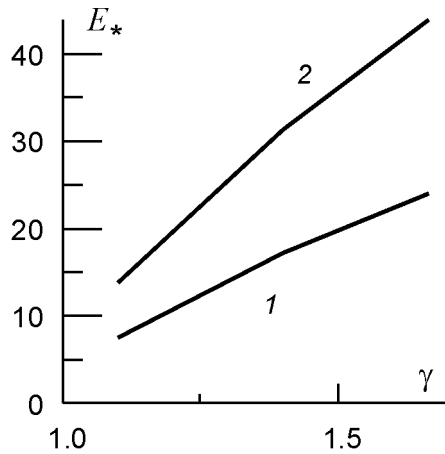


Figure 10. Vortex-source to the stagnation space, initial coordinate is $r_1=1.1$, back coordinate is $r_2=2.1$ (linear law (19), adiabatic index is $\gamma=1.4$, mass flow is $m=m_{\max}/4=0.0647$, circulation is $\Gamma=0.608$): Critical energy parameter value $E_*=1.94165$, critical coordinate $r_*=1.85$ – curve 2, Mach number $M=\sqrt{(u^2+v^2)}/c_s$; 4, radial Mach number $M_r=u/c_s$; Energy parameter value $E_\Delta=1.9415<E_*$ - curve 1 (M), 3 (M_r).

At the circulation equal to zero $\Gamma=0$ the Mach number would nowhere exceed unity (curves 3 and 4).

Conclusions

It is shown that heat addition in a layer in the flow field of a cylindrical or spherical source/sink causes flow choking for the cases of stream to vacuum, to the stagnation zone, from the stagnation space, from the region of the rarefied gas. Critical energy parameter values Q_{cr} , E_{cr} are defined, at which speed of sound is achieved (the Mach number equals unity $M=1$) at the back sections of the heat addition zone $r=r_2$ (source) or $r=r_1$ (sink) for the variants of a prescribed intensity of heat release per unit volume and per unit mass.

For the source at supersonic Mach number $M(r_1) = M_1 > 1$, as well as at the subsonic one $M_1 < 1$, there might be possible a balance of two factors, heat addition and space divergence, at some section r_* ($< r_2$). For the sink both factors act in the same direction and the section of equilibrium r_* is impossible. The section r_* exists in all the situations if $f(r_2)=0$.

In the cylindrical source the critical section r_* is always closer to the back section r_2 as compared to the spherical source. In the flow to the stagnation zone the critical section lies closer to the section r_2 for the E -variant as compared to the Q -variant, all other conditions being the same.

As the initial coordinate r_1 of the heat addition zone grows and its width d is fixed, the coordinate r_* approaches the coordinate r_2 .

Circulation in the cylindrical mass source can essentially increase critical energy parameter values. The increment of critical energy parameter value grows when the adiabatic index increases (in passing from a multi-atomic gas ($\gamma \rightarrow 1$) to a single-atomic one ($\gamma=5/3$) and it rises sharply at the circulation $\Gamma=\Gamma_0/2\pi r_0 u_0$ approaching its maximal value $\Gamma \rightarrow 1$.

In the vortex-source to the stagnation space, the local transonic regions near the critical section r_* are possible, but at the circulation equal to zero in the flow field of a cylindrical mass source the flow is subsonic everywhere.

The work was supported by the State Program № P-09 of the Presidium of Russian Academy of Science.

REFERENCES

1. Kogan M.N., Kucherov A.N. *A stationary heat source in the supersonic flow* / The 8th International Workshop on Magneto-Plasma Aerodynamics. 31 March – 2 April 2009, Moscow. Abstract 2009. P. 68-70; Proceedings 2010 (in print). High Temperature. 2010. **Vol. 48**, N 1 (Additional). P. 85-92.
2. Georgievsky P.Yu., Levin V.A. *Control of flow near different body using local energy addition at supersonic mainstream* // Izvestija RAN. Fluid Dynamics. 2003. N 5.
3. Abramovich G.N. *On heat crisis in gas flow* // Doklady of Russian Academy of Science. 1946. **V. 54**, N 7. P. 579 – 581.
4. Vulis L.A. *On transition through speed of sound in gas flow* // Doklady of Russian Academy of Science. 1946. **V. 54**, N 8. P. 669 – 672.
5. Chaplygin S.A. *Gas jets*. M.: 1902; M.: Gosudarstvennoe Izdanie Tekhnicheskoi i Teoreticheskoi Literatury (GITTL), 1949. – 144p.; Izbrannye trudy po mekhanike i matematike. M.: GITTL, 1954. – 568p.
6. Fabrikant N.Ya. *Aerodynamics*. P. I. M., 1949; *Aerodynamics. General cours*. M.: Nauka, 1964.
7. Mises R. *Mathematical Theory of Compressible Fluid Flow*. New York: Academic Press INC Publishers, 1958.
8. Chernyi G.G. *Gasdynamics*. M.: Nauka, 1988.
9. Raizer Yu.P. *Physics of Gas Discharge*. M.: Nauka, 1994.
10. Ershov A.P., Surkont O.S., Timofeev I.B., Shibkov V.M., Chernikov V.A. *Lateral electric discharges in supersonic airflow. The mechanisms of propagation and instability of a discharge* // Teplofizika Vysokikh Temperatur. 2004. **Vol. 42**, № 4. P. 516 – 522.
11. Gromov V.G., Ershov A.P., Levin V.A., Shibkov V.M. *Lateral electric discharges in su-*

- personic airflows. Simulating of the effects that influence gas heating // Teplofizika Vysokich Temperatur. 2006. Vol. 44. № 2. P. 185 – 194.*
12. Tretyakov P.K., Grachev G.N., Ivanchenko A.I., Kraynev V.L., Ponomarenko A.G., Tischenko V.N. (1994) *Stabilization of optical discharge in a supersonic argon flow // Dokl. Phys. Vol. 39. P. 415.*
 13. Tretyakov P.K., Garanin G.F., Grachev G.N., Kraynev V.L., Ponomarenko A.G., Tischenko V.N., Yakovlev V.I. *The control of supersonic flow over bodies with the use of pulsating optical discharge // Dokl. Phys. 1996. Vol. 41. P. 566.*
 14. Zudov V.N., Tretyakov P.K., Tupikin A.V., Yakovlev V.I. *Supersonic flow over the source // Fluid Dynamics. 2003. № 5.*
 15. Kucherov A.N. Peculiarities in the flow field of cylindrical or spherical source inside energy release region. Preprint TsAGI № 157. M.: Izdatel'stvo TsAGI, 2009.
 16. Kucherov A.N. Thermal crisis in the flow field of cylindrical or spherical source // Journal of Engineering Physics and Thermophysics. 2010. V. 83. №5 (in print).
 17. Kucherov A.N. Curl - Source, Source, and Curl with Space Heat Release // Uchenye Zapiski TsAGI. 1983. V. 14. № 4. P. 47-57.
 18. Kamke E. Differential Gleichungen. Lösungsmethoden und Lösungen. P. I. Gewöhnlicher Differential Gleichungen. 6. Verbesserte Auflage. Leipzig, 1959.

SPECIFIC FEATURES OF SUPERSONIC STREAMLINING FOR ASYMMETRICAL ENERGY SUPPLY INTO EXTERNAL FLOW

Olga Azarova

Dorodnicyn Computing Center of RAS, Moscow, Russia

and

Yuri Kolesnichenko

Joint Institute for High Temperatures of Russian Academy of Sciences, 13/19 Izhorskaya Str., 125412 Moscow
Institute of High Temperatures RAS, Moscow, Russia

Abstract. Interaction of microwave filament regarded as heated rarefied channel with supersonic shock layer is under consideration. Mechanisms of drag force reduction for symmetrically located filament and temporary drag force enhancement for asymmetrically located filament are discussed. The latter is shown to be connected with forming the “heat piston” in front of the body inside a shock layer. Limited length and infinite filaments are considered. Dynamics of local Mach number, parameters in the stagnation point (including its position), drag, lift and pitch forces are researched. Formation of periodical steady flow structures is considered, too.

Nomenclature

M	=	Mach number of oncoming flow
γ	=	ratio of specific heats, $\gamma=1.4$
p_0, ρ_0, u_0, v_0	=	freestream values of pressure, density and longitudinal and normal velocity components
F	=	front surface drag force
D, d	=	diameter of aerodynamic body and filament diameter
α_p	=	degree of gas rarefaction in the filament
Δl	=	filament length
y	=	distance between the axis and the lower filament boundary
p_s, ρ_s	=	pressure and density in the stagnation point

I. Introduction

Flow reconstruction over aerodynamic body under the effect of heat inhomogeneities in a supersonic flow was under the interest from the 80th years of the last century (see [1], survey [2] and additional surveys in [3, 4]). In [5] the possibility of supersonic flow control by a space-distributed energy supply was pointed out. The problem of instabilities generation in such types of flows was initiated in [6]. Effects of flow structure reorganization (including reverse circulation flow generation) caused by the interaction of heated rarefied channel (or heated layer) with a shock layer are established in [7]. In [8, 9] application of this phenomenon for modeling of microwave energy effect on aerodynamic characteristics of bodies for the purpose of flow control improvement was considered. The vortex was established to generate at the first stage of energy release / shock layer interaction, this vortex was shown to be the reason

of the face drag force reduction [8]. Efficiency of this approach was under the interest, too. At the same time this vortex was shown to be responsible for generation of the reversal flow and later for generation of the reverse circulation flow [10]. In [11] the flow reconstruction under the action of microwave filament regarded as longitudinal heated rarefied channel in a supersonic flow is investigated for different body's shapes. Also the results of computation of asymmetrically energy release into a supersonic flow were discussed. Pulsed flows with contact discontinuities instabilities generated via microwave infinite filament / cylinder shock layer interaction were obtained in [12 – 17]. The primary vortex was shown to be caused by the instability of contact discontinuity similar to Richtmyer-Meshkov instability which is generated as the result of microwave filament (regarded as heated rarefied channel) / bow shock wave interaction [12,13]. The lines of vortexes resulting from the shear layer instability were obtained. In [13] it was pointed out that this instability is of Kelvin-Helmholtz type and the mechanism of this instability was established.

Recent experiments [18] showed the possibility of drag force enhancement as the result of the MW energy effect on supersonic shock layer. The enhancement has been registered for limited filament length in particular cases of asymmetrical filament location. In [16] the mechanism of drag force enhancement is established numerically for asymmetrically located filament. The mechanism is shown to connect with forming “heat piston” in front of the body inside a shock layer. Steady flow structures for this case of filament location were obtained and researched in [14, 19, 20].

In this paper the phenomena accompanying asymmetrical location of microwave filament relative to AD body are investigated for wide class of defining flow parameters: rarefaction degree in the filament, impulse time duration and filament

location. Bounded length and infinite filaments are considered. Dynamics of local Mach number, parameters in the stagnation point (including its position) drag, lift and pitch forces are researched.

II. Statement of the problem

Interaction of microwave filament with a shock layer is numerically analyzed on the base of the systems of Euler equations for an ideal gas.

$$\frac{\partial \mathbf{U}}{\partial t} + \frac{\partial \mathbf{F}}{\partial x} + \frac{\partial \mathbf{G}}{\partial r} = \mathbf{0} \quad (1)$$

where

$$\mathbf{U} = \begin{pmatrix} \rho \\ \rho u \\ \rho v \\ E_S \end{pmatrix}, \mathbf{F} = \begin{pmatrix} \rho u \\ p + \rho u^2 \\ \rho uv \\ u(E_S + p) \end{pmatrix}, \mathbf{G} = \begin{pmatrix} \rho v \\ \rho v^2 \\ p + \rho v^2 \\ v(E_S + p) \end{pmatrix}$$

The statement of the problem is analogous to our previous work in [8, 12]. The Mach number of the oncoming flow was 1.89 and 3. On the entrance boundary the parameters of the oncoming flow are used. Reflection (slip) boundary conditions are utilized on the body surface. A no-reflection boundary condition is applied on the exit boundary. Energy deposition by microwave pulse is modeled as the instantaneous creation of a heated finite or infinite rarefied channel ("filament"). The filament enters the computational domain at the entrance boundary ($x=0$) as a channel of low density ρ_f , $\rho_f = \alpha_p \rho_0$ for $0 \leq r \leq 0.5d$. The static pressure and velocity of the channel are equal to those of the undisturbed flow. Thus, the channel is regarded as a heated layer. Non-dimensional undisturbed flow parameters corresponding to the normal conditions are $\rho_0=1$, $p_0=0.2$, $u_0=1$, $v_0=0$. The filament is assumed to arise instantly in the steady flow in front of the bow shock wave at the time moment t_i . Space and time filament characteristics are in agreement with the parameters of the heated areas obtained experimentally as a result of microwave energy injection in air [8, 9]. Experimental filament image on the photograph and schematic sketch for the statement of the computations are presented in Fig. 1 and Fig. 2.

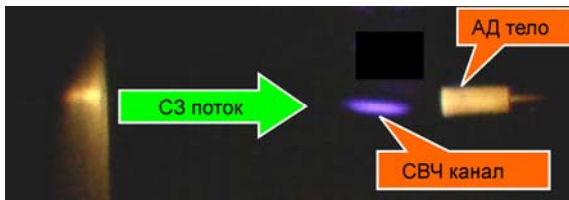


Figure 1. MW filament (experiment)

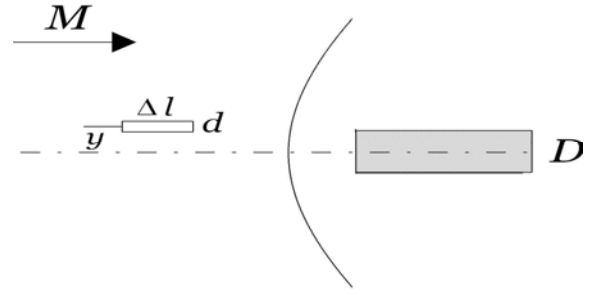


Figure 2. Schematic sketch

Governing dimensionless parameters for the considered cases of the microwave filament / shock layer interaction are presented in Tab.1.

Table 1. Governing dimensionless parameters

Type	Description	Definition	Value
Flow	Mach number	M	1.89, 3
	Specific heats ratio	γ	1.4
	Body's diameter	D	0.2, 0.4
Filament	Density ratio	α_p	0.3 - 0.6
	Diameter	d/D	0.1, 0.125, 0.25, 0.26
	Length (duration)	$\Delta l/D$	3.0, 4.0, ∞
	Location	y/D	-0.05, -0.125, -0.13, 0, 0.08, 0.16, 0.24, 0.25

The base variant of the employed difference scheme is described in [21]. Details of the used schemes modifications are described in [13, 14]. The schemes are second order accurate in space and time. In addition to the conservation property over divergent variables, the schemes are conservative over the divergent variables for space derivatives. This property provides correct computational contact discontinuities and vortices representation. Boundary conditions are incorporated in the calculations without breaking the conservation laws in the calculation area. All calculations have been implemented without introduction of any artificial viscosity into the applied schemes.

III. Results

A. Asymmetrically located limited length filament: “heat piston” effect and drag force enhancement

First we'll demonstrate the effect of front body's surface drag reduction as a result of symmetrically located limited length filament / shock layer interaction (see, also, [8]). Considered dimensionless parameters are presented in Tab. 2. One of the experimental results on drag reduction is presented in Fig.3. In the calculations the drag force reduction has been registered, too. In [8] the phenomenon of drag reduction was pointed out experimentally and numerically. It was shown that the phenomenon is caused by the vortices effect on the front body's surface. The vortices are generated as a result of instability [12] initiated by the bow shock wave / heated channel boundaries (contact discontinuities) interaction. This instability is similar to the Richtmeyer-Meshkov instability. The vortices reach the body and decrease the pressure on the front surface.

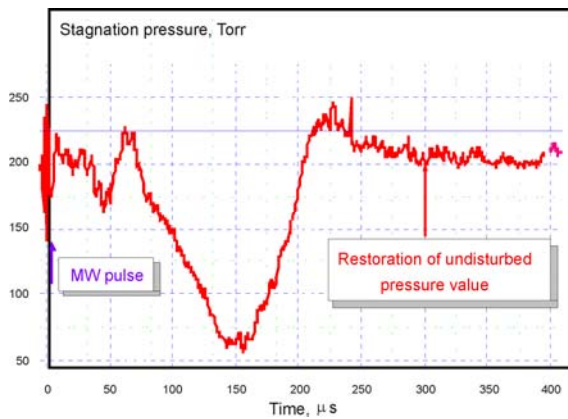


Figure 3. Finite filament / shock layer interaction: dynamics of the stagnation pressure

Table 2. Dimensionless parameters. Case A.

Type	Definition	Value	Details
Flow	M	1.89	
	D	0.2	
Filament	α_p	0.5	symmetrical location
	d/D	0.26	
	$\Delta l/D$	3.0	
	y/D	-0.13	
	t_i	4.01	

Consider the mechanism of this drag reduction [10]. In Fig. 4 the fields of density (in isochors) and velocity are presented for the stage of drag reduction via the enlarged scaled slides. The central area of the increased density and pressure adjacent to the front body's surface is divided into two symmetrical parts by this vortex structure. Upper vortex rotates clockwise and lower vortex rotates counterclockwise. Two streams enveloping these areas below are generated ($t=5.2$). With the help of these streams the values of density and pressure in the front area decrease (the areas of increased density and pressure are “blown out” from the front area). The shock structure moves to the body. At $t=5.4$ two vortex regions occupy all the space between the body and the vortex structure (the streams mention above have disappeared). Two new streams are now generating directed from the body (reverse flow generating), the gas inflow into this front area being locked up by two contact discontinuities located near the angles of the body (i.e. these contact discontinuities are close to tangential ones and gas cannot flow through these discontinuities). Thus, the pressure and density values near the front surface start to decrease. At $t=5.6$ the pressure continues to fall down and near the back side of the vortex structure the streams

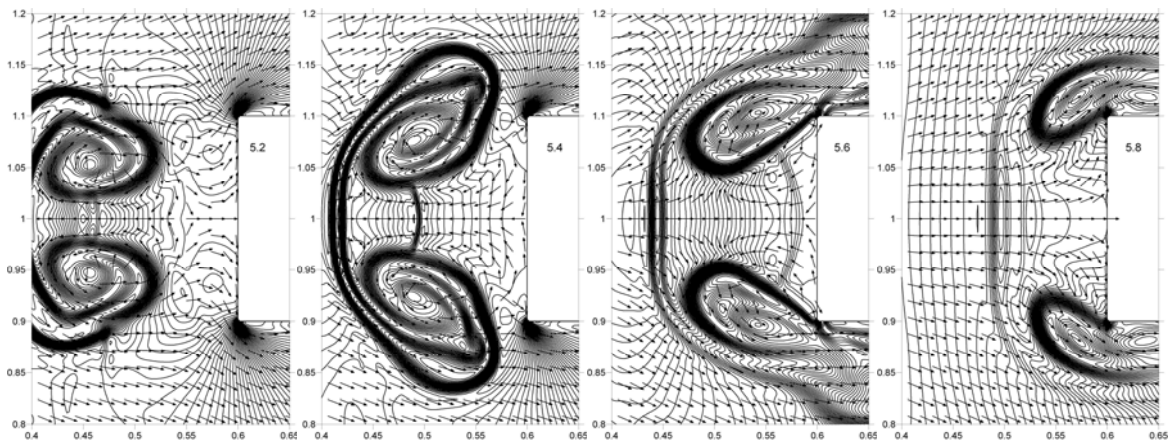


Figure 4. Symmetrically located finite filament / shock layer interaction: density (isochors) and velocity fields [10]

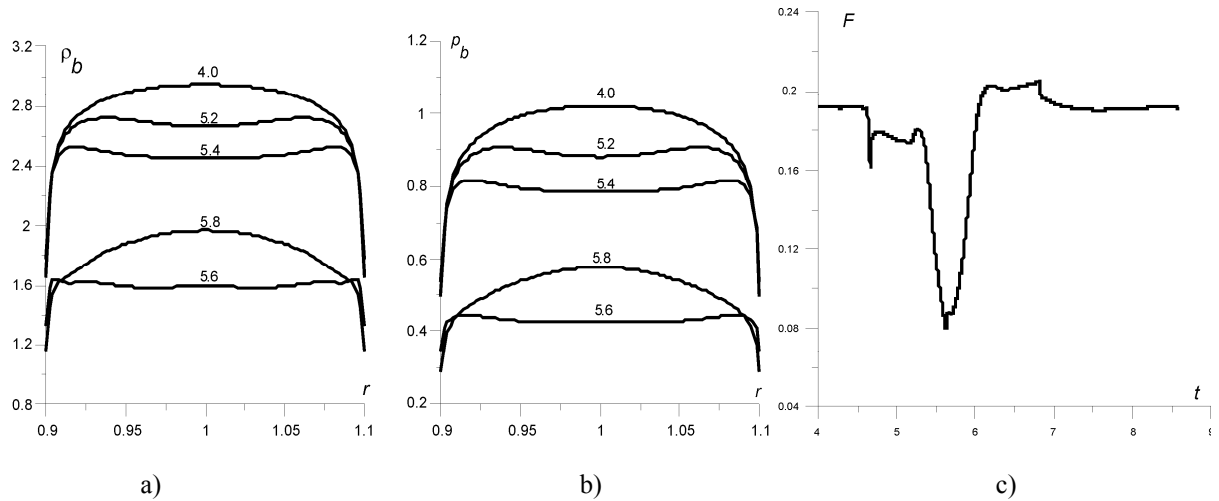


Figure 5. Symmetrically located finite filament / shock layer interaction: a) – density, b) – pressure on the front surface of the body; c) – face drag force dynamics

directed to the body are generating. When these streams reach the body the parameters on the front surface re-establish ($t=5.8$). Note that the weak shock wave arises between the vortices and the pressure decrease is taking place together with this shock wave propagating to the body. Reflection of this shock wave from the body is registered in the experiment as the local non-monotony in the lower part of the pressure dependence on time (see Fig. 3).

In Fig. 6 the appropriate fields of local Mach number M , $M = \sqrt{u^2 + v^2} / c$, are presented. It is seen that the area adjusting to the front surface is subsonic. Note that in the vortices centres the local Mach number M_v , $M_v = \sqrt{(u - u_c)^2 + (v - v_c)^2} / c$, is close to zero (here u_c and v_c – the velocity components of the vortices centres, c – the sound velocity).

B. Asymmetrically located limited length filament: “heat piston” effect and drag force enhancement

Experiments [18] showed the possibility of temporary drag force enhancement as a result of the

asymmetrically located microwave filament / shock layer interaction. For modelling this phenomenon [16] the following flow and filament dimensionless parameters were considered (see Tab.2). Underlined are the parameters of the calculations presented in Fig. 7-10. The reason for the drag enhancement is the formation of a “heat piston” in front of the body [10, 16, 22]. This structure is generated by the action of the lower vortex originating as the result of the instability of the filament boundaries (presenting by contact discontinuities) described in Part A. Consider this processes.

The vortex flow rotates counter clockwise and turns the heated area. This heated area moves to the body together with the flow (because this structure is formed by the contact discontinuities). Near the body the shock structure is decelerated. Cooler gas doesn’t move through the boundaries of this area and has no possibility to flow away with the stream parallel to the front surface, so the pressure and density of the gas between it and the body increase (Fig. 7). Thus, the moving heated area acts like a moving piston and compresses the gas between its boundary and the body. Weak shock wave is registered in front of the heated area in the

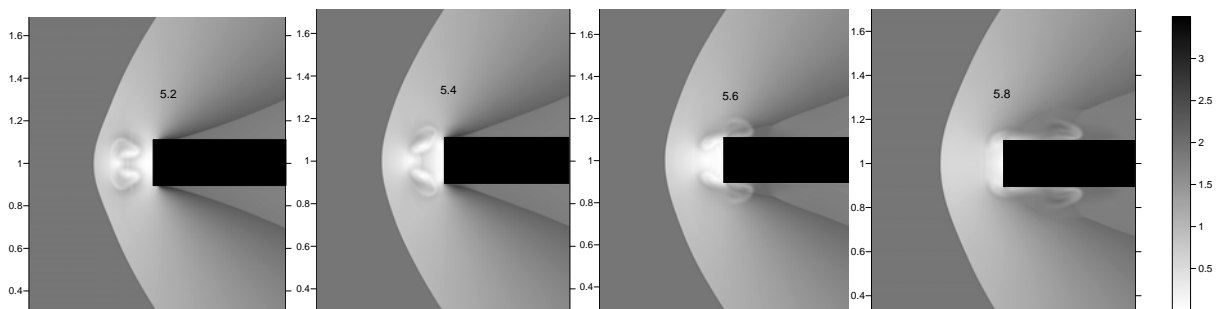


Figure 6. Symmetrically located finite filament / shock layer interaction: fields of local Mach number M

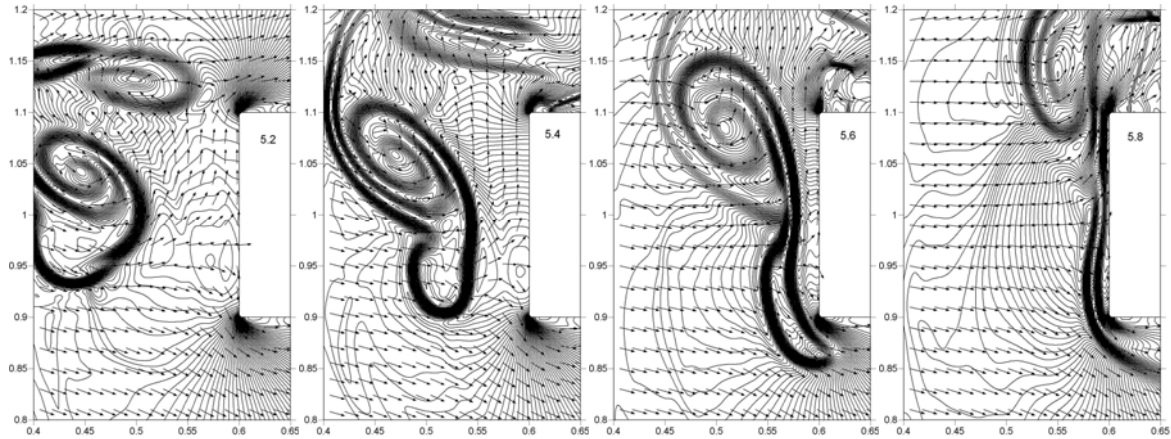


Figure 7. Asymmetrically located finite filament / shock layer interaction: density (isochors) and velocity fields [10]

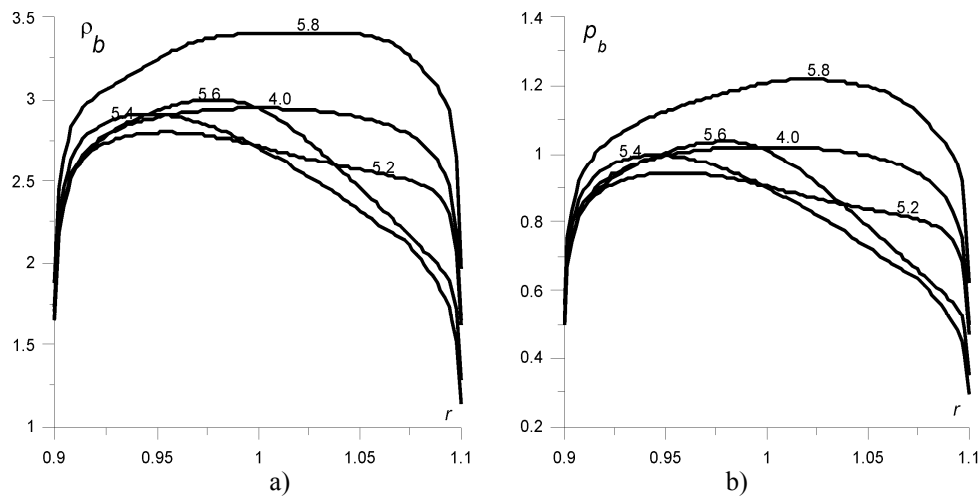


Figure 8. Asymmetrically located finite filament / shock layer interaction: a) – density and b) – pressure on the face of the body

pressure field ($t=6.52$) which strengthens the observed analogy. Pressure and density on the front surface increase together with the “heat piston” moving to the body (Fig. 8). The pressure growth defines the registered drag force enhancement.

Respective dependences of density and pressure on the front body’s surface are presented in Fig. 5a and 5b (time moments are shown near the curves). According drag force dynamics is

presented in Fig. 5c. It is seen that the interaction of the vortex structure with the body face is the reason of obtained drag force reduction.

In [16] it is shown that moving heated area provides a compressed layer near the front body’s surface. In this layer for the considered parameters the pressure value is greater than its stagnation value maximally by 20% and the density value – about 10%. Then the area of increasing values of

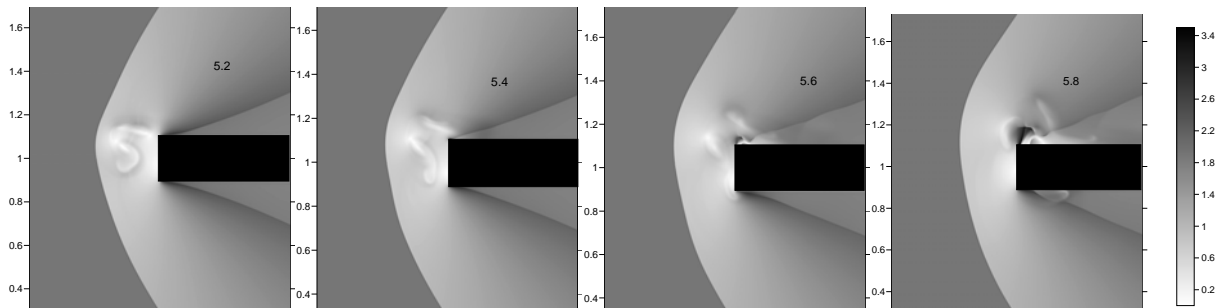


Figure 9. Asymmetrically located finite filament / shock layer interaction: fields of local Mach number

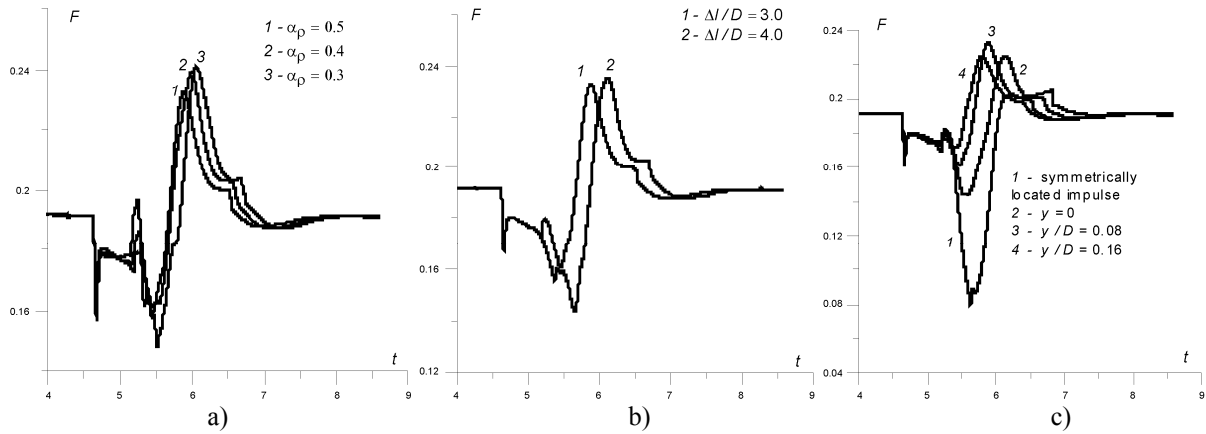


Figure 10. Asymmetrically located finite filament / shock layer interaction: drag force enhancement for governing filament parameters, a) $\Delta l/D=3.0$, $y/D=0.08$, variation of rarefaction degree α_p , b) $\alpha_p=0.5$, $y/D=0.08$, variation of filament length $\Delta l/D$, c) $\alpha_p=0.5$, $\Delta l/D=3.0$, variation of filament location y/D

pressure and density expands from the body. This is strengthened by the braking the shock structure near the body. Fields of Mach number are presented in Fig. 9. Formation of strongly subsonic area is registered in front of the body with increased value of density and pressure. Besides near the body's corner the supersonic area of increased Mach numbers is formed as a result of the shock structure / rarefaction wave interaction.

The observed drag enhancement is based on the generation of a mass of compressed cooler gas near the body via the heated area boundary effect. Fig. 10 presents the dependence of the front surface drag force on the defining filament parameters (α_p , Δl and y). This effect is stronger for smaller rarefaction degree α_p in the channel and greater Δl . For the considered parameters this enhancement has maximal value for $y/D=0.08$. For comparison with the experiments, where the diameter of the MW discharge channel is sufficiently less than in the computations, we consider the value of filament

coordinate location for maximal drag force enhancement as $y_c=y+0.5d=0.205D$. In the experiment this value is $0.25D$. Thus, the coincidence of the simulated and the experimental values is within 20%. Such close coincidence is surprising because in the experiments both the AD body and the MW filament are cylinders (3D case) whereas our model is plane and is of 2D-geometry. Also the effects of viscosity are present only at the scheme level (as the scheme viscosity). We can conclude then that the basic factors defining this phenomenon are weakly dependent on dimensionality of the constituent objects and dissipative effects.

C. Asymmetrically located infinite filament / shock layer interaction

For the interaction of an infinite filament with the shock layer the drag force and stagnation parameters are investigated up to statistically steady state (see also [23]). The dimensionless parameters

Table 3. Dimensionless parameters. Case C.

Type	Definition	Value	Details
Flow	M	1.89	
	D	0.2	
Filament	α_p	<u>0.4</u> , 0.5, 0.6	asymmetrical location
	d/D	<u>0.125</u> , 0.25	
	$\Delta l/D$	∞	
	y/D	0.08, 0.16, 0.24, <u>0.25</u>	
	t_i	<u>3.58</u> , 4.01	

are presented in Table 3.

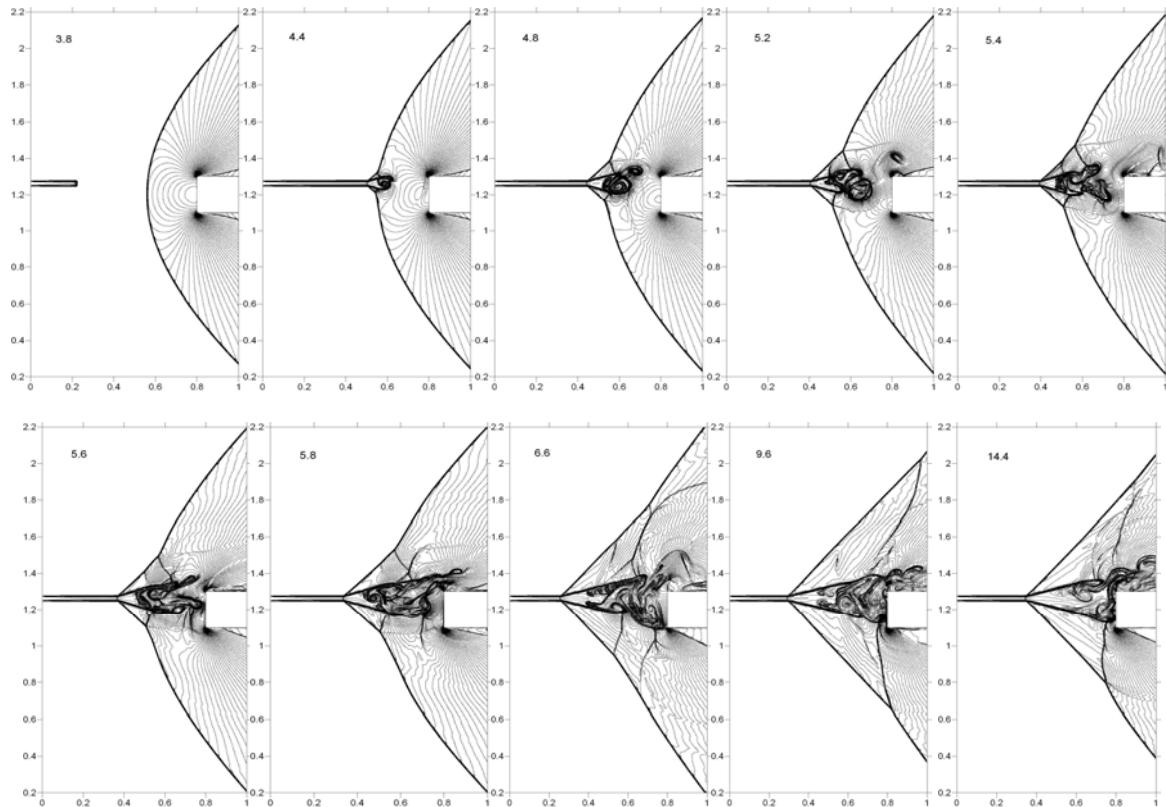


Figure 11. Flow dynamics of the infinite asymmetrically located filament/shock layer interaction, isochors [14]

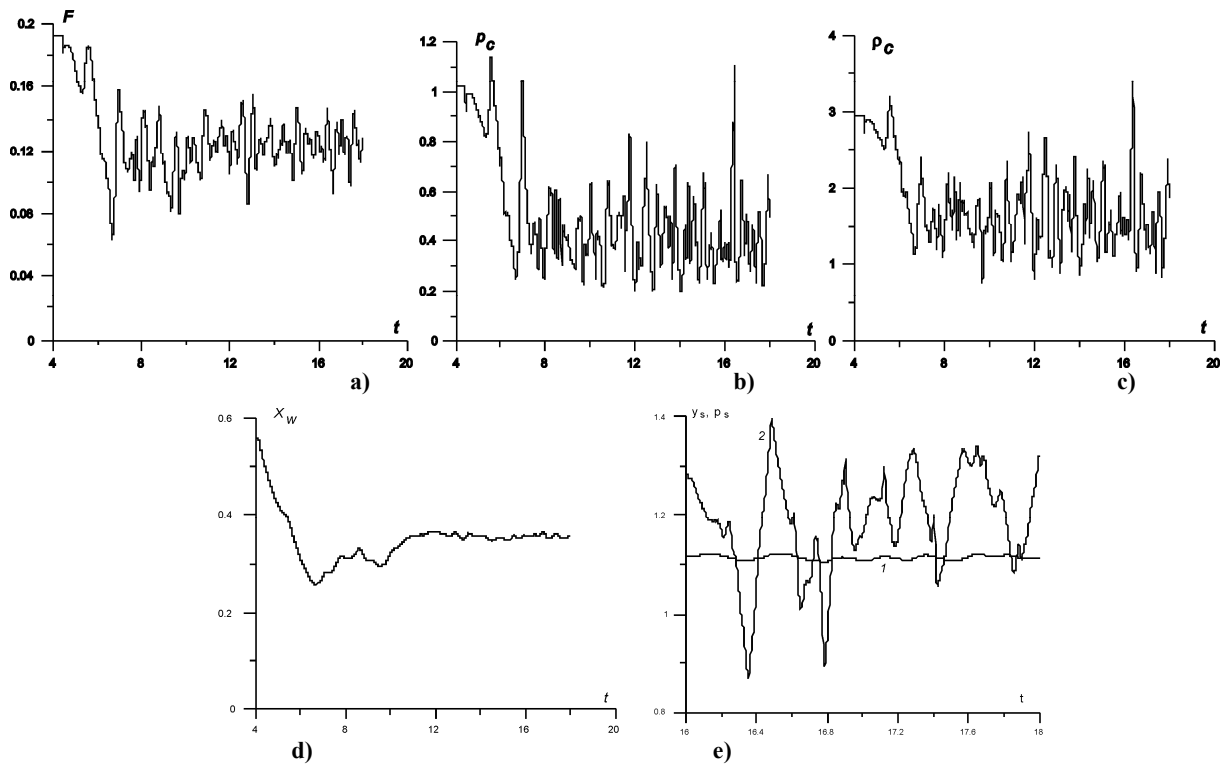


Figure 12. Infinite asymmetrically located filament / shock layer interaction: a) - d) dynamics of defining pulse flow parameters; e) - dynamics of stagnation point y_s on the front body's surface y_s (curve 1) and stagnation pressure p_s (curve 2) [14]

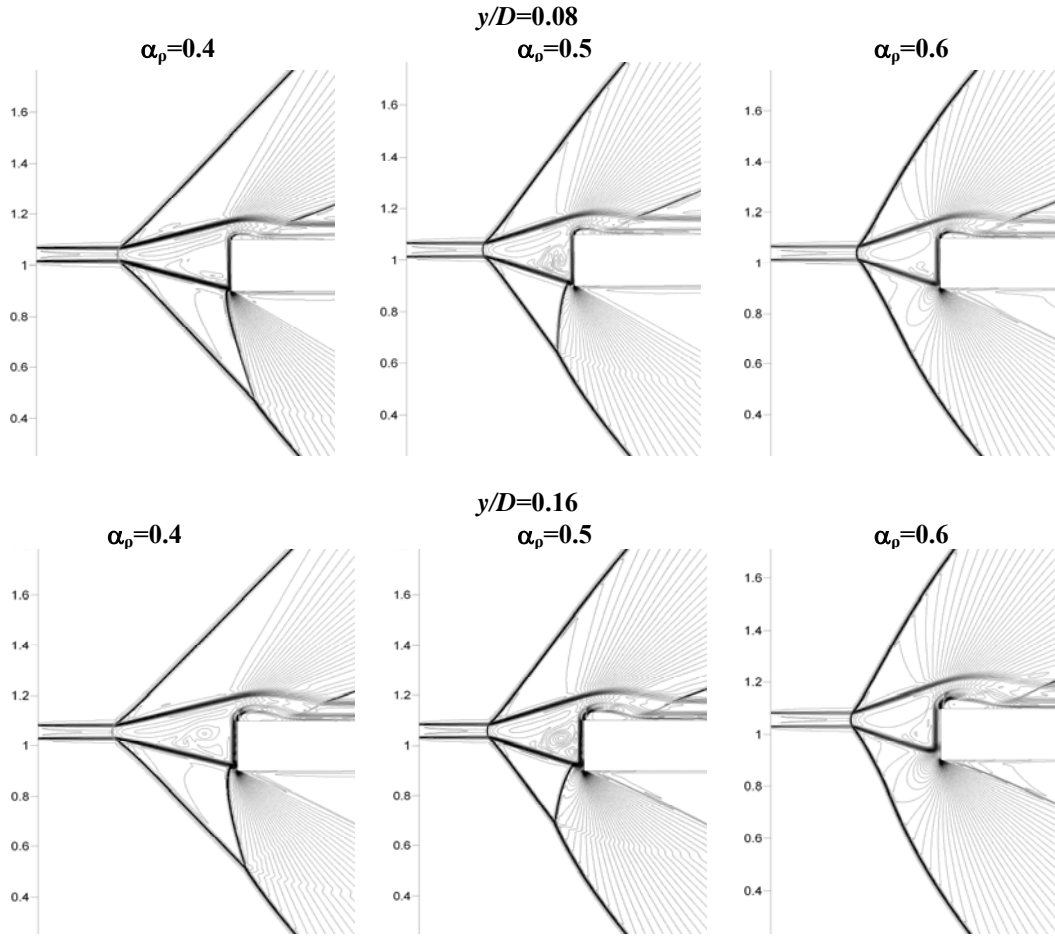


Figure 13. Asymmetrically located filament / shock layer interaction: steady flows for different defining parameters (density, isochors)

Dynamics of the process in isochors is presented in Fig. 11. As compared with the symmetrical case an additional shock wave is generated from the left boundary of the rarefaction wave with the centre in the bottom body's corner (Fig.11, $t > 9.6$). Note that for smaller rarefaction in the filament this shock wave does not appear. The stagnation point is established to be formed in a new position lower the body's face center point.

Fig. 12 presents the force F , pressure p_c and density ρ_c at the center of front surface, the x -coordinate of the point of intersection of the lower channel boundary and the bow shock wave front and the dynamics of the new position of the stagnation point. Here

$$F = \int_{r_b}^{r_b+d} p dr,$$

where r_b is the lower body's r -coordinate. It is seen that the behavior of p_c defines approximately the behavior of F . Some temporary drag force enhancement ("heat piston" effect) relatively the

symmetrically located filament is seen at the beginning of the process (see Fig. 12a - 12c). Note that in this case the pressure in the centre of the front surface is greater than the undisturbed stagnation pressure but the maximal value of the drag force does not exceed its undisturbed value. Thus, the character of pressure in the centre point in this case does not entirely define the character of the drag force. Besides it can be concluded that the presence of the back filament boundary (bounded length filament) plays an important role in drag force enhancement.

It is shown that in statistically steady state the stagnation point is forming in the lower position than that for the case of symmetrical filament location (Fig. 12e), its position dynamics being of pulse character reflecting pulse (stochastic) flow character in whole.

Slides of the steady state in isochors calculated on more roughly grid (with h_x and h_y equal to 0.001) are presented in Fig. 13 for asymmetrical ($y/D=0.16$) infinite filament location. On this grid stochastic character of the processes does not registered in the

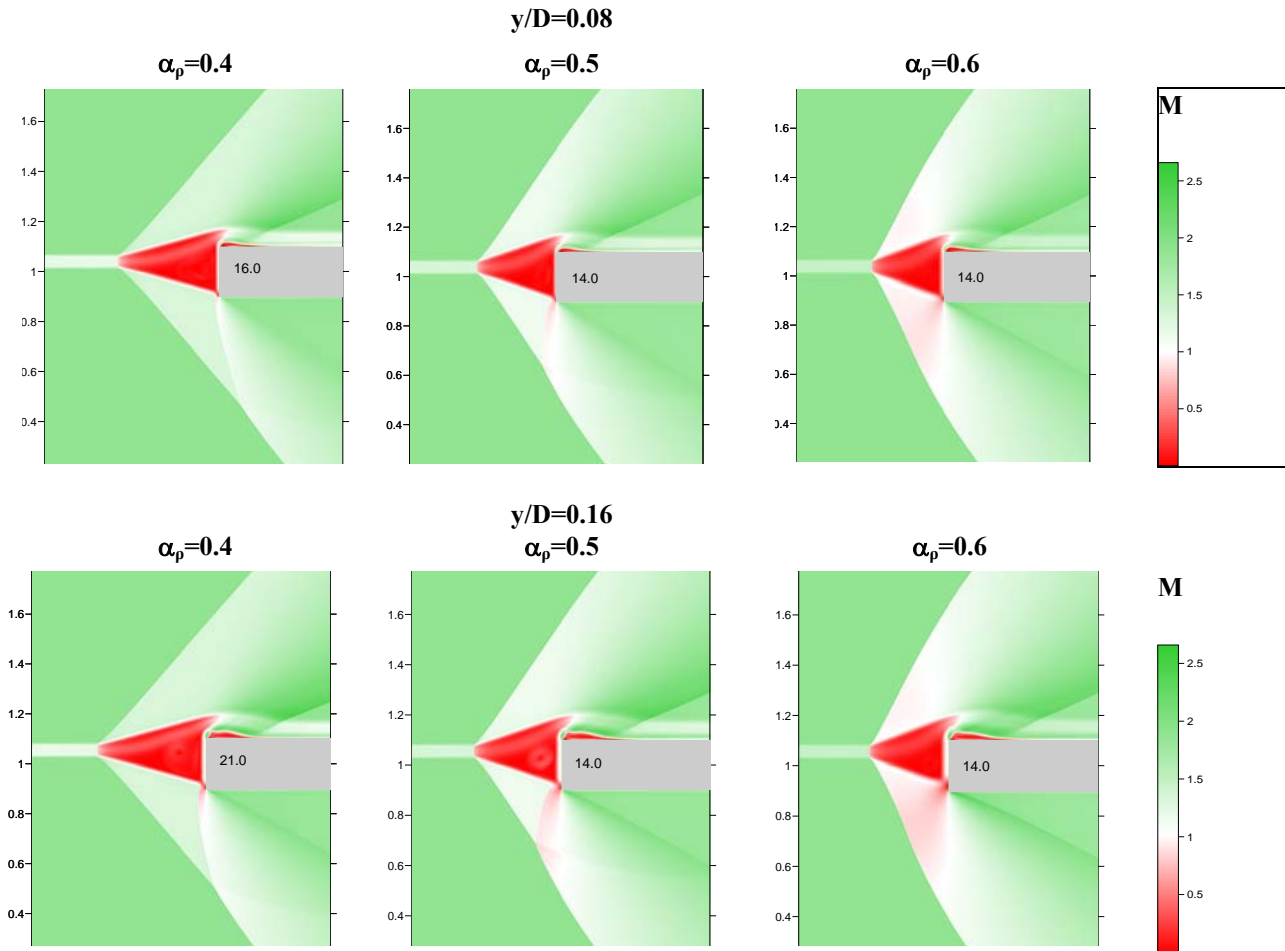


Figure 14. Asymmetrically located filament / shock layer interaction: steady flows for different defining parameters (fields of local Mach number)

steady state but using here difference scheme is established to produce averaged flow characteristics with sufficient accuracy on more roughly grids [13]. In the case of symmetrical filament location the heated flow envelopes the upper and down body's surfaces. For asymmetrical filament location the contact discontinuities form a new structure, the below contact discontinuity turns near the body and becomes parallel to body's front surface dividing the gas near the front surface into cold (adjacent to the front surface) and heat layers. Lower part of the flow decelerates (with new position of stagnation point generation), changes its direction and becomes parallel to the front body's surface.

Near the upper body's corner a new separation area is registered with vortex flow inside of it. The values of pressure and density are decreased in this area. The warm flow envelopes the upper body's surface at some distance from it. The arising shock wave near the upper body's surface is diffracted inside the heated flow. The appropriate fields of Mach numbers are presented in Fig. 14. White color denotes flow transonic areas. In the separation area near the upper body's corner the supersonic area is registered similarly to that

described in Part B. According dynamics of the drag forces for different defining flow parameters is presented in Fig. 15. It can be indicated that the processes are stochastic and for more rarefied channel the large scaled pulsations are registered.

The averaged dependencies of the relative values of stagnation point location, drag force and stagnation pressure over defining flow parameters for asymmetrical filament location are presented in Fig. 16. Here p_{s0} , F_{s0} and y_{s0} – accordingly, stagnation pressure, drag force and stagnation point coordinate (equal to 1) for the flow without filament. It is seen that the stagnation point location on the front of the body is lower and drag force reduction is greater for greater gas rarefaction in the filament (or the greater values of the filament temperature). Note, that these dependencies are close to linear over α_ρ . Dependencies of the relative stagnation pressure on α_ρ for $y/D=0.16$ and 0.24 are more complicated, but for $y/D=0.08$ it is linear, too, and the behavior of drag force is defined by the behavior of the stagnation pressure. In Fig. 17 averaged dependencies of the relative values of stagnation pressure, drag force and y -coordinate of the stagnation point on the body over the release

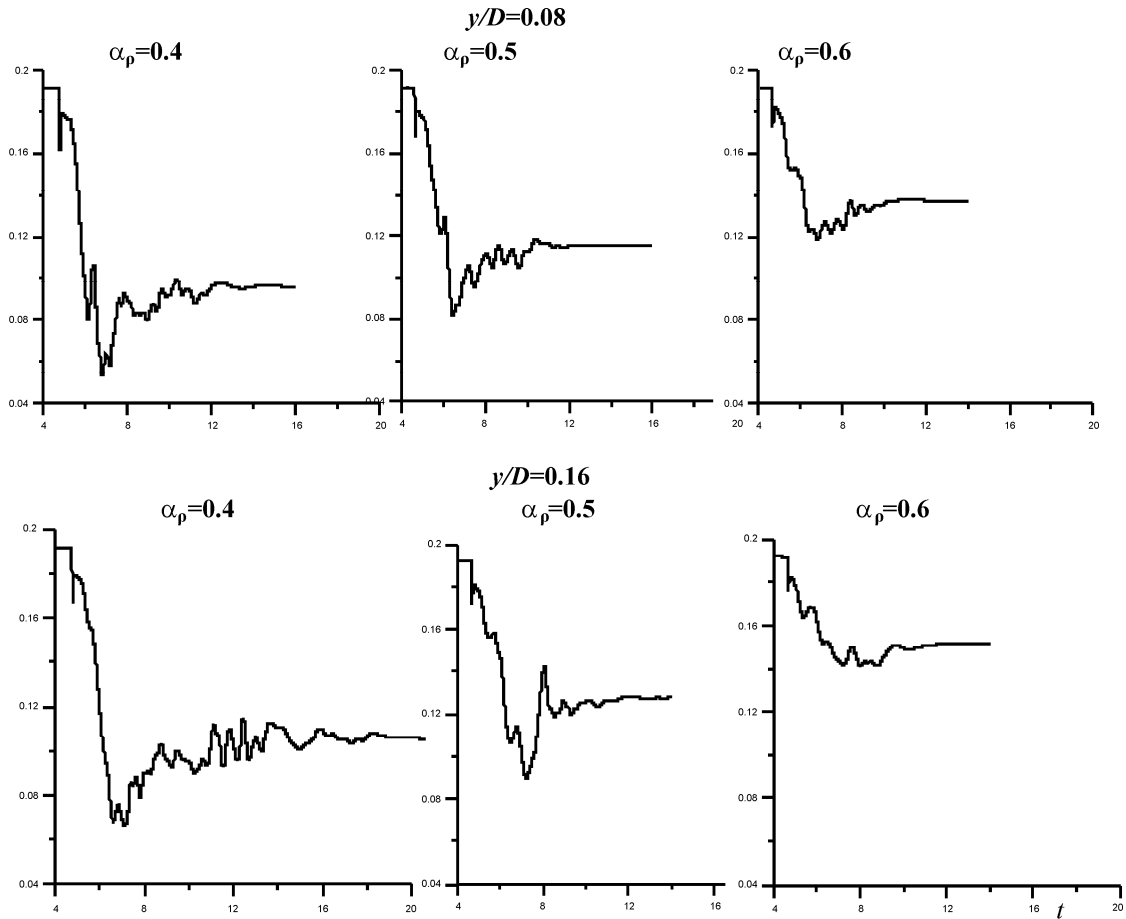


Figure 15. Asymmetrically located filament / shock layer interaction: drag force F dynamics for different defining parameters

filament location are presented for different rarefaction factor in the release filament. The stagnation point location on the front of the body is lower and drag force reduction is greater for greater values of y/D . Note, that these dependencies are linear over the value of the relative distance from filament to the axis of symmetry y/D . Dependencies of the relative stagnation pressure on y/D for different α_p are more complicated.

D. The mechanism of lift/pitch force origination in the case of zero attack angle

If the heated channel/thermal layer is placed up from the axis, only one vortical structure is originated in the steady state instead of two such domains. The warm stream entering the triangle heated area now is not divided and it flows through this area above the vortical structure to the upper corner of the body and then along the upper lateral surface (see Fig. 13). Disposal of a thermal layer up from the axis leads to the overall up shift of the heated triangle area and as a consequence to opening of a lower part of the body to the action of a cold supersonic stream. As a result, new stagnation point

is formed on the front surface near the lower corner of the body, as it was described above in Part C. In this point the pressure value exceeds that for the

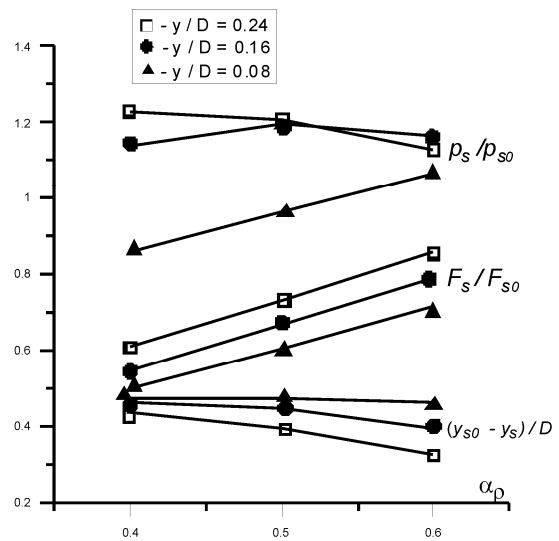


Figure 16. Dependencies of relative values of stagnation pressure, drag force and y -coordinate of the stagnation point on the body over the rarefaction factor in the release filament for different filament locations [23]

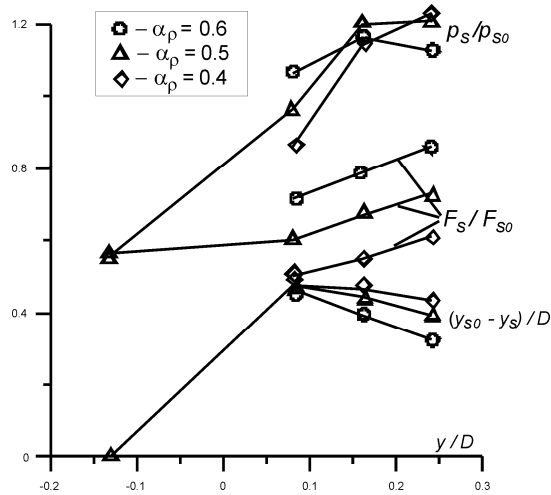


Figure 17. Dependencies of relative values of stagnation pressure, drag force and y-coordinate of the stagnation point on the body over the release filament location for different rarefaction factor in the release [23]

flow without thermal layer by tens of percent. The most part of the stream goes down and then is convected down along the lower lateral surface. The rest (small) part of this cold flow goes up along the front surface of the body pressing the warm triangle structure away from this surface. Reaching the upper corner of the body this cold flow comes into contact with warm flow exiting from the triangle structure, turns to the right and then is convected down along the upper lateral surface, leading to origination of a separated region described in Part C. This separated region occupies the distance of 1...2 body diameters counting downstream from the corner of the body (see Fig. 13, 14).

In Fig. 18 the distributions of a pressure along lateral body surfaces are presented. It is seen that at the lower surface the pressure quickly

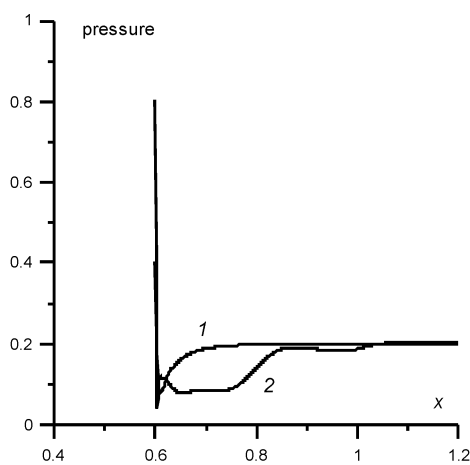


Figure 18. Infinite asymmetrically located filament / shock layer interaction. Pressure on the lateral body's surfaces: curve 1 – on the lower surface, curve 2 – on the upper surface

approaches the static pressure of the oncoming flow. On the contrary, at the upper surface it achieves such a value only at some distance downstream the separated region. Thus, a net force arises as a result of pressure difference which could be distinguished as a lift force if it were not extremely limited in spatial domain of its application. More correct is to determine it as a pitch force. Lift/pitch force is a function of a shift value from the symmetry axis of thermal layer and a degree of rarefaction in it (see Fig. 19). It is seen that in the limits of investigated parameters, this force rises linearly with the shift distance of thermal source from the axis and is approximately inversely proportional to the degree of rarefaction in the source.

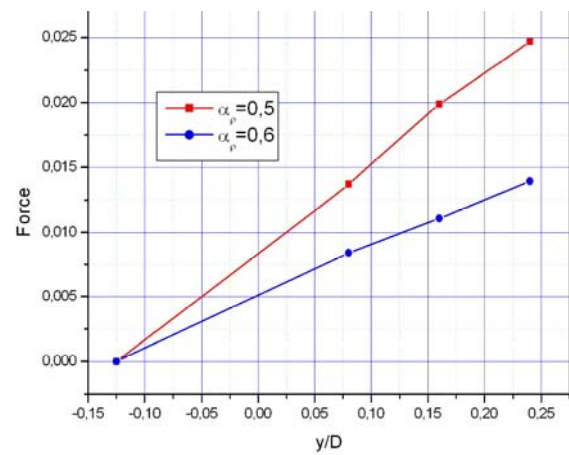


Figure 19. Infinite asymmetrically located filament / shock layer interaction. Dependence of the lift force over y/D for different values of rarefaction degree

Thus, the shift of thermal source from the axis of symmetry leads to origination of a pitch force under the zero angle of attack. Note that while investigating of drag reduction the effect scale was a pressure at stagnation point. In the case of investigation of lift/pitch force such a scale is a static pressure in the oncoming flow.

E. Numerical analysis of periodical steady flow structures accompanying shear layer instability of flat-parallel tangential shock

In the case of an asymmetrical filament location relative to the body (see Part C) another type of instability has been observed near the body's front surface (see [19]). This instability can be characterized as the instability of a flat-parallel tangential discontinuity (which simultaneously in steady state appears to be a contact discontinuity). For the particular set of inflow parameters steady flow structures with some oscillations of the parameters in its (structure elements) are observed in the area of cooler gas between the vertical contact discontinuity and the front surface of the body [14, 19]. Fields of density (in isochors) and velocity in

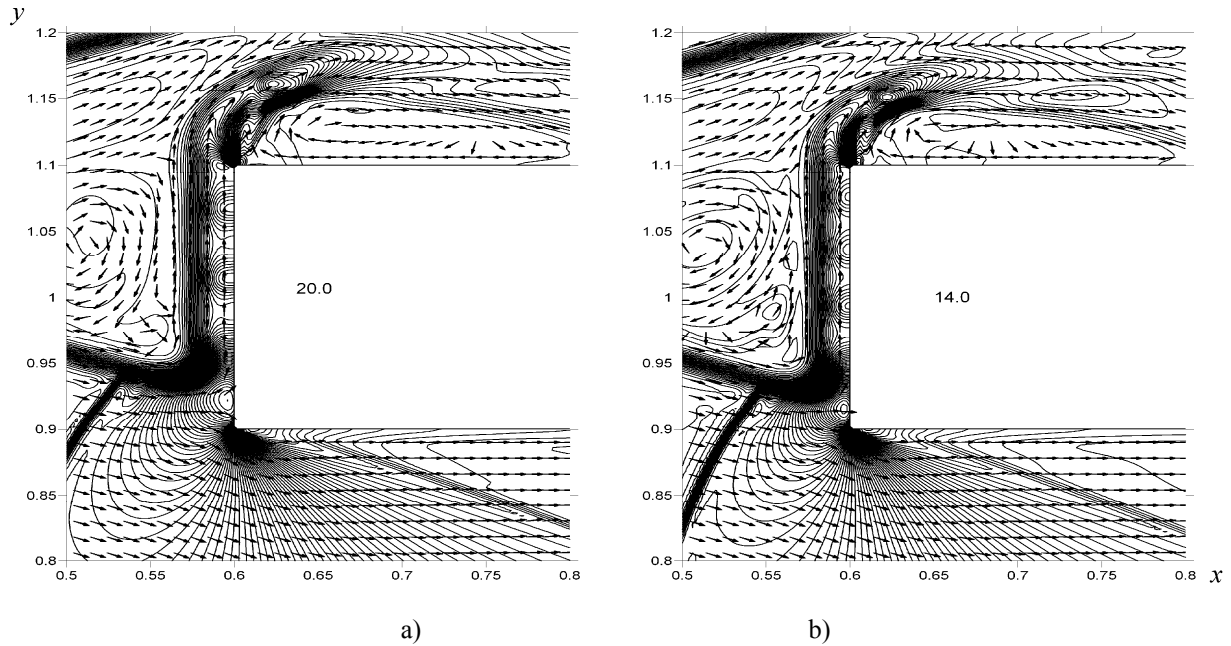


Figure 20. Density (isochors) and velocity in the periodical steady flow structures with two – a) and three – b) elements, $\alpha_p = 0.51201$

the steady flow structures with two and three elements are presented in Fig. 20.

In the dependence on the freestream parameters (including rarefied heated channel parameters) the amount of elements in these steady structures varies from one to four. The flow with one and half element has been observed, too. Transverse velocity component generation during the evolution of the structures shows the presence of the tangential shock instability under these conditions. The mechanism for the generation of these structures is connected with multiple reflection of a primary compression wave inside the flow between the tangential shock and the wall (see [19]). The mechanism is similar to that of generation and forming structures which are accompanying Miles-Ribner instability of super-reflection observed experimentally (in a cylinder flow) in shallow water [24].

Characteristics of these structures were investigated for their dependence on the distance between the heated channel and x -axis, y/D , and the degree of gas rarefaction in the channel α_p . The results are as follows [19, 20]:

- amount of elements in the structures and its length decrease with increasing y/D ;
- period and amplitude of oscillations in structures increase with increasing y/D ;
- amplitude of oscillations in structures increases with decreasing density in the heated channel;
- amount of oscillations in the structures and its period and length are weakly dependent on the degree of rarefaction in the heated channel.

It should be underlined that the structures under consideration are disposed in a very small part ($\sim 1/400$) of the calculation area and the calculations are performed for a time intervals

comparable to the time intervals needed for establishing steady state.

IV. Conclusions

Interaction of microwave filament and a shock layer is analyzed numerically on the base of the Euler system of equations. The filaments are regarded as the heated rarefied channels (heat layers). Investigation of the details of the mechanisms of front body's surface drag force reduction, temporary drag force enhancement and lift/pitch force generation via characteristics and locations of microwave filaments / heat layer in a supersonic flow is implemented. The flow dynamics up to steady states is considered, including the dynamics of drag forces, parameters in the stagnation point and forming new position of the stagnation point for asymmetrical filament location.

It is pointed out that drag reduction for symmetrical filament location is caused by the vortices effect on the front body's surface and is connected with generation of the gas stream directed from the body. Temporary drag increasing is pointed out to base on the generation of a mass of compressed cooler gas near the body via the heated area boundary effect inside the shock layer ("heat piston" effect). It is shown that in statistically steady state in the case of asymmetrically filament location the stagnation point is forming in a new position against that for the case of symmetrical filament location, its dynamics being of pulse character reflecting pulse (stochastic) flow character in whole.

It is also shown that in the case of zero attack angle the shift of thermal source from the axis of symmetry leads to origination of a pitch force,

which is a function of a shift value from the symmetry axis of thermal layer and a degree of rarefaction in it. The mechanism of lift/pitch force origination is revealed. The mechanism of this effect was established to be of vortex nature. For this type of flows the steady flow structures have been obtained and researched.

The phenomena are analyzed for a sufficiently wide class of initial conditions, namely, the freestream parameters and the values of microwave filament characteristics (*i.e.*, Mach number, rarefaction factor, position relative to the body centerline and finite/infinite filament sizes).

Acknowledgements

The work was partially supported by EOARD (ISTC Project 3058p).

References

- Georgievsky, P.Y., Levin, V.A., "Supersonic Flow over Bodies in the Presence of External Energy Input", *Letters in Journal of Technical Physics*, 1988, Vol. 14, 8, pp. 684-687.
- Knight, D., "Survey of Aerodynamic Drag Reduction at High Speed by Energy Deposition", *Journal of Propulsion and Power*, Vol. 24, No. 6, 2008, pp. 1153-1167.
- Zheltovodov, A., "Development of the studies on Energy Deposition for Application to the Problems of Supersonic Aerodynamics", *Preprint No. 10-2002, Khristianovich Inst. of Theoretical and Applied Mechanics*, Novosibirsk, Russia, 2002.
- Fomin, V., Tretyakov, P., and Taran, J.-P., "Flow Control Using Various Plasma and Aerodynamic Approaches (Short Review)", *Aerospace Science and Technology*, Vol. 8, No. 5, July 2004, pp. 411-421.
- Georgievsky, P.Y., Levin, V.A., "Effective Control of Supersonic Flows over Different Bodies by an Energy Input to Ambient Flow", *Proc. 4th Workshop on Magneto-Plasma Aerodynamics in Aerospace Applications*, Ed. by V.A. Bityurin, Moscow, IVTAN, 2002, pp. 40-43.
- Georgievsky, P.Y., Levin, V.A., "Transition to Irregular Regimes of Supersonic Flows over Bodies Initiated by Energy Deposition", *Paper AIAA-2005-1047*, pp. 1-9.
- Artem'ev, V.I., Bergel'son, V.I., Nemchinov, I.V., Orlova, T.I., Smirnov, V.A., Hazins, V.M., "Changing the Regime of Supersonic Streamlining Obstacle via Arising the Thin Channel of Low Density" *Mechanics of Fluids and Gases*, 1989, No 5, pp. 146-151.
- Kolesnichenko, Yu. F., Brovkin, V.G., Azarova, O.A., Grudnitsky, V.G., Lashkov, V.A., Mashek, I.Ch. et al. "Microwave Energy Release Regimes for Drag Reduction in Supersonic Flows" *Paper AIAA-2002-0353*. pp. 1-13.
- Kolesnichenko, Yu. F., Azarova, O.A., Brovkin, V.G., Khmara, D.V., Lashkov, V.A., Mashek, I.Ch. et al. "Basics in Beamed MW Energy Deposition for Flow/Flight Control", *Paper AIAA-2004-0669*, pp.1-14.
- Azarova, O.A., "On Some Mechanisms of Gas Dynamics Established on a Base of Modified Minimum-Stencil Difference Schemes", *Highly Productive Calculations in Problems of Mechanics and Physics*, Ed. by G.P.Prokopov, *Keldysh Inst. of Applied Math. RAS*, 2009, pp. 25-38.
- Azarova, O.A., Grudnitsky, V.G., Kolesnichenko, Yu. F., "Some Gas Dynamics Aspects of Flow Control by MW Energy Deposition", *Proc. 6th Int. Workshop on Magnetoplasma Aerodynamics*, Ed. by V.A. Bityurin, Moscow, Institute of High Temperatures, May 24-27, 2005, Vol. 1, pp. 152-163.
- Azarova, O.A., Kolesnichenko, Yu. F., "On Details of Flow Structure During the Interaction of an Infinite Rarefied Channel with a Cylinder Shock Layer", *Proc. 7th Int. Workshop on Magnetoplasma Aerodynamics*, Ed. by V.A.Bityurin, Moscow, Institute of High Temperatures, 2007, pp. 101-113.
- Azarova, O.A., "A Minimum-Stencil Difference Scheme for Computing Two-Dimensional Axisymmetric Gas Flows: Examples of Pulsating Flows with Instabilities", *Journal of Comp. Math. and Math. Phys.*, 2009, Vol. 49, No 4, pp. 734-753.
- Azarova, O.A., "Modeling of Stochastic Pulsing Flows with Instabilities on the Base of Minimum-Stencil Difference Schemes", *Journal of Comp. Math. and Math. Phys.*, 2009, Vol. 49, No 8, pp. 1-18.
- Farnaz Farzan, Olga Azarova, Yuri Kolesnichenko, Doyle Knight, "Interaction of Microwave Filament and Blunt Body in Supersonic Flow", *Paper AIAA-2008-1356*, pp. 1-24.
- Knight, D., Azarova, O.A., Kolesnichenko, Yu. F., "On Details of Flow Control via Characteristics and Location of Microwave Filament During Its Interaction with Supersonic Blunt Body", *Paper AIAA-2009-847*, pp. 1-21.
- Azarova, O.A., Knight, D., Kolesnichenko, Yu. F., "Instabilities, Vortices and Structures Characteristics During Interaction of Microwave Filaments with Body in Supersonic Flow", *Paper AIAA-2010-1004*, pp. 1-16.
- Lashkov, V.A., Mashek, I.Ch., Anisimov, Yu.I., Ivanov, V.I., Kolesnichenko, Yu.F., Ryvkin, M.I. et. al. "Gas Dynamic Effect of Microwave Discharge on Supersonic Cone-

- Shaped Bodies”, *Paper AIAA-2004-0671*, pp. 1-9.
19. Azarova, O.A. “Modeling of Steady Flow Structures Accompanying Shear Layer Instability”, *Proc. Int. Conf. “Fluxes and Structures in Fluids: Physics of Geospheres”*, Moscow, MSU, June 2009, pp. 22-27.
 20. Azarova, O.A., “Numerical Experiments on Modeling of Steady Structures in Supersonic Flows with Asymmetrical Energy Supply”, *Journal of Comp. Math. and Math. Phys.*, 2010 (to be published).
 21. Belotserkovsky, O.M., Grudnitsky, V.G., Prohorchuk, Yu. A., “Difference Scheme of the Second Order of Precision on a Minimal Stencil for Hyperbolic Equations”, *Journal of Comp. Math. and Math. Phys.*, 1983, Vol. 23, No 1, pp. 119-126.
 22. Doyle Knight, Olga Azarova, Yuri Kolesnichenko, “Drag Force Control via Asymmetrical Microwave Filament Location in a Supersonic Flow”, *Proc. Sixth European Symposium on Aerothermodynamics for Space Vehicles*, Versailles, France, Nov. 3-6, 2008, pp. 1-8.
 23. Azarova, O.A., Knight, D., Kolesnichenko, Yu. F., “Pulsating Stochastic Flows Accompanying Microwave Filament / Supersonic Shock Layer Interaction”, *Shock Waves*, 2010 (under reviewing).
 24. Fridman, A.M., “Prediction and discovery of strongest hydrodynamic instabilities caused by velocity shock: theory and experiment”, *Advances in Physical Sciences*, 2008, Vol. 178, No 3, pp. 225-242.

THE INFLUENCE OF AN ELECTRIC DISCHARGE ON THE FLOW PATTERN OF SUPERSONIC IMPACTING JET

V.M. Fomin, K.A. Lomanovich, and B.V. Postnikov

Khristianovich Institute of Theoretical and Applied Mechanics SB RAS,
Institutskaya str. 4/1, Novosibirsk, 630090, Russia

Abstract. The results of an experimental study in which examined the influence of an electric discharge on the structure of supersonic overexpanded air and methane jet flows ($M=3.5$) impacting a flat face of impermeable cylinder are discussed. The impulse electric discharge was initiated in the gap between the nozzle exit and the obstacle. The influence the geometric parameters of the nozzle-obstacle system on the oscillation frequency of normal compression shocks was examined. It was shown that, following the discharge initiation, the oscillation frequency of the bow shock wave and Mach disk displayed changes. The results obtained in the present study may prove useful in the development of new control methods for supersonic jet flows, and also in the development of high-speed plasma-chemical reactors and gas-spray processes

1. Introduction

Unsteady gas-dynamic regimes may affect performance characteristics of various gas-phase setups. In plasmochemical reactors, for instance, such regimes may have an influence on the yield of final products. Results concerning unsteady and transient regimes can therefore prove useful in modernization and development of advanced high-speed plasmochemical reactors and other gas-phase facilities (see, for instance, [1-5]), and also in solving various applied problems in gasdynamics and magnetoplasma aerodynamics related to the control of supersonic jet flows and jet-obstacle interactions.

Steady and unsteady jet flows impacting onto obstacles were the subject matter of many studies (see, for instance, [6-9]). In overexpanded jets, depending on the nozzle pressure ratio, three

characteristic flow modes are possible. At low overexpansion values, regular reflection of incident compression shock from the jet axis is observed. On decreasing the nozzle pressure ratio below some critical value, irregular reflections appear. If the obstacle is located in the subsonic region behind the central shock, then no bow shock forms at the obstacle.

In [8, 9], it was shown that, in underexpanded jets, unsteady flow regimes may arise in a broad range of gasdynamic conditions and geometric parameters of the nozzle-obstacle system. The ranges of gasdynamic and geometric parameters examined in [8] were as follows: nozzle pressure ratio $n=1\div 55$, Mach number $M=1.0\div 2.0$, relative obstacle diameter $d/D=1\div 8$, and relative nozzle-to-obstacle separation $h/D=1\div 12.5$. In a certain range of governing parameters, when the obstacle exerts an influence on the central compression shock, an

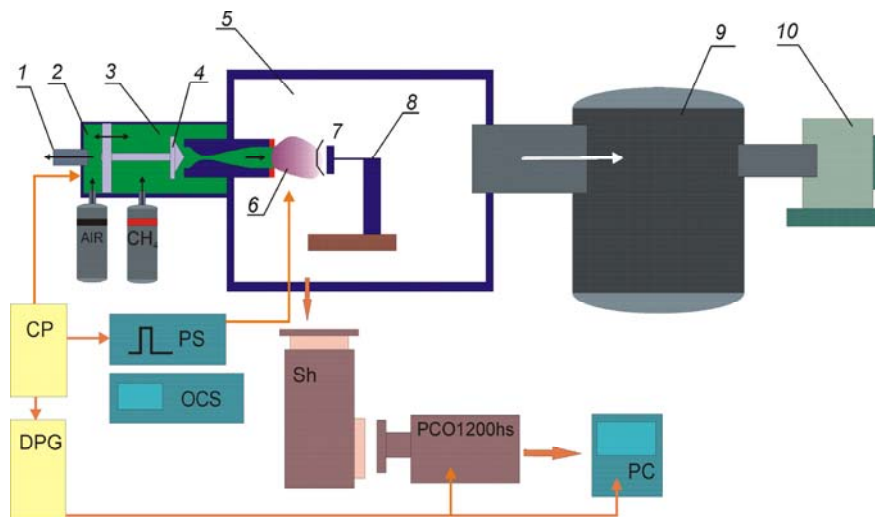


Fig.1. Experimental facility: 1 – pressure release valve for auxiliary gas; 2 – auxiliary-gas chamber; 3 – pre-chamber; 4 – fast valve; 5 – test chamber; 6 – electric discharge area; 7 – obstacle; 8 – pylon; 9 – low-pressure chamber; 10 – backing pump; CP – control panel; PS – power supply; OSC – oscilloscope; DPG – delayed-pulse generator; AIR – air flask; CH₄ – methane flask; Sh – shadow device; PCO1200hs – high-speed video camera; PC – personal computer.

unsteady flow regime arises, in which the compression-shock system displays oscillations. For underexpanded jets, there exists a range of nozzle pressure ratios in which emerging oscillations display a periodic pattern, whereas outside that range an aperiodic “noise” pattern is exhibited. The authors of [9] examined the case in which a supersonic underexpanded jet impacted onto an infinite obstacle: $n=1.5\div 40$, $M=1\div 3$. In those experiments, pressure pulsations at obstacle location were measured. In unsteady regimes, depending on the distance to the obstacle, changes of the frequency and amplitude characteristics of jet shockwave-structure oscillations in front of the obstacle were registered; those changes were also reflected in the pressure pulsations at obstacle location. Low-amplitude oscillations were detected at frequencies up to 20 kHz, and at a 4-kHz frequency five-fold increased pressure pulsation amplitude was registered.

An analysis of phenomena underlying the production of high-amplitude oscillations in impact jet flows was given in [6]. The mechanisms giving rise to such unsteady flow regimes still remain poorly understood. One of the advanced hypotheses relates the manifestation of the unsteadiness with the motion of the triple shock-wave configuration.

2. Experimental facility

The experiments were carried out on the Potok-3 plasmochemical facility, ITAM SB RAS. The facility was a supersonic pyrolytic reactor operated in a pulsed mode (Fig. 1). The 2-liter settling chamber was filled with a gas under study. On initiation of the fast-response pneumatic valve, a supersonic flow, lasting for a period of 500 ms, established in the nozzle. In the downstream region of the nozzle, an obstacle was installed. Energy input into the supersonic flow was organized with the help of an electrode system; as one of the electrodes, the nozzle lip or the obstacle could be used. As an instrument for examining the shock-wave structure in the vicinity of the obstacle, a shadow device of standard optical scheme was employed. Visualization was performed with the help of a PCO 1200hs high-speed video camera capable of registering images at frequencies up to 10 thousand frames per second. Flow regimes emerging in the jet impinging onto an impermeable cylindrical obstacle were examined. The relative obstacle diameters were $d/D=1/3$; 1.0; 1.5; 2.0. The relative distance to the obstacle h/D was varied from 1/3 to 2.0, where h is the distance between the exit plane of the nozzle and the front face of the obstacle. The settling-chamber pressure P was varied in the range from 4 to 12 atm. The conical nozzle was a Mach 3.5 nozzle (air). The gases under study were methane and air. Energy input into the high-speed flow was organized using a

pulsed electric discharge. The duration of discharge was up to 300 ms. A longitudinal-transverse gas discharge has a typical voltage of 60-80 V and a typical current of 50 A, the peak amplitude of transient voltage amounting to 100-150 V. An overexpanded regime of supersonic jet flow (air or methane) was investigated (see Fig. 2 and 3). With the obstacle located in the upstream region of regular reflection, a triple shock-wave configuration, or Mach disc, was formed in the flow.

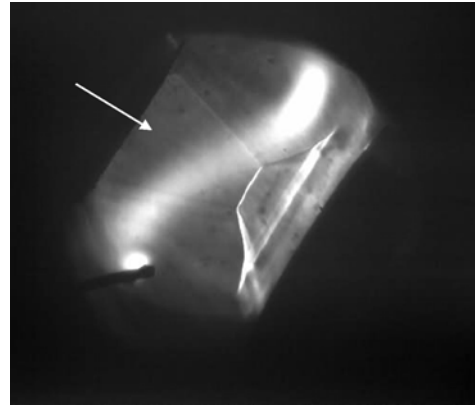


Fig. 2 A typical shadowgraph taken from the air jet flow impinging onto the obstacle at the moment of discharge initiation: $d/D=1.5$; $h/D=1.0$; $n=0.7$; $P=6$ atm.. The flow direction is indicated with the arrow.

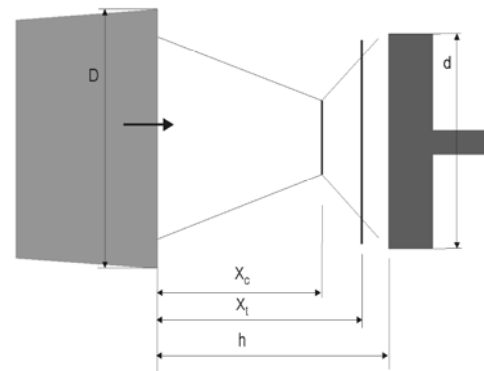


Fig. 3. A simplified gasdynamic pattern of the jet flow: D – nozzle outlet diameter; X_c – distance from the nozzle exit plane to the normal compression shock, or Mach disc; X_t – distance to the bow shock; h – distance to the obstacle; d – obstacle diameter.

3. Experimental results

A proper choice of supply unit, discharge characteristics, electrode arrangement geometry, and parameters of the discharge-initiating circuit has allowed us to organize stable electric-discharge

initiation and burning in the space between the nozzle and the obstacle during the examined flow regime of 150 ms (see Fig. 2).

For identical stagnation pressures, the oscillation frequencies F of the bow shock in air and methane differed in value, these frequencies at nozzle-to-obstacle separation $h/D=1.0$ falling into the range from 250 to 950 Hz. Some minor differences between the cases with methane and air flows were observed. For obstacle with $d/D=1.0$, on increasing the nozzle-to-obstacle separation h/D from $1/3$ to 2.0 , the oscillation frequency of the bow shock decreased from 700 Hz to 300 Hz at $P=4$ atm and from 1800 Hz to 750 Hz at $P=12$ atm (See Fig.4). On increasing the distance to the obstacle h/D from $1/3$ to 2.0 , the interval of Mach disk oscillation frequencies for different relative obstacle diameters shifted from 500–2100 Hz down to 160–550 Hz.

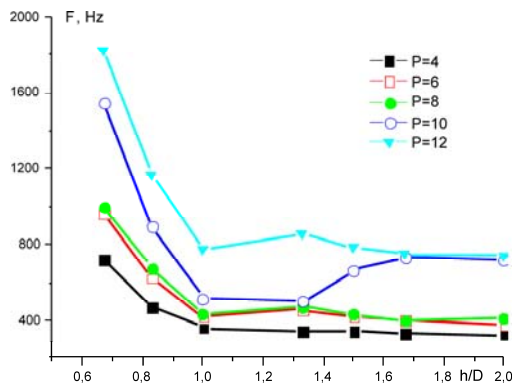


Fig.4. Influence of nozzle-obstacle separation h/D on the oscillation frequency of the bow shock wave $d/D=1.0$ and initial stagnation pressure P from 4 to 12atm.

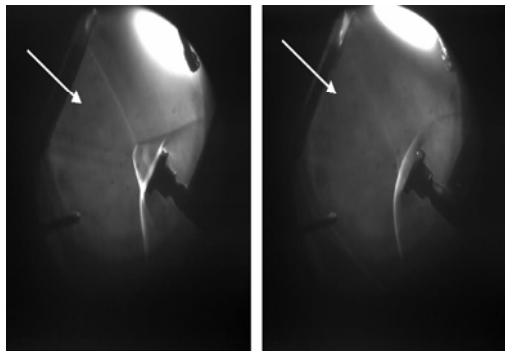


Fig.5. Alteration of flow mode observed on initiation of an electric discharge near the edge of supersonic methane jet: $d/D=1/3$; $h/D=1.0$; $P=6$ atm. The flow direction is indicated with the arrow. Left – flow regime with a central shock, or Mach disc, and with a bow shock at the obstacle. Right – flow regime without a Mach disc.

Apart from the «normal» flow modes, like the one in Fig. 2, in the experiments abnormal flow modes with sudden alteration of shock-wave

configurations were observed. Figure 5 shows successive frames taken from the supersonic flow with initiated electric discharge. Without electric discharge, no alteration of flow modes was observed. A transition is seen possible during which the flow with a normal compression shock, or Mach disc, gives way to a stable regime without Mach disc. A factor probably affecting the transition was the change of nozzle pressure ratio induced by the discharge thermal wake in the mixing layer. Here, the point at which irregular reflections from the jet axis emerged was shifted in the upstream direction and replaced by regular reflection. The obstacle, although located in the downstream region of this point, was also streamlined by supersonic flow.

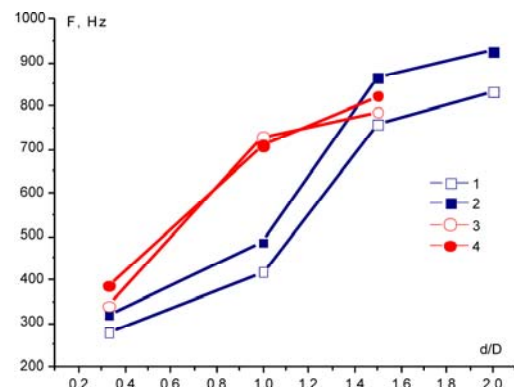


Fig. 6. Influence of the electric discharge on the oscillation frequency of the bow shock wave for various relative obstacle diameters d/D . Data for methane and air are presented, $h/D=1.0$; $P=6$ atm. 1 – air without electric discharge; 2 – air with electric discharge; 3 – methane without electric discharge; 4 – methane with electric discharge.

Experiments showed that, under the action of discharge plasma ignited in the vicinity of the obstacle, the oscillation frequency underwent changes (see Fig. 5). On increasing the relative obstacle diameter d/D , the oscillation frequency grew in value. With the discharge, the frequency response to the external action was more pronounced in air in comparison with methane. For instance, at $d/D=1/3$ and $P=6$ atm the bow-shock oscillation amplitude in air and methane was about $0.35D$ and $0.05D$ respectively with and without ignited discharge. Simultaneously, no transformation of flow pattern similar to that in Fig. 5 was observed in air.

4. Conclusions

New experimental data on the frequency and amplitude characteristics of normal-shock and bow-shock oscillations emerging in supersonic overexpanded air and methane jet flows impacting onto variously sized obstacles installed at a certain distance from the nozzle were obtained for

conditions with and without initiated electric discharge.

The compression-shock oscillation frequency depended on the working-gas (air or methane), on the nozzle-to-obstacle separation, on the relative diameter of the obstacle.

An electric discharge initiated in the space between the nozzle and the obstacle can be used to modify the oscillation frequency of the bow shock wave formed in supersonic methane and air jet flows in the vicinity of the obstacle.

Conditions were identified under which the flow pattern in the vicinity of the flat obstacle suffered dramatic reconstruction on electric-discharge initiation in the mixing layer of the supersonic overexpanded methane jet.

The work was partially supported by the Program for Basic Research of Presidium RAS (project 11.11).

References

1. Patent RU 2222569. (2002). V.M. Fomin, V.N. Parmon, V.P. Fomichev et al. Gas-phase reaction method.
2. N.V. Denisova, B.V. Postnikov, V.M. Fomin. Transverse glow discharge in supersonic air and methane flows. *Fizika Plazmy*, 2006, No. 3, pp. 281-288.
3. N.V. Denisova, V.M. Fomin, B.V. Postnikov. Methane conversion using non-equilibrium discharge plasma. AIAA Paper 2007-4028.
4. V.M. Fomin, A.I. Lebedev, K.A. Lomanovich, B.V. Postnikov. Natural-gas conversion in sub- and supersonic pyrolytic reactors // Proc. 17th ICMHD. Kanagawa, Japan. 2009.
5. V.M. Fomin, B.V. Postnikov, K.A. Lomanovich. Energy input areas initiated by electric discharge in supersonic flow of reactive gases // Proc. 22th ICDERS. Minsk, Belarus. 2009.
6. V.G. Dulov, G.A. Luk'yanov. Gasdynamics of Outflow Processes. – Novosibirsk: Nauka, 1984.
7. V.V. Filatov. Determination of the structure of supersonic overexpanded gas jet over the initial length. – In: *Hydromechanics and Elasticity Theory*. Iss. 13. Dnepropetrovsk: Dnepropetrovsk State University. 1971, pp. 3-11.
8. A.G. Golubkov, B.K. Koz'menko, V.A. Ostapenko, A.V. Solotchin. On the interaction of supersonic underexpanded jet with a finite-size flat obstacle // *Izv. SO AN SSSR. Ser. Techn. Nauk.* No. 13, Iss. 3, 1972, pp. 52-58.
9. B.G. Semiletenko, B.N. Sobkolov, V.N. Uskov, Unsteady interaction of a supersonic jet with infinite obstacle. // *Izv. SO AN SSSR. Ser. Techn. Nauk.* No. 13, Iss. 3, 1972, pp. 47-51.

INVESTIGATION OF VORTEX FLOW INDUCED BY DIELECTRIC BARRIER DISCHARGE IN QUIESCENT AIR

Golub V.V.¹, Saveliev A.S.², Sechenov V.A.², Son E.E.¹

¹Joint Institute for High Temperatures RAS, Moscow

² Moscow Institute of Physics and Technology, Dolgoprudny

Introduction.

One of the most promising methods of airflow control near the surface of aircraft is DBD-actuator. DBD (dielectric barrier discharge [1]) plasma actuator – the electrical device that can transfer small amount of momentum to quiescent or moving air near the surface of solid body. The peculiarity of asymmetric DBD is a presence of areas near the electrodes with huge values of electrical field strength, where the ionization of air and discharge occur. When the high voltage is applied, the partial ionization of air occurs with the generation of different ions (of oxygen, nitrogen), which accelerate due to electrical field. When ions collide with neutral molecules in air, the ions give them momentum, and therefore along the surface of actuator the airflow occurs. The value of airflow jet that induced by DBD is up to 10 m/s and this value is sufficient to have influence on the airflow pattern around the body [2].

Last time many works occurred about the successful delay or even the complete prevention of flow separation from the wing surface with the help of DBD-actuator [2]. There a lot of attention is paid for experimental determination of maximal possible momentum that is transferred to airflow and also for optimization of DBD-actuator characteristics. Though, the gasdynamic processes that occur at initial time moments after voltage applying to actuator have not been investigated completely [3].

This work is devoted for investigation of flow that generates with DBD in quiescent air near the surface of actuator at initial time moment after high voltage applying.

Experimental setup and diagnostics.

The experiments of investigation of unsteady processes that occur in the vicinity of electrodes of electrical device (DBD-actuator) were carried out with the actuator model the sketch of which is presented on Fig. 1. The plexiglas plate of 5 mm thickness and 60 mm on 80 mm dimensions was covered by conducting paint that has high adhesion with plexiglas. After the desiccation and polishing of paint layer its thickness became approximately 0.02 mm. Then the 0.10 mm double-sided scotch tape was stuck on the surface in such way that there were no air bubbles under the tape. The 0.20 mm teflon tape was stuck on above and in

this case there were no air bubbles under the tape. The teflon tape played role of dielectric that separates the electrodes of device. With the help of double-sided scotch tape the copper strip of 0.05 mm thickness was stuck on the teflon in such way that the edges of exposed and encapsulated electrodes have zero overlapping. Therefore, in the discharge device the distance between the electrodes was 0.4 mm. It is necessary to mention that the distance 0.4 mm – was the minimal value in experiments. The width of exposed electrodes was varied from 2 mm to 20 mm.

The power supplying of discharge device was provided by high voltage supply (AC/AC-converter) of altering voltage through the ballast resistor. The adding of active resistance in discharge scheme is necessary, after all, due to high thermal loads on the material of dielectric layer. The limitation of discharge current allows increasing of the life-time of actuator considerably and this fact allows saying about the recurrence of experimental results. The parameters of high voltage supply are below:

- variable amplitude of voltage in range 0 kV – 5 kV;
- maximum power output is 400 W;
- frequency of output voltage is $5.00 \cdot 10^4$ Hz.

In the experiments the value of resistance of ballast resistor was varied from 0 Ohm to 250 kOhm. It is necessary to underline, that the estimated value of actuator reactance, that is a capacitor per se, with that frequency is about 10 MOhm and this value is on two orders greater than the resistance of ballast resistance. The actuator was placed in the airtight working chamber that was equipped with the transparent windows from optical

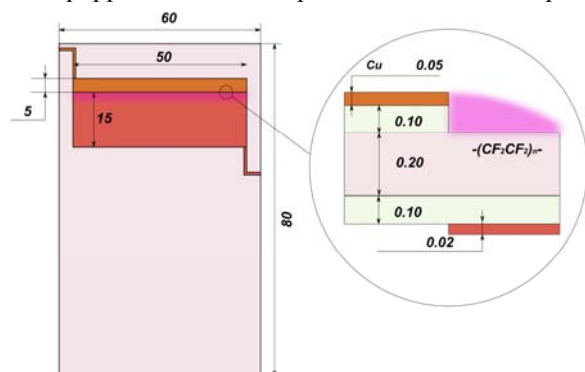


Fig. 1. The scheme of device used in experiments for visualization.

glass for gas flow visualization.

The main experimental methods, used in investigation, were:

- high speed digital schlieren visualization;
- particle image velocimetry;
- measurement of applied voltage and discharge current.

For high speed schlieren visualization the system was developed and it consists of mirror-meniscus schlieren device IAB-451 [4], arc lamp DKSSh-150-1 as light source, high speed digital videocamera Photron FASTCAM SA4 as registering device. The image of slit with 3 mm on 0.4 mm in dimensions was cut buy the Foucault knife by 50%. Then the pattern was projected on the videocamera CMOS-matrix by the lens of variable focus length up to 200 mm. The typical acquisition speed in the experiment was 10^4 fps with exposition time 10 us. On the Fig. 2 the scheme of schlieren visualization near the actuator, placed in the working chamber, surface is presented.

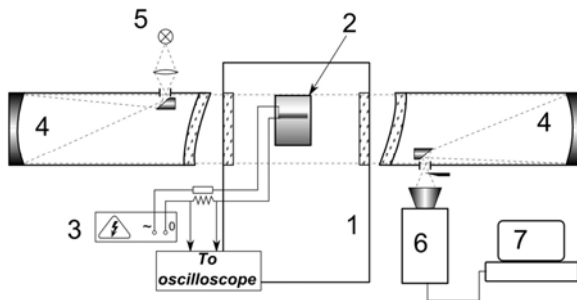


Fig. 2. The scheme of schlieren visualization of flow near the actuator surface. 1 – working chamber, 2 – DBD-actuator, 3 – high voltage supply, 4 – schlieren device IAB-451, 5 – light source, 6 – high speed videocamera, 7 – registering computer.

The actuator was placed with the micrometric screws in such way that its surface and edge of exposed electrode were parallel to optical axis of schlieren device.

For the instantaneous measurement of spatial distribution of velocity vector of flow [5] induced by discharge the system 2D PIV LaVision FlowMaster was used. The microscope MBS-10 was used as lens for PIV-videocamera. The parameters of measurement system are:

- energy of laser pulse is 125 mJ at 6 ns;
- particles of cigarette smoke with diamter about 300 nm as tracers;
- delay between two laser pulses is from 3 us to 5 us;
- delay between discharge start and velocity measurement is from 185 us to 10 ms;
- maximum acquisition speed 14 Hz;
- visible area is 5 mm on 7.5 mm;
- spatial resolution is 70 um;

- synchronization error is 20 ns;
- measurement error is about 2%.

On the Fig. 3 the scheme of measurement of velocity vector spatial distribution is presented.

For the electrical parameters measurements of discharge the digital oscilloscope Tektronix TDS3014B with 100 MHz bandwidth and 1 GS/s discretization, high voltage probe 1:1000 Tektronix P6015A, current probe Tektronix P6021 with the 2 mA/mV sensitivity were used.

Stationary airflow induced by discharge.

The first stage of investigation was the determination of dependence between the velocity of induced air jet and electrical parameters, such as the amplitude of applied to DBD-actuator voltage and the value of active resistance of discharge scheme in stationary case. On the Fig. 4 the experimentally obtained curve of dependence between the maximum velocity of induced by discharge near-wall jet and the amplitude of voltage is presented. In this case the value of resistance of ballast resistor was 160 kOhm. The measurement of velocity was carried out with the PIV, described above.

It was possible due to the high voltage equipment to carry out the investigation of influence of the potential of encapsulated electrode on the parameters of stationary airflow. The investigation was carried out in this way. At first the distribution of velocity vector of induced airflow in case, when the encapsulated electrode was grounded. Then obtained result was compared with the measurement result, obtained in case, when the amplitude of applied potential (in relation to laboratory ground) applied to encapsulated electrode was -1.0 kV and the amplitude of potential applied to exposed electrode was +2.0 kV. And the amplitude of difference of these potentials was the same in first and in second cases and it was 3.0 kV. The value of active resistance of scheme was constant and it was equal to 160 kOhm. It was found that the pattern of induced airflow does not

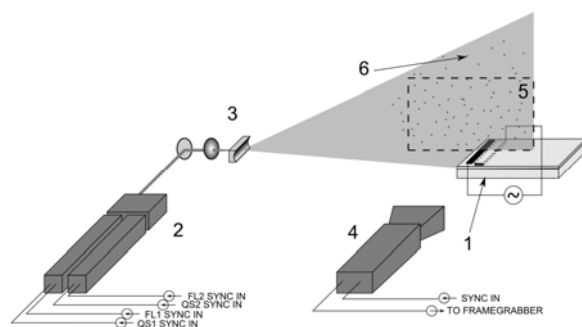


Fig. 3. The scheme of velocity distribution measurement of flow induced by discharge. 1 – DBD-actuator, 2 – double-head Nd:YAG laser, 3 – light sheet optics, 4 – PIV-videocamera, 5 – visible area, 6 – smoke particles.

depend on the potential of encapsulated electrode. In other experiments the encapsulated electrode was grounded.

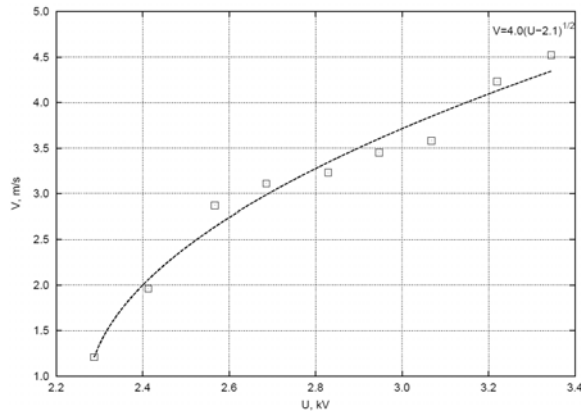


Fig. 4. The dependence between the maximum induced airflow speed and the value of voltage amplitude applied to DBD-actuator.

The investigation of influence of active resistance of discharge scheme value on value of maximum air jet speed was carried out. The range of values of resistor resistance used in experiment was from 1.3 kOhm to 250 kOhm that is much less than reactance of actuator with the frequency 50 kHz. It was found that in this resistance value range the maximum airflow velocity, induced by discharge, changes significantly (Fig. 5).

This phenomenon can be explained by the help of experimentally obtained curves of voltage and discharge in discharge scheme. On the Fig. 6 two examples of these oscillogramms are presented for resistance 12 kOhm and 250 kOhm.

One can see that the value of discharge current undergoes considerable changes in amplitude. It is known [6] that the most efficient discharge stage, from the point of view of creation airflow by DBD, is the negative half-period of

voltage, where the most spatially uniform ionization of air occurs. But at the positive half-period of voltage the formation of localized threads (filaments), which are characterized by high thermalization rate of gas, is observed [7]. One can see that the discharge at the positive half-period is almost suppressed with greater value of resistance.

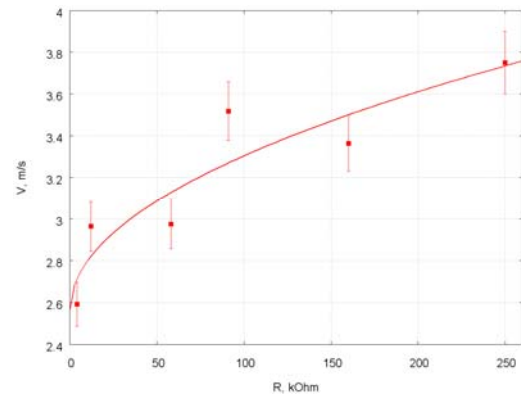


Fig. 5. The dependence between the maximum airflow velocity and the value of active resistance of discharge scheme.

Investigation of the flow formation after voltage applying.

The investigation of unsteady gas flow was carried out with the same methods that are described above. The diagnostic systems were synchronized with the process of DBD initiation. The registration of schlieren pictures of induced by DBD airflow was carried out with the acquisition speed 10^4 fps, and the measurement of flow velocity vector distribution with PIV was carried out with the minimal time step 100 us. The visualization time was 10 ms that corresponds to time of flight of unsteady airflow out of visualization area of space near the actuator

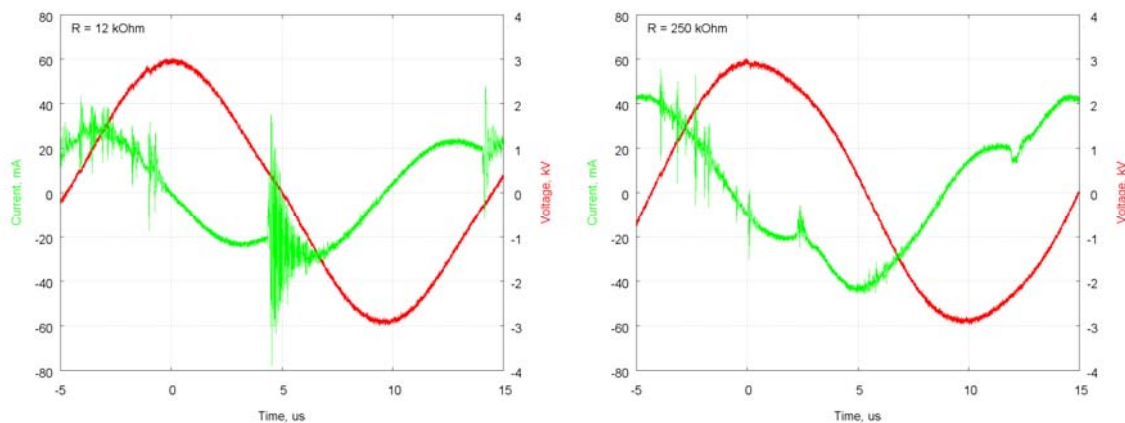


Fig. 6. The typical oscillogramms of voltage and current in the discharge scheme with the resistance values 12 kOhm (top) and 250 kOhm (bottom).

electrodes. The schlieren visualization has shown that in initial time moment after voltage applying on the actuator near the electrode overlapping area the vortex forms, its diameter increase with the course of time and its center shifts in direction of jet propagation. On the Fig. 7 the process of airflow formation is shown schematically.

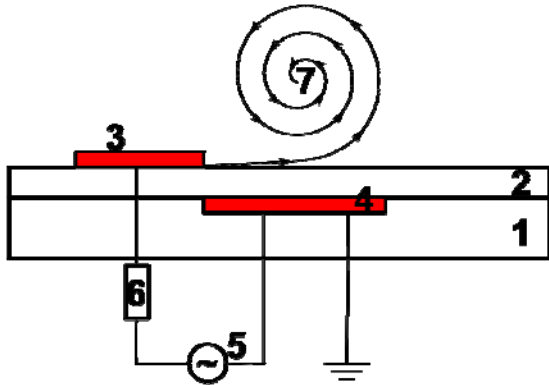


Fig. 7. The scheme of vortex flow formation, caused by DBD. 1 – dielectric, 2 – dielectric layer, 3 – exposed electrode, 4 – encapsulated electrode, 5 – high voltage supply, 6 – ballast resistor, 7 – vortex.

The results of PIV measurements have confirmed this fact. In addition, the high spatial resolution of PIV has allowed reveal the secondary vortex that forms under the surface of exposed electrode. It was found that its dimensions in several times less than in case of main vortex, but the airflow velocity in area of secondary vortex less than in area of main

vortex (Fig. 8).

The main advantage of PIV in comparison to other methods of velocity measurement is the possibility of vorticity measurements at one experiment. It is necessary to mention, the vorticity is a vector quantity. But in this case only one component that has direction perpendicular to the figure 7 plane is important, because in this plane (in plane of light sheet) the flow is quasi two-dimensional.

The values of vorticity were obtained in different time moments up to 10 ms after the discharge start (Fig. 9). It was found that in every time moment the vorticity values in the centers of main and secondary vortices are equal in magnitude but are opposite in sign. From the presented time dependences one can see that the time of vortex flow formation time is about 2 ms and the relaxation time of vorticity is about 5 ms.

Conclusions.

1. The investigation of airflow formation process, induced by dielectric barrier discharge, was carried out.
2. The dependence of the maximum velocity of induced air jet from the amplitude of applied voltage and from the value of active resistance were obtained
3. It was found that in initial time moment of airflow formation under the surface of exposed electrode the secondary vortex occurs.
4. The carried PIV-measurements of induced flow has shown that at each time moment in range

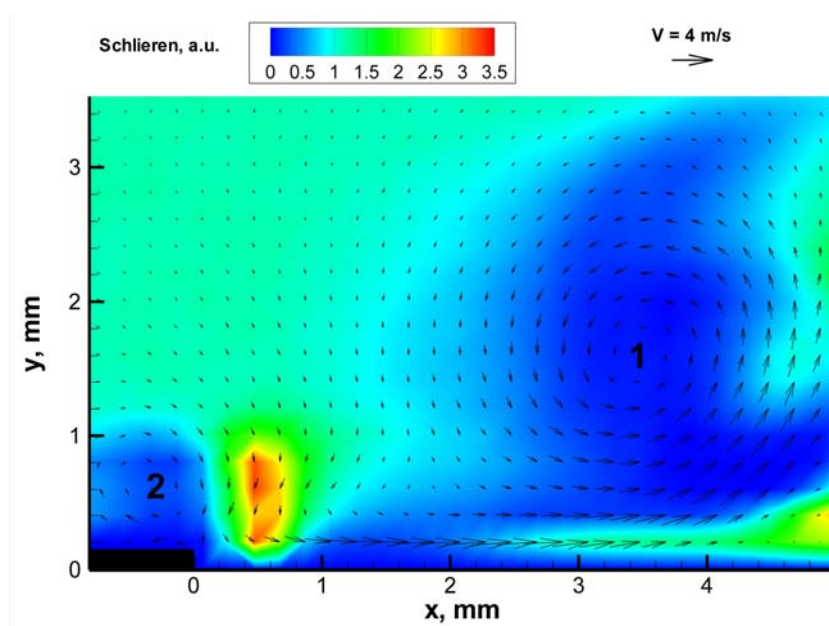


Fig. 8. The schlieren visualization and PIV-measurement at time moment 2 ms after the discharge start with the amplitude of voltage 3 kV. 1 – main vortex, 2 – secondary vortex. The point (0,0) is the edge of exposed electrode. The spatial resolution is decreased in three times for clarity.

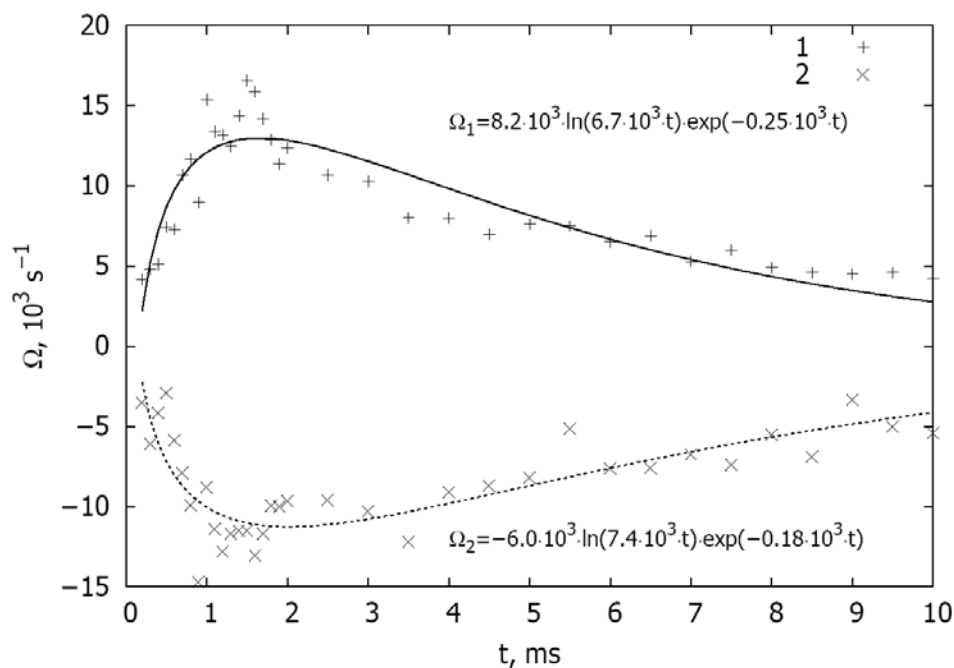


Fig. 9. The dependence of vorticity value from time in area of main (1) and secondary (2) vortex. The numerical coefficients at approximative equations have dimension of 1/s. The voltage amplitude is 3 kV.

from 0 ms to 10 ms after discharge start the values of vorticity in area of main and secondary vortices are related, videlicet these values are equal in magnitude but are opposite in sign.

References.

1. Pietsch G. Peculiarities of Dielectric Barrier Discharges // *Contrib. Plasma Phys.* – 2001. – V.41, N. 6 – P. 620–628.
2. Moreau E. Airflow control by non-thermal plasma actuators // *J. Phys. D: Appl. Phys.* – 2007. – V. 40, N. 3. – P. 605-636.
3. Balcon N., Benard N., Moreau E. // *IEEE Transactions on Dielectrics and Electrical Insulation.* 2009. V. 16 N. 2 P. 463-469.
4. Vasiliev L.A. «Schlieren methods» (in Russian). Moscow:Nauka, 1968.
5. Raffel M. et. al. “Particle Image Velocimetry”. Springer-Verlag Berlin Heidelberg, 2007, PP. 448.
6. S.B. Leonov, D.A. Yarantsev, V.G. Gromovm A.P. Kuriachy. Mechanisms of Flow Control by Near-Surface Electrical Discharge Generation // 43th AIAA Aerospace Sciences Meeting and Exhibit, Reno, NV, 10-13 January 2005, AIAA-2005-0780.
7. Dmitri M. Orlov, Gabriel I. Font, and Daniel Edelstein. Characterization of Discharge Modes of Plasma Actuators // *AIAA-Journal.* Vol. 46, No. 12, 2008. pp. 3142-3148.

TO A THEORY OF GAS DISCHARGE WITH COMPLEX KINETICS IN FREE SPACE

V.L. Bychkov, S.A. Dvinin

M.V.Lomonosov Moscow state university, s_dvinin@mail.ru

Introduction

Chemical waves propagations is a basis for models construction for variety of objects – a gas mixture, chemical reactors, ecological objects, gas discharges. At the description of this wave fronts, as a rule, one starts from the multicomponent diffusion equations of with a nonlinear source [1 – 3]. In spite of the fact that the systems of such equations is widely used in problems of numerical modeling [4 – 7], analytical models (and their properties) are investigated in details only for unicomponent systems [8 – 10]. Its application to set of practically important problems is limited owing to difficult chemical kinetics of real process. Therefore we have actual problem: how to find-out conditions at which it is possible to convert a multicomponent problem to the unicomponent, whether is it possible to accelerate process of phase transition by external influence and if yes, what should be this influence.

The given work deals with the further development of a way of consecutive simplification of multicomponent systems to one diffusion equation with "effective" nonlinear particle source and diffusion coefficients, offered by authors in [11, 12]. Simple expressions for ionization front speed are received. In contrast to the previous model, participation in reactions of the charged particles, excitation of ambipolar field in a multicomponent mix, and also influence of an external field on front propagation are investigated.

1. The multicomponent diffusion equation

1.1 Initial system of the equations

Let's assume, that as a result of discharge development, the medium, consisting from m chemical component, described by local concentration $\mathbf{N}(\mathbf{r}, t) = (n_1, \dots, n_m)$ of particles¹, is transgressed from stationary condition 1 to a condition 2 (fig. 1).

Densities $\mathbf{N}(\mathbf{r}, t)$ is governed by the system of diffusion equations a nonlinear source.

$$\frac{\partial n_i}{\partial t} + \frac{\partial}{\partial x_u} \sum_{j=1}^m (z_j |\mu_{ijuv}| E_w + \mathbf{V}) n_j =$$

¹ Such system describes variety of chemical reactions [1 – 3], and, at the account of ionization and electric fields, – gas discharge [4 – 10].

$$\frac{\partial}{\partial x_u} \sum_{j=1}^m D_{ijuv} \frac{\partial n_j}{\partial x_w} = F_i(\mathbf{N}), \quad (1)$$

$$i = (1 \dots m).$$

Here V – is a speed of an medium element, z_j – is a charge components j in units of electron charge, μ_{ij} , D_{ij} – are tensors of mobility and diffusions, F_j – are the sources of particles. For simplification of calculations the medium is considered homogeneous², u, v, w – are indexes designating space variables x, y, z . Repeating indexes u and w suppose summation. Summation on the indexes designating chemical components, are written out obviously. Transfer coefficients D_{ijxy} is assumed to be independent of concentration, in order to exclude from consideration modes with sharpening [8, 9].

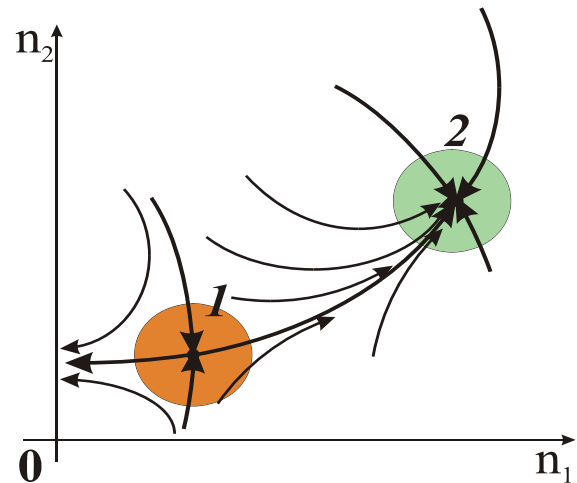


Fig. 1. A phase portrait of system with two stationary points: saddle (1) and stable node (2).

1.2 The reduced system of the equations

В работе [8] был предложен способ сведения In work [8] The way allows to transform the offered system to one diffusion equation with a nonlinear source describing movement along separatrix³

² In most cases it is possible to consider, that $\mu_{ij} = 0$ and $D_{ij} = 0$, when $i \neq j$.

³ The way allowing to calculation separatrix is described in [7], [8]

$$\begin{aligned} \frac{\partial n_0}{\partial t} + \frac{\partial}{\partial x} \mu_{eff}(n_0) E n_0 - \frac{\partial}{\partial x} D_{eff}(n_0) \frac{\partial n_1}{\partial x} \\ = F_{eff}(n_0) + \sum_{j=1}^m \frac{\partial F_{eff}(n_0)}{\partial A_j} A_j(x, t). \end{aligned} \quad (2)$$

and system of the equations for the coefficients A_j describing a deviation from it

$$\begin{aligned} \left(\frac{\partial A_i}{\partial t} - \Lambda_i \right) (\mathbf{N}_i(\mathbf{N}) \cdot \tilde{\mathbf{N}}_i(\mathbf{N})) + \sum_{j=2}^m A_j \left(\frac{\partial \mathbf{N}_j(\mathbf{N})}{\partial t} \cdot \tilde{\mathbf{N}}_i(\mathbf{N}) \right) + \\ \sum_{j=1}^m \sum_{l=2}^m \left(\left(\frac{\partial}{\partial x} E \mu_{ij} A_l \mathbf{N}_l(\mathbf{N}) \right) \cdot \tilde{\mathbf{N}}_i(\mathbf{N}) \right) - \\ \sum_{j=1}^m \sum_{k=1}^m \sum_{l=2}^m \left(\left(\frac{\partial}{\partial x} \left(D_{ij} \frac{\partial}{\partial x} A_l \mathbf{N}_l(\mathbf{N}) \right) \right) \cdot \tilde{\mathbf{N}}_i(\mathbf{N}) \right) = \\ - \left(\sum_{j=1}^m \left(\frac{\partial}{\partial x} E N_j(n_0(x, t)) \mu_{ij} \right) \cdot \tilde{\mathbf{N}}_i(\mathbf{N}) \right) + \\ \sum_{j=1}^m \left(\left(\frac{\partial}{\partial x} \left(D_{ij} \frac{\partial N_j}{\partial n_0} \frac{\partial n_0}{\partial x} \right) \right) \cdot \tilde{\mathbf{N}}_i(\mathbf{N}) \right) \end{aligned} \quad (3)$$

Composed in the right part are responsible for excitation of the higher modes by spatial heterogeneity of the basic function (shift from separatrix I to a close curve II), composed in the second line – of the higher modes interaction among themselves, born by the same heterogeneity and the second term in the first line – for the transformation of modes connected with non stationarity of process. Modes with a speed of approaching to a stationary point above, than the increment of an unstable mode can be considered as quasi stationary, and for them it is possible to neglect derivatives on time in system (3). At construction of system of the equations (2), (3) we have searched solution in a form

$$\mathbf{N} = \begin{pmatrix} n_1 \\ \dots \\ n_m \end{pmatrix} = \mathbf{N}(n_0(x, t)) + \delta \mathbf{N}(x, t). \quad (4)$$

$$\delta \mathbf{N}(n_0(x, t)) = \sum_{i=1}^m A_i(x, t) \mathbf{N}^i(n_0(x, t)) \quad (5)$$

and have projected the equations (1) on a direction of separatrix (the first composed in the expression (4)), and also on eigenfunctions \mathbf{N}_m of linearized systems

$$\Lambda n_i = \sum_{j=1}^m \left(-i \mu_{ij}(\mathbf{kE}) - k^2 D_{ij} + \frac{\partial F_i}{\partial n_j} \right) n_j. \quad (6)$$

The form of eigenfunctions depends on a point in space (more precisely from value of particles densities of in this point of space). The system, conjugated to (6), forms conjugated vectors $\tilde{\mathbf{N}}^i$. We will assume eigenfunctions of a problem (6) to be sorted in decreasing order of eigenvalues.

2. The unicomponent diffusion equation with nonlinear source

2.1 The comparison theorem

It is possible to note one more property of unicomponent solutions, already for the nonlinear equation, for which typical forms of dependence $F(n)$ are shown on fig. 2

$$\frac{\partial n}{\partial t} = D \frac{\partial^2 n}{\partial x^2} + F(n),$$

The property is following from the theorem of comparison for the parabolic equations: the velocity V moving front $n(x - Vt)$ will lay in limits

$$2 \text{Min} \sqrt{D \frac{F(n)}{n}} \leq V \leq 2 \text{Max} \sqrt{D \frac{F(n)}{n}},$$

where the maximum is searched on all separatrix ($n_1 < n < n_2$), and a minimum – on a section from an unstable stationary point to a point in which the maximum is reached.

2.2 Diffusion equation with a convex and not convex source. Active area and a problem on eigenvalues

The formulas received in the previous section allow us to find expression for wave propagation speed in unicomponent system when reaction goes most quickly near to an unstable point of equilibrium 1. Such case is realized most quickly in biological systems [12], [13], however it is not carried out, for example, for a flame propagation [11] (Fig. 2).

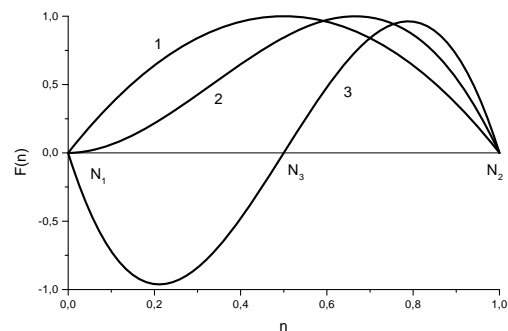


Fig. 2. A typical curve of a nonlinear source $F(n)$: 1 – a convex source, 2 – not convex source, 3. – Phase transition.

Approximations for front velocity at not convex source are known for cases when speed of reaction sharply grows with n (In the case the temperature usually acts as this quality)

$$V = 2 \sqrt{\int_{n_1}^{n_2} 2D_a F_e(n) dn} / (n_2 - n_1),$$

and also for the phase transition close to equilibrium

$$V = \int_{n_1}^{n_2} (F(n) dn) / \int_{n_1}^{n_2} \left(\frac{2}{D} \int_{n_1}^n F(n') dn' \right)^{1/2} dn.$$

It is possible to show, that the area in which speed of chemical reaction is maximum is essential to definition of front speed propagation. For this purpose let's pass from function $n(x-Vt) = n(\zeta)$ to the new unknown variable

$$\psi = \frac{d}{d\zeta} n(\zeta), \quad (7)$$

satisfying to the equation

$$-V \frac{\partial \psi}{\partial \zeta} - \frac{\partial^2 \psi}{\partial \zeta^2} = \Phi(n) \psi, \quad (8)$$

where $\Phi(n) = dF(n)/dn$, or, at the account of the expression (7)

$$-V \frac{\partial \psi}{\partial \zeta} - \frac{\partial^2 \psi}{\partial \zeta^2} = \Phi \left(\int_{-\infty}^{\zeta} \psi(\zeta') d\zeta' \right) \psi,$$

The shape of function $-\Phi(n)$ corresponding to dependences $F(n)$ is shown on fig. 2.

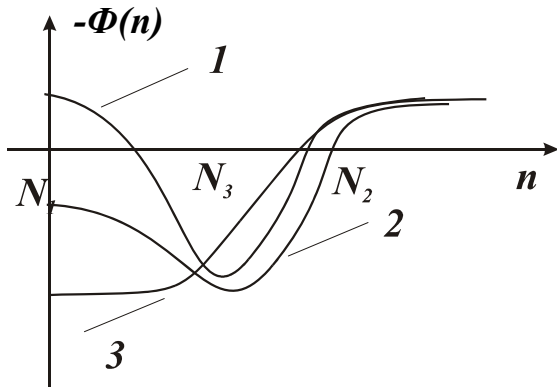


Fig. 3. The Form of function $-\Phi(n)$ corresponding to dependences $F(n)$, shown on fig. 2.

Thus, function ψ_0 represents the solution of a nonlinear eigenvalues problem (8). After the solution of a problem (8), the form of self similar front can be found from the relation (7)

$$n(\zeta) = \int_{-\infty}^{\zeta} \psi(x) dx = N_2 - \int_{\infty}^{\zeta} \psi(x) dx.$$

Behavior of function $\psi(x)$ near to the ends of a

numerical axis it is easily calculated

$$\begin{aligned} \psi|_{x \rightarrow -\infty} &= C_1^- \exp(\Lambda^-(-\infty)x), \\ \psi|_{x \rightarrow \infty} &= C_2^+ \exp(\Lambda_2^+(\infty)x). \end{aligned}$$

where

$$\Lambda^\pm(x) = -V/2 \mp \sqrt{D(x)}, \quad D(x) = V^2/4 - \Phi(n(x)).$$

Then near to points of equilibrium the solution can be received by a method of geometrical optics

$$\psi|_{x \rightarrow -\infty} = \frac{C_1^-}{\sqrt[4]{D(x)}} \exp\left(\int_{-\infty}^x \Lambda^-(x) dx\right), \quad (9)$$

$$\psi|_{x \rightarrow \infty} = \frac{C_1^+}{\sqrt[4]{D(x)}} \exp\left(\int_{\infty}^x \Lambda^+(x) dx\right) \quad (10)$$

For a nonlinear problem the next system of the differential equations follows from (9), (10)

$$\frac{d\psi}{dx} = \Lambda^-(n(x))\psi, \quad \frac{dn}{dx} = \frac{\psi}{\sqrt[4]{D(x)}}, \quad (9a)$$

$$\frac{d\psi}{dx} = \Lambda^+(n(x))\psi, \quad \frac{dn}{dx} = \frac{\psi}{\sqrt[4]{D(x)}}. \quad (10a)$$

which can be easily solved (for example numerically, or by method of successive approximations). First two equations are fair near to negative and second two – the positive end of a numerical axis. As the solution (9) should transforms continuously to (10), it should have branching points, where $\Lambda^+(x) \approx \Lambda^-(x)$ and geometrical optics approach of is not applicable. For finding the solution in this area we will write the equation (8) in the self-conjugated form. It is possible to do, entering new function φ , connected with ψ by parity

$$\psi = \varphi \exp\left(\int V dx\right), \quad (11)$$

Function φ satisfies to the equation

$$\frac{\partial^2 \varphi}{\partial \zeta^2} - U(V, x)\varphi = 0, \quad (12)$$

where

$$U(x) = -(\Phi(n) - V^2/4)$$

is nonlinear potential. As the required solution $n(x-Vt) \equiv n(\zeta)$ is monotonous, the function $\psi(\zeta)$

keeps a sign and has no roots. Near to a bottom of a potential hole the nonlinear potential can be represented as series

$$\Phi = \Phi^{(0)} + \sum_{i=2}^{\infty} \frac{1}{i!} \frac{d^i \Phi^{(0)}}{dn^i} \left(\int_0^{\zeta} \psi(x) dx \right)^i.$$

Substituting the last expression into the equation (12) we will receive

$$V \frac{\partial \psi}{\partial \zeta} - \frac{\partial^2 \psi}{\partial \zeta^2} = \left(\Phi^{(0)} + \sum_{i=2}^{\infty} \frac{1}{i!} \frac{d^i \Phi^{(0)}}{dn^i} \left(\int_0^{\zeta} \psi(x) dx \right)^i \right) \psi$$

In the simplest case

$$\frac{\partial^2 \varphi}{\partial \zeta^2} - \left(\Phi(0) - \frac{1}{2} \Phi''(0) \psi^2(0) x^2 - \frac{V^2}{4} \right) \varphi = 0, \quad (13)$$

The equation (13) – is the equation of harmonic oscillator with potential well depending on amplitude of wave function. The condition of normalization looks like

$$\int_{-\infty}^{\infty} \psi(x) dx = N_2 - N_1, \quad (14)$$

Matching of solutions (9), (10), (13) at the account (14) can be carried out in the various ways and allows to define front velocity V and the wave form $n(x - Vt) = n(\zeta)$. The main assertion in this case is that chemical reaction wave propagation speed for not convex source is defined by chemical kinetics and diffusions features in a vicinity where of a point where $\Phi(n) = dF(n)/dn = 0$.

3. The complicated system of the equations

3.1 Full system of the equations

The system of the equations describing the real gas discharge in addition to (2) – (3) should contain the equations of movement for neutral components

$$\begin{aligned} \frac{\partial N}{\partial t} + \mathbf{u} \nabla N + N \text{div} \mathbf{u} &= \frac{dN}{dt} + N \text{div} \mathbf{u} = 0, \\ \frac{\partial \mathbf{u}}{\partial t} + (\mathbf{u} \nabla) \mathbf{u} &= -\frac{1}{NM} \nabla N k T + \frac{\eta}{NM} \Delta \mathbf{u}, \\ &+ \frac{1}{NM} \left(\xi + \frac{\eta}{3} \right) \text{grad} \text{div} \mathbf{u} - \nu \mathbf{u} \end{aligned} \quad (15)$$

balance of energy equation for heavy gas components,

$$\begin{aligned} \frac{1}{\gamma-1} N k \frac{\partial T}{\partial t} + \frac{1}{\gamma-1} N k (\mathbf{u} \nabla) T \\ + N k T \text{div} \mathbf{u} = \text{div} \chi \nabla T + Q \end{aligned}$$

and the equations of electrons energy balance

$$\begin{aligned} \frac{3}{2} n_e k \frac{\partial T_e}{\partial t} + \frac{3}{2} n_e k (\mathbf{u} \nabla) T_e \\ + n_e k T_e \text{div} \mathbf{u}_e = \text{div} \chi_e \nabla T_e + (\mathbf{j} \mathbf{E}) + Q_{eN} \end{aligned}$$

As movement of the charged particles leads to electric field occurrence, the system should be added by quasistationary Maxwell equations

$$\text{rot} \mathbf{E} = 0, \quad \text{rot} \mathbf{H} = \frac{4\pi}{c} \mathbf{j}, \quad \text{div} \mathbf{E} = 4\pi \rho, \quad \text{div} \mathbf{H} = 0$$

3.2 Conservation laws and system of the reduced equations

Specificity of a considered problem in a homogeneous medium is presence of integrals of movement connected with conservation of matter [16], charge and energy [15]. For flame propagation the fact has been taken into consideration by Burke S.P., Shuman T.E. in work [16]. Let's consider lower as it modifies the procedure offered above. In this case the equations for remaining sizes \tilde{n}_k become

$$\begin{aligned} \frac{\partial \tilde{n}_i}{\partial t} + \frac{\partial}{\partial x_u} (\mu_{ij} \mathbf{u}_{uw} E_w + \mathbf{V}) \tilde{n}_j - \frac{\partial}{\partial x_u} D_{ij} \frac{\partial \tilde{n}_j}{\partial x_w} + \\ \frac{\partial}{\partial x_u} \sum_{j=1, j \neq i}^m \left\{ (\mu_{ij} \mathbf{u}_{uw} E_w + \mathbf{V}) \tilde{n}_j - D_{ij} \frac{\partial \tilde{n}_j}{\partial x_w} \right\} = 0 \quad (16) \\ i = (1 \dots m), \quad i = k. \end{aligned}$$

3.3 System of equations for charged components. Conditions of ambipolarity

In item 3.2 it was pointed out that the law of charge conservation allows us to modify system of the equations. In the same way as in case of chemical reactions, strong electrostatic interaction of particles leads to modification of system of the equations. Let's start with system quasistationary Maxwell equations

$$\mathbf{E} = -\nabla(\varphi_A + \varphi_C), \quad \nabla \left(\left(\sum_i z_i^2 \mu_i n_i \right) \nabla \varphi_C \right) = 0.$$

It is known, that in 1D non-uniform system ambipolar potential satisfies to the equation

$$\nabla \varphi_A = -\mathbf{E} = \left(\sum_i z_i D_i \nabla n_i - e D_e n_e \right) / \left(\sum_i z_i^2 \mu_i n_i + e^2 \mu_e n_e \right).$$

In 2D and 3D systems expression on the right will be not obligatory a gradient, therefore correct record looks like

$$\mathbf{E} = -\nabla \varphi_A = \sum_i z_i D_i \nabla n_i / \sum_i z_i^2 \mu_i n_i + \text{rot} \mathbf{A} \quad ,$$

where vector \mathbf{A} satisfies to the equation

$$\Delta \mathbf{A} = - \frac{\sum_i \sum_{j>i} (z_i D_i z_j^2 \mu_j - z_j D_j z_i^2 \mu_i) [\nabla n_i \times \nabla n_j]}{\left(\sum_i z_i^2 \mu_i n_i \right)^2} .$$

with boundary conditions for \mathbf{A} and $\nabla \varphi_C$

$$([\nabla \times \mathbf{A}] \cdot \mathbf{s}) = 0 \quad \cdot \left(\left(\left(\sum_i z_i^2 \mu_i n_i \right) \nabla \varphi_C \right) \cdot \mathbf{s} \right) = j_{\text{ext}}$$

3.4 Behavior of the solution near to an instability point

The behavior of system of the equations (1) at $n \rightarrow n_1$ can be found by means of Fourier transformation $\delta \mathbf{N}(x, t) = \int d\mathbf{k} \delta \mathbf{N}(\mathbf{k}, t) \exp(i\mathbf{k}\mathbf{r})$, where $\delta \mathbf{N}(\mathbf{k}, t) = \int d\mathbf{r} \delta \delta(\mathbf{r}, t) / 2\pi \exp(-i\mathbf{k}\mathbf{r})$. Fourier image of density satisfies to system of the equations

$$\frac{dn_i}{dt} + ik_u \sum_{j=1}^m \mu_{ij} E_w n_j - k_u k_w \sum_{j=1}^m D_{j, uw} n_j = \sum_{j=1}^m \frac{\partial F_j}{\partial n_j} n_j F_i(\mathbf{N}) .$$

It is possible to present the solution of this system in the form of the sum

$$\delta \mathbf{N}(\mathbf{k}, t) = \sum_{i=1}^m A_i(\mathbf{k}) \mathbf{N}^i(\mathbf{k}) \exp(\Lambda_i t) . \quad (17)$$

Coefficients $A_i(\mathbf{k})$ in (17) is defined by initial conditions.

$$A_i(\mathbf{k}) = \frac{(\delta \mathbf{N}(\mathbf{k}, 0) \cdot \tilde{\mathbf{N}}^i(\mathbf{k}))}{(\mathbf{N}_i(\mathbf{k}) \cdot \tilde{\mathbf{N}}^i(\mathbf{k}))} = \frac{1}{2\pi} \int d\mathbf{r} (\delta \mathbf{N}(\mathbf{r}, 0) \cdot \tilde{\mathbf{N}}^i(\mathbf{k})) \exp(-i\mathbf{k}\mathbf{r}) .$$

In coordinates (\mathbf{r}, t) the solution of the equation (1) can be written down in form

$$\delta \mathbf{N}(\mathbf{r}, t) = \sum_{i=1}^m \int \int \int_{-\infty-\infty-\infty}^{\infty \infty \infty} dk_u dk_w dk_v A_i(\mathbf{k}) \mathbf{N}_i(\mathbf{k}) \exp(\Lambda_i(\mathbf{k})t + i\mathbf{k}\mathbf{r}) .$$

This expression gives a common solution of the problem in linear approach. Asymptotic relation for $\delta \mathbf{N}(\mathbf{r}, t)$ at $t \rightarrow \infty$ usually can be calculated by saddle point method. A stationary point \mathbf{k}_{0i} satisfies to expression

$$\frac{\partial \Lambda_i(\mathbf{k}_{0i})}{\partial \mathbf{k}} t + i\mathbf{r} = 0 .$$

Entering a new variable $\Delta \mathbf{k}_i = \mathbf{k} - \mathbf{k}_{0i}$, and a

designation it is possible to write down parity (17) in a form

$$\delta \mathbf{N}(\mathbf{r}, t) = \sum_{i=1}^m \exp(\Lambda_i(\mathbf{k}_{0i})t + i\mathbf{k}_{0i}\mathbf{r}) \times \int \int \int_{-\infty-\infty-\infty}^{\infty \infty \infty} d\Delta k_u d\Delta k_w d\Delta k_v A_i(\Delta \mathbf{k}) \mathbf{N}_i(\Delta \mathbf{k}) \exp(\Delta \Lambda_i(\Delta \mathbf{k})t) \quad (18)$$

If in a close vicinity of a saddle point there are no special points (pole, branching points, etc.) the argument of exponent can be expanded in series on degrees of $\Delta \mathbf{k}$, leaving only to the second order. Then it is easily calculated

$$\frac{1}{2\pi} \int_{-\infty}^{\infty} d\Delta k \exp(\Delta \Lambda_i''(0) \Delta \mathbf{k}^2 t / 2!) = (\pi \Lambda_i''(k_{0i}) t)^{-1/2} .$$

It is interesting to receive value of integral (18) in system of co-ordinates moving with velocity \mathbf{V} , i.e. if $\mathbf{r} = \mathbf{r} - \mathbf{V}t$. In this case the stationary point satisfy to the equation

$$\frac{\partial \Lambda_i(\mathbf{k}_{0i})}{\partial \mathbf{k}} t + i\mathbf{r} = 0 , \quad (19)$$

and the argument in an exponent before integral $(\Lambda_i(\mathbf{k}_{0i}) + i\mathbf{k}_{0i}\mathbf{V})t$. Thus, in a point, moving with speed \mathbf{V} , the perturbation grows, if $\text{Re}(\Lambda_i(\mathbf{k}_{0i}) + i\mathbf{k}_{0i}\mathbf{V}) > 0$ and also decreases otherwise. Last two parities allow to receive system of the equations for definition of chemical wave propagation speed \mathbf{V} and characteristic size of front of ionization \mathbf{k}_0 at any dispersion law:

$$\begin{aligned} \text{Re} \frac{\partial \Lambda_i(\mathbf{k}_0)}{\partial \mathbf{k}} = 0, \quad \text{Im} \frac{\partial \Lambda_i(\mathbf{k}_0)}{\partial \mathbf{k}} + \mathbf{V} = 0, \\ \text{Re}(\Lambda_i(\mathbf{k}_{0i}) + i\mathbf{k}_{0i}\mathbf{V}) = 0. \end{aligned} \quad (20)$$

In weakly inhomogeneous medium Fourier transform of coefficient $A_i(\mathbf{k})$

$$\begin{aligned} A_i(\mathbf{r}, t) &= \int \int \int_{-\infty-\infty-\infty}^{\infty \infty \infty} dk_u dk_w dk_v A_i(\mathbf{k}) \exp(\Lambda_i(\mathbf{k})t + i\mathbf{k}\mathbf{r}) = \\ &= \int \int \int_{-\infty-\infty-\infty}^{\infty \infty \infty} dk_u dk_w dk_v A_i(\mathbf{k}) \exp\left((\Lambda_i^0 + \Lambda_{iu}^1 k_u + \Lambda_{iuv}^2 k_u k_w)t + i\mathbf{k}\mathbf{r}\right) \end{aligned}$$

satisfies to the equation

$$\frac{\partial A_i}{\partial t} + \frac{\partial}{\partial x_u} \mu_{eff, uv} E_w A_i - \frac{\partial}{\partial x_u} D_{eff, uv} \frac{\partial A_i}{\partial x_w} = \Lambda_i^0 A_i . \quad (21)$$

For record simplification here are entered effective coefficients of mobility and diffusion $\mu_{eff, uv} = \partial \Lambda / \partial \mathbf{k} \partial \mathbf{E}$, $D_{eff, uv}^i = -\partial^2 \Lambda_i / 2 \partial k_u \partial k_w$. Knowing all coefficients $A_i(\mathbf{r}, t)$ it is possible to calculate spatial distributions of particles density using expression (18):

$$\delta \mathbf{N}(\mathbf{r}, t) = \sum_{i=1}^m \left(\mathbf{N}_i(\mathbf{0}) + \frac{\partial \mathbf{N}_i(\mathbf{0})}{\partial k_u} \frac{\partial}{\partial x_u} + \frac{\partial^2 \mathbf{N}_i(\mathbf{0})}{\partial k_u \partial k_w} \frac{\partial^2}{\partial x_u \partial x_w} \right) A_i(\mathbf{r}, t)$$

It follows from the received parities, that propagation speed of reaction front in such medium is defined by the formula

$$V_f = -\mu_{eff}^{11} E_0 + 2\sqrt{D_{eff}^{11} \Lambda_1}$$

4. Example of calculation of effective diffusion and birth coefficients of particles for two-component system

Features which bring in calculation of integral (19) multicomponent media, it is possible to outline qualitatively on an example of the two-componential system described (in linear approach) by the equations:

$$\begin{aligned} \frac{\partial n_1}{\partial t} &= D_{11} \frac{\partial^2 n_1}{\partial x^2} + D_{12} \frac{\partial^2 n_1}{\partial x^2} + G_{11} n_1 + G_{12} n_2 \\ \frac{\partial n_2}{\partial t} &= D_{21} \frac{\partial^2 n_1}{\partial x^2} + D_{22} \frac{\partial^2 n_1}{\partial x^2} + G_{21} n_1 + G_{22} n_2 \end{aligned} \quad (22)$$

Eigenvalues of the given system of the equations can be written out obviously:

$$\Lambda_{1,2} = \frac{(G_{11} + G_{22}) - (D_{11} + D_{22})k^2}{2} \pm \sqrt{\left(\frac{(G_{11} - G_{22}) - (D_{11} - D_{22})k^2}{4} \right)^2 + (G_{12} - D_{12}k^2)(G_{21} - D_{21}k^2)}$$

Solution has saddle points and branching points on a complex plane. It is necessary to notice, that the saddle point (20) is usually displaced from the real axe to the complex plane therefore similar

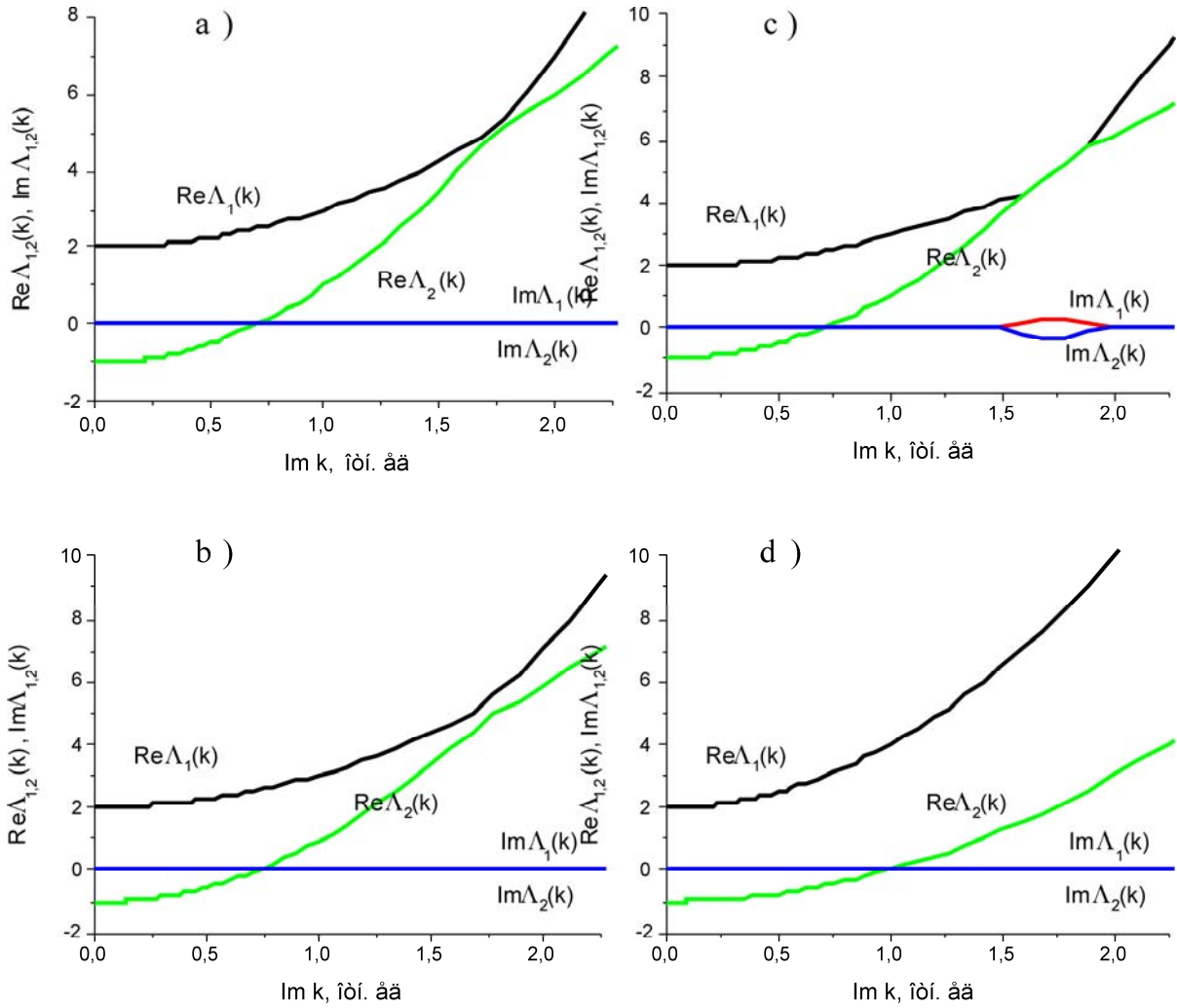


Fig. 4. Possible behavior of dispersive curves on an axis $\text{Re } k=0, -\infty < \text{Re } k < \infty$. a) – intersection of curves in one of points, b) – the interaction leading to increase of distance between eigenvalues, c) – the interaction leading to occurrence of periodic solutions, d) – absence of intersection.

consideration it is necessary to spend not only on the real axis, but also in its some vicinity, where $\text{Im}k \neq 0$. Besides, there can be a question on uniqueness of the solution of system of the equations (20). In system where drift of particles is absent it is sufficient to consider only behavior on real axis enough. (Fig. 4). In many cases dispersion laws are that, that the equation (20) is reduced to one equation

$$\text{Re} \left(\Lambda_i(\mathbf{k}_{0i}) - \mathbf{k}_{0i} \frac{\partial \Lambda_i(\mathbf{k}_0)}{\partial \mathbf{k}} \right) = 0,$$

from which follows, that the characteristic scale of heterogeneity of front is defined by point in which the tangent to a curve $\Lambda(k)$ passes through the beginning of co-ordinates. When the solution is ambiguous, apparently real speed is defined by the solution corresponding to larger density of particles.

Influence of sound waves in case speed of propagation of front is much less than speed of a chemical wave is not significant.

Conclusions

We have proposed a mathematical model of chemical reaction front propagation characteristics calculation in multi component medium. The model is based on a transformation of the balance equation system for different plasma components to one diffusion equation with the nonlinear source. The basis for such a simplification consists in difference of various processes chemical reaction velocities. Use of the given approach allows to reduce essentially volume of numerical calculations at construction of discharge mathematical model. The analysis of the solution of the unicomponent equation of diffusion shows, that in many cases the speed of ionization front propagation defined by speed of chemical reaction and diffusion in the region of phase space near to a point in which speed of reaction is maximum.

References

1. Barenblatt G. I. In a book: Kolmogorov A.N. "The Selected Works. Mathematics and Mechanics", M: Nauka, 1985, pp. 573-578.
2. Volpert A.I. In a book: Petrovsky I.G. "The Selected Works. The Differential Equations. Probability Theory". M.: Nauka, 1985, p. 333-339.
3. Kossyi I.A., Kostinsky A.Y., Matveyev A.A., Silakov V.P. Works of IOFAN. 1994. V.47. P.37-57
4. Babaeva N.Yu., Mnatsakanyan A.R., Naidis G.V. // Fizika Plazmy. 1992. T. 18. C. 1055 – 1063.
5. Popov N.A. Fizika Plazmy, 2003, V. 29, No 8, P. 754-767.
6. Popov N.A. Fizika Plazmy, 2006, V. 32, No3, P. 1-9
7. Aleksandrov A.F., Bychkov V.L., Dvinin S.A., Mikheev V.V., Sviridkina V.S. Prikladnaya Fizika, 2007, No 2, pp. 25-31..
8. Kolmogorov A.N., Petrovskii I.G., Piskunov N.S. Moscow State University Bulletin. Mathematics and Mechanics, 1937, Vol. 1, p. 1. Kolmogorov A.H. "The Selected Works. Mathematics and Mechanics". M: Nauka. 1985. P. 221.
9. Glusberg V.E., Lvovskiy Yu. M. Chemical Physics (USSR), 1982, Vol. 1, p. 1546.
10. Frank-Kamenetskii D.A. "Diffusion and Heat Transfer in Chemical Kinetics", M: Nauka, 1986.
11. Bychkov V.L., Dvinin S.A., Mikheev V.V. 5 International Symposium on theoretical and applied plasma chemistry. Ivanovo. 5-8 September 2008. P. 258-261.
12. Bychkov V.L., Dvinin S.A. The 8th International workshop on magneto-plasma aerodynamics. Moscow, 31 March – 02 April 2009. p. 90 – 91.
13. Samarskij A.A., Galaktionov V.A., Kurdumov S.P., Mikhailov A.P. Modes with sharpening in problems for quasi linear parabolic equations. (In Russian) // M: Nauka. 1987. 480 p.
14. Ahromeeva T.S., Kurdumov S.P., Malinetsky G.G., Samarskij A.A. Structures and chaos in nonlinear media. (In Russian) // M: Nauka. 2008. 488 p.
15. Zeldovich Ja.B., Barenblatt G.I., Librovich J.B., Makhviladze V.G. "Mathematical Burning and Explosion Theory", M: Nauka, 1980.
16. Burke S.P., Shuman T.E. Diffusion flames. Ind. Eng. Chem., 1928, V. 20, N10, p. 998 – 1004.

NUMERICAL SIMULATIONS OF SUPERSONIC FLOW IN CONVERGENT-DIVERGENT DUCT WITH DISCHARGE SUPPLY

A.A. Firsov, S.B. Leonov, A.B. Miller
alexander.a.firsov@gmail.com

Numerical simulation of supersonic flow $M=2$ ($V \sim 500$ m/s) in convergent-divergent duct with near-surface heat sources is described. Influence of power magnitude and position in respect of wedge on the flow structure is investigated. Results comparison of two CFD applications was provided. The main objective of simulations was to obtain the data, which is difficult to be measured experimentally [1].

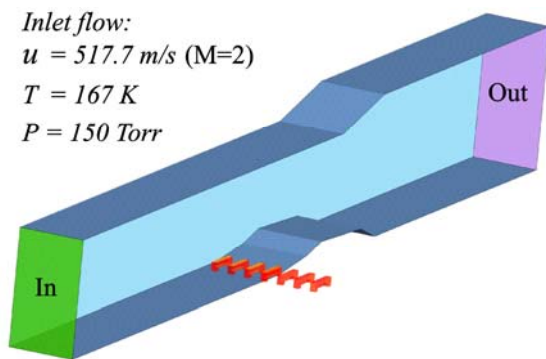


Figure 1. Geometry of computational region.

Calculations of three-dimensional undisturbed flow in experimental set up were executed by using ANSYS™ CFX software and SolidWorks Flow Simulation (SWFS) software. Model of perfect gas in experimental set up was used at modeling supersonic flow. Numerical

modeling of undisturbed flow was based on solution of 3D time-dependent Reynolds averaged Navier-Stokes equations with the utilization of the wide used two-equation SST-model of turbulence and two-equation $k-\epsilon$ -model of turbulence respectively. No-slip and adiabatic conditions were specified on upper, lower, and on lateral walls of the duct. Symmetry conditions were used in central plane of the duct to decrease the calculation domain which contained about $1.7 \times 10^6 - 6 \times 10^6$ mesh points. Inlet of the duct was 72×60 mm, output was 72×72 mm. Direct current electrical discharge between 7 electrodes was simulated by introducing 7 volumetric heat sources. Heat sources were located at $L = 0-40$ mm upstream 1st wedge of convergent-divergent model. The geometry of the whole channel and of the areas of volumetric heat sources is shown in Fig.1.

A comparison of calculated flow structure and experimental schlieren image for undisturbed flow is shown in Fig.2. We can conclude that the volumetric heat sources influence on the flow the same way as the discharge does. In both cases power increase results in crossed shock angle increase and makes crossed shock more strong. Low power (about 4 kW) is insufficient to reduce crossed shocks caused by ramp model. Therefore all other information obtained at our numerical modeling can be used for investigation of discharge influence on undisturbed flow. Crossed shock angle values for heat source position 20mm in front of model are presented in Fig. 4.

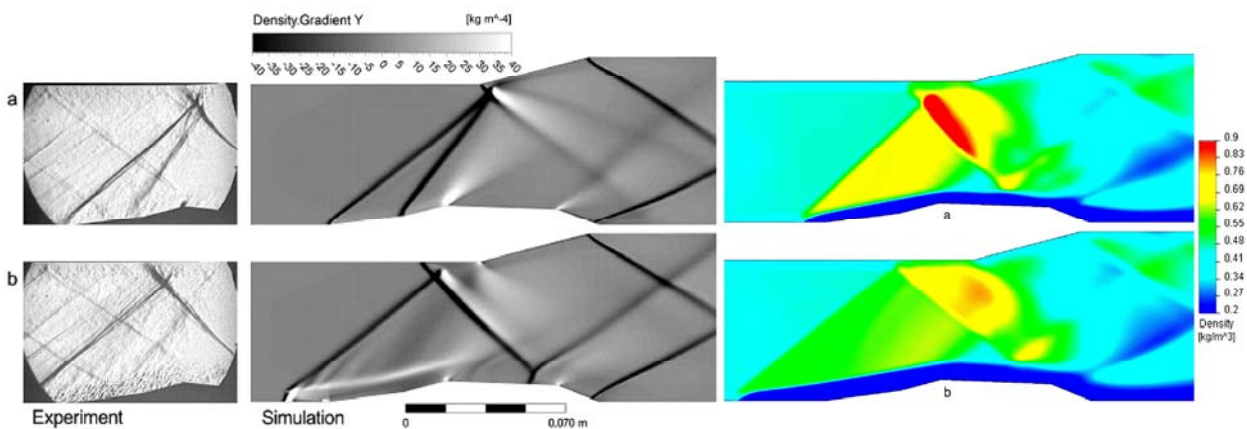


Figure 2. ANSYS: comparison of experimental schlieren image and calculated flow structure.
 $L=20$ mm: a – no discharge, b – discharge: $W=8$ kW.

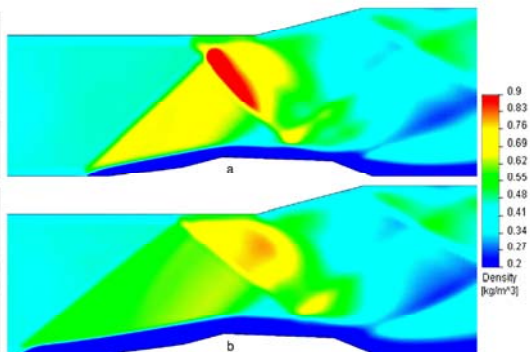


Figure 3. SWFS: density distribution, $W=8$ kW.
 a – $L=10$ mm to 1st wedge ;
 b – $L=40$ mm to 1st wedge.



Figure 4. Crossed shock angle vs Power

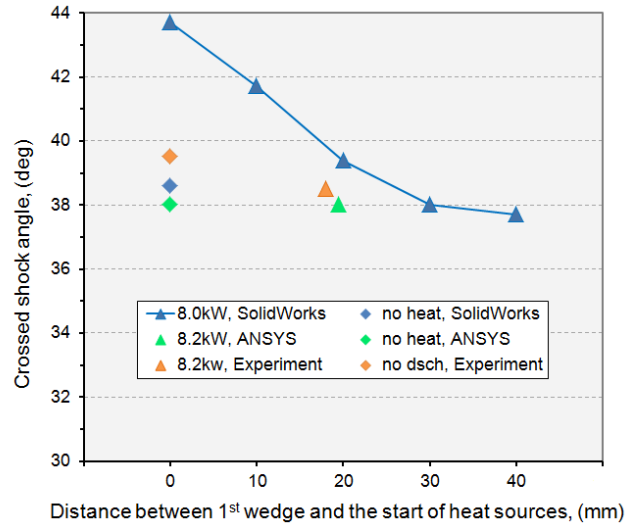


Figure 5. Crossed shock angle vs Distance

Important information that can be obtained by calculation is the three-dimensional structure of crossed shocks. In all cases crossed shock has a plate like form with small curvature near the lateral wall and in case of heat source enabled shock has undulated structure near the down wall caused by discrete heat zone structure. With increase of heat power the undulated shock structure becomes more plane. In case of 4.2kW power flow has complex three crossed shocks structure that can be reduced by power increase.

SolidWorks Flow Simulation was used to carry out investigation of the effect of heat sources location. Illustrations of flow structure for different heat sources location are presented in Fig.3. Location of heat sources on the 1st wedge or at 10mm upstream makes shock angle significantly higher. Heat sources location at 30-40mm upstream 1st wedge makes shock angle less than angle at no-

heat case. Therefore we can modify flow structure by variation of distance between electrodes and the ramp. Increase of distance between 1st wedge and the electrodes location results in not only crossed shock angle decrease. It also contributes to moving of 1st shock reflection point upstream so it may lead to impossibility of flow control. But small distance, especially heat location on 1st wedge, increases the possibility of channel blocking for slightly smaller Mach numbers. So we can conclude that the optimal electrodes location is about 20 mm from ramp. Simulations result of the heat sources location effect is presented in Fig.5.

Heat source filaments make strong influence to static pressure distribution along the channel. Pressure increases in 1st and 2nd model parts at the heat power increase, but decreases in 3rd part. Pressure increasing in 4-6th parts caused by strong reflection of frontal crossed shock and front

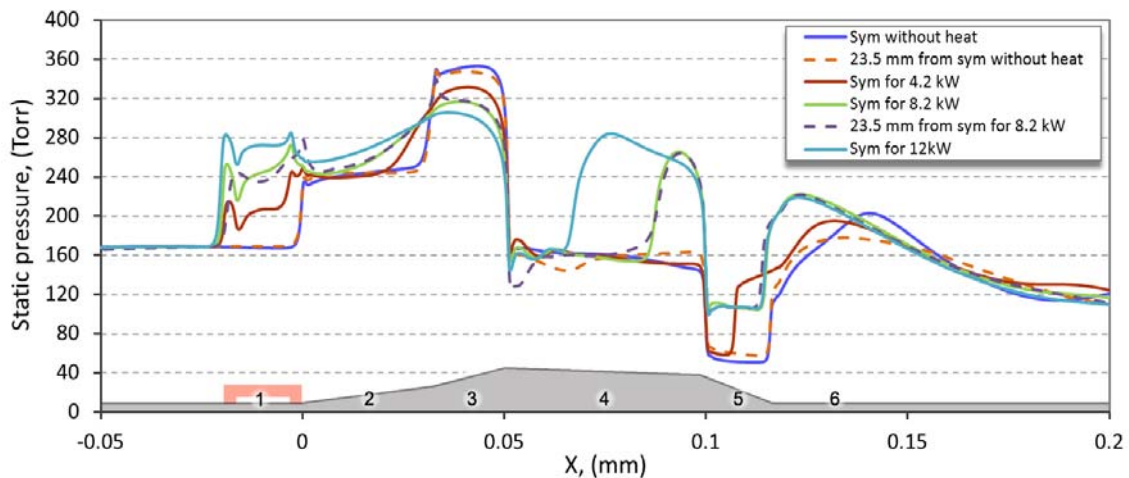


Figure 6. Static pressure distribution along channel.

Temperature, (K)	No heat (0.5mm from down wall)	4.2kW	8.2kW	12kW
2 nd area	283	754	2166	4727
4 th area (back part)	236	290	404	589
6 th area	290	343	412	519

Table Maximum temperature in specified zones.

of this pressure increase moves upstream from 5th to 4th ramp part with power increase. Static pressure distribution is presented in Fig.6. Result comparison for symmetry plane and for plane moved on 23.5 mm to sidewall (this plane is placed between two heat source filaments) leads to conclusion that the discrete heat source structure has no significant influence on static pressure distribution.

Important information was obtained about the air temperature. There are three zones with significant temperature increase in comparison with no-heat case: 2nd area – the end of heat source, 4th area – at the place of crossed shock reflection, 6th area – temperature increase is caused by model geometry. Maximum temperature values are presented in Table

The numerical simulation gives some important details of plasma-flow-model interaction. The following features were considered:

Results obtained by different CFD calculation are in good agreement with experiment and with each other;

Despite of discrete 3D character of the heat source the resulting flow structure looks not very irregular;

Crossed shock angle dependency on power is in good agreement with experiment, but numerical values have small difference;

Low heat power (about 4kW) does not eliminate influence of ramp wedges to crossed shock creation, high power (about 12kW) have strong thermal action to the ramp material, therefore 8kW power source is optimal for ramp crossed shock structure control;

The maximal gas temperature is 2166K at 8.2kW and 4727K at 12kW

The variation of the heat sources location leads to significant modification of the resulting flow structure, particularly increase of distance between 1st wedge and the electrodes location results in crossed shock angle decrease.

Acknowledgement

This work was funded by MBDA-France (F. Falempin supervision)

1. S.B. Leonov, A.A. Firsov, D.A. Yarantsev, F. Falempin, A. Miller - Active Steering of Shock Waves in Compression Ramp by Nonuniform Plasma // 48th AIAA Aerospace Sciences Meeting Including the New Horizons Forum and Aerospace Exposition, 4 - 7 January 2010, Orlando, Florida, AIAA-2010-0261

NONSTEADY-STATE BEHAVIOR OF A “GLIDING ARC” IN AIR FLOW

Yu. D. Korolev, O. B. Frants, N. V. Landl, V. G. Geyman, A. A. Enenko

Institute of High Current Electronics RAS, Tomsk, 634055 Russia,

korolev@lnp.hcei.tsc.ru

The paper deals with the investigation of influence a gas flow and external electric circuit on the properties of so-called gliding arc discharge. Principle of discharge operation is demonstrated in Fig. 1. In most publications [1–3], the discharge properties are interpreted in a framework of steady state models. Such models imply that at initial instant of time the very first breakdown occurs over the shortest distance between the electrodes under that action of voltage V_0 . After that due to gas flow the plasma column moves along the electrode surface, the column length increases with time and the discharge burning voltage increases as well. When the column length reaches a critical value [1], the discharge is extinguished, current is interrupted and new breakdown occurs over the shortest path in the interelectrode gap. So that the above described cycle is repeated. Then in the stage between the successive repeated breakdowns the discharge column is considered as sustaining in steady state conditions with a permanent specific conductivity [2].

In this paper, we demonstrate that with a rather high gas flow the discharge properties are essentially nonsteady state. It resembles the discharge behavior in so-called low-current nonsteady state plasmatron [4]. The principal features of discharge are reduced to the following.

Due to the very first breakdown, a kind of spark discharge appears in the gap. The energy to

the spark is delivered from the capacitance of connecting cable C_c . However, with a low current level from power supply (less that 0.5 A) the discharge is not able to be sustained as a steady state arc. After a time interval of about $1 \mu\text{s}$ the discharge burning regime transforms into a glow mode. So that at the stage of displacement of the discharge column over the electrode surface we deal with a glow type of discharge.

In some regimes, the metal vapor cathode spots arise abruptly and chaotically in the place of glow discharge current attachment at the cathode surface. At these instants of time, the discharge burning voltage sharply decreases as far as the cathode voltage drop region of the glow discharge is bridged by metal vapor plasma. The origin of the arc cathode spot could be initiate the glow to arc transition process [4]. Nevertheless, the lifetime of arc cathode spot is limited. As a result, this spot is extinguished and discharge starts burning in a glow mode again. In such regimes, we can speak of the non-completed glow to spark transitions.

The new spark discharge over a short interelectrode distance appears not due to repeated breakdown after the current interruption in the primary discharge column. In most cases, the spark discharge occurs long before the primary glow discharge current could be interrupted. The phenomenon in its main features resembles rather the glow to spark transition than a repeated

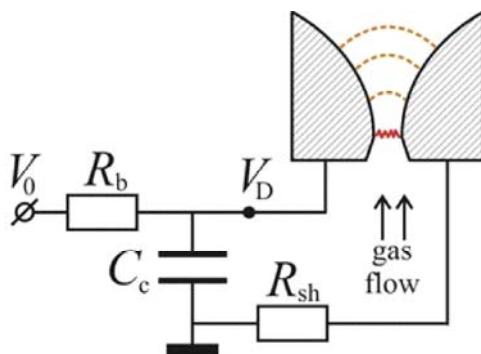


Fig. 1. Principle of gliding arc operation and integral photograph of discharge luminosity ($R_b=10 \text{ kOhm}$, $C_c=300 \text{ pF}$, $V_0=3 \text{ kV}$, $R_{sh}=1 \text{ Ohm}$).

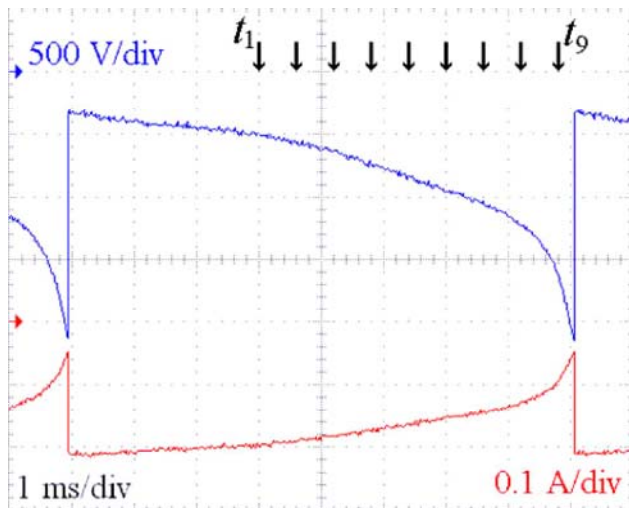


Fig. 2. Voltage and current waveforms and CCD frames of the gap at different instants of time (exposition time – $50 \mu\text{s}$, $V_0=3 \text{ kV}$, gas flow 0.1 g/s).

breakdown of the gap. Correspondingly, the transitions are accompanied by the current pulses with duration of about 100 ns. The pulses appear due to discharging the capacitance C_c across the gap.

The above data had been obtained in the experiments with recording the current and voltage waveforms jointly with photographing of the discharge image by CCD camera. An example of such data for a time interval between successive glow-to-spark transitions is presented in Fig. 2.

The work was supported by the Russian Foundation for Basic Research under the Grants No 08-08-00121 and by Interdisciplinary Integrating Project of Siberian Division RAS No 80.

References

1. S. Pellerin, F. Richard, J. Chapelle, J.-M. Cormier, and K. Musiol, "Heat string model of

bi-dimensional dc Glidarc", *J. Phys. D, Appl. Phys.*, vol. 33, pp. 2407–2419, Oct. 2000.

2. I. V. Kuznetsova, N. Y. Kalashnikov, A. F. Gutsol, A. F. Fridman, and L. A. Kennedy, "Effect of "overshooting" in the transitional regimes of the low-current gliding arc discharge", *J. Appl. Phys.*, vol. 92, no. 8, pp. 4231–4237, Oct. 2002.
3. C. S. Kalra, A. F. Gutsol, A. F. Fridman, "Gliding arc discharge as a source of intermediate plasma for methane partial oxidation", *IEEE Trans. Plasma Sci.*, vol. 33, no. 1, pp. 32–41, Feb. 2005.
4. Yu. D. Korolev, O. B. Frants, N. V. Landl, V. G. Geyman, and I. B. Matveev, "Nonsteady-State Gas-Discharge Processes in Plasmatron for Combustion Sustaining and Hydrocarbon Decomposition", *IEEE Trans. Plasma Sci.*, vol. 37, no. 4, pp. 586–592, April 2009.

INVESTIGATIONS OF THE EROSIVE TYPE DISCHARGE PARAMETERS INFLUENCE ON THE PROCESS OF THE PLASMOIDS FORMATION

A.S.Pashchina, V.I.Nikolaeva, M.K.Sidorenko, V.A.Prudchenko

Joint Stock Company "Scientific Research Institute of Radio Device Instruments", 80, Leningradsky prospect,
Moscow, Russia, 125178

The possibility of the plasmoids performances control is one of actual questions, appears in applied technical problems. At use the erosive type discharge in a pulse mode for the plasmoids formation the possibility of scale (the linear size), energy (energy content) and time (plasmoid lifetime) performances control represents the prime interest.

As a result of experimental researches it is shown, that the plasmoids formation takes place in a restricted range of the erosive type discharge parameters [1, 2, 4]. In particular, there are the limiting values of discharge pulse power density (5 MW/cm³), current increase velocity (500 kA/s), medial current density (10...20 kA/cm²) which excess is accompanied by the plasmoid energy parameters decrease and by intensification of the processes of equilibrium plasma formation in its neighborhood. Essential excess of the specified parameters (for 2...3 orders) is accompanied by the formation of plasma flow that is propagate to a distance, less than 10 calibers from the capillary edge [3]. In this case the plasmoid formation is not observed.

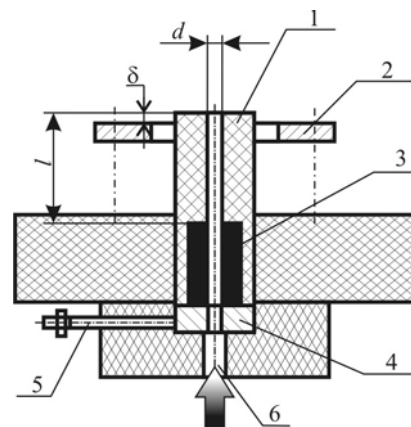
Variation of the full power input into erosive type discharge, at maintenance of power density, can be viewed as one of methods of the plasmoid scale and energy performances control. In particular it can be implemented by the discharge channel volume variation. Besides, the plasmoids performances appears depend in the strong degree on the boundary conditions on the discharge channel outlet, in particular: the shape and the spatial position of the outside electrode (cathode), the condition of atmosphere, magnetic field presence, - that also can be assumed as the additional control possibilities of scale and energy performances.

The experimental bench.

Experimental researches were spent on the erosive type discharger experimental model (fig.1). The discharge channel 1 material is polymethylmetacrylat, used as the plasma source substance. In a carbon anode 3, mounted on the discharge channel 1 inlet, the through hole 6, that provides the compressed gas delivery, is made. During experiments the possibility of the distance δ variation (between the cathode 2 plane and the

channel 1 edge) was provided. Next modifications of channels were used in experiments: the diameter $d=1, 2, 3, 4$ mm and the length $l=3, 5, 10, 15, 20$ mm. The relation of the discharge channel length to the diameter is in a range of values $l/d=2,5...5$.

Capacitors were used as energy source. The maximum energy value of capacitors is 22,5 kJ at the voltage level 5 kV and the net capacity value $C=1800$ uF. Registration of a current, a discharge voltage and the plasmoid radiation in an optical range have been spent during the experiments. The possibility of the compressed gas delivery at redundant pressure level up to 6 Barr was provided. This permitted to study the gas flow influence on the processes of the plasmoids formation.



- 1 – dielectric channel (polymethylmetacrylat)
- 2 – cathode
- 3 – anode (carbon)
- 4 – anode holder
- 5 – anode busbar
- 6 – hole for the forced delivery of air through the discharge channel

Fig. 1. The design scheme of erosive discharger.

Targets of a conductive material, mounted on fixed distance from the discharge channel edge, were used for estimations of the plasmoid energy content. Estimations of the plasmoid energy content were yielded by comparison of the holes sizes, formed in a target as a result of contact interaction with a plasmoid. The plates of conductive material (copper, brass, steel, aluminium) with thickness from 0,2 to 6 mm were used as targets.

The influence of pulse power density, current increase velocity and discharge duration on the plasmoids performances.

Depending on the erosive type discharge pulse power density it is possible to select two modes of plasmoids formation.

The first mode takes place in the range of power density values $0,5...1 \text{ MW/cm}^3$. This mode is characterized by almost silent plasmoid formation, oriented along the discharge channel axis. The plasmoid is characterized by sharply expressed boundaries; the shape is close to cylindrical, pointed to the extremity. For various diameters of the discharge channel (capillary) the plasmoid linear size varies in a range of $10...40 \text{ cm}$, diameter at the basis is about 5 mm . Dynamics of the plasmoid evolution is the smooth length magnification during the discharge. Velocity of the plasmoid length magnification is $30...100 \text{ m/s}$ and depends on the discharge current increase velocity and pulse power density values. Given mode takes place if the discharge current value does not exceed 100 A .

The plasmoid lifetime is exceed duration of the erosive type discharge which in the given experimental series reached up to 50 ms . Long-term enough time prolongs a plasmoid to exist after the discharge termination after that a plasmoid becomes to dissipate. The characteristic plasmoid lifetime, obtained in the given experimental series, is $20...500 \text{ ms}$. The integral plasmoid photo formed in a mode of current restriction, and also the characteristic oscillograms of current, voltage and signal from photodiode, mounted at level of 10 cm relatively to the discharge channel edge, are presented on fig.2.

The maximum plasmoid length received in a current restricted mode is $30...40 \text{ cm}$ for capillary diameter value $d=2 \text{ mm}$. Magnification of the

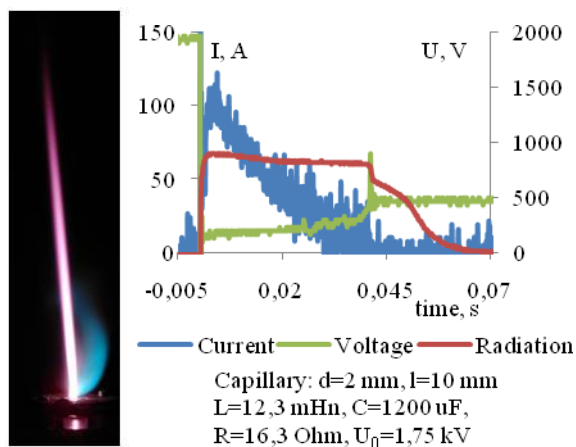


Fig.2. Integral plasmoid photo in current restricted mode, and the typical current, voltage and radiation oscillograms.

discharge channel diameter leads to the plasmoid length reduction. For example, plasmoid length does not exceed 15 cm for the capillary diameter value $d=4 \text{ mm}$. For the capillary diameter value $d=1 \text{ mm}$ the peak value of the plasmoid length in some cases is reached up to $60...80 \text{ cm}$ [1, 5, 6].

The tendency of the plasmoid length reduction while capillary diameter magnification, and, hence, the discharge channel volume (at relation l/d maintenance), can be explained by the pulse power density reduction. In this case also the decrease of the plasmoid energy content can be observed. This was checked by comparison of the contact interaction effects on testing targets.

It is necessary to note essential dependence of the plasmoid linear size from the current increase velocity. The range of current increase velocity values $100...500 \text{ kA/s}$ corresponds to the peak plasmoid linear sizes. Decrease of the current increase velocity leads the plasmoid length reduction. Parallel with the length reduction the upper limit excess causes the intense ionization in plasmoid boundary neighborhood.

The second mode of the plasmoid formation takes place in a range of pulse power density values $1...5 \text{ MW/cm}^3$. A peak current value for given mode is reached up to $2,5 \text{ kA}$, the discharge duration has the order of $2...25 \text{ ms}$. Exterior appearances: on the discharge channel outlet there is a plasmoid formation (the base diameter is nearby $1,5...2 \text{ cm}$) with expressed boundaries, surrounded by breaking up plasma cloud in diameter about $10...15 \text{ cm}$ (fig.3a). Depending on the discharge parameters the plasmoid length can be reached up to 1 m .

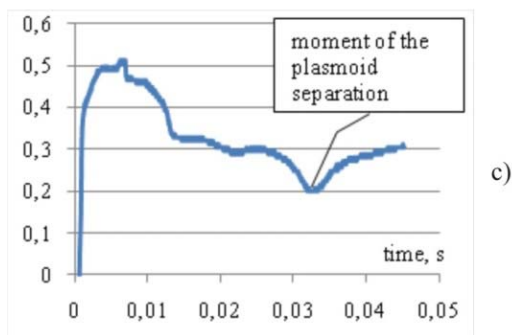
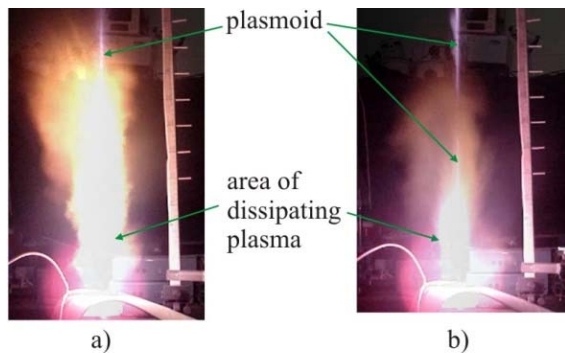
The discharge is accompanied by the strong shock wave formed by gases during the plasma heating and the capillary wall ablation. In some cases the separation of plasmoid and its free motion along the discharge channel axis (fig.3b) is observed, that is registered in the form of surges on the plasmoid radiation oscillogram (fig.3c).

Depending on discharge circuit parameters embodying of two modes is possible - aperiodic, when the discharge duration is restricted by a current half-period (fig. 4a), and periodic one, when the alternating-sign current and voltage oscillations (fig. 4b) takes place during a discharge pulse.

The volume of the breaking up plasma area appears minimal at aperiodic mode. Plasmoid boundaries appear more sharply expressed, than for an oscillating mode. At invariable values of medial power density, current increase velocity and the discharge duration, the energy content and also the plasmoid lifetime appears larger for aperiodic discharge mode (fig.4).

The forced delivery of gas through the discharge channel causes the plasmoid linear size magnification up to $1,5...2$ times. When pulse power density value is lower than $0,5...1 \text{ MW/cm}^3$,

there is the limiting pressure on the discharge channel inlet which excess causes reduction of the plasmoid linear size and energy content. The limiting pressure value varies in the range 1,5...2 Barr [5].



- a) $L=12,3 \text{ mHn}$, $C=1200 \text{ uF}$, $U_0=4,0 \text{ kV}$
 6) $L=49,7 \text{ mHn}$, $C=1200 \text{ uF}$, $U_0=5,0 \text{ kV}$

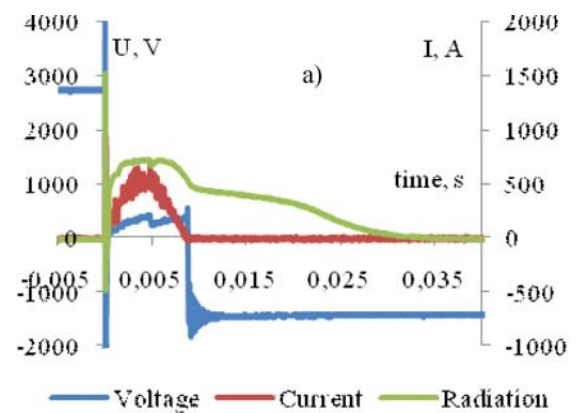
Capillary: $d=4 \text{ mm}$, $l=20 \text{ mm}$
 Inlet capillary pressure $p_x=2 \text{ barr}$

Fig.3. Video frames of the plasmoid formation (a, b), and the plasmoid radiation oscillogram registered by the photodiode (c) for a case of the plasmoid separation and moving.

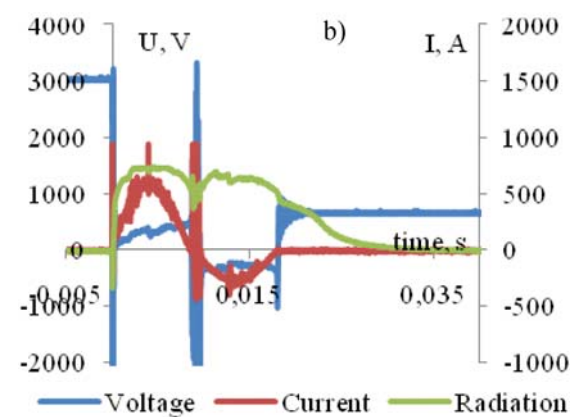
Rising of pulse power density up to 1...5 MW/cm³ and current increase velocity up to 100...500 kA/s causes the limiting pressure value increase. In particular, at magnification of redundant pressure up to 6 Barr it was not possible to find out the tendency of the plasmoid length change, related to presence of critical pressure. In the explored range of redundant pressure values the forced delivery of gas through the discharge channel does not lead to appreciable change in the discharge current and voltage oscillograms. In this case a plasmoid lifetime after the discharge termination is considerably increased (fig.5).

Generally the forced delivery of gas through the capillary provides the discharge localization in the near wall area [3, 5]. Most possibly, it is due to a lapse rate of stagnation pressure in a boundary layer which value reduces in a direction to a capillary wall. Besides discharge stabilization in the near wall area, the forced delivery of gas allows to

reduce the ablation velocity of walls, and hence to raise discharger resource. Also it allows increasing the erosive discharge stage duration during which there is possible to maintenance the plasmoid existence without its fracture. According to spent experiments, in the absence of the forced delivery of gas the optimum duration of this stage does not exceed half-period of the discharge circuit oscillations, defined from requirements when a pulse power density and a current increase velocity are close to the limiting values (5 MW/cm³ and 100...500 kA/s, accordingly). The forced delivery of gas allows increasing the optimum duration of the erosive discharge stage, approximately, to 2...3 times. In current restricted mode the optimum duration of the erosive discharge stage appears essentially longer [6].



Capillary: $d=2 \text{ mm}$, $l=15 \text{ mm}$
 $L=12,3 \text{ mHn}$, $C=600 \text{ uF}$, $U_0=2,5 \text{ kV}$



Capillary: $d=2 \text{ mm}$, $l=15 \text{ mm}$
 $L=12,3 \text{ mHn}$, $C=600 \text{ uF}$, $U_0=3,0 \text{ kV}$

Fig.4. The typical oscillograms of voltage, current, radiation, detected by photodiode, for aperiodic (a) and oscillating (b) discharge modes.

The processes related to plasmoid formation and dynamics are reflected on radiation time dependence. After the discharge termination, which moment corresponds to the beginning of the first

inflexion (the plus inflexion, fig. 5), intensity of radiation decreases linearly on time. After some interval there is a second inflexion (negative) on radiation time dependence after which radiation dependence gets character of a damping exponential curve. The forced delivery of gas through the discharge channel leads preferentially to magnification of the time interval corresponding to linear dumping of radiation intensity. The exponential damping interval changes in a less degree. If to assume, that the exponential damping interval corresponds to plasmoid dissipation time (which on 1...2 orders exceeds plasma recombination time at atmospheric pressure) the linear damping interval can be compared with a plasmoid lifetime.

Excess the upper value of current increase velocity ($dI/dt > 500$ kA/s) leads to considerable decrease of the plasmoid energy performances. In this case change of the plasmoid linear size is inappreciably, however duration of the plasmoid existence after the discharge termination decreases up to 4...5 times (fig.5a and 5b).

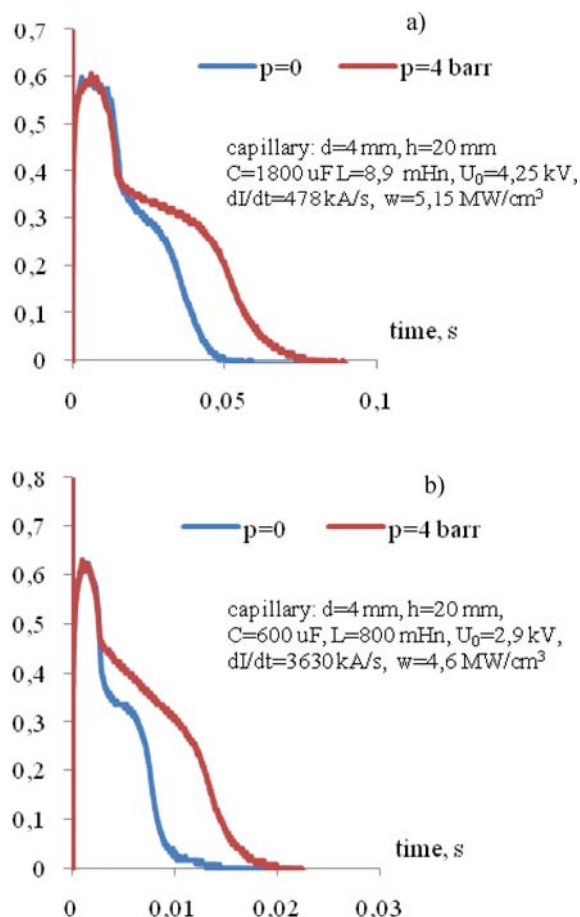


Fig.5. Oscillograms of the plasmoid radiation for the cases with and without forced delivery of gas through the discharge channel for essentially different values of current increase velocity.

Magnification of the erosive discharge integral power at respective increasing of the discharge channel volume (at invariable values of pulse power density and current increase velocity) leads to proportional growth of the plasmoid energy content and to some magnification of the plasmoid linear size. Thus, the plasmoid characteristic size and the energy content appears to be peak in a case when the erosive discharge parameters are closed to critical values (pulse power density $w \sim 5$ MW/cm³, current increase velocity $dI/dt \sim 500$ kA/s). Change of the specified parameters towards diminution, or magnification, is accompanied by decrease of the plasmoid size and energy content.

Influence of the ionic current spatial configuration, formed on the discharge channel outlet, on plasmoid parameters.

It is revealed experimentally, that plasmoid parameters depends on ionic current spatial distribution on the discharge channel outlet in a strong degree. For the used organization scheme of the erosive type discharge the ionic current spatial distribution depends on the shape and the size of the cathode, the cathode position relatively the discharge channel outlet, and also from geometry of the discharge channel outlet profile.

Few variants of ring cathodes with different inside diameters were used in researches. The appreciable distinction of the plasmoid parameters (the linear size and the energy content) depending on the cathode inside diameter value (at the fixed cathode position relatively the discharge channel outlet) was not revealed in experiments.

Change of the cathode position relatively discharge channel edge makes appreciable influence on plasmoid parameters. So, the linear size and the plasmoid energy content appear to be peak in the case when the discharge channel edge raises over a cathode plane.

Replacement of the cathode plane to the level of the discharge channel edge and above is accompanied by reduction of the plasmoid length (fig. 6a-d). Diffusion of the plasmoid boundaries, the breaking up plasma volume magnification in the plasmoid neighborhood is thus observed. So, replacement of the cathode plane to the level of the discharge channel edge leads to plasmoid length diminishing for 10...20 %. The further cathode replacement leads to more essential diminishing of length at some magnification of the plasmoid visible diameter. It is remarkable, that current and voltage time dependences are not change considerably while the cathode replacement. At the same time, the plasmoid lifetime is change enough essentially (fig. 6e). So, the peak value of the plasmoid lifetime is observed if the cathode positions relatively the discharge channel edge in a range of values 0...+3 mm. The cathode

replacement relatively the discharge channel edge in a range of values $-3...+6$ mm is accompanied by the monotonous decrease of the plasmoid energy content.

Change of capillary outlet profile geometry by facet performance (the capillary sizes - $d=2$ mm, $l=10$ mm, a facet depth - 2 mm, a corner value - 120°) has not revealed appreciable influence on the plasmoid shape, size and the energy content in comparison with a case when the capillary edge is not handled. On the contrary, change of the cathode shape yields essentially influence on geometrical and energy plasmoid parameters. The most probable reason of that, in our opinion, is influence of electrical potential distribution which essentially depends on cathode geometry, and in less degree - from density distribution of a gas flow.

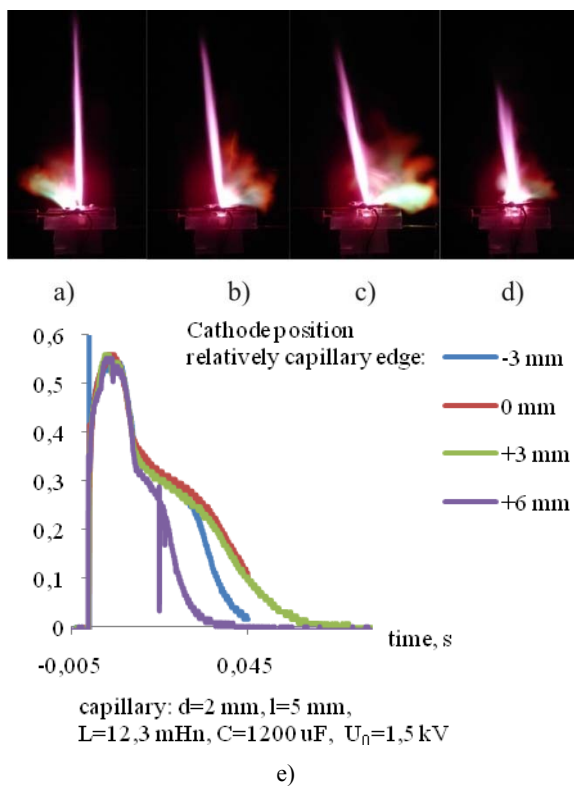


Fig.6. Dependence of geometrical performances (a-d) and plasmoid radiation intensity (e) from the cathode position relatively the capillary edge.

For studying of the cathode shape influence on the plasmoid performances the hollow cylinder has been mounted coaxially to the discharge channel. A cylinder material - aluminium, inside diameter value - 28 mm, height - 30 mm. Essential change of the plasmoid geometrical performances (fig.7a and 7b) is observed in this case, in particular: decrease of the plasmoid linear size, increase of the plasmoid diameter, formation of the breaking up plasma area, expanded while removal from the discharge channel edge. Intensity of the plasmoid radiation

thus decreases (fig.7e), though the radiations duration is little increasing. The character of radiation time dependence becomes close to exponential damping, that is essentially differ from the character of radiation dependence for the case of cathode with initial shape (fig.7a), where there is the linear dumping interval (a corresponding curve in fig.7e). Also the essential decrease of the plasmoid energy content is observed.

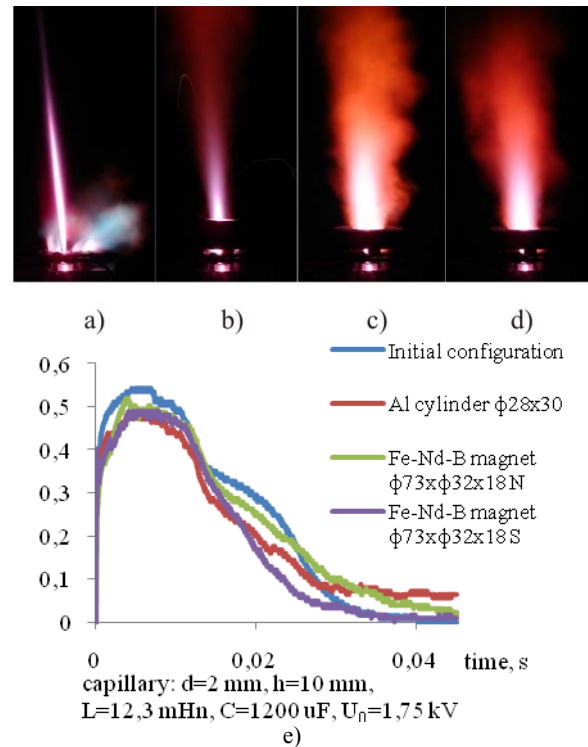


Fig.7. Influence of the cathode geometry and of the magnetic field orientation on the plasmoid geometric performances (a-d) and its radiation intensity (e).

Magnetic field of the ring magnet, mounted coaxially to the discharge channel, leads to more essential influence on plasmoid parameters. The ring magnet with next parameters: the sizes $\phi 73 \times \phi 32 \times 18$, a material - *Fe-Nd-B*, a magnetic intensity near the surface $\sim 1,2$ Tl, - was used in experiments. As far as the magnet material is a conductor, thus changes of the electrical potential distribution, caused by magnet installation, is quite similar to the previous case. However, the magnetic field makes more essential influence on the plasmoid performances (fig.7c and 7d). The length of plasma formation in this case decreases, diameter of the brightest part is increasing till the sizes of the magnet inside diameter, and the volume occupied by the breaking up plasma is increasing. Dependence of the size of the brightest area of plasma formation on the magnetic field direction is observed. The volume of this area appears to be larger while orientation of northern magnet pole

towards the discharge channel (fig.7c), than for the opposite magnetic field direction (fig.7d).

Character of radiation intensity, namely: almost full lack of a linear damping interval and presence of an exponential damping interval, - appears to be similar for a case, when the magnetic field is absent. However, if for a case, when the northern magnetic pole is oriented toward the discharge channel (fig.7c), the character of radiation intensity has little distinctions from an exponential damping, and it is possible to find out signs of the linear damping interval, in a case, when the northern magnetic pole is oriented oppositely (fig.7d), exponential character of radiation damping becomes more expressed (corresponding dependences in fig.7e).

It is necessary to note, that magnet placement on the considerable distances from the discharge channel edge (10...15 cm) does not cause appreciable influence on plasmoid performances.

In these requirements formation of plasma area on the discharge channel outlet (nonuniform localized area with the raised ionization which does not have obviously expressed boundaries) takes place. The similar tendency is observed while changing the cathode spatial position relatively the discharge channel edge, where variation of radial and axial ionic current components relation also takes place (fig.6). Thus, set of the gained data can indicate on the essential role of the ionic current spatial distribution on the discharge channel outlet in mechanisms of plasmoid formation.

Influence of a gas flow on plasmoids performances.

Interaction of the plasmoid with the transversal gas flow which is not touch the removal currents area in the discharge channel edge neighborhood, leads to reduction of the plasmoid sizes (fig.8a and 8b, it is visible the peak intensity area of radiation, gained from video shooting using neutral light filters NS-13 and NS-3). At the redundant pressure value on branch pipe outlet ~6 Barr, the diminution of the plasmoid length reaches 40...50 % of the initial value. Unlike the breaking up plasma area the plasmoid does not drift by a gas flow. Presence of the gas flow does not influence discharge current and voltage time dependences. Radiation time dependences are different in duration of the plasmoid lifetime after the discharge termination. As a rule, duration of the plasmoid lifetime after the discharge termination in the conditions of transversal gas flow changes inappreciably. However in a number of cases magnification of the plasmoid lifetime is observed (fig.8c).

The gas flow action in the discharge channel edge neighborhood on removal currents spatial domain makes essential influence on process of

plasmoid formation and its parameters. In particular, at redundant pressure value on the branch pipe outlet $p \sim 1$ Barr, placed apart ~ 10 cm relatively the discharge channel edge, diminution of the plasmoid length up to 60...80 % is observed. The further magnification of redundant pressure leads to practically full inhibition of plasmoid formation.

In the viewed case the gas flow makes essential influence on electrical potential distribution (and the ionic current density) on the discharge channel outlet, first of all, due to magnification of recombination rate of charged particles. The gained effect is quite similar for cases with influence of the cathode shape and magnetic field on plasmoid parameters. This allows considering the ionic current distribution on the discharge channel outlet as one of the main factors determining the plasmoid formation process.

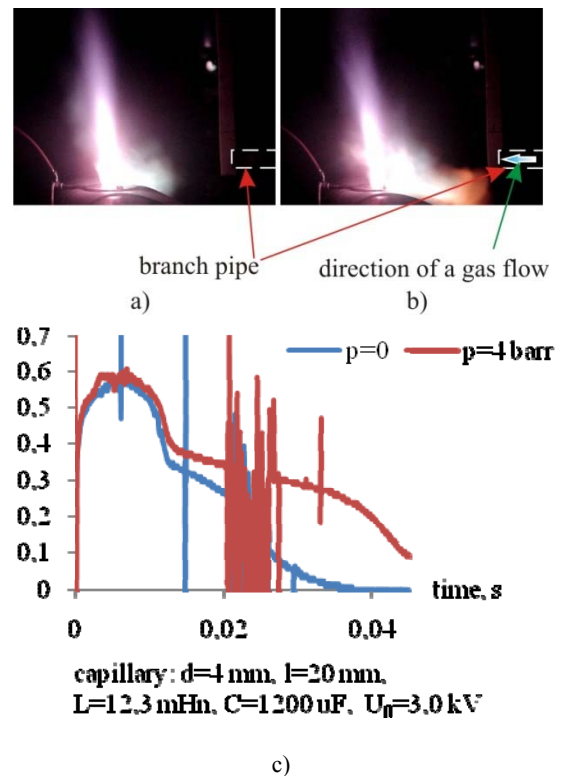


Fig.8. The transversal gas flow influence on the plasmoid sizes.

Conclusions.

Thus, results of experimental researches shows possibility of the plasmoid scale and energy performances control, in particular, due to variation of the erosive discharge integral power (at maintenance of pulse power density and current increase velocity), and also by the means of the erosive discharge stabilization in the near wall capillary area carried out by the forced delivery of gas.

In the technical applied problems it is necessary to consider essential influence of the ionic current spatial distribution on the discharge channel outlet on the plasmoid formation processes. In this connection study of questions related to possibility of minimization of exterior factors influence (in particular, air flows) on removal currents area - on a section between the discharge channel edge and the cathode - is actually. Given questions can be solved both by the means of constructive measures, and by the changes in the organization of the erosive type discharge. First of all, the solution of the specified question is actually for expansion of plasmoid generators applications (for example, for use as the onboard flying vehicles generators for aerodynamic drag decrease, as the plasma antenna, etc.).

This work is executed at the support of the Russian Foundation for Basic Research, the project 07-02-12029.

Literature.

1. *Avramenko R.F., Bahtin B.I., Nikolayeva V.I., Poskacheyeva L.P., Shirokov N.N.* Issledovaniye plazmennikh obrazovaniy, initsiirovaniye erozionnim razryadom. – JTP (Sov.), 1990, v.60, № 12. P.57-64.
2. *Pashchina A.S., Nikolaeva V.I., Sidorenko M.K., Prudchenko V.A.* Researches of the capillary type discharge parameters influence on the process of the plasmoids formation // 3-d International Symposium on Unconventional Plasmas/ Tenth International Symposium on Ball Lightning. Kaliningrad: Kant University, 7-12 July 2008.
3. *Minko L.Ya.* Poluchenije i issledovaniye impulsnikh plazmennikh potokov. Minsk: Nauka i tekhnika, 1970. 184 p.
4. Basic researches of the methods providing stability of plasmoid parameters, formed with the help of the capillary discharge in a pulse-periodic mode/ RFBR project 05-02-08010.
5. Research of the methods of plasmoid formation and the control of their parameters/ RFBR project 07-02-12029.
6. *Avramenko R.F., Nikolayeva V.I.* O sushchestvovanii kvantovomekhanicheskoy energii fona. Eksperimentalniye dannije. Kniga 1. Predvaritelnij nauchno-tekhnicheskij otchet. Moscow: NIIRP., 1984.

PLASMA-ASSISTED MECHANISM OF COOL FLAME APPEARANCE

Bityurin V.A. and Filimonova E.A.

OIVT RAN, Moscow
e-mail: helen@oivtran.ru

Abstract. Multistage inflammation in the propane-air mixture was considered. The longest phase of multistage ignition is an induction time of cool flame appearance. It has been shown by modeling that the operation of discharge in hydrocarbon-oxidizer mixture may reduce the low temperature inflammation stage is appreciably (in tens times and more), due to initial radicals resulted from dissociation of fuel and oxygen by electron impact. At the same time the duration of second (blue) and third (hot) stages remains the unchanged. This effect is associated with a fast appearance of C_3H_7OOH and CH_3OOH , and, as a consequence, a partially release of chemical energy in the system under decomposition of hydroperoxides.

1. Introduction.

Primordially, the interest to low temperature oxidation of fuel-air hydrocarbon mixtures has been associated with the study of combustion in a spark ignition engine (an engine knock) and diesel engine with homogeneous charge (for example, nature gas with air) [1,2]. The appearance of low temperature oxidation of hydrocarbon-air mixtures is accompanied by the fluorescence of formaldehyde (CH_2O) and formyl radical (CHO) with the wave-length of blue spectral region, and the stepped release of fuel mixture chemical enthalpy throughout the organic peroxide decomposition. Multistage inflammation includes the cool flame stage ($T \sim 550-750$ K), blue flame ($T \sim 800-1000$ K) and hot flame ($T > 1000$ K) stages.

At present time, it is actively developed the new area in combustion, namely, plasma assisted combustion. We suggested that under certain conditions generated by exterior source (discharge, laser spark) the onset of multistage inflammation may occur [3]. The results of preliminary calculations showed the radicals (O , H , CH_3 - the dissociation products by direct electron impact) reduce the induction time of cool flame ignition, conserving the duration of blue and hot stages the unchanged [3]. As a result the total induction time becomes smaller. In given work on the basic of developed earlier kinetic mechanism and preliminary results the reason of remarkable reduce of cool flame stage is established. The modeling results were obtained for the mixtures, containing the methane or propane.

2. Description of modeling approach

The initial concentrations of radicals were determined taking into account the treatment of mixture by discharge which is simulated in the approximation of specified electric field. The concentration of primary active particles is estimated through the coefficients of corresponding processes of dissociation and excitation of species

by electron impact and input energy per one molecule. All the kinetic and transport coefficients as functions of the reduced electric field E/n (where E is the electric field and n is the gas density) are obtained by averaging of corresponding cross sections with the electron energy distribution function. The latter is calculated using the BOLSIG+ kinetic code [4].

Initial concentrations of radicals were the inlet parameters for chemical kinetic code. The calculation of inflammation process was carried out using the kinetic code [5] for the constant volume condition with taking into account a heat emission. The cooling of walls was not taken into consideration, and nowadays insufficiently studied peroxide decompositions on the walls was accepted in some reactions just approximately. In experiments the multistage ignition is identified throughout the stepped growth of pressure and light emission. In calculations the identification of those flames is the change of pressure or temperature, and concentrations of the key components.

3. Results and discussion

The basic set of species and reactions of present chemical kinetic code has been used earlier for the description of formation and removal of toxic impurities in the automobile exhaust gases [6], for the simulation of physical and chemical processes in the chemical compression reactor [7], in the study of ignition of fuel-air counter-flow jets by electrical discharge [8] and other tasks. To decide the low temperature inflammation problem that chemical kinetic scheme was added new reactions and components taken from several sources, including [9-11].

In Fig.1 the temperature and OH concentration as the result of modeling for mixture $6.5\%C_3H_8+19.6\%O_2+73.9\% N_2$ are presented. The first peak of OH corresponds to appearance of cool flame (time is 1.16 s) with increase of temperature at 130° , a weak OH peak at time of 1.202 s corresponds to the blue flame stage and the hot

flame arises at time of 1.207s. For this case the concentrations of acetaldehyde (CH_3CHO), and alkyl hydroperoxides $\text{C}_3\text{H}_7\text{OOH}$ and CH_3OOH are showed in Fig.2.

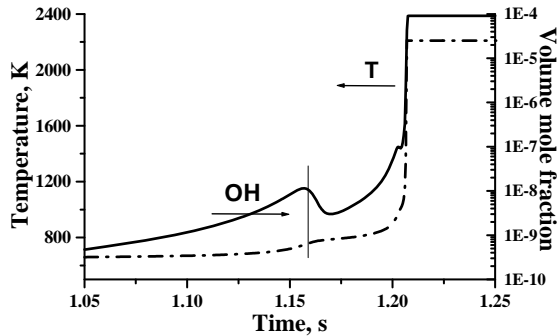


Fig. 1. Temperature and OH concentration in dependence on time in 6.5% C_3H_8 + 19.6% O_2 + 73.9% N_2 mixture. $P_0=5.5\text{atm}$, $T_0=650\text{K}$.

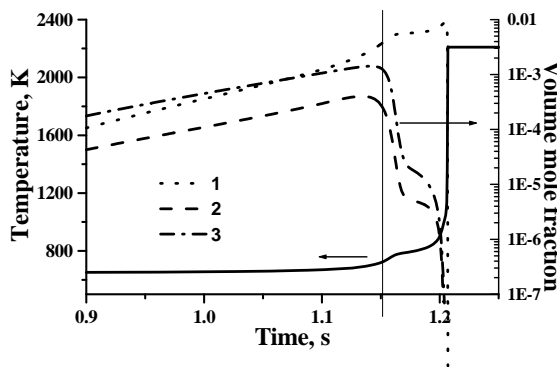


Fig.2. Temperature and component concentrations in dependence on time: "1" is CH_3CHO , "2" is CH_3OOH , "3" is $\text{C}_3\text{H}_7\text{OOH}$. Conditions are in Fig.1.

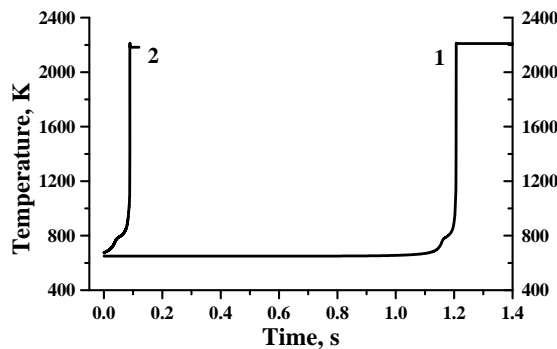


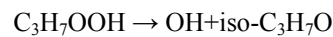
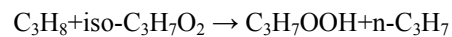
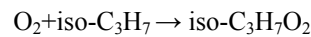
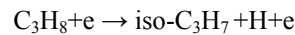
Fig.3. Temperature in dependence on time: "1" is no discharge, "2" is mixture activated by discharge. 6.5% C_3H_8 + 19.6% O_2 + 73.9% N_2 mixture. $P_0=5.5\text{atm}$, $T_0=650\text{K}$.

If the mixture is activated by discharge, the induction time noticeably reduced. In Fig. 3 the

comparison of temperature dependence on time for two cases demonstrates the shift of induction time more than one order of magnitude: from 1.2 s to 0.09 s. The primary concentrations of radicals were calculated using the constant rates of dissociation and excitation for propane-air mixture [12] at the fixed electric field of 200 Td, and in suggestion that the input energy into the system was equal to 0.01 eV/molecule. As a result the concentrations of active particles generated by discharge were $[\text{O}]_0=1500\text{ppm}$, $[\text{H}]_0=500\text{ppm}$, $[\text{n-C}_3\text{H}_7]_0=[\text{iso-C}_3\text{H}_7]_0=[\text{C}_2\text{H}_5]_0=[\text{CH}_3]_0=250\text{ppm}$.

The analysis of leading reactions of cool flame stage in $\text{C}_3\text{H}_8:\text{O}_2$ and $\text{C}_3\text{H}_8:\text{air}$ mixture showed that the preferred mechanism of organic peroxide formation under conditions of alkyl radical production by discharge becomes the way through the formation of propylperoxy radicals iso- $\text{C}_3\text{H}_7\text{O}_2$ and n- $\text{C}_3\text{H}_7\text{O}_2$.

Then the sequence of propylperoxide ($\text{C}_3\text{H}_7\text{OOH}$) formation may be written as follows:



The $\text{C}_3\text{H}_7\text{OOH}$ decomposition with OH production gives the main input in the cool flame inflammation when the enthalpy partially releases, and, as a consequence, the temperature and pressure increase. In contrast, the auto-ignition of CH_4 and C_3H_8 containing mixtures the formation of hydro peroxides for the most part comes from the intermediate product – acetaldehyde.

In assisted ignition by discharge the cool flame induction time is observed both for rich mixture and close to stoichiometric. In rich mixture the leading species are alkyl radicals resulted from dissociation by electron impact. In mixtures close to stoichiometric the main radical is produced by discharge the O atom, which triggers some reactions important for hydro peroxide formation. If the primary radical concentration is ~500-1000 ppm the induction time can be reduced by the order of magnitude and more at the initial temperature of 600-700 K. It depends on mixture.

The simulation results are evidence that the treatment of fuel by gas-discharge plasma is so important as air, moreover, it should be carry out with small amount of oxygen (see above reactions). In accordance with stated above we can await, that the most effective manner of fuel-air mixture preparing is two steps preparing: the first step is treatment by plasma only rich fuel-oxygen mixture, where the only cool flame stage is realized, without transition to hot inflammation, second step is

addition and mixing the prepared mixture with heated air or oxygen (~700 K), because just for rich mixture the cool flame stage is mostly expressed. That fuel preparation one can use, for example, for the diesel engine with homogenous charge (nature gas with air), and also with the purpose of fuel reforming and production of syngas.

4. Conclusion.

The results of multistage inflammation simulation in the discharge system in propane-air mixture showed that the operation of discharge promotes the quick hydro peroxide formation and, as a consequence, a partial release of chemical enthalpy throughout of organic peroxide decomposition. That process results in stepped heat of gas at 50-200 degrees.

Perhaps, it will be able to explain some unaccountable phenomena in experiments of assisted combustion (for example, the fast propagation flame (200 m/s and more) [13] and the low temperature ignition (600-720 K) [14],) if to join the modeling of discharge, hydrodynamics and full chemical kinetic code comprising the description of low temperature inflammation. This is a future work.

This work was supported by Russian Academy of Sciences (the Program of the Basic Research "Fundamental problem of combustion and detonation in energetics")

References

1. *Shtern V.Ia.* Mechanism of Hydrocarbon Oxidation in Gaseous Phase. M.: Academy of Sciences of USSR. 1960. 550 p. (in Russian).
2. *Sokolik A.S.* Spontaneous Combustion, Flame and Detonation in Gases. M.: Academy of Sciences of USSR. 1960. 427p. (in Russian).
3. *Bityurin V.A., Bocharov A.N. and Filimonova E.A.* About low temperature inflammation of propane and acetaldehyde under assisted combustion // 8th Inter. Workshop on Magnetoplasma aerodynamics, Mach 31-April 2, 2009, Moscow, Russia. p. 36-39.
4. BOLSIG+ 2005 CPAT: <http://codiciel.fr/plateforme/plasma/bolsig/bolsig.php>
5. *Bityurin V.A., Bocharov A.N.* MHD Interaction in the Hypersonic Air Flow around a Blunt Body // MZhG. 2006. №5. p.188-203. (in Russian)
6. *Filimonova E.A. and Zhelezniak M.B.* Formation and removal of toxic impurities in the automobile exhaust gases. / In: Combustion and atmospheric pollution, Edited by G.D. Roy, S.M. Frolov, A.M. Starik - Moscow: Torus Press Ltd., 2003. p.483-488.
7. *Bityurin V.A., Bocharov A.N. and Filimonova E.A.* Simulation of the physical and chemical processes in the chemical compression reactor. / In: Combustion and atmospheric pollution, Edited by G.D. Roy, S.M. Frolov, A.M. Starik - Moscow: Torus Press Ltd., 2003. p.188-191.
8. *Bityurin V.A., Bocharov A.N., Filimonova E.A., Klimov A.I.* Study of ignition of fuel-air counter-flow jets by electrical discharge // In Proc. of The 15 Inter. Conf. on Gas Discharges and their Applications, 5-10 Sept., Toulouse, France, P. 973-976. 2004.
9. NIST Chemical Kinetics Database on the Web, <http://kinetics.nist.gov>
10. *Basevich V.Ia., Vedenev B.I. and Arutyunov B.C.* Kinetic Modeling of Appearance and Propagation of Cool Flames in CH₃CHO-O₂ Mixtures. // Khimicheskaja Fizika. 1999. v.18. № 6. p.40-48. (in Russian).
11. *Vedenev B.I. Romanovich L.B., Basevich V.Ia., Arutyunov B.C., Sokolov O.V., Parfenov Y.V.* Experimental Study and Kinetic Modeling of Negative Temperature Coefficient of Reaction Rate in Rich Propane-Oxygen Mixture. // Izvestiya Acadimii nauk. Seriya Khimicheskaja, 1997, №12, p.2120-2124. (in Russian).
12. *Bychkov V.L., Kochetv I.V., Bychkov D.V., Volkov S.A.* Air-Propane Mixture Ionization Processes in Gas Discharges // IEEE Trans. on Plasma Science. 2009, 37, №.12, p.2280-2285.
13. *Kazantzev S.Yu., Kononov I.G., Kossyi I.A., Tarasova N.M., Firsov K.N.* Ignition of combustible gaseous mixture in closed volume initiated by freely localized laser spark. // Fizika plasm, 2009, 35, p.281-288. (in Russian).
14. *Lou G., Bao A., Nishihara M., Keshav S., Utkin Y. G., Adamovich I. V.* Ignition of Premixed Hydrocarbon-Air Flows by Repetitively Pulsed, Nanosecond Pulse Duration Plasma. // 44th AIAA Aerospace Sciences Meeting and Exhibition, Reno, USA, 2006, AIAA Paper 2006-1215.

NUMERICAL STUDY OF PLASMA INITIATED IGNITION STAGES FOR ETHYLENE-AIR MIXTURES

*M. A. Deminsky*¹, *I. V. Kochetov*², *A. P. Napartovich*², *S. B. Leonov*³

¹ State Research Center of Russia “Kurchatov Institute”, Moscow, Russia

² State Research Center of Russia Troitsk Institute for Innovation and Thermonuclear Research (TRINITI), Troitsk, Moscow region, Russia

³ Joint Institute for High Temperature RAS, Moscow, Russia

Abstract. Comprehensive study on processes controlling plasma assisted ignition of ethylene-air mixtures at conditions typical for scramjet combustion chamber. It is shown that at plasma initiation gas heating proceeds by two steps defining two stages of ignition process. On the first stage, the gas is heated due to exothermic reactions involving atomic oxygen and secondary chemical radicals. Temperature increment to the end of this stage for ethylene-air mixture is relatively small. An important effect of this stage is not heating but production of transient species. The second stage is finished by complete combustion.

The first and second stages can be identified through temporal peak intensity in optical spectra from excited OH and CH, respectively.

The calculated whole induction time varies with the particular combustion mechanism exploited. This demonstrates necessity to refine combustion mechanism for conditions typical for scramjet combustion chamber with plasma initiation – one atmosphere pressure, static gas temperature around 700 K and appearance of atomic oxygen.

Introduction

Scramjet combustor is destined for providing flights of hypersonic aircraft at the altitude about 20 km with Mach number M about 8. Head wind is slowed down to $M \approx 2$ in the inlet on a system of attached shocks. Then it comes into combustor. As a result of slowing down, the static gas temperature becomes about 700 K and static gas pressure grows up to about one atmosphere.

Shortening of combustion induction length to the length of combustion chamber is the primary problem for scramjet designers. It is expected that non-thermal plasma may allow diminishing of energy required for faster ignition of air-fuel mixtures [1-3].

Authors of ref. [3] have calculated the threshold energy input required for uniform plasma ignition initiation of a premixed ethylene/air mixture in conditions typical for the scramjet combustor. The reduced threshold energy is as large as 210 J/g. To provide this value rather powerful energy supply is necessary. One of options to get lower threshold energy is usage of a filamentary discharge allowing for utilization of heat released in chemical reactions in locations with high discharge power density. It was shown in [4] that indeed usage of a filamentary discharge can lead to a significant reduction of the reduced threshold energy for ignition of ethylene/air mixture as against uniform discharge.

Mechanisms of plasma induced combustion acceleration are actively discussed in publications: formation of atomic oxygen and other chemical radicals (see f. e. [5]); production of singlet delta oxygen molecules $O_2(a^1\Delta_g)$ [6-7]; chain ion-molecule reactions with radicals as intermediates

[8]. Today, majority of researchers believe that the main precursor responsible for ethylene/air combustion acceleration is the atomic oxygen.

The most important source of atomic oxygen in plasma is dissociation of O_2 molecules in collisions with excited nitrogen molecules and by electron impact. Then oxygen atoms come into fast chemical reactions with hydrocarbons. As a result of these reactions, a number of intermediate products are formed: H_2O_2 , HO_2 , H_2 , CO , CH_2O , CH_2CO , C_2H_3O , C_2H_4O and so on. Heat release in exothermic reactions results in a fast gas heating. Then heating rate diminishes. At low reduced energy density duration of this stage is rather long. Some time later, the second stage follows with fast mixture ignition ending in a complete combustion.

For description of the spontaneous ignition, a number of combustion mechanisms are known: GRI 3.0, Konnov, UBC 2.0. These mechanisms are verified for rather high initial gas temperatures (≥ 1100 K). At lower temperatures, production rate of chemical radicals is too low and subject to strong fluctuations. As a result, induction time in experiments cannot be controlled and fluctuates within large interval. Hence no valid conclusion can be drawn about applicability of known combustion mechanisms at temperatures lower than 1100 K. Plasma activation of gas mixtures results in a large amount of chemical radicals. Then the role of spontaneous fluctuations is negligible, and induction time is well defined quantity. Adequacy of theoretical description of plasma assisted combustion depends on accuracy of chemical reaction rate coefficients adopted for the processes with chemical radicals involved.

Time evolution of gas mixture temperature for conditions of scramjet combustor was studied

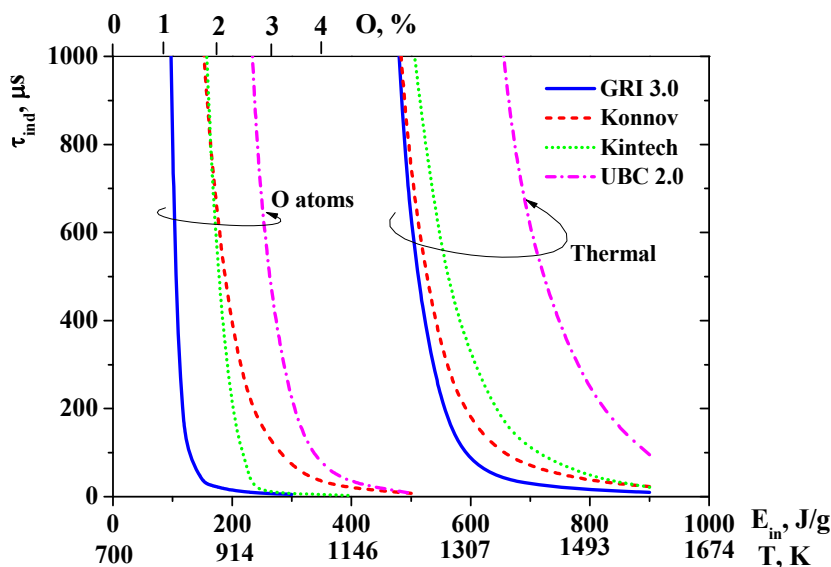


Fig. 1. Comparison of induction time for ethylene/air stoichiometric mixture calculated by different combustion mechanisms for thermal and O-atom initiations. $P_0 = 1 \text{ atm}$, $T_0 = 700 \text{ K}$, $N = \text{const}$.

theoretically in [3] for variable steady state discharge energy input. It was found that temperature growth proceeds in two stages. The present paper aims to give results of more detailed studies on stages of plasma assisted ignition by variation of mixture composition and E/N parameter (E is the electric field strength, N is the gas number density). E/N parameter can be changed within some limits when using different types of a discharge. Uncertainty in predicted induction time value caused by implementation of some mechanism of the spontaneous ignition is discussed.

Numerical model

Induction time predictions in different combustion mechanisms

To illustrate the problem with formulation of combustion mechanism at low temperatures, the induction time for stoichiometric mixture of C_2H_4 with dry air was calculated as a function of initial gas temperature using GRI 3.0, Konnov, UBC 2.0, and Kintech mechanisms (Fig. 1, curves designated as thermal). It is seen that scatter in induction time values at fixed gas temperature is rather large, in particular for UBC 2.0 mechanism versus others. Besides, the calculations were performed for

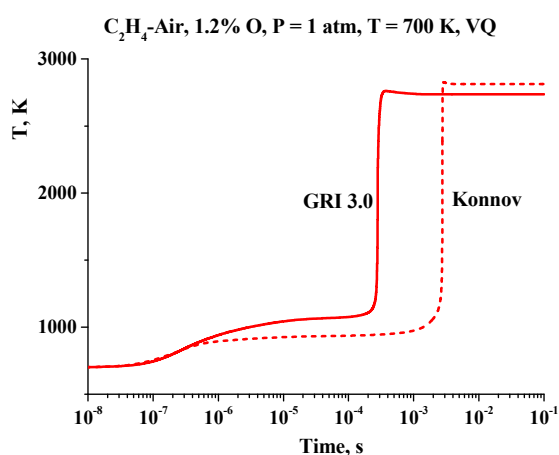


Fig. 2. Calculated temperature evolution at initiation by O atoms for stoichiometric C_2H_4 -air mixture for different combustion mechanisms.

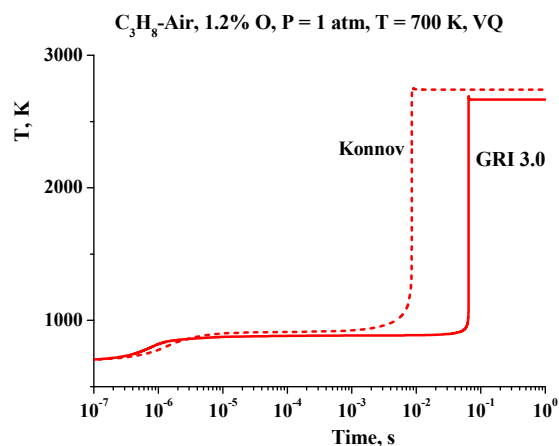


Fig. 3. Calculated temperature evolution at initiation by O atoms for stoichiometric C_3H_8 -air mixture for different combustion mechanisms.

ignition initiation by instant injection of O atoms at fixed initial gas temperature ($T=700$ K, curves are designated as O atoms). The top axis scale is correlated with the scale on the bottom axis by a condition that the chemical potential associated with O atoms is equal to gas enthalpy change at variation of its temperature above 700 K. Comparison of curves for O-atom induced and spontaneous ignition clearly shows that ignition initiation by O-atoms is essentially more energetically efficient than the spontaneous ignition at increased temperature.

For both, ethylene and propane fuels the results of calculations are sensitive to combustion mechanism chosen (GRI 3.0 and Konnov). In particular, GRI 3.0 predicts for C_2H_4 temperature increase at the first stage 370 K in comparison with 250 K predicted by Konnov mechanism. For C_3H_8 both mechanisms predict nearly the same increase of temperature at the first stage (200 K). The inductance times found with usage of GRI 3.0 and Konnov mechanisms differ significantly, and the difference between predicted inductance time values changes a sign by transition from C_2H_4 to C_3H_8 . Earlier the remarkable differences in induction time values calculated with different combustion mechanisms were found in ref. [9] for methane/air ignition as spontaneous, as induced by O-atoms.

It is known that at certain conditions spontaneous ignition of hydrocarbons occurs in a form of a few stages [10]. It manifests itself as step-like increments of gas temperature separated by periods of slow growth. This phenomenon attracts last years much attention. Review article [11] is analyzing processes in “cold” and “blue” flames appearing in a course of oxidation and burning hydrocarbons and their derivatives in gas phase. Light emission observed in flames is mainly due to spontaneous emission from excited electronic states of molecules HCHO (in cold flames) and HCO (in blue flames).

Along with appearance of stages in fuels/air ignition in some cases so-called negative temperature coefficient is observed experimentally (see f.e. [11]). It means that the induction time as a function of temperature is a growing function in some interval of temperature. In a recent paper [12] the combustion mechanism for *n*-butane developed for temperature interval 530-900 K, which predicts for the certain conditions existence of two-stage burning and of negative temperature coefficient.

In order to get better insight into origin of plasma induced two-stage ignition we have analyzed in more detail processes controlling gas heating rate at intermediate times.

Gas heating analysis

Hydrogen combustion

Mechanism of plasma assisted ignition is frequently associated with atomic oxygen production in a discharge. Actually, among products after discharge plasma treatment of a fuel/air mixture there are charged particles and a lot of radicals and electronic excited states of atoms and molecules. To separate effects of charged and excited species and simplify the system under consideration, it is helpful to simulate ignition by fixing an initial concentration of atomic oxygen as a most important reagent with followed calculations performed by purely chemical code. The simplest combustion mechanism takes place for hydrogen/dry air mixture. We are using the mechanism described in detail in [5].

Despite the scatter in induction time values calculated by different combustion mechanisms, calculated time evolution of gas temperature in a course of O-atom induced ignition has similar specific features – appearance of two stages with first fast growth followed by plateau and then the second fast large step.

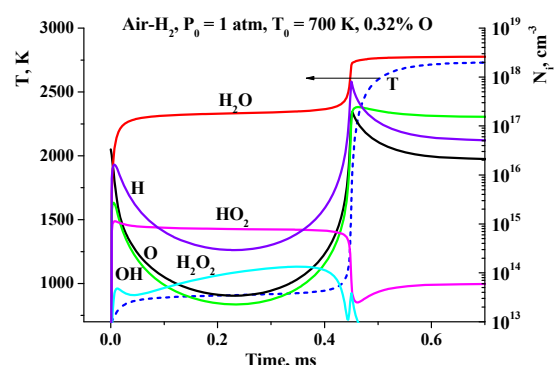


Fig. 4. Evolution of gas temperature and of concentrations of some species. Case of O-atom induced ignition. Stoichiometric H_2 -air mixture.

Fig. 4 shows calculated evolution of gas temperature and of concentrations of some species. Initial equivalence ratio (ER) is taken unity, and O concentration is 0.32%. The gas temperature experiences fast growth within about 20 μ s, then saturates at the level about 900 K till about 0.4 ms. The second fast-growth stage corresponds to the ignition and results in temperature increase up to about 2600 K. In the course of the first stage, H, OH, H_2O , HO_2 и H_2O_2 appear as a result of oxygen atom reactions. After this, the gas temperature is nearly stabilized while H_2O_2 concentration continues to grow slowly. In the end, H_2 is completely burnt and gas temperature is high.

Table 1. List of reactions giving largest input into gas heating rate for the mixture H_2/air (conditions of Figs. 4-6)

№	Reaction
1	$H + HO_2 \rightleftharpoons OH + OH$
2	$OH + H_2 \rightleftharpoons H + H_2O$
3	$H + O_2 + N_2 \Rightarrow HO_2 + N_2$
4	$H + O_2 + H_2 \Rightarrow HO_2 + H_2$
5	$O + HO_2 \rightleftharpoons OH + O_2$
6	$H + HO_2 \rightleftharpoons H_2 + O_2$
7	$O + OH \rightleftharpoons H + O_2$
8	$OH + HO_2 \rightleftharpoons H_2O + O_2$
9	$H + O_2 + O_2 \Rightarrow HO_2 + O_2$
10	$H + OH + M \Rightarrow H_2O + M$
11	$O + H_2 \rightleftharpoons OH + H$

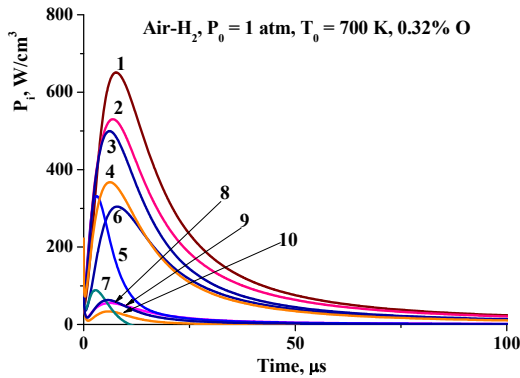


Fig. 5. Heat release rate in reactions listed in Table 1. Case of O-atom induced ignition. Stoichiometric H_2 -air mixture.

To understand why gas temperature grows by two distinct steps, let us analyze individual inputs of specific reactions into the gas heating process. The reactions exerting influence on gas heating rate are listed in Table 1 in the descending order. It is seen that the only primary reaction is #11 in Table 1. This reaction is endothermic one. However, the products in this reaction are high reactive radicals H and OH, which participate in fast exothermic reactions (2-4, 9, 10). It is worth to note that in reactions 3, 4, and 9 the secondary high reactive radical HO_2 is formed involved in exothermic reactions 1, 5, 6, and 8. The role played by selected reactions in gas heating is illustrated in Fig. 5 where the heat release rates expressed in units W/cm^3 are shown as functions of time for reactions 1-10. The heating rates are most intense at times around $10 \mu s$. To clarify the role of gas cooling in reaction 11, Fig. 6 shows the same quantities as in Fig. 4 at fine time scale. It is seen that gas cooling effect in reaction 11 is

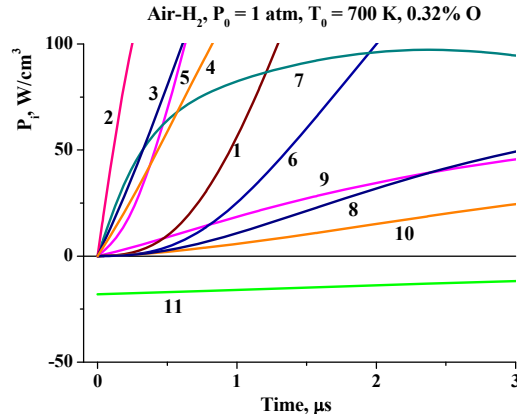


Fig. 6. Heat release rate in reactions listed in Table 1. Case of O-atom induced ignition. (detailed behavior at small times). Stoichiometric H_2 -air mixture.

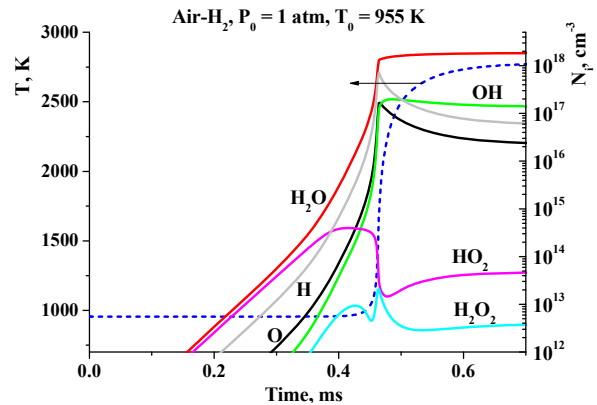


Fig. 7. Evolution of gas temperature and of concentrations of some species at spontaneous ignition. Stoichiometric H_2 -air mixture.

compensated by heat release in secondary reactions on time scale about 100 ns.

It is instructive to compare ignition dynamics induced by an instant injection of O atoms (Fig. 4) with that initiated by an instant increase of gas mixture temperature shown in Fig. 7. The gas temperature increment amplitude ($\Delta T=255 K$) at zero moment was fit to have nearly the same induction time as in case of initiation by O atoms. For comparison purposes, the reduced energy required to heat on 255K is equal to 322 J/g, while for process of 100%-effective dissociation of molecular oxygen to 0.32%O the required reduced energy is equal to 75 J/g. Evolution of gas temperature and particularly of chemical species concentrations at spontaneous ignition differs significantly from their evolution at the O-atom induced ignition. The gas temperature is nearly constant up to the moment of fast ignition, while concentrations of species O, H, OH, H_2O , HO_2 , and H_2O_2 grow monotonously achieving at about 0.4 ms levels comparable to that observed in Fig. 4 at times around 0.05 ms.

Hydrocarbon combustion

For comparison purposes, some simulations were performed with usage of different combustion mechanisms: GRI 3.0, Konnov, UBC, and Kintech (see refs. [13-16]). Actually, evolution of intermediate species in a course of ignition calculated by different combustion mechanisms of hydrocarbons is surprisingly different (see Figs. 8 and 9). In particular, mechanisms GRI 3.0 and Konnov predict qualitatively different time behavior of components HO_2 , CH_2CO , and H_2O_2 .

It is helpful to analyze in detail mechanisms of gas heating on earlier stage of ethylene ignition induced by O-atoms with concentration 1.4%. Reactions giving the largest input into the gas heating rate are listed in Table 2 in the descending order at the time moment 2 μs . In contrast to hydrogen combustion, the primary reactions (2, 11) are exothermic and give the maximal input at times shorter than 100 ns. The secondary reactions (1, 3-10) give an input into heat release rate with maxima around 100 ns. Time evolution of heat release rates in the specified reactions and concentrations of species involved in these reactions are presented in Figs. 10 and 11, respectively.

Таблица 2. List of reactions giving largest input into gas heating rate for the mixture $\text{C}_2\text{H}_4/\text{air}$ (conditions of Figs. 10, 11)

№	Reaction
1	$\text{HCO} + \text{O}_2 \rightleftharpoons \text{HO}_2 + \text{CO}$
2	$\text{O} + \text{C}_2\text{H}_4 \rightleftharpoons \text{CH}_3 + \text{HCO}$
3	$\text{H} + \text{CH}_3 + \text{M} \rightleftharpoons \text{CH}_4 + \text{M}$
4	$\text{O} + \text{CH}_3 \rightleftharpoons \text{H} + \text{CH}_2\text{O}$
5	$\text{H} + \text{HO}_2 \rightleftharpoons \text{OH} + \text{OH}$
6	$\text{O} + \text{CH}_3 \rightleftharpoons \text{H} + \text{H}_2 + \text{CO}$
7	$\text{O} + \text{CH}_2\text{CHO} \rightleftharpoons \text{H} + \text{CH}_2 + \text{HCO}_2$
8	$\text{O} + \text{HCO} \rightleftharpoons \text{H} + \text{CO}_2$
9	$\text{O} + \text{CH}_2 \rightleftharpoons \text{H} + \text{HCO}$
10	$\text{O} + \text{HCO} \rightleftharpoons \text{OH} + \text{CO}$
11	$\text{O} + \text{C}_2\text{H}_4 \rightleftharpoons \text{H} + \text{CH}_2\text{CHO}$

Influence of intermediates on induction time value (O-atom induced ignition)

The performed analysis demonstrated that the role played by O-atoms is not reduced to gas mixture heating. It is of interest to find out to what degree the specific intermediates influence on reduction of ignition time. To achieve this goal the following calculations were performed. While numerically simulating ignition of ethylene induced by a fixed initial concentration of O atoms, the calculations were stopped at the prescribed moment and then continued with a changed set of

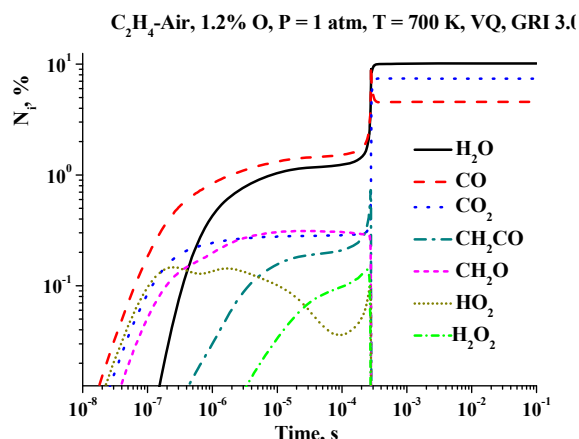


Fig. 8. Calculated evolution of some components at initiation by O atoms for GRI 3.0 combustion mechanism. Stoichiometric C_2H_4 -air mixture.

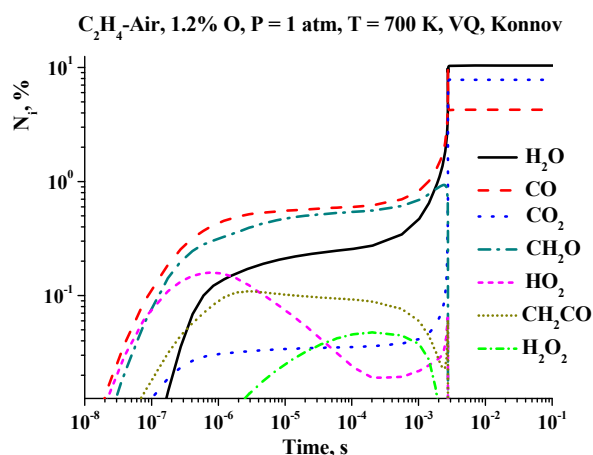


Fig. 9. Calculated evolution of some components at initiation by O atoms for Konnov combustion mechanism. Stoichiometric C_2H_4 -air mixture.

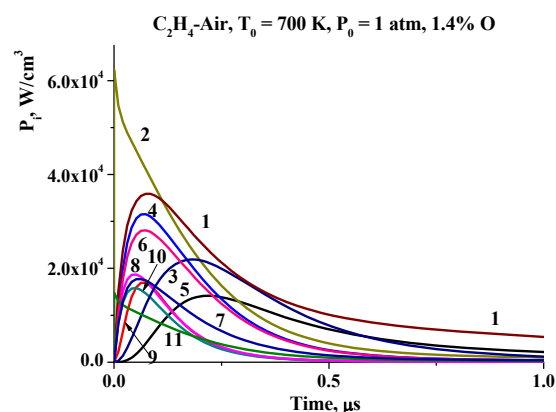


Fig. 10. Heat release rate in reactions listed in Table 2 for O-atom initiation. Stoichiometric C_2H_4 -air mixture.

intermediates concentrations. The role of an individual intermediate was identified by setting zero all intermediates concentrations except the selected one. The results are presented in Figs. 12-14 (vertical arrow indicates the moment of transition to a new set of intermediates). This

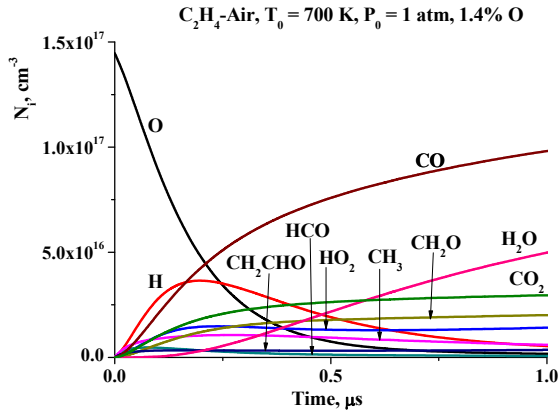


Fig. 11. Calculated evolution of some components at initiation by O atoms. Stoichiometric C_2H_4 -air mixture.

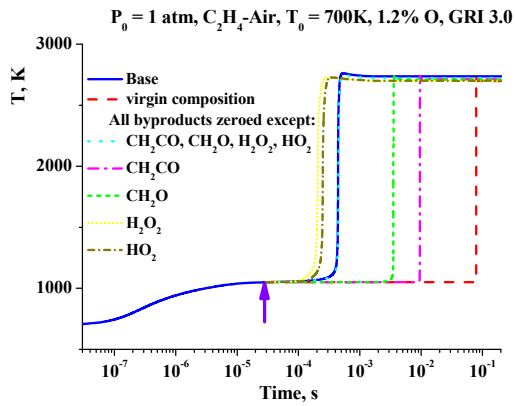


Fig. 12. Calculated temperature evolution at initiation by O atoms for stoichiometric C_2H_4 -air mixture. GRI 3.0 mechanism.

analysis was made with usage of different combustion mechanisms: GRI Mech 3.0, Konnov and Kintech.

The initial O-atom concentration for every combustion mechanism was fit to get the induction time value of the order of a few hundreds of μ s. The “base” curve relates to the non-stop calculations. The longest ignition delay time corresponds to situation when after the stop moment the gas mixture is changed to the stoichiometric ethylene/air mixture. By changing concentrations of intermediates at the continued calculations the mixture composition was found, for which the induction time is exactly equal to that of the “base curve”. The species found are (HO_2 , H_2O_2 , CH_2O) + CH_2CO in frames of GRI 3.0 and Konnov mechanisms. For Kintech mechanism the species are: (HO_2 , H_2O_2 , CH_2O) + H_2 , C_2H_3O and C_2H_4O . The first three species are reproduced in all mechanisms. It is curious that GRI 3.0 mechanism predicts that between actions of three species selected there is some mis-coordination. As result, HO_2 , H_2O_2 , each separately, accelerates ignition in more degree than combination of three species

(HO_2 , H_2O_2 , CH_2O). No such effect is seen in Figs. 13 and 14. Kintech mechanism predicts that C_2H_4O exerts nearly the same influence on induction time shortening as HO_2 , H_2O_2 species.

Influence of intermediates on induction time value (plasma induced ignition)

As the next step in analyzing role played by various byproducts, calculations were performed with help of our numerical model of plasma assisted combustion. The program package Chemical Work Bench (CWB) [16] was used for numerical simulations of plasma assisted combustion in scramjet combustor. This package allows us to integrate a system of kinetic equations for neutral chemical species and charged particles together with gas temperature found from thermal balance equation. The rate coefficients of reactions with electron participation were calculated from electron Boltzmann equation, which was addressed

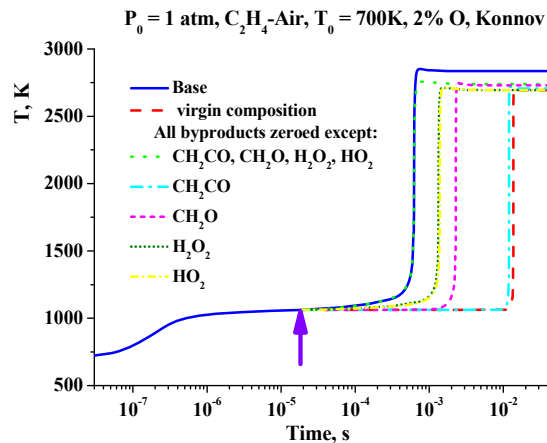


Fig. 13. Calculated temperature evolution at initiation by O atoms for stoichiometric C_2H_4 -air mixture. Konnov mechanism.

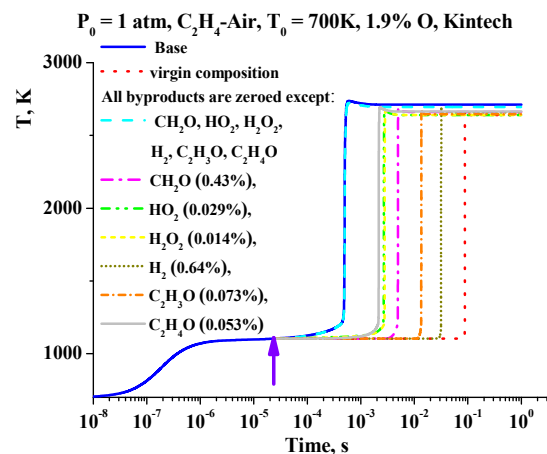


Fig. 14. Calculated temperature evolution at initiation by O atoms for stoichiometric C_2H_4 -air mixture. Kintech mechanism.

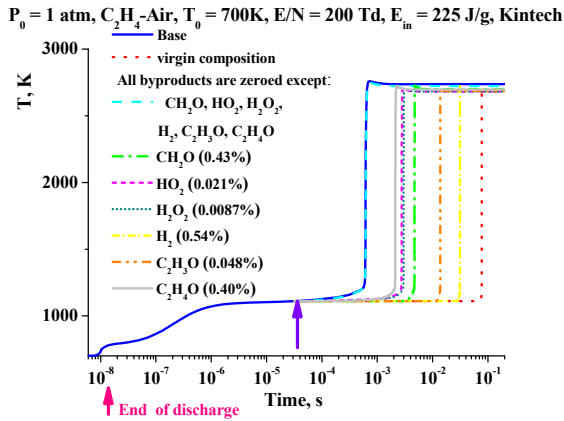


Fig. 15. Calculated temperature evolution at pulse discharge initiation for stoichiometric C_2H_4 -air mixture. Kintech mechanism.

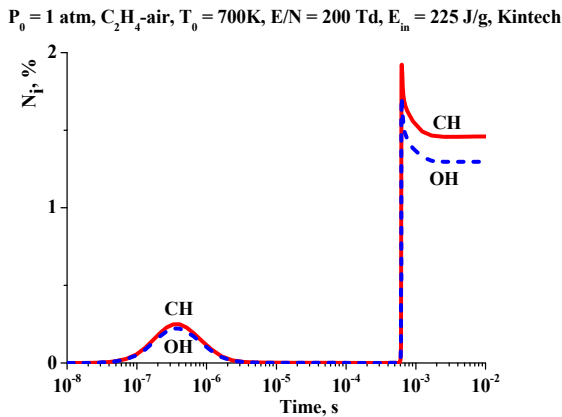


Fig. 16. Calculated evolution of CH and OH concentration at pulse discharge initiation (logarithmic time scale).

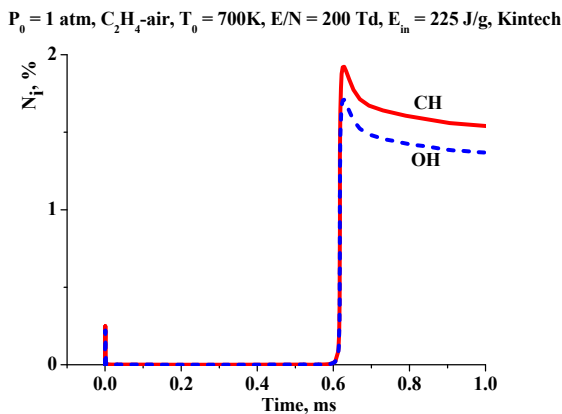


Fig. 17. Calculated evolution of CH and OH concentration at pulse discharge initiation (linear time scale).

as soon as plasma parameters changed in a degree defined through a special criterion. Gas dynamic flow of fuel/air mixture was simulated in approximation of plug-flow model. It was shown earlier [17] that for supersonic flow in scramjet

combustor an additional simplification by setting gas number density constant introduced quite a small error in calculated induction time in comparison with solving a full system of equations for gas dynamic flow. In this work we apply the plug-flow model with fixed gas number density.

The self-consistent electron scattering cross section sets were taken from refs. [18-20] for N_2 , O_2 and C_2H_4 molecules, respectively. Kinetic scheme and rate coefficients for reactions of excited atoms and molecules and for ion-molecular reactions in air are taken from ref. [18].

No experimental data exist about plasma assisted combustion of premixed ethylene/air mixtures for conditions of the scramjet combustor. Therefore, our kinetic model was verified by comparison with experimental data [21-22] for plasma assisted combustion in subsonic flow at room gas temperature and pressure of a few tens of Torr. It was shown in [23] that our model provides reasonably good agreement with experimental data [21-22] on gas heating rate, the threshold energy input and time evolution of atomic oxygen.

We use the simplified approach to modeling pulse gas discharge. The electric field strength set as a constant within some time interval, which was varied from run to run to change the specific energy input (SEI). Calculated evolution of gas temperature of stoichiometric ethylene/air mixture subject to pulse discharge at $E/N=200 \text{ Td}$ with the specific energy input (SEI) 225 J/g (1% O) is shown in Fig. 15 (“base” curve). The first vertical arrow indicates the discharge duration. During the discharge gas is heated in vibrational relaxation processes and due to energy defect released in dissociation processes, both, in direct electron impact and in collisions with electronic excited molecules. After the discharge pulse gas is heated in exothermic reactions involving oxygen atoms and secondary species.

The second arrow indicates the moment when calculations were stopped and continued with changed gas mixture content, as it was done above for O-atom induced ignition. In case of restored gas composition (“virgin” curve) the inductance time is the longest one. Similar to case of O-atom induced ignition, keeping the species HO_2 , H_2O_2 , CH_2O , H_2 , C_2H_3O , and C_2H_4O allows for achieving the same induction time value as in non-stop calculations. The most important species effecting on the induction time are: C_2H_4O , H_2O_2 и HO_2 . This conclusion coincides with the predictions made by Kintech combustion mechanism for O-atom induced ignition.

Light emission from excited states of radicals OH and CH can be used for diagnostics of ignited gas mixture [24]. To evaluate suitability of such a technique the time evolution of these species was calculated for conditions of discharge induced ignition of C_2H_4 /air mixture. Figs. 16 and 17 show

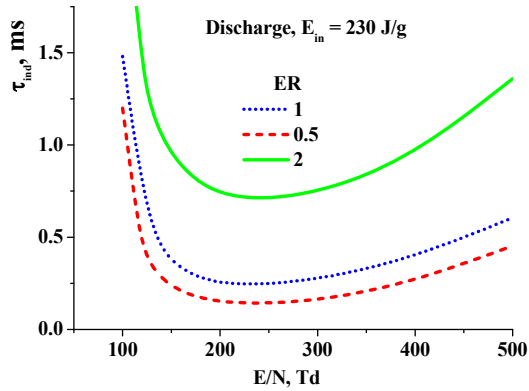


Fig. 18. Induction time as a function of E/N for various mixtures C_2H_4 -air. $T_0=700$ K, $P_0=1$ atm.

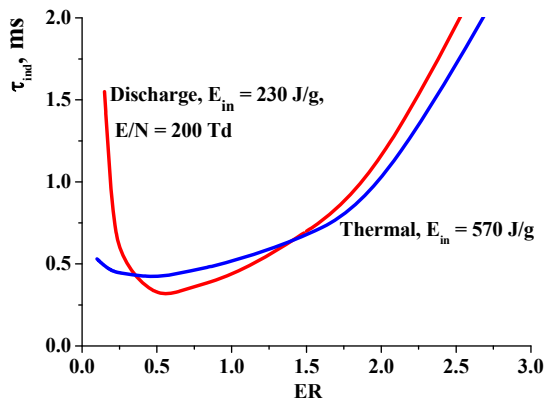


Fig. 19. Induction time as a function of equivalence ratio for discharge and thermal initiation.

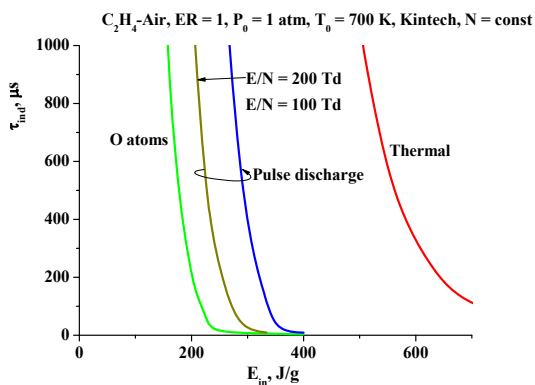


Fig. 20. Calculated induction time as a function of the SEI for initiation by thermal heating, pulse discharge with given E/N, and O-atom injection.

calculated evolution of CH and OH concentrations after discharge pulse initiation. The first peak reflects formation of CH and OH radicals in the discharge, while the second peak corresponds to ignition. Fig. 17 demonstrates that the respective peaks in evolution of CH and OH concentrations

are rather narrow in comparison with duration of a whole ignition processes and can serve as reliable indicators for moments of the first and second stages of ignition. Evaluations demonstrate that the position of the second peak in CH and OH concentrations is equal with accuracy better than 2% with the peak position in dT/dt . However, at the first stage the peak in the temperature growth rate dT/dt curve is broadened due to direct discharge heating and cannot serve as a good indicator. Both CH_3 and OH concentrations have a clear maximum at the first stage, and these peaks practically coincide in position.

Influence of E/N parameter and mixture composition on induction time

Existing discharge techniques allow one to vary in some limits the E/N parameter in plasma. The theoretical calculations can give a guideline for choice a most appropriate discharge technique. Fig. 18 shows calculated induction time for varied gas composition as a function of the E/N parameter. The curves for different gas contents characterized by Equivalence Ratio (ER) have a broad minimum at about (230-250) Td. Location of this minimum is determined by existence of a maximum in E/N dependence of electron energy fraction spent to radical production. The more dilute fuel the shorter is the induction time at the fixed E/N parameter.

Fig. 19 shows induction time as a function of ER for pulse discharge initiation and thermal heating. The energy required to heat the fuel/air mixture to temperatures at which induction time is about 1 ms is about 2.5 times higher than the energy deposited in the pulse discharge at $E/N=200$ Td. This ratio is kept on the same level at variation of ER down to about 0.2 (high diluted fuel). The final plot for dependence of calculated induction time on the SEI for various methods of ignition initiation is presented in Fig. 20. The Kintech combustion mechanism [16] was used, and results are presented for thermal initiation, for ignition induced by pulse discharges with $E/N=100$ and 200 Td, and for O-atom injection. This plot demonstrates that hypothetical injection of atomic oxygen is the energetically best method. However, there is no means to realize such method. Usage of a short pulse discharge with high value of E/N parameter is the method approaching by efficiency to the hypothetical O-atom injection.

Conclusion

Numerical modeling of plasma or O-atom assisted ignition of hydrogen and hydrocarbons premixed with air demonstrates appearance of two stages in evolution of gas temperature and chemical species. At the first stage O atoms and other radicals produced by a discharge convert into some

intermediate species. Chemical reactions on this stage are, as a rule, exothermic resulting in a fast gas heating stopped at some level. The second stage corresponds to complete burning of a fuel. Further evolution of combustion process between these stages proceeds with rather slow growth of gas temperature. In this interval, chemical reactions take place between intermediate species. For ethylene/air mixture the most important intermediates strongly influencing on the induction time are HO₂, H₂O₂, CH₂O, CH₂CO, H₂, C₂H₃O, and C₂H₄O species. Various combustion mechanisms predict different roles played by these species in the ignition. The first three species are found as most important in the following combustion mechanisms: GRI Mech 3.0, Konnov and Kintech.

It is shown numerically that the first and second stages in ignition process can be detected by emission from excited OH and CH molecules.

The large scatter in values of induction time predicted for plasma induced ignition predicted with different combustion mechanisms is convincing evidence that further improvement of combustion mechanism is required for conditions typical for scramjet combustors: static gas pressure 1 atm., temperature 700 K.

References

- Leonov S., Bityurin V., Bocharov A. et al., 2002, Hydrocarbon fuel ignition in separation zone of high speed duct by discharge plasma. *Proc. 4th Workshop "PA and MHD in Aerospace Applications"*. M: IVTAN.
- Starikovskaia S. M., Plasma Assisted Ignition and Combustion, 2006, *J. Phys. D: Appl. Phys.*, **39**, R 265.
- Kochetov I. V., Leonov S. B., Napartovich A. P., 2006, Plasma ignition of combustion in a supersonic flow of fuel-air mixture: Simulation problem, *High Energy Chemistry*, **40**, 98.
- Napartovich A. P., Kochetov I. V., Leonov S. B., 2010, Numerical modeling of ignition premixed ethylene-air mixture by system of microdischarge, *Teplofiz. Vys. Temp.*, **48**, 60.
- Napartovich A. P., Kochetov I. V., Leonov S. B., 2005, Study of dynamics of air-hydrogen mixture ignition by non-equilibrium discharge in high-speed flow, *Teplofiz. Vys. Temp.*, **43**, 677.
- Starik A. M., Kozlov V. E., Titova N. S., 2010, On the influence of singlet oxygen molecules on the speed of flame propagation in methane-air mixture, *Combustion and Flame*, **157**, 313.
- Popov N. A., The influence of nonequilibrium excitation of the ignition of hydrogen-oxygen mixtures, 2007, *Teplofiz. Vys. Temp.*, **45**, 296.
- Starik A. M., Titova N. S., 2002, Kinetics of ion formation in the volumetric reaction of methane with air, *Combustion, Explosion, and Shock Waves*, **38**, 253.
- Napartovich A. P., 2009, Problems of modelling of non-thermal discharge evolution in chemically unstable gas mixtures, *Aerospace Thematic Workshop: Fundamentals of Aerodynamic Flow and Combustion Control by Plasmas*, Les Houches, France.
- Sokolik A. S., 1940, Self-ignition and combustion in gases, *Usp. Phys. Nauk*, **23**, 209.
- Basevich V. Ya., Frolov S. M., 2007, Kinetics of "blue" flames in the gas-phase oxidation and combustion of hydrocarbons and their derivatives, *Usp. Khim.*, **76**, 927.
- Strelkova M. I., Safonov A. A., Sukhanov L. P. et al, 2010, Low temperature n-butane oxidation skeletal mechanism, based on multilevel approach, *Combustion and Flame*, **157**, 641.
- Smith G. P., Golden D. M., Frenklach M., Moriarty N. W., Eiteneer B., Goldenberg M., Bowman C. T., Hanson R. K., Song, S., Gardiner W. C. Jr., Lissianski V. V. and Qin Z. GRI Mech 3.0 (1999) http://www.me.berkeley.edu/gri_mech/
- Konnov A.A. Detailed reaction mechanism for small hydrocarbons combustion. Release 0.5 , 2000 <http://homepages.vub.ac.be/~akonnov/>
- Huang J. and Bushe W. K., 2006, "Experimental and kinetic study of autoignition in methane/ethane/air and methane/propane/air mixtures under engine-relevant conditions," *Combustion and Flame*, **144**, 74, <http://kbspc.mech.ubc.ca/kinetics.html>
- KINTECH. *Kinetic technologies. Chemical Workbench* (<http://www.kintech.ru>).
- Leonov S. B., Yarrantsev D. A., Napartovich A. P., Kochetov I. V., 2006, Plasma-Assisted Combustion of Gaseous Fuel in Supersonic Duct, *IEEE Transactions on Plasma Science*, **34**, 2514.
- Y. S. Akishev, A. A. Deryugin, V. B. Karalnik, I. V. Kochetov, A. P. Napartovich, and N. I. Trushkin, 1994, Numerical simulation and experimental study of an atmospheric-pressure direct-current glow discharge, *Plasma Phys. Rep.*, **20**, 511.
- Ionin A.A., Kochetov I.V., Napartovich A.P. Yuryshv N.N., 2007, Physics and Engineering of Singlet Delta Oxygen Production in Low-Temperature Plasma, *J. Phys. D: Appl. Phys.* **40**. R25.
- Hayashi M., 1990, "Electron collision cross sections determined from beam and swarm data by Boltzmann analysis" in "Nonequilibrium Processes in Partially Ionized Gases" Eds. M. Capitelli and J. N. Bardsley, NATO ASI Series B: Physics v. 220, p.333, Plenum Press, N-Y.
- Mintusov E., Serdyuchenko A., Choi I., Lempert W.R., Adamovich I.V., 2009,

- Mechanism of plasma assisted oxidation and ignition of ethylene–air flows by a repetitively pulsed nanosecond discharge, *Proceedings of the Combustion Institute*, **32**, 3181–3188.
22. Uddi M., Jiang N., Mintusov E., Adamovich I. V., Lempert W. R., 2008, Atomic Oxygen Measurements in Air and Air/Fuel Nanosecond Pulse Discharges by Two Photon Laser Induced Fluorescence, *AIAA-2008-1110 PAC*.
 23. Napartovich A. P., Kochetov I. V., Deminsky M. A., Potapkin B. V., 2008, Modeling of oxygen dissociation in gas mixture by pulse-periodic discharge, *Proceeding of the V International Symposium on Theoretical and Applied Plasma Chemistry, Ivanovo State University of Chemistry and Technology, Ivanovo, Russia*, **1**, 262.
 24. Chintala N., Bao A., Lou G., Adamovich I. V., 2006, Measurements of combustion efficiency in nonequilibrium RF plasma-ignited flows, *Combustion and Flame*, **144**, 744.

PROCESSES RESPONSIBLE FOR NEAR-THE-AXIS IGNITION OF METHANE-OXYGEN MIXTURE BY MEANS OF RING-SHAPED ELECTRIC DISCHARGE

E.M.Barkhudarov, N.K.Berezhetskaya, V.A.Kop'ev, I.A.Kosy, V.A.Levin¹, I.S.Manuilovich¹, V.V.Markov¹, N.A.Popov², M.I.Taktakishvili, S.M.Temchin

A.M.Prokhorov General Physics Institute of RAS, Moscow, 119991, Russia

¹Institute of Mechanics, Moscow State University, Moscow, Russia

²D.V.Skobel'syn Institute of Nuclear Physics, Moscow State University, Moscow, Russia

Abstract. Results are presented from experimental studies of ignition of a stoichiometric methane—oxygen mixture in a closed chamber by ring electric discharge. It is shown that the process of fast (explosive) ignition of the reactor volume starts on the axis of the ring, near its center, i.e., at a distance from the annular region of power deposition. Experimental evidence suggests that the ignition of a combustible gas mixture near the axis is triggered by strong gas-dynamic perturbations converging to the axis, radially propagating from the ring discharger.

I. Introduction

In an aviation engines with high-speed fuel/air mixtures the flame initiating system has a critical influence on misfire or cycle-to-cycle variations. For improve of igniters action various ignition systems have been proposed and tested [1-4]. These include high-energy spark plugs, plasma jet igniters, rail plug igniters, laser-induced ignition, torch jet igniters etc. Over last decade, considerable progress has been made in studies of non-equilibrium plasma assisted combustion. A review of recent experimental work in this field is given in [5-7].

The aim of the present paper is to study the processes of ignition of gas mixtures under the action of still untapped and non understood axisymmetric (ring) electric discharges. A particular feature of the action of ring discharges on a gas medium is that the possibility exists of initiating combustion of the gas mixture not only in the immediate vicinity of a ring discharge, but also near the axis of the ring through the presence of a converging toroidal wave generated by the discharger.

The cumulative effect of convergence of a non-one-dimensional shock wave was first demonstrated by the example of a ring-shaped shock wave in air, in experiments performed at the General Physics Institute [8,9]. The experiments have shown that the geometry of the wave (i.e. whether it is one-dimensional or non-one-dimensional) is not essential to the end results. Shock waves investigated in those experiments were ring-shaped (toroidal), apparently non-one-dimensional. It was found that the amplitude of a shock wave generated by a ring electric-discharge increases gradually as it approaches the center of the ring. Generally, the effect of cumulative amplification of a noncylindrical (nonspherical)

shock wave converging toward the axis is nontrivial, because in contrast to a one-dimensional wave, there may be hydrodynamic energy outflow along the axis.

Theoretical analysis performed in [10] has shown that the amplitude of a ring shock wave (as with spherical and cylindrical waves) increases without bound if dissipative processes are ignored. An unbounded increase in the energy of a convergent shock wave, which is indicative of a cumulative process, still remains a key problem in both theoretical and experimental research. In other words, it is necessary to identify mechanisms that limit the values of the gas temperature T_g on the focus in real experiments.

The further step toward the solution of the above problem has been taken in recent experiments [11-13] for studying a toroidal shock wave generated in atmospheric-pressure air by ring electric discharge. It was shown that the shock wave converges at the axis of the ring. A mathematical model describing the focusing of a non-one-dimensional shock wave was constructed, and the results of calculations were compared with the experimental results. The energy released in the ring discharge was estimated from calculations given a good fit to the experimentally observed dynamics of both a toroidal shock wave convergent toward the axis and axial shock waves (Mach waves) accompanying the cumulative process of focusing. With the assumption that the model adequately describes actual gas flows at a given level of released energy, the gas temperature was estimated near the cumulation region located on the axis at some distance from the center of the ring. In particular, for a ring discharger of radius ~ 5 cm with released energy of about 200 J, the gas temperature on the axis of the ring at a distance of about 1 cm from its center was estimated as 6000 K. The energy is transferred from a discharge

toward the axis through gas-dynamic perturbations caused by the discharge itself.

The results obtained in [11-13] allow us to make an assumption that, with a ring discharger employed as an initiator, the ignition may be induced not only in the region of energy release (an annular plasma layer), but also outside of this region – at the center of the ring. In the present paper, we report on results of the first experiments with the use of a ring discharge in a combustible (methane—oxygen) mixture in closed volume and describe characteristic features of the initiation of combustion in a gas medium by this discharger.

Both the above experiments and the calculations, being important for fundamental physics, were stimulated by the applied problem – the initiation of combustion of fuel-air streams in the axial region of a ramjet aviation engine. Schematically method of supersonic gas ignition is shown on the Fig. 1. Considering the obtained in [11-13] results from this scheme viewpoint, we note that the heating of a gas to the mixture ignition temperature occurs in relatively small volumes, while the temperature remains high for a short (microseconds) time. For this reason, we are not in position to assert that the ignition of a fuel-air stream is realizable. However, this possibility must not be ruled out, especially as a success was achieved in a series of experiments on the initiation of combustion of gas mixtures by laser sparks, microwave discharges and gliding surface discharges [14-17]. It has been found that high-temperature microscopic plasma objects generated by discharges have an abnormally long lifetime, eventually causing combustion of a gas mixture throughout the gas volume.

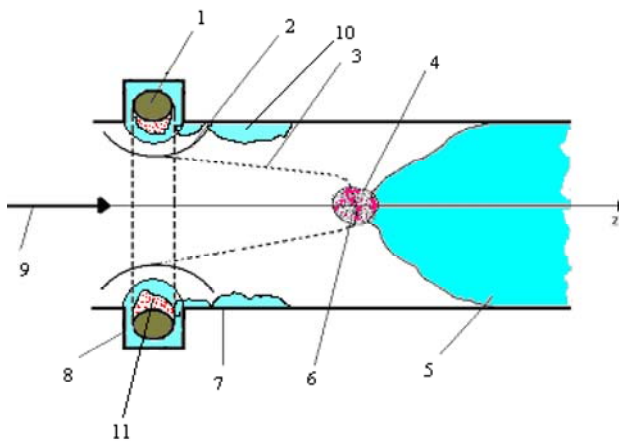


Figure 1. Scheme of supersonic gas ignition by cumulating shock wave.

1-annular electric discharger; 2- toroidal shock wave; 3- trajectory of toroidal shock wave front; 4- region of combustion ignition; 5- burning gas; 6- point of toroidal shock wave focusing; 7- combustion chamber; 8- annular slot; 9- inflammable gas mixture flow; 10 – periphery combustion wave initiated by annular gliding surface discharge; 11 – gliding surface discharge plasma.

II. Experimental layout

To study the action of a ring electric discharge on a chemically active (combustible) gas, we designed, assembled and put into operation an experimental device shown schematically in Fig. 2. A cylindrical organic-glass reactor chamber is 100 mm in diameter and 70 mm in height. Its ends are covered with plane-parallel quartz windows. The chamber is evacuated to a pressure $p_0 < 0.1$ Torr and is filled with a stoichiometric mixture $\text{CH}_4:\text{O}_2 = 60:120$ Torr or oxygen (to a pressure $p \approx 180$ Torr).

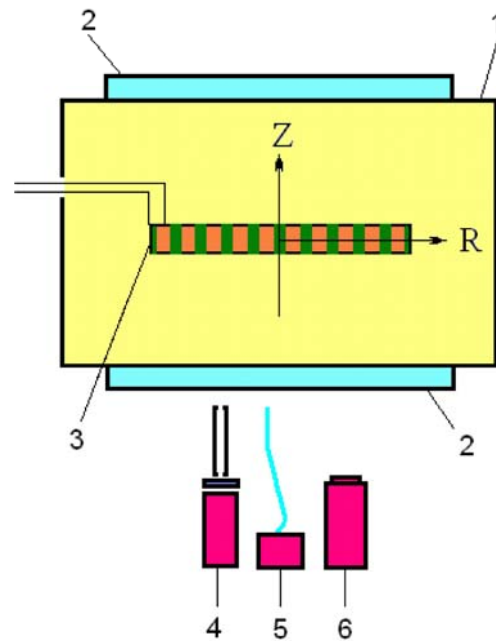


Figure 2. Schematic of the experiment: 1-vacuum chamber, 2-quartz windows, 3- ring discharger, 4- collimated photomultiplier, 5- spectrograph, 6- image converter camera.

As an electric-discharge initiator of combustion of a gas mixture, we used an annular multielectrode system [18] placed inside the chamber. This discharger is a system of insulated ring electrodes (titanium, stainless steel) around a high-voltage metal return conductor. The inner diameter of the ring is about 5.5 cm. Figure 3 shows a photograph of the discharger ready to use and a photograph of the operating discharger under a high-voltage pulse exciting the gliding surface discharge. A high-current gliding surface discharge was excited along the dielectric surface upon switching on a high-voltage pulse of amplitude $U \leq 20$ kV and duration $\tau_h \approx 15 \mu\text{s}$. On the side nearest to the chamber axis, the annular electrodes had sharpeners intended to localize regions where gliding surface discharge should be excited. When a high-voltage pulse is applied to the discharger, these regions give rise to a sequence of plasmoids, which are primary sources

for gas heating, production of chemically active particles and generation of UV radiation affecting the surrounding gas. The energy released in discharge during one pulse was ≈ 40 J. The volume of an electric-discharge plasma produced by released energy is estimated as ≈ 2 cm³.

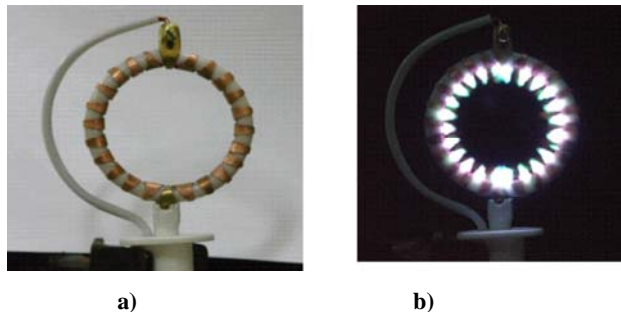


Figure 3. Photograph of the electric discharger generating an annular plasma layer: a) before mounting at the experimental bench; b) in operating condition during high-voltage pulse.

To study a glow accompanying the discharge processes and the combustion of the gas mixture, we used an FEU-60 collimated photomultiplier with a spatial resolution of ≈ 8 mm at the chamber axis. For the same purposes, we used an FER-7 optical streak camera. The radiation of the band of OH radicals was selected from the spectrum with the help of ZhS-20 and UFS-2 filters placed in front of the photomultiplier. In the absence of filters, the photomultiplier signal showed the time behavior of the radiation integrated over the spectrum.

Spectral characteristics of the radiation emitted from the discharge region and the combustion zone were studied with the help of AvaSpec-3648FT spectrograph, which allowed measurements of the spectrum in the wavelength range $\lambda = 200 - 800$ nm with a time resolution as high as 10 μ s.

Gas-dynamic perturbations of the medium were recorded using shadow photography according to the scheme presented in Fig.4. A system of lenses (2), (4), incorporated in a telescope, forms a paraxial beam of a pulsed nitrogen laser ($\lambda = 337.1$ nm) in the direction perpendicular to the cross-section of the ring discharger, which is excited by high-voltage pulses of a power supply. The laser beam passed through the cross-sectional area of the discharger is recorded with the help a photographic camera (10). A series of photographs was taken successively by varying a delay time of the laser pulse with respect to trigger pulse of the discharger (τ_d). In this way, we traced the time variation of the shadow pattern formed by gas-dynamic perturbations in the plane of the ring, in particular, by a toroidal shock wave propagating from the discharger.

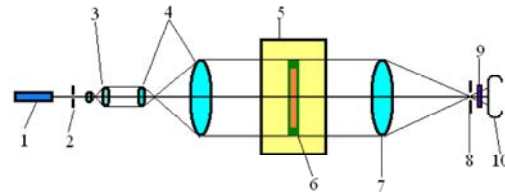


Figure 4. Schematic of the experiment using shadow photography:

1-nitrogen laser; 2, 8- apertures; 3- objective for preliminary expansion of the laser beam; 4-telescope; 5- vacuum chamber, 6- ring-discharge initiator; 7-collecting lens; 9-filter; 10- photographic camera.

Figure 5 shows the ‘refraction’ detector scheme which allows local gas-dynamic perturbations in the plane of a ring discharge to be detected with a high temporal and spatial resolution. A paraxial narrow (~ 1 mm in diameter) beam of a helium-neon laser (4) passes through the plane of a ring discharge and falls within the aperture of a diaphragm (6) placed in front of a photomultiplier (5). The photomultiplier signal is fed into an oscillograph. Refraction of the laser beam passing through the medium with gas-dynamic perturbations causes its deflection from the axis of the aperture and, as a result, the photomultiplier signal decays.

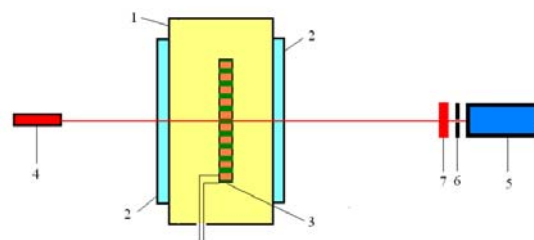


Figure 5. Scheme of refraction measurements.

1-vacuum chamber; 2-quartz windows; 3-ring electric discharger; 4- helium—neon laser; 5- FEU-60 photomultiplier; 6-diaphragm; 7-interference filter.

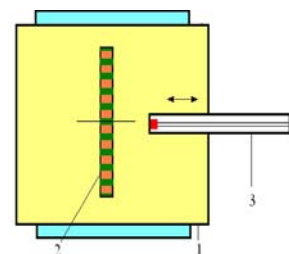


Figure 6. Scheme of piezoelectric transducer measurements. 1-vacuum chamber; 2-ring discharger; 3- piezoelectric transducer.

In Fig. 6 is shown the scheme for measuring gas-dynamic perturbations with the help of a piezoelectric transducer (IPC[®] 132A32 microsensor).

III. Experimental results

Figure 7 shows typical photomultiplier signals corresponding to the radiation of the OH band observed in the plane of the ring at different distances from the axis (the working gas is a methane—oxygen mixture).

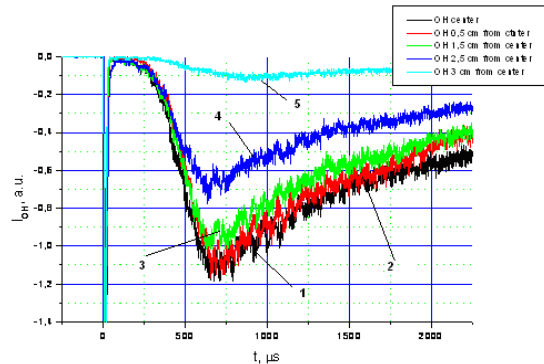


Figure 7. Photomultiplier signals recording the OH band radiation from the reactor at different distances R from the center of the ring. 1- $R=0$; 2- $R=0.5\text{cm}$; 3- $R=1.5\text{cm}$; 4- $R=2.5\text{cm}$; 5- $R=3.0\text{cm}$

Figures 8 shows typical photomultiplier signals corresponding to the radiation of the OH band observed at different values of the energy released in the ring discharge (the working gas is a methane—oxygen mixture). The radiation is received from the central region of the ring. The curves are normalized to peak values of the radiation intensity in the initiated flame.

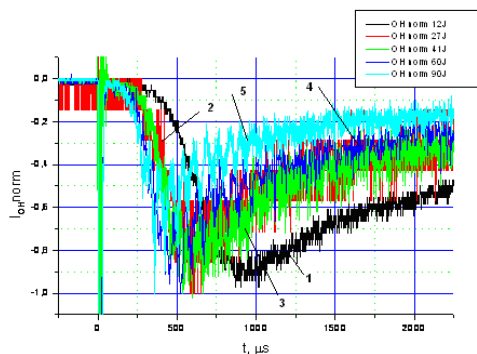


Figure 8. Photomultiplier signals recording the OH band radiation from the reactor at different values of energy W released in the ring discharge. 1- $W=12\text{J}$; 2- $W=27\text{J}$; 3- $W=41\text{J}$; 4- $W=60\text{J}$; 5- $W=90\text{J}$

Figures 9 and 10 show typical photographs of streak images of the FER-7 camera, which are taken when its slit is oriented in the radial direction and along the axis Z of the ring, respectively. The

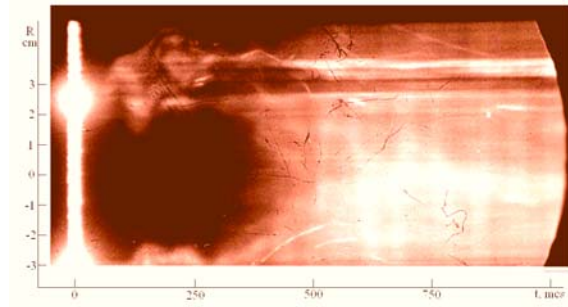


Figure 9. Typical streak images of glow in the reactor. The slit of the streak camera is oriented in the radial direction of the ring discharger.

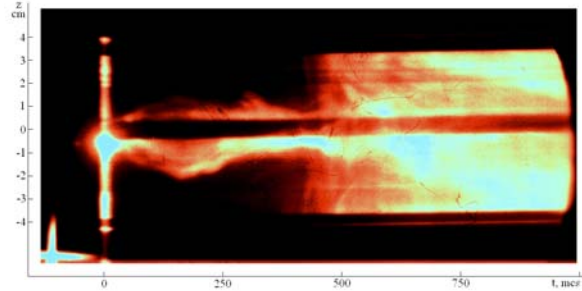


Figure 10. Typical streak images of glow in the reactor. The slit of the streak camera is oriented along the Z axis.

temporal and spatial scales are indicated in the figures.

Figure 11 shows typical spectra of the radiation from the reactor, which are obtained with

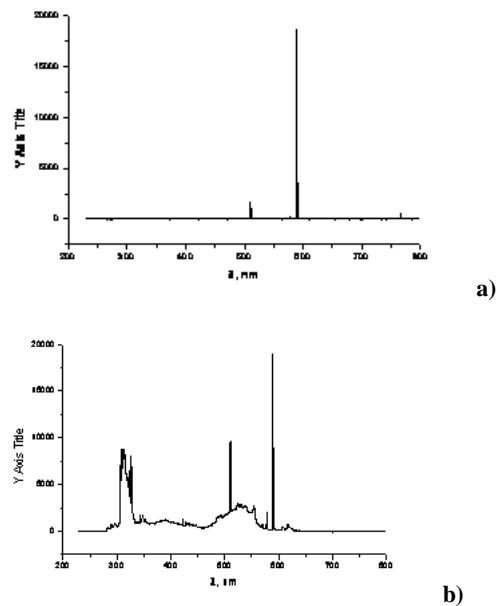
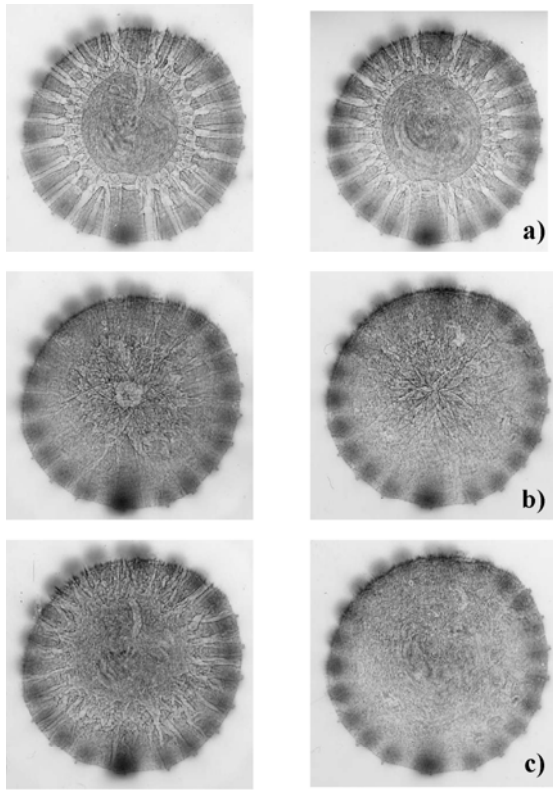
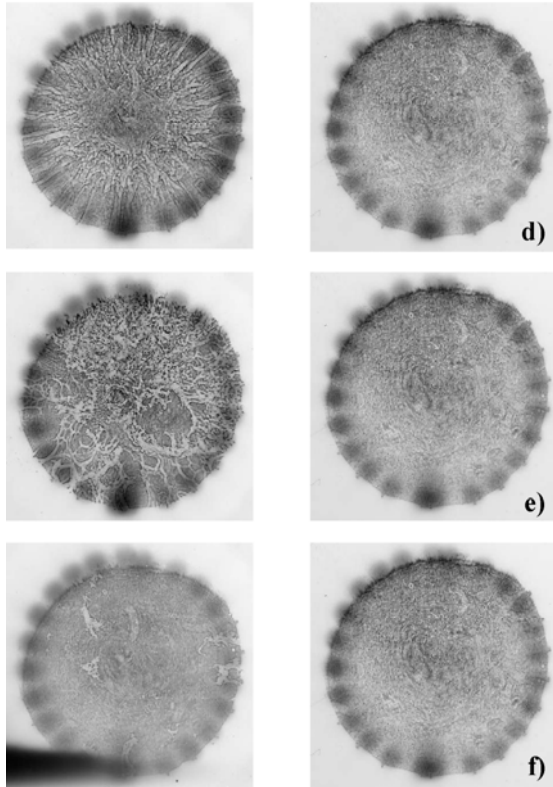


Figure 11. Typical optical radiation spectra measured at different delay time t with respect to the discharger trigger pulse. a) $t=100\mu\text{s}$; b) $t=900\mu\text{s}$.



1 cm



1 cm

Figure 12. Shadow photographs taken at different delay time t with respect to the discharger trigger pulse. Left column – discharge in a $\text{CH}_4:\text{O}_2$ mixture; right column – discharge in O_2 . Delay time in μs : a) 10; b) 30; c) 80; d) 100; e) 500; f) 600.

an exposure time of 200 μs . The delay time with respect to the discharger trigger pulse is indicated in the figure. At a delay time of 100 μs , the spectrum exhibits the lines $\lambda = 510.55 \text{ nm}$ (copper) and $\lambda = 589 \text{ nm}$ (sodium). At delay times in the interval 300–600 μs , the band corresponding to the OH radical appears in the spectrum. At delay times of about 500 μs and more, brightness of the OH band reaches its maximum, and a continuum appears in the spectral region 450–600 nm, where the bands of C_2 , CO, CO_2 molecules also show.

Figure 12 shows typical shadow photographs taken in the direction orthogonal to the plane of the ring when operating with a methane–oxygen mixture ($\text{CH}_4:\text{O}_2$) and oxygen (O_2). The delay time with respect to the discharger trigger pulse is indicated in the figure.

Figure 13 compares typical ‘refraction’ signals measured when operating with a noncombustible gas (oxygen, 180 Torr) and a methane–oxygen mixture; Fig. 14 compares typical signals from the piezoelectric transducer under these conditions.

In Fig. 15, the time corresponding to the maximum intensity of the OH band (see Fig. 8) is plotted vs. the energy released in the ring discharge.

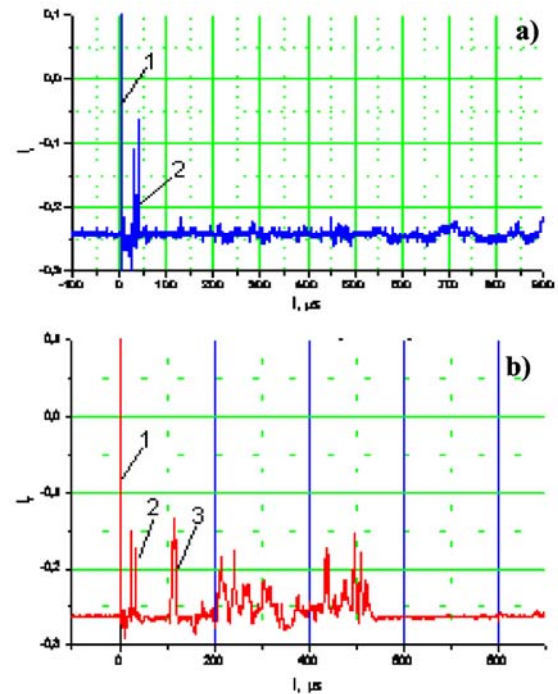
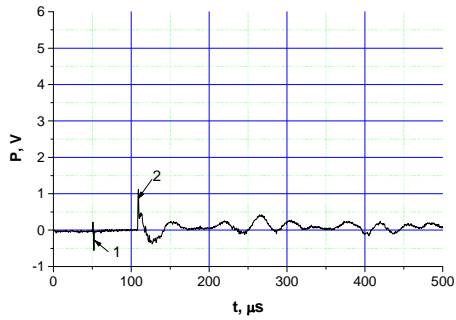
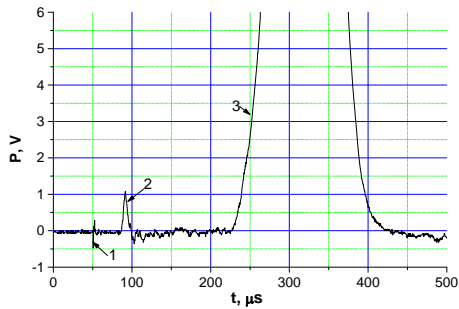


Figure 13. Signal from the refraction detector. a) Discharge in O_2 ; b) Discharge in a $\text{CH}_4:\text{O}_2$ mixture.



a)



b)

Figure 14. Signals from the piezoelectric transducer. A) Discharge in O_2 ; b) Discharge in a $CH_4:O_2$ mixture. $L=5$ cm.

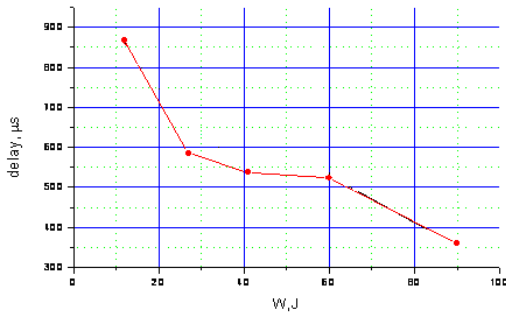


Figure 15. Time corresponding to the maximum intensity of the OH band vs. the energy W released in the ring discharge.

IV. Discussion of experimental results

Analysis of experimental results allows us to conclude that the geometry of the electric-discharge initiator, namely its ring geometry, plays a decisive role in the process of ignition of a combustible gas mixture as well as in the dynamics of the flame propagation inside the combustion chamber.

As we might expect, the ignition of a gas mixture begins near the annular plasma layer (see Fig. 9). In this case, the flame advances into the surrounding gas at low velocities, which do not exceed the velocity of usual deflagration waves. As a consequence, the flame initiated by the annular plasma layer is confined to this region during the time interval under observation. A peculiarity of the

phenomenon under study is that an extremely fast process of flame propagation throughout the reactor starts in the region situated at a distance from the annular region of energy release – at the axis of the ring, near its center.

Oscillograms of photomultiplier signals and FER-7 streak images of a glow in the reactor allow us to distinguish three characteristic time intervals (phases), as illustrated by Fig. 16, which shows a photomultiplier signal, a streak picture and several shadow pictures taken at different delay times.

The first phase is a very short period Δt_1 (in this case $\Delta t_1 \cong 5 - 10 \mu s$), when a discharge is excited along the initiator surface and an annular plasma layer forms. The energy is released to a gas layer adjacent to the inner surface of the discharger through gas-discharge plasma.

The second phase is associated with a feeble glow, recorded in the streak picture and identified as a wave propagating from the ring to the axis (Fig. 9). The duration of this phase, in which the photomultiplier signal becomes zero (Figs. 7, 8), is $\Delta t_2 \cong 200 - 300 \mu s$.

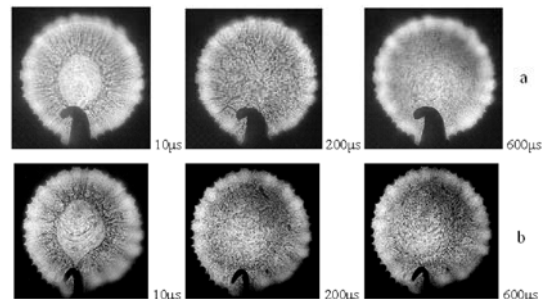
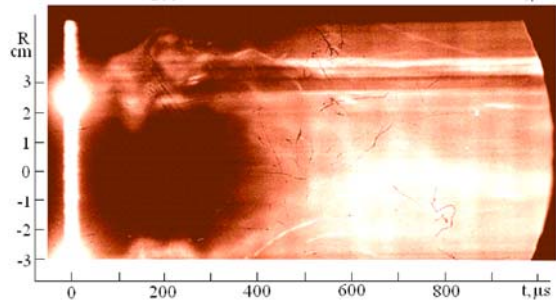
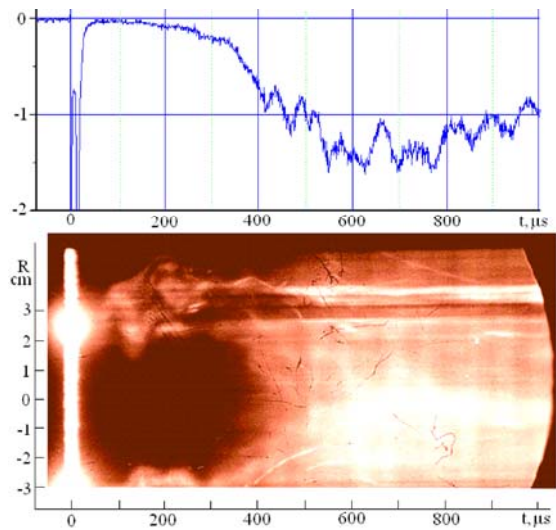


Figure 16. Three photographic layers show, from top to bottom: a) a photomultiplier signal measuring the reactor radiation integrated over the spectrum; a streak image of glow in the reactor, the slit of the streak camera being oriented in the radial direction of the discharger; typical shadow pictures of gasdynamic processes in the plane of the ring during discharge in a methane-oxygen mixture;

The third phase is associated with a fast volume combustion of the mixture, recorded in the streak picture as a bright burst of duration $\Delta t_3 \cong 5\text{--}10$ ms.

The presence of three phases with their characteristic features is typical of previous experiments in closed quartz tubes filled with a methane—oxygen mixtures, where the combustion was initiated by high-power linear gliding discharges [17], microwave discharges on plane metal—dielectric targets [16], laser sparks [14,15]. Though seemingly identical to the sequence of events in [14-17], the initiation of combustion in the present experiments demonstrates also its distinctive features, especially, in the second phase of the process, when the combustible gas is being prepared to the fast ('explosive') combustion. The features peculiar to the initiation of combustion by a ring discharge show up if we consider in more detail the experimental results concerning the measurements of radiation and gas-dynamic characteristics of the methane—oxygen medium in the phase preceding the ignition.

Shadow photographs of gas-dynamic perturbations in the cross-sectional plane of the ring discharger demonstrate that the processes of formation of a ring (toroidal) shock wave, its convergence toward the axis and reflection at the axis proceed in almost the same way in the combustible (methane—oxygen) and noncombustible (oxygen) medium (see Fig. 12). In this initial phase ($t \leq 60 \mu\text{s}$), a glow is visible only in a layer of discharge plasma adjacent to the inner surface of the ring (Fig. 9), whereas neither the photomultiplier nor FER-7 detects glow inside the ring.

The optical radiation from the reactor is absent in noncombustible gases (oxygen) at all time $t > 100 \mu\text{s}$. At this post-discharge time in chemically inactive gases, the indications of the presence of gas-dynamic perturbations against the background are missing from the shadow photographs and the refraction detector signals (see Fig. 12 and Fig. 13). However, the absence of any consequences of the ring discharge at delay times $> 100 \mu\text{s}$ is characteristic of only discharges in oxygen. An essentially different type of situation occurs in methane—oxygen mixtures. In this case, a feeble but well-defined glow appears within $50\text{--}60 \mu\text{s}$ in the streak image. This glow is identified as a wave which propagates accelerating from the surface of the ring toward its axis (Fig. 9). The average velocity of the wave is on the order of $5 \cdot 10^4$ cm/s. Gas-dynamic processes do not cease: a radially convergent gas-dynamic wave appears in the shadow photograph; behind its front are seen local gas density perturbations, mostly in the form of extended inhomogeneities (see Figs. 12c, 12d). (Perturbations of this sort are detected by the refraction detector as well (Fig. 13b)). The average

velocity of this second convergent wave is nearly equal to the velocity of the first glow wave ($\sim 5 \cdot 10^4$ cm/s). Collapse of the second gas-dynamic wave at the axis of the ring ($t \cong 100 \mu\text{s}$) is recorded by the refraction detector (see peak 3 in Fig. 13b) as well as by shadow photography.

In the context of gas dynamics, the ignition process in oxygen may be interpreted as the following sequence of events: the excitation of a shock wave by discharge, the cumulative process of convergence of this wave toward the axis, its reflection at the axis and reverse motion from the center of the ring. At this point, the gas-dynamic response of the medium to the ring discharge ceases. Other chemically rare gases behave in a similar manner [8,9]. In the methane—oxygen medium, however, the process is modified – there appears a second radial convergent wave focusing at the axis and causing the ignition of the methane—oxygen mixture.

Flame initiated at the axis of the ring, in the vicinity of its center is accompanied by a combustion wave, which at a velocity higher than 10^5 cm/s travels in both the axial and radial directions, and within $100 \mu\text{s}$ and even sooner, combustion occurs throughout the reactor volume. Note that velocity of a fast combustion wave is close to the velocity of detonation wave in a methane-oxygen gas mixture [19]. That detonation wave plays an important role in a volumetric combustion processes in the reactor is also indicated by data of measurements made with help of a piezoelectric transducer. It can be seen from Fig. 14b that the transducer (located on the Z axis, at a distance $L=5$ cm from the plane of the ring discharger) detects an arrival of an extremely strong shock wave (peak 3 in Fig. 14b) that can be identified as a detonation wave accompanying the second cumulative shock wave propagating along the Z axis.

Subsequently, when the intensity of radiation, associated with flame, reaches its maximum and then slowly decreases ($t \geq 600 \mu\text{s}$), the field of shadow photographs becomes free from local inhomogeneities represented perturbations of the medium (see Fig. 12f). At the same time, characteristic fluctuations, which are due to perturbations of the medium, disappear from the refraction detector signal (Fig. 13b). The results obtained late in the post-discharge phase with the help of shadow photography and refraction measurements testify to the volume combustion of the mixture throughout the reactor and to the equalization of the gas temperature (apparently, at a level of the equilibrium burnout temperature of a stoichiometric methane—oxygen mixture).

Of particular interest is the mechanism for formation of a feeble glow wave convergent at the axis and preceding the ignition. This wave exhibit properties similar to feeble glow waves –

predecessor events, discovered in [14-17] during the process of initiation of combustion of a methane—oxygen mixture in closed chambers by different types of high-power electric discharge. As in the present experiment, these so-called ‘incomplete combustion waves’ propagate from localized discharges into the surrounding gas at velocities far exceeding the velocity of a usual deflagration wave. (Even taking into account the gas-dynamic entrainment of a burning medium, this velocity cannot exceed $4 \cdot 10^3$ cm/c [14,16,19].) The nature of ‘incomplete combustion waves’ remains an open question. The present experiment allows us to assume that one of the factors, which play a part in the formation of this phenomenon, is a peculiar kind of ‘chemical’ instability related to the production of excited particles and radicals in local overheated regions behind the front of a feeble glow wave. These active particles stimulating the heating promote the ignition of the gas throughout the volume. It may well be that a feeble glow recorded in the FER-7 streak pictures is due to emission from the OH radicals.

In addition, the possibility of the flame front accelerating substantially under the action of weak shock waves must be taken into account [20,21]. In [22], the mechanism underlying the deflagration-to-detonation transition was studied analytically and numerically. It is shown that a preheated zone forms ahead of a deflagration wave front, between the flame front and the shock front. In the presence of the preheated zone, the gas temperature, density and pressure profiles change substantially within the flame. These processes lead to the flame front acceleration up to its transformation into detonation mode. It is not improbable that this mechanism works in some ways in our experiment, where the ring discharger provides multiple interactions of weak gas-dynamic perturbations with the flame front.

Thus, the possibility of ignition at the axis, proposed and studied in [11,13], was checked experimentally. A ring electric discharge provides ignition of a combustible methane—oxygen medium at a distance from the region of energy release, i.e., in the axial region near the center of the ring. In real situation, however, the process turns out to be more complicated than expected. Combustion is initiated not by the first (toroidal) shock wave generated by an annular plasma layer, but by the second gas-dynamic wave emerging with some delay time with respect to the first wave. The mechanism for formation of this wave needs clarification, and the construction of a model for describing the processes ensuring the ignition at the reactor axis calls for further investigation.

Yet another advantage of the ring discharger, in addition to the capability of initiating combustion at a distance from the region of energy release, is a short induction time (from switching on

the discharger to the appearance of flame). The induction time depends markedly on the energy released in the discharge: its value decreases with increasing energy and reaches ~ 350 μ s at $W \cong 90$ J (Fig. 15). The dependence of this sort unambiguously points to the fact that the mechanism for initiating the volume combustion by a ring discharge in a closed chamber can in no way be explained by a usual deflagration wave excited by discharge.

Turning our attention to the problem of ring-shape discharger application in an aviation engines (see Fig. 1) we can emphasize that high-speed jet combustion on its axis in fact could be expected. In this case it will be easy to estimate axial downstream distance ΔZ between ring plane and point at which cumulative toroidal shock wave acting like igniter gets axis:

$$\Delta Z \approx 3 R M ,$$

where R is ring radius and M – is Mach velocity of jet. This estimation bases on the fact that average velocities of cumulative toroidal shock wave and wave reflected from axis are close to the speed of sound (see [9,10]).

V. Conclusions

The present experiments have demonstrated the effect of ignition of a stoichiometric mixture at a certain distance from the initiator – a multielectrode discharge system generating an annular plasma layer which is a source of gas-dynamic perturbations converging toward the axis.

The gas-dynamic processes of the ring discharge in a methane—oxygen medium are more intricate than those in chemically inactive gases. The distinctive feature of this discharge is generation of the second wave of strong gas-dynamic perturbations, which is also converging toward the axis. The ignition occurs when the second wave is approaching the axis.

The induction times at initiation of combustion by a ring discharge turn out to be much shorter in comparison with linear gliding discharges, microwave discharges at plane targets, and lasers sparks with nearly the same energy released.

This work was supported by the Presidium of the Russian Academy of Sciences (Fundamental Problems of Mechanics, program P-11), the International Science and Technology Center (project no. 3833p), and the Council of the Russian Federation Presidential Grant for State Support of Leading Scientific Schools (project no. NSh-452.2008.2).

References

- [1] *J.D.Dale, M.D.Checkel and P.R.Smy.* // Prog. Energy Combustion Sci. , 23: 379-398 (1997).
- [2] *J.D.Dale and A.K.Oppenheim,* SAE Paper No 810146.
- [3] *R.G.Kingdon and F.G.Weinberg,* Sixteenth Symposium (International) on Combustion, The Combustion Institute, Pittsburgh, pp. 747-756, (1977).
- [4] *M.H.Morsy, Y.S. Ko and S.H. Chung,* Laser – Induced Ignition Using a Conical Cavity in CH₄-Air Mixtures // Combustion and Flame, 119: 473-482, (1999).
- [5] *A.Yu. Starikovskii,* // Proc. Combust. Inst., v. 30, p. 2405, (2005).
- [6] *S.M.Starikovskaya,* // J. Phys. D: Appl. Phys., v. 39, R265, (2006).
- [7] *I.V.Adamovich, I. Choi, N. Jiang et al.,* // Plasma Sources Sci. Technol., v. 18, 03418 (13pp), (2009).
- [8] *N.K.Berezhetskaya, E.F. Bol'shakov, S.K. Golubev et al.,* Gas-dynamic Phenomena Accompanying a Ring Surface Discharge // Sov. Phys. JETP, v.60, p. 1108 (1984).
- [9] *I.A. Kossyi, K.V. Krasnobaev, I.V. Sokolov, V.E. Terekhin,* Cumulation of Schock Waves Excited by an Axisymmetric Gliding Discharge // Kratk. Soobshch. Fiz., No. 11. p. 3 (1987) [in Russian].
- [10] *I.V. Sokolov.* Hydrodynamic Cumulative Process in Plasma Physics // Sov. Phys. Usp., v. 33 p. 960 (1990).
- [11] *E.M.Barkhudarov, T.S.Zhuravskaya, I.A.Kossyi, V.A.Levin, V.V.Markov, N.A.Popov, N.M.Tarasova, S.M.Temchin and M.I.Taktakishvili.* Axisymmetric Electric Discharge as a Means for Distant Heating of Gas Media // Plasma Physics Reports, 2009, V. 35, No 11, pp. 924-932.
- [12] *Eduard M.Barkhudarov, Igor A. Kossyi, Vladimir A. Levin, Vladimir V. Markov, Nikolay A. Popov, Merab I. Taktakishvili, Saveliy M. Temchin, Tatiana A. Zhuravskaya.* Formation of Toroidal Explosion Wave for Initiation of Detonation // 22nd ICDERS, July 27-31, 2009, Minsk, Belarus, Proceedings.
- [13] *E.M.Barkhudarov, T.S.Zhuravskaya, I.A.Kossyi, V.A.Levin, V.V.Markov, N.A.Popov, N.M.Tarasova, S.M.Temchin and M.I.Taktakishvili.* Axisymmetric Electric Discharge as a Method for Gas Heating Distance // The 8th International Workshop on Magneto-Plasma Aerodynamics (Abstracts) Moscow, 2009, pp. 88-89.
- [14] *S.Yu. Kazantsev, I.G.Kononov, I.A.Kossyi, N.M.Tarasova and K.N.Firsov.* Ignition of Combustible Gas Mixture by a Laser Spark Excited in the Reactor Volume // Plasma Physics Reports, 2009, V. 35, No 3, pp. 251-257.
- [15] *I.A.Kossyi, V.P.Silakov, N.M.Tarasova and D. Van Wie.* Long-Lived Plasmoids Generated by Surface Laser Sparks in Combustible Gas Mixtures // Plasma Physics Reports, 2006, V. 32, No 4, pp. 349-351.
- [16] *I.A.Kossyi, N.K.Berezhetskaya, S.I.Gritsinin, V.A.Kop'ev, V.P.Silakov, N.M.Tarasova and D. M. Van Wie.* Abnormal Long-lived Plasmoids Produced by Surface Microwave Discharge or Surface Laser Spark in a Combustible Gas Mixture // 44th AIAA Aerospace Sciences Meeting and Exhibit, Reno, Nevada, 2006, Report AIAA-2006-1213.
- [17] *N.K.Berezhetskaya, S.I.Gritsinin, V.A.Kop'ev, I.A.Kossyi, P.S.Kuleshov, N.A.Popov, A.M.Starik and N.M.Tarasova.* Ignition of a Combustible Gas Mixture by a High-Current Electric Discharge in a Closed Volume // Plasma Physics Reports, 2009, V. 35, No 6, PP. 471-483.
- [18] *Barkhudarov E.M., Midivnishvili M.O., Sokolov I.V. et al.* Experimental Simulation of Hydrodynamic Phenomena Accompanying Laser Beam Interactions in a Gas // Laser and Particle Beams. 1991. V. 9. № 2. P. 421.
- [19] *A.S. Sokolik.* Self-Ignition, Flame, and Detonation in Gases // Acad. Nauk SSSR, Moscow, 1960 [in Russian].
- [20] *Elaine S. Oran, Vadim N. Gamezo* Origins of the deflagration-to-detonation transition in gas-phase combustion // Combustion and Flame, 2007, v. 148, pp. 4-47.
- [21] *Bazhenova T.V., Golub V.V.* Application of gas detonation under the controlled frequency regime (overview) // Fizika Goreniya i Vzryva, 2003, V. 39, No 4, pp. 3-21, (in Russian).
- [22] *Lieberman M.A., Kuznetsov M., Ivanov A., Matsukov I.* Formation of the preheated zone ahead of a propagating flame and the mechanism underlying the deflagration-to-detonation transition // Phys. Lett., A. 2009. V. 373, P. 501-510.

ULTRA-LEAN FLAMES STABILIZATION BY HIGH-VOLTAGE NANOSECOND PULSED DISCHARGE

Andrei Nikipelov^{1,2}, Ilia Popov², Giuseppe Correale², A. Rakitin², A. Starikovskii^{2,3}

1 – Moscow institute of physics and technology, Dolgoprudny, 141700, Russia

2 – NEQLab Research BV, The Hague, 2521 AL, The Netherlands

3 - Drexel Plasma Institute, Drexel University, Philadelphia, PA

1. Introduction

Strict environmental regulations on emissions levels in combustion chambers of all kinds recently led to the development of various lean combustion concepts. One of the key problems in these systems is flame stabilization at equivalence ratios as low as 0.05–0.2. These conditions ensure very low NO_x production rate, but at the same time require careful design of the burner, the combustion chamber and the flow pattern inside to provide stable flame attachment and combustion completeness.

One of the approaches for lean flame stabilization is the application of plasma-assisted burners, also referred to as plasmatrons. Mainly plasmatrons are based arc, spark, or microwave discharges, since they have been thoroughly studied and present relatively simple designs with low costs. The general problems of these approaches are significant energy consumption and short life cycles due to overheating and erosion of electrodes. The best examples provide 100 operating hours while the necessary life cycle is approximately 1000 hr for industrial applications.

One of the main features of nanosecond gas discharge is its efficiency in production of nonequilibrium low-temperature plasma with high concentration of active radicals. This is due to the high values of reduced electric fields (50–500 Td) which are present in the discharge channels at typical pulse voltages of 10–20 kV. Under such high fields, the energy input into the gas is branched between rapid heating and radical production, which is mostly atomic oxygen in 1D excited state, as was shown in [1]. Also shown was that atomic oxygen is extremely efficient in starting chain reactions and, thus, in promoting ignition. Though most of PAC (plasma-assisted combustion) and PAI (plasma-assisted ignition) papers showing considerable plasma effect are devoted to mixtures with equivalence ratio in the range of 0.7–1.2 [2], it is clear that radical introduction into preheated rich hydrocarbon-air mixtures with stoichiometric ratios up to 3.5 should promote oxidation reactions and change overall reaction time.

High pulse amplitude up to 15–20 kV and short pulse duration of 10–20 ns enable discharge development in a wide range of pressures, temperatures, and gas compositions with relatively low pulse energy. This makes it possible to use this type of discharge in industrial devices where operating conditions vary significantly and where limited energy consumption is important. Low average current through the plasmatron also leads to long life of the electrodes, making it suitable for long-term operation.

2. Experimental Setup

The study was performed for premixed preheated flows of up to 100 standard liters per minute (slpm) in the moderate discharge power range of 40 to 200 W measured 'from the plug'. The experimental setup consisted of the following systems (Fig. 1): high-voltage pulse generator (1), fuel-air supply, premixing and preheating system (2), plasmatron (3), reaction chamber (4), ground electrode (5), high-voltage electrode/swirler (6), heat insulation (7), ungrounded thermocouple (8),

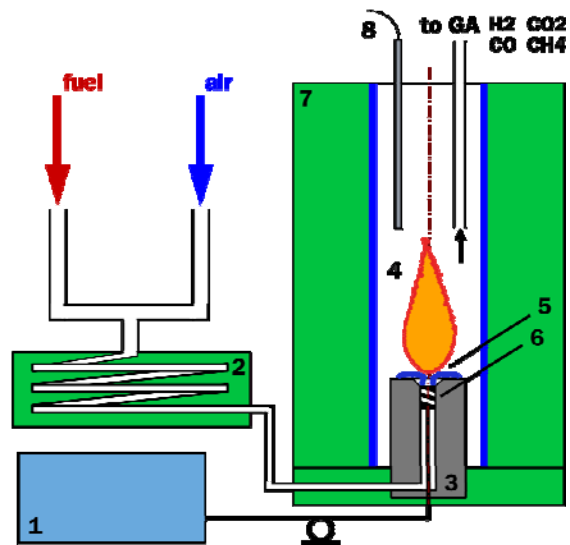


Fig. 1: Scheme of experimental setup for plasma-assisted flame stabilization.

multi-channel gas analyzer, and a 500 MHz oscilloscope not shown in the scheme.

Room air and methane or diesel fuel vapours were premixed and preheated in the heat exchanger which is a part of the supply system (2). The heat exchanger is a stainless steel coil wrapped in a heating tape and thermal insulation. In the case of diesel fuel, it also acted as the evaporator, producing a hot air–vapour mixture. The air flow was delivered from a pressurized central supply and controlled with a flow meter with a built-in high precision valve. Air expenditure rate was up to 100 standard liters per minute (slpm), the pressure at the inlet of the heat exchanger was up to 3 bars. Methane was supplied from a gas cylinder with a pressure reducer and a flow meter with a built-in high precision valve. Diesel fuel was delivered from a fuel tank by a digitally controlled peristaltic pump. The pump provided a constant expenditure with an outlet pressure of up to 7 bars. The maximum expenditure was 18 ml/min.

Table 1: Operational condition during flame stabilization tests.

Outlet pressure	1 bar
Flow temperature	600 C for CH ₄ 350 C for vaporized diesel
ER, lean	0,03 – 0,4
ER, rich	2,0 – 3,3
Gas flow rate	Up to 100 slpm
Discharge power	40-200 W

Digital controllers defined the temperature of the fuel–air heater and the plasmatron body temperature. It enabled to keep the temperature of the flow in the range of 20–600 C at the outlet. The plasmatron was also wrapped in thermal insulation and a heating tape with the temperature matching that of the evaporator to prevent condensation when working with diesel vapor and to provide a constant temperature of the flow. The total power consumption of the heaters was 200–500 W, depending on the temperature and the flow rate required. The study was conducted under the operating conditions summarized in Table 1.

The mixed flow to be ignited was directed through the plasmatron into the thermally insulated chamber (4). The chamber was made of a SiC tube, wrapped in 50 mm Fiberfrax thermoinsulating blankets and enclosed in a stainless steel cylinder. The discharge developed inside the nozzle of the plasmatron, starting from the high-voltage electrode which also acted as a swirler. Figure 2



Fig. 2: Uncovered plasmatron photo at an exposure of 1/30 s.

shows a top view of it with consequent sparks with an exposure time of 1/60 s. The discharge is produced by 15 kV pulses generated at a frequency of 10 kHz in a 60 slpm air flow. The same discharge is shown in Fig. 3 at an exposure time of 1/350 s. During the experiments, temperature and composition (CO, CO₂, CH₄) of the flow at the outlet of the plasmatron were measured. The gas for analysis was sampled 5 cm above the plasmatron. Thethermocouple measurement of the products temperature were carried out in the same spot.

3. Ultra-lean flame stabilization tests

The first set of experiments was conducted

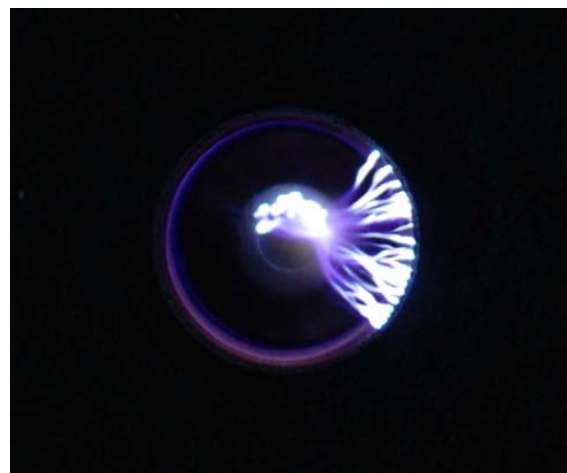


Fig. 3: Spark rotation in the preheated methane–air flow, 1/500 s exposure.

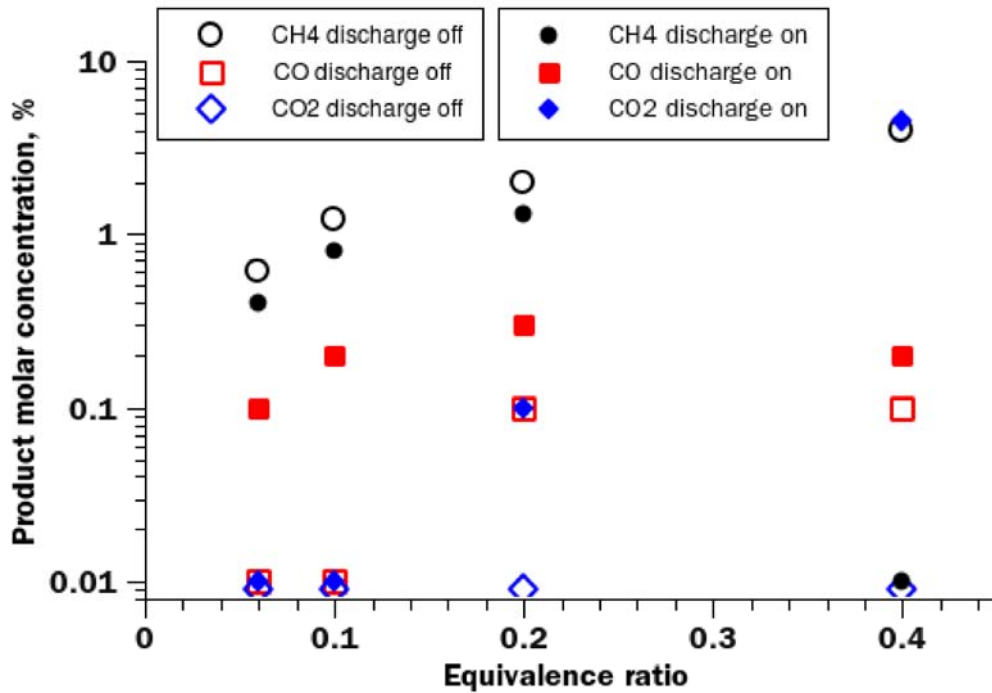


Fig. 4: Plasma-assisted stabilization of premixed methane-air flame. Inlet temperature: 400 C. Flow rate: 30 slpm.

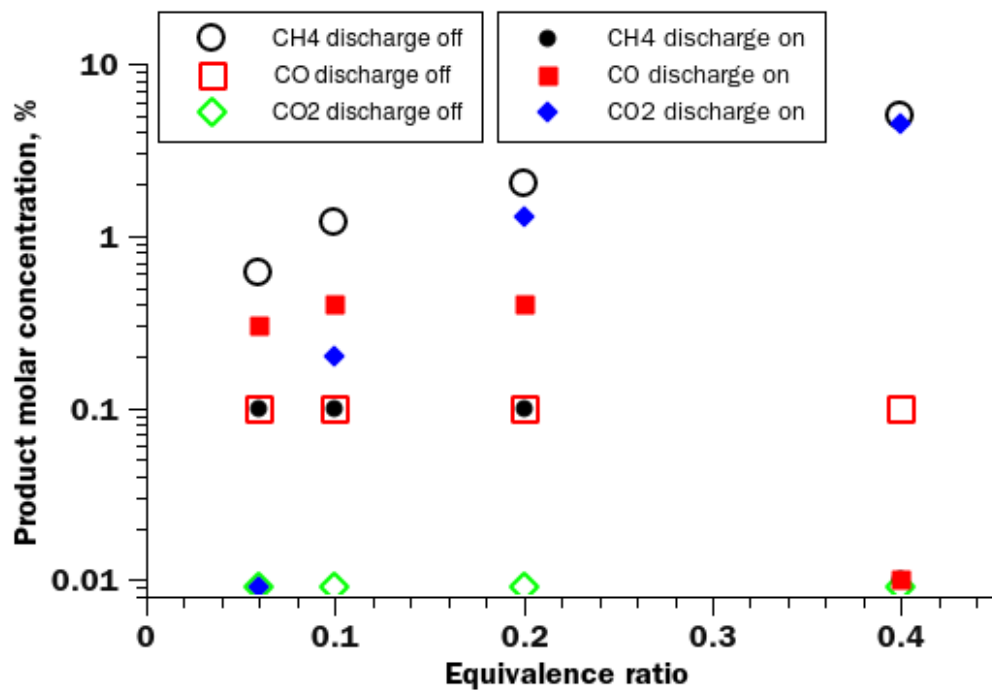


Fig. 5: Plasma-assisted stabilization of premixed methane-air flame. Inlet temperature: 580 C. Flow rate: 60 slpm.

with methane. It has relatively high ignition threshold and very well known rates of reactions. Figures 4 and 5 contain data on the products of ignition of premixed methane-air flow with inlet temperatures of 400 C and 580 C by repetitive nanosecond spark discharge. The gas flow rate was 30 and 60 slpm, the equivalence ratios ranged from 0.06 to 0.4. For the 400 C flow, the discharge

action was very modest: only 10% of methane were oxidized into CO and, probably, into CH₃OH. For 580 C, 90–95% of methane were oxidized, into CO and CO₂, mostly.

The spark starting point was evenly distributed over the cylindrical high-voltage electrode with two consequences: first, no electrode erosion was observed because no spot on the

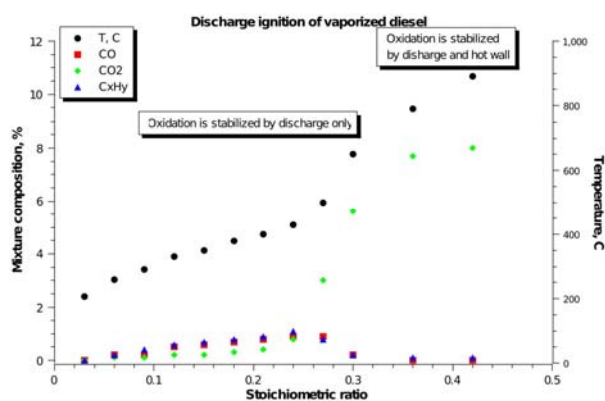


Fig. 6: Ignition of lean diesel vapour-air mixture.

electrode was overheated; and second, each channel treated a fresh volume of gas, providing distributed ignition. The nanosecond spark created radicals during the streamer phase and increased temperature during the arc phase faster than radicals recombined. Non-thermally created radicals initiated chain reactions within times shorter than those of gas mixing, thus efficiently igniting the flow in the afterglow of the nanosecond spark. This is the main advantage of the nanosecond spark over the conventional one. In conventional spark, almost all the energy input goes into heating. With comparable energy input, most of the heat would have been dissipated before ignition occurred.

It is important that no flame front was observed during the discharge initiated combustion at equivalence ratios 0.06–0.2. This implied that volumetric combustion and heat release took place. Since the temperature increase for lean flames is moderate, a combustion chamber design with reverse flows may be reasonable to obtain better completeness of oxidation. Another way to suppress CO yield is to increase the inlet temperature. This will be illustrated further on on the example of lean diesel fuel vapour combustion.

These were performed in the same conditions as the tests with methane. Air flow at 60 slpm was mixed with liquid diesel fuel and fed into the stainless steel coil of the evaporator. Precautions were made to prevent ignition inside the coil and a special design of heater geometry was developed for this task. Temperature of the mixture to be processed by the discharge was 220 C. The equivalence ratio was controlled by the pump expenditure, which was increased in steps.

The results are presented in Fig. 6 as product composition versus equivalence ratio, with discharge on and off. When the discharge was off, CO, CO₂ and CH₄ levels were 0–0.1%, which proved that no oxidation took place on the surface of the steel evaporator. After each change of

expenditure (and, thus, equivalence ratio), the discharge was turned off to find the conditions when ignition was stabilized at the outlet of the plasmatron or on a hot ceramic wall of the thermally insulated volume. Note “Oxidation is stabilized by discharge and hot wall” in Fig. 6 implies that after the ignition by the discharge heat release from combustion was sufficient to increase temperature of thermally insulated ceramic tube to such extent, that turning off discharge would not affect product composition since combustion was stabilized on the hot ceramic tube wall. Note “Oxidation is stabilized by discharge only” means that flame was immediately blown off upon discharge turning off.

4. Discussion

4.1. Plasmatron with a swirler

As was mentioned above, the radical responsible for ignition promotion under these conditions is atomic oxygen. It is produced in the discharge by electron impact dissociation and by dissociative quenching of excited nitrogen molecules on oxygen. The concentration of O atoms in the plasma channel after discharge propagation can be estimated by solving Boltzmann equation in two-term approximation for typical reduced electric field values. It can be then taken as the initial condition for kinetics modelling of the ignition process.

Numerous experiments that had been performed previously on the facility combining a shock tube and a high-voltage (up to 150 kV) discharge chamber [3, 4] enabled validation of a kinetic mechanism for plasma-assisted ignition of saturated hydrocarbons from methane up to pentane [5]. It showed, however, that radical introduction is efficient for ignition only in the case if the temperature is above or slightly below the self-ignition threshold.

For ignition of mixtures at temperatures below the ignition threshold, it is crucial to add some heat, thus increasing the temperature along with the introduction of radicals, since the chain reactions only start efficiently if the temperature is close to the autoignition threshold. At lower temperatures, the radicals recombine quickly without starting the chains. This scenario is realized in case of application of uniform discharges (for example, radio-frequency discharge with the same power as a high-voltage nanosecond pulsed discharge), which couple energy volumetrically. Specific energy input per gas particle is low in this case, and temperature increase is limited to several K, which makes radicals production inefficient for ignition.

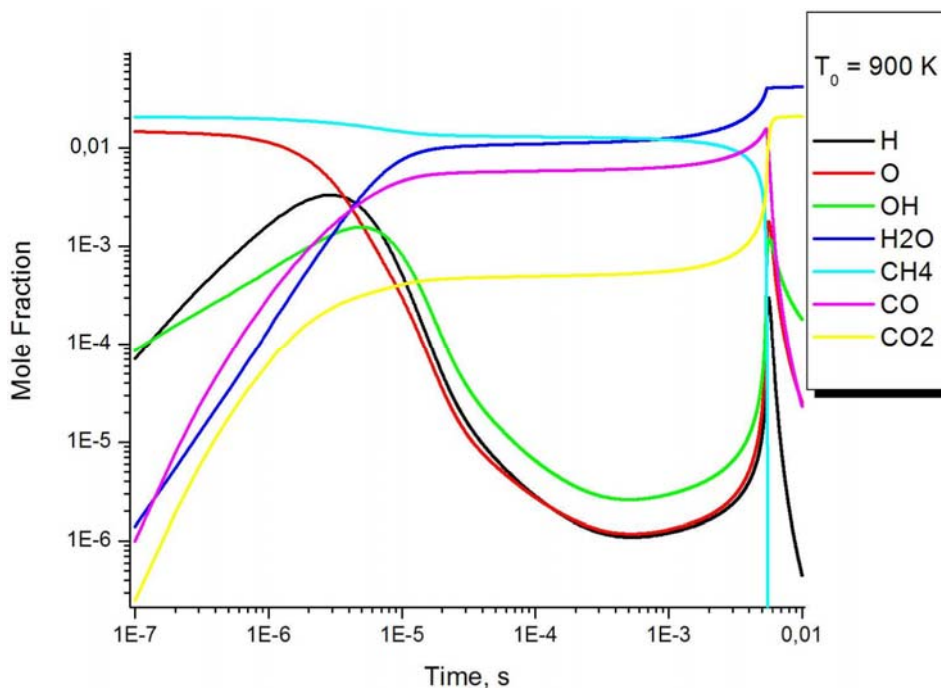


Fig. 7: Calculated kinetic curves for methane–air mixture ignition at $ER = 0.25$, $T = 750$ K. Discharge produces 1.5% of atomic oxygen in the mixture and increases the temperature to 900 K.

On the other hand, adding only heat would require significantly more energy. This scenario is realized in case of application of conventional spark discharges in which most of the energy is branched into direct heating due to lower reduced electric field values in the channel.

The short duration of nanosecond sparks makes it possible to apply high voltage and, hence, obtain high reduced electric field values in the gap, while keeping the overall energy input low (within 40 mJ in a single pulse under our conditions). This in turn enables both radical production and temperature increase due to the high electric field value, while operating at frequencies up to 1–10 kHz and consuming 40–200 W “from the plug”. Thus, repetitive nanosecond sparks provide the mechanism for lean flame stabilization at relatively low temperatures since they efficiently release heat and produce radicals simultaneously.

This has been supported by zero-dimensional simulation of chemical kinetics in lean methane–air mixture processed by a high-voltage nanosecond discharge. The mixture at an ER of 0.25 was preheated up to 750 K. The discharge was modelled as introduction of 1.5% of atomic oxygen and a temperature increase of 150 K, which roughly corresponds to the energy input in a single spark under the experimental conditions. Results of the calculations are shown in Fig. 7 in terms of kinetic curves for different species. The kinetic mechanism used here is described in [6]. It is clearly seen that ignition delay time in this case is

several milliseconds and corresponds to typical diffusion times for a single streamer channel. It should be noted that the ignition delay time in this range of parameters is extremely sensitive to the energy input. For example, a two-fold increase of the energy deposition reduces the ignition delay time by more than two orders of magnitude. Thus, kinetic modeling also predicts the possibility to control ignition and flame stability with relatively low energy price.

As compared to ignition, for flame stabilization it is also important to arrange proper interaction between the flow and the discharge. For that, the flow pattern was modelled with a CFD tool. No chemistry or discharge effect were taken into account. For creating the geometry and generating the meshes, SALOME application version 4.1.4 was used. It is an open-source integrated environment for managing geometry and meshing. Default automatic meshing algorithm was used, with the fineness factor of 0.14. The mesh produced consisted of about 350 000 tetrahedrons. The faces which presented inlets and outlets were grouped to set the boundary conditions. For the simulations, OpenFOAM toolkit version 1.5 was used. A transient turbulent compressible solver with LES turbulent model and perfect gas thermophysical model was selected.

The tested plasmatron featured a flow pattern which guaranteed that the spark hits fresh gas portions each time, due to the swirling element and the overall design of the burner, except for the

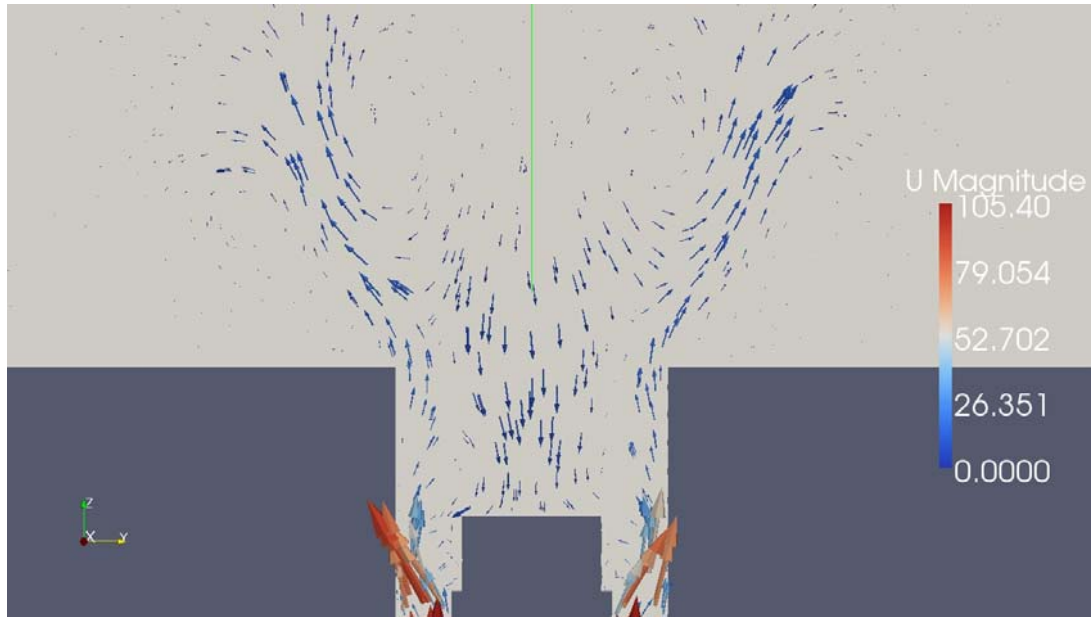


Fig. 8: Z component of flow velocity at the outlet of the plasmatron. Numerical simulation results.

regions of reverse flow. This can be estimated from the maximum spark diameter (1 mm), maximum frequency applied (10 kHz), and the z-component of gas velocity derived from the CFD modelling and presented in Fig. 8.

4.2. Another approach: multi-jet plasmatron

It is mainly the discharge frequency that defines the mode of discharge development (localized spark, distributed spark, or diffuse) for a certain geometry of electrodes, and only the sparks were able to ignite lean flows in the experiments. In order to increase the efficiency of ignition and to decrease the overall energy input to the system, various plasmatron geometries were designed and tested. Currently a so-called multi-jet plasmatron with the spark developing along the flow is being tested. This concept ensures that consequent sparks hit the same gas volume several times, hence increasing the temperature of the channel in steps until it is close to the self-ignition threshold when the introduction of non-thermal radicals is most efficient.

Such flow-discharge interaction makes possible the ignition of colder flows and to decrease the ignition threshold in terms of frequency to as low as 2 kHz as compared to 8 kHz for the same conditions in the swirler-type plasmatron discussed above. This corresponds to a decrease in the required generator power from 200 to 40 W for stabilization of a methane-air flame at an equivalence ratio of 0.3. The flow of 60 slpm

was preheated up to 350 C. This gain in efficiency demonstrates the high sensitivity of the ignition efficiency to the geometry of the plasmatron, which provides space for design optimization at various operating conditions.

5. Conclusions

In this paper the concept of plasma-assisted combustion has been applied to develop an ignition and flame stabilizing system for a wide range of fuels, equivalence ratios, gas pressures, and temperatures. A series of plasmatrons based on repetitively pulsed nanosecond high-voltage discharge has been developed.

The optimal configuration and discharge parameters for ultra-lean ($ER > 0.03$) and ultra-rich ($ER < 3.3$) flame stabilization have been found experimentally.

The air flow pattern has been simulated numerically with OpenFOAM package in two various plasmatron geometries to optimize the discharge-flow interaction. Significant differences in the patterns have been shown by the model and confirmed by the experiments.

Kinetic modelling in zero-dimensional approach has supported the experimental results as well. Further comparison with enhanced modeling taking into account discharge effect and actual flame propagation will allow to obtain insight into the mechanisms of plasma-assisted flame stabilization.

Acknowledgements

Plasmatron designing and testing have been carried out in the framework of the research and development project at NEQLab Research BV aimed at the realization of a commercially perspective compact catalyst-free reforming technology.

References

1. Starikovskii, A. Y., "Plasma Supported Combustion," Proceedings of the Combustion Institute, 30th International Symposium on Combustion, Chicago, USA, 2004, p. 326.
2. Starikovskaia, S. M., "Plasma assisted ignition and combustion," *J. Phys. D: Appl. Phys.*, Vol. 39, 2006.
3. Kosarev, I., Kindusheva, S., Aleksandrov, N., Starikovskaia, S., and Starikovskii, A., "Kinetics in Gas Mixtures for Problem of Plasma Assisted Ignition," 45th AIAA Aerospace Sciences Meeting and Exhibit, AIAA, Reno, USA, 2007, paper 2007-1386.
4. Starikovskii, A. Y., Anikin, N. B., Kosarev, I. N., Mintoussov, E. I., Nudnova, M. M., Rakitin, A. E., Roupasov, D. V., Starikovskaia, S. M., Zavialov, I. N., and Zhukov, V. P., "Nanosecond Pulsed Discharges for Plasma Assisted Combustion and Aerodynamics," *Journal of Propulsion and Power*, Vol. 24, No. 6, 2008.
5. Kosarev, I. N., Aleksandrov, N. L., Kindysheva, S. V., Starikovskaia, S. M., and Starikovskii, A. Y., "Kinetics of ignition of saturated hydrocarbons by nonequilibrium plasma: CH₄-containing mixtures," *Combustion and Flame*, Vol. 154, No. 3, 2008.
6. Aleksandrov, N. L., Kindysheva, S. V., Kukaev, E. N., Starikovskaya, S. M., and Starikovskii, A. Y., "Simulation of the Ignition of a MethaneAir Mixture by a High-Voltage Nanosecond Discharge," *Plasma Physics Reports*, Vol. 35, No. 10, 2009, pp. 867—882.

THE EFFECT OF NONEQUILIBRIUM EXCITATION ON THE IGNITION OF HYDROGEN-OXYGEN MIXTURES

N. A. Popov

Skobel'tsyn Research Institute of Nuclear Physics, Moscow State University, Moscow, 119992 Russia

e-mail: NPopov@mics.msu.su

Abstract. The effect of various radicals and excited particles on the induction delay time reduction is discussed when analyzing the ignition of combustible mixtures under nonequilibrium conditions. A review is made of experimental and theoretical investigations of the effect of hydrogen and oxygen atoms, electronically excited $O_2(a^1\Delta_g)$ molecules on the induction times and on shift of the ignition temperature limits of hydrogen-oxygen mixtures. The addition of oxygen and hydrogen atoms to a combustible mixture may cause a significant reduction of the induction times and the lowering of the ignition temperature limit of combustible mixtures. However, the latter effect is observed only in the vicinity of the ignition limit. In the region of relatively low initial temperatures, the shift of the ignition limit is largely associated with the heating of mixture owing to recombination of atomic particles being added. In so doing, the nonequilibrium pattern of the impact hardly shows up.

Molecules of singlet delta oxygen (SDO) $O_2(a^1\Delta_g)$ may be involved in both chain initiation reactions and chain branching reactions. A kinetic model describing the impact of the admixture of SDO molecules $O_2(a^1\Delta_g)$ on the evolution of the composition of hydrogen-oxygen mixtures was worked out. There was shown in the framework of this model the possibility of describing all the main experimental data on the dynamics of quenching of singlet oxygen in $H_2 : O_2$ gas mixtures in the temperature range of $T_0 = 300 - 1050$ K. Most of the acts of interaction between singlet oxygen molecules and atomic hydrogen $O_2(a^1\Delta_g) + H$ lead to quenching of $O_2(a^1\Delta_g)$. Efficiency of this interaction channel is more than 80% and fraction of the reaction $H + O_2(a^1\Delta_g) \rightarrow OH + O(^3P)$ was only in 10-20%. The impact of the admixture of SDO molecules on the ignition of $H_2 : O_2$ mixtures was investigated. The dominant process determining the degree of impact of $O_2(a^1\Delta_g)$ is its deactivation by molecules of HO_2 . As a result, in $H_2 : O_2$ mixtures of high pressure, where the density of produced HO_2 molecules can be high enough, the effect of singlet oxygen on the ignition time of these mixtures turns out to be relatively weak. This effect becomes even less noticeable if admixtures of atomic oxygen are present in the mixture. The last case is typical when the electric discharge systems are used for production of singlet oxygen. Presence of even small (10^{-4}) initial concentration of atomic oxygen reduces the effect of $O_2(a^1\Delta_g)$ admixtures on the processes of ignition only to additional heating of the mixture in the process of SDO deactivation

INTRODUCTION

Considerable recent attention has been given to the problem of fast ignition of combustible gas mixtures, which is motivated by a possibility of applying the obtained results in the design of engines and various plasmachemical systems. It is common knowledge that, in most cases of practical importance, the ignition of combustible mixtures is achieved by increasing their temperature to values exceeding the ignition temperature. The effect of an additional nonequilibrium excitation can be twofold: (i) a shorter induction period of a combustible mixture; (ii) a lower ignition temperature T_g^* , i.e., the ignition of a mixture at initial temperatures below T_g^* . In this case, the effect of the nonequilibrium excitation might be reckoned as substantial if the ignition temperature of the mixture is reduced by the value that considerably exceeds its heating due to relaxation of the excitation energy.

In recent years, several methods have been proposed for nonequilibrium initiation of the combustion in gas flows. Takita et al. [1] reported a significant increase in the velocity of combustion wave as a result of direct injection of arc DC discharge plasma into a gas mixture. Besides, the feasibility of initiating the combustion

by pulsed high-current DC discharges [2-8], by RF and microwave discharges [9-13], and by electron beams [14, 15] is being investigated. A review of some recent works on the ignition of combustible gas mixtures by means of electric discharges and on the stabilization of the combustion is given by Starikovskaia [3].

An analysis of kinetic processes which are initiated by electric discharges and affect the ignition of combustible gas mixtures is rather complicated, because the discharge is accompanied by excitation of various degrees of freedom of the mixture molecules. The same problems complicate a comparative analysis of different types of electric-discharge systems. Depending on a value of the reduced electric field E/N in a particular discharge, different species of chemically active particles dominate the mixture. At large values of E/N in the discharge, most of the discharge energy goes into ionization and dissociation of molecules in the mixture [16, 17]. At relatively low values of E/N , there take place an effective excitation of the electronic states $O_2(a^1\Delta_g)$, $O_2(b^1\Sigma_g^+)$ [18, 19] and vibrational degrees of freedom of molecules [16, 17].

Apparently, we must first analyze the effect of different chemically active particles on the

characteristics of the ignition process. It is only after this that it will be possible to identify a set of particles and their ratios which have an optimal effect on ignition. It is only then that it will be possible to formulate the problem of determining the characteristics of electric discharges which enable one to produce the desired chemically active particles in optimal ratios.

1. THE EFFECT OF HYDROGEN AND OXYGEN ATOMS ON THE IGNITION OF H₂ : O₂ MIXTURES

A number of papers are available at present, which deal with the investigation of additions of chemically active radicals on the shift of temperature ignition limits [20 - 26] and on the times of induction [14, 15, 27-29] in hydrogen-containing and hydrocarbon mixtures. These investigations involved the use of UV radiation, electric discharge, electron beam etc. for obtaining the initial concentration of chemically active particles.

Nalbandyan [21] investigated the effect of UV photolysis on the ignition temperature of a stoichiometric hydrogen-oxygen mixture at pressure $P = 2$ to 30 torr. The experiments were performed in a quartz tube 2.7 cm in diameter, whose walls were treated with hydrofluoric acid. The radiation source was provided by a DC discharge in hydrogen, and the intensity of radiation was adjusted by varying the discharge current $I = 0.1 - 1$ A. A quartz membrane was used to identify a spectral region $\lambda \leq 175$ nm corresponding to Schumann-Runge continuum of absorption of oxygen.

The possibility was demonstrated of some lowering of the temperature ignition limit ΔT_g^* of H₂ : O₂ mixtures. For example, at $P = 20$ torr, the maximal value of ΔT_g^* was 27 K at the radiating discharge current of 1 A. The intensity of the UV radiation source in the range of $\lambda \leq 175$ nm was determined by the number of water molecules formed as a result of photolysis of H₂ : O₂ mixtures at room temperature. It was assumed that two atoms of oxygen are formed upon absorption of each radiation quantum and, with time, are converted to H₂O.

Nalbandyan [21] further investigated the effectiveness of chain chemical reactions depending on the initial gas temperature. This effectiveness is characterized by the chain length ϕ which was determined as the ratio of the rate of production of water molecules at a given gas temperature to the rate of production at $T_0 = 300$ K,

$$\phi = \frac{dH_2O}{dt} \bigg/ \left(\frac{dH_2O}{dt} \right)_{T=300}$$

As was already noted, the latter rate is defined by the intensity of the source of UV radiation. The experimental data of [21], as well as the results of calculation of the dependence of chain length ϕ on the gas temperature under the effect of radiation of discharge with current $I = 150$ mA, are given in Fig.1. One can see in the figure that the chain pattern of the process starts showing up only in the region of temperatures close to the ignition limit. At low temperatures, the production of radicals as a result of UV photolysis leads only to heating of the mixture.

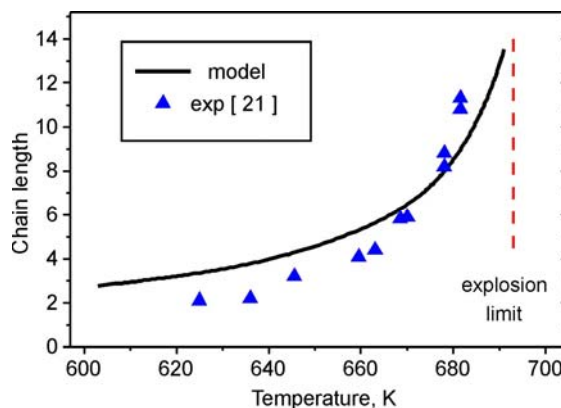


Fig. 1. The chain length in a mixture of H₂ : O₂ = 2 : 1 at $P = 20$ torr and discharge current $I = 150$ mA as a function of the initial temperature of gas: the points indicate the experiment of [21], the curve - calculation, and the dashed curve - the temperature limit of autoignition for the conditions of [21].

The absorption of radiation by oxygen in the region of Schumann-Runge continuum is accompanied by dissociation of O₂, with one of the atoms being formed in the excited O(¹D) state [30],
 $O_2(X^3\Sigma_g^-) + h\nu \rightarrow O(^3P) + O(^1D)$.

This results in a rapid production of H and OH radicals during the quenching of O(¹D) atoms by hydrogen [31],

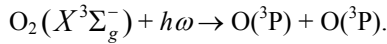


The results of the impact of UV radiation were simulated by introducing a source of atomic oxygen (O(³P) + O(¹D)) of intensity $\nu_{O_2} \cdot [O_2]$. The calculation results given in Fig. 1 correspond to the value $\nu_{O_2} = 4.5 \cdot 10^{-5} \text{ s}^{-1}$ and, as one can see, agree with the experimental data. The existing differences may be associated with the fact that, under conditions being considered ($P = 20$ torr), an important part is played by heterogeneous reactions on the discharge tube surface [32]. These processes are not known well enough at present. In order to increase the importance of the part played by the volumetric reactions, it is necessary to make a transition to higher pressures. However, problems

arise in this case, which are associated with the nonuniformity of absorption of radiation by oxygen in the Schumann-Runge continuum.

Many experiments on the initiation of ignition of combustible mixtures by means of UV photolysis were conducted by using the focused laser radiation [22-24]. Most frequently in these experiments, a breakdown a fast gas heating occur on the focus of the laser beam with the resulting formation of a high-temperature region, where the combustion is then initiated. In this case, the probability for the ignition depends substantially on characteristic dimensions of this high-temperature region, since a critical question is of whether the mixture has time to ignite during its cooling by heat conduction. Such experiments with laser radiation have much in common with the combustion initiation by spark electric discharges [33].

Lavid et al. [24] used the focused radiation of an ArF laser ($\lambda = 193$ nm) for igniting atmospheric-pressure $H_2 : O_2$ mixtures. During the pulse, most of the energy of absorbed photons is spent for dissociation of oxygen molecules rather than for gas heating,



In this case, the temperature of mixture turns out to be below the limit of ignition, and reactions involving $O(^3P)$ and H atoms, OH radicals, and other play an important part in the initiation of combustion. The transverse dimension of the excitation zone in the focused laser beam was relatively small ($R \approx 0.4$ mm [24]). Therefore, similar to [22, 23], the probability of ignition was affected both by the diffusion “departure” of radicals from the excitation zone and by the rate of cooling down of this region due to heat conduction. Figure 2 gives the minimal values of the initial concentration of $O(^3P)$ atoms, required for the ignition of a stoichiometric $H_2 : O_2$ mixture at $P = 1$ atm, as a function of the initial gas temperature. Note that both the calculation (curves) and experimental (symbols) results [24] indicate that very significant (in excess of 10^{16} cm^{-3}) concentrations of oxygen atoms are required for the ignition of this mixture at temperatures below the ignition limit. In view of the small size of the excitation zone, the temperature limit of ignition of the mixture under consideration is higher than 880 K [33]. The results of calculations performed within a uniform 0-D model [47] (curve 1) lie markedly below the experimental data. As was already mentioned, this is indicative of the important part played by diffusion and heat conduction processes in determining the ignition temperature.

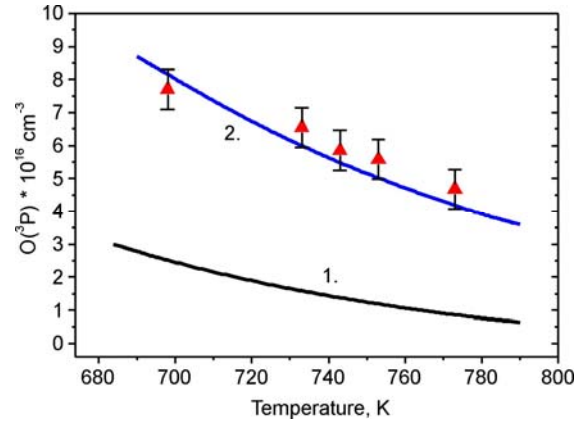


Fig. 2. The minimal initial concentration of $O(^3P)$ atoms required for the ignition of a stoichiometric $H_2 : O_2$ mixture at $P = 1$ atm as a function of gas temperature: the symbols indicate the experiment of [24], and the curve indicates the calculation by the 0-D model (curve 1) and by the 1-D model (curve 2).

To analyse the effect of diffusive and thermal conductivity processes on determination of ignition temperature in $H_2 : O_2$ mixtures the comparison of calculation results executed in the frame of uniform (0-D) model and one dimensional (1-D) axisymmetric model has been performed. In the latter the corresponding diffusive terms for all considered components have been inserted in the balance equation. The values of diffusive coefficients D_k and their dependences on temperature were estimated using the data [36]. Apart from the thermal conductivity term was included in the equation for temperature. In the calculation of thermal conductivity coefficient λ_{ef} of multicomponent mixture the following expression has been used:

$$\lambda_{ef} = 0.5 \cdot \left(\sum_k \lambda_k X_k + \left(\sum_k \frac{X_k}{\lambda_k} \right)^{-1} \right), [36]$$

where the X_k is the mole fraction of main components, and λ_k are the corresponding values of thermal conductivity coefficients.

In calculations in the frame of one dimensional (1-D) model the initial distribution of $O(^3P)$ atom density and gas temperature were assumed as Gaussian with $R_0 = 0.4$ mm [24]. Then, under consideration of this simulation the values of temperature and atom concentrations at laser channel axis are given.

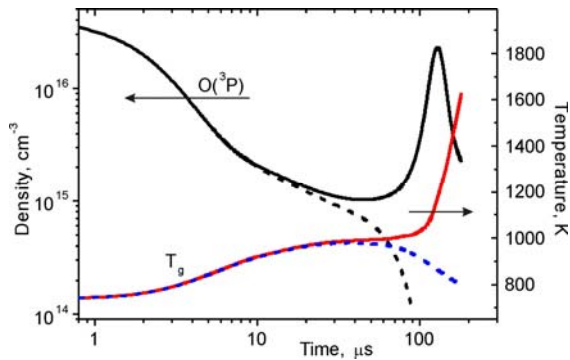
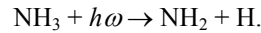


Figure 3. Temporal dynamics of the temperature and the density of atoms $O(^3P)$ at the axis for a stoichiometric $H_2 : O_2$ mixture at $P = 1$ atm, $T_0 = 740$ K and initial concentrations: $[O]_0 = 5.6 \cdot 10^{16} \text{ cm}^{-3}$ (solid lines) u $[O]_0 = 5.5 \cdot 10^{16} \text{ cm}^{-3}$ (dashed lines).

As example, in Figure 3 the simulation results (in frame of 1-D model) of the time dependence of O atom concentration and temperature at laser channel axis in mixture of $H_2 : O_2 = 2 : 1$ at $P = 1$ atm and $T_0 = 740$ K with two different initial $O(^3P)$ concentrations ($[O]_0 = 5.6 \cdot 10^{16} \text{ cm}^{-3}$ and $[O]_0 = 5.5 \cdot 10^{16} \text{ cm}^{-3}$) are demonstrated. As one can see in spite of very small change of $[O]_0$, in first case the ignition of mixture occurs, but in the second one does not take place. This example is evidence that in calculations described above the accuracy of determination of $O(^3P)$ concentration needed for mixture ignition is rather high.

The minimal atom concentrations $[O(^3P)]_{\min}$, needed for ignition of $H_2 : O_2$ mixture in the range of $T_0 = 690 - 790$ K are presented in Figure 2. Apparently, the 0-D model (curve 1) and 1-D model (curve 2) obtained results differ from each other in 3-5 times. That difference increases with gas temperature. The 1-D model results (curve 2) agree with experimental data [24]. The shown calculation results were executed in conditions of stoichiometric mixture of $H_2 : O_2 = 2 : 1$. Similar results were obtained for other $[H_2]/[O_2]$ values as well (in the work [24] that ratio was varied from 0.4 to 4).

The experimental investigation of kinetic mechanisms of the effect of radical's initial density on the ignition time requires the development of a rather uniform and extended excitation region. Such experiments were described by Chou and Zukowski [25], who investigated the pulsed UV photolysis of stoichiometric $H_2 : O_2$, $H_2 : \text{air}$, and $CH_4 : O_2$ mixtures with additions of molecules of ammonia NH_3 . The initial temperature of mixture was 300 K, with pressure $P = 1$ atm. The radiation of ArF laser on wavelength $\lambda = 193$ nm, which is effectively absorbed by NH_3 molecules, was used for production of radicals [30],



The power of laser radiation was sufficient for decomposition of all available molecules of ammonia. This provided for spatially uniform production of radicals of preassigned initial concentration equal to the concentration of NH_3 . Chou and Zukowski [25] assumed that the reactivity of the NH_2 radicals being formed is relatively low; therefore, the main result of the impact of UV radiation on the characteristics of ignition is the production of atomic hydrogen with concentration $[H]_0 = [NH_3]$.

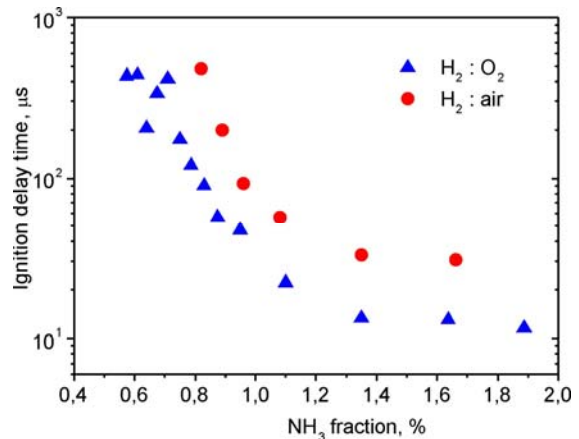
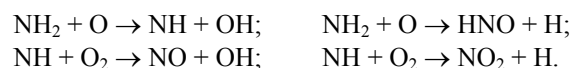


Fig. 4. The induction period for stoichiometric mixtures of $H_2 : O_2$ and $H_2 : \text{air}$ excited by a pulsed source of UV radiation as a function of the initial fraction of NH_3 molecules in the mixture: $P_0 = 1$ atm, $T_0 = 300$ K; the symbols indicate the experiment of [25].

Figure 4 gives the ignition times of stoichiometric mixtures of $H_2 : O_2$ and $H_2 : \text{air}$ at $P = 1$ atm and $T_0 = 300$ K as a function of the fraction of NH_3 in the mixture [25]. The ignition of a 2- $H_2 : O_2$ mixture could be experimentally accomplished for a fraction of ammonia molecules of 0.6 - 0.7%. The calculation results indicate that initial concentrations of hydrogen atoms $[H]_0/M = [NH_3]/M \geq 2\%$, are required for the ignition of the mixture under consideration. This is three times higher than the experimentally obtained values. The reason for discrepancy between the calculation and experimental data may be as follows. Indeed, NH_2 radicals formed as a result of UV photolysis of ammonia hardly react with O_2 and H_2 molecules. However, a fairly fast reaction of NH_2 with $O(^3P)$ atoms may occur, which causes the emergence of additional channels of production of hydrogen radicals H and OH, as well as nitrogen oxides [34],



The latter is especially important because it is known [20, 33 and 35] that nitrogen oxides cause a significant reduction of the induction times and the ignition temperature limit of high-pressure hydrogen-oxygen and hydrogen-air mixtures. Therefore, Chou and Zukowski [25] managed to accomplish the ignition of hydrogen-oxygen mixtures (with additions of ammonia) at atmospheric pressure and $T_0 = 300$ K as a result of their nonequilibrium excitation by ArF laser radiation. However, the use of NH_3 additions results in a significant complication of the ignition kinetics of $\text{H}_2 : \text{O}_2$ mixtures, which makes the interpretation of the results quite difficult.

Starikovskaia et al. [28] investigated the effect of pulsed UV photolysis, caused by the ArF laser radiation, on the induction times of $\text{O}_2 : \text{N}_2\text{O} : \text{H}_2 : \text{Ar} = 3 : 11 : 32 : 54$ mixture. The absorbed energy was $W = 2$ to 4 mJ/cm^3 , with $P_0 = 0.3 - 0.7$ atm and $T_0 = 850 - 1300$ K. The measurements were performed in a shock tube behind reflected shock wave. The induction times were determined by the dynamics of radiation intensity of OH^* excited state. In the mixture under investigation, the radiation at $\lambda = 193$ nm is largely absorbed by N_2O molecules [30],

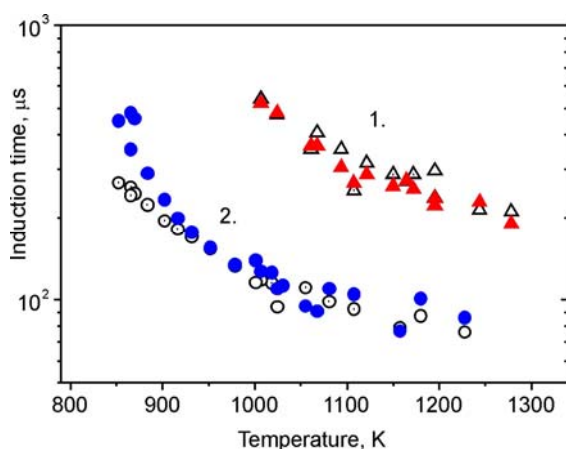
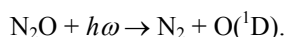


Fig. 5. The time of induction for a mixture of $\text{O}_2 : \text{N}_2\text{O} : \text{H}_2 : \text{Ar} = 3 : 11 : 32 : 54$ ($P = 0.3 - 0.6$ atm) as a function of initial temperature: (1) autoignition, (2) impact of UV radiation; solid symbols - experiment, hollow symbols - calculation [28].

Therefore, the impact of the ArF laser pulse leads to the production of excited atoms whose concentration under the conditions of [28] reaches a value of $[\text{O}(^1\text{D})]/[\text{M}] = (1 \pm 0.5) \cdot 10^{-3}$. The results of such impact are given in Fig. 5 which shows the dependences of the induction times for the given mixture on the initial temperature, experimentally obtained both in the mode of autoignition (symbols) and in view of UV

photolysis (points). One can see in Fig. 5 that the use of UV radiation makes for a significant reduction of the induction times and for the lowering of the ignition temperature limit by 100 - 150 K. At the same time, the laser pulse proper is capable of gas heating by no more than 5 - 10 K.

Starikovskaia et al. [28] used unfocused laser radiation to accomplish a fairly uniform excitation of combustible mixture. The concentration of excited atoms being formed was determined by the results of measurements of absorbed energy. Additions of $\text{O}(^1\text{D})$ make it possible to significantly reduce the induction times. The simulation results of [28] agree with the experimental data (Fig. 5); however, the required additions of $\text{O}(^1\text{D})$ atoms $[\text{O}(^1\text{D})]/[\text{M}] = 3 \cdot 10^{-4}$ turn out to be approximately three times less than the measured values.

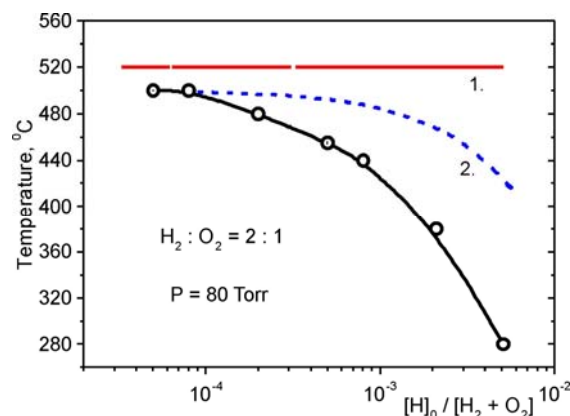


Fig. 6. The ignition temperature of a mixture of $\text{H}_2 : \text{O}_2 = 2 : 1$ as a function of the fraction of hydrogen atoms at $P = 80$ torr. The points indicate calculation [26], curve 1 - temperature limit of ignition for the given conditions [33], and curve 2 - variation of the ignition temperature because of autoheating of the mixture as a result of recombination of hydrogen atoms.

Seleznev et al. [26] performed numerical investigations of the effect of hydrogen and oxygen atoms additions on the ignition temperature of a stoichiometric $\text{H}_2 : \text{O}_2$ mixture in a wide range of pressures ($P = 1$ to 10^4 torr). Given by way of example in Fig. 6 are the results of calculation of the shift of ignition limits as a function of the initial fraction of hydrogen atoms at $P = 80$ torr (points) [26]. Note that the experimentally obtained value of the ignition temperature of unexcited mixture (curve 1) given in [33] somewhat exceeds the calculated values. Also given in Fig. 6 for comparison are our estimates of the variation of ignition temperature because of heating of the mixture as a result of recombination of hydrogen atoms H_0 . One can see that additions of hydrogen atoms in excess of $3 \cdot 10^{-3}$ are required for a more significant (over 200 K) reduction of the ignition

temperature limit. In so doing (according to the data of [26]), the effect of heating of the mixture is of significant importance because it leads to an increase in the effectiveness of chain chemical reactions (see Fig. 1) initiated by additions of H.

A fairly uniform excitation of a mixture may be accomplished by using short-pulse high-current discharges [37] which propagate in the form of a fast ionization wave (FIW). Owing to the high values of reduced field E/N , which may be realized under these conditions, the most part of electron energy is delivered for the ionization and dissociation of mixture molecules.

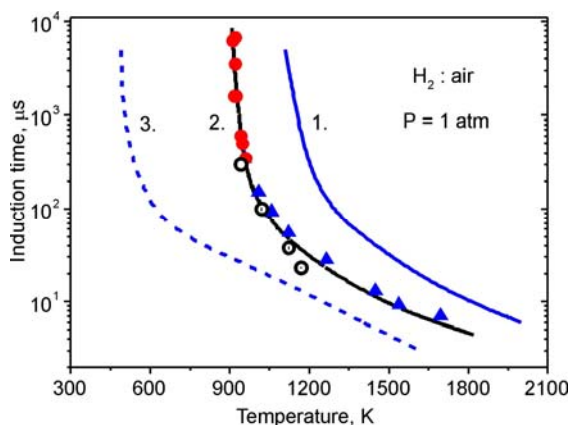


Fig. 7. The temperature dependence of the time of induction of a stoichiometric mixture of H_2 : air, $P = 1$ atm. Curves 1 and 2 indicate autoignition, curve 3 - additional excitation by a high-current discharge; symbols, experiment [35, 38]; curves 1 and 3, calculation [29].

Starikovskii [29] gives the results of theoretical investigations of the induction times dependence on the initial temperature for stoichiometric H_2 : O_2 , H_2 : air, and CH_4 : air mixtures. Comparison is made of the ignition delay times of these mixtures with and without a pulsed high-current discharge impact. Figure 7 gives the results of calculations of [29] for a stoichiometric H_2 : air mixture at $P = 1$ atm. Under these conditions, according to [29], the use of additional discharge excitation makes it possible to reduce the ignition temperature in the vicinity of the ignition limit by 500 - 600 K. Also given in this figure are the experimental data on the induction times of this mixture borrowed from [35, 38]. These data differ very significantly from the calculation results of [29] for the times of autoignition. Therefore, it is difficult to make the final inference about the degree of temperature ignition limit reduction of using the numerical simulation results of [29].

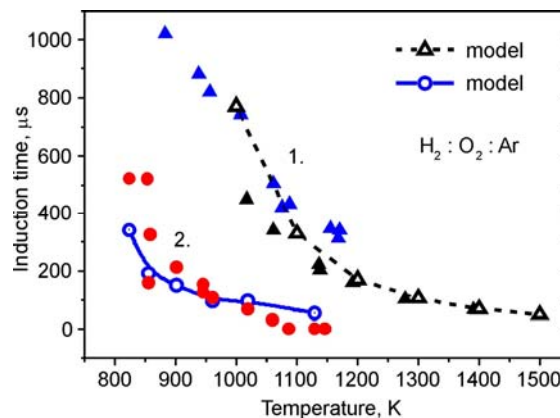
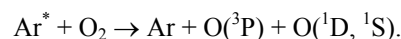


Fig. 8. The time of induction for a stoichiometric mixture of H_2 : O_2 : $Ar = 12 : 6 : 82$ ($P = 0.3-0.6$ atm) as a function of initial temperature: (1) autoignition, (2) in view of the impact of discharge; solid symbols, experiment [4]; hollow symbols, calculation [4].

Bozhenkov et al. [4] performed experimental investigations of the effect of a fast ionization wave on the induction times of H_2 : O_2 : $Ar = 12 : 6 : 82$ mixture in the temperature range of $T_0 = 800 - 1400$ K ($P_0 = 0.25 - 0.75$ atm). The discharge input energy did not exceed 30 - 50 mJ/cm³. The measurement results given in Fig. 8 indicate that the use of this discharge enables one to reduce the ignition temperature by 200 - 250 K. Bozhenkov et al. [4] used the results of measurements of the dynamics of electric field $E(t)$ for the numerical simulation of the discharge impact and for the determination of the hydrogen and oxygen atoms density produced in the discharge. The obtained concentrations of atoms were used as the initial conditions in calculating the ignition delay time of the considering mixture. The results of simulation of autoignition and of the effect of discharge on the induction time agree with the experimental data (Fig. 8).

Note that Bozhenkov et al. [4] described the production of hydrogen and oxygen atoms in the discharge in view of only the dissociation of H_2 and O_2 molecules by electron impact. However, in a mixture with more than 80% Ar (H_2 : O_2 : $Ar = 12 : 6 : 82$) at high E/N values, a very significant additional channel of dissociation is provided by the processes of quenching of metastable electronically excited atoms of $Ar^* = Ar(^3P_0, ^3P_2)$, for example [39],



The inclusion of these reactions must more than double the initial atom concentration and reduces the predicted induction delay times accordingly. In this case, agreement with the experimental data may be impaired.

Therefore, the addition of oxygen and hydrogen atoms to a combustible mixture enables one to significantly reduce the induction times and the ignition temperature of mixtures. However, in the zone of relatively low initial temperatures, the shift of the ignition limit is largely associated with the heating of mixture due to the recombination of the atomic particles being added. In so doing, the nonequilibrium character of the impact hardly shows up. Therefore, it is of interest to search for other forms of nonequilibrium excitation (for example, the introduction of non-equilibrium concentrations of electronically- and vibrationally excited particles).

2. THE EFFECT OF $O_2(a^1\Delta_g)$ ON THE IGNITION DELAY TIME AND THE FLAME PROPAGATION VELOCITY IN HYDROGEN-OXYGEN MIXTURES

Investigations have been continued recently of the processes which define the initiation of combustion and detonation in combustible mixtures in the presence of excited oxygen molecules $O_2(a^1\Delta_g)$ [40-46]. In [41, 42], it was suggested (apparently for the first time) to use reactions involving $O_2(a^1\Delta_g)$ for explaining the observed increase in the rate of flame propagation in $H_2 : O_2$ mixtures after the impact of electric discharge. This phenomenon was experimentally investigated by Basevich and Kogarko [40, 41] who used a glow discharge ($I = 5$ to 85 mA) for exciting a flow of molecular oxygen. After the discharge, molecular hydrogen was added to the flow. The resultant mixture contained $7\% H_2 + 93\% O_2$ and the products of impact of the discharge, namely, atoms of $O(^3P)$ and molecules of ozone and singlet oxygen $O_2(a^1\Delta_g)$ and $O_2(b^1\Sigma_g^+)$ (mixture pressure $P_0 = 50$ torr, $T_0 = 293$ K). This

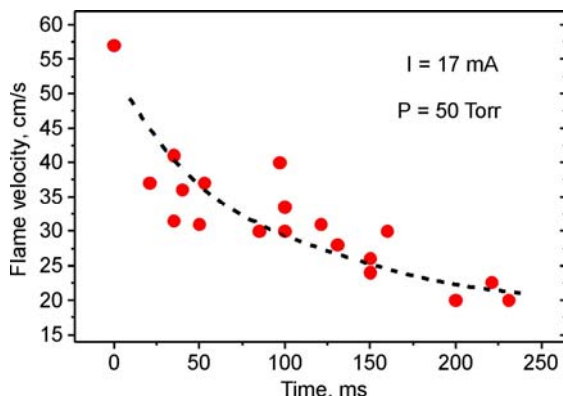


Fig. 9. Flame propagation velocity vs. the duration of a pause between the end of the discharge and the ignition time of a $7\% H_2 : 93\% O_2$ mixture at $P = 50$ Torr and discharge current $I = 17$ mA [41].

mixture was ignited by a pulsed spark discharge with subsequent measurement of the normal rate of flame propagation and of the axial profile of gas temperature.

In the case of discharge currents higher than 17 mA, the velocity of combustion wave almost doubled. In so doing, the gas temperature in the discharge increased by no more than $5 - 10$ K. The measurement results of [41] are given in Fig. 9. For current $I = 17$ mA, the characteristic time during which the discharge has a significant effect on the flame velocity is approximately 0.2 s. Note that the pause increase is accompanied by a significant variation of the content of active particles before the front of combustion wave with an almost unchanged concentration of stable products (ozone and nitrogen oxides).

The characteristic time of loss of $O(^3P)$ atoms is defined by their conversion to ozone and amounts to several milliseconds under conditions of [41]. The quenching of $O_2(a^1\Delta_g)$ largely occurs on O_2 molecules and in reactions with ozone with a characteristic time of 0.15 s, which is comparable with the measured time of impact of discharge [41]. The calculation results of [42] supported the assumption that the effect of glow discharge in oxygen on the flame propagation velocity is most likely associated with the involvement in combustion of the molecules of $O_2(a^1\Delta_g)$ produced in the discharge.

In papers [44-46], the results from theoretical research of the impact of $O_2(a^1\Delta_g)$ on the ignition delay time of $H_2 : O_2 : O_2(a^1\Delta_g)$ mixtures are presented. There was shown a possibility of a sufficient reduction in the temperature threshold of ignition and in the induction times of hydrogen-oxygen mixtures when the fraction of singlet oxygen (SDO) is $[O_2(a^1\Delta_g)/O_2] \geq 1\%$. One of the

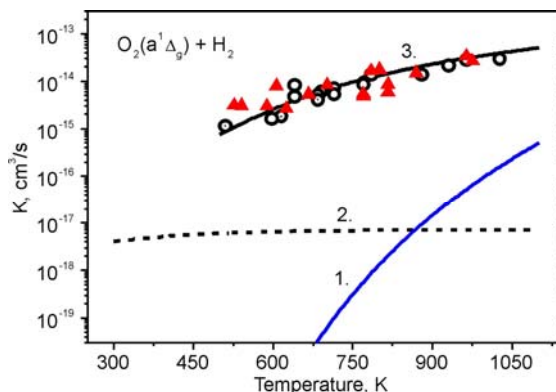


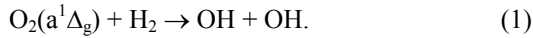
Figure 10. Dependences of reaction rate coefficients on the temperature: 1 - $O_2(a^1\Delta_g) + H_2 \rightarrow 2.OH$ [45]; 2 - $O_2(a^1\Delta_g) + H_2 \rightarrow O_2 + H_2$ [49]; 3 - experimental data [50].

Table 1. The reactions with the $O_2(a^1\Delta_g)$, $O_2(b^1\Sigma_g^+)$ participation in $H_2 : O_2$ mixtures

No	Reaction	Rate coefficient, cm^3/s	Reference
1.	$O_2(a^1\Delta_g) + H_2 \rightarrow OH + OH$	$2.8 \cdot 10^{-9} \cdot \exp(-17906/T)$	[45]
2.	$O_2(a^1\Delta_g) + H_2 \rightarrow O_2 + H_2$	$4.5 \cdot 10^{-18} \cdot (T/300)^{0.5}$	[49]
3.	$O_2(a^1\Delta_g) + H \rightarrow O(^3P) + OH$	$\alpha \cdot 6.5 \cdot 10^{-11} \cdot \exp(-2530/T)$	[47*]
4.	$O_2(a^1\Delta_g) + H \rightarrow O_2 + H$	$(1-\alpha) \cdot 6.5 \cdot 10^{-11} \cdot \exp(-2530/T)$	[47*]
5.	$O_2(a^1\Delta_g) + HO_2 \rightarrow O_2 + HO_2^*$	$2.0 \cdot 10^{-11}$	[55]
6.	$O_2(a^1\Delta_g) + O_2 \rightarrow O_2 + O_2$	$2.2 \cdot 10^{-18}$	[48]
7.	$O_2(a^1\Delta_g) + O_2(a^1\Delta_g) \rightarrow O_2(b^1\Sigma_g^+) + O_2$	$2.4 \cdot 10^{-17}$	[48]
8.	$O_2(b^1\Sigma_g^+) + H_2 \rightarrow O_2(a^1\Delta_g) + H_2$	$1.0 \cdot 10^{-12}$	[48]
9.	$O_2(b^1\Sigma_g^+) + N_2 \rightarrow O_2(a^1\Delta_g) + N_2$	$4.9 \cdot 10^{-15} \cdot \exp(-253/T)$	[48]
10.	$O_2(b^1\Sigma_g^+) + O_2 \rightarrow O_2(a^1\Delta_g) + O_2$	$4.0 \cdot 10^{-17}$	[48]

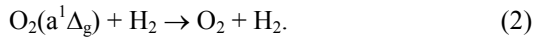
[*] The coefficient $\alpha \cong 0.2$ is determined in the given work (see below).

important processes that determine the efficiency of the impact of SDO on the ignition of combustible mixtures is the following:



This process can result in a sufficiently more rapid production of chemically active particles by the adding of SDO. The rate of reaction (1) sufficiently increases with the rise of gas temperature. The corresponding dependence $k_1(T)$ got in [45] is shown in Fig. 10 (curve 1).

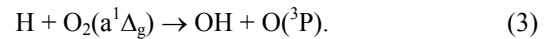
Along with this, quenching of $O_2(a^1\Delta_g)$ by molecules of hydrogen is also possible:



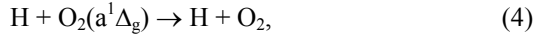
The rate of reaction (2) at $T = 300$ K was measured in several experiments (see review [48]). The results from calculations of the dependence of the rate of this reaction on temperature are given in [49]. The approach adopted in this work is based on assumptions that the spin ban on the transition $O_2(a^1\Delta_g) \rightarrow O_2(X^3\Sigma_g^-)$ is withdrawn by taking into account spin-orbit interaction inside the O_2 molecule, the kinetic energy of relative motion is a lot more than the potential energy of interaction of molecules and the transition probability is small. The last two conditions allow us to apply perturbation theory. The results from calculation of the dependence $k_2(T)$ [49] are shown in Fig. 10 (curve 2). Also here (curve 3), the results of

measuring the effective quenching rate of $O_2(a^1\Delta_g)$ got in paper [50] are also presented in the temperature range $T = 500 - 1000$ K. In this paper the temporal dynamics of $O_2(a^1\Delta_g)$ quenching in a $H_2 : O_2$ mixture (with the fraction of hydrogen less than 2-3%) was measured. In [50], the main mechanism of SDO quenching was associated with reaction (2). As it is seen from Fig. 10, the experimentally obtained rates of $O_2(a^1\Delta_g)$ losses far exceed both the rate of reaction $k_1(T)$ [45] and the rate of SDO deactivation $k_2(T)$ [49]. One of the reasons for such difference can be the fact that the analysis of experimental results [50] does not take into account the specifics of considered mixture in which the chain chemical reactions can proceed in the temperature range of $T_0 = 500 - 1000$ K. As a result, particles that are actively involved in the SDO deactivation are produced, for example, H and HO_2 . Therefore, a further numerical analysis of experimental results [50] is necessary to determine the possible reasons for the high rate of $O_2(a^1\Delta_g)$ losses under these conditions.

Another important process for the combustion problems is the following:

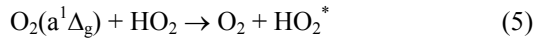


This reaction was investigated experimentally in [51, 52] in the temperature ranges of $T = 300 - 431$ K and $T = 520 - 930$ K, correspondingly. The total rate of processes (3) and (4) was measured in these papers:



and, according to paper [52], reaction (3) is dominant. However, it was shown in more recent studies [53] that $k_3 / (k_3 + k_4) \leq 0.1$ in the temperature range of $T = 300 - 437$ K. Thus, the ratio between the reaction rates $k_3 : k_4$ remains unknown.

In [53, 54], the following process was involved to explain the experimental results concerning the dynamics of the concentration of atomic hydrogen when $\text{O}_2(a^1\Delta_g)$ molecules were added to a mixture of $\text{H} : \text{H}_2 : \text{O}_2$:



The rate of this reaction is $k_5 = 2.0 \cdot 10^{-12} \text{ cm}^3/\text{s}$, according to [53, 54]. In paper [55], higher rates of SDO quenching by HO_2 molecules were reported which amounted to $k_5 = 3.0 \cdot 10^{-11} \text{ cm}^3/\text{s}$. Consequently, reaction (5) can also effect the dynamics of $\text{O}_2(a^1\Delta_g)$ and the ignition time of $\text{H}_2 : \text{O}_2 : \text{O}_2(a^1\Delta_g)$ mixtures.

In [47], a model of ignition of hydrogen-oxygen mixtures is described. In this section, the system of reactions [47] was supplemented by processes involving singlet oxygen molecules $\text{O}_2(a^1\Delta_g)$ and $\text{O}_2(b^1\Sigma_g^+)$. These processes are given in Table 1. The aim of this investigation is to analyze the results from the named experiments and to explain the discrepancy of obtained there data. Based on this analysis, the recommendations concerning the rates of the main processes involving $\text{O}_2(a^1\Delta_g)$ (1-5) will be provided which will make it possible to estimate the impact of SDO molecules on the induction time and ignition threshold shift for $\text{H}_2 : \text{O}_2$ mixtures.

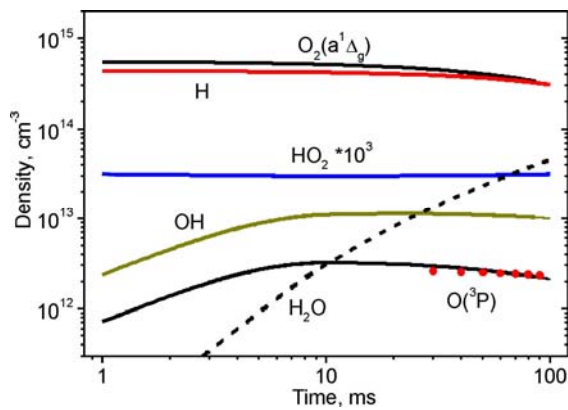


Figure 11. Dynamics of the main components of the mixture $\text{H}_2 : \text{O}_2 : \text{O}_2(a^1\Delta_g) : \text{Ar}$ at $T = 300$ K and at the ratio of reaction rates $k_3 : k_4 = 2 : 8$. Dots correspond to the calculated values of $2.17 \cdot [O(^3P)]$ at $\text{O}_2(a^1\Delta_g) = 0$.

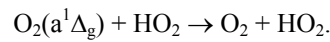
The initial concentrations of components are: $\text{Ar} = 9.1 \cdot 10^{15} \text{ cm}^{-3}$; $\text{O}_2 = 5.3 \cdot 10^{15} \text{ cm}^{-3}$; $\text{H}_2 = 7.4 \cdot 10^{14} \text{ cm}^{-3}$; $\text{H} = 4.4 \cdot 10^{14} \text{ cm}^{-3}$ and $\text{O}_2(a^1\Delta_g) = 5.5 \cdot 10^{14} \text{ cm}^{-3}$.

In all the further considered experiments (except in cases explicitly stated) studies were carried out in a flow reactor with a system of flows mixing. The $\text{O}_2(a^1\Delta_g)$ molecules were produced, typically, in a microwave discharge (in oxygen or $\text{O}_2 : \text{Ar}$ or $\text{O}_2 : \text{He}$ mixtures). The $\text{O}(^3P)$ atoms, which are also produced in the discharge, were removed in reactions with mercury oxide HgO , which coated the walls of the tube. Hydrogen atoms were produced in a microwave discharge in argon (or helium) with the admixture of H_2 .

In [51], the quenching of the $\text{O}_2(a^1\Delta_g)$ molecules by atomic hydrogen was studied in a mixture of $\text{H}_2 : \text{O}_2 : \text{Ar}$ at $P = 0.3 - 0.9$ torr. The experiments were conducted both in the presence of $\text{O}(^3P)$ atoms and with the removal of them. After mixing the flows of excited hydrogen and oxygen, dynamics of the variation of O , H , and also OH and $\text{O}_2(a^1\Delta_g)$ densities was studied using the electron-paramagnetic-resonance (EPR) spectrometer. Based on these data, the rate of $\text{O}_2(a^1\Delta_g)$ deactivation by the hydrogen atoms ($k_3 + k_4$) was determined at $T = 300 - 431$ K. To reduce the probability of heterogeneous losses of active particles, the tube walls were covered with orthoboric acid. As a result, it was achieved that the reactions at the surface had practically no effect on the dynamics of the main studied components and this was verified experimentally.

As an example, Fig. 11 shows the results from calculating the dynamics of the main components of the mixture which has the following initial composition: $\text{Ar} = 9.1 \cdot 10^{15} \text{ cm}^{-3}$, $\text{O}_2 = 5.3 \cdot 10^{15} \text{ cm}^{-3}$, $\text{H}_2 = 7.4 \cdot 10^{14} \text{ cm}^{-3}$, $\text{H} = 4.4 \cdot 10^{14} \text{ cm}^{-3}$, $\text{O}_2(a^1\Delta_g) = 5.5 \cdot 10^{14} \text{ cm}^{-3}$, $T_0 = 300$ K. Under these conditions the main losses of SDO molecules occur in the reactions with H atoms, the decay of $\text{O}_2(a^1\Delta_g)$ being monoexponential [51]. It is therefore necessary that the hydrogen number density $\text{H}(t)$ varies only slightly in time. As it is seen from results of calculations presented in Fig. 11, this condition is fulfilled.

In [53], another mechanism of SDO quenching associated with reaction (5) was proposed to explain the experimental results [51]:



According to the calculations given in Fig. 11, the number density of $\text{HO}_2(t)$ within the considered time interval remains practically constant, being $\cong 3 \cdot 10^{10} \text{ cm}^{-3}$ total. In this case, the frequency of $\text{O}_2(a^1\Delta_g)$ quenching in the reaction (5) does not exceed $\nu_a \leq 0.6 \text{ s}^{-1}$, which is much lower than the experimentally observed value for these conditions $\nu_a \cong 8 \text{ s}^{-1}$ [51]. So, the proposed in [53] mechanism of $\text{O}_2(a^1\Delta_g)$ quenching is enabled in conditions of experiment [51].

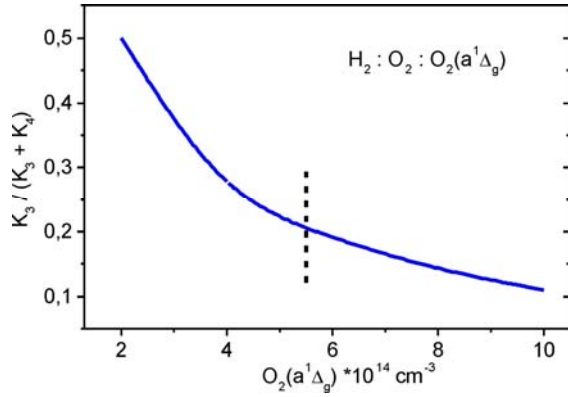


Figure 12. Relative fraction of the reaction (3) ($k_3/(k_3 + k_4)$) versus the concentration of admixed $O_2(a^1\Delta_g)$ molecules for the conditions of Fig. 11. Dashed curve corresponds to the measured in [51] concentration $O_2(a^1\Delta_g) = 5.5 \cdot 10^{14} \text{ cm}^{-3}$.

It was also shown in [51] that the concentration of atomic oxygen is increased under these conditions by adding molecules of $O_2(a^1\Delta_g)$. These data can be used to determine the fractions of reaction channels (3) and (4). According to [51], the addition of $O_2(a^1\Delta_g)$ molecules with number density $5.5 \cdot 10^{14} \text{ cm}^{-3}$ to the studied mixture increases the concentration of atomic oxygen by a factor of 2.17. To receive in the calculations the value of $\xi = [O(^3P)]/[O(^3P)]_0 = 2.17$, it is necessary that the ratio of reaction rates $k_3 : k_4$ was about 2 : 8 (see Fig. 12). It is good to mention that taking into account the uncertainty associated with the heterogeneous recombination of atomic oxygen on the walls of the tube has practically no effect on the value of ξ (in the frequency range $\nu_{\text{get}} = 2 - 20 \text{ s}^{-1}$).

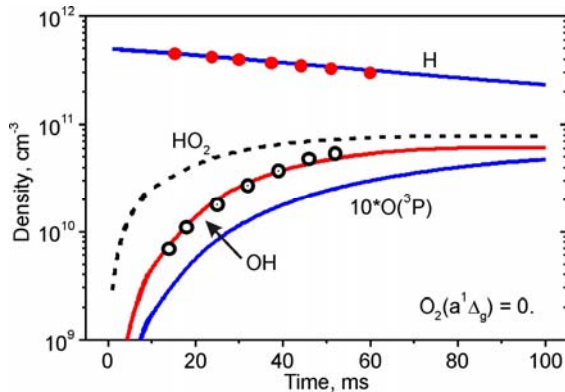


Figure 13. Temporal dynamics of the main components of the mixture $He = 3.3 \cdot 10^{16} \text{ cm}^{-3}$, $O_2 = 6.0 \cdot 10^{15} \text{ cm}^{-3}$, $H = 5.0 \cdot 10^{11} \text{ cm}^{-3}$, $O_2(a^1\Delta_g) = 0$ at $T = 300 \text{ K}$. Signs correspond to the experimental data [53].

The reaction $H + O_2(a^1\Delta_g) \rightarrow OH + O$ was also studied in [53] under the conditions $T = 295 - 423 \text{ K}$, $P = 0.5 - 7 \text{ torr}$. Here, as in [51], the mixing

of hydrogen and oxygen flows excited by microwave discharges took place. The densities of O and H atoms were measured by the absorption of diagnostic radiation having wavelengths $\lambda = 130.5 \text{ nm}$ and $\lambda = 121.6 \text{ nm}$, correspondingly. To determine the number density of OH radicals, there was used the laser-induced fluorescence (LIF) technique for the transition $OH(X^2\Pi, v = 0) \rightarrow OH(A^2\Sigma, v' = 0)$ ($\lambda = 308.2 \text{ nm}$). The content of $O_2(a^1\Delta_g)$ was determined by the value and dynamics of the photo ionization current occurring as the radiation of Ar lamp ($\lambda = 106.7 \text{ nm}$) was absorbed by SDO molecules.

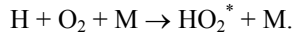
Figure 13 shows the experimental data [53] and the calculation results of the temporal dynamics of some components produced in a mixture of $He = 3.3 \cdot 10^{16} \text{ cm}^{-3}$, $O_2 = 6.0 \cdot 10^{15} \text{ cm}^{-3}$ and $H = 5.0 \cdot 10^{11} \text{ cm}^{-3}$ at $T = 300 \text{ K}$. The main reactions determining the change of density of H and $O(^3P)$ atoms and OH and HO_2 molecules in this case are the following:

- (6) $H + O_2 + M \rightarrow HO_2 + M$,
- (7) $H + HO_2 \rightarrow OH + OH$,
- (8) $OH + OH \rightarrow O + H_2O$,
- (9) $O + HO_2 \rightarrow OH + O_2$,
- (10) $O + OH \rightarrow H + O_2$.

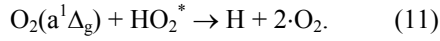
It should be noted that, in order to agree the results of calculations with the experimental data on the $OH(t)$ dynamics, the rate of reaction (7) was taken equal to $k_7 = 3.8 \cdot 10^{-11} \text{ cm}^3/\text{s}$ [53] which is 1.7 times less than recommended in [56]. Studies [53, 54] and [56] were performed using identical method and even with the same diagnostics (absorption of UV radiation and LIF). One of the reasons for the pointed out difference in results can be the errors in determining the absolute values of the number density of atomic H. As shown by our calculations, a decrease of the absolute values of $[H]_0$ concentration by approximately 22 - 25% allows to agree data on the value of k_7 , i.e. to describe measured in [53] dynamics of $OH(t)$ at a value of $k_7 = 6.6 \cdot 10^{-11} \text{ cm}^3/\text{s}$ [56].

Adding of $O_2(a^1\Delta_g)$ molecules to the mixture results in a sufficient increase in the concentration of produced $O(^3P)$ atoms, but it decreases OH concentration and the rate of hydrogen atoms losses [53, 54]. To explain such dynamics $H(t)$, we should assume the possibility of losses of HO_2 molecules in the reaction involving $O_2(a^1\Delta_g)$. The production of hydrogen atoms should also take place in this reaction.

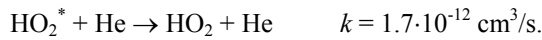
It is well-known that HO₂ molecules are produced in a highly excited state in the process (6):



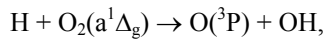
In this paper, the reaction of dissociation of produced in (6) HO₂^{*} molecules was additionally considered to explain the results [53, 54].



Additionally, the possible quenching of HO₂^{*} molecules was taken into account [54]:



The results from the comparison between calculated and experimental profiles of the main considered components are given in Fig. 14. The initial conditions were taken the same as in Fig. 13 but the addition of O₂(a¹Δ_g) = 2.6·10¹⁴ cm⁻³ was taken into account. The presented calculated curves were obtained at k₁₁ = 5.0·10⁻¹⁰ cm³/s. Just as in [51], the production of O(³P) atoms in these conditions is determined by the reaction (3):



which allows to determine the fraction of this channel $\alpha = k_3/(k_3 + k_4)$. The presented in Fig. 14 simulation results were obtained at $\alpha = 10\%$. It is good to mention that taking into account the possible errors in determining [H]₀ (mentioned above), i.e. decreasing of the initial number density of H by 25%, results in an increase of α up to 16 - 17%, which is close to the values obtained in the processing of experimental data [51].

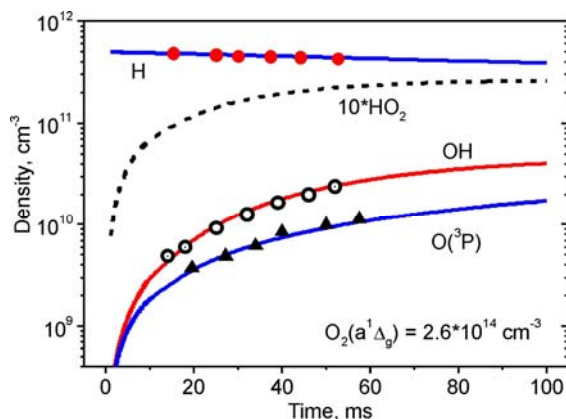


Figure 14. Temporal dynamics of the main components of the mixture for the conditions of Fig. 13 at O₂(a¹Δ_g) = 2.6·10¹⁴ cm⁻³. Signs correspond to the experimental data [53].

It is noted in [53] that the time profiles of O(³P) concentration change with increasing pressure of the mixture in the range of P = 0.1 - 7 torr. This may indicate that the factor α depends on pressure. However, other explanations of this phenomenon are possible (for example, reduction of the characteristic diffusion time and, correspondingly, the rate of heterogeneous losses of O(³P) with increasing pressure). Since the experimental data on the dependence of the concentration of atomic oxygen on pressure is not given in [53], then it is difficult to make a final conclusion on the causes of this phenomenon.

Thus, a comparative analysis of experimental results [51] and [53, 54] allows making the following conclusions. In [51], due to the low pressure of mixture, the degree of conversion of atomic hydrogen to HO₂ is low during the considered times. Therefore, the main contribution to the O₂(a¹Δ_g) quenching occurs due to the reactions with atomic H, and quenching by HO₂ can be neglected. In [53, 54] (due to higher pressure), atomic hydrogen is quickly converted to HO₂ and the reactions between SDO molecules and HO₂ became dominant (HO₂ can be produced in both the ground and excited states). The results from numerical simulations of data [51] and [53] concerning the production of atomic oxygen O(³P) point out that the fraction of reaction (3) is $\alpha = 15 - 20\%$, the value of α changing slightly in the temperature range T = 295 - 420 K.

Effect of O₂(a¹Δ_g) admixtures on the ignition of H₂ : O₂ mixtures

Here we analyze the effect of the obtained data on the rates of reactions involving singlet oxygen (3-5) on the ignition of hydrogen-oxygen mixtures. The calculations of the dependence of the ignition times of these mixtures on temperature were performed for different proportions of the processes involving O₂(a¹Δ_g). The rate constant of reaction (1) was taken similar as in [45] (Table 1) while the fraction of reaction (3) $\alpha = k_3 / (k_3 + k_4)$ was varied from 0.1 to 1. Figure 15 presents the results of calculations of ignition times of stoichiometric H₂ : air mixture (in the case of $\alpha = 0.2$) at P = 1 atm and at different initial concentrations of singlet oxygen O₂(a¹Δ_g) and O(³P) atoms. All results were compared with curve 1 obtained at concentrations [O₂(a¹Δ_g)₀] = [O(³P)]₀ = 0. Curve 2 corresponds to the initial ratio [O₂(a¹Δ_g)]/[O₂]₀ = 1%. As can be seen, the addition of 1% O₂(a¹Δ_g) does not lead to a sufficient decrease in the temperature threshold of ignition which distinguishes the obtained results from those given in papers [44, 45].

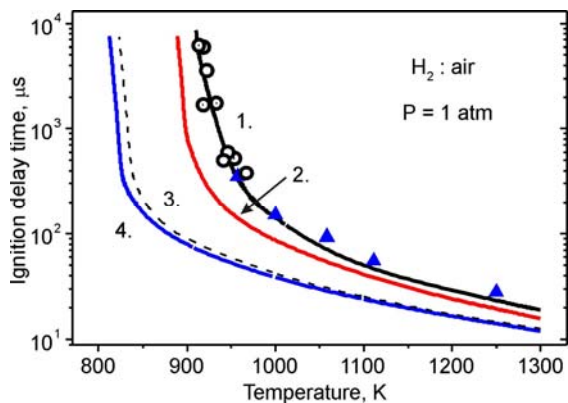


Figure 15. Dependences of the ignition time of a stoichiometric H_2 : air mixture on the initial temperature ($\alpha = 0.2$) at $P = 1$ atm and at the various admixtures of $O_2(a^1\Delta_g)$ and $O(^3P)$. Signs correspond to the experimental data [35, 38], curves correspond to the results of calculations without admixtures (curve 1) and with the admixtures of 1% $[O_2(a^1\Delta_g)]/[O_2]$ (curve 2); 0.1% $[O(^3P)]/[O_2]$ (curve 3) and 1% $[O_2(a^1\Delta_g)]/[O_2]$ + 0.1% $[O(^3P)]/[O_2]$ (curve 4).

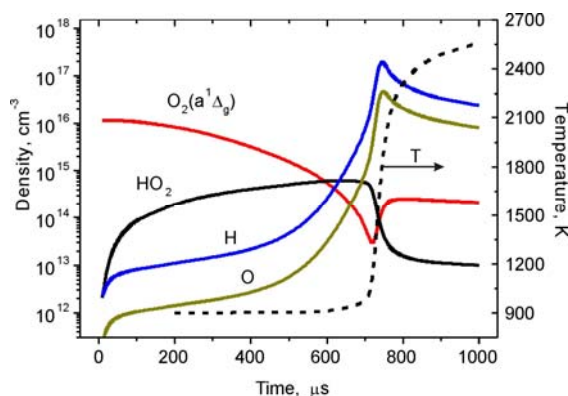


Figure 16. Temporal dynamics of the temperature and the concentrations of some components of a stoichiometric mixture of H_2 : air at $P = 1$ atm, $T_0 = 900$ K and $[O_2(a^1\Delta_g)]/[O_2]_0 = 1\%$.

Figure 16 shows calculations of the temporal dynamics of concentrations of the main components and the temperature of the H_2 : air mixture at $P = 1$ atm, $[O_2(a^1\Delta_g)]/[O_2]_0 = 1\%$, $T_0 = 900$ K. Number density of HO_2 molecules is $(1 - 6) \cdot 10^{14} \text{ cm}^{-3}$ over times of $t = 100 - 700 \text{ } \mu\text{s}$ which leads to a rapid quenching of $O_2(a^1\Delta_g)$ molecules by these particles. During the ignition time ($\tau_{ind} \cong 740 \text{ } \mu\text{s}$) the concentration of singlet oxygen is reduced by more than 100 times. Let us note some increase in the concentration of $O_2(a^1\Delta_g)$ molecules over times of $720 - 780 \text{ } \mu\text{s}$ which is associated with the intensification of the process: $O + OH \rightarrow H + O_2(a^1\Delta_g)$ (the rate constant $k(T)$ was taken from [44]). In addition, the rate of SDO quenching by the

HO_2 molecules decreases over these times as their density falls.

Thus, as follows from the calculations presented in Fig. 15, a relatively small effect of admixtures of $O_2(a^1\Delta_g)$ molecules on the ignition of hydrogen-oxygen mixtures occurs due to the rapid quenching of SDO by HO_2 molecules. These molecules are actively produced in H_2 : O_2 mixtures under considered conditions.

One of the main studied now sources of singlet oxygen is an electrical discharge [18], which allows to achieve a sufficiently high degree of excitation of $[O_2(a^1\Delta_g)]/[O_2]$. This is confirmed by experimental results ([18-19] etc.) obtained for different types of discharges. However, as SDO is generated in electric discharge, a great deal of energy can be expended for the dissociation of O_2 . In this case it is necessary to consider the total effect (admixtures of $O_2(a^1\Delta_g)$ and atomic oxygen) on the ignition of combustible mixtures.

An example of such a calculation is presented in Fig. 15 (curves 3 and 4) which shows the dependences of ignition times of H_2 : air mixture on initial temperature with admixtures of $[O(^3P)]/[O_2] = 0.1\%$ (curve 3) and with the joint effect of 1% $O_2(a^1\Delta_g)$ and 0.1% $O(^3P)$ (curve 4). Adding to the H_2 : air mixture 0.1% of oxygen atoms results in the sufficient decrease in the induction time and in the temperature threshold of ignition of considered mixture. Additional admixing of another 1% $O_2(a^1\Delta_g)$ to this mixture does not give noticeable improvement in ignition characteristics, as is evident from comparison of curves 3 and 4. That is, in presence of even a small initial concentration of atomic particles in a mixture, the effect of SDO admixtures is reduced compared with the unexcited mixture. The reason for this is that the addition of $[O(^3P)]_0$ atoms leads to reducing the role of reaction (1) as a process of chain initiation. The contribution of the reaction of chain branching (3) is also small at the given temperatures [47]. Therefore, under considered conditions, the effect of admixtures of singlet oxygen is reduced only to additional heating of the mixture in the process of its deactivation.

CONCLUSIONS

The results of our analysis lead to the following conclusions. The addition of oxygen and hydrogen atoms to a combustible mixture may result in a significant reduction of the induction delay time of H_2 : O_2 mixtures. Such reduction may be attained with a relative concentration of additions exceeding 10^{-3} . The introduction of atomic particles provides a further possibility of reducing the ignition temperature of mixtures. However, this effect shows up only in the vicinity of the ignition limit. In the zone of relatively low

initial temperatures, the shift of the ignition limit is largely associated with the heating of mixture owing to recombination of atomic particles being added. In so doing, the nonequilibrium character of the impact hardly shows up.

A kinetic model describing the effect of the admixtures of molecules of singlet delta oxygen $O_2(a^1\Delta_g)$ on the evolution of the hydrogen-oxygen mixtures was worked out. The dynamics of SDO quenching in $H_2 : O_2$ mixtures was calculated for the experimental conditions [51-54] in the temperature range of $T_0 = 300 - 1050$ K. The possibility of describing the entire set of the experimental data [51-54] in the framework of the model was illustrated.

The effect of admixtures of singlet oxygen molecules $O_2(a^1\Delta_g)$ on ignition of $H_2 : O_2$ mixtures was studied. The SDO molecules can also participate both in the reactions of chain initiation ($O_2(a^1\Delta_g) + H_2 \rightarrow OH + OH$), and in the reactions of chain branching ($O_2(a^1\Delta_g) + H \rightarrow OH + O$). By comparing the results of calculations with experimental data, the following conclusions on the rates of these processes can be drawn. Most of the acts of interaction of SDO molecules with atomic hydrogen $O_2(a^1\Delta_g) + H$ leads to quenching of $O_2(a^1\Delta_g)$ molecules (reaction 4). Share of this channel is more than 80% and the reaction of chain branching is observed only in 15 - 20% of cases. It is not possible to determine the rate constant of the process $O_2(a^1\Delta_g) + H_2 \rightarrow OH + OH$ (1) on the basis of available experimental data. So, the values of $k_1(T)$ still remain undetermined.

An important process that determines the effect of SDO molecules on the ignition characteristics of hydrogen-oxygen mixtures is its deactivation by HO_2 molecules. According to [55, 57], this reaction is very effective. As a result, in $H_2 : O_2$ mixtures at high pressure, where the concentration of produced HO_2 molecules can be high enough, the effect of singlet oxygen on the ignition times of these mixtures is relatively weak. This effect becomes even less noticeable if the mixture contains admixtures of atomic oxygen. The last case is typical when the electric discharge systems are used for production of singlet oxygen. Presence of even small (10^{-4}) initial concentration of atomic oxygen or ozone reduces the effect of $O_2(a^1\Delta_g)$ admixtures on the processes of ignition only to additional heating of the mixture in the process of SDO deactivation

ACKNOWLEDGMENTS

This work was partially supported by Russian Agency of Technologies and Innovations (Contract no 02.740.11.5108), the International Science and Technology Center (project no. 3833p) and Grant

for Support of Leading Scientific Schools (Grant no. 3322.2010.2).

REFERENCES

1. Takita K., Moriwaki A., Kitagawa T., Masuya G. Ignition and flame-holding of H_2 and CH_4 in high temperature airflow by plasma torch // *Combustion and Flame*. 2003. V. 132. P. 679-689.
2. Starikovskii A.Yu. Plasma supported combustion // *Proc. Combustion Institute*. 2005. V. 30. P. 2405-2417.
3. Starikovskaia S.M. Plasma assisted ignition and combustion // *J. Phys. D: Appl. Phys.* 2006. V. 39. R265-R299.
4. Bozhenkov S.A., Starikovskaia S.M., Starikovskii A.Yu. Nanosecond gas discharge ignition of H_2 and CH_4 - containing mixtures // *Combustion and Flame*. 2003. V. 133. No 1-2. P. 133-146.
5. Pancheshnyi S.V., Lacoste D.A., Bourdon A., Laux C.O. Ignition of propane-air mixture by a repetitively pulsed nanosecond discharge // *IEEE Trans. Plasma Sci.* 2006. V. 34. № 6. P. 2478-2487.
6. Leonov S.B., Biturin V.A., Yarantsev D.A. Plasma-induced ignition and plasma-assisted combustion in high speed flow (Issue «Nonequilibrium processes») // *TORUS PRESS*. 2005. V. 2. P. 104-115.
7. Brown M.S., Forlines R.A., Ganguly B.N. Dynamics of hydrocarbon-based pulsed DC discharge for ignition application // 44th AIAA Aerospace Sciences Meeting and Exhibition (9-12 January, 2006, Reno). AIAA 2006-0611.
8. Lou G., Bao A., Nishihara M., Keshav S., Utkin Yu.G., Rich J.W., Lempert W.R., Adamovich I.V. Ignition of premixed hydrocarbon-air flows by repetitively pulsed, nanosecond pulse duration plasma // *Proc. Combustion Institute*. 2007. V. 31. P. 3327-3334.
9. Chintala N., Bao A., Lou G., Adamovich I. Measured of combustion efficiency in nonequilibrium RF plasma-ignited flows // *Combustion and Flame*. 2006. V. 144. P. 744-756.
10. Shibkov V.M., Chernikov A.P., Ershov A.P. et al. Ignition of the supersonic propane-air mixture with the help of the surface microwave discharge // *The 5th Workshop on Magnetoplasma Aerodynamics for Aerospace Applications*. Moscow. 2003. P. 162-165.
11. Berezhetskaya N.K., Gritsinin S.I., Kop'ev V.A., Kossyi I.A., Popov N.A., Silakov V.P., Van Wie D.M. Microwave discharge as a method for igniting combustion in gas mixtures // 43th AIAA Aerospace Sciences Meeting and Exhibit. 2005. Reno. AIAA 2005-0991.

12. *Esakov I.I., Grachev L.P., Bychkov V.L., VanWie D.M.* Investigations of undercritical MW discharge with volumetrically-developed streamer structure in propane-air supersonic stream // 44th AIAA Aerospace Sciences Meeting and Exhibition (9-12 January, 2006, Reno). AIAA 2006-0790.
13. *Ikeda Y., Nishiyama A., Kaneko M.* Microwave enhanced ignition process for fuel mixture at elevated pressure of 1 MPa // 47-th AIAA Aerospace Sci. Meeting and Exhibit (January, 2009, Orlando). AIAA 2009-223.
14. *Gerasimov G.Ya.* Ignition of hydrogen-air mixtures exposed to ionizing radiation // *Khim. Vys. Energ.* 2002. V. 36. No 6. P. 408-412.
15. *Pushkarev A.I., Remnev G.E.* Initiation of hydrogen oxidation by pulsed electron beams // *Physics of Combustion & Explosion.* 2005. V. 41. No. P. 46-51.
16. *Raizer Yu. P.* Gas Discharge Physics. Berlin: Springer. 1991.
17. *Rusanov V.D., Fridman A.A.* Physics of Chemically Active Plasma, Moscow: Nauka, 1984.
18. *Ionin A.A., Klimachev Yu.M., Kotkov A.A., Kochetov I.V., Napartovich A.P., Seleznev L.V., Hager G.D.* // Non-self-sustained electric discharge in oxygen gas mixtures: singlet delta oxygen production // *J. Phys. D: Appl.Phys.* 2003. V. 36. P. 982-989.
19. *Vasiljeva A.N., Klopovsky K.S., Kovalev A.S., Lopaev D.V., Mankelevich Y.A., Popov N.A., Rakhimov A.T., Rakhimova T.V.* // On the possibility of O₂(¹Δ_g) production by a non-self-sustained discharge for oxygen-iodine laser pumping // *J.Phys. D: Appl.Phys.* 2004. V. 37. P. 2455-2468.
20. *Semenov N.N.* Chain Reactions. Moscow: Nauka, 1986 (in Russian).
21. *Nalbandyan A.B.* Photochemical Oxidation of Hydrogen // *J. Phys. Chem.* 1946. V. 20. No 11. P. 1259-1272 (in Russian).
22. *Lavid M., Stevens J.G.* Photochemical ignition of premixed hydrogen/oxygen mixtures with excimer lasers // *Combustion Flame.* 1985. V. 60. P. 195-202.
23. *Lucas D., Dunn-Rankin D., Hom K., Brown N.J.* Ignition by excimer laser photolysis of ozone // *Combustion Flame.* 1987. V. 69. P. 171-184.
24. *Lavid M., Nachshon Y., Gulati S.K., Stevens J.G.* Photochemical ignition of premixed hydrogen/oxygen mixtures with ArF laser // *Combust. Sci. & Tech.* 1994. V. 96. P. 231-245.
25. *Chou M-S., Zukowski T.J.* Ignition of H₂/O₂/NH₃, H₂/Air/NH₃ and CH₄/O₂/NH₃ mixtures by excimer-laser photolysis of NH₃ // *Combustion Flame.* 1991. V. 87. P. 191-202.
26. *Seleznev A.A., Aleinikov A.Yu., Yaroshenko V.V.* Effect of radiolysis on displacement of explosion limit for hydrogen/oxygen gas mixtures // *Chem. Phys.* 1999. V. 18. No 5. P. 65-71.
27. *Baratov A.N., Shebeko Yu.N. Korol'chenko A.Ya.* Influence of active centers produced by an external source on the induction period of self-ignition hydrogen/oxygen gas mixtures // *Kinetics and Catalysis.* 1986. V. 27. No 2. P. 482-485.
28. *Starikovskaia S.M., Anikin N.B., Kosarev I.N., Popov N.A., Starikovskii A.Yu.* Analysis of Ignition by Nonequilibrium Sources. Ignition of Homological Series of Hydrocarbons by Volume Nanosecond Discharge // 44th AIAA Aerospace Sciences Meeting and Exhibition (9-12 January, 2006, Reno). AIAA 2006-0616.
29. *Starikovskii A.Yu.* Ignition initiation by pulsed high-current discharge in gas // *Phys. Combustion & Explosion.* 2003. V. 39. N 6. P. 12-19.
30. *Okabe H.* Photochemistry of small molecules // J. Willey & Sons Inc., NY. 1978.
31. *Baulch D.L., Cox R.A., Hampson R.F., Kerr J.A.* Kinetic and photochemical data for atmospheric chemistry // *J. Phys. Chem. Ref. Data.* 1984. V. 13. No 4. P. 1259.
32. *Klopovsky K.S., Lopaev D.V., Popov N.A., Rakhimov A.T., Rakhimova T.V.* // Heterogeneous quenching of O₂(¹Δ_g) molecules in H₂ : O₂ mixtures // *J. Phys. D: Appl. Phys.* 1999. V. 32. P. 3003-3012.
33. *Lewis B., van Elbe G.* Combustion, Flame and Explosions in Gases. New York: Academic Press. 1961.
34. *Baulch D.L., Cobos C.J., Cox R.A. et al* Summary table of evaluated kinetic data for combustion modelling // *Combust. Flame.* 1994. V. 98. No 1. P. 59-79.
35. *Slack M., Grillo A.* Investigation of hydrogen-air ignition sensitized by nitric oxide and nitrogen dioxide // NASA Report CR-2896. 1977.
36. *Warnatz J., Maas U., Dibble R.W.* Combustion: physical and chemical fundamentals, modeling and simulations, experiments, pollutant formation. Berlin: Springer. 2001.
37. *Starikovskaia S.M., Kukaev E.N., Kuksin A.Yu., Nudnova M.M., Starikovskii A.Yu.* Analysis of spatial uniformity of the combustion of a gaseous mixture initiated by a nanosecond discharge // *Combustion & Flame.* 2004. V. 139. P. 177-187.
38. *Schultz E., Shepherd J.* Validation of detailed reaction mechanisms for detonation simulation // California Institute of Technology Graduate Aeronautical Laboratories Technical Report FM 99-5. 2000. 230p.

39. *Delacroix G., Ferreira K.M., Rikar A. Metastable Atoms and Molecules in Ionized Gases* // in: Principles of laser plasma, G. Bekefi Ed. John Wiley & Sons Inc. NY. 1976.
40. *Basevich V.Ya., Kogarko S.M.* Mechanism governing the effect of glow-discharge products on the velocity of hydrogen/oxygen flames in combustion peninsula // *Kinetics & Catalysis*. 1965. V. 6. No 1. P. 23 (in Russian).
41. *Basevich V.Ya., Kogarko S.M.* Mechanism governing the effect of glow-discharge products on the velocity of hydrogen/oxygen flames in combustion peninsula // *Kinetics & Catalysis*. 1966. V. 7. No 3. P. 393-400 (in Russian).
42. *Basevich V.Ya., Belyaev A.A.* Calculation of acceleration of hydrogen/oxygen flame on additions of singlet oxygen // *Chem. Phys.* 1989. V. 8. No 8. P. 1124-1127.
43. *Klopovsky K.S., Lopaev D.V., Popov N.A., Rakhimov A.T., Rakhimova T.V.* // Heterogeneous quenching of $O_2(^1\Delta_g)$ molecules in $H_2 : O_2$ mixtures // *J. Phys. D: Appl. Phys.* 1999. V. 32. P. 3003-3012.
44. *Starik A.M., Titova N.S.* Initiation of combustion and detonation in combustible mixtures at excitation of molecular hydrogen to the $O_2(a^1\Delta_g)$ state // *Chem. Phys.* 2001. V. 20. P. 17-25.
45. *Starik A.M., Titova N.S.* On kinetic mechanisms for combustion initiation in hydrogen/oxygen mixtures at excitation of electron degrees of freedom of oxygen molecules by laser radiation // *JTP* 2003. V. 73. No. 3. P. 59-68.
46. *Starik A.M., Titova N.S.* On kinetics of detonation initiation in supersonic flows of $H_2 + O_2$ (air) mixtures at excitation of O_2 molecules by resonance laser radiation // *Kinetics & Catalysis*. 2003. V. 44. No 1. P. 35-46.
47. *Popov N. A.* The effect of nonequilibrium excitation on the ignition of hydrogen-oxygen mixtures // *High Temp.* 2007. V. 45. P. 261.
48. *Morozov I.I., Temchin S.M.* Kinetics of reactions of singlet oxygen in gaseous phase // *Plas. Chem.* No 16. Moscow: Energoizdat. 1989. P. 39-67.
49. *Kustarev V. G.* Recommended data for the rate constants of singlet oxygen $O_2(^1\Delta_g)$ deactivation in gas phase // *Itoqi nauki i tekhniki. Kinet. Catal.* 1991 (Moscow, VINITI) V. 24. P. 71.
50. *Borrell P., Richards D.S.* Quenching of singlet molecular oxygen $O_2(a^1\Delta_g)$ by H_2 , D_2 , HCl , and HBr // *J. Chem. Soc. Faraday Trans. II*. 1989. V. 85. P. 1401-1411.
51. *Cupitt L.T., Takacs G.A., Glass G.P.* Reaction of hydrogen atoms and $O_2(^1\Delta_g)$ // *Intern. J. Chem. Kinet.* 1982. V. 14. P. 487-497.
52. *Basevich V.Ya., Vedenev V.I.* Rate constant for reaction $H + O_2(a^1\Delta_g) = OH + O$ // *Chem. Phys.* 1985. V. 4. P. 1102-1106.
53. *Hack W., Kurzke H.* Kinetic study of the elementary chemical reaction $H + O_2(^1\Delta_g) = OH + O(^3P)$ in gas phase // *J. Phys. Chem.* 1986. V. 90. P. 1900.
54. *Hack W., Kurzke H.* The production of H atoms in the energy-transfer reaction of $O_2(^1\Delta_g)$ with $HO_2 (X^2A')$ // *Chem. Phys. Lett.* 1984. V. 104. P. 93.
55. *Podolske J.R., Johnston H.S.* Rate of the resonant energy-transfer reaction between $O_2(^1\Delta_g)$ and HOO // *J. Phys. Chem.* 1983. V. 83. P. 626.
56. *Sridharau U. C., Qiu L. X., Kaufman F.* Kinetics and product channels of the reaction of HO_2 with O and H atoms at 296 K // *J. Phys. Chem.* 1982. V. 86. P. 4569.
57. *Becker K. H., Fink E. H., Langen P., Schurath U.* Near infrared emission bands of the HO_2 radical // *J. Chem. Phys.* 1974. V. 60. P. 4623.

LIQUID AND GASEOUS HYDROCARBON FUELS IGNITION IN THE AIR STREAM WITH THE HELP OF A DISCHARGE CREATED IN A PROGRAMMABLE PULSE MODE

V.M.Shibkov, V.A.Bityurin, A.A.Karachev, R.S.Konstantinovskii, P.V.Kopyl, L.V.Shibkova
Faculty of Physics, Moscow State University, 119991, Moscow, Russia,
shibkov@phys.msu.ru

Abstract. In the paper the influence of a non-equilibrium plasma on ignition and combustion of hydrocarbon fuel is studied. Process of ignition of thin liquid hydrocarbon films with the help of a surface microwave discharge created in a mode of double pulses, as a first step to programmable regime, was studied too. The ignition of a propane-air high speed flow with use of combined discharge was experimentally investigated.

I. Introduction

For several decades the scientists have been discussing the question of possible ways of efficient control of combustion processes with the help of various physical influences. Interest to an intensification of combustion with use of various forms of the gas discharge with reference to supersonic plasma aerodynamics recently has essentially risen. Under conditions of low-temperature plasma there is an opportunity of generation of active particles in result of molecules dissociation by electronic impact, electron-ionic and ion-molecular reactions, and also reduction in a threshold of chemical reactions with participation of the vibrationally-excited reagents. Therefore essentially not thermal mode of ignition is possible when the creating time of active particles occurs by electronic impact practically on all an extent of reaction. Methods of ignition and combustion control of the air-hydrocarbon streams, based on generation of electric discharges, are represented now by the most perspective.

A variety of types of electric discharges allows changing over a wide range a ratio between contributions of various mechanisms. Application of the combined discharges of various types can provide necessary rate and intensity of combustion. Studying of process of ignition and combustion of air-hydrocarbon mixtures under conditions of low-temperature plasma is of great importance as from the point of view of basic researches of mechanisms and kinetics of atom-molecular transformations at presence of strong electric fields, and the analysis of some applied tasks. One of practical problems is development of physical principles of the direct-flow jet engine. For reduction of its longitudinal size it is necessary to provide fast volumetric ignition of hydrocarbon fuel under conditions of high-speed streams, and for this purpose maximum to reduce an induction period.

For stationary work of the direct-flow air-breathing engine at use of non-stationary non-

equilibrium low-temperature plasma for ignition of air-hydrocarbon mixtures it is necessary to optimize a mode of initiation of the pulsed discharge, i.e. the value of energy put into plasma, pulse duration and frequency of following of the microwave pulses. It can be carried out at creation of the discharge in a mode of a programmable pulse [1]. Such discharge is the self-sustained-non-self-sustained discharge. In a programmable pulse mode gas breakdown and creation of plasma is carried out with the help of a short powerful pulse, or a pack of short powerful pulses, and maintenance of the formed plasma and energy input occurs during the long low-power pulse following with some time delay after the first pulse, or a pack of short powerful pulses. It is also possible to create the discharge in a programmable mode when low-power pulse is switched on time, equal to duration of a pack of the short powerful pulses.

Till now kinetics of ignition of hydrocarbon fuel in conditions of the low-temperature plasma of the gas discharge existing at high values of the reduced electric field remains not up to the end clarify. Therefore for deeper understanding of the physical and chemical processes proceeding at initiation of ignition of gaseous fuel with the help of the low-temperature plasma, it is necessary alongside with experimental researches to carry out mathematical modelling of influence of gas discharge on initiation of combustion.

For the purposes of plasma aerodynamics we use some types of a self-sustained gas discharge, namely, the microwave discharge which is created by a surface wave on a dielectric body, streamlined by a high-speed gas stream, the freely localized microwave discharge, created by focused beam of electromagnetic energy, and the pulsed electrode transversal surface or volumetric discharges [2-17]. It is known, that self-sustained microwave discharges, as well as high-voltage nanosecond electrode discharges, exist at high values of the reduced electric field. However, high

value of the reduced electric field can be supported during long (hundreds microseconds) time under conditions of a microwave discharge in contrast the nanosecond high-voltage discharge. Therefore features of self-sustained microwave discharges are very perspective from the point of view of the fast reliable ignition of high speed air-hydrocarbon flows. However, as well as for other types of the gas discharges, combustion of high speed combustible flow under condition of microwave discharges stops, as soon as the supply of microwave energy is switched off.

For stationary combustion of hydrocarbon-air mixture at use of non-stationary low-temperature plasma it is necessary to optimize a mode of initiation of the pulsed discharge, i.e. the value of energy put into plasma, pulse duration and frequency of following of the microwave pulses. It can be carried out at creation of the discharge in a mode of a programmable pulse [1].

In a programmable pulse mode gas breakdown and creation of plasma is carried out with the help of a short ($\tau_1 = 5-20 \mu\text{s}$) powerful pulse (Fig. 1, a), or a pack of short powerful pulses (Fig. 1, b,c), and maintenance of the formed plasma and energy input occurs during the long ($\tau_2 > 1 \text{ s}$) low-power pulse following with some time delay ($\tau_{\text{del}} = 10-100 \mu\text{s}$) after the first pulse (Fig. 1, a), or a pack of short powerful pulses (Fig. 1, b). It is also possible to create the discharge in a programmable mode when low-power pulse is switched on during time ($\tau_2 > 1 \text{ s}$), equal to duration of a pack of the short powerful pulses (Fig. 1, c) following with pulse-repetition frequency of $f = 10-100 \text{ Hz}$.

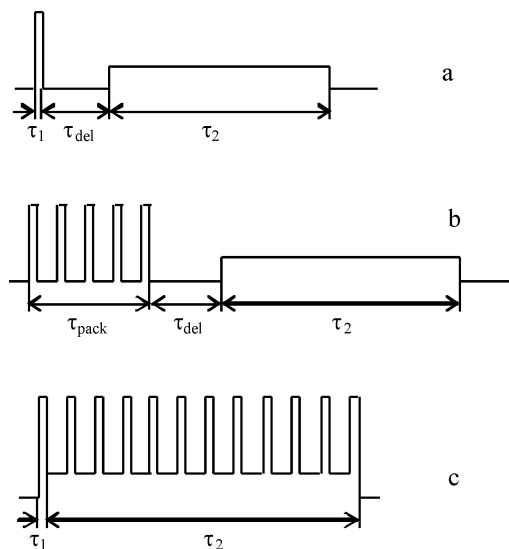


Figure 1. Time diagrams of gas discharge creation under condition of programmable pulse mode.

It is very well-known, that in the motionless gas secondary breakdown becomes easier in comparison with primary breakdown (look Fig. 2 and Fig. 3) [1, 18].

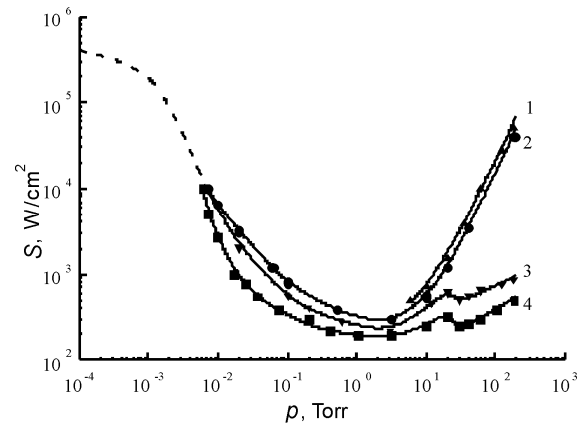


Figure 2. Threshold characteristics of the microwave breakdown for various modes: 1 – monopulse mode ($\tau = 10 \mu\text{s}$); 2 – continuous mode ($\tau > 50 \mu\text{s}$); 3 – two pulses ($\tau_1 = 10 \mu\text{s}$, $\tau_2 = 50 \mu\text{s}$); 4 – two pulses ($\tau_1 = 50 \mu\text{s}$, $\tau_2 = 50 \mu\text{s}$).

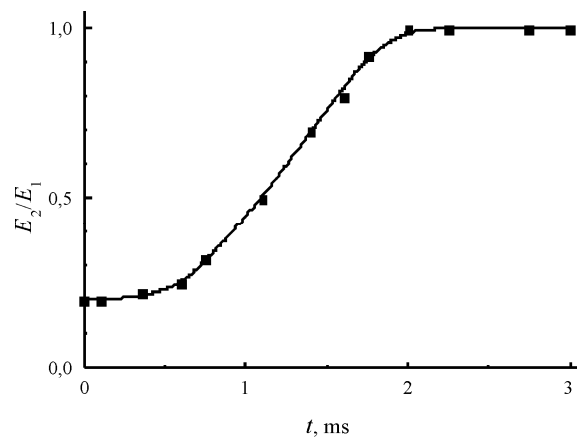


Figure 3. Dependence of amplitude of a longitudinal electric field at the beginning of the second pulse on a time interval between pulses. The discharge in helium at duration of first and second pulses $\tau = 100 \mu\text{s}$, a discharge current $i = 0.15 \text{ A}$, pressure of helium $p = 0.8 \text{ torr}$.

It is connected to that fact that plasma deionization occurs during some time after switch off of the first pulse of energy, thus the great number of the charged particles can remain to the moment of switch on of the second pulse. Presence in gas of the long-living excited particles also makes easier repeated breakdown as ionization of gas in this case can realize electrons with small energies due to step processes with participation of excited long-living atoms and molecules. Heating of gas during the first pulse at high pressures also results in decrease in secondary breakdown due to reduction of gas density in the zone of the discharge existence.

With reference to ignition of motionless air-hydrocarbon mixtures during the first pulse reforming of hydrocarbon fuel (molecules

dissociation, creation of the charged and excited particles, active radicals, and also heating of fuel) can occur, that should lead to decrease of induction period during the second pulse and to increase in combustion completeness.

As to ignition of high-speed air-hydrocarbon streams the mode of programmable pulses can be used in such combination when the discharge during the first pulse is created before an entrance of combustor where a preparation of fuel takes place whereas during a repeated pulse low-temperature plasma is created in the basic chamber of combustor with the time delay determined in the speed of movement of reformed fuel and distance between area of preliminary excitation of fuel and the combustor chamber.

For a general chemical reaction $A \rightarrow B$ of n^{th} order, the Damköhler number is defined as $D_a = kC_0^{n-1}t$, where: k is rate constant of kinetics reaction, C_0 is initial concentration, n is reaction order, t is time. The Damköhler number represents a dimensionless reaction time. It provides a quick estimate of the degree of conversion (X) that can be achieved in continuous flow reactors. If $D_a < 0.1$, then $X < 0.1$, if $D_a > 10$, then $X > 0.9$. In continuous or semibatch chemical processes, the general definition of the Damköhler number is: $D_a = \tau/t_r$, where τ is the mean residence time, t_r is reaction time.

In conditions of external ignition with the help of a self-sustained pulsed ($\tau \leq 10^{-4}$ s) a surface microwave discharge an induction period of a high-speed air-hydrocarbon stream on a smooth surface of the antenna changes from 10^{-5} s up to 10^{-4} s. Thus for a smooth surface of the antenna the mean residence time $\tau = (3-6) \cdot 10^{-4}$ s whereas at use as a stagnant zone of various cavities (the closed and open types) resident time can reach some milliseconds. In this case the Damköhler number $D_a > 10$, that is $X > 0.9$.

In conditions of the self-sustained pulsed discharge combustion occurs only during duration of a pulse. At use of a programmable regime of creation of the discharge we hope to carry out full combustion in a continuous mode.

Influence of non-equilibrium plasma on ignition and combustion of air-hydrocarbon flow is studied in the report on example of ignition of liquid thin hydrocarbon films (alcohol, gasoline, kerosene) and gaseous hydrocarbon (propane) with the help of the discharge created in a mode of a programmable pulse.

II. Experimental Installation

Experiments were carried out on the installation consisting of a vacuum chamber, a receiver of a high pressure of air, a receiver of a high pressure of propane, a system for mixing

propane with air, a system for producing a supersonic gas flow, two magnetron generators, two systems for delivering microwave power to the chamber, rectangular aerodynamic channels, a synchronization unit, and a diagnostic system. The basic component of the experimental setup is an evacuated metal cylindrical chamber, which serves simultaneously for supersonic flow creation, and as a tank for the expiration of gases or combustion products. The inner diameter of the vacuum chamber is 1 m, and its length is 3 m. A supersonic flow was produced by filling the vacuum chamber with air through a specially profiled Laval nozzle. In our experiments, we used rectangular nozzle designed for a Mach number of $M = 2$.

The microwave source is a pulsed magnetron generator with parameters: the wavelength is $\lambda = 2.4$ cm, the pulse duration is $\tau = 5-150$ μs , the pulsed microwave power is $W < 200$ kW, and the period-to-pulse duration ratio is $Q = 1000$. Microwave power was delivered to the discharge chamber through a 9.5×19 -mm rectangular waveguide. The input microwave power was measured with the help of a directional coupler installed in the waveguide so that a fraction of microwave power was directed to the measuring arm containing an attenuator and a section with a crystal detector. All the components of the microwave transmission line were sealed. To avoid electric breakdowns inside the waveguide, it was filled with an insulating gas (SF_6) at a pressure of 4 atm. The vacuum system of the chamber allows us to vary the pressure over a wide range from 10^{-3} to 10^3 torr.

The supersonic stream is created at filling a pressure chamber with air through specially shaped Laval nozzle, established on a tube of the electromechanical valve. Two electromechanical valves fixed on an external surface of the chamber, hermetically connect the channel to a receiver of a high pressure ($p_1 = 1-6$ atm) air and a receiver of a high pressure ($p_2 = 3-5$ atm) propane. Air or air-propane mixture originally goes into the mixing device, established in a subsonic part of a channel. Directly behind the mixer the supersonic nozzle is arranged. For synchronization of electromechanical valves and the discharge the special circuit providing a time delay between inclusion of the discharge and opening of the valves is used. In conditions of experiments the electromechanical valve could open on 0.3-2 s. During same time the surface microwave discharge was created. Thus at use of a surface microwave discharge the direction of a supersonic stream was opposite to a direction of distribution of an SMD. The system of synchronization allows to enter air, propane or a propane-air mixture into the aerodynamic channel with the fixed delays under the relation to each other. The synchronization system also allows to create a surface microwave discharge or in a mode

of a single pulse, or in a pulsed-periodic mode. Thus it is possible to change in a wide range of duration of pulses, frequency of their following, number of pulses in a pack. Ignition was investigated in conditions of a high-speed stoichiometric propane-air stream with Mach number $M = 2$. Pressure p_0 of motionless air in the vacuum chamber changed from 10 up to 100 Torr.

The combined discharge is offered with the purpose of reduction of an induction period and increase of an intensification of combustion of a high speed stream of hydrocarbon fuel. The discharge represents a combination of the pulse-periodic surface microwave discharge and the direct current discharge created in a recirculation zone of the aerodynamic channel. Thus surface microwave discharge serves for the several purposes. First, it facilitates initiation of the direct current discharge. Second, effective energy contribution to plasma takes place under conditions of the microwave discharge. It leads to effective creation of the active radicals, excited and charged particles, and also to intensive volumetric illumination of gas flow by ultra-violet radiation. These factors can result in fast ignition of a gas mixture. The direct current discharge serves for the contribution of a thermal energy to gas and stabilization of combustion of a high speed stream of hydrocarbon fuel.

With the purpose of check of efficiency of the combined discharge for its use in plasma aerodynamics the laboratory model of the aerodynamic channel with the different stagnant zones, allowing to carry out researches on combustion hydrocarbon fuel, has been developed and made. Microwave energy was entered into the channel with the help of the rectangular antenna. On its external surface a pulse-periodic microwave discharge was created. Microwave power, pulse duration and repetition frequency of pulses could vary in a wide range. Under experimental conditions direct current discharge pulse duration did not exceed 1.5 s, which was defined by design features of experimental installation. A voltage on an electrode gap and a discharge current could also vary in a wide range.

We used various types of the stagnant zones: a reverse step, a rectangular cavity with various depths of forward and back walls, a rectangular cavity with angled rear-wall, and a rectangular cavity. The aerodynamic channel with various types of the stagnant zones used in experiments is schematically represented in Fig. 4. Points (1)-(4) show position of pressure gauges, and a point (5) shows a position of electrodes for creation of the direct current discharge. The stream of gas is directed from right to left and represented by an arrow. Pressure gauges of (1)-(4) allowed to measure distribution of pressure in various points of the aerodynamic channel and to register ignition of a propane-air stream on change of pressure in the

channel. Specially developed system allowed to smoothly move the electrodes serving for creation of a direct current discharge. It allowed creating the DC in different places of a stagnant zone. In experiments the discharge was created both about a bottom of a cavity and in a free stream is higher than a stagnant zone

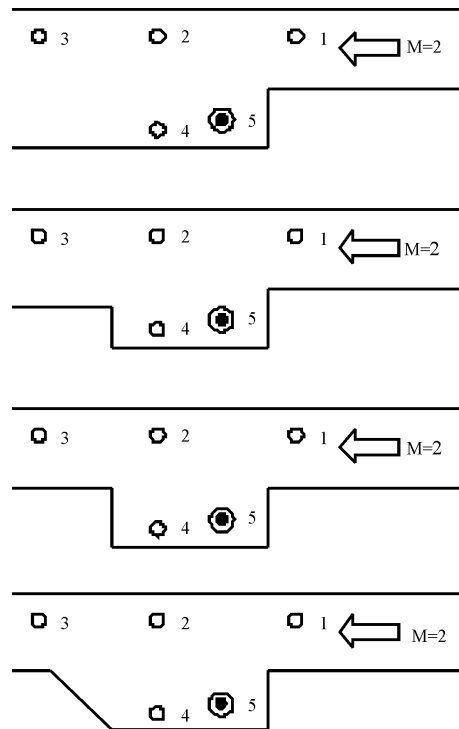


Figure 4. The circuit of the aerodynamic channel with a stagnant zone: a reverse step (a), a rectangular cavity with various depths of forward and back walls (b), a rectangular cavity (c) and a rectangular cavity with an angled rear-wall. 1, 2, 3, 4 – location of pressure gauges, 5 – location of electrodes for creation of a DC discharge.

As a direct current source for creation of the transversally-longitudinal electrode discharge the power supply with a voltage up to 5 kV, a discharge current up to 20 A and at a pulse duration up to 1.5 s was used. For external ignition gaseous and liquid hydrocarbons the combined discharge was created on an external surface of the dielectric antenna, streamlined by a high-speed stream of air (look Fig. 5).

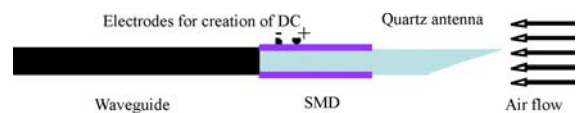


Figure 5. The circuit of creation of the combined discharge for external combustion without stagnant zone.

In experiments the following diagnostic methods were used: process of ignition and combustion of a high speed stream of hydrocarbon fuel was fixed on a video camera; photos of the

channel were registered; the time dependence of plasma radiation was fixed at ignition of a high speed stream; the time dependence of signals from pressure gauges were registered; the spectrum of the discharge was fixed; the current of the electric probe placed on an exit of the aerodynamic channel was fixed.

III. Experimental results

At first the dielectric antenna has been placed in a stagnant zone of the aerodynamic channel and experiments were fulfilled under condition of combined discharge. The results of internal combustion of a propane-air stream under condition of combined discharge, received at use of a rectangular cavity with angled rear-wall and a rectangular cavity with various depths of forward and back walls on a wide wall of the aerodynamic channel as flame stabilizers and flame holders are submitted in Fig. 6 and Fig. 7 at microwave pulse duration $\tau=10^{-5}$ s, repetition frequency of microwave pulses $f=100$ Hz, duration of direct current discharge $t=1$ s, and time exposure is 20 ms.



Figure 6. The general view of the combined discharge created in a high speed propane-air stream in a rectangular cavity with angled rear-wall on a wide wall of the aerodynamic channel.



Figure 7. The general view of the combined discharge created in a high stream of propane-air ($M=2$) in a rectangular cavity with various depths of forward and back walls on a wide wall of the aerodynamic channel at microwave pulse duration $\tau=10^{-5}$ s, repetition frequency $f=100$ Hz, duration of direct current discharge $t=1$ s, and time exposure is 20 ms. The propane-air flow is directed from right to left.

In this case gas breakdown and fast ignition of supersonic air-hydrocarbon stream occurs with the help of powerful pulse-periodic surface microwave discharges, and stabilization of combustion is carried out at a supply of electric energy in a stagnant zone with the help of a direct current electrode discharge.

Time dependence of pressure in the aerodynamic channel with a stagnant zone under condition of combustion of high-speed air-propane flow is present in Fig. 8 at experimental conditions $v_{\text{flow}} = 520$ m/s, $\tau_{\text{MW}} = 30$ μ s, $f = 100$ Hz, $W = 55$ kW, $N = 100$, $\tau_{\text{DC}} = 1$ s, $i = 12$ A. One can see, that after some time delay after switching on of the combined discharge there is a stabilization of combustion.

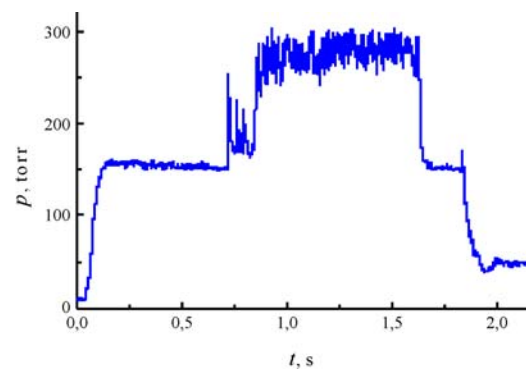


Figure 8. Time dependence of pressure in the aerodynamic channel with a stagnant zone under condition of combustion of high-speed air-propane flow.

These experiments show, that the combined discharge created in a stagnant zone in the aerodynamic channel, results in fast ignition and stabilization of propane-air stream combustion. However, efficiency of combustion of a high-speed air hydrocarbon stream not so good. It is difficult to receive regular stable combustion. Repeatability of process is low.

External combustion of thin liquid hydrocarbon films under condition of transonic air flow one can see in Fig. 9.

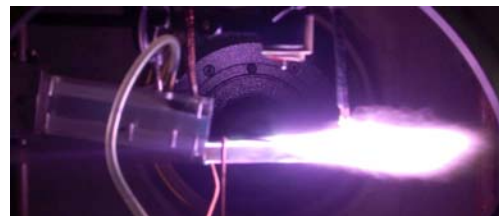


Figure 9. External combustion of thin liquid hydrocarbon films under condition of transonic ($M = 1$) air flow at atmospheric pressure in chamber.

In the paper process of ignition of thin liquid hydrocarbon films with the help of a surface microwave discharge created in a mode of double pulses, was also studied. The block of synchronization allowed to create a surface microwave discharge in a mode of pair pulses, independently to change duration of the first and the second pulses, to change frequency of their following, and also a time delay of the second pulse concerning the first one at identical value of pulsed power in both pulses. The time diagram of a mode of pair pulses is submitted in Fig. 10.



Figure 10. The temporal diagram of a mode of pair pulses.

Surface microwave discharge was created at the first pulse duration $\tau_1 = 5 - 150 \mu\text{s}$, the second pulse duration $\tau_2 = 5 - 150 \mu\text{s}$, the time delay of the second pulse concerning the first one $t_{\text{del}} = 5 \mu\text{s} - 100 \text{ms}$, the identical value of pulsed power in both pulses $W_1 = W_2 = 20 - 75 \text{kW}$.

The time dependences of intensities of flame luminescence in area of plasma-stimulated ignition in a mode of double pulses are submitted in Fig. 11. Surface microwave discharge was created during second pulse at its delay $t_{\text{del}} = 2 \text{ms}$ concerning the first pulse. It is visible, that the period of an induction during the second pulse is much less.

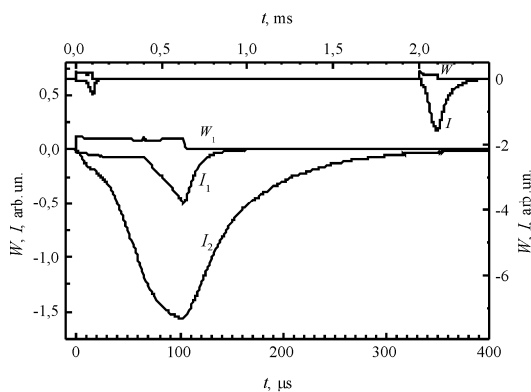


Figure 11. Time dependences of intensities of flame luminescence in area of plasma-stimulated ignition in a mode of pair pulses at a delay of the second pulse $t_{\text{del}} = 2 \text{ms}$ concerning the first one.

Dependence of the maximal intensity of the flame luminescence, achievable during the second microwave pulse, from a delay of the second pulse in relation to forward front of the first pulse is submitted in Fig. 12 at identical duration of first

and second pulses $\tau_1 = \tau_2 = 50 \mu\text{s}$ and pulsed power $W = 55 \text{kW}$. It is visible, that the received dependence of intensity has no monotonic character with a minimum at $t_{\text{del}} = 200 \mu\text{s}$. It is possible to explain this minimum that fact, that some time is required, that the oxygen which has burned down during the first pulse, has arrived again in area of combustion.

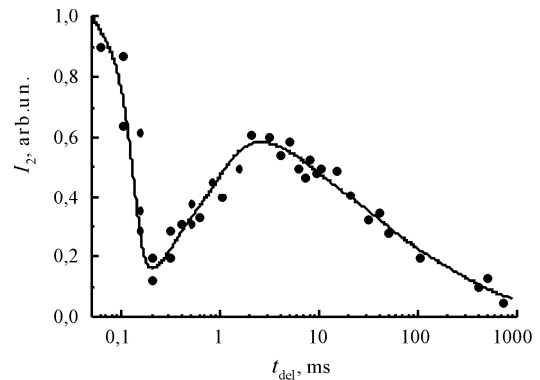


Figure 12. Time dependence of the flame luminescence maximal intensity, which achieves during the second microwave pulse, on time delay of the second pulse in relation to forward front of the first one.

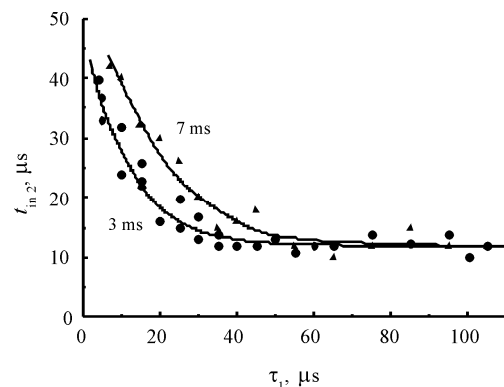


Figure 13. Induction periods during repeated ignition vs the first pulse duration at various time delays of the second pulse.

Dependences of the induction periods at repeated ignition on duration of the first pulse are submitted in Fig. 13 at various time delays of the second pulse in relation to the first one. It is visible, that the period of an induction during secondary ignition strongly depends on duration of the first pulse at any delays of the second pulse in relation to the first pulse.

IV. Mathematical Modeling

To determine the influence of the plasma effects on the ignition of fuel gas mixtures, a kinetic model is developed in [19-21]. Model of hydrocarbon-air mixture ignition takes into account the influence of the electric field on the processes

of molecular dissociation and production of active radicals and excited and charged particles (electrons, positive and negative ions) under the conditions of non-equilibrium gas discharge plasma. The model of the plasma-stimulated ignition of the air-hydrocarbon mixture is based on the system of equations governing the oxidation processes in such mixture and including the non-stationary kinetic equation for the electron energy distribution function, equation of energy, equation of particle density (concentration) variation, and equation of state. The mixture ignition under the impact of the low-temperature microwave discharge plasma at high values of the reduced electric field is calculated using a model accounting for dissociation of molecules and occurrence of active radicals and charged particles. As the gas temperature under microwave discharge conditions increases at a rate of about 10^2 K/ μ s, the modeling is performed under the assumption that, after the electric field is switched on, the gas temperature increases instantly up to certain initial value, T_0 . The energy loss and the active particle diffusion are not taken into account.

The mathematical modeling of the plasma-stimulated ignition is performed by the example of a steady propane-air mixture. To determine the influence of various channels on ignition of the fuel mixture, a kinetic model is taken including 130 components and 1314 direct and reverse reactions (including 89 processes with electron participation), kinetics of the nitrogen and hydrogen vibration levels, and also the Boltzmann equation for the function of the electron distribution over the energies. The transport cross sections of the electron scattering on the H_2 , N_2 , O_2 , H_2O , CH_4 , C_2H_2 , C_2H_4 , C_2H_6 , and CH_2O are taken from [22-24]. In the modeling, the following components are taken into account: the neutral nonexcited particles H , H_2 , N_2 , N , NH , NH_2 , NH_3 , N_2H , N_2H_2 , N_2H_3 , N_2H_4 , N_2O , NO , NO_2 , NO_3 , NHO , HNO , HNO_2 , HNO_3 , O , O_2 , OH , H_2O , HO_2 , H_2O_2 , O_3 , C , C_2 , CH , CH_2 , CH_3 , CH_4 , C_2H , C_2H_2 , C_2H_3 , C_2H_4 , C_2H_5 , C_2H_6 , CO , CO_2 , HCO , CH_2O , CH_3O , CH_2OH , CH_3OH , CH_3O_2 , CH_3OOH , C_2HO , CH_2CO , CH_3CO , CH_3CHO , C_2H_5O , $C_2H_5O_2$, $C_2H_5O_2H$, CN , C_2N , C_2N_2 , HCN , NCO , C_3H_4 , C_3H_5 , C_3H_6 , $n-C_3H_7$, $iso-C_3H_7$, C_3H_8 , C_3H_5O , $C_3H_5O_2$, $C_3H_5O_2H$, C_3H_6O , $n-C_3H_7O$, $iso-C_3H_7O$, $n-C_3H_7O_2$, $iso-C_3H_7O_2$, $n-C_3H_7O_2H$, $iso-C_3H_7O_2H$; the electron-excited oxygen molecules $O_2(a^1\Delta_g)$, $O_2(b^1\Sigma_g^+)$; the oxygen atoms $O(^1D)$; the electron-excited nitrogen molecules $N_2(A^3\Sigma_u^+)$, $N_2(B^3\Pi_g)$, $N_2(C^3\Pi_u)$, $N_2(D^3\Sigma_u)$, $N_2(a^1\Pi_g)$, $N_2(b^1\Pi_u)$, $N_2(a^1\Sigma_g^+)$, $N_2(11.87)$, $N_2(a^1\Sigma_u^-)$; the nitrogen atoms $N(^2D)$, $N(^2P)$; the hydrogen molecules $H_2(c^3\Pi_u)$, $H_2(a^3\Sigma_g^+)$, $H_2(e^3\Sigma_u^+)$, $H_2(d^2\Pi_u)$; the hydrogen atoms $H(2s)$ + $H(2p)$; the positive ions H^+ , H_2^+ , H_3^+ , H_5^+ , O^+ , O_2^+ , OH^+ , H_2O^+ , C^+ , CH^+ , CH_2^+ , CH_3^+ , C_2^+ , C_2H^+ , $C_2H_2^+$, $C_2H_3^+$, $C_2H_4^+$, $C_2H_5^+$, $C_2H_6^+$, C_3^+ , $C_3H_2^+$, $C_3H_3^+$, $C_3H_4^+$, $C_3H_5^+$,

$C_3H_6^+$, $C_3H_7^+$, $C_3H_8^+$; the negative ions H^- , O^- , OH^- , CH_4^- ; and electrons e . The rate constants for the reactions taken into account in the model, depending on the electron and gas temperatures, are calculated on the basis of the data [21, 25-30].

At first, the electron energy distribution function and the electron temperature depending on the reduced electric field for the stoichiometric propane-air mixture are calculated. Then, modeling is performed of the fuel mixture ignition process at the initial gas temperature of 300 K, the neutral particle concentration of 10^{18} cm^{-3} , initial electron concentration of 10^3 cm^{-3} , and various values of the reduced electric field $E/n = 100$ -200 Td. The modeling shows that, under the microwave discharge, the induction period decreases and the ignition mechanism changes as compared to autoignition.

The radical and active particle birth process accelerates significantly in the presence of the discharge. Here, the ionization frequency increases rapidly and the avalanche development delay time decreases with increasing electron temperature, that is, with increasing reduced electric field strength. During the avalanche development, not only the charged particle concentration increases sharply, but also the concentrations of radicals and active particles. This naturally causes significant shortening of the induction period.

Fig. 14 shows the comparison of the calculation results for monopulse mode of microwave discharge creation (curve 1) and programmable mode discharge creation (curve 2).

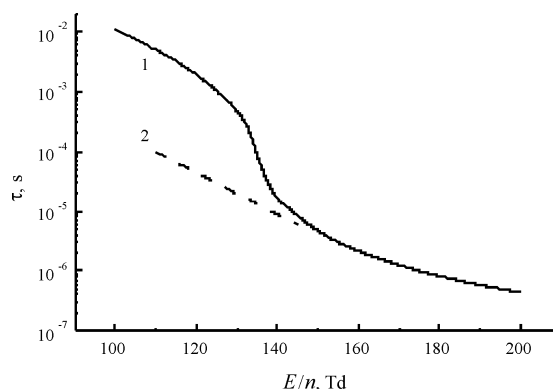


Figure 14. Dependence of an induction period on the reduced electric field. 1 – monopulse mode $\tau = 10$ ms; 2 – programmable mode, duration of first pulse $\tau_1 = 1.95$ μ s, reduced electric field $(E/n)_1 = 150$ Td, duration of second pulse $\tau_2 = 10$ ms, reduced electric field $(E/n)_2$ changes from 110 up to 150 Td. Initial gas temperature of 300 K, the neutral particle concentration of 10^{18} cm^{-3} , initial electron concentration of 10^3 cm^{-3} .

The simulation reveals the strong influence of the reduced electric field on the induction period. Results of mathematical modelling also show, that ignition in a monopulse mode occurs through 100 μ s at value of reduced electric field

$E/n = 135$ Td. However the same result can be received at use of programmable mode of creation of the microwave discharge at $E/n = 110$ Td. In this case spent power is reduced in 1.5 times.

V. Conclusion

Received results testify to efficiency of use of the combined microwave discharge in plasma aerodynamics. However it is necessary to find the optimum modes of creation of the discharge and the optimum configuration of the aerodynamic channel for stabilization and increase in completeness of combustion of hydrocarbon fuel.

VI. Acknowledgments

This work was partially supported by the Russian Foundation for Basic Research (grant # 08-02-01251-a and grant # 11-02-01091-a).

VII. References

1. A.S.Zarin, A.A.Kuzovnikov, V.M.Shibkov. Freely localized microwave discharge in air. Moscow, Oil & Gas. 1996 (In Russian).
2. Shibkov, V.M., Vinogradov, D.A., Voskanyan, A.V. et al., *Vestn. Mosk. Univ. Ser. 3 Fiz. Astron.*, 2000, vol. 41, no. 6, p. 64.
3. Shibkov, V.M., Aleksandrov, A.F., Ershov, A.P. et al., *Vestn. Mosk. Univ., Ser. 3 Fiz. Astron.*, 2004, vol. 45, no 5, p. 67.
4. Shibkov, V.M., Ershov, A.P., Chernikov, V.A., and Shibkova, L.V., *Zh. Tekh. Fiz.*, 2005, vol. 75, no 4, p.67.
5. Shibkov, V.M., Dvinin, S.A., Ershov, A.R, and Shibkova, L.V., *Zh. Tekh. Fiz.*, 2005, vol. 75, no.4, p.74.
6. Shibkov, V.M., Aleksandrov, A.F., Ershov, A.P. et al., *Fiz.Plazmy*, 2005, v.31, no.9, p.857.
7. Dvinin, S.A., Shibkov, V.M., and Mikheev, V.V., *Fiz. Plazmy*, 2006, vol. 32, no. 7, p. 654.
8. Shibkov, V.M., Dvinin, S.A., Ershov, A.P. et al., *Fiz. Plazmy*, 2007, vol. 33, no. 1, p. 77.
9. Shibkova, L.V., *Vestn. Mosk. Univ., Ser. 3 Fiz. Astron.*, 2007, vol. 48, no. 5, p. 62.
10. Shibkova, L.V., Ignition of Alcohol under Conditions of Surface Microwave Discharge in Air, *Preprint of Dept. of Physics, Moscow State Univ., M.: 2007*, no.4.
11. Shibkova, L.V., Physical Processes in Moving Plasma of Multicomponent Inert and Chemically Active Mixtures, *Extended Abstract of Doctoral (Phys.-Math.) Dissertation*, Moscow: Joint Inst. for High Temperatures, Russ. Acad. Sci., 2007.
12. Aleksandrov, A.F., Shibkov VM., and Shibkova, L.V., *Vestn. Mosk. Univ., Ser.3: Fiz., Astron.*, 2008, vol. 63, no. 5, p. 68.
13. Aleksandrov, A.F., Shibkov, V.M., and Shibkova, L.V., *Vestn. Mosk. Univ., Ser. 3: Fiz., Astron.*, 2008, vol. 63, no. 6, p. 65.
14. Shibkov, V.M., and Shibkova L.V., *Technical Physics*, 2009, vol.54, no.10, p.1467.
15. Shibkov V.M., Shibkova L.V., Karachev A.A., *High Temperature*, 2009, vol.47, no.5, p.620.
16. Aleksandrov A.F., Shibkov V.M., and Shibkova L.V. *High Temperature*, 2010, vol.48, no.5, p.611.
17. Shibkov, V.M., and Shibkova L.V., *Technical Physics*, 2010, vol. 55, no. 1, p.59.
18. L.V.Shibkova, V.M.Shibkov. Discharge in mixtures of noble gases. Moscow, Fizmatlit, 2005 (In Russian).
19. Shibkov, V.M., Aleksandrov, A.F., Chernikov, V.A., Ershoy, A., and Shibkova, L., *J. Propul. Power*, 2009, vol. 25, no. 1, p. 123.
20. Shibkov, V.M., Gromov, VG., and Konstantinovskij, R.S., Influence of Gas Discharge Plasma on Combustion of a High-Speed Hydrocarbon Flow, in *Advanced Combustion and Aerothermal Technologies: Environmental Protection and Pollution Reductions*, Syred, N. and Khalatov, A., Eds., New York (United States): Springer, 2007, p. 413.
21. Konstantinovskii, R.S., Shibkov, V.M., and Shibkova, L.V, *Kinet. Katal.*, 2005, vol. 46, no. 6, p. 821.
22. Toshizo Shirai, Tatsuo Tabata, Hiroyuki Tawara, and Yukikazu Itikawa, *At. Data Nucl. Data Tables*, 2002, vol. 80, no. 2, p. 147.
23. Brunger, M.J. and Buckman, S J., *Phys. Rep.*, 2002, no. 357, p. 215.
24. Sobrinho, A.A., Machado, L.E., Michelin, S.E., Mu-Tao, L., and Brescansin, L.M., *J. Mol. Struct.: THEOCHEM*, 2001, vol. 539, nos. 1-3, p. 65.
25. Dautov, N.G. and Starik, A.M., *Kinet. Katal.*, 1997, vol. 38, no. 2, p. 207.
26. Starik, A.M., Titova, N.S., and Yanovskii, L.S., *Kinet. Katal.*, 1999, vol. 40, no. 1, p. 11.
27. Starik, A.M. and Titova, N.S., *Kinet. Katal.*, 2003, vol. 44, no. 1, p. 35.
28. Matveev, A.A. and Silakov, V.P., Non-Equilibrium Kinetic Processes in Low-Temperature Hydrogen Plasma, *Preprint of the General Physics Institute of the Russian Academy of Science*, Moscow, 1994, no. 8 [in Russian].
29. Matveyev, A.A. and Silakov, V.P., Theoretical Study of the Role of Ultraviolet Radiation of the Non-Equilibrium Plasma in the Dynamics of the Microwave Discharge in Molecular Nitrogen, *Preprint of the General Physics Institute of the Russian Academy of Science*, Moscow, 1998, no. 7 [in Russian].
30. Islamov, R.Sh., Kochetov, I.V., and Pevgov, VG., Analysis of the Processes of Interaction of Electrons with Oxygen Molecules, *Preprint of the P. N. Lebedev Physics Institute of the Academy of Sciences of the Soviet Union*, Moscow, 1977, no. 169 [in Russian].

LOW-ENERGY ELECTRON ATTACHMENT AND DETACHMENT IN VIBRATIONALLY EXCITED OXYGEN AND AIR

N L Aleksandrov*, E M Anokhin
Moscow Institute of Physics and Technology
[*nick_aleksandrov@mail.ru](mailto:nick_aleksandrov@mail.ru)

Abstract. Three-body electron attachment to O₂ molecules and electron detachment from O₂⁻ ions have been theoretically studied in vibrationally excited oxygen and air. Assuming that electron attachment and detachment proceed via the formation of vibrationally excited temporary O₂⁻ ions, the rates of these processes were determined on the basis of the statistical approach for the vibrational transfer and relaxation in collisions between O₂⁻ ions and O₂ molecules. The calculated attachment and detachment rate constants turned out to agree well with available measurements in unexcited oxygen. This method was extended to calculate attachment and detachment rates in vibrationally excited oxygen and air. It was shown that the effect of vibrational excitation on electron detachment is profound, whereas attachment of low-energy electrons to vibrationally excited O₂ is inefficient. The calculated rate constants were used to simulate the formation and decay of an electron-beam-generated plasma in air at elevated vibrational temperatures. The calculations showed that vibrational excitation of molecules leads to orders of magnitude increase in the plasma density and in the plasma lifetime, in agreement with available observations.

1. Introduction

Three-body attachment to O₂ to form O₂⁻ ions is one of the dominant mechanisms of the loss of low-energy electrons in non-equilibrium uniform plasmas in oxygen, air and other O₂-containing mixtures. Electron attachment can be somewhat balanced by electron detachment from negative ions at high gas temperatures or at sufficiently high densities of atoms and excited particles. Formation and decomposition of O₂⁻ ions have been studied for the most part at room gas temperature, whereas electron and ion temperatures could be elevated due to application of electric field. Little is known about the rates of electron attachment and detachment in vibrationally and electronically excited gases [1].

It was experimentally shown in [2-4] that the vibrational excitation of electron-beam-generated, nonequilibrium O₂:N₂ plasma with CO laser leads to a two orders of magnitude increase in the plasma free electron lifetime. This effect was ascribed to complete mitigation of rapid three-body electron attachment to molecular oxygen due to electron detachment from O₂⁻ ions in collisions with vibrationally excited molecules. It was mentioned that the mitigation of electron attachment could be important to a variety of potential aerodynamic applications of high pressure, low temperature air plasmas [5]. In addition, the rates of electron attachment and detachment in vibrationally excited gases are necessary to simulate the properties of various gas discharges [6].

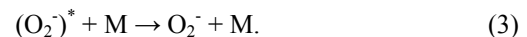
The effect of vibrational excitation on electron detachment from O₂⁻ ions has not been studied till now, whereas three-body electron attachment to vibrationally excited oxygen,



was studied only theoretically in [7] where the rate constant of reaction (1) was calculated under the assumption that M = O₂ is an unexcited molecule. In this work, the approach used in [7] is generalized to consider reaction (1) when the third body is a vibrationally excited O₂ molecule and to consider the reverse reaction, electron detachment from O₂⁻, in a vibrationally excited gas. The rate constants for these reactions are calculated at various vibrational temperatures and, using the results obtained, the production and decay of an electron-beam-generated plasma is simulated in O₂-containing mixtures under the conditions of the experiments [2-4]. Preliminary results of this work were published in [8].

2. Theoretical approach

The three-body electron attachment to O₂ molecule proceeds in two stages [9, 10],



In the first stage, the electron is captured by the molecule into a vibrationally excited temporary negative-ion state (O₂⁻)^{*} (process (2)). This excited molecular ion may subsequently autoionize into a free electron and a neutral molecule (the reverse process) or exceeding energy of the molecular ion may be removed in a collision with a third body M (process (3)). The states of O₂⁻ with vibrational quantum numbers $i > 3$ are temporary and the states with $i \leq 3$ are stable. At not-too-high pressures the lifetime of (O₂⁻)^{*} for electron emission is much shorter than that for the quenching by the third body and the rate of electron attachment varies as the square of pressure.

The rate constant of the three-body electron attachment to $O_2(v=0)$ (v is the vibrational quantum number) can be written as [10, 11]

$$k_a(v=0) = \frac{2^{1/2} \pi^2 \hbar^3}{m^{3/2}} \frac{g_{ion}}{g_e g_M} \sum_{j \geq 4} f(\varepsilon_j) k_q^j \frac{\Gamma_0^j}{\Gamma^j}, \quad (4)$$

where j is the vibrational quantum number of the O_2^- ion, m is the electron mass, g_{ion} , g_M and g_e are the statistical weights of the O_2^- ion, the O_2 molecule and the electron, respectively, k_q^j is the rate constant for quenching of the j -th state of the ion with energy ε_j , Γ^j and Γ_0^j are, respectively, the total and partial (relative to decay into the initial state $e + O_2(v=0)$) width of the j -th state of the O_2^- ion, and $f(\varepsilon)$ is the electron energy distribution function normalized such that

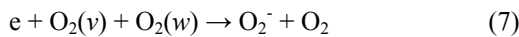
$$\int_0^\infty f(\varepsilon) \varepsilon^{1/2} d\varepsilon = 1. \quad (5)$$

Equation (4) is easy to extended to describe three-body electron attachment to the $O_2(v > 0)$ molecule (reaction (1)). In this case, we have [7]

$$k_a(v) = \sum_j k_a^j(v) \tau_j k_q^j = \frac{2^{1/2} \pi^2 \hbar^3}{m^{3/2}} \frac{g_{ion}}{g_e g_M} \sum_j f(\varepsilon_j - \varepsilon_v) k_q^j \frac{\Gamma_v^j}{\Gamma^j}, \quad (6)$$

where $k_a^j(v)$ is the rate constant of the electron capture by the $O_2(v)$ molecule into the temporary negative-ion state $O_2^-(j)$ with the lifetime τ_j , ε_v is the energy of the $O_2(v)$ molecule with respect to $O_2(0)$, and Γ_v^j is the partial width of the j -th state of the O_2^- ion relative to the decay into the $e + O_2(v)$ state. The summation is performed over all autoionization levels of the ion, lying above the v -th vibrational state of the initial molecule.

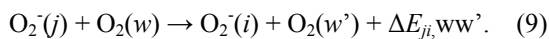
Expression (6) could be used to calculate the rate coefficient for the process



In this case, k_q^j must be replaced by $k_q^j(w)$, the rate constant for quenching of the j -th state of the ion by the $O_2(w)$ molecule. In a vibrationally excited gas this rate constant is expressed as

$$k_q^j(w) = \sum_{i \geq 3} \sum_{w'} k_{ji,ww'}, \quad (8)$$

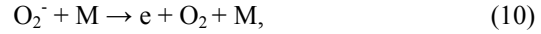
where $k_{ji,ww'}$ is the rate constant of the reaction



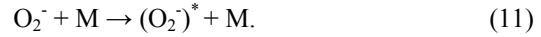
Here, w and w' are the vibrational quantum numbers of O_2 , respectively, before and after the collision with the O_2^- ion and $\Delta E_{ji,ww'}$ is the energy released in reaction (9). At present values of $k_q^j(w)$

cannot be determined semi-empirically for $w > 0$ and, in this work, they are calculated.

Three-body electron attachment to O_2 is described by reactions (2) and (3). It is reasonable to expect that the reverse process, electron detachment from O_2^-



proceeds in a similar way. In this case, a stable O_2^- ion is excited into a vibrationally excited temporary negative-ion state $(O_2^-)^*$ in a collision with M



Then, the excited ion autoionizes into a free electron and a neutral molecule



For simplicity let us consider electron attachment and detachment in pure oxygen; that is, $M = O_2$. The rate of reaction (10) can be calculated in a vibrationally excited gas if the rate constants of reaction (9) are available. At not-too-high gas pressures the rate of reaction (12) is much higher than the rate of reaction (3), $\tau_j N_M k_q^j \ll 1$ (N_M is the gas number density of particles M), and the rate constant for electron detachment (reaction (10)) is expressed as

$$k_d = \sum_{i \geq 3} \sum_{j > 3} \sum_w \sum_{w'} k_{ij,ww'} \delta_i \delta_w, \quad (13)$$

where δ_i and δ_w are the fractions of the stable $O_2^-(i)$ ions and $O_2(w)$ molecules, respectively. Here, the right-hand side of equation (13) is averaged over initial states of the system and summed over all final states leading to electron detachment. Thus, rate constants for the exchange of energy between vibrational and translational (VT) modes and between different vibrational (VV') modes in collisions between O_2^- and O_2 (reaction (9)) are required to calculate the rates of electron attachment and detachment in vibrationally excited oxygen.

In this work, we used the statistical theory to calculate quantitatively the rate constants for reaction (9) and, based on these calculations, to determine the rates of electron attachment and detachment in vibrationally excited oxygen. The statistical (or phase space) approach has been widely used for chemical kinetics of neutral gases and for ion-molecule reactions (see [12, 13] and references cited therein). Based on the statistical theory, vibrational relaxation of molecular ions was considered in [14] (see also [15] and references cited therein).

The statistical treatment assumes strong coupling collisions between reactants with the

formation of an intermediate complex that decomposes according to the relative phase space available to each product state, while total energy and angular momentum are conserved. The statistical approach is based on a hypothesis and the results must be subjected to comparison with experiment to test the validity of the hypothesis. When verified, this approach may provide a simple method to obtain reasonable answers, particularly for complex systems in which other methods are difficult or impossible to apply. In addition, the statistical treatment is complementary to much more sophisticated approaches, like quantum scattering theory and classical dynamical calculations [12].

In this work, according to the common statistical treatment of ion-molecule collisions, the rate constant of reaction (9) was expressed at $\Delta E_{ji,ww'} > 0$ as

$$k_{ji,ww'} = k_L P_{ji,ww'} \quad (14)$$

where k_L is the Langevin collision rate coefficient, $P_{ji,ww'}$ is the probability that the intermediate complex formed in a collision between $O_2^-(j)$ and $O_2^-(w)$ decomposes into $O_2^-(i)$ and $O_2^-(w')$. The probability $P_{ji,ww'}$ is [14, 15]

$$P_{ji,ww'} = \frac{(E - \varepsilon_i - \varepsilon_{w'})^{5/2}}{\sum_i \sum_{w'} (E - \varepsilon_i - \varepsilon_{w'})^{5/2}} \quad (15)$$

where $E = \varepsilon_T + 2\varepsilon_R + \varepsilon_j + \varepsilon_w$ is the total energy of the colliding particles, $\varepsilon_T = 3k_B T/2$ is their average translational energy in the center-of-mass frame, $\varepsilon_R = k_B T$ is the average rotational energy of each molecule, ε_j and ε_w are, respectively, the initial vibrational energies of the ion and molecule and ε_i and $\varepsilon_{w'}$ are their vibrational energies after the collision. The values of the vibrational energies were calculated accounting for vibrational anharmonicity with the spectroscopic constants taken from [16]. Equation (15) is valid only for exothermic processes with $\Delta E_{ji,ww'} > 0$. To satisfy detailed balancing, the probability for any endothermic reverse process was calculated using the probability of the corresponding direct process with the equation

$$P_{ij,w'w} = P_{ji,ww'} \exp(-\Delta E_{ji,ww'}/k_B T) \quad (16)$$

Equation (15) follows from the simplest version of the statistical treatment when ignoring the conservation of total angular momentum. In the zero approximation, this seems to be reasonable for vibrational relaxation of molecular ions. Indeed, it was shown in [14] (see also [15]) that, in this case, taking into account the conservation of total angular momentum is much more computational time-consuming, whereas this leads only to an 1-3 %

change in the calculated results. In addition, our calculation with regard to the conservation of total angular momentum for reaction (9) substantiated this statement.

When calculating attachment and detachment rates, by analogy with our previous works [7, 11], the values of ε_j , I^j and Γ_v^j were taken from [17]. We neglected the spin-orbit splitting of the vibrational levels of the $O_2^-(^2\Pi_g)$ ions; this splitting is around 0.02 eV [16] and is close to the uncertainty in the location of the levels.

3. Validation of theoretical approach

To validate the statistical approach used, we calculated attachment and detachment rate constants under conditions under which measurements are available. For validation of the statistical distribution between various channels of the reactions, it was important to make comparison between calculation and experiment in the case when several vibrational states of temporary or stable O_2^- ions simultaneously play a part in these processes.

Attachment rates have been reliably measured in drift-tube experiments [18] in which electrons are heated in an external electric field and, when captured by O_2 molecules, form temporary O_2^- ions in different vibrational states. Using equation (4), we calculated the attachment rate constant in unexcited oxygen under the conditions of the drift-tube experiments [19, 20] and compared the results with these measurements. The electron energy distribution function was calculated for various values of the reduced electric field E/N , N is the gas number density, using a numerical solution of the electron Boltzmann equation in the classical two-term approximation [18]. Here, we used the standard BOLSIG+ software [21] and electron cross sections given therein. Figure 1 compares the calculated results and measurements [19, 20] as a function of the characteristic electron energy $3D/2\mu$, where D is the transverse electron diffusion coefficient and μ is the electron mobility. The ratio $3D/2\mu$ is equal to the average electron energy when the electron energy distribution is a Maxwellian one. The values of D/μ were also calculated for various ratios E/N using the BOLSIG+ software.

There is good agreement between the calculated attachment rate constant and measurements. Figure 1 also shows the calculated rate constant for electron attachment proceeding only via the first temporary O_2^- state (the first term in the sum on the right-hand side of equation (4)). Comparison of this constant with the total attachment constant testifies that electron attachment proceeds via the first temporary O_2^- state only at low values of D/μ and that the contribution of higher temporary states to electron attachment increases with D/μ . The statistical

approach used agrees well with the experiments for all values of D/μ under consideration and, consequently, describes properly not only the quenching rate constants for temporary O_2^- states, k_q^i , but the ratios between them as well.

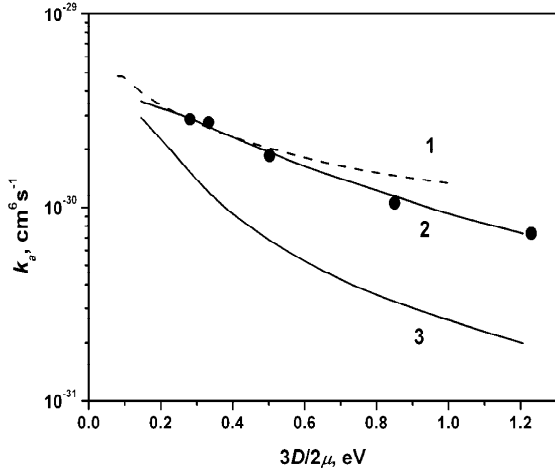


Figure 1. The rate coefficient of three-body electron attachment in oxygen at $T = 300$ K as a function of the characteristic electron energy, $3D/2\mu$. Points correspond to the measurements [20] for 2.8 kPa, curve 1 corresponds to the measurements [19]. Curves 2 and 3 give, respectively, our calculations when considering all temporary states of O_2^- and only the first one.

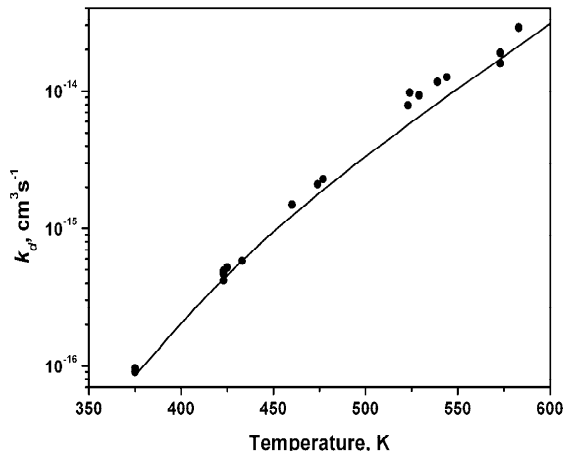


Figure 2. The detachment rate constant for O_2^- ions in oxygen as a function of the gas temperature. Points correspond to the measurements [22] and solid curve corresponds to our calculations.

Detachment rate constant for stable thermal O_2^- ions (reaction (10)) colliding with O_2 has been measured only in the gas temperature range $375 < T < 600$ K [22]. Based on the statistical approach, we calculated this rate constant using expressions (13) - (15). Figure 2 compares the calculated results with the rate constant measured in [22]. Here, it was assumed that the vibrational distributions of stable O_2^- ions and O_2 molecules were in equilibrium at

the gas temperature T . There is good agreement between the calculated and measured detachment rate constants.

4. Electron attachment in vibrationally excited oxygen

Based on statistical approach, attachment and detachment rates can be calculated under conditions when vibrational temperatures of O_2 and O_2^- differ from gas temperature and even when vibrational distributions are non-equilibrium. We used the statistical theory to calculate the values of k_q^j for $M = O_2(v)$ with $v > 0$ and to determine the three-body attachment rate for vibrationally excited third particles. The constants k_q^j were determined from equations (8), (14) and (15). Vibrational distribution for O_2 was assumed to be an equilibrium one with a temperature T_v , whereas the gas temperature was $T = 300$ K. Using the calculated quenching rate constants k_q^j , from (6) we determined the rate constants $k_a(v)$ for reaction (1) with $M = O_2$. It was assumed that electrons are heated in oxygen by an external electric field and the electron energy distribution and characteristic energy were calculated by the BOLSIG+ software.

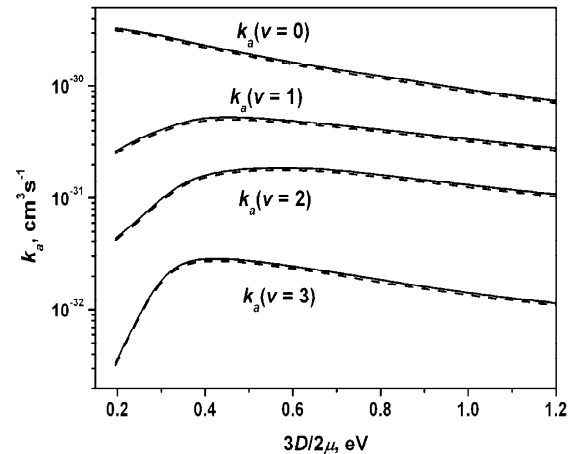


Figure 3. The rate constant of three-body electron attachment to $O_2(v)$, $k_a(v)$, at $T = 300$ K as a function of the characteristic electron energy, $3D/2\mu$. The solid curves correspond to $M = O_2$ at $T_v = 300$ K and dash curves correspond to $M = O_2$ at $T_v = 2500$ K.

Figure 3 shows the calculated values of $k_a(v)$ at $T = 300$ K as a function of the characteristic electron energy. These constants were averaged over vibrational states of $M = O_2$ with various vibrational temperatures T_v . The calculations show that the attachment rates are almost independent of the vibrational temperature of the third body, $M = O_2$; an increase in T_v from 300 to 2500 K led only to a $\sim 4\%$ decrease in the attachment rates. The effect of vibrational excitation on three-body electron attachment is mainly associated with excitation of a

molecule capturing an electron in reaction (2) and causes an orders of magnitude decrease in $k_a(v)$ with increasing v . This effect is more profound for low characteristic electron energies when the process proceeds only via the lowest temporary state. The trends observed are due to that the rate constant of the electron capture by $O_2(v)$ into the temporary negative-ion state $O_2^-(j)$, $k_a^j(v)$, is directly proportional to the partial width Γ_v^j and consequently to the Franck-Condon factor G_{fv}^j [17]. The number growth causes G_{fv}^j for the transition $O_2^-(j) - O_2(v)$ with $j \geq 4$ to exponentially decrease and the attachment rate to $O_2(v)$ is much smaller at higher number v .

5. Electron detachment in vibrationally excited oxygen

We consider electron detachment proceeding via temporary O_2^- ions (reactions (11) and (12)). Consistent description of electron detachment in vibrationally excited oxygen must be based on the balance equations for electrons and master equations for temporary and stable O_2^- ions in various vibrational states. The equation for electrons is written as

$$\frac{dn_e}{dt} = -n_e N \sum_{j>3} k_a^j + \sum_{j>3} \frac{n_j}{\tau_j}, \quad (17)$$

where n_e is the electron density, N is the gas number density for O_2 molecules,

$$k_a^j = \sum_v k_a^j(v) \delta_v, \quad (18)$$

is the average rate constant of electron capture by the O_2 molecule into the temporary negative-ion state $O_2^-(j)$ with the lifetime τ_j and density n_j . The constant k_a^j is averaged over vibrational $O_2(v)$ states with the fractions δ_v .

The master equations for temporary $O_2^-(j)$ ions are

$$\frac{dn_j}{dt} = n_e N k_a^j - \frac{n_j}{\tau_j} + N \sum_{i \neq j} k_{ij} n_i - n_j N \sum_{i \neq j} k_{ji}, \quad (19)$$

where $j > 3$ and

$$k_{ij} = \sum_w \sum_{w'} k_{ij,ww'} \delta_w. \quad (20)$$

The master equations for stable $O_2^-(i)$ ions with $i \leq 3$ are

$$\frac{dn_i}{dt} = -n_i N \sum_{j \neq i} k_{ij} + N \sum_{j \neq i} k_{ji} n_j. \quad (21)$$

Let us consider electron detachment from O_2^- ions in vibrationally excited oxygen. To separate this process from electron attachment, we assume that the density of free electrons can be neglected, $n_e \approx 0$. Then, we have

$$\frac{dn_e}{dt} = k_d N n_n, \quad (22)$$

where $n_n = \sum_{i \leq 3} n_i$ is the total density of stable negative ions. Here, the detachment rate constant k_d is approximately written as

$$k_d = \sum_{i \leq 3} \delta_i \sum_{j>3} \frac{k_{ij}}{1 + N \tau_j k_q^j}, \quad (23)$$

where

$$k_q^j = \sum_{i \leq 3} k_{ji}$$

is the rate constant for quenching of the temporary $O_2^-(j)$ state.

We determined the detachment rate coefficient based on a numerical solution of equation (17) and (19) or from (23). The results obtained were the same. Figure 4 shows the calculated detachment rate constant, k_d , as a function of the vibrational temperature of O_2 , T_v , for $T = 300$ K and for sufficiently low gas densities to satisfy the condition $N \tau_j k_q^j \ll 1$ when the second term in the denominator on the right-hand side of (23) is negligible. For comparison the curve corresponding to the calculation at $T = T_v$ is also presented in figure 4.

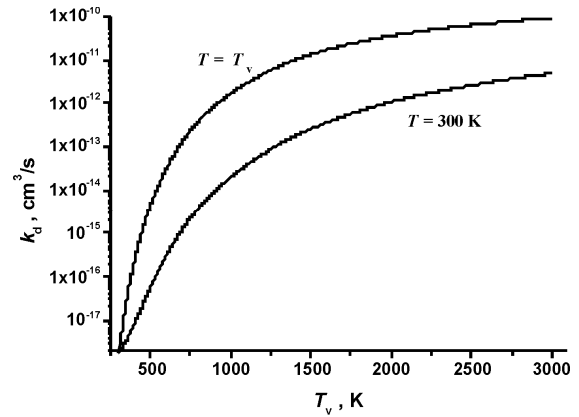


Figure 4. The detachment rate constant as a function of vibrational temperature of O_2 for $T = 300$ K and for $T = T_v$.

It follows from the calculations that the detachment rate at $T = 300$ K increases by six orders of magnitude as T_v rises from 300 to 2500 K. This agrees with the suggestion made in [2-4] to explain these observations. The value of k_d at $T =$

300 K and $T_v = 2500$ K is lower than that at $T = T_v = 2500$ K by a factor of ~ 26 . At $T < T_v$ the contribution of detachment from excited ions to the total detachment rate is less important as compared to the contribution at $T = T_v$ because of a lower vibrational population of stable O_2^- ions in the first case.

6. Plasma production and decay in vibrationally excited oxygen-containing mixtures

In the previous Sections, we considered electron attachment and detachment in pure oxygen. To extend these results to O_2 -containing mixtures, it is necessary to consider reactions (1) and (10) when M is not O_2 . When taking these reactions into account, our results could be applied in many practically important cases. For instance, the rate of reaction (1) for $M = N_2$ is orders of magnitude lower than that for $M = O_2$ [9, 10] and the same is expected for the reverse reaction. In this case, we can neglect the processes with $M = N_2$ and directly extend the results obtained assuming that N and gas pressure are, respectively, the gas number density and partial pressure of oxygen in air or other $N_2:O_2$ mixtures. The results considered could be used also under the conditions of the experiments [2-4] in which $N_2:O_2$ mixtures with a small addition of CO were considered. The effect of CO on electron attachment and detachment is expected to be negligible because of small density of these molecules and because these processes with $M = CO$ seems to be similar to the processes with $M = N_2$.

In experiments [2-4], time-resolved measurements have been performed of the electron density in electron-beam-generated, CO laser excited nonequilibrium plasma. Experiments were carried out in air and some other $N_2:O_2$ mixtures at 40 kPa [4] and 100 kPa [2, 3]. It was shown that vibrational excitation of all molecules to vibrational temperatures of order 2000 K with only a small increase in heavy-species rotational/translational temperature leads to an increase in the plasma lifetime by around two orders of magnitude. Based on the analysis of measurement results and kinetic modeling, the authors concluded that the increase in plasma lifetime is due to an increase in the detachment rate by at least four to five orders of magnitude (compared to equilibrium detachment in a cold gas). As a result, under such conditions, electron attachment to O_2 was completely mitigated by electron detachment and the plasma decay was controlled by electron-ion and ion-ion recombination.

We simulated the formation and decay of electron-beam-generated plasma in vibrationally excited $N_2:O_2$ mixtures under the conditions corresponding to the experiments [2-4]. For this

purpose, we solved numerically the coupled rate equations for electron and negative ion densities

$$\frac{dn_e}{dt} = S - \beta_{ei}n_en_p - k_aN_{O_2}^2n_e + k_dN_{O_2}n_n \quad (24)$$

$$\frac{dn_n}{dt} = k_aN_{O_2}^2n_e - k_dN_{O_2}n_n - \beta_{ii}n_pn_nN \quad (25)$$

using the quasineutrality condition

$$n_p = n_e + n_n \quad (26)$$

Here, S is the ionization rate by high-energy electron impact, n_p is the density of positive ions, β_{ei} and β_{ii} are, respectively, electron-ion and three-body ion-ion rate constants and N_{O_2} and N are, respectively, the oxygen and total gas number densities. Numerous calculations showed that the dominant positive ion species in dry air plasma at high (around 100 kPa) pressures is O_4^+ , whereas other ions are fast (at times much shorter than plasma lifetimes) transformed into O_4^+ due to charge transfer and ion-molecule reactions (see, for instance, [23, 24]). In the absence of heating electric fields, dissociative electron attachment to form O^- ions is unimportant and it is expected that negative ion composition in $N_2:O_2$ mixtures is dominated by O_2^- . Therefore, we considered only O_4^+ and O_2^- ions and took the values of β_{ei} and β_{ii} for these ions from [25]. The values of S , gas temperature, T , vibrational temperature of O_2 , T_v , and electron temperature, T_e , were taken by analogy with [2-4]. In [4], the value of T_e was not given and here we assumed $T_e = T_v$, due to electron heating in superelastic collisions with vibrationally excited molecules. The rate constants k_a and k_d were taken from [25] for unexcited mixtures and were calculated by analogy with previous Sections of this work for vibrationally excited mixtures.

Figure 5 shows the calculated evolution in time of the electron density at 40 kPa under the conditions typical to the experiment [4] and at 100 kPa under the conditions typical to the experiment [2, 3]. For comparison, the results calculated in unexcited gases are also given. Our calculations show that vibrational excitation of molecules leads to an increase by more than an order of magnitude (i) in quasi-steady electron density in the electron-beam-generated plasma and (ii) in the plasma lifetime.

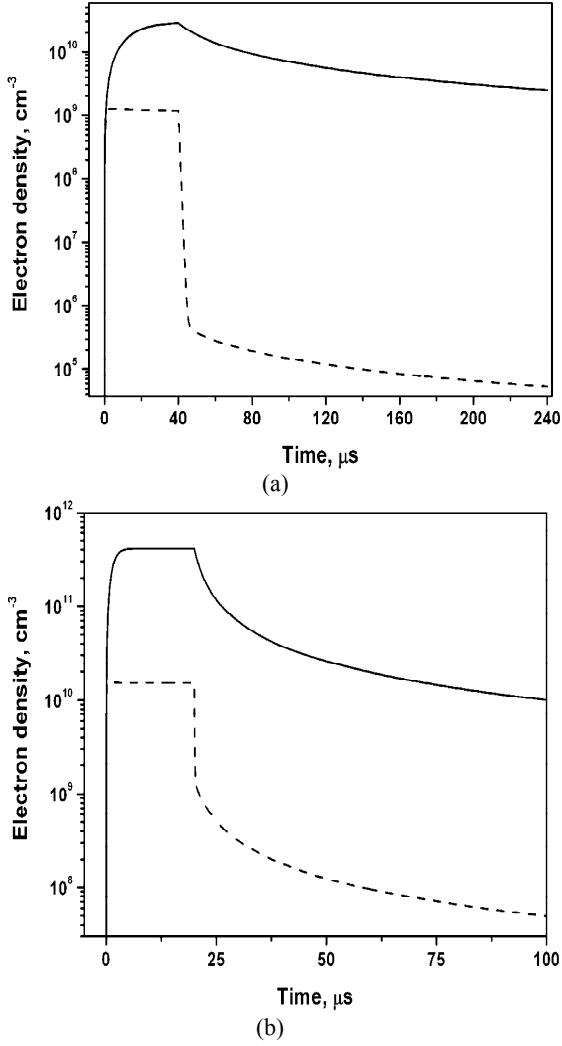


Figure 5. The evolution in time of the electron density in electron-beam-generated plasma. (a) $N_2:O_2 = 9:1$, $p = 40$ kPa, a $40 \mu s$ electron beam pulse duration, (solid curve) $T_v = T_e = 2500$ K and $T = 350$ K and (dash curve) $T_v = T_e = T = 300$ K; (b) $N_2:O_2 = 4:1$, $p = 100$ kPa, a $20 \mu s$ electron beam pulse duration, (solid curve) $T_v = 2500$ K $T_e = 5000$ K and $T = 560$ K and (dash curve) $T_v = T_e = T = 300$ K.

Figure 6 shows the calculated $1/n_e$ against the time plot during the plasma decay in the excited mixtures. Good linear behavior of such plots means that the plasma decays as if the loss of electrons were dominated by electron-ion recombination. The calculations show that, under the conditions considered, the effective electron-ion recombination coefficient is

$$\beta_{eff} = \beta_{ei} + \beta_{ii}v_a/v_d, \quad (27)$$

where $v_a = k_a N_{O_2}^2$ and $v_d = k_d N_{O_2}$ are the frequencies of electron attachment and detachment, respectively. Equation (27) was derived in [26] (see also [6]) under the assumptions that $v_a, v_d \gg \beta_{ei}n_p, \beta_{ii}n_p$, which are satisfied under the conditions

studied. Figure 6 also shows the plots calculated when neglecting electron attachment and detachment processes and consequently $\beta_{eff} = \beta_{ei}$. Comparison of the plots in this figure shows that the contribution of the last term on the right-hand side of (27) is only about 20 %; that is, electron attachment is almost totally balanced by detachment and the plasma decay is mainly governed by electron-ion recombination, in agreement with the conclusions made in [2-4].

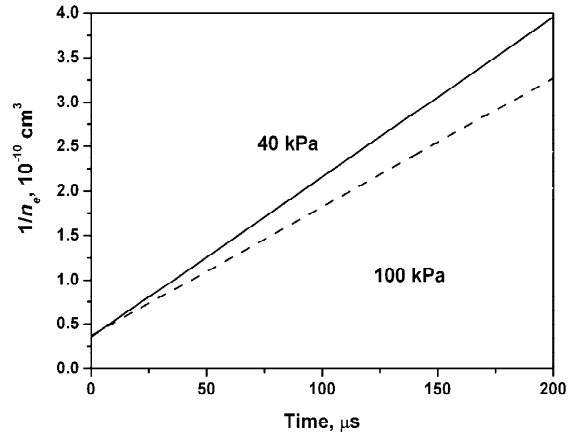


Figure 6. The calculated $1/n_e$ against the time plot during the plasma decay in the excited mixtures. The solid curves correspond to the same conditions as those for the solid curves in Figure 5 (a) and (b) and dash curves correspond to the calculations for the same parameters when neglecting electron attachment and detachment processes.

Table 1. The time $\tau_{1/2}$ it takes to reduce initial electron density by half.

Gas mixture	P , kPa	Calc. for $T_v = T = T_e = 300$ K	Calc. for $T_v = 2500$ K, $T < T_v, T_e \geq T_v$	Meas.
$N_2:O_2=9:1$	40	0.4 μs	20 μs	6 μs [4]
$N_2:O_2=4:1$	100	0.04 μs	2 μs	5 μs [2, 3]

Table 1 presents the time $\tau_{1/2}$ it takes to reduce initial electron density by half after the electron beam is turned off; this time was determined from the calculated plots in figure 5 and from the experimental curves presented in [2-4]. The calculated results and measurements agree qualitatively. Quantitative disagreement between calculations and measurements seems to be primarily induced by an experimental error, which could be sufficiently large because of a strong nonuniformity of the excited region in the plasma. In particular, to reach good agreement between the measurements and numerical modeling under the assumption of a uniform plasma region, the authors of [4] had to use $\beta_{ei} = 1.1 \times 10^{-5} \text{ cm}^3 \text{ s}^{-1}$, the value which is much higher than the typical

recombination rate constants for O_4^+ and similar ions [25, 27]. It was mentioned in [4] that the measured too high rate of plasma decay could be explained by electron attachment in regions located at some distance from the CO laser centerline in which T_v is moderate and attachment is not totally mitigated by detachment. In addition, there is a calculation error of the calculations associated with uncertainty in the values of β_{ei} and β_{ii} ; for instance, β_{ei} given in [25] differs by a factor of three from that given in [27]. Finally, the effect of vibrational excitation on β_{ei} (for O_4^+) and on β_{ii} has not been studied and deserves a special consideration.

7. Conclusions

Based on the statistical approach, the rates of vibrational relaxation of O_2^- in collisions with O_2 were determined. These rates were used to obtain the rates of three-body electron attachment and detachment from O_2^- ions in oxygen under the assumption that these processes proceed via vibrationally excited temporary O_2^- ions. This approach was validated by comparison of the calculated results with measured attachment rates for nonthermal electrons in heating electric fields and with measured detachment rates in oxygen heated to 600 K.

Solving numerically the master equations for temporary and stable O_2^- ions, attachment and detachment rates were calculated in vibrationally excited oxygen when vibrational temperature of O_2 is higher than the translational temperature. The rates of three-body electron attachment to excited O_2 molecules were orders of magnitude lower than the rate of attachment to unexcited molecules. It was shown that the detachment rate increases by six orders of magnitude as the vibrational temperature of O_2 rises from 300 to 2500 K at room translational temperature.

Using the calculated attachment and detachment rates, the formation and decay of an electron-beam-generated plasma in $N_2:O_2$ mixtures was numerically simulated at elevated vibrational temperatures. It was shown that vibrational excitation of molecules leads to orders of magnitude increase in the plasma density and in the plasma lifetime, in agreement with available observations.

References

1. Christophorou L G and Olthoff J K 2000 *Adv. Atom. Mol. Optical Physics* **44** 155
2. Palm P, Plonjes E, Adamovich I V and Rich J W 2002 AIAA paper number 2002-2224 33rd *Plasmadynamics and Lasers Conference (Maui, Hawaii, May 20-23)*
3. Rich W, Adamovich I V, Lempert W, Vidmar R and Barker B 2004 *In: Non-Equilibrium Air*

Plasmas at Atmospheric Pressure Ed. Becker K H, Kogelschatz U, Schoenbach K H and Barker R J (Bristol: IOP)

4. Frederickson K, Lee W, Palm P, Adamovich I V, Rich J W and Lempert W R 2007 *J. App. Phys.* **101** 093302
5. Bletzinger P, Ganguly B N, Van Wie D and Garscadden A 2005 *J. Phys. D: Appl. Phys.* **38** R33
6. Raizer Yu P 1991 *Gas Discharge Physics* (Berlin: Springer)
7. Aleksandrov N L and Konchakov A M 1984 *High Temp. (USSR)* **22** 205
8. Aleksandrov N L and Anokhin E M 2009 *J. Phys. D: Appl. Phys.* **42** 225210
9. Massey H 1976 *Negative Ions* (Cambridge: Cambridge University Press)
10. Smirnov B M 1982 *Negative Ions* (New York: McGraw-Hill)
11. Aleksandrov N L 1988 *Soviet Phys. Uspekhi* **31** 101
12. Light J C 1968 *Disc. Faraday Soc.* **44** 14
13. Nikitin E E and Umanskii S Ya 1974 *Chemistry of plasmas* ed B M Smirnov (Moscow: Atomizdat) No 3 p 8 (in Russian)
14. Karachevtsev G V 1970 *Khim. Vys. Energii* **4** 387 (*High Energy Chem.*)
15. Karachevtsev G V and Talrose V L 1987 *Chemistry of plasmas* ed B M Smirnov (Moscow: Energoatomizdat) No 14 p 255 (in Russian)
16. Radtsig A A and Smirnov B M 1985 *Reference data on atoms, molecules and ions* (Berlin: Springer)
17. Parlant G and Fiquet-Fayard F 1976 *J. Phys. B: Atom. Molec. Phys.* **9** 1617
18. Huxley L G H and Crompton R W 1974 *The diffusion and drift of electrons in gases* (New York: Wiley)
19. Chanin L M, Phelps A V and Biondi M A 1962 *Phys. Rev.* **128** 219
20. Grunberg R 1969 *Z. Naturforsch.* **24a** 1039
21. Hagelaar G J M and Pitchford L C 2005 *Plasma Sources Sci. Technol.* **14** 722
22. Pack J L and Phelps A V 1966 *J. Chem. Phys.* **44** 1870
23. Akishev Yu S, Derugin A A, Karalnik V B, Kochetov I V, Napartovich A P and Trushkin N I 1994 *Plasma Phys. Rep.* **20** 511
24. [Aleksandrov N L and Bazelyan E M 1999 *Plasma Sources Sci. Technol.* **8** 285
25. Kossyi I A, Kostinsky A Yu, Matveyev A A and Silakov V P 1992 *Plasma Sources Sci. Technol.* **1** 207
26. Napartovich A P, Naumov V G and Shashkov V M 1975 *Fiz. Plazmy* **1** 821
27. Florescu-Mitchell A I and Mitchell J B A 2006 *Phys. Rep.* **430** 277

MODELING OF TOLUENE CONVERSION IN NON-THERMAL NITROGEN PLASMA

M. A. Deminsky¹, I.V. Kochetov², A.N. Trushkin², S. Ya. Umanski³

¹ State Research Center of Russia "Kurchatov Institute", Moscow, Russia

² State Research Center of Russia Troitsk Institute for Innovation and Thermonuclear Research (TRINITI), Troitsk, Moscow region, Russia

³ Institute of Chemical Physics RAS, Moscow, Russia

Abstract. The kinetic model of the destruction of toluene in non-thermal nitrogen plasma is formulated in the report. Reactions of C₇H₈ with nitrogen molecules in the N₂ (A) and N₂ (a') states play a major role in the mechanism of toluene removal. Conversion channels of toluene and their relative probabilities have been chosen based on analysis of the heat of reaction, the law of conservation of spin, as well as experimental data on the composition of by-products. Results of numerical simulation of the destruction of toluene in nitrogen plasma produced by dielectric barrier discharge are also presented.

Numerical calculations were performed for the experimental conditions: gas pressure and temperature were equal to P = 1 atm and T = 300 - 600 K, respectively, specific energy input into the gas varies between Q = 0 - 400 J/liter, initial toluene concentration values: 100 and 400 ppm. Calculated concentrations of toluene and several by-products (C₂H₂, CH₄, HCN) at the output of gas-discharge reactor, as a function of energy deposited in the gas are presented in the work. The results of numerical simulation were compared with experimental data. This comparison shows good agreement between the calculated and experimental data.

Introduction

Toluene (C₇H₈) is one of the most widely used organic solvents in modern industry. Toluene vapours are also present in considerable concentration in the exhaust gases of internal combustion engines. The problem of waste gas cleaning from C₇H₈ (and other volatile organic solvents) is very relevant and there are few, if any, economically viable solutions. Researchers in many developed countries (USA, France, Japan, etc.) are seeking new efficient methods for cleaning contaminated gas streams. The development of electrical methods of gas treatment, based on the creation of high concentration of chemically active and environmentally friendly particles by a non-thermal plasma in the contaminated gas without appreciable heating of the treated gas stream is one of the promising directions. Produced reactive particles react with the pollutant molecules and decompose the harmful pollutants. The set of the basic reactions that determines the chemical kinetics in the activated gas flow is determined by the composition of the processed gas and the type of electrical discharge used to generate non-thermal plasma. Recently, some experimental studies on the destruction of low concentration toluene (at the level of 100-400 ppm) in a non-thermal nitrogen plasma at atmospheric pressure generated by a dielectric barrier discharge appeared in the literature [1-3]. The results of these studies clearly demonstrate the high reactivity of nitrogen plasma [2] and air plasma [3] with respect to toluene. Meanwhile, in the well-known works on toluene removal from exhaust gases [4], where nitrogen is the dominating component, the reactivity of the excited nitrogen is not taken into account. To a large

extent, this situation is due to the fact that the toluene reactions with excited nitrogen were not represented in the literature until recently. In such a situation carrying out of experiments on toluene removal under simplified (as much as possible) experimental conditions where the number of active components is insignificant and is supposed unequivocal interpretation of the results obtained, is rather valuable as allows to identify most reliably channels of pollutant conversion and to choose speed constants of the basic reactions. To make similar conclusions for the real polluted gas (for example, air) is much more difficult and less reliable. Obviously, the determination of the mechanism of toluene conversion in nitrogen plasma is not only scientific interest but also has considerable practical interest owing to choosing the treatment conditions under which the generation of excited nitrogen components is most effective.

Model description

Kinetic model of conversion of toluene in non-thermal nitrogen plasma is formulated and the results of numerical simulation of the toluene destruction in nitrogen plasma of dielectric barrier discharge are presented in the report. Numerical calculations have been performed for the experimental conditions of [2], the gas pressure was equal to P = 1 bar, gas temperature varied in the range of T = 300 - 600 K. Unfortunately, data on nitrogen purity used in experiment are not represented in [2]. We accept that it does not contain impurity. A repetition frequency of unipolar voltage pulses in [2] ranged f = 0-200 Hz, discharge pulse current duration at half amplitude level was equal to 50 ns. Specific energy input into the gas

was varied by changing the pulse repetition frequency of current pulses at a fixed volume gas flow and was ranged within the $Q = 0 - 400 \text{ J / liter}$. It was accepted as initial approach in numerical modeling unlike experiment that all energy was entered into gas for one pulse. Obviously, that such approach leads to increase in initial concentration of the excited nitrogen components produced in the discharge in comparison with [2] where energy was entered into the gas by small portions. High concentration of excited nitrogen components can lead to their mutual destruction, for example, $\text{N}_2(\text{A}^3\Sigma_u^+)$ molecules due to the Pooling reaction and, accordingly, to the useless partial loss of energy reserved at electronic levels. It is supposed in future to complicate numerical model by taking into account the repeated pulse energy input. The experiments [2] were carried out for two values of initial concentration of toluene: 100 and 400 ppm. Concentrations of toluene and several by-products (C_2H_2 , CH_4 , and HCN) at the output of gas-discharge reactor, depending on the specific energy input in the gas are presented in the paper.

Since the gas discharge in molecular gases at atmospheric pressure is often a sharply non-uniform in space and time dependent plasma process, the correct self-consistent description of plasma-chemical reactor should be based on nonstationary three-dimensional model of gas discharge and plasma chemical processes. It is a difficult task and exact description is not possible currently for several reasons. Therefore various simplifying assumptions in numerical modeling are made. One of these assumptions concerns the effective reduced electric field in the discharge E / N (where E - electric field, N - total density of neutral particles), which corresponds to the main production of chemically active species. Really there are various regions with different value of E / N in streamer-type discharges (pulsed corona, dielectric barrier discharge). The reduced electric field in the streamer head, E / N , is equal to 500-1000 Td ($1 \text{ Td} = 10^{-17} \text{ V cm}^2$), in accordance with [5], $E / N \sim 20 \text{ Td}$ in the plasma channel of the primary streamer [6], $E / N = 70 - 100 \text{ Td}$ in the secondary streamer channel [6]. It is assumed in [7] for plasmachemical processes modeling (based on the results of two-

dimension numerical simulation of the streamer propagation) that generation of all excited particles, atoms and radicals occurs in the streamer head at $E / N = 900 \text{ Td}$. The fraction of the input electrical energy, which is released in the streamer head and spent for the generation of chemically active species, is a fitting parameter in such model. However, the results of resent experimental works [6,8,9] indicate that the basic production of excited particles, atoms and radicals in pulsed corona and dielectric barrier discharge does not occur in the streamer head, but in the channel of the secondary streamer, where the most part of energy input occurs at a value of reduced electric field $E / N = 70 - 100 \text{ Td}$. Taken into account these results, the kinetic Boltzmann equation for a function of electron energy distribution at a value of reduced electric field $E / N = 50 - 500 \text{ Td}$ was numerically solved in this study to determine the rates of various processes occurring in the discharge by collisions with electrons, resulting in an producing of excited particles. The calculated densities of chemically active components produced by the discharge were specified as initial parameters for the system of differential equations of non-equilibrium chemical kinetics. Under the simulation of plasma chemical processes. it was assumed that these processes do not affect the properties of the discharge. The validity of this approach depends on the chemical nature and concentration of pollutants, the rate of non-equilibrium chemical reactions in the plasma, the pulse repetition frequency, the concentration of by-products, etc. A good reason for this approach in this paper is the weak dependence of the discharge parameters (amplitude and duration of the current pulse, energy input into the discharge, etc.) on the initial concentration of toluene and pulse repetition rate, observed in the experiment [2]. Reactions of the excited nitrogen component production in the discharge are presented in table 1.

Electron cross sections with nitrogen molecules were taken from [10]. Dissociation sections of nitrogen molecules with excited nitrogen atoms (N^2D) formation were taken from [11].

Processes with the participation of toluene given in [2] are the basis of the kinetic model. The

Table 1

No	Reaction	Energy threshold, eV	Source
1	$\text{N}_2 + e \rightarrow \text{N}_2(\text{A}^3\Sigma_u^+) + e$	6,17	[10]
2	$\text{N}_2 + e \rightarrow \text{N}_2(\text{a}^1\Sigma_u^-) + e$	8,40	[10]
3	$\text{N}_2 + e \rightarrow \text{N}_2(\text{Esum}) + e$	7,35	[10]
4	$\text{N}_2 + e \rightarrow \text{N}(\text{A}^4\text{S}) + \text{N}(\text{A}^4\text{S}) + e$	9,76	[10]
5	$\text{N}_2 + e \rightarrow \text{N}(\text{A}^4\text{S}) + \text{N}(\text{N}^2\text{D}) + e$	12,14	[11]

Table 2

№	Reaction	$k(T=298\text{ K}), \text{ cm}^3/\text{c}$	$A, \text{ cm}^3/\text{s}^{(a)}$	n	$E_a, \text{ kcal/mol}$	Ref.
1	$\text{N}_2(\text{A})+\text{C}_6\text{H}_5\text{CH}_3 \rightarrow \text{C}_6\text{H}_5+\text{CH}_3+\text{N}_2$	$6 \cdot 10^{-11}$	$6,0\text{e-}11$	0	0	Estimation
2	$\text{N}_2(\text{A})+\text{C}_6\text{H}_5\text{CH}_3 \rightarrow \text{C}_6\text{H}_5\text{CH}_2+\text{H}+\text{N}_2$	$6 \cdot 10^{-11}$	$6,0\text{e-}11$	0	0	Estimation
3	$\text{N}_2(\text{A})+\text{C}_6\text{H}_5\text{CH}_3 \rightarrow \text{C}_6\text{H}_4\text{CH}_3+\text{H}+\text{N}_2$	$6 \cdot 10^{-11}$	$6,0\text{e-}11$	0	0	Estimation
4	$\text{N}_2(\text{a}')+\text{C}_6\text{H}_5\text{CH}_3 \rightarrow \text{C}_5\text{H}_6+\text{C}_2\text{H}_2+\text{N}_2$	$6 \cdot 10^{-11}$	$6,0\text{e-}11$	0	0	Estimation
5	$\text{N}(\text{D})+\text{C}_6\text{H}_5\text{CH}_3 \rightarrow \text{C}_6\text{H}_5\text{CH}_2+\text{NH}$	$3 \cdot 10^{-11}$	$3,0\text{e-}11$	0	0	[12]
6	$\text{H}+\text{C}_6\text{H}_5\text{CH}_3 \rightarrow \text{C}_6\text{H}_6+\text{CH}_3$	$1.4 \cdot 10^{-14}$	$1,4\text{e-}13$	2	6,87	[13]
7	$\text{N}_2(\text{A})+\text{N}_2(\text{A}) \rightarrow \text{N}_2(\text{B,C})+\text{N}_2$	$4.5 \cdot 10^{-10}$	$4,5\text{e-}10$	0	0	[13]
8	$\text{N}_2(\text{B})+\text{N}_2 \rightarrow \text{N}_2(\text{A})+\text{N}_2$	$3 \cdot 10^{-11}$	$3,0\text{e-}11$	0	0	[14]
9	$\text{N}+\text{CH}_3 \rightarrow \text{HCN}+\text{H}_2$	$2.9 \cdot 10^{-11}$	$3,9\text{e-}11$	0	0,84	[2]
10	$\text{N}+\text{CH}_4 \rightarrow \text{HCN}+\text{H}_2+\text{N}$	$1 \cdot 10^{-14}$	$1,0\text{e-}14$	0	0	[13]
11	$\text{N}+\text{C}_2\text{H}_2 \rightarrow \text{HCN}+\text{CH}$	$5.4 \cdot 10^{-15}$	$5,4\text{e-}15$	0	0	[13]
12	$\text{C}_6\text{H}_5+\text{H}_2 \rightarrow \text{C}_6\text{H}_6+\text{H}$	$4.2 \cdot 10^{-21}$	$9,7\text{e-}14$	2,4	50	[13]
13	$\text{N}+\text{CH} \rightarrow \text{CN}+\text{H}$	$2.1 \cdot 10^{-11}$	$2,1\text{e-}11$	0	0	[2]
14	$\text{N}_2(\text{A})+\text{HCN} \rightarrow \text{products}$	$6 \cdot 10^{-12}$	$6,0\text{e-}12$	0	0	[13]
15	$\text{H}+\text{HCN}+\text{N}_2 \rightarrow \text{H}_2\text{CN}+\text{N}_2$	$3.2 \cdot 10^{-40}$	$7,7\text{e-}31$	0	63,68	[13]
16	$\text{H}+\text{CH}_3+\text{N}_2 \rightarrow \text{CH}_4+\text{N}_2$	$2 \cdot 10^{-26}$	$2,48\text{e-}26$	-1,2	0,6	[2]
17	$\text{CH}+\text{CH} \rightarrow \text{C}_2\text{H}_2$	$2 \cdot 10^{-10}$	$2,0\text{e-}10$	0	0	[2]
18	$\text{N}+\text{N}+\text{N}_2 \rightarrow \text{N}_2+\text{N}_2$	$1 \cdot 10^{-33}$	$1,0\text{e-}33$	0	0	[13]
19	$\text{C}_6\text{H}_5 \rightarrow \text{C}_2\text{H}_2+\text{C}_4\text{H}_3$	$3.6 \cdot 10^{15}$	$3,3\text{e+}33$	-17	1,13	[13]
20	$\text{C}_6\text{H}_5+\text{H} \rightarrow \text{C}_6\text{H}_6$	$1.6 \cdot 10^{-10}$	$1,63\text{e-}10$	0,2	0	[13]
21	$\text{H}+\text{H}+\text{N}_2 \rightarrow \text{H}_2+\text{N}_2$	$6 \cdot 10^{-33}$	$6,0\text{e-}33$	-1	0	[13]
22	$\text{CN}+\text{H} \rightarrow \text{HCN}$	$1.7 \cdot 10^{-10}$	$1,73\text{e-}10$	0	0	[13]
23	$\text{C}_6\text{H}_6+\text{N}_2(\text{A}) \rightarrow \text{products}$	$1.6 \cdot 10^{-10}$	$1,6\text{e-}10$	0	0	[13]
24	$\text{N}(\text{D})+\text{N}_2 \rightarrow \text{N}+\text{N}_2$	$1.7 \cdot 10^{-14}$	$1,7\text{e-}14$	0	0	[12]

a) For the rate constant calculation we used such conventional formula: $k = A \left(\frac{T}{298} \right)^n e^{-\frac{E_a}{RT}}$.

table 2 provides a complete list of reactions with the corresponding rate constants, which are included in a plasma model for the transformation of toluene in nitrogen plasma. It is necessary to pay attention first of all on the reaction (1-4) of metastable electronically excited nitrogen molecules $\text{N}_2(\text{A}^3\Sigma_u^+)$ and $\text{N}_2(\text{a}'^1\Sigma_u^-)$ with toluene, from which toluene conversion process starts, and which are the major contributors to toluene removal. It should be noted that only the reaction $\text{N}_2(\text{A}^3\Sigma_u^+)$ with other aromatic hydrocarbon benzene C_6H_6 is known at present [15,16]:

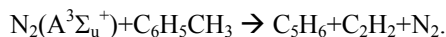


with constants equal to $1,6 \cdot 10^{-10} \text{ cm}^3\text{s}^{-1}$ [15], $3,2 \cdot 10^{-10} \text{ cm}^3\text{s}^{-1}$ [16].

We are not aware of direct experimental evidence of the reactions (1-4). The inclusion of

reactions (1-4) in the destruction mechanism of toluene is based on the known experimental fact [15] that the rate of quenching reactions of $\text{N}_2(\text{A}^3\Sigma_u^+)$ by a number of hydrocarbons increases with their complexity. The presence of by-products methane CH_4 and hydrogen cyanide HCN of toluene decomposition strong evidences in favor of reactions (1-3), in which there is production of H atoms and methyl group CH_3 . The relative probability of reactions (1-3) can be estimated on the basis of exothermic effect of reactions. It seems that the reaction (2) is the most probable, because 2.3 eV release. Reactions of (1,3) have approximately the same probability, because they release 1.7 eV and 1.3 eV, respectively. However, the difference between the rate constants of reactions (1,3) and reaction (2) should not be significant, since all these reactions are highly exothermic. Rate constants of reactions (1-3) are

assumed to be equal to each other in our calculations. Generation of noticeable amount of acetylene C_2H_2 at the exit of plasma-chemical reactor indicates that the reactions of C_7H_8 conversion occur with the the toluene ring cleavage. In [2] the following reaction is proposed as such a reaction:



However, the electronic energy supply of the molecule $N_2(A^3\Sigma_u^+)$ is sufficient to overcome the reaction energy barrier, analysis of this reaction initial and final products is indicative of its low probability due to non-conservation of spin. In this paper, reaction (4) as a cleavage toluene ring reaction is proposed, in which nitrogen molecules in the metastable triplet state of $N_2(A^3\Sigma_u^+)$ are replaced by a molecules in the metastable singlet state $N_2(a^1\Sigma_u^-)$, with a rate constant equal to the rate constant of reaction (1-3). The molecules $N_2(a^1\Sigma_u^-)$ production rate is approximately two times less than the molecules $N_2(A^3\Sigma_u^+)$ production rate at the reduced electric field $E/N = 70 - 100$ Td. The absolute values of the rate constants of reactions (1-4) were taken equal to $0, 25 k_b$, where k_b - rate constant of $N_2(A^3\Sigma_u^+)$ with benzene. We accept followed by [2] that $k_b = 2.4 \cdot 10^{-10} \text{ cm}^3 \text{ s}^{-1}$ (the mean value of two known ones).

Reactions (5) and (6) contribution is significantly smaller than the contribution to the toluene removal in comparison with reactions (1-4): their contribution does not exceed 10% and 5% respectively. However, their inclusion in the mechanism of toluene conversion improves the agreement between the results of numerical simulation and experimental data. Pooling reactions (7) have a noticeable effect on the molecules $N_2(A^3\Sigma_u^+)$ balance at small toluene concentrations only. Chemical Workbench code (CWB) [17], carrying out the solution of equations of chemical kinetics with the participation of electronically excited atoms and molecules were used for modeling. Stationary Boltzmann equation in two-term approximation was solved [10] to calculate the electron energy distribution function. We used the cross sections of electron interactions with nitrogen molecules according to [10, 11].

Comparison of simulation results with experiment.

Calculation of the electron energy distribution function and concentration of chemically active particles produced in the discharge was carried out at reduced electric field E/N ranged in 50-1000 Td. The agreement between model and experimental results on toluene removal degree at $E/N=900$ Td (streamer's head) was obtained provided that the specific deposited energy

was equal to 12% of experimentally measured one. The best agreement between model and experimental results was reached at $E/N=70-80$ Td under the condition of the main excited particles in the secondary streamer production.

Comparison of simulation results with experimental data [2] was performed both in share of toluene removal and on the composition and concentration of by-products depending on the specific energy input of the discharge. Fig. 1 shows the results of comparison of numerical calculations with experimental data [2] for the toluene removal as function of specific energy input for two values of initial toluene concentration.

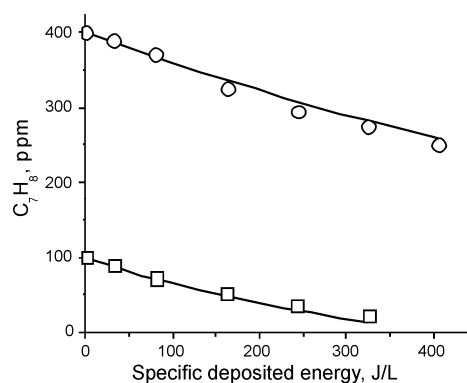


Fig.1. Dependence of the toluene concentration at the reactor outlet on the specific energy input. $[C_7H_8]_0 = 100$ ppm (squares) and 400 ppm (circles), $T = 323$ K. Markers show experiment [2], lines show modeling results.

It is seen that the results of numerical simulations are in good agreement with experimental data.

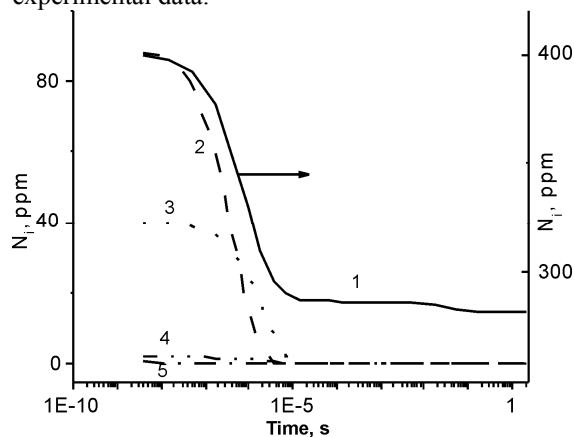


Fig. 2. Calculated time dynamics of toluene and excited nitrogen species. The initial concentration of toluene $[C_7H_8]_0 = 400$ ppm, the gas temperature $T = 323$ K, the specific energy input -325 J / liter. 1 - Toluene, 2 - $N_2(A^3\Sigma_u^+)$, 3 - $N_2(a^1\Sigma_u^-)$, 4 - $N_2(Esum)$, 5 - $N(2D)$

In Fig.2 the calculated dependences of remaining toluene and active nitrogen species concentration versus time are shown. Figure 2 shows the calculated curve of concentration of toluene, depending on the time. It is clear that there are two distinct stages in the toluene destruction dynamics: fast (characteristic time ≈ 5 microseconds) and slow (characteristic time ≈ 100 ms). Major toluene removal occurs during fast stage, slow stage contributes a smaller role in the toluene destruction.

Comparison of the dynamics of the toluene destruction with the behavior of the main active components of nitrogen (Figure 2) shows that all active components of molecular nitrogen are spent during the rapid removal stage (during 5 μ s).

The slow removal of toluene at times $t > 5$ microseconds is due to nitrogen atoms produced by gas discharge (reactions (5, 6)). The increase of the $N_2(A^3\Sigma_u^+)$ concentration (Fig. 2) immediately after the end of the discharge is due to the cascade processes from the upper electronic states of N_2 molecules (reaction (8)). It is seen from Fig. 2 that about 93% of produced molecules $N_2(A^3\Sigma_u^+)$ and $N_2(a^1\Sigma_u^-)$ are spent on the destruction of the toluene molecules. Energy price ε of removal of one toluene molecule obtained in the numerical calculations is equal to $\varepsilon \approx 1150$ eV / molec. This value is very close to the experimentally measured $\varepsilon \approx 1200$ eV / molec [2].

In Fig. 3, the results of numerical simulation of some turned out by-products of toluene decomposition at the initial concentration of $[C_7H_8]_0 = 400$ ppm are presented and compared with experimental data. This comparison shows good agreement between the calculated and experimental data [2].

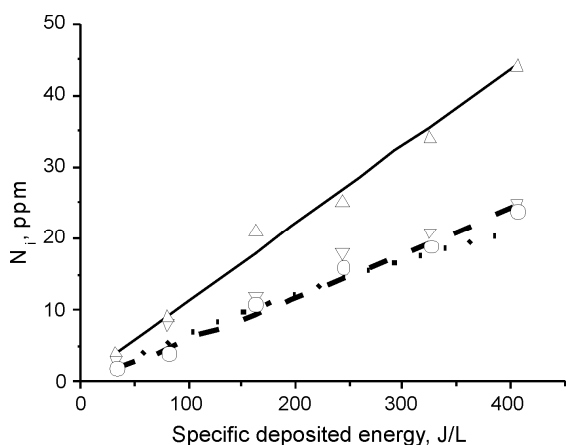


Fig. 3. Dependence of the by-product concentration at the reactor outlet on the specific energy input. $[C_7H_8]_0 = 400$ ppm, $T = 323$ K. Markers show experiment, lines show the results of simulation: \square , --- - HCN; Δ , -- - C_2H_2 ; \circ , ··· - CH_4 [2].

In Fig. 4 the kinetic curves of some by-products of toluene conversion, which were detected in the experiment [2], are shown.

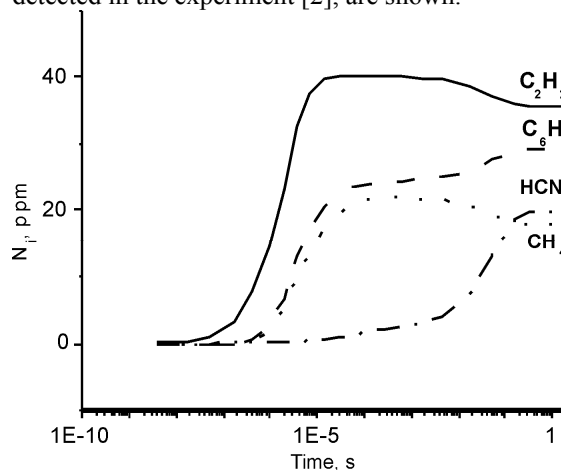


Fig.4. Dynamics of the main by-products of toluene decomposition. The initial concentration of toluene $[C_7H_8]_0 = 400$ ppm, the gas temperature $T = 323$ K, the specific energy input -325 J / l. Lines: — C_2H_2 , ---- C_6H_6 , ··· CH_4 , ···· HCN.

It should be noted on the rapid increase of acetylene C_2H_2 during the toluene decomposition. The dynamics of its increase is highly correlated with the stage of fast toluene destruction. This fact indicates that the proposed reaction (4), occurring with cleavage of the benzene ring and leading to the fast formation of C_2H_2 really takes place. Other reactions of acetylene formation (17-19) have a much lower rate of C_2H_2 production under experimental conditions [2]. Acetylene concentration increases proportionally to the specific energy input (Fig. 3) observed in the experiment. This fact indicates that produced C_2H_2 is weakly destroyed by the discharge. Model dynamic behavior of C_2H_2 (Fig. 4) was generally consistent with this statement, but there is a small (about 10%) destruction of acetylene at large times owing to the reaction (11).

Similar conclusions can be made with regard to methane. Quantitative comparison of model and experimental results shows that the destruction of CH_4 at large times owing to the reaction (10) reaches 20% (Fig. 4). Such rate of methane decomposition leads to a decrease of about 12% of the calculated CH_4 concentration compared with the concentration experimentally measured at high specific energy input (Fig. 3).

In Fig.5 the temporal dynamics of HCN generation and destruction rates owing to reactions (9 -11, 14, 22) are shown. Numerical calculations demonstrated that the HCN destruction owing reaction (15) is not significant under the experimental conditions [2].

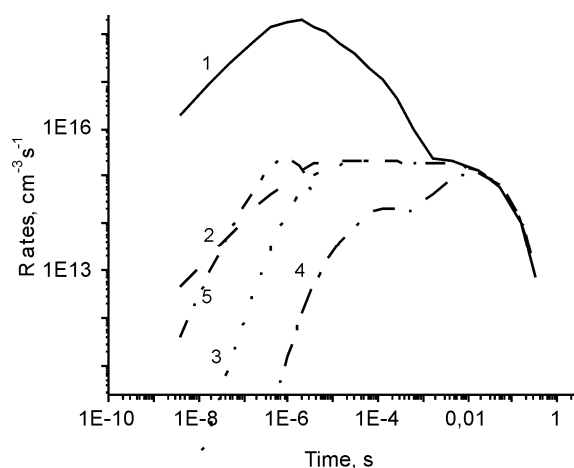


Fig. 5. Temporal dynamics of HCN generation and destruction rates owing to reactions (9 -11, 14, 22). The initial concentration of toluene $[C_7H_8]_0 = 400$ ppm, the gas temperature $T = 323$ K. 1 – (9); 2 – (11); 3 – (10); 4 – (22); 5 – (14).

It is seen that reaction (9) provides the highest rate of HCN production, however the high rate of hydrogen cyanide production, is partially compensated by a high rate of its destruction owing to the reaction (14). After the $N_2(A^3\Sigma_u^+)$ molecules have completely disappeared and the reaction of the HCN destruction (14) have terminated, the concentration of hydrogen cyanide began to monotonically increase over time (Fig. 4). Sharp increase in the HCN concentration occurs at large time (10^{-2} - 10^{-1} s). In Fig. 5 it is shown that all reactions (9-11, 22) make about equal contribution to the increase of the HCN concentration at this stage.

In Fig. 4 the dynamics of benzene production under the toluene decomposition is also presented. The presence of this by-product at the output of plasma-chemical reactor is mentioned in many experimental studies on the toluene removal (see, for example [2]), but quantitative data are not known in the literature yet.

Conclusion

In this paper we developed a model of plasma-chemical conversion of toluene in non-thermal nitrogen plasma. Reactions of C_7H_8 with nitrogen molecules in the $N_2(A^3\Sigma_u^+)$ and $N_2(a^1\Sigma_u^-)$ states play a major role in the mechanism of toluene destruction. Conversion pathways of toluene and their relative probabilities have chosen based on analysis of the heat of reaction, the law of conservation of spin, as well as experimental data on the composition of by-products. Comparison of the results of numerical calculations performed in the framework of this model with experimental data [2] on the degree of toluene removal, the composition and concentration of by-products of

toluene decomposition, versus the specific energy input was carried out. It is shown that simulation results are in good agreement with the experimental data.

References

1. Z. Falkenstein. Effect of the O_2 concentration on the removal efficiency of volatile organic compounds with dielectric barrier discharges in Ar and N_2 . - *J. Appl. Phys.* (1999), v. 85, № 1, pp. 525-529.
2. N. Blin-Simiand, F. Jorand, L. Magne, S. Pasquiers, C. Postel, J.-R. Vacher. Plasma Reactivity and Plasma-Surface Interactions During Treatment of Toluene by a Dielectric Barrier Discharge.- *Plasma Chem Plasma Process* (2008), v. 28, pp. 429-466.
3. Yu. S. Akishev, V. B. Karal'nik, I. V. Kochetov, A. E. Monich, A. P. Napartovich, and N. I. Trushkin. On synergetic effects at destroying of toluene and TCE by non-thermal plasma of DC glow discharge and streamer corona at atmospheric pressure.- in *Proc. 16th ISPC*, (2003) Jun 22-27, p. 226, Taormina, Italy.
4. T. Yamamoto, P.A. Lawless, M. K. Owen, D. S. Ensor and C. Boss. Decomposition of VOC by a packed-bed reactor and pulsed corona reactor.- *Non-Thermal Plasma Techniques for Pollution Control* (NATO ASI series, Part B) ed B.M. Penetrante and S.E. Schultheis (Berlin: Springer), pp,223-37.
5. N.Yu. Babaeva and G.V. Naidis. Two-dimensional modelling of positive streamer dynamics in non-uniform electric fields in air.- *J. Phys.D: Appl. Phys.* (1996),v. 29, pp.2423-31.
6. O. Eichwald, O. Ducasse, D. Dubois, A. Abahazem, N. Merbahi, M. Benhenni and M. Yousfi. Experimental analysis and modelling of positive streamer in air: towards an estimation of O and N radical production. - *J. Phys.D: Appl. Phys.* (2008),v. 41,234002 (11pp).
7. V.A. Biturin, E.A. Filimonova, G.V. Naidis. Simulation of Naphthalene Conversion in Biogas Initiated by Pulsed Corona Discharges – *IEEE Transactions on Plasma Science* (2009), v. 37, pp. 911-919.
8. R. Ono and R. Oda. Spatial distribution of ozone density in pulsed corona discharges observed by two-dimensional laser absorption method - *J. Phys D: Appl. Phys.* (2004), v. 37, pp. 730-735.
9. R. Ono and R. Oda. Measurement of gas temperature and OH density in the afterglow of pulsed positive corona discharge - *J. Phys D: Appl. Phys.* (2008), v. 41, 035204 (11pp).
10. O. Eichwald, O. Ducasse, D. Dubois, A. Abahazem, N. Merbahi, M. Benhenni and m. Yousfi. Experimental analysis and modelling of

- positive streamer in air: towards an estimation of O and N radical production- *J. Phys D: Appl. Phys.* (2008), v. 41, 234002 (11pp).
11. Diatko N. A., Kochetov I. V., Napartovich A. P., Taran M. D., 1984, *TVT*, **22**, №6, 1048-1054. (In Russian).
 12. E. C. Zipf, R. W. McLaughlin On the dissociation of nitrogen by electron impact and by E. U. V. photo-absorption. *Planetary and space science*, 1978, v. **26**, p. 449.
 13. J. T. Heron. Evaluated chemical kinetics data for reactions of N (2D), N(2P), and N₂ (A³Σ_u⁺) in the gas phase.- *J. Phys. Chem. Ref. Data*, (1999), v.28, no. 5, pp.1453-83.
 14. W. Mallard, F. Westley, J. Herron and D. Frizzell. NIST Chemical Kinetics Database (version 2Q98) (Gaithersburg, MD: National Institute of Standards and Technology).
 15. V. Guerra, J. Loureiro. Electron and heavy-particle kinetics in a low pressure nitrogen glow discharge.-*Plasma Sources Sci. Technol.*, (1997), v.6, p 361.
 16. J. Meyer, D. Klosterboer, D. Setser. Energy Transfer Reactions of N₂ (A³Σ_u⁺). IV. Measurement of the Radiative Lifetime Study of the Interaction with Olefins and Other Molecules. – *J. Chem. Phys.* (1971), v. 55, p.2084-90.
 17. S. Suzuki, T. Suzuki, H. Itoh. Determination of Collisional Quenching Rate Coefficient of N₂ (A³Σ_u⁺) by Air Pollutants. – In: *Proc 28th ICPIG*, (2007) July 15-20, Prague, Czech Republic.
 18. KINTECH. Kinetic technologies. Chemical Workbench (<http://www.kintech.ru>).

DETONATION INITIATION THROUGH A GRADIENT MECHANISM WITH APPLICATION OF NONEQUILIBRIUM NANOSECOND DISCHARGE

A. Rakitin^{1,2}, A. Starikovskii^{1,3}

1 – Moscow institute of physics and technology, Dolgoprudny, 141700, Russia

2 – NEQLab Research BV, The Hague, 2521 AL, The Netherlands

3 - Drexel Plasma Institute, Drexel University, Philadelphia, PA

1. Introduction

The current investigation of the mechanisms of gaseous detonation initiation is related to the problem of the pulsed detonation engine (PDE) concept realization. The combustion of a fuel–oxidizer mixture in a PDE is a decreasing–volume process that occurs at higher pressures and temperatures, as compared with the conventional constant–pressure combustion, and allows one to achieve a significantly higher thermodynamic efficiency. A detonation wave may be formed by a direct initiation or through a deflagration to detonation transition (DDT) process. For a direct detonation initiation, an ignition source of a considerable energy is required. A stoichiometric propane–air mixture may be ignited with a spark discharge with an energy of 1 mJ, whereas, for a direct initiation of a spherical detonation in the same mixture, a minimum energy of 300 kJ is required [1]. When initiated by a lower energy source in a sufficiently long tube, a DDT may occur through flame front acceleration. The typical DDT length amounts to several tens of tube diameters. Thus, since DDT length and time are crucial parameters for PDE applications, one of the key issues is the reduction of the transition length and time in detonation tubes under the minimum energy of initiation.

The most common method of DDT facilitation and length reduction is the application of various types of obstacles that turbulize the flow and increase the flame velocity. This method was proposed by Shchelkin [2], who used wire spirals inside the tube for flow turbulization. The method has since been widely applied in a number of works [3–7]. A modification of this method is the application of a two–chamber initiating system [8]. The first, smaller auxiliary chamber is used for primary ignition by a weak ignition source, whereas the mixture in the main chamber is ignited by flame jets bursting out of the auxiliary chamber. Detonation initiation by shock wave focusing with shaped reflectors (experimental [9, 10]) and with regularly spaced shaped obstacles (numerical [11]) was also proven to be possible. In the latter work, the focusing effect of shaped obstacles upon the shock–to–detonation transition was emphasized in the calculations with rectangular shaped obstacles,

where no focusing occurred and detonation was not observed under identical conditions. A number of research groups carried out experimental investigations of ignition and detonation initiation by nonequilibrium pulsed corona discharges [12]. The experiments confirmed that ignition delay times decreased substantially in comparison to spark initiation.

The concept of detonation initiation through a gradient mechanism was theoretically introduced by Zeldovich [13]. According to this work, an ignition delay time (or induction time) gradient formed due to a corresponding temperature gradient leads to the onset of a spontaneous combustion wave. The mixture first ignites at the point with the lowest delay and then propagates by spontaneous ignition with a velocity D_{sp} determined by the shape of the gradient. Depending on the value of D_{sp} , different modes of flame propagation can be realized. When D_{sp} exceeds the Chapman–Jouguet velocity D_{CJ} , a detonation wave can emerge from a constant–volume explosion as the spontaneous wave decelerates to the D_{CJ} value. This case was numerically studied in a series of papers overviewed in [14], where the detonation wave always occurred from a hot spot in the region between the shock wave and the turbulent flame. Various scenarios of hot spots formation due to shock–flame interaction and the role of their structure were also discussed in that paper. When D_{sp} falls into the interval between the speed of sound and D_{CJ} , the spontaneous wave propagating over the induction time gradient can become coupled with the compression wave and thus evolve into a detonation wave through shock amplification and acceleration. A similar concept of the shock–wave amplification by coherent energy release (SWACER) was introduced in [15] where this process was investigated in more detail. Another numerical study presented in [16] summarized the different scenarios occurring under different gradient profiles and, thus, different D_{sp} values. Experimentally, the idea of coupling the shockwave with the ignition was used for the detonation wave formation in [17] where the mixture was ignited by a set of properly synchronized spark plugs installed along the detonation tube. It resulted in a significant reduction of the DDT length and the initiation

energy under accurate synchronization of the ignition sources.

Pulsed discharge in the form of a fast ionization wave (FIW) was proposed as a tool for DDT length and time reduction in [18]. In this paper, the nonequilibrium plasma of a high-voltage nanosecond gas discharge was used for simultaneous preexcitation of the gas and for the reduction of ignition delay time in a bulk volume. The calculations performed for hydrogen-air and methane-air mixtures showed that the ignition threshold shifted by 400 K under an energy deposition of 0.4 J/cm³ in the methane-air mixture. It was also shown that the typical time for chemical energy release had to be shorter than that of the gas-dynamic processes to form a detonation wave. Thus, for DDT length reduction, it is desirable that the sonic speed and, hence, the temperature be as low as possible, which is realized in a nonequilibrium plasma of a high-voltage nanosecond gas discharge.

It is important that this kind of discharge, developed in a chamber of a proper geometry, is capable of instantly ionizing, exciting, and heating the gas in a bulk volume. The main channel of energy deposition is governed mostly by the reduced electric field (E/N) value. Under certain experimental parameters, an excited species concentration gradient may be formed over a considerable distance. The non-uniform gas excitation by the discharge results in an ignition delay time gradient formation and, hence, the possible DDT through a gradient mechanism. Due to the spatial homogeneity of this kind of discharge, it is possible to form the gradient in a large volume rather than only in the close vicinity of hot spots. Thus, the nanosecond discharge is very promising for detonation initiation and DDT facilitation from a number of points of view. To realize the advantages of this initiation method, a proper geometry and parameters of the discharge chamber are required.

Relying on these results, Zhukov and Starikovskii carried out experiments on detonation initiation by this kind of discharge [19–21]. A 131-cell discharge chamber with a distributed electrode system was developed and patented [22]. A study of the discharge development with an ICCD camera showed that the discharge was distributed over the cross-section of the chamber, filling a significant portion of the cells. This was achieved due to the short rise time and width of the high-voltage nanosecond pulse. The experiments were carried out in propane-oxygen and propane/butane-oxygen mixtures diluted with nitrogen at initial pressures from 0.15 to 0.55 bar. It allowed us to achieve a DDT length of 130 mm in a smooth tube with an inner diameter of 140 mm in a C₃H₈ + 5O₂ mixture at an initial pressure of 0.3 bar and a discharge energy of 70 mJ. The discharge development and the detonation wave formation were studied with a fast ICCD camera, pressure

transducers, and infrared sensors. It was found that the efficiency of the distributed nanosecond detonation initiation strongly depended on the nitrogen dilution level and initial mixture pressure, whereas the dependence upon the discharge energy was weak. This research was continued by Zhukov, Rakitin, and Starikovskii in [23], which also included a study of the effect of different discharge types upon DDT in smooth tubes. For that, experiments on detonation initiation by a high-voltage microsecond discharge were carried out in a different distributed electrode system that included 28 discharge cells. Each cell geometry was analogous to the one described in [22]. Due to the long pulse rise-time, the discharge was localized in only one cell. The results were compared to those obtained for the nanosecond discharge initiation. At the same time, the study of the latter was extended to higher pressures, which allowed us to make the comparison in a wider range of initial parameters. The experimental results demonstrated a higher efficiency of the nanosecond initiating system in terms of DDT length and time in comparison with the discharge chamber of a similar geometry with microsecond spark. At the same time, the ignition delay times under the microsecond excitation in all the mixtures under study were significantly lower, as compared to the nanosecond ignition due to the localized nature of the energy deposition in the microsecond discharge.

The multi-cell distributed electrode systems described above were too complicated to carry out a detailed study of the processes occurring inside the discharge chamber. To clarify the mechanisms leading to DDT promotion under different discharge development modes, a detonation tube with a single-cell discharge chamber has been assembled [24]. The chamber geometry has remained similar to the cell geometry of the multi-cell distributed electrode systems described previously. At the same time, it allows one to perform detailed diagnostics inside the discharge cell and the detonation tube. The parameters of the setup also allow us to investigate different discharge development modes in the same tube geometry. A gradient mechanism of deflagration-to-detonation transition similar to that proposed by Zeldovich has been observed experimentally under initiation by a streamer discharge. The mixture inside the discharge channel was excited non-uniformly by the streamer, thus forming an excited species concentration gradient. The gradient corresponded to that of ignition delay time. The hottest spot with the shortest ignition delay was at the high-voltage electrode tips. Originating at this point, the spontaneous combustion wave started propagating along the channels at a velocity over 1500 m/s and accelerated up to the CJ velocity value at the channels output. The initiation energy was, by an order of magnitude, lower for the streamer mode

when compared to the spark initiation under the experimental conditions, whereas the DDT time was 3 times longer.

The current paper focuses on further study of this mode of detonation initiation with regard to its future application in pulsed detonation engines. To enhance the efficiency of the gradient formation in terms of energy input, we are using a four-cell discharge chamber mounted to the same tube with 2×2 cm cross-section. Each of the discharge cells is nevertheless of the same geometry as the ones used in all previous setups. This has eventually allowed us to initiate detonations in nitrogen-diluted mixtures under significantly lower energy inputs, taking the concept closer to applications.

2. Experimental Setup

For a more detailed study of the gradient mechanism, a four-cell Plexiglas discharge chamber was designed. The scheme is shown in Fig. 1. The geometry of each discharge cell remained the same. Each cell contains a pin-like high-voltage electrode (1) which is immersed into a 6.5 mm-diameter channel (2). The channels length is 150 mm. Replacement of the electrodes allows to vary the interelectrode distance and, thus, the reduced electric field value under the same pulse parameters. The four channels are led into a square detonation tube (2×2 cm) through a converging reducer (3). The diameter of the channels inside the reducer is 9 mm. The convergence angle is 24° . The diameter of the reducer outlet is 20 mm, which matches with the inlet of the detonation tube. The reducer is manufactured of aluminium and is grounded, serving as the ground electrode. The whole Plexiglas discharge section is also covered with

grounded shield (4). The shield includes a longitudinal gap for visual observation of the processes inside one channel. Discharge propagation is also enhanced by four grounded plates (5) which are fixed into narrow slits inside the chamber between the discharge channels. The plates stretch along the whole chamber, increasing the capacitance of the electrode system and the transverse reduced electric field in the channels. In comparison to the single-cell geometry, the volume of the potentially excited gas mixture is increased fourfold.

3. Discharge Development: Gradient Shape

The construction of the four-cell discharge chamber implied that only relatively low-amplitude pulses could be used. The vast majority of DDT experiments was carried out under a pulse amplitude of 50 kV. Under such conditions, the discharge propagated as a streamer in a wide pressure range above 0.1–0.15 bar depending on the gas. It allowed to study the gradient mechanism extensively. At the same time, it would demonstrate how that kind of DDT occurred under low energy inputs.

The discharge propagation mode was controlled in every experiment by the same back-current shunt used with the single-cell chamber. The shunt provided the data on both the propagation mode and the energy input value in the experiment. Both the spark mode and the streamer mode were registered. However, due to the different geometry and pulse amplitude, the pressure ranges differed substantially from those observed for the single-cell chamber. The incident pulse energy, the reflected pulse energy, and the energy input are shown in the figures. It is seen that

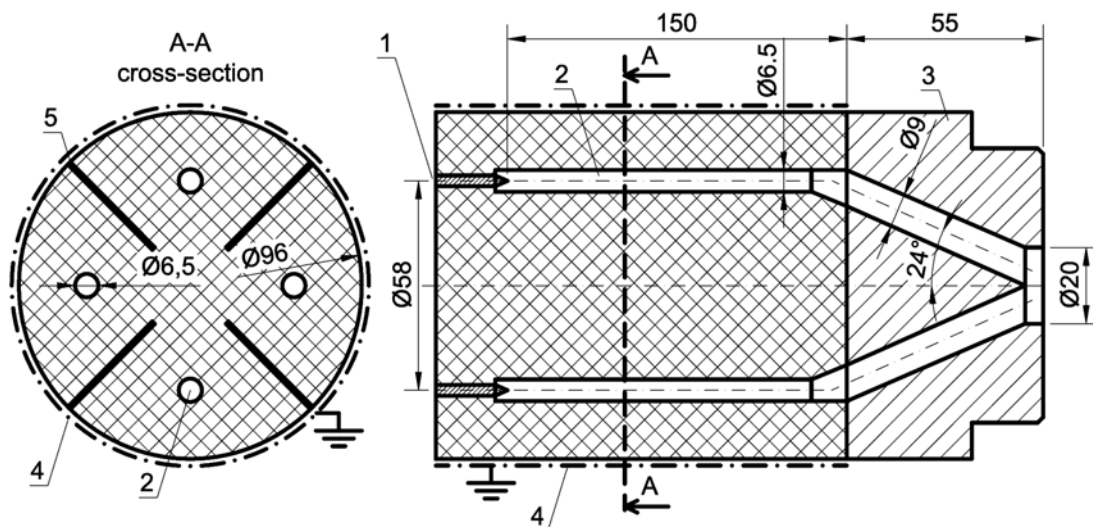


Fig. 1: Four-cell discharge chamber: the scheme. (1) - high-voltage electrode, (2) - discharge channel with a diameter of 6.5 mm, (3) - converging reducer, (4) - coaxial grounded shield, (5) - grounded plates.

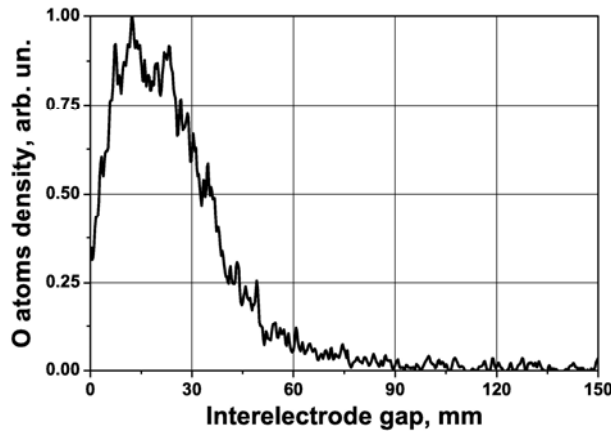


Fig. 4: O atoms density distribution over the interelectrode gap in one of the four channels.

almost 90% of the pulse energy is deposited into the gas in spark mode, which is accounted for by the multi-cell geometry of the discharge chamber.

In order to estimate the shape of the excited species gradient, streak imaging has also been performed for the discharge in air at 1 bar. The imaging could only be performed in the one discharge channel not completely covered by the shield. However, the discharge was expected to develop similarly in all the channels due to the symmetry of the chamber. The pulse voltage was typical for the DDT experiments and amounted to 50 kV. An estimation of the O atoms concentration gradient along the interelectrode gap was obtained by integrating the intensity over the discharge duration. The resulting distribution is presented in Fig. 2. The relatively low reduced electric field value (25 Td) results in a low streamer velocity (1.5 mm/ns). For that reason, the streamer only propagates over the portion of the channel next to the high-voltage electrode. That is also clearly seen from the O atoms concentration gradient shape, which spans over ≈ 5 cm in comparison with the 10 cm in the single-channel case under a higher reduced electric field value (40 Td).

4. Gradient Mechanism Under Different Conditions

The first series of experiments was carried out in the undiluted propane-oxygen mixture. As was seen from the streak image, only the gas in the region next to the high-voltage electrode was notably excited. Since these conditions are suitable for detonation initiation by the gradient mechanism, temporally resolved imaging of the ignition inside the discharge channels was performed to confirm that. The sequence of images at 0.6 bar is shown in Fig. 3.

The non-uniformity of ignition and the trajectory of the flame wave propagation are clearly seen here. The mixture was first ignited close to the high-voltage electrode after a delay of 30–40 μ s.

The overall results for the streamer mode in the undiluted propane-oxygen mixture are plotted as x-t diagrams in Fig. 4. The negative region of the horizontal axis corresponds to the discharge channel, its outlet coinciding with zero. The points in this area correspond to the propagation of the spontaneous combustion wave registered with the high-speed imaging for the cases at 0.3 and 0.6 bar. All the traces show that detonation waves had been formed before the waves reached the first sensor in the tube. It is seen that detonation formation was preceded by the propagation of the combustion waves inside the discharge channels at Mach numbers over 2.

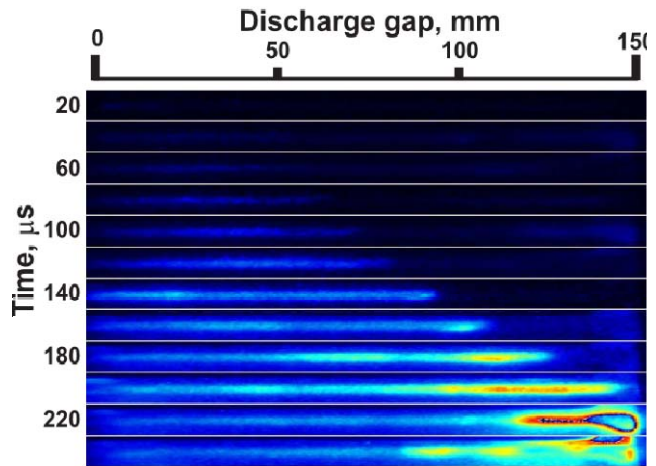


Fig. 2: Time-resolved ICCD imaging of propane-oxygen mixture ignition inside the discharge chamber. Initial pressure: 0.6 bar.

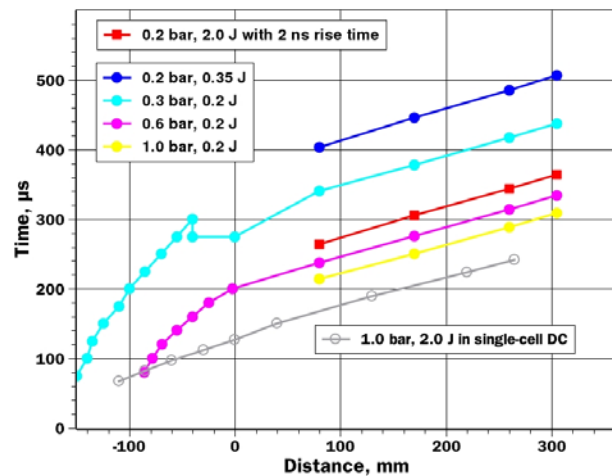


Fig. 3: X-t diagrams of detonation formation at initial pressures of 0.2–1 bar. Undiluted mixture.

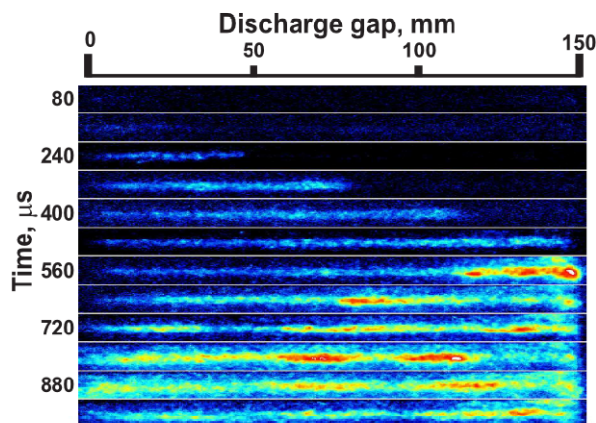


Fig. 6: Time-resolved ICCD imaging of propane–oxygen–nitrogen mixture ignition inside the discharge chamber. Initial pressure: 0.5 bar.

However, the CJ velocity was only reached outside the discharge chamber.

The overall detonation formation time decreases with pressure rise under close energy input values. This is due to the similar dependency of ignition delay time upon mixture pressure. On the other hand, the formation time also decreases with energy input rise. For a clear comparison, the data points for the experiment in a transient mode at 0.2 bar under 2 J of energy input are plotted in the same figure (blue squares). Under an initial pressure of 0.2 bar, the arrival time of the detonation wave to the position of the first sensor decreased from 400 μs under the initiation energy of 0.35 J to 260 μs under 2 J. The higher energy input under the same pulse amplitude was due to a different pulse shape with a short rise time of 2 ns. Another comparison can be made with detonation initiation by streamer discharge in the single-cell discharge chamber [24]. The $x-t$ diagram for the case at 1 bar of initial pressure is also plotted as the gray line. The higher energy input of 2 J together

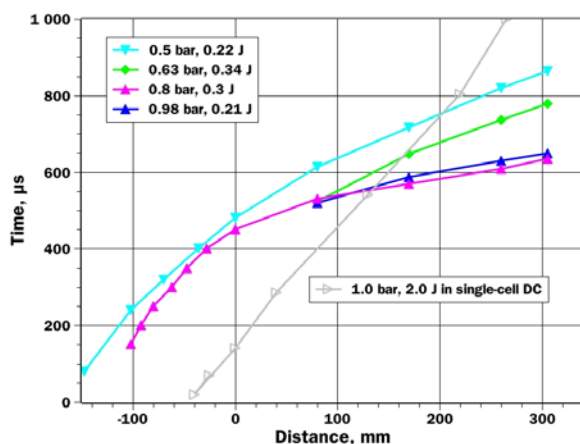


Fig. 5: $X-t$ diagrams of detonation formation at initial pressures of 0.5–1 bar. Diluted mixture.

with the smaller volume of the excited gas in the single-cell DC results in a slightly shorter delay than in the experiment in the four-cell DC at the same initial pressure. However, the detonation formation distance is below 3 transverse tube sizes in all the tests in streamer mode.

Experiments in propane–oxygen mixture diluted with 40% of nitrogen were only carried out in streamer mode at initial pressures higher than 0.2 bar. Under relatively low pressures of 0.2–0.5 bar, only deflagration modes were observed in this mixture. The flame wave and the shock wave propagated at supersonic velocities in all experiments, being coupled along the tube. The temporally resolved imaging at 0.5 bar in Fig. 5 also indicated that the gradient mechanism is as well effective in diluted mixtures. It allowed the flame wave to accelerate inside the discharge channel up to <500 m/s, which resulted in a shock wave formation in the detonation tube, travelling at a velocity of <1000 m/s. Such deflagration velocity is typically enough for an adiabatic explosion to occur within a short distance further downstream, leading to an onset of a CJ detonation.

The increased initial pressure together with the gradient mechanism lead to CJ detonation in the diluted mixture under energy inputs of 0.2–0.3 J. The results are presented for four pressure values of 0.5, 0.63, 0.8, and 1 bar in Fig. 6. At 0.63 bar, the shock/flame velocity remained <1000 m/s, though the deflagration wave arrival time decreased as compared with the case of 0.5 bar. A CJ detonation wave was first observed at 0.8 bar of initial pressure. The propagation of the spontaneous combustion wave inside the discharge channel at this pressure is shown in Fig. 7. The ignition delay time was within 100 μs , and the wave accelerated up to 800 m/s by the end of the channel.

At the initial pressure of 1 bar, the shock waves arrived at the first sensor after 0.5 ms for both cases, whereas a shorter delay was expected under a higher pressure. The effect of pressure rise could be compensated by a lower energy input (0.2 J for 1 bar experiment compared to 0.3 J for the case at 0.8 bar). Additionally, an $x-t$ diagram of the experiment at 1 bar in the same mixture in the single-cell DC is plotted in the same figure for comparison (gray line). The data points are based on the IR data and correspond to the flame wave propagation. Even though the initiation energy was by an order of magnitude higher (2 J), only a deflagration wave with a velocity of 600 m/s was observed. Furthermore, in this case the shock wave propagated ahead of the flame wave with a slightly higher velocity. That resulted in the decoupling of the shock–flame complex and in the eventual deceleration of both waves.

5. Discussion of Experimental Results

The condition for the gradient mechanism to lead to detonation wave formation is that

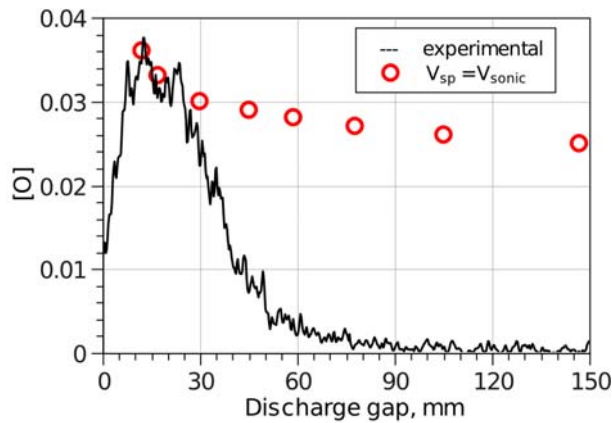


Fig. 7: Calculated O atoms concentration distribution over the interelectrode gap, corresponding to the propagation of the spontaneous combustion wave at sonic velocity.

spontaneous combustion velocity D_{sp} is greater than sonic velocity V_s and less than Chapman–Jouguet velocity D_{CJ} . Spontaneous combustion wave velocity D_{sp} , or the ignition pattern inside the discharge channels in general, is determined by the temperature gradient and by the axial distribution of radicals produced by the discharge. Knowing the temperature and the radical concentration at different points along the channel, it is possible to evaluate the corresponding ignition delay time distribution using 0D chemical kinetics equations. Taking into account that $D_{sp} = (d\tau/dz)^{-1}$, where z is the axial coordinate along the channel, this will allow us to estimate whether the gradient condition can be fulfilled for the conditions in Fig. 3. To estimate the absolute values of these parameters, energy branching of the 200 mJ put in into the gas by the discharge was considered. It is known that, for reduced electric field values of <100 Td, 20–30% of energy input is branched into direct heating of the gas by rapid plasma thermalization during the first microsecond [26]. Taking into account that the total volume of the four discharge channels is 20cm^3 , the volume-averaged heating by this mechanism amounts to 6 K. As for the radical production, it has been shown in [11] that O atoms are produced at an overall energy price of <10 eV. This results in the volume-averaged concentration of atomic oxygen of 0.03%. To obtain the actual peak values of the temperature increase and O production in the area next to the high-voltage electrode, it is necessary to take into account the spatial non-uniformity of excitation. The axial non-uniformity is represented by the normalized relative distribution in Fig. 2 with the mean value being close to 0.2. This yields the cross-section averaged values of 30 K and 0.15% for the temperature increase and O concentration at the maximum point, respectively. It has to be noted that even though the distribution presented in Fig. 2 has been measured at 1 bar, the ignition pattern and delay time were very close to those at 0.6 bar. The radial non-uniformity is due to discharge attachment to

the dielectric walls of the channels and is hard to estimate directly. The typical value for streamer transverse size at these discharge parameters is ≈ 1 mm [27]. It corresponds to a peak temperature increase of 700 K and to the production of 3.5% of O. The chemical kinetics calculation performed under these conditions using the reaction mechanism described in [28] yields an ignition delay time of 33 μs , which agrees with the experimentally observed result.

In order to check if the gradient condition has been fulfilled, the mechanism described above has been applied to find the O concentration distribution which corresponded to the propagation of the spontaneous combustion wave at sonic velocity. The initial conditions for the kinetic calculations were obtained basing on the estimated values of peak temperature increase and radical production corrected by accounting for the longitudinal distribution. The result is shown with red points in Fig. 8 together with the experimental distribution (black line). The condition on the gradient holds if the slopes of the two curves coincide in some region. It can be seen that it is the case within <20 mm from the peak. This demonstrates that within roughly 10 calibers of the discharge channel the velocity of the spontaneous combustion wave is close to the sonic speed and the gradient mechanism of detonation initiation is feasible.

References

1. Bull, D. C., Elsworth, J. E., and Hooper, G., "Initiation of Spherical Detonation in Hydrocarbon/Air Mixtures," *Acta Astron.*, Vol. 5, No. 11, 1978, pp. 997–1008.
2. Shchelkin, K. I., "Initiation of Detonation in Gases in Rough Tubes," *Technical Physics*, Vol. 17, No. 5, 1947, pp. 613.
3. Brown, C. J. and Thomas, G. O., "Experimental Studies of Ignition and Transition to Detonation Induced by the Reflection and Diffraction of Shock Waves," *Shock Waves*, Vol. 10, No. 1, 2000, pp. 23–32.
4. Sorin, R., Zitoun, R., and Desbordes, D., "Optimization of the Deflagration to Detonation Transition: Reduction of Length and Time of Transition," *Shock Waves*, Vol. 15, No. 2, 2006, pp. 137–145.
5. Smirnov, N. N. and Nikitin, V. F., "Effect of Channel Geometry and Mixture Temperature on Detonation-to-Deflagration Transition," *Combustion, Explosion, and Shock Waves*, Vol. 40, No. 2, 2004, pp. 186–199.
6. Cooper, M., Jackson, S., Austin, J., Wintenberger, E., and Shepherd, J. E., "Direct Experimental Impulse Measurements for Detonations and Deflagrations," *Journal of*

- Propulsion and Power , Vol. 18, No. 5, 2002, pp. 1033–1041.
7. Frolov, S. M., “Liquid-Fueled, Air-Breathing Pulse Detonation Engine Demonstrator: Operation Principles and Performance,” *Journal of Propulsion and Power* , Vol. 22, No. 6, 2006, pp. 1162–1169.
 8. Higgins, A. J., Pinard, P., Yoshinaka, A. C., and Lee, J. H. S., “Sensitization of Fuel-Air Mixtures for Deflagration to Detonation Transition,” *High-Speed Deflagration and Detonation: Fundamentals and Control*, edited by G. Roy, S. Frolov, D. Netzer, and A. Borisov, Elex-KM Publ., Moscow, Russia, 2001, pp. 45–62.
 9. Achasov, O. V., Labuda, S. A., Kondrashov, V. V., Penyazkov, O. G., Pushkin, R. M., Tarasov, A. I., and Shabunya, S. I., “Focusing of Shock Waves on Reflection from Concave Curvilinear Surfaces,” *Journal of Engineering Physics and Thermophysics*, Vol. 65, No. 5, 1993, pp. 1073–1077.
 10. Achasov, O. V. and Penyazkov, O. G., “Some Gasdynamic Methods for Control of Detonation Initiation and Propagation,” *High-Speed Deflagration and Detonation: Fundamentals and Control* , edited by G. Roy, S. Frolov, D. Netzer, and A. Borisov, Elex-KM Publ., Moscow, Russia, 2001, pp. 31–44.
 11. Semenov, I., Frolov, S., Markov, V., and Utkin, P., “Shock-to-Detonation Transition in Tubes with Shaped Obstacles,” *Pulsed and Continuous Detonations*, edited by G. Roy, S. Frolov, and J. Sinibaldi, Torus Press, Moscow, Russia, 2006, pp. 159–169.
 12. Cathey, C., Wang, F., Tang, T., Kuthi, A., Gundersen, M. A., Sinibaldi, J. O., Brophy, C., Barbour, E., Hanson, R. K., Hoke, J., Schauer, F., Corrigan, J., and Yu, J., “Transient Plasma Ignition for Delay Reduction in Pulse Detonation Engines,” 45th AIAA Aerospace Sciences Meeting and Exhibit, AIAA, Reno, USA, 2007, paper 2007-443.
 13. Zeldovich, Y. B., Librovich, V. B., Makhviladze, G. M., and Sivashinskii, G. I., “On the Onset of Detonation in a Nonuniformly Heated Gas,” *J. Appl. Mech. Tech. Phys.*, Vol. 11, No. 2, 1970, pp. 264–270.
 14. Oran, E. S. and Gamezo, V. N., “Origins of the deflagration-to-detonation transition in gas-phase combustion,” *Combustion and Flame*, Vol. 148, No. 1–2, 2007, pp. 4–47.
 15. Lee, J. H. S., “Initiation of Gaseous Detonation,” *Annual Review of Physical Chemistry*, Vol. 28, 1977, pp. 75–104.
 16. Kapila, A. K., Schwendeman, D. W., Quirk, J. J., and Hawa, T., “Mechanisms of Detonation Formation due to a Temperature Gradient,” *Combustion Theory and Modelling*, Vol. 6, No. 4, 2002, pp. 553–594.
 17. Frolov, S. M., Basevich, V. Y., Aksenov, V. S., and Polikhov, S. A., “Detonation Initiation by Controlled Triggering of Electric Discharges,” *Journal of Propulsion and Power* , Vol. 19, No. 4, 2003, pp. 573–580.
 18. Starikovskii, A. Y., “Deflagration-to-Detonation Control by Non-Equilibrium Gas Discharges and Its Applications for Pulsed Detonation Engine,” 39th AIAA/ASME/SAE/ASEE Joint Propulsion Conference and Exhibit, AIAA, Alabama, USA, 2003, paper AIAA2003-4686.
 19. Zhukov, V. P. and Starikovskii, A. Y., “Effect of a Nanosecond Gas Discharge on Deflagration to Detonation Transition,” *Combustion, Explosion, and Shock Waves*, Vol. 42, No. 2, 2006, pp. 195–204.
 20. Zhukov, V. P., Rakitin, A. E., and Starikovskii, A. Y., “Initiation of Detonation by Nanosecond Gas Discharge,” 44th AIAA Aerospace Sciences Meeting and Exhibit, AIAA, Reno, USA, 2006, paper 2006-952.
 21. Starikovskii, A. Y., Anikin, N. B., Kosarev, I. N., Mintoussov, E. I., Nudnova, M. M., Rakitin, A. E., Roupasov, D. V., Starikovskaia, S. M., Zavalov, I. N., and Zhukov, V. P., “Nanosecond Pulsed Discharges for Plasma Assisted Combustion and Aerodynamics,” *Journal of Propulsion and Power* , Vol. 24, No. 6, 2008.
 22. Starikovskii, A. Y., “The Method of Initiation of Ignition, Intensification of Combustion or Reforming of Fuel-Air and Fuel-Oxygen Mixtures,” patent PCT/IB 2006/003106, 2006.
 23. Zhukov, V. P., Rakitin, A. E., and Starikovskii, A. Y., “Effect of High-Voltage Pulsed Discharges on Deflagration to Detonation Transition,” *Journal of Propulsion and Power* , Vol. 24, No. 1, 2008, pp. 88–93.
 24. Rakitin, A. E. and Starikovskii, A. Y., “Mechanisms of Deflagration-to-Detonation Transition Under Initiation by High-Voltage Nanosecond Discharges,” *Combustion and Flame*, Vol. 155, 2008, pp. 343–355, doi:10.1016/j.combustflame.2008.05.019.
 25. Kaneshige, M. and Shepherd, J. E., “Detonation Database,” Technical report fm97-8, GALCIT, California Institute of Technology, 1997.
 26. N. A. Popov, Investigation of the mechanism for rapid heating of nitrogen and air in gas discharges, *Plasma Physics Reports* 27 (10) (2001) 886.
 27. S. Pancheshnyi, M. Nudnova, A. Starikovskii, Development of a cathode-directed streamer discharge in air at different pressures: Experiment and comparison with direct numerical simulation, *Physical Review E* 71 (1) (2005) ID 016407.
 28. V. P. Zhukov, V. A. Sechenov, A. Yu. Starikovskii, Self-ignition of a lean mixture of n-pentane and air over a wide range of pressures, *Combustion and Flame* 140 (3) (2005) 196–203.

SUBMICROSECOND DISCHARGE IN NONHOMOGENEOUS MEDIA AND IN HIGH-SPEED FLOW

Firsov A. A., Isaenkov Y. I., Leonov S. B., Shurupov M. A., Yarantsev D. A.,
JIHT RAS, Moscow, 125412, Russia, leonov@ihed.ras.ru

Abstract. A subject of this work is the dynamics of long filamentary pulse discharge generated along the contact zone of two co-flown gases. Two main ideas are discussed: the mechanism of lateral jets generation after the discharge run and the mechanism of the discharge localization in a mixing layer of two gases. The effects found are supposed to be used for high-speed combustion enhancement owing to nonequilibrium excitation of air/fuel composition and mixing acceleration of nonpremixed multicomponents flow.

1. Introduction

The result of interaction of a pulsed filamentary discharge with a surrounded gas strongly depends on the discharge decay mechanism, which is a function of the discharge electrical and geometrical parameters. At adequate high power deposition (no exact criteria currently), the turbulent gas motion develops in a cooling post discharge channel, replacing molecular heat conduction as the dominant mechanism of the heat transfer. As a result, the rates of cooling and expansion of the channel increase considerably. The turbulent motion arisen in the immediate vicinity of boundary between two gases may significantly increase the rate of mixing, which may in turn be used to control the mixing rate in high speed directly fuelling combustors, as well as others [1–4].

A simple theoretical model of the post-discharge channel cooling has been proposed in [5–7], which takes into account the development of turbulence and its effect on the channel expansion process. In recent experiments [8–10] it has been shown that there is another, much faster, mechanism of the afterspark channel expansion. The expansion is driven by high velocity radial jets formed during the afterspark channel development. It can not be described by the conventional model of turbulent expansion. The second discussed idea is the filamentary discharge localization and movement in medium at gradient concentration of two dissimilar components [11]. It is considered that the interaction can be controlled thoroughly, because the discharge position and dynamics in mixing layer enable to be steered by the discharge parameters and physical properties of the gases.

2. Lateral jets formation

Breakdown of the gap and afterspark channel cooling / expansion are studied for $D=5\text{-}7\text{cm}$ gap (1) in air at standard conditions, (2) in alternative gases, and (3) in high-speed airflow. An important feature of the power supply is a high

speed of the voltage rise, $dV/dt > 10^8$ V/s [9–10]. Typical discharge parameters are as follows: the breakdown voltage $V > 100$ kV, the peak current $I = 1\text{--}3$ kA, duration of current pulse $\tau = 50\text{--}90\text{ns}$, and the pulse energy release $E = 1\text{--}3$ J. Typical voltage-current and power characteristics of the discharge are presented in Fig.1.

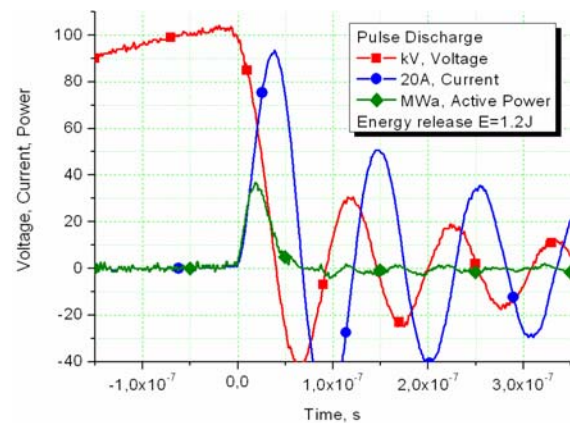


Fig.1. Voltage-current-power characteristics of electrical pulse. Energy deposition in this particular case is 1.2 J.

The visualization of the plasma filament and the thermal distortion, generated by the spark in ambient conditions and high-speed flow was performed by a fast-gated camera, by schlieren method, and by line-scan (streak) camera. The light flash of the schlieren device has duration of 100 ns, and is precisely synchronized with the discharge phase and triggered CMOS camera, whose shutter is tuned for duration of 10–300 μs . The frame rate was typically 2 kHz, and the early stage of the discharge was recorded due to variation of the first frame delay time.

Duration of electrical pulse at described test conditions was much shorter than a characteristic gasdynamic time: $\tau = d/u_s$, where d is characteristic dimension, u_s is the sonic velocity. It means that the gas is heated instantly in terms of the medium movement. All gasdynamic sequences (shock wave

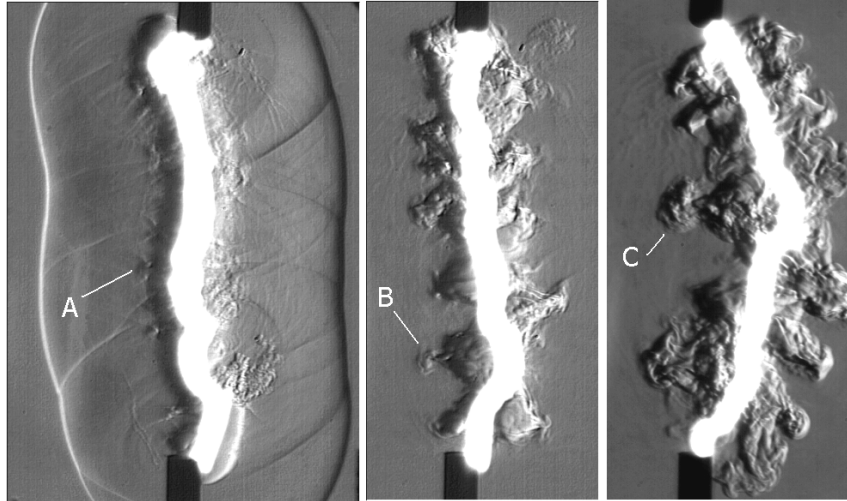


Fig. 2. Expanding afterspark channel, obtained by schlieren technique: delay 50, 220 and 300 μ s. Interelectrode gap is $D=60$ mm. "A" - the starting phase of instability, "B" - the fast jet development, and "C" - the final stage of the jet expanded from a concave part of the channel.

run away and channel expansion) appear after the discharge current stop. The shock wave expansion induced by the pulse discharge follows the asymptotic theory for a strong cylindrical shock wave [12-13] for the first tens microseconds

$$R_{SW} = \alpha(\gamma) \times (E_1 / \rho_0)^{1/4} \times t^{1/2}; \quad \alpha(\gamma) \approx 1,$$

where E_1 [J/m] is the energy release per unit length, ρ_0 is the ambient density, and $r=c_p/c_v$ is the specific heat ratio. In a few microseconds the shock wave is separated from the heated channel.

During the first stage of the expansion, $t < 50 \mu$ s, the post-discharge channel looks as a classical cylindrical thermal cavity. At $t = 80-150 \mu$ s (the exact time depends on the conditions), the shape of the after-spark channel becomes unstable, as shown in Fig.2. The physical mechanism of this phenomenon may be summarized as follows. The cooling of the axial zone leads to pressure decrease with the subsequent reverse gas movement. Such a movement becomes unstable due to the Rayleigh-Taylor mechanism [13]. The estimate of the instability development time of $\approx 100 \mu$ s coincides with the experimentally observed value. The plasma luminosity is not rejected in Fig.2, which allows one to detect the locations of preferential jet directions. The strongest cumulative flow is clearly associated with the curvature of the initial plasma channel. The jets tend to form at concave parts of the channel. Note that no jets were observed, when the deposited power was lower than 10MW.

The experimental results thus demonstrate that the latter stage of channel expansion is characterized by the formation of intensive lateral jets followed by fast gas turbulization in a significant volume, comparable to the gap distance.

Analysis of the experimental data shows that the size of the perturbed region is several times larger than it has to be appeared, if only conventional laminar or turbulent diffusion mechanisms were considered. Two more observations can be drawn from these results. First, the diameter of the plasma zone after the fast expansion is about 8 mm, and second, the average speed of the disturbance propagation observed in the experiment exceeds 100 m/s.

The presented results suggest the following mechanism of jet formation. At concave sides of the plasma channel, the shock wave propagation results in strong compression followed by strong rarefaction behind the shock. At convex sides, the shock wave is diverging, and thus is characterized by smaller compression followed by weaker rarefaction when compared with the concave sides. As a result, a pressure gradient builds up, with pressure decreasing from convex to the opposite concave sides. This causes jet formation outside of the concave regions, with the general direction of jets from concave to convex.

3. Discharge localization

The next important idea is the discharge's filament localization under nonhomogeneous medium. It was found experimentally that the discharge closely follows a boundary between two gases in most of the cases at the air--fuel--plasma interaction [11]. The explanation of this fact includes the idea that the discharge localization is managed by the rule of minimal electrical field, required for the discharge maintenance, along the line of breakdown. It can be supposed that the discharge "prefers" the path in the fuel, oxidizer, or between them depending on conditions and the phase of discharge development. For the short-

pulse discharge, the physical mechanism appears as follows. The first stage of the spark breakdown is the multiple streamers propagation from the “hot” electrode toward the grounded one. In case of high-power electrical source, the streamers occupy a huge volume of gas, covering all possible paths for further development. This statement is illustrated by the well-adjusted schlieren photo of the streamers’ phase in Fig. 3, where the spark phase was prevented owing to voltage reduction. The next phase consists of the real selection of the discharge path among multiple channels with nonzero conductivity. It is the key point – the channel appears to be the best in terms of the current increase, i.e. possessing higher conductivity and lower inductivity. If the media is nonhomogeneous, the favorite path may not be the shortest one. Sometimes, even double- and triple-channel structures were observed.

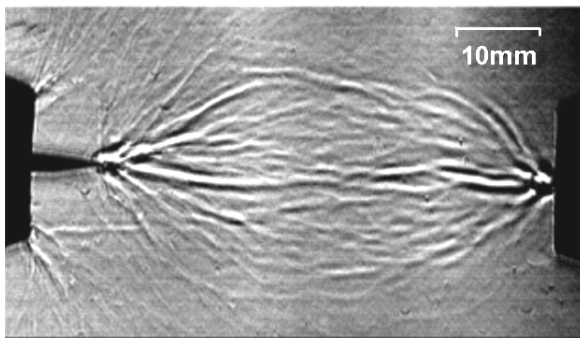


Fig.3. Schlieren image of streamer phase of the discharge development. The photo is taken in 0.5ms after the shot.

Figure 4 shows the results of calculations [11] of discharge properties in ethylene–air mixture (for CO₂–Air mixture, the picture is not so clear). Here, the coefficient of the ionization rate minus the rate of attachment is presented for variable-

reduced electrical field. It is known that the best conditions for discharge development may be realized in reach mixture, but not in air or ethylene. This statement is confirmed by measuring the history of E/N and resistance in high-current phase of the discharge at a study of the discharge parameters in different gases (see Fig. 9). Besides discharges in air and ethylene, the experiments were fulfilled for discharge in CO₂ (one of the combustion products) and in vicinity of boundary between air and CO₂. The weak laminar jet of secondary gas was arranged between two electrodes: CO₂ jet in air and air jet in CO₂. The typical schlieren image of the discharge breakdown at the presence of two gases is shown in Fig. 5. The discharge position between two gases and strong disturbance of the boundary has been recognized. In the last particular case, when the discharge can select the path, it mostly locates in air, but in immediate vicinity of secondary gas (CO₂)

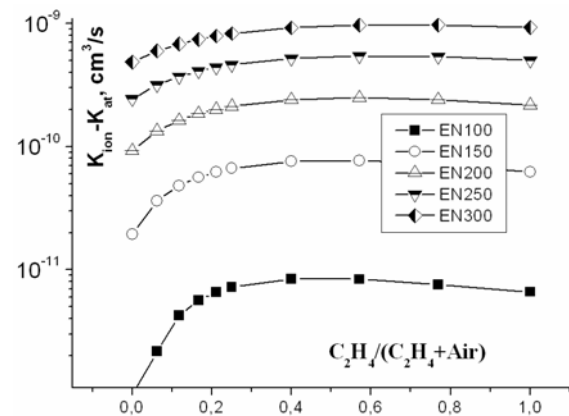


Fig.4. Calculated coefficient of ionization taking into account the electrons attachment in air, ethylene and their mixture.

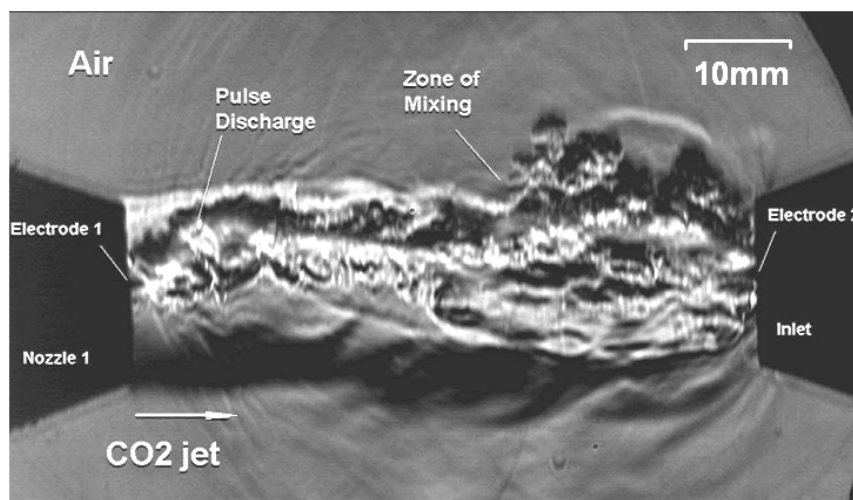


Fig.5. Schlieren image of the discharge interaction with CO₂ jet in Air. The photo is taken in 0.2ms after the shot.

This statement is confirmed by measuring history of E/N and the discharge channel resistance in high-current phase of the discharge. Being excited in CO₂ or in Air the discharge possesses remarkably different electrical parameters. In case of CO₂ jet in Air and Air jet in CO₂ both the measured parameters are close to air but not to CO₂, as it is shown in Fig.6.

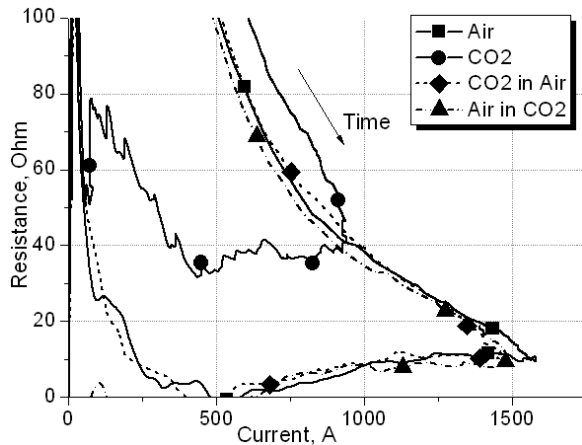


Fig.6. Experimentally obtained dynamics of discharge channel resistance in Air, CO₂, air jet in CO₂ and CO₂ jet in air.

4. Filamentary high-power discharge in high-speed flow

The experimental approach includes the following key points: supersonic duct-driven airflow $M=2$ and $M=2.5$; direct injection of gaseous fuel (co-flow/wall jet of model gas, gaseous fuel, He or CO₂, preliminary); transversal short-pulse repetitive electrical discharge, crossing air-fuel-air zone or along air-fuel boundary; plasma-induced artificial turbulence; zone of improved mixing.

The high-speed experimental facility consists of blow-down wind tunnel PWT-50, system of the pulse-repetitive discharge feeding (pulse-repetitive discharger PD3-100/2.5), and diagnostic equipment. The gas dynamic (GD) duct

includes rectangular test channel made of insulating materials with two opposite electrodes installed transversally in respect of the flow. The pulse transversal discharge was excited by means of the pulse-repetitive power supply of the discharge made on the base of Tesla transformer. Two experimental series were performed in accordance with the particular schemes, Fig.7 (1) study of pulse discharge dynamics in subsonic and supersonic flow at interaction with co-flowing plane jet of secondary gas; and (2) study of pulse discharge dynamics in subsonic and supersonic flow at interaction with jet of secondary gas directly injected from the wall. Three main methods were applied for the visualization of plasma-flow interaction: instant schlieren images; schlieren-streak records; and schlieren based sensors records.

The data below correspond with the first scheme in Fig.7. Three experimental series were fulfilled to study the discharge interaction with two-phase flow:

- Discharge through the jet of secondary gas (CO₂), no external flow;
- Discharge in external flow with a central body without the second gas injection;
- Discharge through co-flowing jet of second gas in supersonic airflow.

The Figures 8 show the typical schlieren photos for the third case. It should be considered that the observation of schlieren images is insufficient to have deep quantitative analysis of the discharge generation effect on the mixing processes. But some qualitative conclusions could be made. The influence of the discharge on visible appearance of the jet is recognized at time delay about $70\mu s$ and later. At the same time the discharge affects the jet very locally, in the place of immediate intersection. The Fourier analysis of the plasma -induced perturbation didn't demonstrate significant changes.

The second experimental scheme in Fig.7 was explored in subsonic and supersonic flow. Two secondary gases were used: CO₂ as a model of hydrocarbon gaseous fuel, and He as a model of hydrogen. The jet was injected orthogonally to the

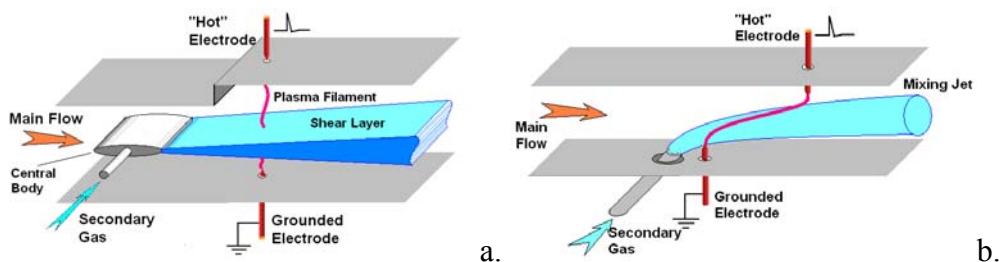


Fig.7. Experimental schemes.

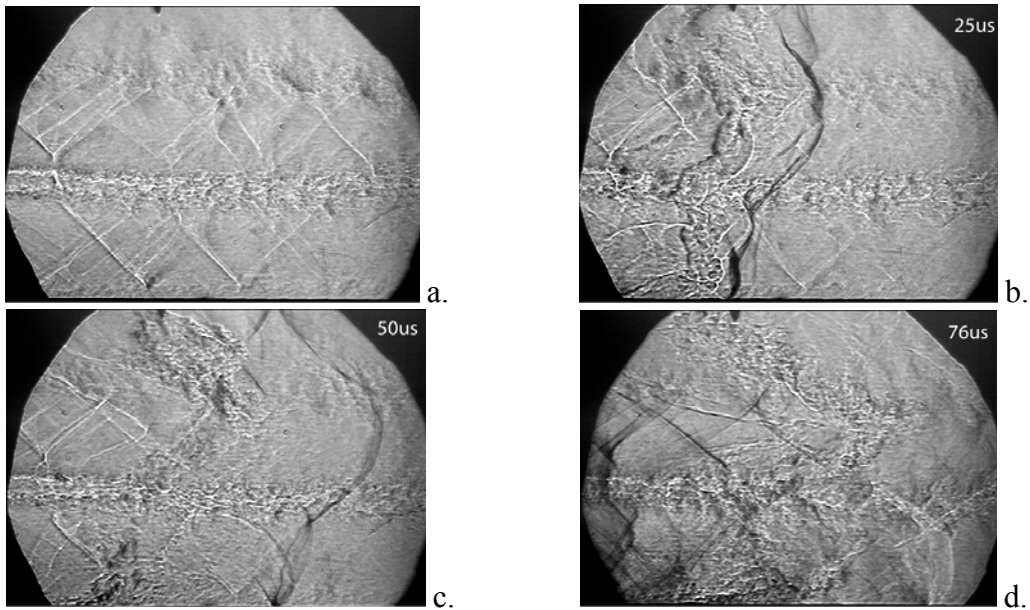


Fig.8. Discharge interaction with CO₂ jet in $M=2$ flow.
Left, top – initial structure, right and bottom – 25, 50 and 76 μ s after the discharge.

wall through $D=4\text{mm}$ orifice with the sonic velocity. The grounded electrode was combined with the nozzle. The “hot” high-voltage electrode was installed on the opposite wall of the duct a bit downstream in respect of the grounded one.

Before presentation of the results obtained it is important to remind one feature of the discharge behavior near the boundary of two different gases. As there were announced in Ref.14, “On one side, the breakdown voltage is lower in a fuel (experimentally and by the calculations, as well), on the other side the discharge channel loses the resistance much faster in the air. A priori it is difficult to predict the discharge filament location,

when the electrodes position is close to boundary of two different gases. Special tests were performed to clarify this point experimentally. It was found, that in the most cases the discharge was located inside a mixing layer between the gases”. This fact may be principally important for a practical implementation. The physical mechanism of this phenomena is considered in section 3.

Flow parameters were $M=0.3$ and 2.5 ; $P_{st}=400$ and 125Torr . Injected gases were CO₂ and He. Schlieren photos in Fig.9 demonstrate CO₂ jet in flow, discharge operation without CO₂ jet and discharge with jet under conditions of subsonic (top series) and supersonic (bottom series) flow.

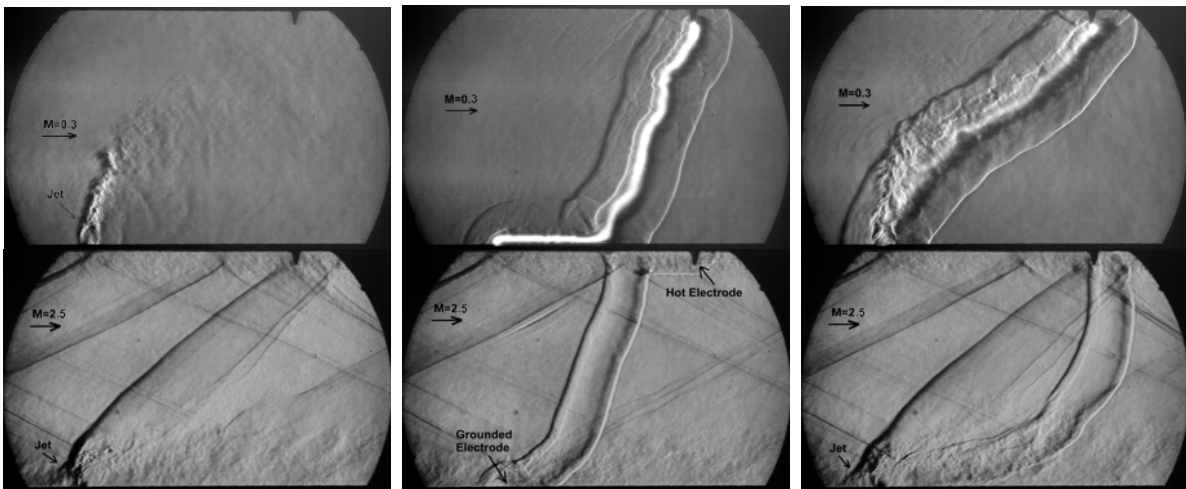


Fig.9. Typical schlieren images of the discharge operation in the airflow with jet. Top line– subsonic flow, $M = 0.3$; bottom line – supersonic flow, $M = 2.5$. Left column – CO₂ jet within the flow; middle column – discharge within the flow; right column – the discharge and the jet both.

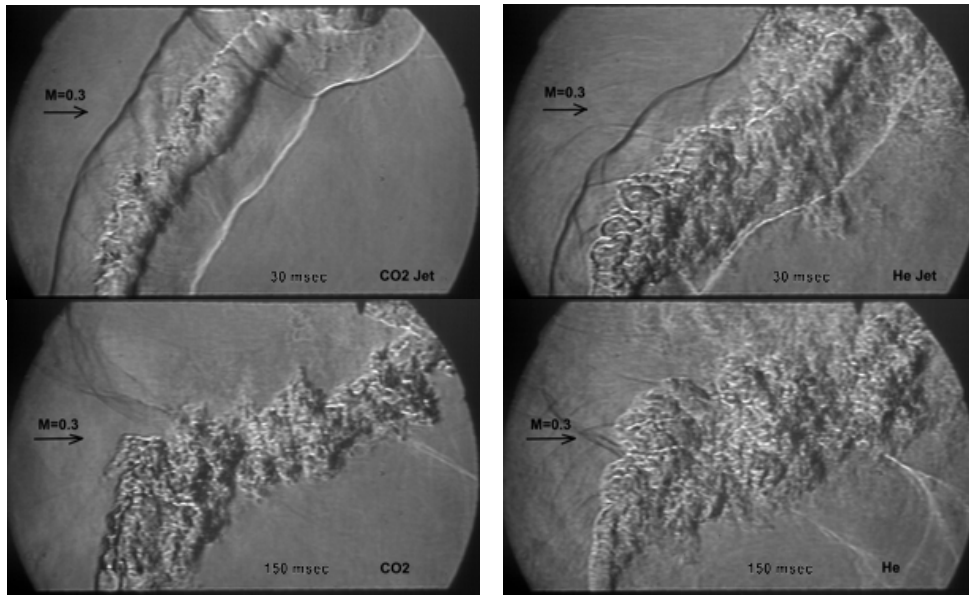


Fig.10. Schlieren photos of the discharge interaction with CO₂ jet (left) and He jet (right). $M=0.3$. Top row – time delay 30 μ s; bottom row – 150 μ s.

It is clearly seen, that discharge breakdown occurs along the jet. This fact was proved during number of experiments. Localization of the discharge's filament may vary from run to run in the experimental mode without jet, but it doesn't vary significantly in different runs with jet injection. The shock wave arises on the jet in the supersonic flow as it is seen in Fig.18, but the discharge doesn't "feel" it. It means that the type of gas injected is more important for the breakdown than a strong density gradient.

CO₂ jet models the hydrocarbon fuel jet. Helium jet was used in order to model hydrogen fuel because breakdown voltages for both gases are definitely lower than in air. The schlieren photos of the discharge's interaction with CO₂ jet and He jet in the subsonic ($M=0.3$) airflow at different delays are shown in Fig.10.

Helium jet itself occurs more turbulent in airflow than CO₂ jet, discharge interaction with helium jet is stronger than with CO₂ jet.

Comparison between schlieren photo of the CO₂ jet in Fig.9 and schlieren photo of the discharge interaction with CO₂ jet at delay 150 μ s in Fig.10 allows concluding that the discharge strongly influences on jet mixing with subsonic airflow. A several times longer distance is needed to analyze the discharge influence on jet appearance in supersonic flow. It was made using the second window of the test section to confirm the previous conclusion.

5. Conclusions

The paper raises new questions regarding the evolution of well-known long spark discharge

in air and nonhomogeneous media. Two experimentally found features of such a discharge were under consideration, namely (1) the mechanism of jet's instability of after-spark channel and (2) the mechanism of discharge filament localization in the presence of mixing layer (boundary) of two gases. In practical approach, the two gases might be a fuel and oxidizer. On the one side, the breakdown voltage is lower in a fuel (experimentally and by the calculations, as well), and on the other side, the discharge channel loses the resistance much faster in the air. A priori, it is difficult to predict the discharge filament location, when the electrodes position is close to the boundary of two different gases. Special tests were performed to clarify this point experimentally. It was found that in most cases, the discharge was located inside a mixing layer between the gases. The discharge disposition into a mixing layer and the instability development are favorable for kinematic mixing. This fact may be principally important for practical implementation.

Experimental results presented in this work demonstrate that turbulent and directed motion arising in the after-spark channel can essentially enhance the rate of fuel-gas mixing, which may control the mixing rate in engines with high-speed combustor.

The experimental work in JIHT RAS was funded through EOARD-ISTC project #3793p. Some parts of this work were supported by RFBR grant #10-08-00952a. The authors express their gratitude to Prof. A. Napartovich and Dr. I. Kochetov of TRINITY for calculations fulfilled and multiple discussions on plasma kinetics.

REFERENCES

1. J.P.Greig, R.E.Pechacek, M.Raleigh, "Channel cooling by turbulent convective mixing," *Phys. Fluids*, Vol. 28, No. 8, 1985, pp. 2357–2364.
2. J.M.Seiner, S.M.Dash, and D.C. Kenzakowski, "Historical survey on enhanced mixing in scramjet engines," *J. Propul. Power* 17, 1273 (2001)
3. E.J.Gutmark, K.C.Schadow, and K.H.Yu, "Mixing enhancement in supersonic free shear flows," *Annual Rev. Fluid Mech.* 27, 375 (1995)
4. N.T.Clemens & M.G.Mungal "Large Structure and Entrainment in the Supersonic Mixing Layer," *J. Fluid Mech.*, Vol. 284, 171-216, (1995).
5. M.N.Shneider, "Turbulent decay of after-spark channels", *Phys. Plasmas*, Vol. 13, 073501 (2006)
6. M.N.Shneider, "The effect of residual current on turbulent cooling of after-spark channels," AIAA Paper 2000-0721, Reno, NV, January 10-13, 2000.
7. S.B.Leonov, Y.I.Isaenkov, M.N.Shneider, "Suppression of the turbulent decay of an afterspark channel with residual current," *Physics of Plasmas*, Vol. 14, 2007, 123504.
8. Y.I.Isaenkov, S.B.Leonov, D.A.Yarantsev, "Properties of Filamentary Electrical Discharge in High-Enthalpy Flow," AIAA Paper 2005-0159
9. S.B.Leonov, D.A.Yarantsev, "Instability in Post-Discharge Thermal Cavity," *IEEE Transactions, Plasma Science*, Vol. 36, No. 4, 2008, p. 978.
10. M.Shneider, S.Leonov, Y.Isaenkov, S.Noethnagel, S.Gimelshein, "Jet Regime of the Afterspark Channel Decay", AIAA-2009-691, 47th AIAA Aerospace Sciences Meeting, Orlando, Florida, Jan. 5-8, 2009
11. S.B.Leonov, Y.I.Isaenkov, A.A.Firsov, "Mixing Intensification in High-Speed Flow by Unstable Pulse Discharge, 40th AIAA PDL Conference, San-Antonio, June 22-25, 2009, Paper AIAA-2009-4074
12. L.I.Sedov, "Similarity and dimensional analysis in mechanics". Academic Press, New York (1959)
13. Ya.B.Zel'dovich, Yu.P. Raizer, "Physics of shock waves and high-temperature hydrodynamic phenomena", Plenum Press, New York 1 (1966)
14. Sergey B. Leonov, Yury I. Isaenkov, Dmitry A. Yarantsev, Igor V. Kochetov, Anatoly P. Napartovich, Michail N. Shneider "Unstable Pulse Discharge in Mixing Layer of Gaseous Reactants", 47th AIAA Aerospace Sciences Meeting and Exhibit (Orlando, FL, USA, 5-8 January 2009), AIAA-2009-0820.

THE FORMATION OF POSITELY CHARGED PLASMA STRUCTURE IN NANOSECOND DISCHARGE WITH SLOT CATHODE

N.A. Ashurbekov, K.O. Iminov, O.V. Kobzev, V.S. Kobzeva

Dagestan State University
Makhachkala, 367025, Russia, nashurb@mail.ru

The parameters of visualized plasma structures (plasmoids) forming by means of nonlinear interaction of electric field with streams of charged particles in self-organizing plasma are intensively investigated in recent years [1, 2]. Despite a large number of works devoted to studies of such structures in underionized plasma, the problem of current and electric field focusing into plasma structures in high-voltage nanosecond discharges still remains unsolved. In this connection, of special interest is the investigation of conditions and mechanisms of self-organization of a positively-charged plasma structure in pulse nanosecond discharges, in which a beam of fast electrons with the energy of up to several keV is formed in the process of gas electric breakdown [3, 4].

This work is devoted to the study of plasma structure in nanosecond discharge with a slot cathode. The discharge occurred in the discharge chamber with a slot cathode, whose design is described in detail in [3]. The spatial-temporal distribution of optical irradiation of the discharge was registered by CCD-matrix and photomultiplier tube.

Systematic experimental studies of electric properties and spatial dynamics of optical irradiation of the discharge depending on the amplitude of voltage (U_0) applied to the discharge interval have been carried out. In particular, it has been established that with the increase of value U_0 from 1 to 5 kV, the value of burning voltage U_b

increased from 600 to 1650 V, while the value of discharge current I_p increased from 10 A to 450 A, with the time of the main energy contribution τ , determined by the half-width of current pulse, decreasing from 250 ns to 5 ns. Figure 1 shows the typical pictures of spatial distribution of optical irradiation between the electrodes and in the slot of the cathode. With the increase of value U_0 , an egg-shaped plasma clot appears at the slot exit (Fig. 1a). Further increase of U_0 results in the growth of size and irradiation intensity of this plasma formation, and at $U_0 \sim 5$ kV the plasmoid completely blocks the entrance to the slot and reaches its bottom (Fig. 1c).

The values of the main discharge parameters corresponding to the conditions of Fig. 1, are presented in the table. The given medium tension of electric field $-E/N$, was calculated by the value of the discharge burning voltage at the time of current maximum. To calculate the concentration of electrons by the current in the discharge volume, approximation for electrons' drift velocity in argon, of special purity $V_e = 0,9 \cdot (E/N(Td)/10)^{0,9} \cdot 10^4$ (m/c) was applied. In the conditions under investigation there occurred a pulse breakdown of overvoltage interval. The value of overvoltage coefficient was calculated as $K_t = (U_0 - U_b) / U_b$.

Short typical times of discharge burning ($\sim 10 - 50$ ns) and big values of electric field tension considerably decrease the role of ions and gas particles transfer processes in the formation of plasma structures, which allows to investigate the impact of

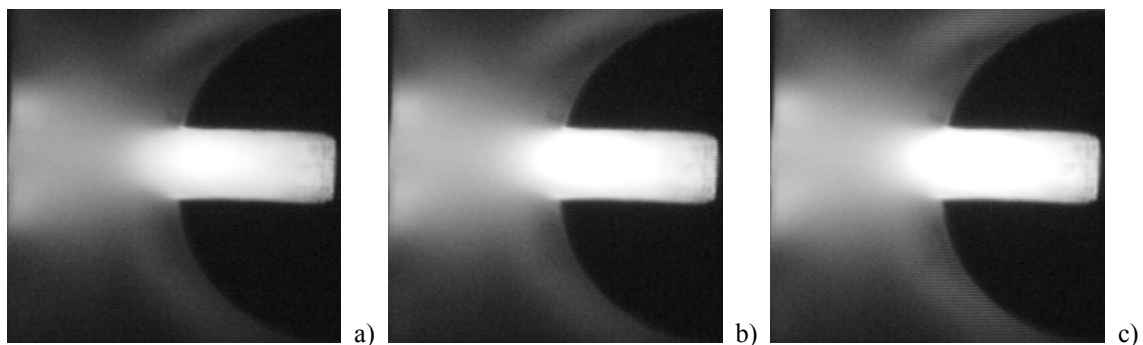


Fig. 1. Optical pictures of discharge luminescence in argon $p = 5$ torr.

Table. Parameters of discharge in argon

<i>Fig. 1.</i>	U_b, V	I_p, A	$E/N, Td$	$n_e, 10^{12} cm^{-3}$	$K_b, \%$	τ, ns
<i>a</i>	920	230	909	1.2	110	60
<i>b</i>	1000	320	1010	1.5	207	50
<i>c</i>	1120	450	1111	1.9	208	50

ionization and electrons transfer processes on the formation of plasma structures – plasmoids. The estimates provided in [4] demonstrate that for all conditions investigated, the accelerated electrons run length in plasma exceeds the width of cathode cavity. For the conditions of Fig. 1a, fast electrons, starting from the side surfaces of the slot, traverse the cathode cavity up to ten times and perform over 50 ionization acts. With the growth of value U_0 from 3 to 5 kV, the distance covered by fast electron increase and the number of ionization acts increases many times (Fig. 1b and 1c).

Since the main part of fast electrons, starting from the sides of the slot, make oscillatory movement in the cavity, they produce additional ionization. This additional ionization and the shift of electrons towards the anode under the influence of external field, result in the sharp growth of electrons concentration at the exit from the slot and the formation of dense cathode plasma that further functions as plasma electrode. The experimental field draws out free electrons from the plasma electrode, which leads to the formation of an area with excessive positive volume discharge. With the disturbance of neutrality, there appears an internal electric field directed to the centre of the area with excessive positive volume discharge and considerably outsize the external field. Free electrons rush to that area, which results in the cumulation of electric field density and the growth

of electrons concentration towards the centre of the area.

Thus, under the conditions investigated, there seems to be the formation of an attractor (plasmoid), with cumulative streams (beam of electrons) performing the focusing and carrying-out of electrons from the area of cumulator [2]. The increase in the size of plasmoid with the growth of the field applied, observed in the experiment, is connected with the growth of the area drawing out electron from the slot of the cathode.

This study was financially supported by the Federal Special-Purpose Programme «Scientific and Scientific-Pedagogical Personnel of Innovative Russia» for 2009 – 2013, project NK – 105P/1; NK-182P/7.

References

1. Dem'yanov A.V., Mazalov D.A., Napartovich A.P. et al. // JETP. 1996. V. 110. № 4 . Pp. 1266 – 1272.
2. Vysikailo F.I. // JETP. 2004. V. 125. № 5. Pp. 1071 – 1081.
3. Ashurbekov N.A., Iminov K.O., Kobzeva V.S., et al. // TVT. 2007. V. 45. № 4. Pp. 485 – 491.
4. Ashurbekov N.A., Iminov K.O., Kobzeva V.S., et al. // Izvestiya vuzov. Fizika. Tomsk. 2009. № 4. Pp. 37 – 44.

REMARKS ON GROUND-BASED MHD EXPERIMENTS

V.A. Bityurin, A.N. Bocharov, N.A. Popov

Joint Institute of High Temperatures of Russian Academy of Sciences, Moscow, Russia

Abstract. More than 50 years MHD flow control is the subject of intensive studies. As far as aerospace application is concerned, its potential could be utilized through, for instance, mitigation of heat loads on the spacecraft surface while re-entry path. The feasibility of heat flux mitigation was shown in many studies to associate with increase of bow shock stand-off distance, and, consequently, decrease of the mean temperature gradient across the shock layer. This can be characterized as direct MHD effect due to electromagnetic forces acting in ionized gas behind a strong shock. Another feasibility of heat flux mitigation proposed recently also utilizes action of electromagnetic force, but the primary goal of the idea is to decelerate the vehicle before it comes into thermally dangerous atmosphere [8,9,10].

The interest to magneto-aerodynamic heat flux mitigation has been renewed for the last several years due to publications on the preparation of flight experiments in this subject [1,2,12]. In this relation results of on-ground experiments on magneto-aerodynamic heat flux mitigation [1,2] are quite exciting since they may be a base for flight experiments.

The goals of the current paper are as follows. First, an attempt is made to assess one of the typical computational MHD model from the viewpoint of their ability to capture the key effects in magneto-aerodynamics including both flight conditions and the conditions of on-ground experiments. The second goal is to evaluate the typical experiments in magneto-aerodynamics from the viewpoint “what was observed and what is behind the observations”. Such formulation is essentially motivated by the author’s own experience in conducting and interpreting on-ground experiments in MHD hypersonic flows.

Four problems are considered in the paper. Problem 1 is well known experiment by R.W. Ziemer [3] recently numerically simulated by R.W. MacCormack [6]. In Problem 2 the experiments [4,5] and theoretical work [7] are discussed concerning the MHD effects in non-equilibrium argon plasma flows. Problem 3 is the most interesting (at the moment) one as the results of the works [1,2] are discussed. In Problem 4 the author’s experience in observing the hypersonic MHD flows is summarized.

Numerical simulations made with the computational model [9,10] have shown that the features of MHD flows (MHD features) in Problems 1 and 2 (change in the bow shock stand-off distance and change in the surface heat flux) are really due to the MHD interaction, or are due to MHD effects. At first sight, the flow analyzed in papers [1,2] (Problem 3) is similar to that from experimental works [4,5] and Problem 2. However, application of the same physical and computational model to simulate MHD in hypersonic argon plasma flow didn’t reveal any significant MHD effects in the region of interest. Such situation could be classified as “MHD features were experimentally detected (decrease in surface heat flux at the presence of magnetic field), while MHD effects were not confirmed numerically”. This is opposite to the situation considered in Problem 4: no MHD features (change in the bow shock stand-off distance) were experimentally detected in the expected location. At the same time, MHD effects were experimentally proven to be available.

1. Problem 1. Magnetohydrodynamic Interaction in Electromagnetic Tube [3].

In this Section the well known work by Ziemer [3] is considered. This is one of the first clear experimental demonstration of strong MHD effect in air plasma. In particular, it was noticed that large increase in the bow shock stand-off distance, 7.5 times at magnetic induction 4 Tesla, was detected. Experiments were carried out in electromagnetic tube. At one end of tube the electric discharge was initiated, which generated strong primary shock moving toward the other end of tube. At this end the cylindrical model was mounted with the electromagnet inside. MHD effects were studied in the region behind the secondary shock appearing after the primary shock arrived to the model. These studies seem to be a good candidate for validation of numerical models developed for magneto-aerodynamics. Some additional challenge for simulations arises from very short test times. First, the time needed for the primary shock to arrive to the model is about several tens microseconds, which is comparable with the time for magnetic field to achieve its

maximum value. Second, the primary shock reflected from the end wall may effect on the MHD flow behind the secondary shock. Therefore, the main concern is about the time needed for establishing quasi-steady flow behind the secondary shock. The quasi-steady formulation of the problem has been recently realized by R.W. MacCormack [6], and good qualitative agreement between numerical and experimental results was shown.

Numerical problem formulation considered in the paper is close to experimental one. 2D axi-symmetric air flow in the tube of diameter of 76 mm is simulated. The radius of cylindrical model (with hemi-spherical cap) is 20 mm, its length is 46 mm. The flow characteristics specified at the inlet station correspond to the gas behind the primary shock. Two cases are simulated designating moderate and strong MHD interaction cases. For the first case, static pressure behind the primary shock is $P_1 = 5717\text{Pa}$, velocity is $V_1 = 6715\text{ m/s}$, static temperature is $T_1 = 6049\text{K}$. These data are taken from the original paper [3] and correspond to the Mach number $M_1 = 21$, determined for undisturbed air in the tube ($P_0 = 9\text{Pa}$, $T_0 = 273\text{K}$). For the second case, $P_1 = 5300\text{Pa}$,

velocity is $V_1 = 11000$ m/s, static temperature is $T_1 = 12000$, $P_0 = 3$ Pa, $T_0 = 273$ K, Mach number $M_1 = 38$. In both cases the equilibrium air composition was specified at the inlet. In particular, $(n_e/n_0)_1 = 4.4 \cdot 10^{-4}$ in the first case, and $(n_e/n_0)_1 = 0.317$ in the second. Here, n_e is electron number density, n_0 is total number density. The MHD model of thermochemical non-equilibrium air [9,10] was used in simulations. The steady magnetic field from the coil similar to those described in paper [3] was specified. In all calculations characteristic value of magnetic induction $B^* = 4\pi I$ (the field at the critical point of hemisphere) was taken. The surface of the model, as well as the walls of the tube were considered as non-catalytic and iso-thermal, with wall temperature $T_w = 273$ K. Two kinds of calculations were done, steady and time-dependent. The formulation of steady problem is similar to those of paper [6]: the computational domain is not restricted with the tube walls. In time-dependent calculations the magnetic field is switched on when the primary shock arrives to the model.

The steadiness of the MHD flow behind the secondary shock can be seen in Fig.1. Here, the pressure field at several time moments is shown for both cases, $M_1 = 21$ and $M_1 = 38$. In first case the steady flow is established for 20 – 30 μ s. In the second – for less than 10 μ s. Comparison with steady calculations shows the same flow features in the region behind the secondary shock and the hemi-spherical part of the model. The flow downstream the leading part of model differs significantly for time-dependent and steady calculations. Conclusion concerning the steadiness of the MHD flow behind the secondary shock made in paper [3] was also confirmed in current simulations.

Increase in the bow shock (secondary shock in the considered setup) stand-off distance is typically treated as the evidence of MHD interaction. The distributions of temperature along the stagnation streamline are shown in Fig.2. In the flow case $M_1 = 21$ the stand-off distance increases in 3.2 times, while in $M_1 = 38$ case it increases in 9.4 times. Note, that in second case magnetic Reynolds number is estimated to be $Re_m \sim 0.72$. Taking into account high magnetic Reynolds number effects should decrease the stand-off distance. In the first case $Re_m \sim 0.14$.

Another feature of MHD interaction is considered to be a decrease of the surface heat flux. This feature is represented in Fig.3 for both Mach number cases. 60% decrease in peak heat flux (at critical point) was calculated for $M_1 = 21$ case and almost three-fold decrease – for strong MHD interaction case, $M_1 = 38$.

Thus, both typical features of MHD interaction, increase in bow shock stand-off distance and decrease of the heat flux were revealed in experimental work and confirmed by numerical

calculations (in paper [6] and in current paper). One can say that these features are due to primarily MHD interaction and are not the consequence of other effects like influence of the reflection of primary shock from the wall. As far as numerical model is concerned, we believe it is suitable to simulate complicated MHD flows under re-entry conditions or those considered in the paper.

2. Problem 2: MHD Interaction in Non-Equilibrium Argon Plasma Flow [4,5].

The argon plasma flows are widely used in on-ground experiments in magneto-aerodynamics. The main advantage of ionized argon flow is that it can be obtained for the cost less than, for example, air flow. Even small ionization degree, say of order of 10^{-4} , may provide an electrical conductivity level sufficient for detecting remarkable MHD effects in the region of interest. In this Section the numerical simulations of MHD flow around a blunt body are considered analogous to those reported in well known papers [4,5] (see also recent paper [7]). These investigations are interesting for simulations for several reasons. They are representative of many on-ground studies in magneto-aerodynamics, so many typical features of non-equilibrium flows are exposed. While experimental conditions differ considerably from flight that, it is nevertheless necessary for the numerical models to deal with flows generated in the existing ground facilities. Third reason to consider problem [4,5] associates with the analogous Problem 3 from the following Section and will be discussed there.

Scheme of experiments [4,5] are principally those as in the previous Problem 1. The supersonic flow around cylinder with hemispherical end is considered. Magnetic field is generated by the coil at the nose of the model and is similar to the field of magnetic dipole. The argon plasma is generated by the arc heater and then is expanded in the supersonic nozzle. It was assumed in original papers [4,5] as well as in paper [7] that flow in the test section is frozen due to expansion in the nozzle. That is, both electron concentration and electron temperature don't change in the test section. The following free-stream flow data were specified in the calculations. Density is $1.035 \cdot 10^{-4}$ kg/m³, velocity is 3000 m/s, static temperature is 1100K, Mach number 4.75, electron temperature was estimated as 3900K. The key parameter is electron number density. In [4,5] it was estimated as $4 \cdot 10^{19}$ m⁻³ (ionization degree is 2.5%), while in paper [7] it was estimated to be 10^{19} m⁻³ (ionization degree is 0.625%). The latter estimate was made based on the Saha equation in which stagnation pressure and temperature in arc heater were used, 0.49atm and 9700K, respectively. This estimate is also used in the current paper. The radius of hemisphere (same as cylinder radius) is 38.1 mm, the model's surface

temperature was taken to be 300K. The scaling value of the magnetic induction B^* is the value of induction at critical point of the model.

Numerical formulation is, in general, close to that used in Problem 1. Instead air 3-species non-reacting argon plasma flow is considered (Ar, Ar⁺, and e⁻). Transport properties of the flow are estimated from cross-section data given in paper [11]. It is assumed that cross-sections with participating electrons are determined by the electron temperature. The latter is determined from the solution for corresponding transport equation [10], in which elastic collisions dominate. As the composition of argon plasma is considered to be given, the electron temperature is the main factor determining electrodynamics around the model. Example of the distribution of electron temperature near the model is shown in Fig.4. It can be seen that this distribution correlates well with the distribution of the magnetic field. The main processes occur in rather thin layer near the spherical part of the model surface in angle sector 20 – 60 degrees relative to the stagnation line. In this layer the level of electrical conductivity is rather high (600-800 Sm/m) while Hall parameter is rather small (less than 4). These two factors provide an MHD interaction intensity sufficient for detecting. Fig.5 shows the gas temperature field for non-MHD and MHD flow around the model. Change in bow shock position is clearly seen. Position of bow shock for three values of characteristic magnetic field is shown in Fig.6. Also, relative increase in bow shock stand-off distance, $(d_m - d_0)/d_0$, is shown in rectangles. In current paper stand-off distance was estimated at $T_s=4000K$. Good agreement with data reported in papers [4,7] is observed for $B^*=0.28Tl$. At larger value, $B^*=0.45Tl$, the stand-off distance is within experimental uncertainty. The data reported in paper [7] are slightly less than those reported in original paper [4] and in the current one. This is probably due to the fact that additional heating of electron gas was not considered in paper [7]. Another feature of MHD interaction, change in surface heat flux, is shown in Fig.7. Data obtained here for $B^*=0.28Tl$ agree well with those reported in paper [7].

Conclusions made from considering Problem 2 are as follows. The features of MHD (increase in bow shock stand-off distance and decrease in the surface heat flux) are due to the MHD interaction. We also believe that the model of non-equilibrium argon plasma flow developed in the paper is capable of capturing the key processes in the systems like those considered here. Attempt was made to take into account possible chemical reactions (electron impact ionization of argon atom and three-body recombination), but no principal differences from the frozen plasma case was revealed. It appeared that electron temperature is high enough to provide electrical conductivity, but

it is rather small to change significantly plasma composition.

3. Problem 3: The Newest Experiments in Argon Plasma Flow [1,2].

As was already mentioned, the papers [1,2] are of special interest because they are considered as important stage for the first flight experiment on electromagnetic heat shield test. As in papers [4,5], the effect of magnetic field on the model's surface heat flux is studied in papers [1,2]. Experiments were carried out in the hypersonic flow of non-equilibrium argon plasma. Decrease of the heat flux was reported to be 46 – 85% at characteristic magnetic induction value of order of 0.5Tl depending on the cylindrical model leading part, hemispherical or rectangle. This flux decrease was estimated assuming the equilibrium irradiation from the surface, which temperature was decreasing in 16 – 44% depending on the model design.

In this Section the attempt is made to numerically simulate the argon plasma flow around a cylindrical model under experimental conditions. One of the model design considered here is a cylinder (cylinder axis is aligned with the main flow direction) of diameter of 70 mm. Electromagnet is positioned within the model. Details can be found in [1,2]. The free-stream flow is specified as follows. Measured parameters (just before the shock at the stagnation line): velocity is 2150 m/s, gas temperature is 180 K, electron number density is $2.8 \cdot 10^{17} m^{-3}$, electron temperature T_e is 6600 K, Pito pressure is 550 Pa. Calculated parameters: gas density is $1.19 \cdot 10^{-4} kg/m^3$, static pressure is 4.47 Pa, argon atoms number density is $1.79 \cdot 10^{21} m^{-3}$, ionization degree is $n_e/n_0 = 1.56 \cdot 10^{-4}$. From these data estimate to free-stream electron conductivity can be obtained with using cross-sections data from paper [11]:

$$\sigma = e^2 n_e / (m_e \nu_e) \sim 260 Sm/m \quad (1)$$

Here, σ is coefficient of electrical conductivity, e is electron charge, m_e is electron mass, ν_e is mean electron collision frequency. Electron-neutral collisions make the primary contribution to electron collision frequency. For e -Ar collisions, cross-section is about $Q_{ea} \sim 3A^2$. Note, that characteristic conductivity value is of the same order as those in Problem 2 from the previous Section. Though free-stream electron number density in Problem 2 is almost 40 times more than in Problem 3, the collision-frequency is almost in same ratio higher. This is because the main contribution to the mean electron frequency is due to electron-ion collisions, which cross-section value is estimated as $Q_{ei} \sim 160A^2$. So, the ratio n_e/ν_e is almost same for both Problem 2 and Problem 3. Using commonly used estimation for the magnetic parameter

$$S_{mhd} = \sigma B_*^2 D / (\rho_\infty U_\infty) \quad (2)$$

one could expect very similar effects of magnetic field in both MHD flows (Problem 2 and Problem 3): $S_{mhd} \sim 8.2$ for Problem 2, and $S_{mhd} \sim 8.7$ for Problem 3. The principal difference between these two MHD flows relates with Hall effect, which is characterized by Hall parameter, $\beta_e = \omega_e / \nu_e$ ($\omega_e = eB_*/m_e$ is Larmour frequency). Hence, Hall effect in Problem 2 is quite moderate and doesn't dramatically influences on the MHD interaction. Unlike Problem 2 Hall effect is crucial for Problem 3, and no remarkable MHD effects should be expected including increase in bow shock stand-off distance and heat flux mitigation. This conclusion is in contradiction with the experimental results of papers [1,2].

Two-dimensional numerical simulations of the flow were carried out with the same model described shortly in Section 2 and with the inflow data given above. Several flow fields are presented in Fig.8 for the characteristic value of magnetic induction $B^*=0.45Tl$ (magnetic induction at the critical point). One can see that distribution of electron temperature and electric conductivity is quite similar to those from Problem 2. The difference between two flows is that conductivity drops with rising the electron temperature, as e-n collision cross-section increases with T_e . In Problem 2 Column collisions dominate for which $Q_{ei} \sim 1/T_e^2$. At the same time Hall parameter is much higher in Problem 3 (Fig.8d) than in Problem 2 (Fig.4c). So, it is difficult to explain experimental results [1,2] in terms of typical MHD flow models.

In attempting to explain experimental results we exclude for a moment from consideration such factors like current leakages feeding the electromagnet and possible change in catalytic properties of the model surface due to the induced electric fields. Generation of voltage of order of 5 – 10 V is absolutely possible within the typical MHD model like that exploited in current work. This voltage may be applied to the small region near, for example, the nozzle exit (realization of such possibility depends on boundary conditions, which are not known). If so, local energy input localized in this region could lead to heating the gas thus changing the free-stream flow characteristics. More probably, energy input will lead to decrease of free-stream Mach number, or velocity. As consequence, the surface heat flux $q_w \sim \rho U^3 / 2 \cdot St$ (St – Stanton number) should also decrease. To recognize whether such mechanism is valid or not, one should know more about geometry of the test section, about material of the walls including the walls of the nozzle, and about grounding conditions.

Another possible reason for the induced electric field to influence on the flow relates with functioning of the arc heater. For example, arc

heater used in works [4,5] was functioning at voltage 28V and current 960A. Applied magnetic field could induce the voltage 5 – 10V in the electric circuit including the arc heater itself. Thus, induced voltage could effect on the functionality of arc heater and, as consequence, on the flow.

In both cases considered above one should know more about facility. Typical set of free-stream gasdynamic data is not sufficient for accurate interpretation of the results. At the moment we believe that experimental results reported in papers [1,2] associate with indirect influence of the magnetic field like that discussed above. Direct effect of magnetic field should associate with the action of electromagnetic forces.

4. Problem 4: MHD Interaction in Seeded Airflow [8].

The Problem 3 could be characterized as the presence of MHD features in the absence of MHD interaction. In this Section we consider our own experience in MHD flow control, which looks opposite to the previous one. That is, no expected MHD features were detected, whereas MHD interaction took place. Such a conclusion has been made from analysis of MHD flow around circular cylinder [8]. In general, experimental setup is close to those considered above. The magnetic field generated by the current flowing along the cylinder axis. So, the plane of magnetic field is the plane of the flow. Ionization in hypersonic airflow (Mach number $\sim 8 - 15$) was provided with injection of easy-ionized atoms (Na, K) and was estimated to be 1 – 2%. Originally, attention has been paid to the detection of change in bow shock position when magnetic field is on. However, no change has been revealed.

Numerical analysis showed that no change in bow shock position should be expected. Fig.9 demonstrates this. Curves 0, 1 and 2 show position of the bow shock under experimental conditions and for several kinds of grounding. It is seen that magnetic field does influence on the flow, however the bow shock near the model surface is rather stable. Intensive MHD interaction occurs in other places. Combination of factors, namely configuration of magnetic field, the presence of ionization in the free-stream flow, and electric boundary conditions, specify interaction in such a way that the region near the bow shock is MHD acceleration zone. The electromagnetic force is directed toward the model surface; therefore no increase in stand-off distance could take place. The bow shock stand-off distance could be increased in two cases. First, the Hall effect should be small (Curve 3 in Fig.9), which seems impossible in low-density poorly-ionized flows. Or, second, remarkable ionization should take place behind the shock as in real flight case. In this case the Hall

effect is essentially suppressed due to boundary conditions.

“Useful” MHD interaction occurs mainly in the wake of cylinder – in the region of MHD generation. After it has been recognized the setup has been changed. The MHD flow over the wedge clearly demonstrated the presence of MHD effects resulting in “useful” changes in the flow pattern: increase in angle between the shock and model’s surface, and even the power extraction.

Conclusions

Four typical examples were considered in the paper concerning the interpretation of on-ground experiments in magneto-aerodynamics. A wide range of possible situations was demonstrated: the detected MHD flow features are due to MHD effect; MHD features are exposed, while MHD effects are not; MHD features are not detected, while MHD effect is present. The main conclusion from these examples is that commonly used set of so called free-stream parameters is, in general, insufficient to correctly interpret experimental observations.

Currently used numerical MHD models are capable of interpreting the key processes taking place in the test sections of on-ground facilities. There many successful attempts known from the literature to numerically simulate MHD flows under experimental conditions. At the same time the situation related with MHD flow considered in papers [1,2] (Problem 3) could be characterized as challengeable. At the moment it is not clear for authors whether the model is insufficient to predict quite impressive experimental results or still unknown facility/flow features could effect on the flow.

Finally, we would like to mention once again that real flight conditions are principally different from those typically realized in on-ground facilities. In real flight ionization could take place only in the shock layer. If the temperature within the layer is high enough to provide high degree of ionization, Hall parameter is small due to high electron collision-frequencies. In this case assessments of MHD effects should be close to classic that known from 1950th. At moderate vehicle velocities, when ionization degree is not so high, Hall effect would be a critical factor effecting on MHD flow. However, the role of Hall effect is significantly reduced due to the presence of non-conductive boundaries like bow shock and the vehicle surface (ideally). This doesn’t mean that Hall effect plays no role. This just means that the role of factor $1/(1+\beta_e^2) \sim 10^{-2} - 10^{-4}$ (β_e – electron Hall parameter) becomes not so critical. Hall effect does influence the flow structure but it doesn’t suppress the “positive” magneto-aerodynamic effects like surface heat flux mitigation.

Unfortunately, it is very difficult to reproduce the ionization behind a strong shock in on-ground experiments.

References

1. *Gülhan, B. Esser, U. Koch, F. Siebe, J. Riehmer, D. Giordano, D. Konigorski*, “Experimental Verification of Heat-Flux Mitigation by Electromagnetic Fields in Partially-Ionized-Argon Flows”, JOURNAL OF SPACECRAFT AND ROCKETS, Vol. 46, No. 2, March–April 2009.
2. *A. Gülhan, B. Esser, U. Koch, F. Siebe, J. Riehmer, D. Giordano, D. Konigorski*, “Experiments on Heat-Flux Mitigation by Electromagnetic Fields in Ionized Flows”, 40th AIAA Plasmadynamics and Lasers Conference 22-25 June 2009 San Antonio, TX, USA, AIAA-2009-3725.
3. *Ziemer, R.W.*, “Experimental Investigation in Magneto-Aerodynamics”, ARS Journal, Vol.29, Sept. 1959, pp.642-647.
4. *Kranc, S., Yuen, M. C., and Cambel, A. B.*, “Experimental Investigation of Magnetoaerodynamic Flow around Blunt Bodies”, Tech. rep., National Aeronautics and Space Administration, Washington, D.C., August 1969, NASA CR-1392.
5. *Nowak, R. J., Kran, S., Porter, R. W., Yuen, M. C., and Cambel, A. B.*, “Magnetogasdynamic Re-Entry Phenomena”, Journal of Spacecraft, Vol. 4, No. 11, November 1967, pp. 1538-1542.
6. *R.W. MacCormack*, “ Non-Equilibrium Ionized Flow Simulations within Strong Electro-Magnetic Fields”, 48th AIAA Aerospace Sciences Meeting, 4-7 January 2010, Orlando, Florida, AIAA Paper 2010-225.
7. *N. J. Bisek, I.D. Boyd, and J. Poggie*, “Numerical Study of Magnetoaerodynamic Flow around Hemisphere”, 48th AIAA Aerospace Sciences Meeting, 4-7 January 2010, Orlando, Florida, AIAA Paper 2010-227.
8. *Bityurin V., Bocharov A., Baranov D. and Bychkov S.* Power Extraction Experiment with a Surface MHD Generator in Hypersonic Airflow // 38th AIAA Plasmadynamics and Lasers Conference In conjunction with the 16th International Conference on MHD Energy Conversion. Miami, FL: AIAA-2007-3882, 25–28 June 2007.
9. *Bityurin V.A., Bocharov A.N., Popov N.A.* Non-Equilibrium Effects in MHD Parachute Concept: Induced Electric Field Effects // 47th AIAA Aerospace Sciences Meeting & Exhibit AIAA. Reno. NV Paper 2009-1230, 5–8 January 2009.

10. *Bityurin V.A., Bocharov A.N.* MHD Flow Control in Hypersonic Flight. V. 2 // The 15th International Conference on MHD Energy Conversion. Moscow, 24–27 May 2005. P. 429.

11. *R.S. Devoto*, “Transport coefficients of ionized Argon”, *Physics of Fluids*, Vol.16, No.5, May 1973.
 12. *Journal Aerospace America*, December 2009, p.12.

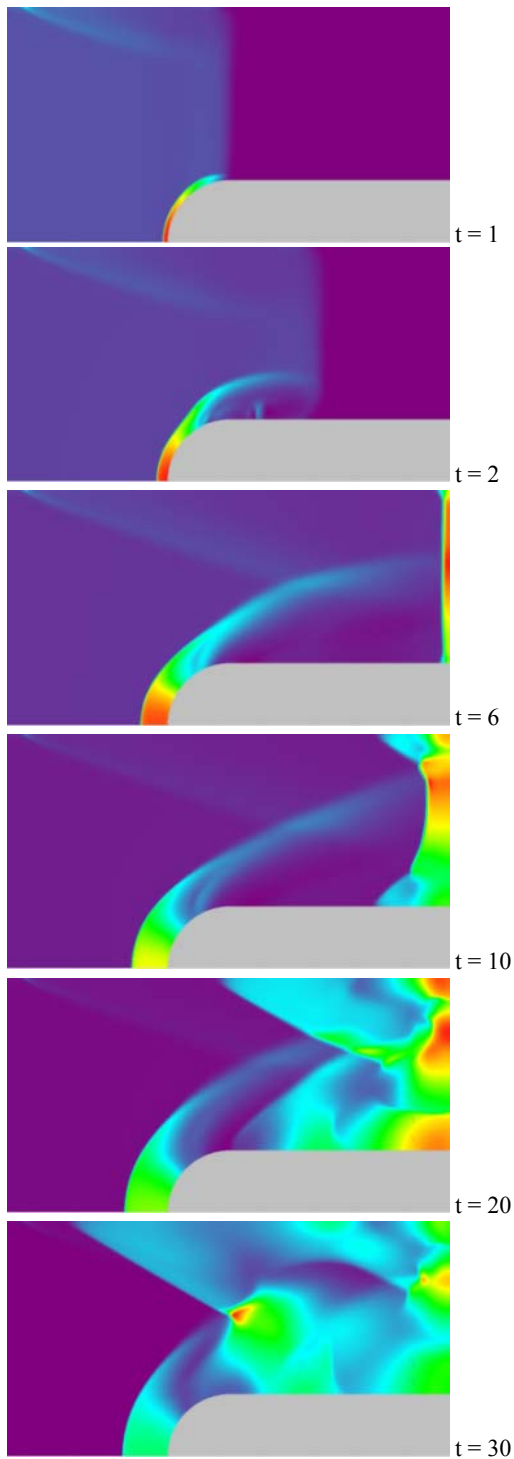


Fig.1a. Evolution of pressure in Problem 1. $M_1=21$, $B^*=4Tl$. Time is given in μs .

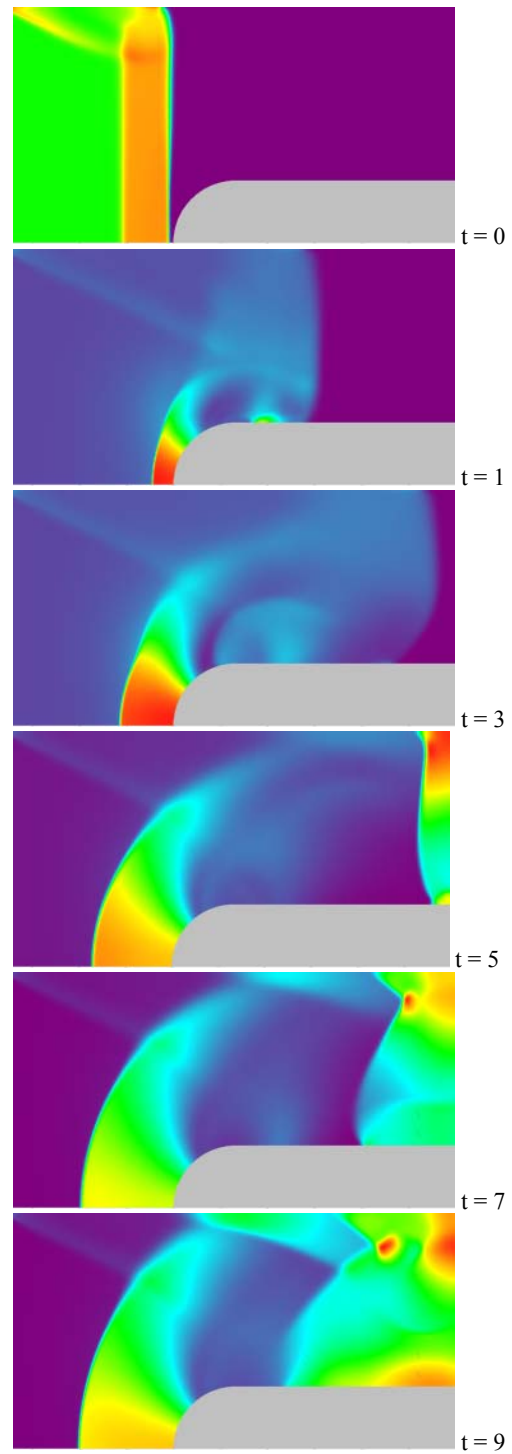


Fig.1b. Evolution of pressure in Problem 1. $M_1=38$, $B^*=4Tl$. Time is given in μs .

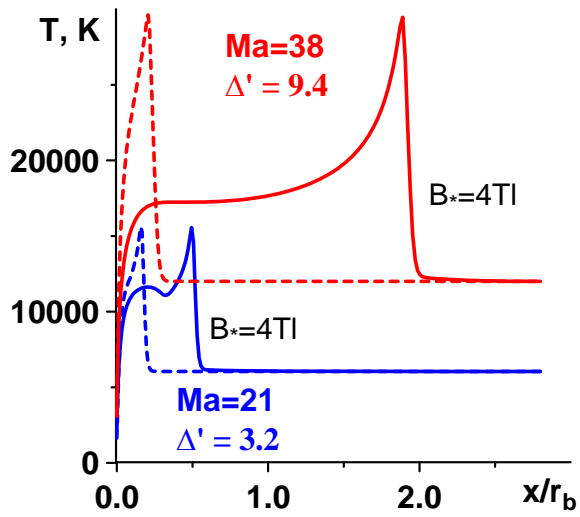


Fig.2. Distribution of temperature along stagnation streamline for Problem 1. Blue lines – $Ma_1=21$, red lines – $Ma_1=38$. Dotted lines – $B^*=0$, solid lines – $B^*=4Tl$. $r_b=1\text{cm}$ – nose radius.

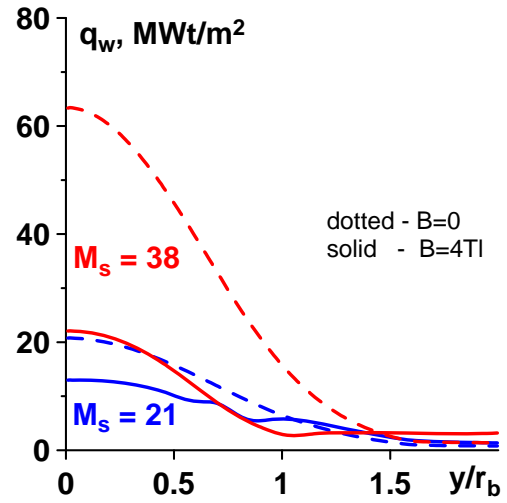


Fig.3. Distribution of the heat flux density over the model surface for Problem. Blue lines – $Ma_1=21$, red lines – $Ma_1=38$. Dotted lines – $B^*=0$, solid lines – $B^*=4Tl$. $r_b=1\text{cm}$ – nose radius.

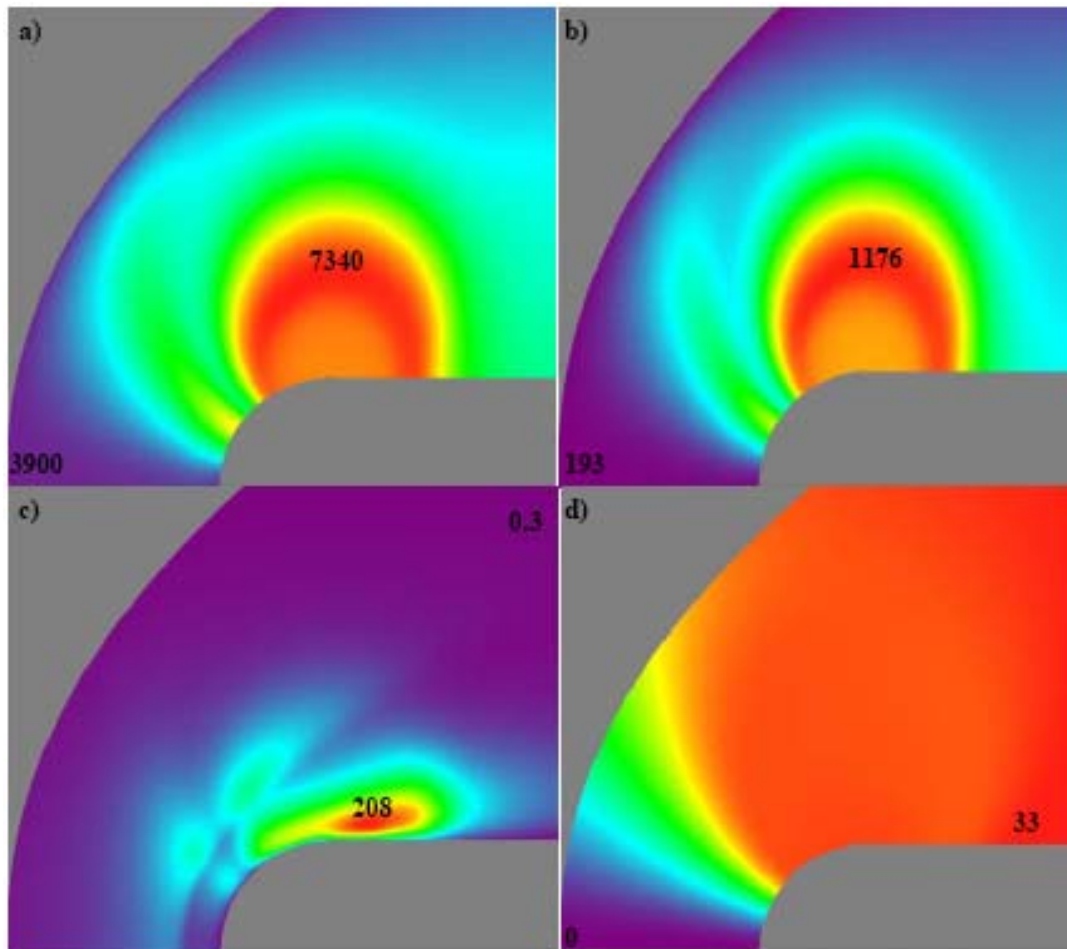


Fig.4. Distribution of electron temperature (a), electric conductivity (b), Hall parameter (c), and electric potential (d) for Problem 2. $B^*=0.45Tl$.

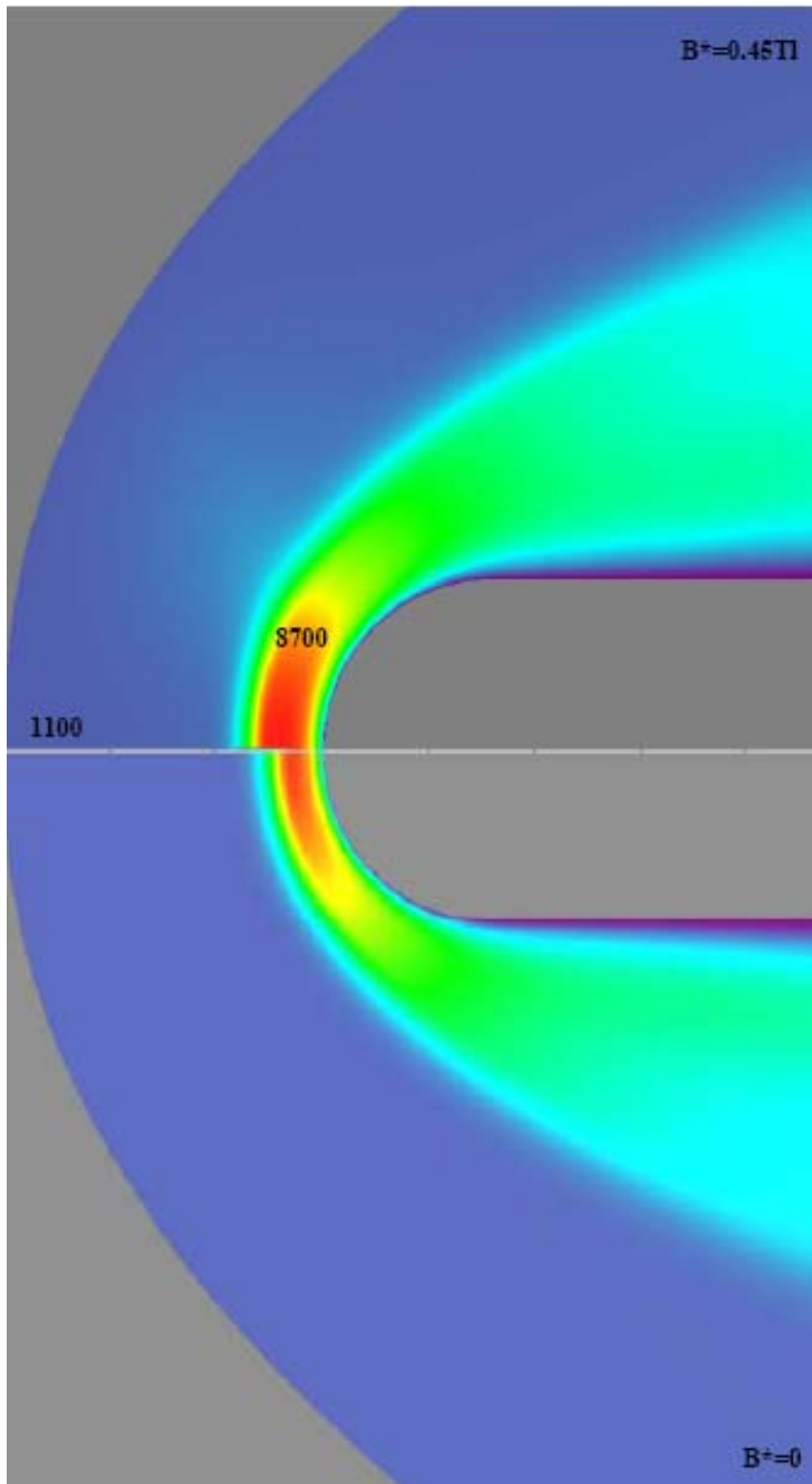


Fig.5. Gas temperature without magnetic field (bottom) and with magnetic field (top) for Problem 2.

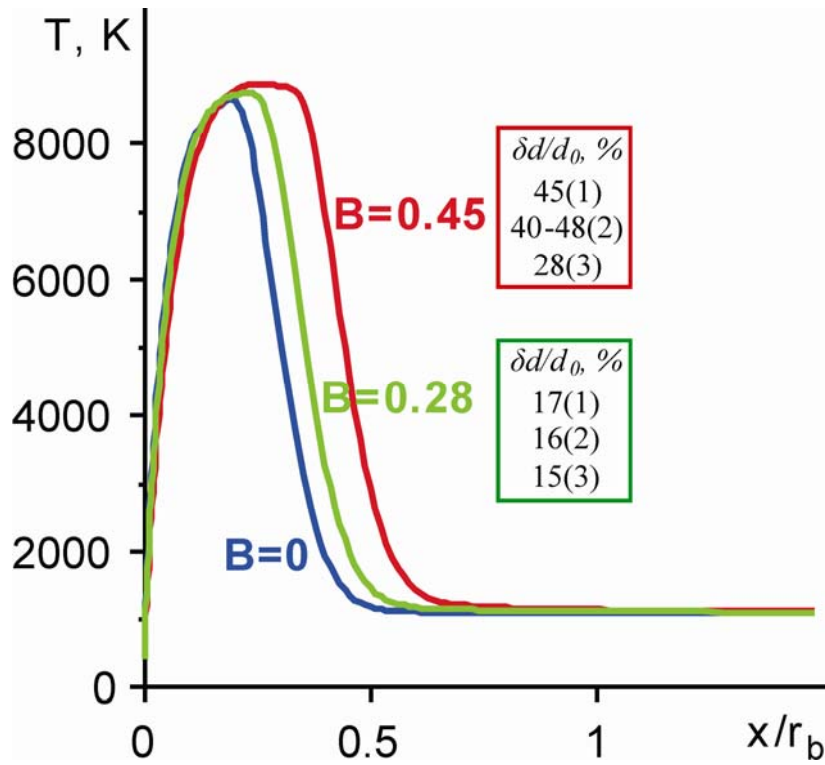


Fig.6. Distribution of gas temperature along the stagnation streamline and increase in standoff distance due to magnetic field for Problem 2. [1] – this paper, [2] – paper⁴, [3] – paper⁷.

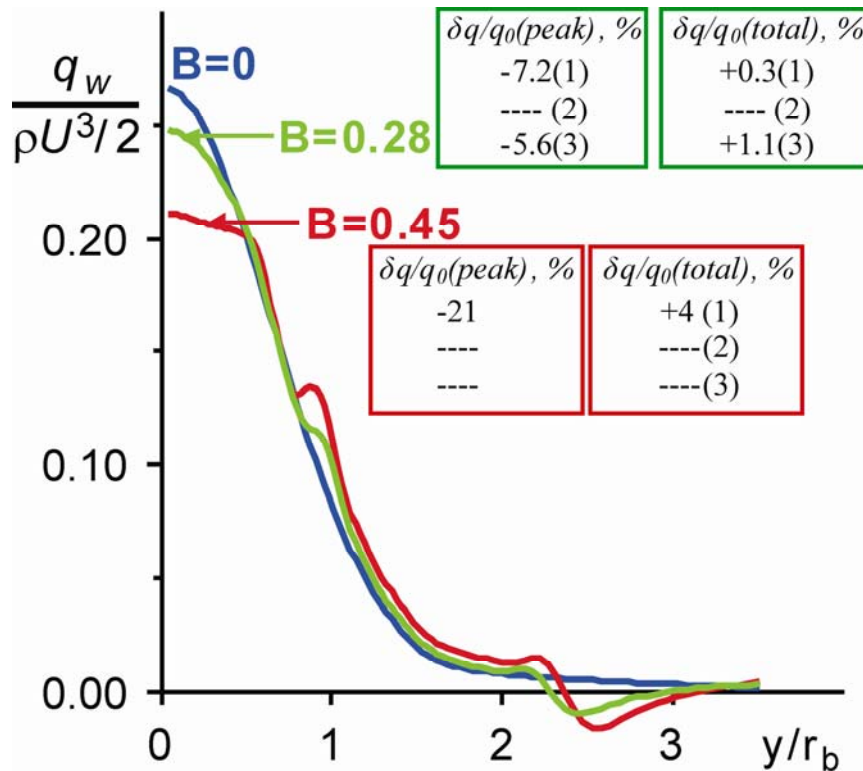


Fig.7. Surface heat flux and change in heat flux due to magnetic field for Problem 2. [1] – this paper, [2] – paper [4], [3] – paper [7].

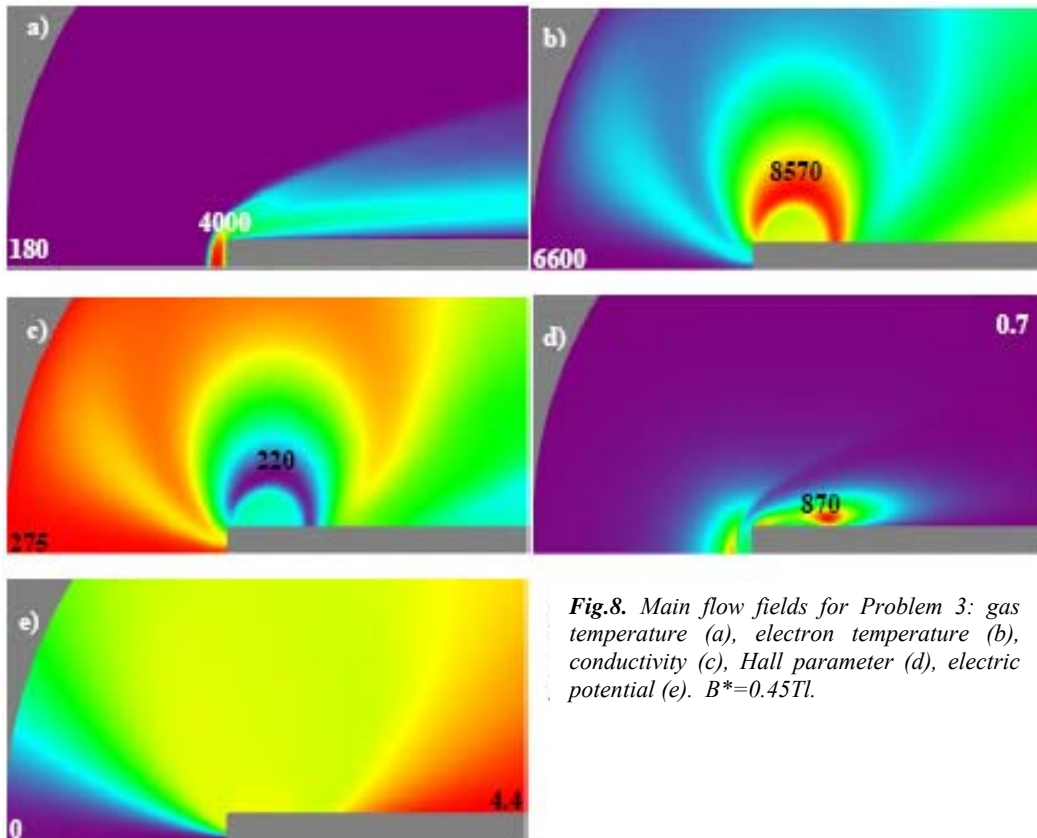


Fig.8. Main flow fields for Problem 3: gas temperature (a), electron temperature (b), conductivity (c), Hall parameter (d), electric potential (e). $B^*=0.45Tl$.

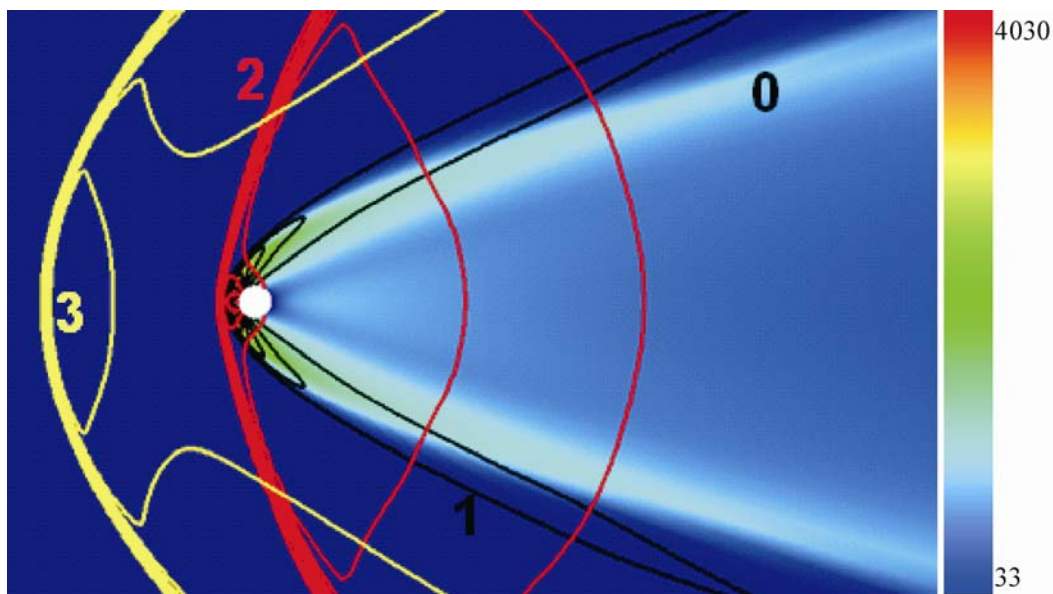


Fig.9. Effect of plasma model and boundary conditions on the position of bow shock in Problem 4 (flow around circular cylinder). 0 – $B^*=0$; 1 – $B^*=1.5Tl$, frozen conductivity, grounded walls (experimental conditions); 2 – $B^*=1.5Tl$, frozen conductivity, isolated walls; 3 – $B^*=1.5Tl$, frozen conductivity, Hall effect canceled.

INVESTIGATION OF THE AIR FLOW AROUND A WEDGE AT $M = 6$ UNDER THE LOCAL MHD-INFLUENCE

V.E. Podzin, V.P. Fomichev, A.B. Shevchenko, M.A. Yadrenkin

Khristianovich's Institute of Theoretical and Applied Mechanics SB RAS
630090, Novosibirsk, Russia,

fomichev@itam.nsc.ru, yadrenkin@itam.nsc.ru

The hypersonic flow around a wedge at $M = 6$ and the local pulsing magnetohydrodynamic influence (MHD) on the flow ahead of the wedge has been studied experimentally by the photo technique. It is demonstrated that the slope of the attached shock wave can be increased by 10 - 12 degrees. It has been shown that the flow backup to its initial state during one pass of the MHD-interaction region over the wedge surface. The settling time of the flow is less than 3 μ s.

Introduction

Hypersonic vehicles developing stimulates the great interest to the application of new MHD-techniques to improve scramjet operation [1]. It is possible to study the MHD-control of the hypersonic air flow over the compression surfaces [2, 3] simulating the flow around a wedge. A number of experimental and numerical investigations has shown that the localized MHD-interaction in the hypersonic flow ahead of the wedge results in the alteration of the slope angle of the attached shock wave. Results of the numerical and experimental research of the MHD-interaction in the air flow over the wedge at $M = 8$, the wedge's apex angle of 30 degrees, are presented in [4, 5]. The data has been obtained at the free flight conditions at the altitude of 30 - 50 km. It is shown that the slope of the shock wave can be increased by 6 - 8 degrees at the free-stream Mach number of $M = 8$. In the experimental investigations, the time of the external ionization of the flow is about 100 μ s. Therefore there is a question whether the studied flow is quasi-steady or not. To solve this problem, the air flow around the wedge has been studied experimentally. Taking into account that the Mach number decreases at the MHD-interaction, the tests have been performed at free-stream Mach number $M = 6$, the flow ionization duration is 120 and 12 μ s.

Test rig and test conditions

Experimental study of the MHD-interaction has been carried out at the MHD-test rig, based to a shock tube [18, 20]. Gas heated by reflected shock wave in a settling chamber accelerates up to $M = 6, 8, 10$ in the wind tunnel nozzle. Cross section of the flow is round with diameter 105 mm. The test rig allows to simulate a hypersonic flow, which is typical for the flight altitude of 30-50 km with $M = 6, 8, 10$. Model is a wedge with the apex angle of 30 deg. B-field generated by an electromagnet is up to 2.5 T. The

external flow ionization is initiated by the pulse electric discharge similarly to [4]. Electrical and gas-dynamic measurements permitted to obtain information about plasma discharge and MHD-interaction parameters.

Following parameters are measured in each experiment to investigate the MHD-interaction: shock wave parameters, gas parameters in the nozzle prechamber, parameters of ionizing discharge and MHD-interaction parameters. Optical visualization of the oblique shock wave generated by the wedge is also used as a method of the study. P_0 and T_0 , parameters in the nozzle prechamber, have been defined by measurements of pressure in the prechamber using a piezoelectric transducer and the calculated speed of the shock wave in the channel of the shock wind tunnel.

Operating characteristics of the pre-ionizers are defined by measurements of the current and voltage of the pulse discharge. The current is measured with the help of high-frequency transformers of the current; the voltage is measured using a voltage divisor with an induction - output signal.

MHD-interaction parameters are defined using the value of the total current measured in the interaction zone and voltage on MHD-electrodes. The total current is measured using current transformers, the voltage is measured using a voltage divisor with an inductive connection to an oscillograph. All the measurements of the electrical parameters are implemented using the current transformers. That allow performing the signal transmission to oscillograph without a galvanic coupling in the range of frequency from 100 Hz up to 107 Hz.

Location of the shock generated by the wedge is defined by two photographs taking consistently. The photographs obtained by shadow technique based on AVT [23] (adaptive visualizing transparencies). The first image is registered before the ionizer switches on; the second one is registered with 50-100 μ s delay, at the moment of the MHD-interaction. Accuracy of measurements is determined by accuracy of electronic devices and

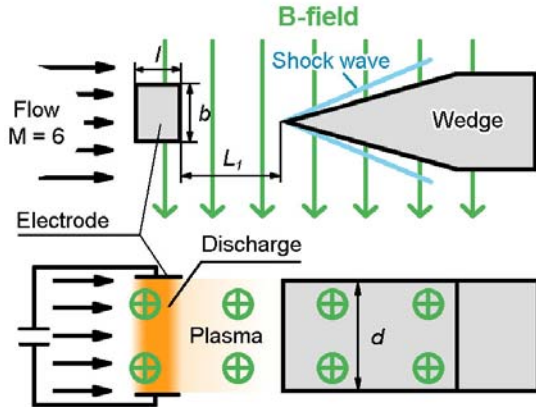


Figure 1. Schematic of the experiment.

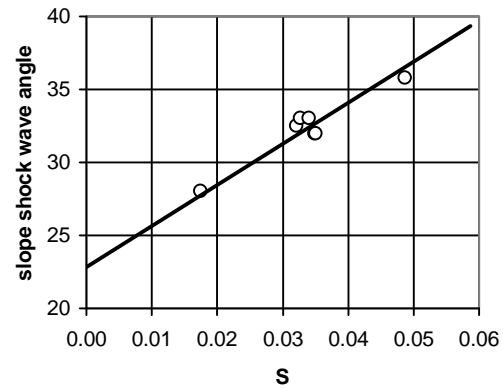


Figure 2. Dependence of the slope wave angle on the MHD-interaction parameter at $M = 6$.

gauges, used in tests (piezoelectric transducers and current transformers), this error is less than 5-10 %.

Figure 1 presents the schematic of the experiment. Wedge width is $d = 50$ mm, length and height of the electrodes are $l = 25$ mm and $b = 15$ mm accordingly, electrode-wedge distance is $L_1 = 5$ mm. Test conditions are: static pressure in the flow $p_s = 11.6$ Torr, gas density is $\rho_s = 0.019$ kg/m³, temperature is $T_s = 287$ K, flow velocity is $V = 1983$ m/s, Mach number is $M = 5.8$. Flow parameters correspond to the atmospheric conditions at the altitude of 29 km. Magnitude of the magnetic field is of 0.34 T. The Schlieren pictures of the flow are taken with the frequency of 330,000 fps. The exposition time is of 1.2 μ s.

Intensity of the MHD-interaction is estimated by the Stewart number which can be written with use of the measured current in the circuit of the MHD - electrodes as

$$S = \frac{IB}{kb\rho w^2},$$

where I is the current magnitude, B - magnetic induction, ρ - density of the flow, V - flow velocity, b - size of an electrode in direction normal to the free flow direction and along the magnetic field, k is a coefficient, which allows to taking into account the deviation of the effective area of discharge from the electrode surface area equal to product bl . Magnitude of the coefficient is higher than 1, and, most likely is less than 10. Theoretically, it can be assessed using either a photo of the discharge, by the size of the glowing discharge area, or analyzing the data on the current distribution in the region of the MHD-interaction, which can be calculated. For instance, $k \approx 1,4$ obtained by pictures of the luminous discharge region has been taken in the present work.

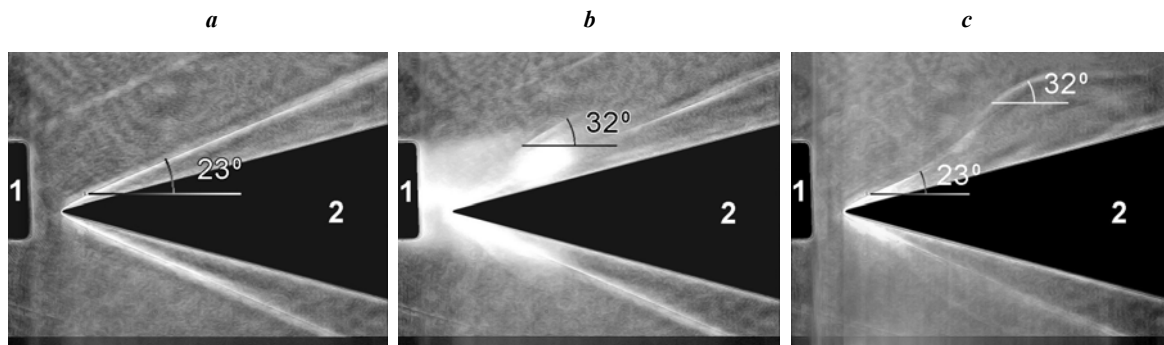


Figure 3. Schlieren-photos of the uniform flow around the wedge (a), and the MHD-disturbed flow (b), (c).

1 – electrodes, 2 – wedge.

Results and discussion

In the experiments with the flow ionization time of $120 \mu\text{s}$, the slope angle of the attached shock wave over the wedge increases by 10–12 degrees, the magnitude of the MHD-interaction parameter is around $S \approx 0.035$. Figure 2 presents the slope wave angle depending on a magnitude of MHD-interaction parameter.

The study of the flow around the wedge at the ionization time of $12 \mu\text{s}$ has permitted one to obtain information about the time of the flow settling over the wedge surface. Figure 3 presents the photos of the flow obtained in the uniform flow (*a*) and in the flow with the MHD-disturbance region (*b*) and (*c*), which show the passing of the disturbed region in the streamwise direction. One can see that the shock wave generated by the wedge has a curved shape. The central part of the disturbed region is placed about the wedge side center, Figure 3, *c*. Comparing the photos of the uniform flow and the flow with the MHD-disturbance, we see that the flow near the wedge apex is almost non-disturbed in both cases.

The slope angle of the oblique shock wave in the apex region is equal to 23 degrees, which relates to the flow over the wedge at $M = 5.8$. The slope angle of the oblique shock wave in the wedge side center is equal to 32 degrees, which relates to the flow around the wedge at $M = 3$. The time interval between two frames is of $3 \mu\text{s}$. It can be seen that the slope angle is unchanged in the MHD-disturbance region passing the wedge. Comparison of two consequent pictures (Figure 3) permits to conclude that the flow settling time is less than $3 \mu\text{s}$ at test conditions.

Conclusions

Experimental research results of the MHD-interaction in the hypersonic air flow over the wedge at $M = 6$ and the local pulsing MHD-influence on the flow ahead of the wedge has shown that slope angle of the attached shock wave

over the wedge might be increased by 10–12 degrees at the magnitude of the MHD-interaction parameter is about $S \approx 0.035 - 0.045$.

It has been shown that the flow backup to its initial state during one pass of the MHD-interaction region along the model surface. The flow settling time is less than $3 \mu\text{s}$ at test conditions.

References

1. I.A. Golovnov, G.A. Pozdnyakov, S.S. Pravdin, V.E. Podzin, T.I. Pushkareva, V.M. Fomin, V.P. Fomichev, V.I. Yakovlev. An experimental complex to simulate and study the MHD-interaction in a hypersonic flow / Preprint No. 7-2003, ITAM SB RAS, Novosibirsk, 2003, 26 p.
2. Fomin V.M., Fomichev V.P., Golovnov I.A., Korotaeva T.A., Pozdnyakov G.A., Pravdin S.S., Shashkin A.P., Yakovlev V.I. Study of MHD-interaction in hypersonic streams//AIAA 2004-1193, 2004.
3. V.A. Bitjurin, A. N. Bocharov. The study of the hypersonic MHD flow above the wedge // Inter. Confer. ICMAR 2004, Part V, P. 18-23.
4. Fomin V.M., Maslov A.A., Korotaeva T.A., Shashkin A.P., Malmuth N.D. Simulation of the MHD-Effect Upon a Flow around a Wedge// 15th Int. Conf. on MHD energy conversion and 6th Int. Workshop on MPA, Moscow, May 24-27, 2005, Proc. V.2, p.583.
5. V.M. Fomin, V.P. Fomichev, T.A. Korotaeva, A.A. Maslov, A.A. Pavlov, A.I.A. Pavlov, S.S. Pravdin, A.P. Shashkin, V.I. Yakovlev, N.D. Malmuth, P. Smereczniak, J. S. Silkey. Initiation of nonequilibrium conductivity of a hypersonic flow and MHD-interaction. // AIAA 2007-1376, 45th AIAA Aerospace Sciences Meeting and Exhibit, Reno, Nevada, 2007, 11p.

ELECTROGASDYNAMIC AND MAGNETOHYDRODYNAMIC CONTROL OF SUPERSONIC BODY STREAMLINE

A.V.Erofeev, T.A.Lapushkina, S.A.Poniaev

Ioffe Physical Technical Institute of the Russian Academy of Sciences
26 Polytekhnicheskaya str., St.Petersburg, 194021, Russia
alex.erofeev@mail.ioffe.ru

1. Introduction

The actuality of the investigations on control of supersonic flows does not change in time in spite of a large number of works in the aerodynamics. This work is in series of works [1-3] concerned with possibility to control the shock-wave configuration by non-mechanical methods. The two types of action on supersonic flow structure were considered: electrogasdynamic (EGD) realized due to heating of a gas in gas discharges of high intensity, and magnetohydrodynamic (MHD) by action of Lorentz force appeared at magnetoinduced current or organized in gas discharge electric current at transversal magnetic field.

The aim of this work is to show possibility to control position of the bow shock-wave arising due to supersonic streamlining of a semicylindrical body both by EGD and MHD methods at surface discharge near the front part of the model.

The main task of the work is to investigate how the bow shock-wave position change:

1. At increase of near surface gas discharge intensity on nose part of the body and EGD

interaction parameter, i.e. a ratio between heat of a gas in the discharge and doubled kinetic

energy of the flow in unit volume $N = \frac{jE\Delta t}{\rho u^2}$;

2. At increase of MHD interaction in near surface region after bow shock wave due to increase Stewart parameter, i.e. a ratio between work of ponderomotive force in an interaction zone and doubled kinetic energy of the flow in unit

volume $St = \frac{jBL}{\rho u^2}$.

Where j is current density, E is electric field intensity, Δt is interaction time, B is magnetic field induction, L is width of interaction zone, ρ and u are density and velocity of incoming flow.

2. Experiment arrangement.

Experiments were conducted at the setup based on a shock tube. Figure 1 shows a scheme of the gasdynamic range. A working chamber in the form of a supersonic nozzle with the walls inclined at 11° to the axis was connected to the butt end of a low-

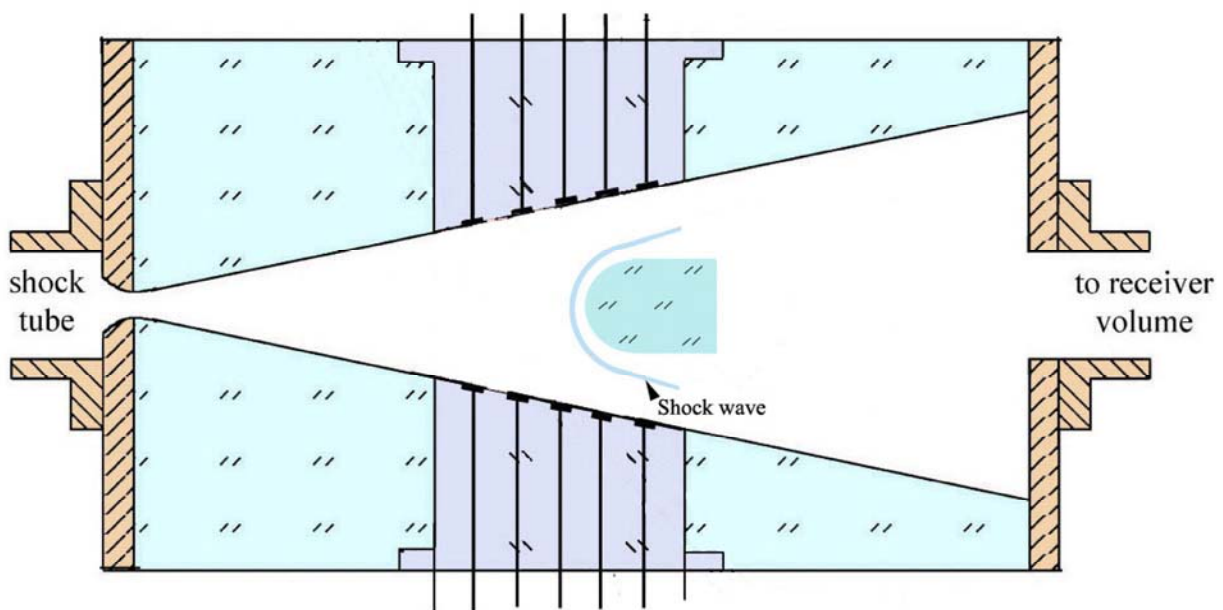


Figure 1. Setup scheme.

pressure chamber. A set of copper electrodes was mounted into the upper and lower nozzle walls. At a distance of 20 cm from the nozzle entrance, at its axis, a body in the form of a half-cylinder was placed. The radius of the cylindrical part was 1.5 cm and the total length of the body was 3.8 cm. The body was placed in such a manner that the flow passed through the region of three pairs of electrodes before it reached the body. Figure 1 schematically shows the bow shock formed at supersonic body streamline. The set-up includes additionally the system of gas discharge creation on the basis of thyatron schemes, long lines collection and system of pulse homogeneous magnetic field creation across flow in all working chamber with magnetic induction value up to 1.5 T and duration of stationary region of action about 600 mks.

Xenon was used as a working gas. Such a choice allows us to model plasma, electrogasdynamic and magnetohydrodynamic influence upon supersonic streamline of aircraft head parts without additional energy expenditures on ionization, which is required in air experiment.

For investigation next working regime of the shock tube was chosen: moving gas (hydrogen) pressure is $p_1=21$ atm, pressure in the low pressure chamber $p_2=30$ Torr, shock wave Mach number in shock tube is $M_2=8$. This regime is characterized by such named sew together contact surface in the region of the shock tube end, that allows homogeneous flow of ionise xenon in nozzle with duration about 600 mks.

The feature of presented gas discharges is that discharge is switched on in the ionized flow with some conductivity. The gas compressed in the shock tube stagnates before the nozzle inlet, is ionized thermally by means of transition of flow kinetic energy into heat, and then enters the nozzle. In the end of shock tube homogeneous xenon plasma with next parameters is created: atom and electron temperature is $T_5=9600$ K, conductivity is $\sigma_5=3600$ S/m, ionizing degree is $\alpha_5=5 \cdot 10^{-2}$. In the process of moving along nozzle gas is expanded in spite of this gas temperature decreases more quickly than electron temperature owing to comparatively long relaxation time of xenon [4]. In result before gas discharge the flow of already inhomogeneous plasma moves toward body with next parameters: Mach number is $M=4.3$, gas temperature is $T_h=1600$ K, electron temperature is $T_e=4600$ K, conductivity is $\sigma=600$ S/m, ionization degree is $\alpha=2 \cdot 10^{-3}$, flow velocity is $u=1.6 \cdot 10^3$ m/s, gas density is $\rho=0.127$ kg/m³. The doubled kinetic energy in volume unit is $\rho u^2=3.25 \cdot 10^5$ J/m³.

Flow visualization was realized by means of schlieren system with light source from semiconductor laser with electronic radiation pumping with pulse duration about 20 ns. Schlieren pictures were recorded directly to the digital photo camera Canon EOS 300D matrix. The main

obstacle to obtain a good quality of pictures was bright own plasma radiation. For lowering of it filter with bandwidth in the region of laser wavelength 656 nm and narrow collimator before knife was placed. Plexiglass windows decreased the quality of imagers too. From schlieren pictures of flow the distance d along nozzle axis from bow shock wave to the body's nose part was determined and bow shock wave shift from first position d_0 without any action was investigated depending on organized flow conditions.

2. Surface discharge near the front edge of the model.

Body in a form of semicylinder with horizontal electrodes on the nose part was made for investigation of near surface discharge influence on bow shock wave position. Electrodes arrangement is shown on figure 2.

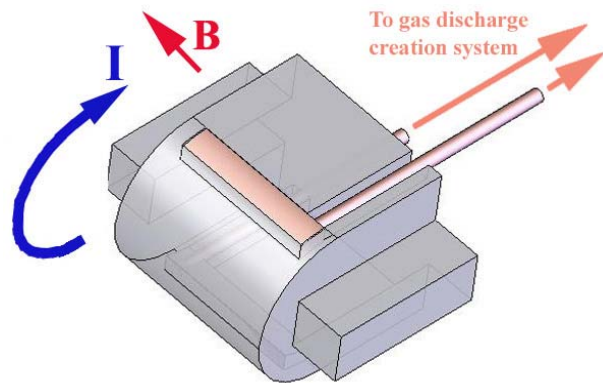


Figure 2. Body with horizontal electrodes.

When gas discharge is organized using these electrodes discharge current embraces the nose part of the body by half-circle trajectory as shown on Figure 3. When magnetic field is switched on electrical current vector remains orthogonal to the

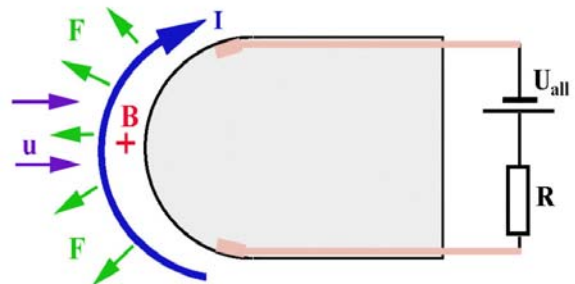


Figure 3. Illustration of ponderomotive force action at near surface gas discharge.

magnetic field induction vector and Lorentz force acts on gas in direction from body. If current source polarity is changed current changes its direction to opposite one and Lorentz force action has direction to body. In that way we can control bow shock wave position used the near surface discharge and external magnetic field which compressed or expanded the gas in depends from current direction.

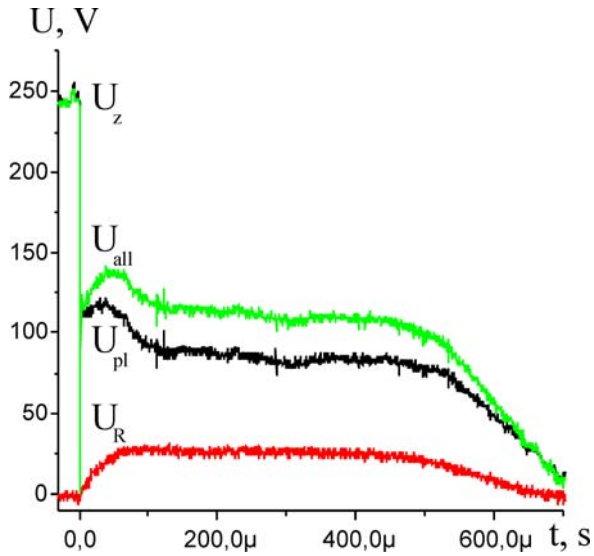


Figure 4. Voltage at near surface gas discharge in xenon.

Near surface discharge in the nose part of the model is created by mean of current source named long line, which connected with model electrodes through diagnostic resistance R as schematic shown on figure 3. Before experiment long line is charged up to predetermined voltage U_z . Ionized flow coming to body initiates the discharge; it allows excluding additional electrical key in

circuit, plasma flow is key. In this part experimental data of investigation of EGD and MHD action on flow parameters at discharge organized in such manner.

Oscillograms of voltage in electric circuit are presented on Figure 4. U_z is long line charge voltage, U_{all} is general voltage which comes from long line to circuit, U_{pl} voltage on plasma space, U_R is voltage on diagnostic resistance $R=0.05$ Ohm.

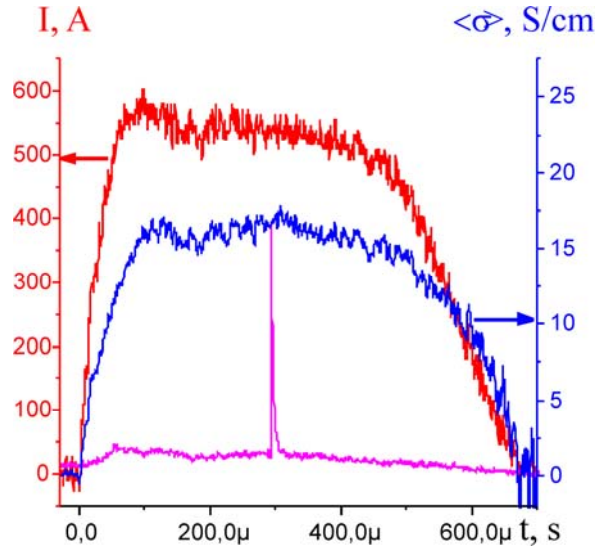


Figure 5. Oscillograms of current (red curve) and integral conductivity (blue curve) of xenon plasma at near surface gas discharge. Magenta curve is diagnostic laser pulse.

On Figure 5 you can see how discharge current (red line) and integral plasma conductivity $\langle\sigma\rangle$ (blue line) is changed in discharge. Current value was changed by means of changing of long line charge voltage. Discharge duration is determined

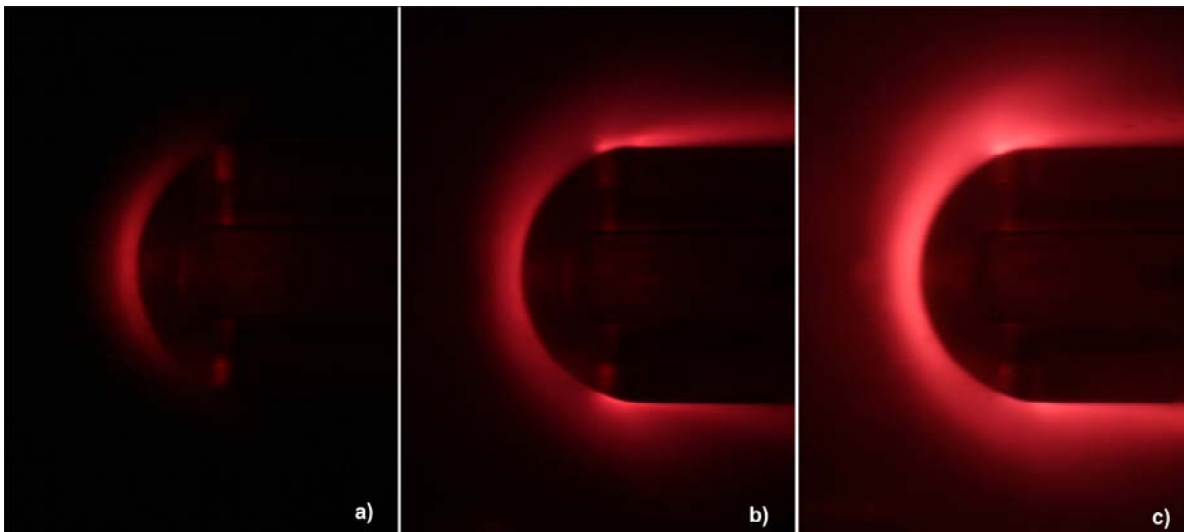


Figure 6. Xenon plasma luminosity at different intensity of near surface gas discharge without magnetic field. a) $j=0$; b) $j=2.2 \cdot 10^6$ A/m²; c) $j=6.9 \cdot 10^6$ A/m².

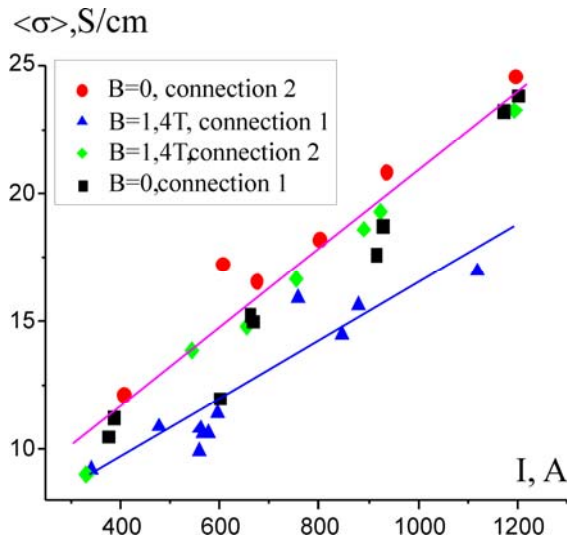


Figure 7. Xenon plasma conductivity with near surface gas discharge current.

by time of plasma flow around body that is duration of xenon flow in nozzle. Time of bow shock wave formed near model about 100 mks from flow beginning, next 400 mks is time of stationary flow around body. Flow diagnostic is realized on this period. Light pulse of schlieren system laser is shown on figure 5 by magenta line in the bottom. Schlieren picture is fixed in period of stationary flow in 330 mks after flow beginning.

Changing of discharge current direction is carried out by means of changing of long line connection polarity. When current runs from bottom electrode to top one as on Figure 3 it is connection 1. In this case in magnetic field Lorentz force will be directed from model. When current is organized from top electrode to bottom one (connection 2) Lorentz force action changes its direction to model. If we change near-surface

discharge current value and its direction we change intensity and direction of EGD and MHD action on bow shock wave position and flow parameters.

Integral pictures of plasma luminosity in near surface region at different intensity discharge without magnetic field are present on Figure 6. You can see that luminosity embraces the front model edge. It is diffuse and light intensity increases with discharge current intensity increasing. Plasma conductivity in discharge region increases too.

Dependence of plasma conductivity from discharge current is presented on Figure 7. Conductivity obtained in discharges at different current direction and with or without magnetic field are presented by correspond color and form points. You can see that conductivity increases with current increasing. Without magnetic field conductivity value doesn't depend from current direction. In magnetic field at connection 2 conductivity has the same value as in discharge without magnetic field at the same discharge intensity. At connection 1 conductivity is smaller. It necessary to note that in this case voltage polarity in discharge circuit is the same as polarity of magnetoinduce electromotive force, which induced in ionized gas flow moved in cross magnetic field.

In the first stage of investigations of near-surface discharge influence on flow around body process the EGD action was studied. Schlieren pictures of body streamline at different discharge intensities without magnetic field are present on the Figure 8. You can see that bow shock wave moves from body with discharge current rising, the distance from model to bow shock wave increases. That is happen due to gas hitting in gas discharge behind bow shock wave. As result of hitting gas pressure increases in discharge region directly ahead of model, it leads shock wave moving away from body.

In the next work stage the investigation were carried out how MHD interaction influences on

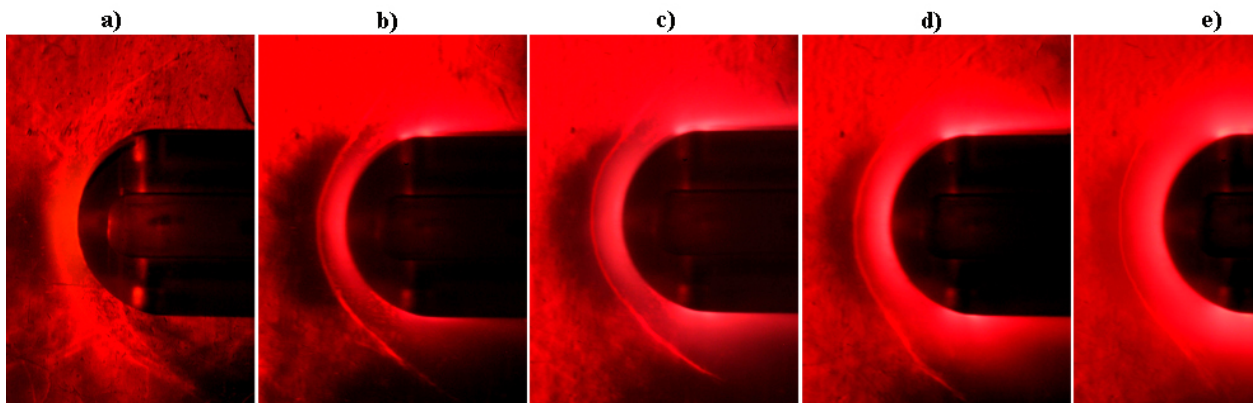


Figure 8. EGD action. Flow picture changing with near-surface discharge intensity increasing in xenon.

a) $j=0$; $N=0$; b) $j=2.2 \cdot 10^6$ A/m², $N=0.68$; c) $j=3.8 \cdot 10^6$ A/m², $N=1.33$;
d) $j=5.3 \cdot 10^6$ A/m², $N=2.08$; e) $j=6.8 \cdot 10^6$ A/m², $N=2.95$.

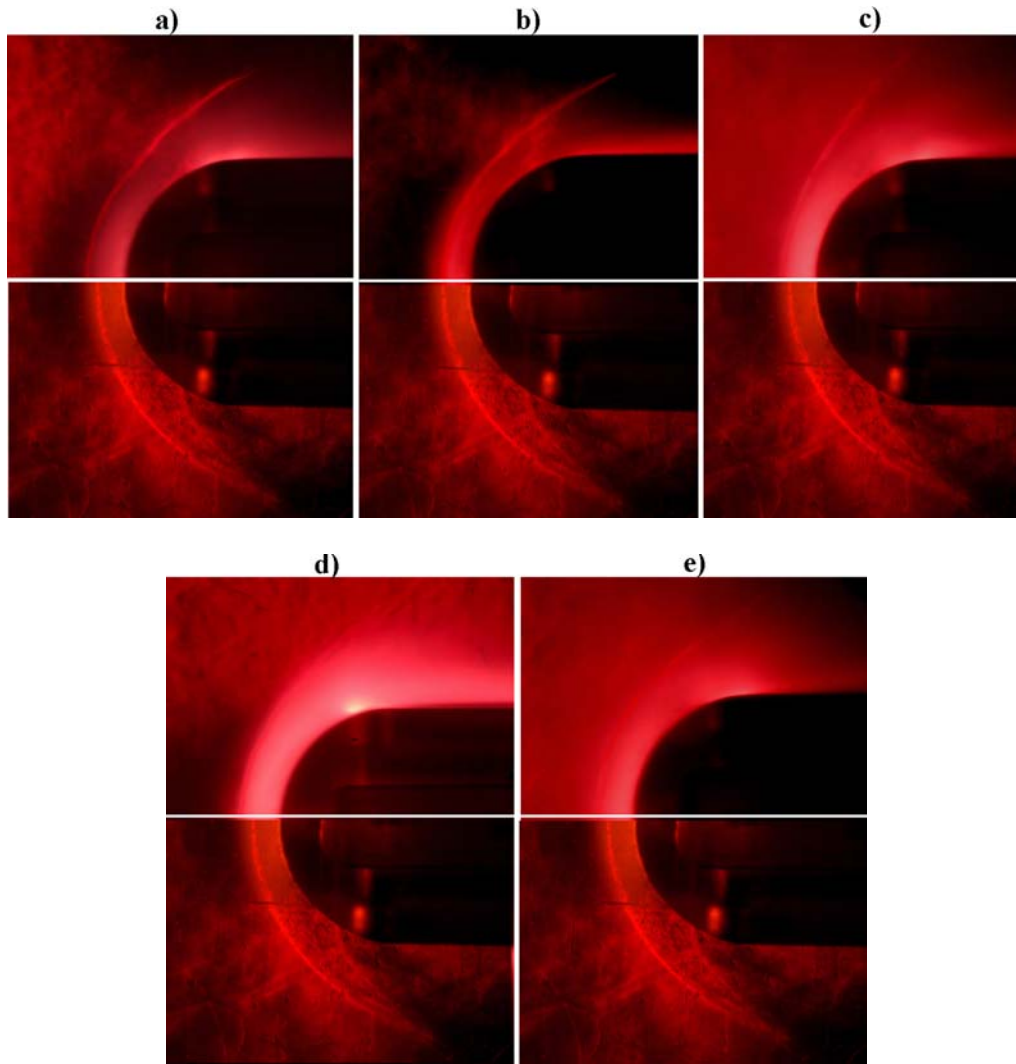


Figure 9. Changing of bow shock wave position at MHD action:

- a) $B=0, j=3.5 \cdot 10^6 \text{ A/m}^2$ (600A);
- b) connection 1, $B=1.4\text{T}, j=3.5 \cdot 10^6 \text{ A/m}^2$ (600A);
- c) connection 2, $B=1.4\text{T}, j=3.5 \cdot 10^6 \text{ A/m}^2$ (600A);
- d) connection 1, $B=1.4\text{T}, j=5.0 \cdot 10^6 \text{ A/m}^2$ (800A);
- e) connection 2, $B=1.4\text{T}, j=5.0 \cdot 10^6 \text{ A/m}^2$ (800A).

flow pictures at the background of gas hitting in discharge. On Figure 9 schlieren pictures of body streamline obtained in experiments at different intensity and direction MHD action are presented. For clearness all pictures in bottom part are combined with schlieren flow picture without any actions. Figures 9 a, b, c are obtained at the same discharge intensity $j=3.5 \cdot 10^6 \text{ A/m}^2$ ($I=600\text{A}$). Streamline picture on Figure 9 a is obtained without magnetic field. There is wave moving from first position away from body. Picture on Figure 9 b is obtained for connection 1 with magnetic field $B=1.4\text{T}$. In this experiment there is shock wave approaching to model, wave approaches to body most strong above and below central model axis. It should note that in this case Lorentz force action directs from model but bow shock wave approaches

to model. Apparently, it takes place due to Lorentz force promotes to remove gas from body behind bow shock wave more quickly, it leads to gas pressure decreasing near body surface and wave approaching to body. Picture obtained with magnetic field $B=1.4 \text{ T}$ at connection 2 is shown on Figure 9 c. There is addition wave moving away from body in compare with wave position in discharge at the same intensity without magnetic field (Figure 9 a)

It takes place due to increasing of pressure behind bow shock wave under action of Lorentz force directed to body in this case; it leads to additional shift of bow shock wave. Pictures on Figures 9 d, e are obtained with MHD interaction at two different connections but at more intensive discharge $j=5.1 \cdot 10^6 \text{ A/m}^2$ ($I=900\text{A}$). In both cases

there is wave moving away from body independent of current flow direction because in more insensitive discharge gas hitting action starts to prevail under MHD interaction, EGD action is stronger than MHD one.

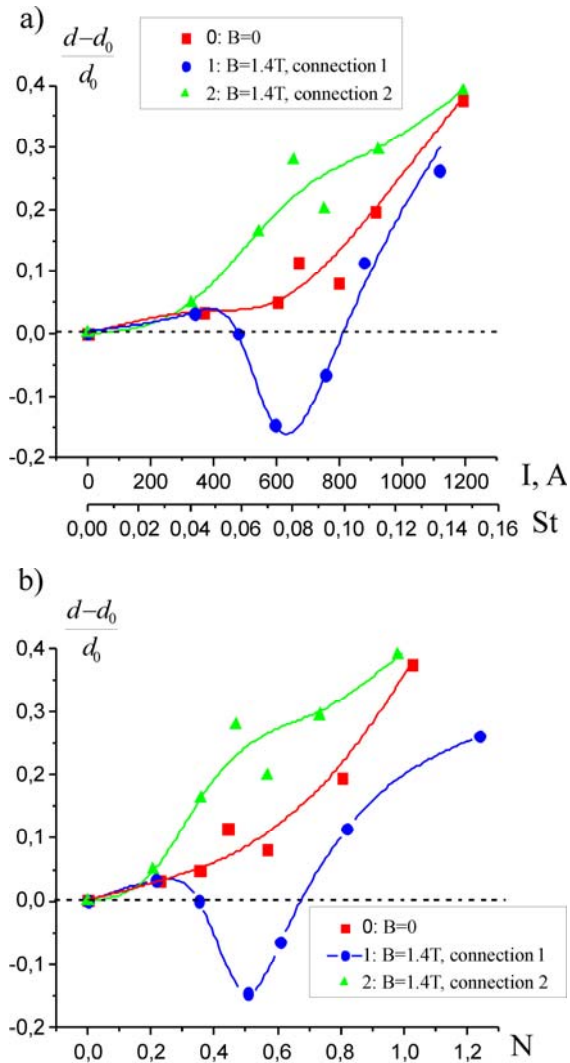


Figure 10. Relative bow shock wave shift at different intensities of EGD and MHD action at near surface discharge in xenon.

On Figure 10 a there are changing curves of bow shock wave shift $d-d_0$ with electrogasdynamic and magnetogidrodynemic action at different intensity and direction in dependence from discharge current value and Stewart parameter. All data is normalized on bow shock wave position without any actions d_0 . Curve 0 (red squares) is obtained at investigation of bow shock wave position with increasing of near surface gas discharge current without magnetic field, only at EGD action. You can see increasing of distance from body to shock wave with current increasing. Curve 1 (blue circles) is obtained with magnetic field 1.4 T at near surface current from bottom to top (connection 1). You can see that at

small current there is shock wave approaching to model, wave shift is negative. Then there is wave moving away from body with current increasing. Curve 2 (green triangles) is MHD interaction at connection 2 (current from top to bottom) when ponderomotive force directs to model. In this case there is increasing of bow shock wave shift from body in compare with EGD action without magnetic field. It is significant that apparent shift of bow shock wave under MHD action is observed at current value about $I=450-800A$ and Stewart parameters $St=0.06-0.1$. The EGD action starts to dominate with subsequent current increasing. At large-scale current value curves 0, 1 and 2 are near resemblance practically.

On Figure 10 b these data is given in dependence from EGD action parameters N . Hear it is necessary to take note of fact that maximum wave shift at MHD action at connection 1 when Lorentz force directs from body (blue curve) is reached at much more greater EGD action parameter then at EGD action without magnetic field or at MHD interaction in connection 2. At connection 1 Lorentz force action on gas removing from body prevents to wave moving away from body as effect of gas hitting and pressure increasing behind bow shock wave.

Individual experiments shown that bow shock wave position in region of visible MHD action doesn't depend from how appointed Stewart parameter is reached by discharge current increasing or magnetic field value one. At equal Stewart parameters bow shock wave positions coincide. EGD and MHD flow control of bow shock wave position at surface discharge near the front model edge is possible by means of changing of parameters N and St . MHD action allows to move the shock wave away from body as well as to bring the wave nearer.

3. Experiments in air flow.

In the work prior experiments of investigation of body streamline particularizes by air supersonic flow at presence of surface discharge near the front model edge were carried out. In these experiments an air was used as working gas instead of xenon. Working regime was chosen from next reasons: the length of ionised gas zone must be more longer then length of MHD interaction zone, particles concentration in working zone is $N=10^{23}-10^{24} m^{-3}$, at expansion in nozzle gas temperature T_h must keep below condensation temperature of air components and probable molecular admixtures, temperature of thermally heated air behind reflected shock wave in the end of shock tube mustn't to exceed temperature at which there is appreciable changing of air molecular composition. Experiments were carried out at next condition in shock tube: shock wave Mach number in shock

tube is $M_2 = 6$, initial pressure and temperature of working gas is $p_I = 34$ Torr, $T_I = 300$ K. In region of model position $X_0 = 20$ cm: $M = 4.3$, $T_h = 395$ K, $u = 1.87 \cdot 10^3$ m/s, $N = 5.34 \cdot 10^{23}$ m⁻³, $\rho = 0.026$ kg/m³. The doubled kinetic energy in volume unit is $\rho u^2 = 9,06 \cdot 10^4$ J/m³.

In present experiments of EGD action on flow picture without magnetic field were carried out. Discharge in near surface region was switched on with similar method by means of voltage supply from long line. Experiments were carried out with minimal long line charge voltage $U_z = 500$ V at which disruptive discharge arises when air flow comes to body. Voltage applied to circuit in this case is about 300 V. Current and conductivity oscillograms in air are shown on Figure 11. It is clear that stationary flow duration in air is 150 mks that is more less then one in xenon. Average plasma conductivity is $\langle \sigma \rangle \approx 6$ S/cm, it is acceptable for realization of EGD and MHD action. Lighting pulse of laser in schlieren system is added on the Graph 11 (bottom curve), picture of flow around model was fixed in 90 mks after streamline start.

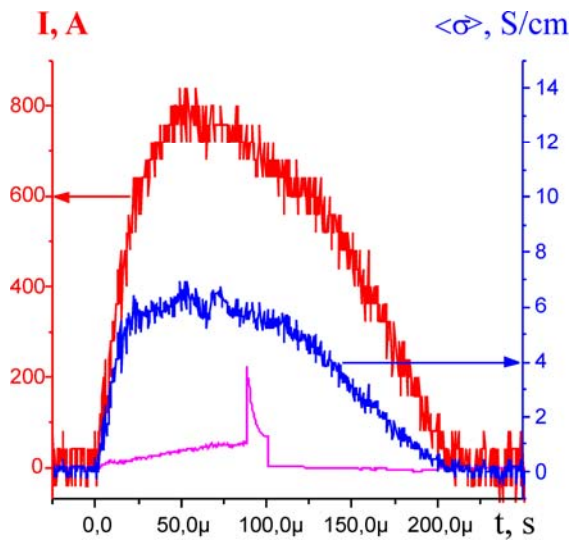


Figure 11. Oscillograms of current (red curve) and integral conductivity (blue curve) of air plasma at near surface gas discharge. Magenta curve is diagnostic laser pulse.

Figure 12 demonstrates the changing of bow shock wave position at surface discharge near the front model edge (top part of photo) in comparison with streamline picture without external actions (bottom part of photo). You can see that bow shock wave moves away from first position, relative

shock wave shift is $\frac{d - d_0}{d} = 0,24$. In this case

EGD action parameter is $N_{air} = 5.4$, it is more higher then at the same shock wave shift in xenon $N_{xe} = 0.86$, but this shift in air is obtained at more

less discharge current $I_{air} = 720$ A then current in xenon $I_{xe} = 970$ A (figure 10).

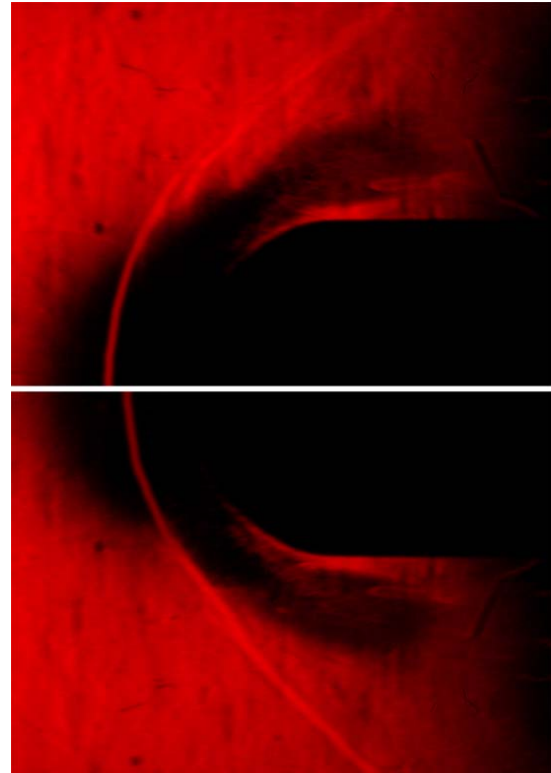


Figure 12. Schlieren pictures of body streamline in air flow: top picture is obtained at near surface discharge $j = 4.1 \cdot 10^6$ A/m², $N = 5.4$ without magnetic field; bottom picture is obtained without external action.

4. Conclusions

In this work an investigations on gas discharge influence of different configuration and intensity on position of bow shock wave arising due to streamlining of semicylindrical body by a supersonic flow were carried out. A possibility to control of bow shock-wave position by plasma, electrogasdynamic and magnetohydrodynamic methods were considered.

It was shown that

1. The bow shock wave shifts at electrogasdynamic method due to discharge in near surface region in the nose part of the body behind shock wave. This method is concerned with heat action of the discharge. An increase of the distance between the shock wave and the body is the result of pressure increase behind shock wave due to strong heat of a gas in the discharge. By changing gas heating degree namely parameter of electrogasdynamic action N it is possible to change the bow shock-wave position.

2. At switching-on of external magnetic field orthogonal to the flow and near surface gas discharge current it is possible to make magnetohydrodynamic control of the bow shock-wave position by Lorentz force effect. At changing of gas discharge current direction to opposite one the Lorentz force direction also changing. In this case Lorentz force removes gas from model or presses gas to model, i.e. increase or decrease pressure behind bow shock wave. By changing direction of Lorentz force and MHD interaction parameter St it is possible to change the bow shock-wave position as to move wave away from body as to approach it to body.
3. Preliminary experiments with air plasma were also carried out. It was shown that it is possible to make EGD action on shock wave configuration at organizing a surface discharge near nose part of the body.

Acknowledgments

This work is supported by the Program #11 of the Presidium of Russian Academy of Sciences and

grant RFBR #08-01-00330a.

References

1. S. V. Bobashev; A. V. Erofeev; T. A. Lapushkina; S. A. Poniaev; R. V. Vasil'eva; D. M. Van Wie. Effect of Magnetohydrodynamics Interaction in Various Parts of Diffuser on Inlet Shocks: Experiment - Journal of Propulsion and Power, 2005, 0748-4658, vol.21, no.5. P.831-837.
2. T. A. Lapushkina, S. V. Bobashev, R. V. Vasil'eva, A. V. Erofeev, S. A. Poniaev, V. A. Sakharov and D. Van Wie. Influence of electric and magnetic fields on the shock wave configuration at the diffuser inlet. - Technical Physics, V.47, N4, 2002, p. 397 – 405.
3. R. V. Vasil'eva, A. V. Erofeev, T. A. Lapushkina, S. A. Poniaev, S. V. Bobashev, D. M. Van Wie. Characteristics of a magnetogasdynamic diffuser under different modes of electric current switching. - Technical Physics, V.50, N9, 2005, p. 1132-1138.
4. Raizer, Yu.P. Gas discharge physics. Springer, 2001, 449 p.

THEORETICAL AND EXPERIMENTAL RESEARCHES OF THE PHENOMENON OF THE CURRENT CRISIS IN THE COAXIAL PLASMA ACCELERATOR WITH THE CONTINUOUS ELECTRODES

A.N. Kozlov

Keldysh Institute of Applied Mathematics, Russian Academy of Sciences,
Miusskaya square, 4, Moscow, 125047, Russia, ankoz@keldysh.ru

Abstract. This paper reports the results of numerical studies of axisymmetric flow in a plasma accelerator with the impenetrable equipotential electrodes. The calculations were performed using a two-dimensional two-fluid magnetohydrodynamic model taking into account the Hall effect and the conductivity tensor of the medium. The lead numerical experiments have allowed to investigate the features of the plasma dynamics in a vicinity of the electrodes and to execute the comparison to the available experimental data.

Introduction

Till now it has not been developed the MHD-model of the plasma flow which would describe in the adequate image the processes near to the electrodes and the phenomenon of the current crisis in the elementary plasma accelerators with continuous impenetrable electrodes [1]. During too time the corresponding experimental researches which have revealed the phenomenon of the current crisis are executed already enough for a long time, and also the theoretical substantiation of the reasons of occurrence of this phenomenon is given. Besides, the various modifications of the quasi-steady plasma accelerators (QSPA) are offered and tested (see, for example, [2-6]), which allow if not completely, at least, partially to solve a problem of interaction of the plasma streams with electrodes.

It is necessary to remind that the elementary plasma accelerators consist of two continuous coaxial electrodes connected to an electric circuit. The gas which is ionizing in an interelectrode interval moves continuously between the electrodes. The electric current flowing along an internal electrode generates an azimuthal magnetic field and the plasma is accelerated along an axis of system under the action of the Ampere force $\frac{1}{c}[\mathbf{j}, \mathbf{H}]$. Last experimental development [6] based on the theoretical analysis [7-10] corresponds the ion current transport regime with the penetrated electrodes at the presence of an additional longitudinal magnetic field. This field allows to reduce essentially the area of an anode stream caused by the plasma inflow through the anode. In this case researches have shown that in a vicinity of electrodes the formation of the boundary layers and the occurrence of any instability are not observed. Generation of the high-speed streams of plasma in QSPA is of interest for the solution of problems of injection in the various thermonuclear installations, of the interactions of plasma with materials, realizations of some technological

applications, and also for the perspective development of the electrojet plasma engines.

In practice the continuous impenetrable electrodes continue to be used in a lot of cases. The theoretical analysis [1] of the plasma dynamics across a magnetic field $H = H_\varphi$ in a vicinities of the equipotential impenetrable electrode ($\mathbf{E} \perp \mathbf{V}$, $V_n = 0$, $E_\tau = 0$) has been spent on the basis of the generalized Ohm's law. As $\mathbf{V}_e \neq \mathbf{V}_i$, the account of the Hall effect and parameter $\omega_e \tau_e$ leads to the occurrence of the longitudinal Hall's component of a current $|j_{||}| \cong \omega_e \tau_e |j_{\perp}|$ and to the pushing of plasma from the anode. In turn the concentration reduction in a vicinity of an electrode increases the parameter $\omega_e \tau_e$ and increases a current along the anode and the pushing of plasma from an electrode even more. As a result under certain conditions there can be a full reorganization of the flow structure. The large-amplitude oscillations occur in the accelerator. In experiments this phenomenon exerts the greatest effect on the volt-ampere characteristics. When the discharge current in the system is higher than a certain critical value J_{cr} , the discharge voltage begins to grow rapidly and the system prevents the passage of currents of the greater value. The experiments have shown that up to critical regimes will be defined by the discharge current $J_p < J_{cr} = K \sqrt{J_{\dot{m}}}$, where K is the empirical constant which magnitude is defined basically by the geometry of electrodes, and $J_{\dot{m}} = e \dot{m} / m_i$ is the flow rate \dot{m} expressed in the current units.

In theoretical and numerical researches the influence of boundary layers on the basic stream is realized through the boundary conditions which should consider the character of the interaction of plasma with the surface of metal or insulator. Earlier the simplified numerical models (see, for example, [11, 12]) which did not include the dependence of coefficients in the equations and boundary conditions

from parameter $\omega_e \tau_e$ were used. The former level of models excluded an opportunity of the comparison with the theory of the phenomenon of the current crisis. Besides in the previous numerical models the dimensionless parameters were used mainly. Such practice did not promote the comparison with the experimental data. In calculations the so-called anode explosions which occurrence was treated on the basis of the theory were observed, but in any way it did not confirm the theory. Differently the numerical models used earlier did not allow to reveal the true nature of processes.

The present researches are directed on the detailed studying of the plasma dynamics in the coaxial accelerator with the continuous electrodes on the basis of the full MHD model according to [13]. The various modifications of two-fluid MHD model answer the statement of the various boundary conditions and have been used earlier for the comparison of the two-dimensional axisymmetric numerical and analytical models [4,14], and also for the analysis of the ion current transport regime in QSPA with the penetrated electrodes at the presence of an additional longitudinal magnetic field [10]. At the given stage it is a question of numerical researches of the processes near to the electrodes and the plasma dynamics in QSPA with continuous electrodes at the presence of the unique azimuthal component of the magnetic field.

1. Formulation of the problem.

In the given work the two-dimensional two-fluid numerical model which allows to study the plasma dynamics in the accelerator with continuous electrodes at the various values of the plasma parameters on an input in the channel is considered. The basis of model is made with the MHD equations taking into account the Hall effect ($\mathbf{V}_e \neq \mathbf{V}_i$), the conductivity tensor of the medium and the dependence of the transport coefficients in the magnetic field from $\omega_e \tau_e$. Following [13] we consider that plasma is quasineutral $n_i = n_e = n$ and ignore the inertia of electrons ($m_e \ll m_i$). In the examined range of the problem parameters the standard estimates of the heat transfer and the characteristic time of the energy exchange between the components show that $T_i \cong T_e = T$. In this paper we will restrict ourselves to the dynamics of a hydrogen plasma ($Z=1$, $m = m_i = m_p$) often used in experiments.

The simple transformations of the initial transport equations using the magnetic field induction equation and the above assumptions yield the following system of equations [15]:

$$\frac{\partial \rho}{\partial t} + \text{div} \rho \mathbf{V} = 0 ; \quad \rho \frac{d \mathbf{V}}{d t} + \nabla P = \frac{1}{c} [\mathbf{j}, \mathbf{H}]$$

$$\rho \frac{d \varepsilon}{d t} + P \text{div} \mathbf{V} = Q - \text{div} \mathbf{q} + \frac{k}{e(\gamma-1)} (\mathbf{j}, \nabla) T + \frac{P_e}{e} \text{div} \frac{\mathbf{j}}{n}$$

$$\frac{1}{c} \frac{\partial \mathbf{H}}{\partial t} = -\text{rot} \mathbf{E} ;$$

$$\mathbf{E} = -\frac{1}{c} [\mathbf{V}_e, \mathbf{H}] - \frac{1}{e n} \nabla P_e + \frac{1}{e n} \mathbf{R}$$

$$\mathbf{j} = \frac{c}{4\pi} \text{rot} \mathbf{H} = e n (\mathbf{V}_i - \mathbf{V}_e) ;$$

$$\frac{d}{d t} = \frac{\partial}{\partial t} + (\mathbf{V}, \nabla)$$

$$P = P_i + P_e = 2 (c_p - c_v) \rho T ; \quad \varepsilon = 2 c_v T$$

Here $\mathbf{V} = \mathbf{V}_i$, P is the total pressure, $\rho = m n$ is the heavy-particle density, \mathbf{j} is the electric current, and \mathbf{q} is the heat flux. The transport coefficients in the magnetic field depend on the parameter $\omega_e \tau_e$, where

$$\omega_e = \frac{e H}{m_e c} \quad \text{is the electron cyclotron rotation frequency,} \quad \tau_e = \frac{3 \sqrt{m_e} (k T)^{3/2}}{4 \sqrt{2} \pi \lambda e^4 Z^2 n} \quad \text{is the time}$$

between electron-ion collisions, and λ is the Coulomb logarithm.

The force of friction between the components of the medium $\mathbf{R} = \mathbf{R}_j + \mathbf{R}_T$ is the sum of the friction force \mathbf{R}_j due to the presence of the relative velocity $\mathbf{u} = \mathbf{V}_e - \mathbf{V}_i = -\mathbf{j}/e n$ and the thermal force \mathbf{R}_T dependent on the temperature gradient. According to [13], we have

$$\mathbf{R}_j = \frac{e n}{\sigma} \left(A_1(x) \mathbf{j}_{//} + A_2(x) \mathbf{j}_{\perp} + \frac{A_3(x)}{H} [\mathbf{H}, \mathbf{j}] \right)$$

$$\mathbf{R}_T = -k n \left(B_1(x) \nabla_{//} T + B_2(x) \nabla_{\perp} T - \frac{B_3(x)}{H} [\mathbf{H}, \nabla T] \right)$$

$$\text{where } \mathbf{j}_{//} = \frac{1}{H^2} (\mathbf{j}, \mathbf{H}) \mathbf{H} \quad \text{and}$$

$$\mathbf{j}_{\perp} = \frac{1}{H^2} [\mathbf{H}, [\mathbf{j}, \mathbf{H}]]$$

are the vector components parallel and perpendicular to the magnetic field; $A_{1,2,3}$ и $B_{1,2,3}$ are known functions of the variable quantity $x = \omega_e \tau_e$; $\sigma = e^2 n_e \tau_e / m_e$ is the electrical conductivity of the medium. The electron heat flux also consists of two

flows: $\mathbf{q}_e = \mathbf{q}_j^e + \mathbf{q}_T^e$. The heat flux \mathbf{q}_T^e due to the temperature gradient can be ignored since $q_T^e \ll q_j^e$. In addition, the ion heat flux is much smaller than the electron heat flux ($q_i \ll q_e$) and hence it can also be ignored. Then

$$\mathbf{q} = \mathbf{q}_e + \mathbf{q}_i \approx \mathbf{q}_j^e = -\frac{kT}{e} (B_2(x) \mathbf{j} + \frac{B_1(x) - B_2(x)}{H} (\mathbf{j}, \mathbf{H}) \mathbf{H} + \frac{B_3(x)}{H} [\mathbf{H}, \mathbf{j}])$$

The total heat release due to collisions is equal to

$$Q = Q_i + Q_e = \frac{1}{en} (\mathbf{R}, \mathbf{j}).$$

The experimental researches (see, for example, [2-6, 16]) and estimates of the parameters in the considered range indicate that using the classical transport coefficients is to a certain extent justified in numerical solutions not only of this problem but also a large number of other plasmadynamic problems (see, for example, [16, 17]).

Parameters of the problem. Equations are transformed and written in dimensionless form. As the normalizing quantities we use the following dimensional constants: the channel length L and the characteristic values of the concentration n_0 ($\rho_0 = m n_0$), temperature T_0 , and azimuthal magnetic-field component at the channel inlet $H_0 = H_\varphi^0 = 2 J_p / c R_0$. Here R_0 is the radius of the outer electrode; J_p is the discharge current in the system. Using this values the pressure is normalized by the quantity $H_0^2 / 4\pi$, the characteristic velocity by $V_0 = H_0 / \sqrt{4\pi \rho_0}$, time by $t_0 = L / V_0$, the electric field intensity by $E_0 = H_0 V_0 / c$, and the current density by the quantity $j_0 = c H_0 / 4\pi L$. The initial dimensional quantities are related to the dimensionless parameters used in the problem as follows: $\xi = \frac{c}{eL} \sqrt{\frac{m}{4\pi n_0}}$ is the local exchange parameter characterizing the role of the Hall effect in the two-fluid regime; $\beta = 8\pi P_0 / H_0^2$ is the ratio of the gas and magnetic pressures at the inlet ($P_0 = k n_0 T_0$); $\nu = \frac{1}{\text{Re}_m} = \frac{c^2}{4\pi L V_0 \sigma}$ is the magnetic viscosity which is inverse proportional to the magnetic Reynolds number corresponding to Spitzer

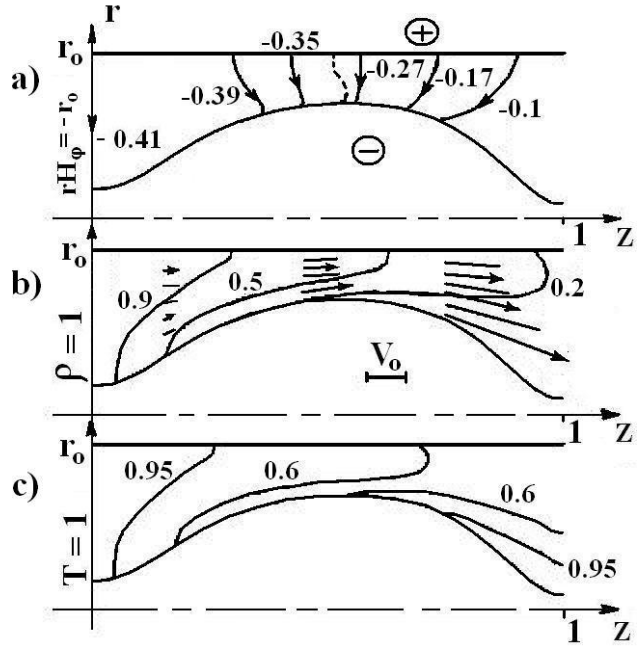


Fig. 1. The example of the transonic plasma flow.

conductivity. Using ξ and ν we obtain the value of the fourth dimensionless parameter participating in the problem $x = \omega_e \tau_e = \frac{\xi H}{\nu \rho}$.

In the plasma flow the dimensionless conductivity depends on the temperature: $\text{Re}_m = \sigma_0 T^{3/2}$; the parameter $\omega_e \tau_e$ can also have the different values at each points of the channel. According to the lead [2-6] and perspective experimental researches we choose as the characteristic units of a problem, for example, the following values: $n_0 = 10^{16} \text{ cm}^{-3}$; $T_0 = 1 \text{ eB}$; $J_p = 500 \text{ kA}$; $L = 1.2 \text{ m}$; $R_0 = 0.5 \text{ m}$. The given values are used for calculation of the base variant. In this case, the values of the dimensionless parameters of the problem are $\beta = 0.1$; $\xi = 0.0019$; $\sigma_0 = 91.1$. If $T = 1$ and $\rho = 1$ we have $\omega_e \tau_e = 0.17$ and $\nu = 0.011$.

In fact the dimensionless parameters, along with the equations and boundary conditions, determine the plasma flow in the channel. Thus it is not necessary to forget that in space of the dimensionless parameters β , ν , ξ , and $\omega_e \tau_e$ only very small area answers the physically admissible values of the initial dimensional parameters n_0 , T_0 , J_p , and L . It should be noted that in modern plasma accelerators we have $\beta \ll 1$. Therefore the temperature background has an insignificant effect on the plasma flow dynamics. Accordingly the radiation

transport is not a necessary element of this study and can be taken into account in the following.

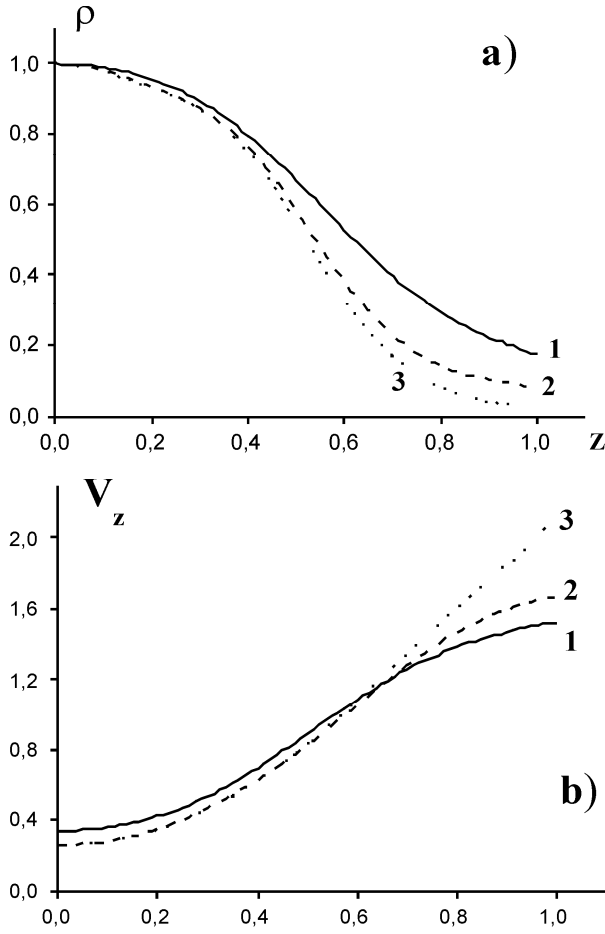


Fig. 2. Distributions of a) density and b) longitudinal component of velocity along the anode for the various values of the characteristic plasma concentration on the input: solid curves 1- $n_0=10^{16} \text{cm}^{-3}$, dashed curves 2 - $n_0=0.22 \cdot 10^{16} \text{cm}^{-3}$, and dashed-and-dotted lines 3 - $n_0=0.18 \cdot 10^{16} \text{cm}^{-3}$

Features of numerical model. At the presence of the unique azimuthal components of a magnetic field and under condition of the axial symmetry of flow ($\frac{\partial}{\partial \varphi} \equiv 0$) it is had as a result the

five equations for the variables ρ , V_z , V_r , H_φ , and T or the entropy S . The electric current in plasma is defined by means of the relations $j_r = -\frac{1}{r} \frac{\partial r H_\varphi}{\partial z}$

$$\text{and } j_z = \frac{1}{r} \frac{\partial r H_\varphi}{\partial r}.$$

For the given electrode profiles the curvilinear computation domain in the variables (r, z) is mapped to a unit square $0 \leq y, z \leq 1$ by means of the relations $r = (1-y)r_k + yr_a$ where

functions $r_k(z)$ and $r_a(z)$ also describe accordingly the profiles of the cathode and the anode. Taking into account of the Jacobean of the map the initial unsteady MHD equations are written in the new variables in divergent form. The numerical solution of the problem is based on the coordinate split. We use the SHASTA-FCT algorithm [18] for the hyperbolic part of the differential equations and the flux sweep method [19] for the parabolic part describing the diffusion of the magnetic field. The numerical solution of the problem is performed until the establishment of flow. Use of this method is also justified by the fact that the characteristic relaxation time is much smaller than the discharge time. Therefore a qualitative analysis of the processes is based on the obtaining of the quasi-steady-state solutions. The quality assurance of the numerical experiments was carried out by means of the test calculations on the various grids.

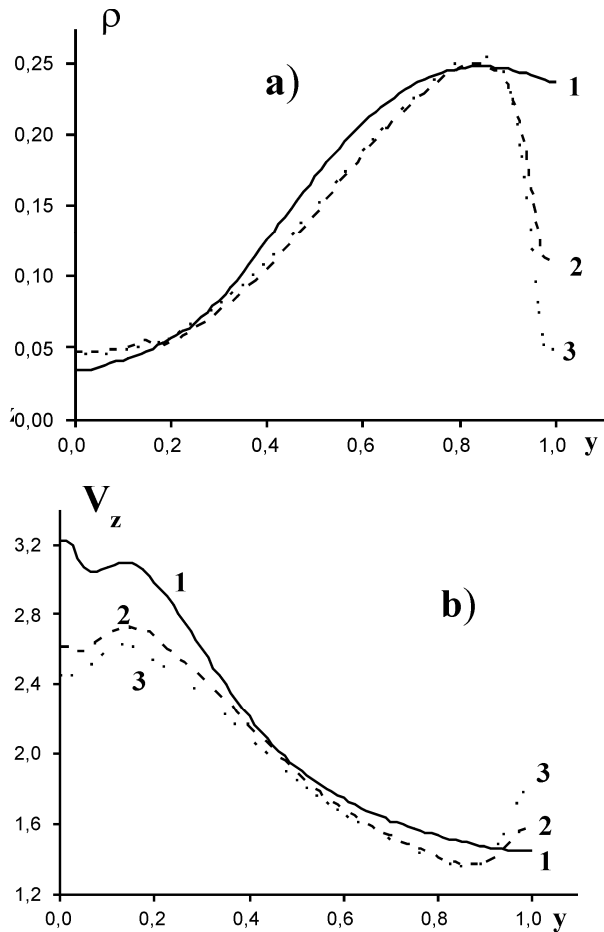


Fig. 3. Distributions of a) density and b) longitudinal component of velocity in the cross-section direction at $z = 0.875$.

Boundary conditions. At the channel inlet $z = 0$ the conditions of the subsonic plasma flow with the known distributions of the density $\rho(r) = f_1(r)$ and temperature $T(r) = f_2(r)$ are imposed. In the

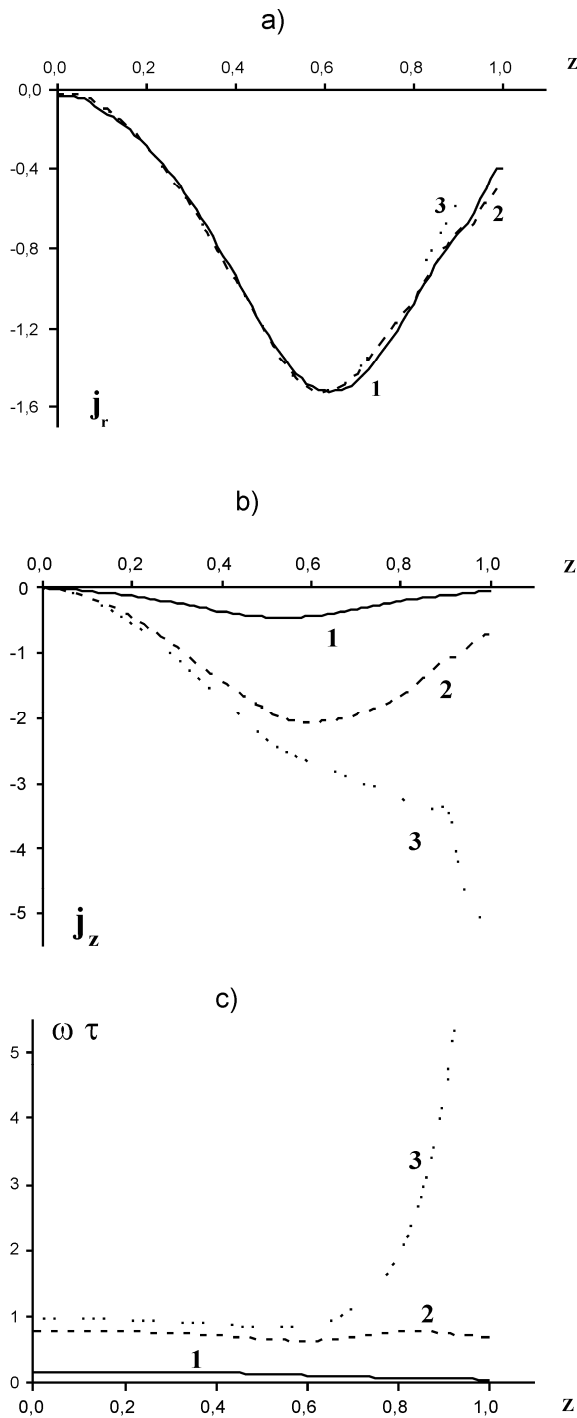


Fig. 4. Distributions of a) radial, b) longitudinal components of current and c) parameter $\omega_e \tau_e$ along the anode for various values n_0 .

given work we shall consider that $\rho=1$ and $T=1$ at the input. Ignoring the additional equation of the electric circuit we can assume that the current has a constant value and enters to the system only through the electrodes, i.e. $j_z = 0$ at $z = 0$ or

$|r H_\varphi| = r_0 = const$ where $r_0 = R_0 / L$. The plasma moves in a certain direction, for example, along the coordinate lines. The channel geometry can be determined using the analytical constructions [9]. The electrode shape corresponding to these constructions (Fig. 1) allows to realize the transonic flow. In the central narrowest part of the channel there is transition through the fast magnetosonic wave velocity or velocity of a signal [1] in the absence of a longitudinal magnetic field. Therefore at the outlet for hypersonic flow the free outflow conditions are specified.

The boundary conditions assumes that the electrodes $r_a(z)$ and $r_k(z)$ are equipotential ($E_\tau = 0$)

2. Results of calculation of plasma flow.

The steady-state transonic plasma flow is presented in fig. 1 for the specified above characteristic parameters of a problem. Figure demonstrates: **a** - the electric current (j_z, j_r) (contour lines of functions $r H_\varphi = const$) and line of transition through velocity of a signal (dashed line); **b** - a projection of velocity of the ion component on a plane (r, z) in the various points of the channel and distribution of the contour lines for density $\rho(z, r)$; **c** - distribution of temperature $T(z, r)$. The polarity of electrodes specified in fig. 1a answers the standard experimental researches. The scale of vectors in fig. 1b is allocated and defined by the characteristic velocity V_0 .

We can see in fig. 1a (dashed curve) that in the middle of the channel the velocity of the stream passes through the velocity of signal $V_s = \sqrt{V_T^2 + H^2 / \rho}$. Here $V_T = \sqrt{\gamma P / \rho}$ is the thermal gasdynamic velocity of a sound. According to fig. 1b the acceleration of plasma depends from value r in a considered case of the uniform inflow of plasma $\rho=1$. At smaller values r the acceleration and velocity is greater.

The change of value of the characteristic plasma concentration n_0 at the inlet leads to the qualitative reorganization of the plasma flow in a vicinity of the external anode. The distributions of a) density ρ and b) longitudinal component of velocity V_z along the anode are presented in fig. 2 at the various values n_0 . Solid curves 1, dashed curves 2 and dashed-and-dotted curves 3 in figs. 2-4 answer to values $n_0 = 10^{16} \text{ cm}^{-3}$,

$n_0 = 0.22 \cdot 10^{16} \text{ cm}^{-3}$, and $n_0 = 0.18 \cdot 10^{16} \text{ cm}^{-3}$ accordingly. The decrease of parameter n_0 conducts to the formation of the obviously expressed layer in the vicinity of anode. It is visible in fig. 2 that for rather small values n_0 the leaving of plasma from the anode under the action of the Hall's component of the current leads to the essential decrease of the density ρ and the significant increase of the longitudinal components of velocity V_z in a vicinity of an electrode at $z > 0.6$, i.e. on a outlet part of the anode. In fig. 3 for the specified above three values n_0 the distributions of a) density ρ and b) longitudinal components of velocity V_z in a cross-section direction are represented at $z = 0.875$. The given figure illustrates the formation the layer in the vicinity of anode adequating to the more high-velocity stream of the rarefied plasma more brightly. In the absence of diffusion for the ideally conductivity plasma it would be possible to speak about the formation of the tangential break in a vicinity of the anode. The surface of such break would represent itself the conic surface. The directing of the conic surface would cross the anode under a sharp corner at values $z \approx 0.5$. It is necessary to notice that also as in the presented work the any correct research of dynamics of the plasma adjoining to a surface of electrodes assumes the account of the finite plasma conductivity and the accurate realization of the boundary conditions on electrodes.

The coordination of the presented two-fluid MHD-model with the theory of the phenomenon of the current crisis is based on the appeared opportunity to investigate the behavior of the plasma currents in a vicinity of electrodes together with the respective alteration of the coefficient $\omega_e \tau_e$ depending on the parameters of a problem. The distributions of a) radial j_r and longitudinal j_z components of a current, and also c) parameter $\omega_e \tau_e$ along the anode for specified above three values n_0 of the characteristic concentration of plasma at the inlet are presented in fig. 4. If the distribution of a radial current practically does not vary that the distribution of a longitudinal current j_z along an electrode essentially depends on values n_0 . The decrease of parameter n_0 leads to the essential growth of value $|j_z|$. The essential growth of a variable $\omega_e \tau_e$ is simultaneously observed. When $n_0 = 0.18 \cdot 10^{16} \text{ cm}^{-3}$ we have $\omega_e \tau_e = 18.9$ on a outlet part of the anode (the curve 3 in fig. 4c corresponds to values $0 < z < 0.9$). All distributions answer the stationary flows calculated by means of the relaxation method. After the relaxation to the steady state flow the further calculation within the limits of any time interval and any quantity of steps on time

gives a root-mean-square deviation of the solutions which are not exceeding 0.3 % for all MHD-variables.

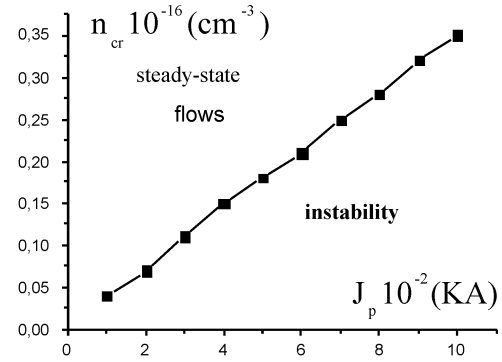


Fig. 5. The critical values of the characteristic plasma concentration at the inlet in the accelerator channel.

Even greater decrease of the characteristic concentration of particles up to value $n_0 = 0.17 \cdot 10^{16} \text{ cm}^{-3}$ conducts to the qualitative reorganization of processes. The flow is not become stationary. On the contrary the fast increase of values $|j_z|$ and $\omega_e \tau_e$ in the vicinity of the outlet part of the anode in the full conformity with the theoretical prediction of development of the phenomenon of the current crisis is observed. Thus the density in the vicinity of the anode has very small values $\rho < 0.01$ and its further decrease made calculation not possible and not correct within the framework of MHD-model. Accordingly for the given magnitude of a discharge current $J_p = 500 \text{ kA}$ the value $n_0 = 0.18 \cdot 10^{16} \text{ cm}^{-3}$ can be considered as the critical value of the characteristic plasma concentration n_{cr} . If $n_0 > n_{cr}$ we have the laminar stationary flows. In case of $n_0 < n_{cr}$ the quickly increasing instability describing the phenomenon of the current crisis is observed.

As a result of a series of calculations for the various values of the discharge current J_p the critical values of the characteristic plasma concentration n_{cr} at the inlet in the accelerator channel presented in fig. 5 have been certain. It has appeared that in a plane of variables (J_p, n_{cr}) the boundary between the laminar and unstable modes is the linear function represented in figure. The important characteristics of flow are the mass flux \dot{m} and the integrated exchange parameter $\xi_\Sigma = \frac{J_p}{J_m}$ where $J_{\dot{m}} = e \dot{m} / m_i$ is the mass flux expressed in current units. The dimensionless mass flux

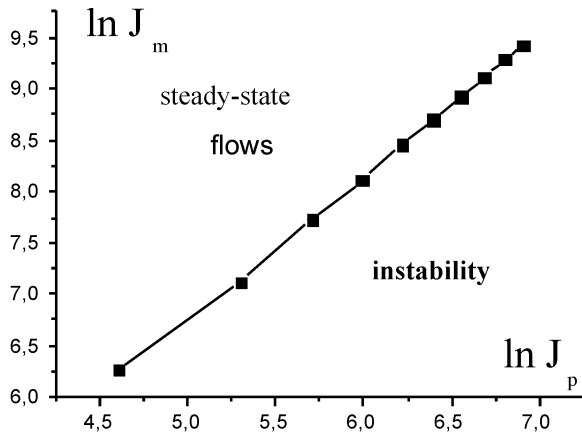


Fig. 6. The boundary between the steady-state and instability modes of flow.

$\hat{m} = 2\pi \int_{r_k}^{r_a} r \rho V_z dr$ can be defined in any cross-section of the channel for the stationary plasma streams considering that the conservation laws are carried out during the calculations with a good degree of accuracy. The chosen units of measure allow to define easily the dimensional magnitude of any value including the mass flux \hat{m} (g/s). For example, the variant of calculation in case $n_0 = 0.18 \cdot 10^{16} \text{ cm}^{-3}$ and $J_p = 500 \text{ kA}$ gives the values $\hat{m} = 49.08 \text{ g/s}$ and $\xi_{\Sigma} = 0.1$.

As it was specified in introduction the experiments lead to the following approximate

relation $\frac{J_{cr}^2}{J_m} \approx K$ in which the critical value of a

discharge current J_{cr} participates and the constant

K depends basically on the geometry of the channel. It is obvious that the given relation can be used for definition of the critical value of the mass flux at the certain value of the discharge current. To each point of the graph represented in fig. 5 there corresponds the magnitude \hat{m} which allows to calculate easily \hat{m} , J_m and $\ln J_m$. In fig. 6 the corresponding graph is presented in the plane of variables $(\ln J_p, \ln J_m)$. As it has appeared this graph defines also the linear dependence equivalent to those that is represented in fig. 5. By means of fig. 6 it is easy to calculate the coefficient α in relations $\ln J_m = \alpha \cdot \ln J_p - \ln K$

or $\frac{J_p^\alpha}{J_m} \approx K$ which define the critical values of the

mass flux at the certain discharge current or on the contrary the critical values of the discharge current at the known mass flux. Calculations lead to value $\alpha \cong 1.44$.

Thus the results of the numerical experiments allow to speak about the comprehensible qualitative conformity with the available approximate experimental data.

Conclusions

The prominent features of the flow dynamics in a vicinity of the anode in the channel of the plasma accelerator with continuous electrodes are revealed. Researches have confirmed the theory of the phenomenon of current crisis. The formation of a layer near to the anode and the occurrence of the processes which proceed to the current crisis are revealed. As a result of a series of calculations the comparison to the experimental data defining the presence of the critical modes has been executed in the terms of the values J_p and \hat{m} .

The work has been executed at the financial support of Russian Foundation of Basic Research (grant 09-01-12056) and Russian Academy of Science (the program No. 14 of the basic researches of Presidium RAS, the project - 301).

References

1. Morozov A.I. Introduction in plasmadynamics. Moscow. Fizmatlit. 2008.
2. Belan V.G., Zolotarev S.P., Levashov V.F., Mainashev V.S., Morozov A.I., Podkovirov V.L. and Skvortsov Iu.V. Experimental study of a quasi-stationary plasma accelerator power supplied by inductive and capacitive energy storage devices. // Sov. J. Plasma Phys. 1990. V. 16, P. 96.
3. Tereshin V.I., Bandura A.N., Byrka O.V., Chebotarev V.V., Garkusha I.E., Landman, I., Makhlij V.A., Neklyudov, I.M., Solyakov D.G., Tsarenko A.V. Application of powerful quasi-steady-state plasma accelerators for simulation of ITER transient heat loads on divertor surfaces. // Plasma Phys. Contr. Fusion. 2007. V. 49. P. A231-A239.
4. Ananin S.I., Astashinskii V.M., Kostyukevich E.A., Man'kovskii A.A. and Min'ko L.Ya. Interferometric studies of the processes occurring in a quasi-steady high current plasma accelerator. // Plasma Physics Reports. 1998. V. 24. P. 936.
5. Dyakonov G.A., Tikhonov V.B. Experimental investigation of the influence of acceleration channel geometry and external magnetic field on modes of plasma flow in coaxial quasi-stationary plasma accelerator (QSPA) P-50A. // Rus. J. Plasma Phys. 1994. V. 20. P. 533.
6. Kozlov A.N., Drukarenko S.P., Klimov N.S., Moskacheva A.A., Podkovyrov V.L. The experimental research of the electric characteristics of discharge in the quasi-steady plasma accelerator with the longitudinal magnetic field. // Problems of Atomic Science and

- Technology. Series: Plasma Physics. 2009. No. 1. P. 92-94.
7. Kozlov A.N. Influence of a longitudinal magnetic field on the Hall Effect in plasma accelerator channel. // *J. Fluid Dynamics*. 2003. V. 38. P. 653-661.
 8. Kozlov A.N. Dynamics of the rotating flows in the plasma accelerator channels with a longitudinal magnetic field. // *J. Plasma Physics Reports*. 2006. V. 32. No. 5. P. 378-387.
 9. Kozlov A.N. Basis of the quasi-steady plasma accelerator theory in the presence of a longitudinal magnetic field. // *J. Plasma Physics*. 2008. V. 74. No. 2. P. 261-286.
 10. Kozlov A.N. Two-fluid magnetohydrodynamic model of the plasma flows in the quasi-steady-state accelerator with a longitudinal magnetic field. // *J. of Applied Mechanics and Technical Physics*. 2009. V. 50. No. 3. P. 396-405.
 11. Encyclopedia of low-temperature plasma. / Edited by V.E. Fortov. Moscow: Yanus-K. 2007. V. IX-2. P. 334-369.
 12. Kozlov A.N. Plasma dynamics peculiarities in the process of the flow stabilization in QSPA. // *Sov. J. Plasma Phys.* 1992. V. 18. 369.
 13. Braginskii S.I. Transport phenomena in plasma. // *Reviews of Plasma Physics* (ed. V.A. Leontovich). New York: Consultants Bureau. 1966. V. 1. P. 253.
 14. Kozlov A.N. Modeling of rotating flows in the plasma accelerator channel with longitudinal magnetic field. // *Problems of Atomic Science and Technology. Series: Plasma Physics* (10). 2005. No 1. P. 104-106.
 15. Kozlov A. N. Numerical model of rotating axisymmetric plasma flows. Comparison with the analytical model. // Preprint No. 48. Keldysh Institute of Applied Mathematics. Moscow. 2004.
 16. Astrelin V. T., Burdakov A. V. and V. V. Postupaev V. V. Inhibition of thermal conduction and generation of ionic-sound waves during plasma heating by an electronic beam. // *Fiz. Plazmy*. 1998. V. 24. No. 5. P. 450-462.
 17. Barmin A. A. and Uspenskii V. S. Study of the nonsteady propagation of an ionizing shock wave in a magnetic field. // *J. of Applied Mechanics and Technical Physics*. 1989. V. 3. P. 356-362.
 18. Oran E.S. and Boris J.P. Numerical simulation of reactive flow. New York: Elsevier. 1987.
 19. Degtyarev L.M. and Favorsky A.P. Flux variant of implicit method for numerical problem with sharp changing coefficient. // *Numerical Mathem. and Mathem. Phys. Journal*. 1969. V. 9. No. 1. P. 211-218.

STUDY OF SHOCK WAVE IMPACT ON GAS INHOMOGENEITY PRODUCED BY PULSE GAS DISCHARGE

V.P. Fokeev, Yu.I. Grin

Institute of Mechanics, Lomonosov Moscow State University,
1 Michurinsky pr., Moscow 119192, Russia,
vfokeev@imec.msu.ru

Shock wave – gas inhomogeneity interaction takes place in many gasdynamic processes. Two types of gas inhomogeneity are researched experimentally and numerically most of all. The very first, it is the extreme case of lengthy gas inhomogeneity thin layer (flow lengthwise direction) realized by heat or light gas layer, when the dimension of interaction region is much larger than gas inhomogeneity transversal dimension [1-6]. It is significant, for this case, that incident shock wave propagates lengthwise the boundary separating two examined gases, and this boundary is thin contact discontinuity region of gas parameters (density). This gives large-scale flow restructurisation and λ -shock configuration formation in more dense gas. However, it is [7] numerically showed that λ -shock configuration is formed at shock wave impact on infinitely thick step (layer) of light gas. This indicates determinant role of shock front orientation with regard to two gases contact boundary position.

The second type of gas inhomogeneity is characterized by the sameness and finiteness of the transversal and longitudinal gas inhomogeneity dimensions, and its ordinarily spherical form [8-16]. That gas inhomogeneity is realized by short pulse of energy input into a small volume (laser spark in experiment [8,10], numerical simulation [9-11,14]) or by spherical volume of spatially homogeneous light gas (in experiment soup film bubble filled with light gas [12,15,16], numerical simulation [13,15,16]). Shock wave – spherical gas inhomogeneity interaction is accompanied by evolution of the angle between shock front and gas inhomogeneity boundary, and, as a result, different

shock configurations are realized as for shock wave refraction at inclined shock impact on a boundary separated two different gases. This interaction is studied now at research of the effects on shock wave configuration [6-11, 14] in connection with plasma aerodynamics problems, and at research of gas inhomogeneity deformation [12, 16] and development of bubble boundary instability in connection with inertial thermo-nuclear fusion problems [15, 16].

The present study associated with the last works [12-16], but given one has following peculiarities: gas inhomogeneity (ellipsoid or sphere) was created by pulse gas discharge and has diffusive boundary and it is not essentially uniform inside his volume. The aim of this paper is continuation of the works [19, 20] where the effect of gas discharge on shock wave Mach reflection was studied as research of shock wave front evolution during impact on gas discharge gas inhomogeneity.

The experiments are carried in a shock tube in air at initial pressure 4000Pa (30Torr) and incident shock Mach number 2.2 – 2.4. The pulse discharge of 0.1-2.5ms duration was initiated before the shock arrival at interaction region in dielectric experimental chamber of 72*72mm cross-section between electrodes (gap – 17mm) located on shock tube axis. The energy input was about several Joules. Visualization of the evolution of quasi-spherical gas inhomogeneity and interaction with incident shock is carried out by shadowgraphie with shadow device TE-19 and digital camera DICAM-Pro.

Some Features are revealed using shock tube

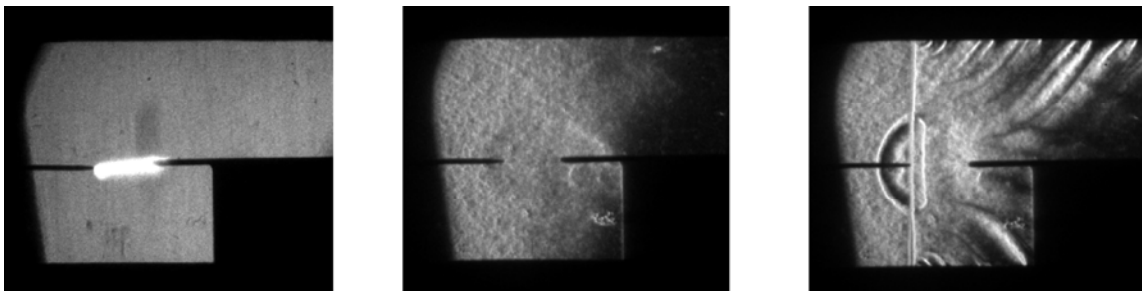


Fig.1.

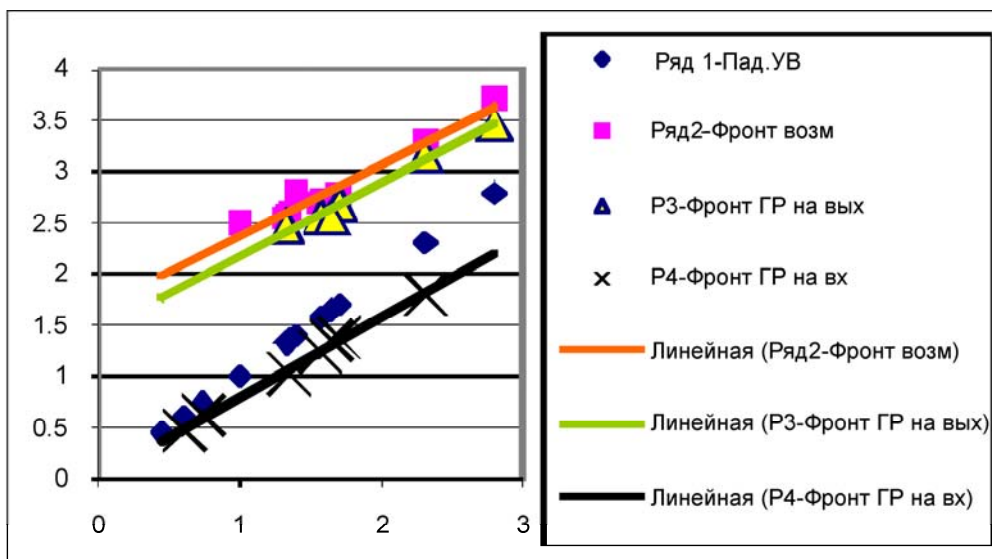


Fig.2.

experiments:

On Fig.1, for gas discharge duration of 1.6ms, the gas discharge region (at the left), produced gas inhomogeneity (in the center), and the picture of the interaction of shock with gas inhomogeneity (on the right) are presented.

On Fig.2 positions of different characteristic points of the flow in function of the incident shock position are presented. Hear diamonds – incident shock; squares – positions of shock passed through gas inhomogeneity; triangles – positions of following gas inhomogeneity boundary; crosses – positions of inhomogeneity boundary at incident shock entry. We can see the different point velocities, and by extrapolation we can find a point of incident and transmitted shocks joining.

Further study of this interaction will be undertaken for additional data on triple-shock configuration parameters.

References

1. Glowacki W.J., Kuhl A.L., Glaz H.M., Ferguson R.E. Shock wave interaction with high sound speed layers. // 15th ISSW, Proceedings, Berkeley, 1985, p.187-194.
2. Mirels H. Interaction of Moving Shock with Thin Stationery Thermal Layer. // 16th Intern. Symp. On Shock Tubes and Waves, Aachen, 1987, p.177-183.
3. Bergelson V.I., Nemchinov I.V. et al. Doklady, 1987, v.296, №6, p.554-557 (in Russian)
4. Bergelson V.I., Nemchinov I.V. et al. Eng. Fiz. J, 1993, т.65, №3, с.302-305. (in Russian)
5. Lashin A.M., Starikovskiy A.Yu. Thermophysics, 1996, т.34, №1, с.98-108 (in Russian).
6. Georgievskiy P.Yu., Levin V.A. Izv. Ran., MZhG, 1993. №4. С. 174-183. (in Russian)
7. Georgievskiy P.Yu., Levin V.A., Sutyurin O.G. MZhG, 2010, №2, 126-134 (in Russian).
8. Tretyakov P.K., Garanin A.F. Matemat. Modelir., Aerodyn and Phys. Gasodyn. Ed. Fomin V.M., ITAM, Novosibirsk, 1995, p.70-78 (in Russian).
9. Yan H., Adelgren R., Elliott G. et al. Laser Energy Deposition in Quiescent Air and Intersecting shocks. //The Fourth Workshop on Magneto-Plasma Aerodynamics for Aerospace Applications. Ed. V.A. Bityurin, Moscow, IVTAN, pp. 68-77, 2002.
10. H. Yan, R. Adelgren, G. Elliott, D. Knight., M. Ivanov, D. Khotyanovskiy, T. Beutner. Control of Mach Reflection — Regular Reflection Transition in Dual Solution Domain by Laser Energy Deposition. // Fifth WSMFA, IVTAN, Moscow April 7-10, p.217-222, 2003
11. Khotyanovskiy D.V., Kudryavtsev A.N., Ivanov M.S. Effects of a single-pulse energy deposition on steady shock wave reflection. // Shock Waves, 2006, v.15, N.5, p. 353-362
12. Haas J.-F., Sturtevant B. Interaction of Weak shock Waves with Cylindrical and Spherical Gas Inhomogeneities // J. Fluid Mech. 1987, vol.181, p.41-76
13. Picone J.M., Boris J.P., Oran E.S. et al. Rotational motion generated by shock propagation through a nonuniform gas. Proceed. Of the 15th Intern. Symp. On Shock

- waves and Shock Tubes, Berkeley, California, 1985, ed.D.Bershader and R.Hanson, Stanford Univ.Press,1986.
14. Babaeva N.Yu., Naidis G.V. Simulation of Shock Wave Proragation in Gas Discharge Plasma Region. // Perspectives of MHD and Plasma Technologies in Aerospace Applications, ed. V.Bityurin, IVTAN, Moscow, p.108-111, 1999.
 15. Anderson M. H. et al. Shock tube investigation of hydrodynamic issues related to inertial confinement fusion. // Shock Waves (2000) 10: 377-387.
 16. Ranjan, D., Niederhaus, J., Oakley, J., Anderson, M., and Bonazza, R., "Experimental investigation of shock-induced distortion of a light spherical gas inhomogeneity," 26th International Symposium on Shock Waves, Paper 2960, Gottingen, Germany, 2007
 17. Henderson L.F., Colella P., Puckett E.G. On the refraction of shock waves at a slow-fast gas interface. J. Fluid Mech., 1991, 224, p.1-27.
 18. Samtaney R., Pullin D.I. Self-similar hypervelocity shock interactions with oblique contact discontinuities. Shock Waves, 1998, 8, p.299-310.
 19. Fokeev V.P., Grin Yu.I., Levin V.A. et al. The influence of Gas Discharge on Propagation of Triple-Shock Mach Configuration – Numerical and Experimental Investigations // The Fifth Workshop on Magneto-and Plasma Aerodynamics for Aerospace Applications. Ed. V.A. Bityurin, Moscow, IVTAN, pp. 234-239, 2003.
 20. Fokeev V.P., Grin Yu.I., Levin V.A. Effect of Pulse Gas Discharge on Shock Wave – Cone Interaction. // 15th International Conference on MHD Energy Conversion and 6th Workshop on Magnetoplasma Aerodynamics, Moscow, Mai 24-27, 2005, Proceedings, Ed. V.A. Bityurin, IVTAN, Moscow, 2005, vol.3, p.796-802.

FEATURES OF CONVERGING SHOCK WAVE BEHAVIOUR INFLUENCED BY MEDIUM THERMODYNAMIC NON-IDEALITY

A.V. Konyukhov, A.P. Likhachev, and V.E. Fortov*

Joint Institute for High Temperatures, Russian Academy of Sciences

Izhorskaya ul. 13 bld. 2 Moscow 125412, Russia

*apl@ihed.ras.ru

Abstract. The nonlinear analysis of the problem of the stability of the converging shock waves in media with arbitrary equation of state is conducted on the basis of numerical modelling. The behaviour of viscous converging shock waves in the ambiguous representation Hugoniot regions as well as in the region of the neutral stability is considered. The solutions for converging and plane shock waves are compared.

Introduction

In our previous works [1-4] we have shown that the linear theory of the plane shock wave stability in media with arbitrary equation of state [5,6] permits to check the Hugoniot for fragments in which the shock wave stability is violated, but it improperly determines the boundaries of these fragments as well as features of the observed shock anomalies. In particular, the Hugoniot fragment meeting to either of two linear criteria of the shock wave instability $L < -1$ or $L > 1 + 2M$ (the notations are the same as in the works cited above) is always overlapped by the region of the ambiguous representation of the shock discontinuity. When the shock wave belongs to the ambiguous representation region conditioned by the instability criterion $L < -1$ fulfilment, the initial shock splits into composite (incomplete or complete) compression wave. If the ambiguity is associated with the condition $L > 1 + 2M$, the shock front acquires unsteady cellular structure. The latter is explained by the switching of the shock parameters between the admissible wave configurations. The switching is induced by the transverse waves which propagate along the shock front from the post-shock side. The spontaneous sound emission from the neutrally stable shock waves (condition $L_0 < L < 1 + 2M$) is not observed. If the emission is forced, acoustic waves downstream the shock front are damped but much slower than that for absolutely stable shock waves.

Clearly, it is not possible to extend automatically the results obtained to converging cylindrical or spherical shock waves – if just for their geometry and intensity growth in the converging process. Meantime, the problem of their stability is the more so actual that converging shock waves are powerful and frequently used tool to achieve extremely high compression [7-9]. The thermodynamic properties of shock compressed matter may be far from ideal; however the problem

of converging shock wave stability for arbitrary thermodynamic properties has yet to be considered. The solution of this problem is additionally complicated by the fact that converging shock may lose their spatial symmetry (peculiar instability kind) taking polygonal (polyhedral) shape periodically varied in time (see, i.e., [10]).

In the given paper the nonlinear analysis of the problem aforementioned is conducted on the basis of numerical modelling. The behaviour of viscous converging shock waves in the ambiguous representation Hugoniot regions as well as in the region of the neutral stability is considered.

1. The numerical model

The problem has been considered in one- and two-dimensional formulations in the viscous heat-conductive model:

$$\left. \begin{aligned} \partial_t \rho + \nabla \cdot (\rho \mathbf{v}) &= 0, \\ \partial_t (\rho \mathbf{v}) + \nabla \cdot (\rho \mathbf{v} \otimes \mathbf{v} + p \delta - \boldsymbol{\tau}) &= 0, \\ \partial_t (\rho E) + \nabla \cdot (\rho \mathbf{v} (E + p/\rho) - \boldsymbol{\tau} \cdot \mathbf{v} + \mathbf{q}) &= 0, \\ E &= e + 0.5 \mathbf{v}^2. \end{aligned} \right\} \quad (1)$$

The model equation of state [4]

$$e(p, V) = (1 - \exp(-p^2) + \varepsilon V p^2)(4 - \exp(-(4 - V)^2)) \quad (2)$$

has been used in calculations: The viscous stress tensor $\boldsymbol{\tau}$ and heat flux density \mathbf{q} have been determined by the expressions:

$$\boldsymbol{\tau} = \frac{1}{Re} (\nabla \otimes \mathbf{v} + (\nabla \otimes \mathbf{v})^T) - \frac{2}{3} \nabla \cdot \mathbf{v}, \quad (3)$$

$$\mathbf{q} = -\frac{1}{Re Pr} \nabla i, \quad (4)$$

were i is enthalpy, The second viscosity is disregarded in Eq. (3); the model character of Eq. (4) is caused by the incomplete form of the model equation of state (2).

The second order TVD scheme with upstream differences based on the algorithm [11] with the extension [12] to an arbitrary equation of state has been used to determine inviscid fluxes through the numerical cell boundaries. The terms of the equations associated with the inclusion of viscosity and heat conduction were approximated in a standard second order symmetric scheme. The introduction of physical diffusion and dissipation makes it possible to a certain extent to suppress the influence of the numerical effects of the motion of the shock wave through the grid cells on the solution, but does not affect choice of the solution in the region of its nonuniqueness [13]. The grid step size and Reynolds number Re have been taken from the condition of the resolution of the shock wave structure (no less than ten grid steps); the Prandtl number Pr has been taken to be 1.

2. Ambiguous representation of converging shock waves (one-dimensional analysis)

The process of the shock wave converging can be considered as “sliding” along Hugoniot from the initial state to the focus with very large pressure. Let converging shock wave pass on its way through the region of ambiguous representation or arise inside this one. The one-dimensional description of the shock wave behavior in the converging process is valid if the solution keeps the cylindrical (spherical) symmetry. This fact may be checked in the following two-dimensional calculations.

The one-dimensional analog of the system of equations (1) has been solved. The equation of state (2) permits to build Hugoniot curve including segments associated with linear criteria of the instabilities of both types and neutral stability obtained for the case of plane shock waves. The

Hugoniot curve used in calculations is shown in Fig. 1a in $p-V$ and $p-u$ coordinates. Intervals AB and EF are the instability regions meeting conditions $L < -1$ and $L > 1 + 2M$, respectively; intervals AC and DG are regions of shock wave ambiguity conditioned by fulfillment of these criteria.

The initial conditions for radial flow with converging shock wave have been assigned in the form:

$$(\rho, \mathbf{v}, p) = \begin{cases} (\rho_0, 0, p_0), & r \leq r_0 - \delta \\ (\rho_1, u_1, p_1), & r > r_0 + \delta \end{cases}, \quad (5)$$

where the parameters with subscripts 0 and 1 correspond to the Hugoniot relations. In the interval $r_0 - \delta < r < r_0 + \delta$ a monotonic smoothing of the discontinuity is specified, which can be considered as a weak structure perturbation of the shock front at the initial instant. The value of δ is taken to be equal to five grid steps. Grid cell number is 10^3 , the average grid step (the grid is condensed to the centre of converging) is correspondingly 10^{-3} . The symmetry condition has been assigned in the focus; the nonreflecting conditions are specified at the external boundary.

The calculations have been shown that converging shock waves passing through or initiated inside the ambiguity region AC (Fig. 1a) (remind this region is associated with fulfillment of the instability condition $L < -1$) split into composite (incomplete or complete) compression wave, i.e. behave like plane shock waves [4]. The example of such splitting for the case of the spherical shock wave is presented in Fig. 1b. The initial shock wave position on the Hugoniot is just above point B. It is seen that the shock wave splits immediately with creation of complete composite compression wave, i.e. two like-directed shock waves divided by isentropic compression wave [4]. This structure is preserved until leading shock approaches the focus. The closed shock is behind the leading one that is

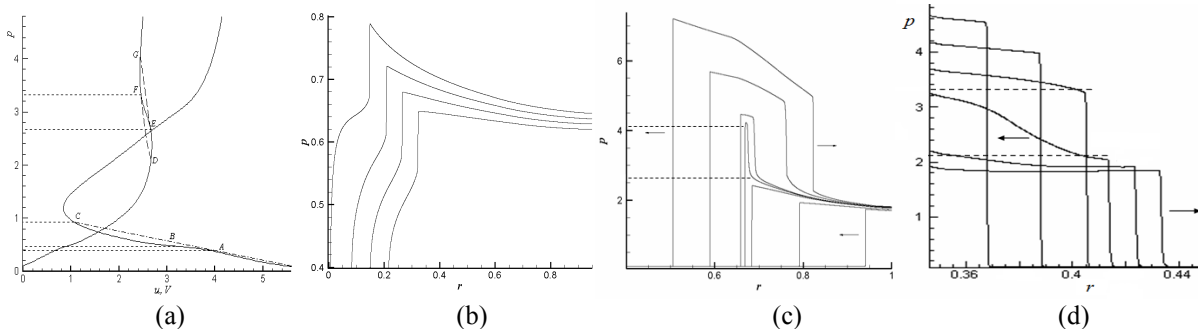


Figure 1

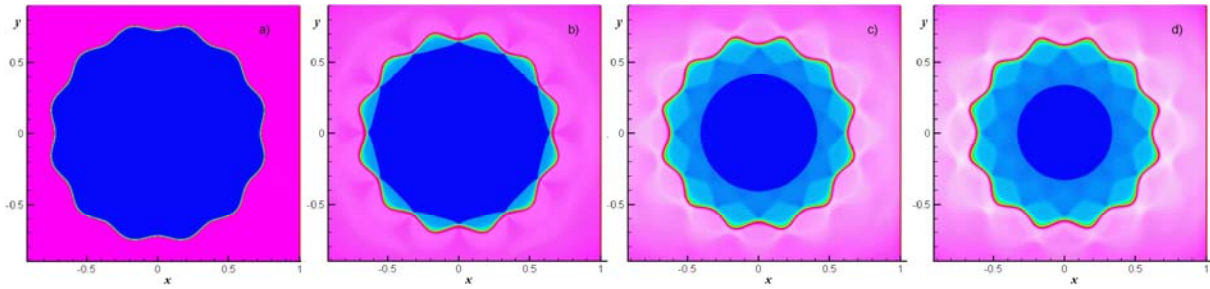


Figure 2

the condition of such wave configuration existence [4]. The pressure drop on the closed shock wave remains practically constant up to the focus neighborhood when reflected and converging elements of the composite compression wave begin to interact of one another. The study of this stage of the process was not conducted because it requires very fine grid. Note the simulation of cylindrical and spherical converging shock wave behavior in this Hugoniot region has given the same results.

The simulation of the converging shock wave passage through the ambiguity region DG (Fig. 1a) (as mentioned above this region is associated with the criterion $L > 1 + 2M$ fulfillment) has demonstrated fundamental distinction from the plane shock wave behavior. If the plane shock belongs to this region, it breaks up always. The choice of resulting wave configuration (oppositely directed two shocks or shock wave and rarefaction wave) is defined by the position inside the interval DG and initial perturbation type (weak compression or rarefaction wave). This fact predetermines the inception of cellular structure of shock wave in multidimensional case [4]. By contrast the converging shock keeps absolutely stable in interval DE and breaks up in interval EG; moreover, only configuration with two oppositely directed shock waves arises.

The example for the case of the spherical converging shock wave is presented in Fig. 1c. The initial shock wave position on the Hugoniot is just below point D. It is seen that inside interval DE the converging shock wave doesn't break up. Note the similar results were obtained for the case of diverging shock waves. As it is shown in Fig. 1d, the diverging shock runs into the ambiguity region DG from the side of larger pressure. In interval FG it keeps absolutely stable; in interval DF the diverging shock breaks up into oppositely directed shock and a rarefaction waves. Other configurations do not arise.

3. Ambiguous representation of converging shock waves (two-dimensional analysis)

The problems considered in previous chapter have been also solved in two-dimensional

approximation. The initial data have been assigned as follows:

$$(\rho, \mathbf{v}, p) = \begin{cases} (\rho_0, 0, p_0), & r \leq r_0 + A \cos(n\varphi) - \delta \\ (\rho_1, u_1, p_1), & r > r_0 + A \cos(n\varphi) + \delta \end{cases} \quad (6)$$

where parameters with index '0' and '1' correspond to the Hugoniot relations, r_0 is the radius of the shock wave in initial state, A is an amplitude of the initial periodic perturbation of the of the shock surface, r and φ are cylindrical coordinates. As in one-dimensional formulation monotonous smoothing of the discontinuity has been performed. The calculations have been carried out in square computational region with 10^6 cells. The grid is strongly condensed to the focus. The boundaries are disposed so far from the initial position of the discontinuity that they do not affect the shock behavior up to its approach to the centre.

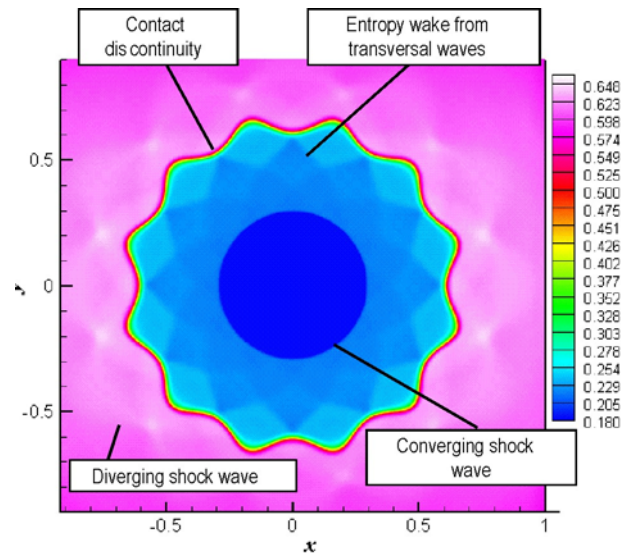


Figure 3

The two-dimensional solution for the cylindrical converging shock wave passing through the interval AC has the one-dimensional structure describing above. This result is predictable because

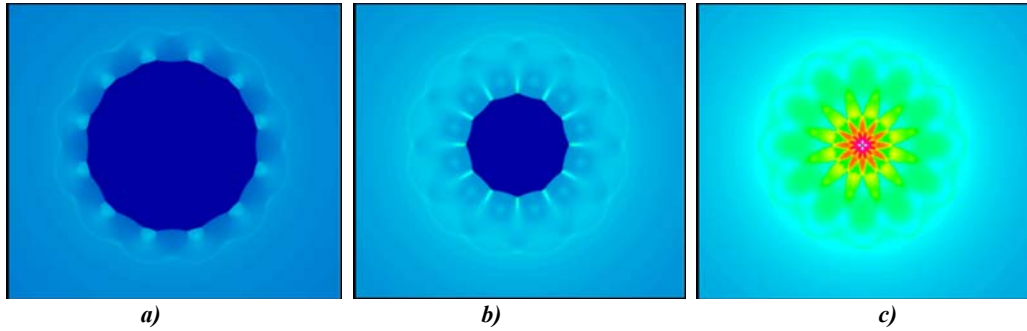


Figure 4

composite compression wave is only admissible wave configuration. The differences might be expected for converging shock waves passing through or arising inside the interval DG because two admissible splitting wave configurations (oppositely directed two shock waves or shock and rarefaction waves) are possible in principle. Nevertheless one- and two-dimensional solutions coincide again in basic features. Fig. 2 demonstrates the density distribution at initial state and three following instants of time. The main elements of the structure arising are shown in Fig. 3.

The initial bend of the shock surface leads to the transversal pressure nonuniformity in the post-shock flow region: behind convex and concave shock wave fragments pressure becomes less and more respectively (here “convexity” means the bend to the centre side). The concave fragments reach in first the point E at the Hugoniot curve and break up into two oppositely directed shock waves. The three-wave configurations arising as result of their interaction move towards to one another. After their merging the break up structure takes the final form: one shock wave of polygonal shape runs to the centre and other shock wave diverges outward. Hereafter the first acquires the cylindrical symmetry and its convergence to the center occurs in a classical manner quantitatively reproducing the Guderley’s solution. The diverging shock wave interacts with incoming waves and keeps periodical structure. Note the attenuation of transverse waves in the region behind converging shock is exceptional phenomenon. It is known from the study of the stability of the converging shock waves in ideal and weakly non-ideal gas [10, 14, 15] that such shocks are unstable from the point of view of the formation of the polygonal structure with the three-wave configurations at the nodal points. This fact is confirmed by our simulation of the converging shock wave behavior. The results obtained are presented in Fig. 4, where pressure distribution at three successive points of time is

shown. This phenomenon is important because may lead to reduction of the cumulation effect. One can assume that the tendency toward the restoration of the spatial symmetry of the perturbed converging shock waves is connected with low medium compressibility; however, this fact requires checking and explanation.

4. Converging shock waves in neutral stability region (two-dimensional analysis)

The two-dimensional problem of the passage of the cylindrical converging shock wave through the neutral stability region (the linear criterion $L_0 < L < 1 + 2M$) has been solved. Unlike previous considerations the wide-range equation of state of magnesium [16] has been applied. The phase diagram built on the basis of this equation of state is shown in Fig. 5; the Hugoniot used in calculations is marked by letter A.

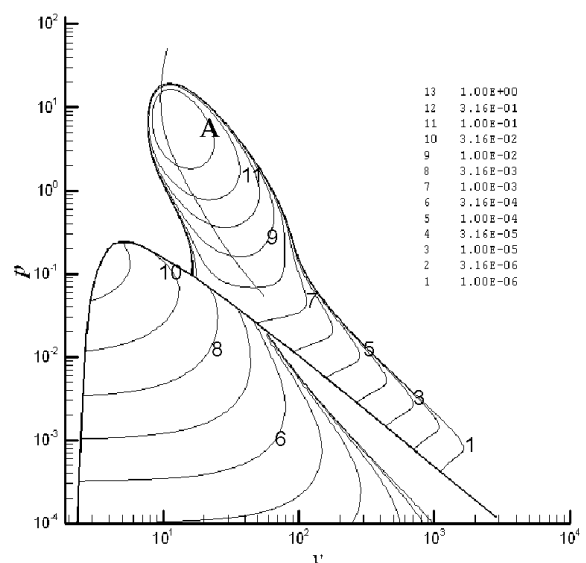


Figure 5

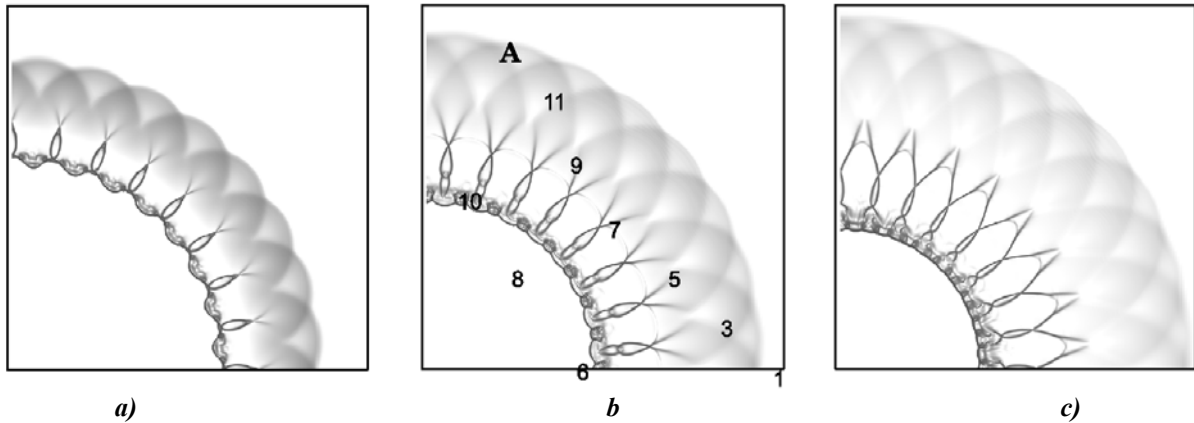


Figure 6

The solution obtained is presented in Fig. 6. The density gradient distribution is shown at three successive points of time. Unlike the case of plane shock wave the perturbations at the front of the converging shock wave do not damp. After exit from the neutral stability region the shock wave becomes stable, and the perturbations attenuate gradually.

Acknowledgments

This work was supported by the Presidium of the RAS (basic research Programs “Investigation of Matter under Extreme Conditions” and “Basic Problems of Interaction Mechanics in Technical and Nature Systems”) and by the Russian Foundation for Basic Research (project No. 08-08-01067-a).

References

1. Konyukhov A. V., Likhachev A. P., Fortov V. E., et al., 2004, Numerical modeling of shock-wave instability in thermodynamically nonideal media. *JETP*, 98, 811-819.
2. A. V. Konyukhov, A. P. Likhachev, V. E. Fortov, et al., 2007, Interaction between a composite compression wave and a vortex in a thermodynamically nonideal medium. *JETP*, 104, 670.
3. A. V. Konyukhov, A. P. Likhachev, V. E. Fortov, et al., 2009, On neutral stability of a shock wave in real media. *JETP Letters*, 90, 18-24.
4. V. Konyukhov, A. P. Likhachev, V. E. Fortov, et al., 2009, Stability and ambiguous representation of shock wave discontinuity in thermodynamically nonideal media. *JETP Letters*, 90, 25-31.
5. D'yakov S. P., 1954, Shock wave stability. *Zh. Eksp. Teor. Fiz.*, 27, 288-295 (in Russian).
6. Kontorovich V. M., 1957, On shock wave stability. *Zh. Eksp. Teor. Fiz.*, 33, 1525-1526 (in Russian).
7. Schwendeman, D. W., Whitham, G. B., 1987, On converging shock waves. *Proc. R. Soc. Lond. A*, 413, 297-311.
8. Wu J.T., Neemeh R.A., Ostrowski P.P., 1981, Experiments on the stability of converging cylindrical shock waves. *AIAA J*, 19, 257-258.
9. Takayama K., Onodera O., Hoshizawa, 1984, Experiments on the stability of converging cylindrical shock waves. *Theor. Appl. Mech.*, 32, 305-329.
10. Whitham, G. B., 1974, *Linear and Non-linear Waves*. NY: Wiley.
11. Roe P. L., 1981, Approximate Riemann solvers, parameter vectors, and difference schemes. *J. Comput. Phys.*, 43, 2, 357.
12. Glaister P., 1988, An approximate linearized Riemann solver for the Euler equations for real gases. *J. Comput. Phys.*, 74, 2, 382.
13. Menikoff R., Plohr B.J., 1989, The Riemann problem for fluid flow of real materials. *Rev. Mod. Phys.*, 61, 75.
14. Eliasson, V., Apazidis, N. & Tillmark, N., 2007, Controlling the form of strong converging shocks by means of Disturbances. *Shock waves*, 17, 29-42.
15. Wu C.C., Roberts P.H., 1996, Structure and stability of a spherical shock wave in a van der Waals gas. *Quarterly Journal of Mechanics and Applied Mathematics*, 49 (4), 501-543.
16. Lomonosov I. V., Fortov V. E., Khishchenko K. V., Levashov P. R., , 2002. *Proc. "Shock Compression of Condensed Matter – 2001"*. New York: AIP, 111.

SHOCK WAVE PROPAGATION IN THE STATIONARY DUSTED PLASMA OF THE GLOW DISCHARGE IN THE DIFFERENT GASES

A.S.Baryshnikov, I.V.Basargin, M.V.Chistyakova

Ioffe Physico-Technical Institute of RAS,

26 Politechnicheskaya, S.Petersburg, 194021, E-mail: al.bar@mail.ioffe.ru

1. Installation.

1.1 Description of the installation.

Experiments were conducted on the electric discharge shock tube of Ioffe Institute. It consists of cylindrical camera (1) with an inside diameter of 300 mm and with a height of 400 mm, supplied with receiver (length of 1000 mm, the diameter of 200 mm) and with electromagnetic shock tube (EMST) (2). Installation was pumped out to $P \approx 0,05$ Tor by pump (12) through gate (11). Gas inlet was achieved through gate (13), and its pressure was controlled by manometers (14). The glow discharge in the camera was created between the conical copper electrodes water-cooled: by anode (5), with the diameter of 30 mm, and by cathode (6), with the diameter of 50 mm. The anode was introduced into the camera by means of the vacuum seal through the flange from organic glass. The distance between the electrodes was equally to 65 mm. The nourishment of camera was achieved from the powerful, adjustable, high-voltage source with the use of ballast resistance. The value of voltage could vary from 1 kV to 10 kV, current - from 0,25 to 2,5 A. The current strength was controlled on the ammeter.

The maximum speed of shock wave - to 1,6 km/s, pressure in the camera 4000 PA. In the experiments the time profiles of the signal from the end of piezoelectric pickup streamlined with the incident shock wave were obtained. They correspond to the distribution of pressure behind the wave.

Experiments were conducted in the transonic regimes of shock wave propagation. Such regimes with difficulty yield to numerical simulation, those more in the plasma, and at the same time precisely these regimes are interesting for the practice. The experimental form of the distribution of pressure after shock wave in the plasma differs significantly from form in the gas without the plasma. "Two-wave" form in the plasma makes it possible to hope for reductions in the expenditures of energy of the motion of gas for an increase in the entropy in the shock wave, as this occurs in the case of the mechanical method of splitting wave, for example on the conical surfaces.

1.2. Modernization of installation.

It is necessary to note that before beginning studies for increasing the accuracy of measurement was accomplished the extensive work

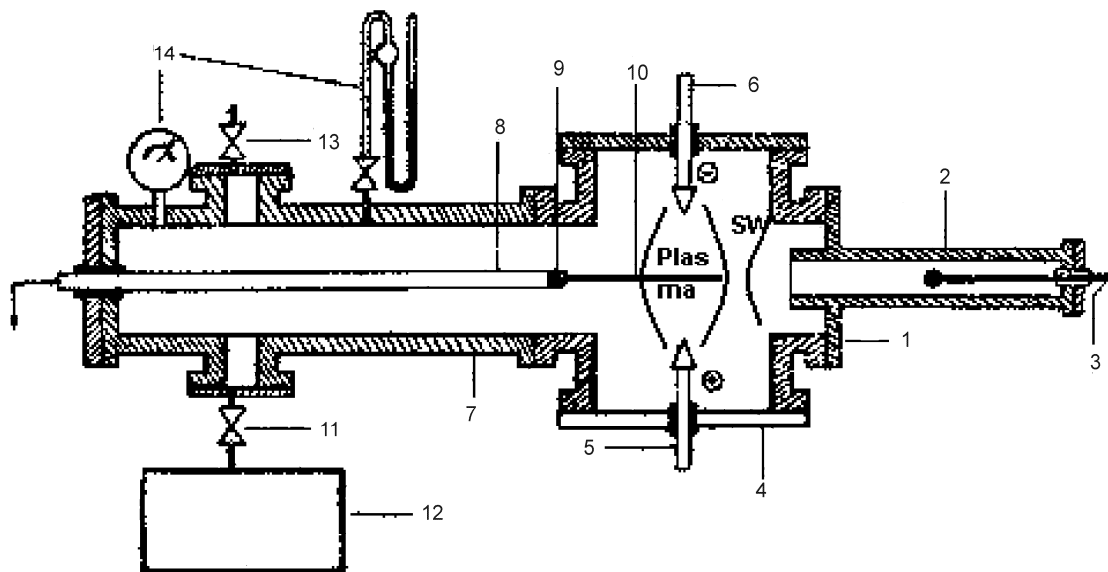


Fig.1. Installation diagram.

1- camera; 2- electromagnetic shock tube, 3- central electrode (EMST); 4- flanges from organic glass, 5- the anode, 6- cathode; 7- receiver; 8 - rod; 9- piezoelectric pickup; 10- quartz rod; 11- gate of evacuation; 12- pump; 13- gate of gas inlet; 14- manometers.

on the modernization of the system of the registration of signal in schlieren system. Usually the use of the Foucault's knife and the photoelectric pickup has small signal-to-noise ratio with the presence of electrical interference. The application of prism instead of the Foucault's knife and the operational amplifier significantly improved use of schlieren of system. Prism divides light ray into two rays. Light modulation with shock wave leads to an increase of the intensity of light in one ray and its decrease in other. Output electrical signals from two photoelectric receivers are united at the entrance of operational amplifier that gives the doubling of the value of useful signal and the considerable weakening of cophasal interferences to 80-100 decibel. The accomplished work considerably improved the accuracy of the measurement of the impact velocity wave.

In addition, a new, modern Board recording system, increasing the number of points of registration on the order. As a result of processing the results do not permit smoothing. This allowed to significantly greater attention averaging values in different experiments, each point of registration. Moreover, accomplished work made this averaging as rational processing because at smoothing there is no sense in averaging. Accomplished work significantly improved measurement accuracy. At present it is 1 to 2%.

2. Dustiness.

In the work the influence of dustiness only on the waveform in the positive column of discharge with different concentrations of dustiness was studied.

Carbonic dust was used as the dust. Dust possesses exceptional dryness and dispersiveness. As show photographs from the electron microscope, specks have sizes, compared with the sizes of nanos-particle. The diameter of specks is 150 nm.

2.1. Small dustiness.

The study of waveform from the piezoelectric pickup was conducted in accordance with the plan of studies in air and in nitrogen with concentration of dust, which varied in the environment of concentration of approximately 20 mg to the cubic meter. In this case the luminous flux of the laser, which controlled the dustiness of working volume, decreased in transit through working volume by 4%.

With the first shot of shock wave the dust rises into the atmosphere, and then, the concentration of dust in practice is supported by constant due to the intensive convective motions of gas, that one can see well on the motion of the

separate large particles of the dust with the observation of the discharge through the window.

Studies showed that for the presented concentrations the signals from piezoelectric pickup differed not more than to 3% from each other, which indicates the very small influence of dustiness in this range of concentrations on the distribution of pressure behind the shock wave in the plasma of air and nitrogen (Fig.2).

Bearing in mind the theoretical works [3,4], and also work [5], in which it was indicated the significant role of the dustiness of the atmosphere to the appearance of the studied effect, and in order to explain nature of the studied effect, besides the studies indicated investigation of influence of the dustiness in the considerably larger concentration (10 times) in the argon plasma were conducted also. Argon was selected in order to exclude chemical reactions with the dust in the plasma. First studies in the argon plasma for the small concentration of dust were carried out at the same concentration, as for air and nitrogen, and then - for the concentration 10 times of greater.

2.2. High dustiness - preliminary results.

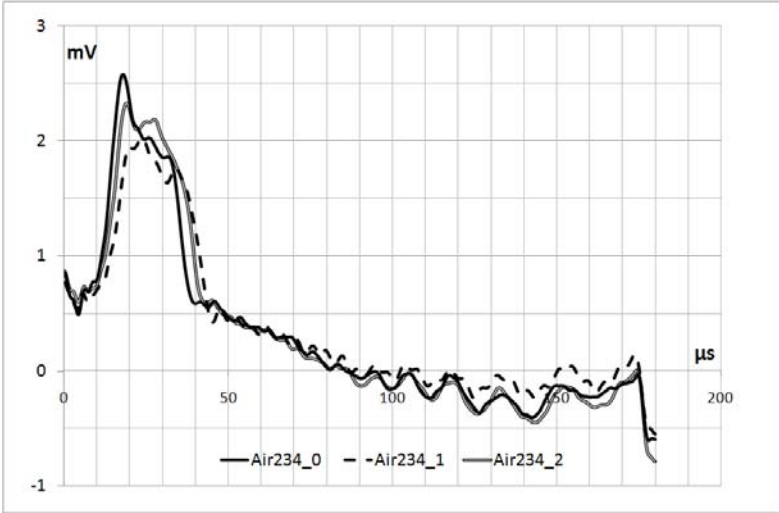
The dustiness of the atmosphere was controlled by the absorption of laser beam in the positive column of discharge. In the experiments for the small concentration it was absorbed by 4% of emission of laser, and for the high concentration - 31%. Thus, in the last experiments the concentration of dust was increased almost 10 times in comparison with the concentration of dust in the first experiments. Measurements, as in the case air and nitrogen, were carried out at a distance by 20 mm after the center of discharge, 20 mm before the center and in the center of discharge.

The comparison of experimental results in the case "small" and "large" dustiness shows that, conditionally speaking "small" dustiness, which in reality composes 4% of absorption of the radiant flux of laser beam, practically does not influence waveform both in air and in nitrogen (Fig.2).

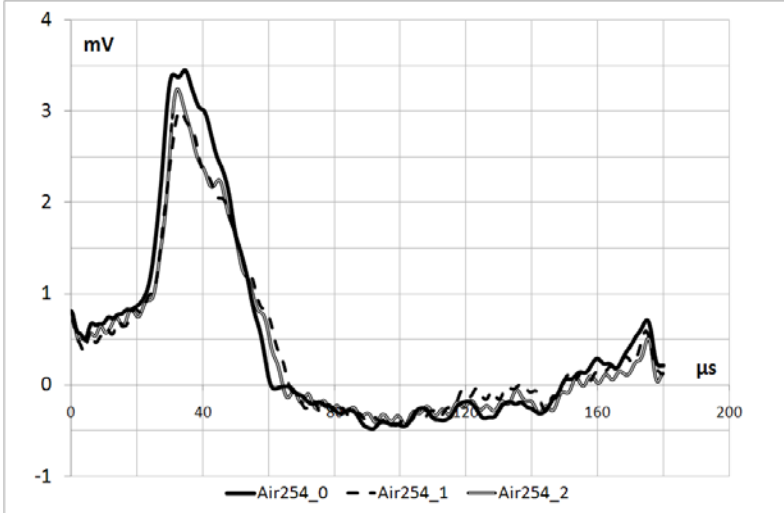
At the same time the dustiness, conditionally named "large" dustiness, and which composes only 31% of absorption of the radiant flux of laser beam, influences waveform from the piezoelectric pickup.

However, this influence strongly depends on the speed at the point, at which were conducted the tests. At a distance 20 mm of the center of the discharge, when the speed of the motion of shock wave in the discharge is maximum, influence, both in the amplitude of second wave and on the distance from the forerunner to the second wave, exceeds the frame of 10%. Thus, this influence can be considered significant. It is here necessary to note that with "small" dustiness of 20 mg/m³ its influence on the waveform in argon is considerably

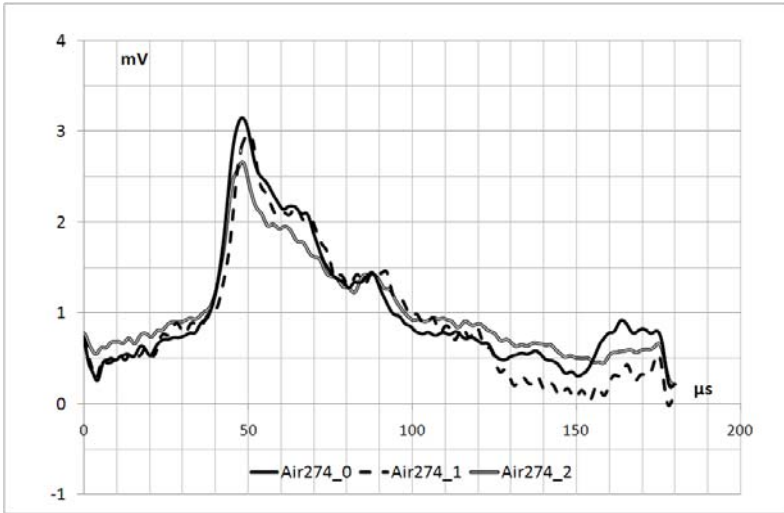
below at all three points exactly as for air and for nitrogen (see Fig.2).



a)



b)



c)

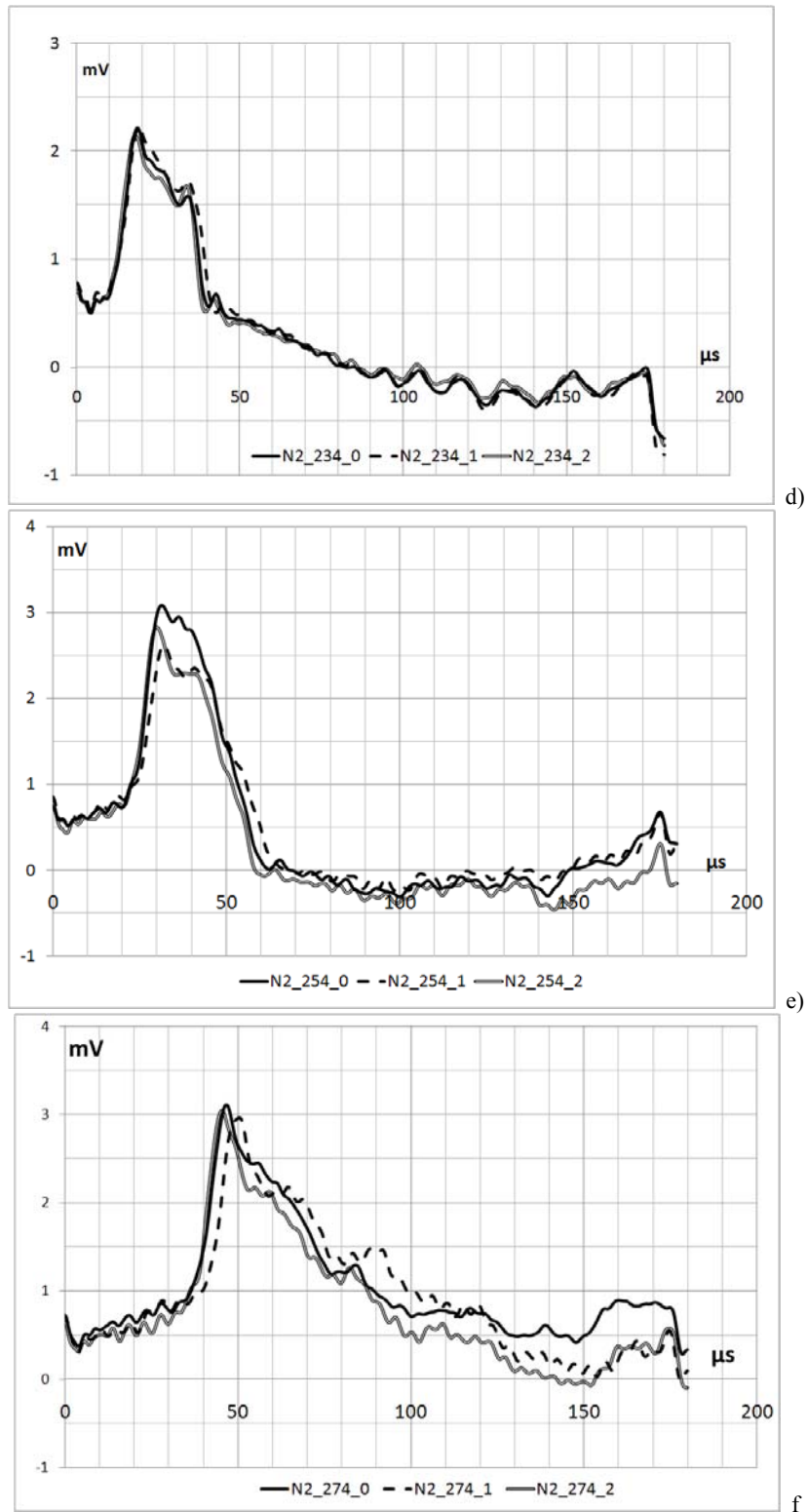


Fig.2. a) - f). Weak influence of dustiness on the form of the distribution of pressure behind the shock wave in the plasma of the glow discharge for the small concentration of dust (20mg in m^3) for air (Air) and nitrogen (N_2). 2- maximum dustiness (20mg in m^3), 1- dustiness is two times lower, 0 - without the dust. 234 - point 20 mm prior to center, 254 - center of discharge, 274 - 20 mm after center. The initial velocity of shock wave at the output from the electric discharge shock tube of 1,6 km/s.

In the Center and at a distance of 20 mm behind the center impact of dust at large concentrations (200 mg/m^3) in the form of signal is much smaller and is approximately 3%. Due to the symmetry of the discharge, the dustiness is also symmetrical and cause of separating, apparently, is the speed of shock wave. As experiments show, shock wave speed when passing discharge is reduced. At 20 mm from the Centre of speed is approximately 1.5 km/s, in the Center-1.3 km/s, and at a distance of 20 mm for Centre-1.1 km/s. Thus, when the speed is reduced of 30% dustiness influence decreases in 3 times (in the center of the discharge the dustiness can be significantly reduced). There is a strong dependence of dustiness effect on shock wave speed.

2.3. High dustiness - refined results

The next step consisted in conducting experiments in the upgraded installation with increased measurement precision by increasing the registration point to order, and at the expense of averaging at each point registration number experiments. In this study there was an averaging of 10 experiments. The measurement results are presented in Fig. 4-6. Experiments carried out under the same conditions. Dustiness was high (200 mg/m^3), because at such mass concentration of dust effect of dust was observed in the pressure distribution behind shock wave in preliminary experiments.

Experiments were also conducted in the upgraded installation and in dusty air, nitrogen and argon without the ignition of glow discharge. Influence of made virtually no. For example, distribution of pressure in the air in the middle of discharge is presented (Fig. 4).

Начальная скорость ударной волны на выходе из электромагнитной ударной трубы составляла 1,6 км/с. Мелкодисперсная углеродная пыль, которая использовалась для запыления плазмы, обладает низкой энергией сродства с электроном. Возможно, это является причиной, по которой не наблюдается электризация пыли. Наблюдается равномерное распределение пыли по пространству в свободных конвекционных потоках.

Initial shock wave speed on the output from electromagnetic shock tube was 1.6 km/s. The fine carbon dust which was used for dusty plasma has low energy electron affinity with electron. Perhaps this is the reason why there was no electrization of dust. There is a uniform distribution of dust for space in free convection flows.

Main results in plasma in glow discharge are two facts unexplained now. The first fact; the impact of dust on the pressure distribution behind shock wave in the air is minimal (Fig. 5) and is limited to only a small effect on the pressure

distribution only at high speeds shock wave. Amplitude secondary wave in the air a bit increases (Fig. 5). The upper part of the secondary waves in air also changes its form (Fig. 5).

The second fact: under the same initial conditions in argon plasma influence is pronounced. Dustiness of argon plasma leads, unlike air plasma, to significantly increase of amplitudes of secondary wave (Fig. 6).

2. Conclusion.

The influence of carbon dust on the pressure distribution behind shock wave in atmosphere of air and argon in plasma of glow discharge and without plasma is investigated. Increasing the natural dustiness in 10 times, as in the air and argon, influence of dustiness on pressure distribution behind shock wave in the atmosphere without plasma practically is not observed. Influence of dustiness evident in argon plasma of glow discharge (in the case of increasing of natural level of dust in 10 times).

The influence of dustiness in plasma of glow discharge in air is not essential. The same behavior is observed in nitrogen. In argon plasma dustiness leads to a substantial increase of amplitude of secondary wave. Preliminary experiments have shown that the impact of dustiness strongly depends on the speed of shock wave. For stronger shocks influence of dustiness is greater. More precise studies have shown that such behavior is more common for plasma air than for argon plasma. The difference in influence of dust in argon and in the air can be associated with that in plasma of molecular gases there is excitation of vibration levels of state, which at collisions with fine carbon dust may be occurred in equilibrium with the kinetic energy of dust particle.

References

1. Klimov A.I., Bityurin V., Kharitonov A., et al., Shock Wave Propagation through Non-Equilibrium Cluster Plasma, AIAA Paper 2002-7978, 40th AIAA Aerospace Science Meeting & Exhibit, Reno NV, P.8 Anatoly Klimov.
2. Akishev YU.S., Deryugin A.A., Karalnik V.B., Kochetov I.V., Napartovich A.P., Trushkin N.I. Experimental study and the numerical simulation of the glow discharge of the direct current of atmospheric pressure. Physics of plasma. 1994. V.20. №6. P.571-584. [in Russian]
3. Velikodnyy V.YU., Bityurin V.A. Propagation and the structure of shock wave front in the ion plasma with the presence of the negatively charged nanos-particle (clusters, specks). Applied physics, 2002, №5, P.90-98. [in Russian]

4. Popel S.I., Golub A.P., Loseva T.V., Binkhem R., Benkadda S. Formation of shock-wave structures in the dust plasma. *Physics of plasma*. 2001. V.27. №.6. P.483-490. [in Russian]
5. Zobnin A.V., Usachev A.D., Petrov O. F, Fortov V.E. Dust-acoustic instability in the plasma of induction gas discharge. *Journal of Experimental and Theoretical Physics*, 2002, V. 122, N. 3 (9), P. 500-512. [in Russian]
6. Baryshnikov A.S., Basargin I.V., Chistyakova M.V. Influence of moistening the atmosphere and its dustiness on the effect of the destruction of shock wave in the plasma of the glow discharge. *Letters into the Journal of Technical Physics*, 2008, V.33, N.10, P.54-57. [in Russian]
7. Baryshnikov A.S., Basargin I.V., Chistyakova M.V. Experimental and theoretical study of splitting effect of shock wave in glow discharge in dry, dusted and humid air and nitrogen. The 7th Workshop on Magneto-Plasma-Aerodynamics in Aerospace Applications, Moscow, 17-19 April, 2007, IVTAN, P. 174-178

SPEED LIMITS AT PROPAGATION OF SHOCK WAVE IN MULTICOMPONENT DISPERSIVE MEDIUM

Yu.L. Serov

Ioffe Institute RAS, 26 Polytechnicheskaya,
194021 St.-Petersburg, Russia, E-mail: yuserov@mail.ioffe.ru

Introduction

Physical processes related to the propagation of high-speed shock waves in a dispersive medium (gas-plasma mixture) need further investigation. Gas-dynamic processes in rarefied dispersive media are determined by their specific nonlinear properties [1]. Usually it is supposed, that the physical effects accompanying the propagation of a shock wave in a weakly ionized plasma are the same with effects in a heated gas. However, it is true only for range of small speeds of a shock wave. Many researchers observed significant differences in the propagation of shock waves in plasma and hot gas [1,2]. The nature of these anomalies has been unclear for a long time. It has appeared, the problem of unusual interaction of shock waves with plasma should be considered with laws of electrodynamics and nonlinear ionic acoustics. The new mechanism of interaction of plasma component has been found out at propagation of a shock wave in weakly ionized medium [3, 4]. It has allowed to develop a nonlinear ionic-sound model of interaction of shock waves with dense weakly ionized medium [5-7] which describes many observable abnormal resonant effects with high accuracy [8]. It is obvious, that similar electrodynamic nonlinear plasma effects can be observed at propagation of shock waves in plasmas of a various kind. From this point of view, shock waves in reacting gases are very interesting. In such gases, the gas-plasma medium with various ions and groups of nonequilibrium electrons is formed in the front of the shock wave. This situation arises for example at a detonation. Thus, in a nonlinear resonant plasma dynamics point of view, detonation waves can be considered as a special case of shock waves in a gas-plasma medium. In fact, there is a significant similarity of a gas detonation with ionizational instability of shock waves even in detailed attributes. Both ion-acoustic shock waves in plasma and detonation waves arise in the certain resonant ranges of speeds. In particular, the influence of plasma resonant ion-

acoustic effects on a gas detonation is presented in ref. [9,10]. It is shown, that the maximal speed of a detonation in a gas mixture coincides with the maximal phase speed of a soliton bunch in products of reaction.

Up to this moment, the real physical mechanisms of detonation are poorly investigated and the detonation theory is far from being complete. Currently, the detonation is considered to be a thermal effect, where a shock wave and chemical reaction support intensity of shock interaction. Existing theory relates detonation limits with energy losses in the propagation of the shock wave [11] or with kinks at the front of the detonation wave which result in gas ignition [12]. Considering the chemical reaction as an energy source for detonation and using the thermodynamic approach we can investigate the basic laws of the detonation process. However, the more detailed understanding of physical mechanisms in detonation is important. In this paper we present the further investigation on nonlinear ion-acoustic interaction and its effect on propagation of a detonation wave.

The nonlinear ion-acoustic mechanism of interaction of plasma components

The important role of nonlinear ion-acoustic interaction in plasma shock waves has been detected in ballistic experiments [4, 5]. Detailed experimental study of physical processes in dense plasma near the hypersonic body revealed the existence of ion-acoustic soliton bunch in the front of a shock wave, which is caused by non-linear interaction of plasma components.

We can observe two additional peaks of radiation on the forward front of the shock wave, which are related with soliton bunch formed in photo-ionizational plasma in Fig.1. The analysis of ballistic experiments has shown, that there is a correlation between existence of an abnormal flow and soliton bunch. It was revealed, that the high-speed border of existence of an abnormal flow of supersonic bodies in dense collisional plasma

coincides with the maximal phase speed of a soliton bunch formed in plasma [4, 5, 8]. There is an ionizational instability, which destroys a front of shock wave at the speed, related to the maximal phase speed of a soliton bunch.

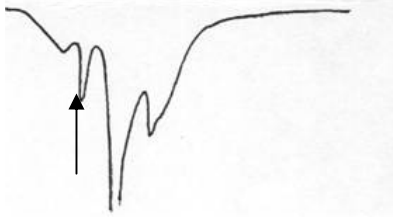


Fig.1. Ballistic apparatus; signal of radiation from multiplier, sphere, xenon, $C = 2260$ m/s, soliton package on a front of a bow shock (it is marked by an arrow), $M_i = 1,3$.

Theoretical model. The physical model of observable anomalies in dense collisional plasma is considered in ref. [5-7]. The solution of the dynamic equations of three-component plasma accounted for nonlinearity and dispersion has shown that, indeed, the soliton bunch is formed in the field of plasma shock wave and the “Houston’s horse” effect is realized. This model is in a good agreement with the results of high-speed ballistic experiments and other experiments on instability of plasma shock waves. According to our model, the equations of a shock wave in dense three-component plasma can be reduced to the nonlinear equation for potential. In the extreme case, if we neglect collisions between ions and neutral particles and utilize the nonlinearity of the equation for the electric field, it leads to the well-known Sagdeev equation:

$$2D\psi'' = -\frac{d\phi(\psi)}{d\psi} \quad (1)$$

$$\phi(\psi) \equiv 1 - \exp\psi + M_i^2 [1 - (1 - 2M_i^{-2}\psi)^{1/2}],$$

$$\psi \leq \psi_*; \quad \psi_* \equiv 0,5M_i^2,$$

where D is the Debye radius, M_i is the ionic Mach-number. The Debye radius characterizes dispersive properties of plasma. This equation has the soliton solution in the range of ionic Mach-numbers $1 < M_i \leq 1,6$, ($M_i = V/V_{is}$, where V is speed of a shock wave, $V_{is} = \sqrt{T_e/m_i}$ is speed of an ionic sound). Equation, which serves as a better approximation and includes an elastic ion-neutral collisions, electronic heat conductivity, ionic viscosity, nonlinearity and dispersion is derived and analyzed in [7]:

$$-V'''' - 2D^2V_{is}^2(1 - Vc^{-1}) + V''\eta c\rho_0^{-1} \\ (1 - Vc^{-1})^2 + V[(c - V)^2 - V_{is}^2] - V_0V(c - V)(V - V_n) \approx 0 \\ V_0 \equiv V_{in}[1 - V_n(\zeta)V^{-1}] + \alpha^{-1}V_{is}^2kn_0 \quad (2)$$

In the given problem stationary perturbation in weakly ionized not isothermal plasma was investigated. The fields depend on $\zeta = x - ct$, where x, t , coordinates and time, c is speed of moving of a shock wave, n is concentration, indexes i, e, n correspond to ions, electrons and to neutral particles, α is a factor of electronic heat conductivity, η is factor of dynamic viscosity. In the equation (2) members nonlinear on Vc^{-1} , an elastic ion-neutral impacts, electronic heat conductivity, ionic viscosity and a dispersion are considered. If we take into account the collisions, the equation has a solution similar to those of Sagdeev equation. In fact, even strong dissipation does not destroy sharp resonant effect. Analytical estimations and numerical analysis [7] have shown that specific ion-acoustic shock wave is formed in a shock wave precursor. The analysis of the equation (2) has confirmed the existence of soliton bunch in dense collisional plasma in the field of a shock wave when shock wave speed is in resonant range $1 < M_i \leq \sqrt{3}$, which is similar to data of ballistic experiments. Ion-acoustic soliton bunch, arising at $M_i > 1$, leads to development of instability of a shock wave. With increase of ionic Mach number both the amplitude of a bunch grows and the factor of ionization in bunch increases. The analysis [7] has shown that at critical value of ionic Mach-number $M_i \approx \sqrt{3}$ there is an explosive instability. The finite increment in speed of neutral component shock wave leads to infinite increase of soliton bunch amplitude of ionic component. When ionic Mach-number approaches its critical value, the ionization factor comes to $\alpha \approx 1$. The strongest interaction between charged and neutral components takes place in this area of highly-ionized bunch. It is the moment of the greatest instability, which is followed by the collapse of the soliton bunch and destruction of the shock wave (see Fig. 2, 3).

Nonlinear interaction in the oxygen-hydrogen mixture

Let us start with simple problem of propagation of shock waves in a combustible gas mixture with a minimum quantity of components. The solution of this task facilitates the understanding of the problem of propagation of shock waves in more complex gas-plasma systems. The most simple object is the mixture of hydrogen and oxygen. It is necessary to investigate the kinetic scheme of formation of ion-acoustic soliton bunch

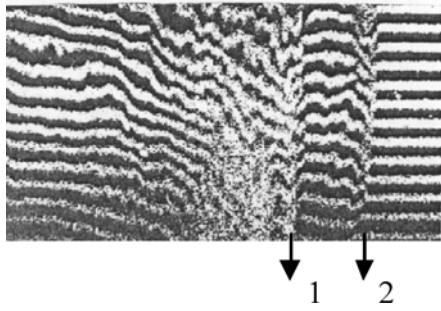


Fig. 2. Interferogram of a shock wave in xenon [14]; $M = 25$, $M_i = 1,5$; 1 - front of a gas-dynamic shock wave, 2 - front of an ion-acoustic shock wave in precursor.

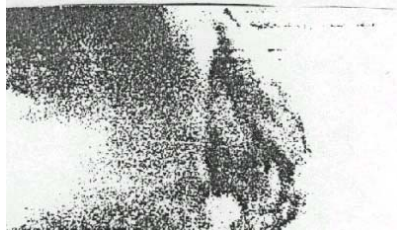


Fig. 3. Interferogram of a shock wave in xenon [14]; collapse of a shock: destruction of the wave front and transition to multyflow movement at $M=27,1$; $M_i = 1,6$.

in the oxygen-hydrogen plasma near the shock front by means of multifluid model. The solution of the whole problem appears at first sight rather complicated due to consideration of all the resonance and metastable levels, which can participate in the formation of the electron energy distribution due to collisions of the second kind. However, the task becomes much simpler if you consistently take into account only the most populated metastable energy terms of the molecules. Such terms are the lowest metastable terms of molecular oxygen. These terms give the largest contribution to the formation of the electron energy distribution in the wave front. In fact, the energy of chemical reactions at explosive decomposition is usually not sufficient for direct population of high energy levels of atoms. Metastable terms of atomic

oxygen with higher energy have lower population and can be considered in the second turn.

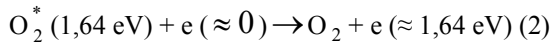
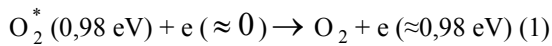
Also, the solution of problem is facilitated by the fact that due to the small atomic and molecular weight of hydrogen its ions can form only high speed plasma dynamical resonances, which in this case we do not consider. In addition, atoms of hydrogen has highly located and poorly populated levels of energy which cannot give the appreciable contribution to the energy distribution of electrons and cannot form a bunch. There is no low metastable term in molecular hydrogen, therefore it is possible neglect a role of atoms and molecules of hydrogen in formation of nonlinear plasma-dynamical resonances in a hydrogen-oxygen mixture. Two main types of ions - O^+ with the ionization potential $I = 13,62$ eV and O_2^+ ($I=12,08$ eV) are formed at propagation of a shock wave in oxygen. Thus molecular oxygen has a special role in an oxygen-hydrogen mixture. It has low located metastable power terms $O_2 (a^1\Delta_g)$ and $O_2 (b^1\Sigma_g^+)$ which have energy $E = 0,98$ eV and $E = 1,64$ eV. These terms are easily populated at collisions and take part in formation of electron energy distribution in the wave front. The molecule of oxygen possesses the lowest ionization potential. Energy of excitation is easily transferred from atoms to molecular terms, which leads to prevalence of oxygen molecular ions in oxygen-hydrogen plasma, so the concentration of oxygen atomic ions can be neglected. Furthermore, the oxygen molecular ions are massive and can form lowest-speed resonances in plasma of H_2+O_2 mixture. Two large groups of electrons with energy $E=0.98$ eV and $E=1.64$ eV are formed as a result of second kind collisions of excited molecules with slow electrons. The molecular oxygen ions are also produced as a result of step-wise excitation. Thus it appears that the ions of molecular oxygen and two groups of electrons form the lowest speed plasma dynamic resonances $\sqrt{T_e/m_i} < C \leq 1,63 \sqrt{T_e/m_i}$ in a mixture of hydrogen and oxygen. The source of these electrons are the two lower metastable term of molecular oxygen (Table 1).

Table 1. Ranges instability of the shock waves in oxygen, associated to population of the terms $O_2 (a^1\Delta_g)$ and $O_2 (b^1\Sigma_g^+)$.

Energy of electrons E (eV)	ion	range of instability of the shock wave (km / sec) $\Delta C = V_{is} \div 1,63 V_{is}$	collapse of the shock wave (km / sec)
0,98	O_2^+	1,72 ÷ 2,8	2,8
1,64	O_2^+	2,2 ÷ 3,58	3,58

Table 2. Speed limits of detonation and the corresponding nonlinear resonance ranges

Mixture	Limits of detonation experiment [15] (m / sec)	The range of existence of a soliton bunch $\Delta C = V_{is} \div 1,63 V_{is}$ calculation (m/sec)
$(2H_2 + O_2) + kO_2$	1707 ÷ 2814	1720 ÷ 2800
$kH_2 + O_2$	1707 ÷ 3532	1720 ÷ 2800 (O_2^+ , E=0,98 eV); 2200 ÷ 3580 (O_2^+ , E=1,64 eV); Total 1720 ÷ 3580



Depending on conditions different speed range $\Delta C = V_{is} \div 1,63 V_{is}$, with soliton bunch can be realized. It depends on the population of the metastable terms, which is determined by the energy input, as well as the density of the medium, as the collisions devastate metastable terms. If the energy of shock waves and chemical reaction is enough to populate a term $O_2(a^1\Delta_g)$, but not enough to populate a term $O_2(b^1\Sigma_g^+)$ with energy $E = 1.64$ eV, the soliton bunch is formed only in the range of $\Delta C = 1,70 \div 2,8$ km / sec (Table 1). The second range of $\Delta C = 2,2 \div 3,6$ km / sec occurs with greater energy deposition at the expense of a term $O_2(b^1\Sigma_g^+)$ with energy $E = 1.64$ eV. In Table 2, these ranges are compared with the known speed ranges of detonation in an oxygen- hydrogen mixture. At increase in energy of a shock wave higher power levels of atoms and molecules can be populated. Metastable terms of atom of oxygen

$O(^1D)$ with energy $E = 1,97$ eV, $O(^5S)$, $E = 3,15$ eV, and also $O(^1S)$ with energy $E = 4,19$ eV are located the following on energy behind metastable terms of a molecule of oxygen. At collisions of the second kind with participation of these terms groups of electrons with corresponding energy $E = 1,97$ eV, $E = 3,15$ eV, $E = 4,19$ eV can be formed. As a result the ranges of instability $\Delta C = 2,4 \div 3,9$ km/s (ion O_2^+ , electrons $E = 1,97$ eV), $\Delta C = 3,06 \div 5$ km/s (ion O_2^+ , electrons $E = 3,15$ eV), $\Delta C = 3,46 \div 5,6$ km/s (ion O_2^+ , electrons $E = 4,19$ eV) will arise. Strong instability at speed of a shock wave of 3,9 km/s is really registered in experiments [16] on research of ionizational instability in oxygen. Ranges of instability can arise also at participation of resonant terms [9]. For example, due to two-step reaction with participation of resonant term $O^*(9,52 \text{ eV})$ the group of electrons can be formed.

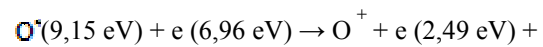
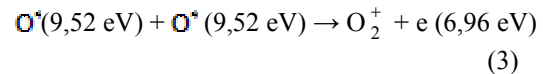


Table 3. Comparison of the phase velocity of the soliton bunch with a maximum speed overcompressed detonation of oxygen-hydrogen mixture $4H_2 + O_2$

Energy of electrons E (eV)	ion	The phase velocity of the bunch (km/s)	Pressure of mixture (Torr)	Speed limit of overcompressed detonation; experiment [17] (km/s)
1,97	O_2^+	2,42 ÷ 3,9	80	3,9
2,49	O_2^+	2,73 ÷ 4,45	200	4,5

$$e (\approx 0 \text{ eV}) \quad (4)$$

As a result the range of instability of shock wave $\Delta C = 2,73 \div 4,45 \text{ km/s}$ (ion O_2^+ , electrons $E = 2,49 \text{ eV}$), will be generated (Table 3). In oxygen there may be other more high-speed ranges of nonlinearity, which can occur at high velocities of the shock wave. Two-step reaction similar to reaction (3) - (4) is realized for example in the ionization instability in xenon [9]. Thus, in a reacting oxygen-hydrogen gas mixture due to ions of oxygen the following ranges of instability of the shock wave, connected with nonlinear ion-acoustic interaction can consistently realize: $\Delta C = 1,70 \div 2,8 \text{ km/s}$; $\Delta C = 2,2 \div 3,6 \text{ km/s}$; $\Delta C = 2,4 \div 3,9 \text{ km/s}$; $\Delta C = 2,73 \div 4,45 \text{ km/s}$; $\Delta C = 3,06 \div 5 \text{ km/s}$; $\Delta C = 3,46 \div 5,6 \text{ km/s}$. The speed limits of a detonation close to values of 2,8 km/s, 3,6 km/s; 3,9 km/s; 4,45 km/s are registered in experiments (see tables 2,3). Experimental data at higher speeds are absent in the literature. Thus, experiments in the oxygen-hydrogen mixture show that the physical mechanism of detonation, which determines the nature and speed limits of detonation, is associated with non-linear processes in a dispersive gas - plasma medium that occurs during the explosion. All the registered speed limits of detonation D for the oxygen-hydrogen mixture at various pressure: $D = 2,8 \text{ km/s}$, 3,6 km/s, 3,9 km/s, 4,5 km/s [17] coincide with the maximal phase speeds of soliton bunches, realized in the field of a shock wave in plasma of oxygen $D = 1,63 V_{is}$. Phase velocity of soliton bunches is determined by a consistent population of metastable terms of oxygen. In turn, the population of terms is associated with the frequency of collisions and, therefore, depends on the pressure of medium. Because of this, the detonation velocity depends on the pressure.

Detonation of the condensed explosives at change of density

Various explosives differ by energy of explosion. Detonation speed increases with increase in explosion energy. It is shown in [18] that the detonation velocity of condensed explosives corresponds to the speed of soliton bunches, which are formed in the reaction products of decomposition of explosives. The heat of explosion determines the population of the metastable low-energy terms of atoms and molecules formed in the decomposition products of explosives. There are only eight such metastable terms in explosives, which have element structure C-O-N or C-O-N-H. These are terms with energy from C_{met}^* (1,26 eV) up to NO_{met}^* (4,7 eV). Non-equilibrium electron groups are formed in the front of the shock wave as a result of second kind collisions of excited atoms with slow electrons. Ions are also formed. Owing to these eight groups of electrons and to ions of six kinds ($C^+ - CH^+ - O^+ - N^+ - NH^+ - NO^+$) the limited number of soliton bunches is formed. We


consider the ions CH^+ and NO^+ as they have low potential of ionization and can prevail in plasma at explosive decomposition. The more heat of explosion is produced, the higher energy terms of atoms and molecules become populated. As a result, both the electron energy and phase speed of ion-acoustic soliton increase. It is due to the described factors, that the detonation speed has a discrete set of values.

The energy released during the explosion, also depends on the density of the explosive. Change of density of each explosive leads to change of population of metastable terms and subsequently to change of resonant ranges, which determines the detonation speed. Let us consider these factors now.

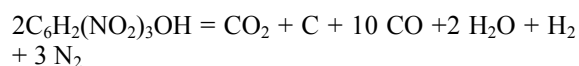
Table 4. Trinitrophenol.

Density, g / cm ³	Velocity of detonation, m / sec	Soliton bunch	Phase velocity of soliton bunch, m/sec
0,97	4965	$C^*(1,26 \text{ eV}), N^+$	3080 ÷ 5000
1,32	6190	$O^*(1,97 \text{ eV}), CH^+$	3800 ÷ 6200
1,41	6510	$C^*(2,68 \text{ eV}), O^+$	4000 ÷ 6500
1,6	7350	$O^*(3,15 \text{ eV}), NH^+$	4450 ÷ 7300
1,62	7200	$C^*(2,68 \text{ eV}), CH^+$	4400 ÷ 7200
1,70; 1,77	7480	$C^*(2,68 \text{ eV}), C^+$ $O^*(3,15 \text{ eV}), N^+$ $N^*(3,58 \text{ eV}), O^+$	4600 ÷ 7500 4600 ÷ 7500 4600 ÷ 7500

Table 5. Pentaerythrit

Density, g / cm ³	Velocity of detonation, m / sec	Soliton bunch	Phase velocity of soliton bunch, m/sec
0,65	4400	C* (1,26), O ⁺	2730 ÷ 4440
0,8	4900	C* (1,26), N ⁺	3000 ÷ 4900
1,0	5500	 (1,64), N ⁺	3340 ÷ 5450
1,17	6110	O* (1,97), CH ⁺	3780 ÷ 6150
1,2	6300	O* (1,97), C ⁺	3920 ÷ 6400
1,4	7100	N* (2,38), C ⁺	435 ÷ 7100
1,5	7520	N* (3,58), O ⁺	4600 ÷ 7500
1,6	8300, 7900	N* (3,58), CH ⁺ , N ⁺	5100 ÷ 8300, 4900 ÷ 8000
1,72	8350	N* (3,58), CH ⁺	5100 ÷ 8300

2,4,6-trinitrophenol (TNP), (Picric acid, Melinit). **C₆H₂(NO₂)₃OH**. Yellow crystal substance under normal conditions. Brisant explosives. Density is 1,8 g/cm³, heat of explosion - 4,02 MJ/Kg. Reaction of decomposition:



Products of explosion in the closed bomb: 71,05 % CO, 3,42 % CO₂, 0,34 % O₂, 1,02 % CH₄, 13,8 % H₂, 21,1 % N₂. Picric acid was used in World War I for filling shells to three-inch guns. It was also used to equip anti-tank mines in wooden cases during the Second World War. Experiments show, that the detonation speed depends on explosive density. It is usually supposed, that detonation speed continuously follows after change of density wave velocity. However, we can show, that detonation speed changes discretely. Let us compare known detonation speeds with speeds of soliton bunches whose formation is possible for the given substance. We shall compare known speeds of a detonation with speeds of soliton bunches whose formation is possible for the given substance.

Table 4 shows, that the maximum phase speeds of low-speed soliton bunches coincide with detonation speeds for various densities of TNP substance.

If energy increases the higher metastable terms of atoms and molecules become populated and the phase speed of soliton bunch grows. Sequence of population of metastable terms in compound of type C-O - N - H is follows: 0,98 eV (O₂^{*}), 1,26 eV (C*), 1,64 eV (O₂^{*}), 1,97 eV (O*), 2,38 eV (N*), 2,68 eV (C*), 3,15 eV (O*), 3,58 eV (N*), 4,19 eV (O*), 4,7 eV (NO*). Detonation comes to an end in some phase of decomposition before the stage of formation of end-products. At

the maximal density of picric acid, 1.77 g/cm³ three soliton bunches correspond to detonation velocity D = 7480 m/sec. However most likely the detonation in this case is connected with a bunch [C* (2,68 eV), C⁺], as the maximal speed of a detonation of the trotyl, having close heat of explosion of 4,23 MJ/Kg is unequivocally connected with a term C* (2,68 eV) [18].

Pentaerythrit (Pentaerithrityl Tetranitrate). **(CH₂ONO₂)₄C**. It is a crystal powder of white color. Powerful and sensitive explosive. It detonates at impact. The burning of leaky charges is unstably and it can pass in a detonation. Heat of explosion is 5.76 MJ/Kg. Density is 1.77 g/cm. It is applied for filling of the detonators, detonating cords, ammunition, in mixtures and alloys. Table 5 presents the results of comparing the velocity of detonation of pentaerythrit of different densities with phase velocities of soliton bunches. All range of detonation velocities of 4400 ÷ 8350 m/sec is the imposition of ranges of existence of soliton bunches associated with the population of the six metastable terms of C* (1,26eV) to N* (3,58eV). Metastable term N* (3,58eV) is the highest term populated at a detonation of pentaerythrit. Comparison shows, that the maximal phase speeds of low-speed soliton bunches coincide with speeds of a detonation at various substance densities.

There are general laws which describe the detonation physics of both density increase and explosive energy increase. When the heat energy increases due to higher density, the higher metastable terms of atoms and molecules get populated and the energy of electrons increases, which causes the increase of phase velocity of a soliton bunch. The same effect can be obtained with more powerful explosive. Higher metastable terms are populated and energy of the electronic groups

forming a soliton bunch grows. Consequently, the collapse of the shock wave (Fig. 3) occurs at a higher speed corresponding to the detonation velocity $D = 1,63 V_{is}$.

Thus the velocities of detonation of explosives

- have discrete values;
- are the limiting propagation velocities of shock waves in a multicomponent dispersion medium;
- are the maximum phase velocities of soliton bunches in multifluid system with different ion sound velocities.

References

1. М.Я. Иванов, Л.В. Терентьева. Элементы газодинамики диспергирующей среды. М. Информконверсия. 2002.
2. Gloersen P. Some Unexpected Results of Shock-Heating Xenon. Phys. Fluids. 1960.V.3, 6, pp.857-870.
3. R. Fowler, G. Paxton, H. Hughes, Electrons as a Shock Driver Gas. Phys. Fluids 4, 234 – 237 (1961).
4. Ю.Л. Серов, И.П. Явор. Волны заряда в ионизованном газе перед гиперзвуковым телом. ЖТФ, т. 66, в. 11, 1996, стр.181-186.
5. Yu.L.Serov. Experimental Investigation of a Supersonic Sphere Motion in Plasma on Ballistic Apparatus. Proc. 2nd Weakly Ionized Gases Workshop, Norfolk, 1998, pp.32-45.
6. V.A.Pavlov, Yu.L.Serov. Supersonic Motion of a Body in Weakly Ionized Plasma: Phenomena of Trans-Ion-Acoustic Plasma Dynamics. 3rd Weakly Ionized Gases Workshop, Norfolk, 1999, AIAA-99-4852.
7. V.A.Pavlov. Ion-Acoustic "Houston's Horse" Effect. Plasma Physics Reports, 2000, V.26, No.6, pp.507-511.
8. V.A. Pavlov. Weakly Ionized Plasma in a Supersonic Plasma Flow. Plasma Physics Reports, v.28, №6, 2002, pp.479-483.
9. Yu.L. Serov. Ion-Acoustic Model of Instability of Strong Shock Waves. J. Actual Problems of Aviation and Aerospace Systems. Kazan-Daytona Beach. №2(18), 2004, pp.49-55.
10. V.A. Pavlov, Yu.L. Serov. PLASMA MODEL OF DETONATION – I: THEORETICAL DESCRIPTION OF PLASMA DETONATION. Proc. of 7th Workshop on Magneto-Plasma Aerodynamics. Moscow, Russia, March 27-29, 2007.
11. V.A. Pavlov, Yu.L. Serov. PLASMA MODEL OF DETONATION – II: Nonlinear interaction and limits of propagation of a detonation in combustible gas mixtures. Proc. of 7th Workshop on Magneto-Plasma Aerodynamics. Moscow, Russia, March 27- 29, 2007.
12. Я.Б. Зельдович. Теория горения и детонации газов. М.-Л. Изд.-во АН СССР, 1944.
13. К.И. Щёлкин, Я.К. Трошин. Газодинамика горения. Изд. АН СССР, М., 1963.
14. Ф.В. Шугаев. Отчёт МГУ №277(1979), тема29/79.
15. B. Lewis, G. Elbe. Combustion, flames and explosions of gases. Acad. Press Inc., 1961.
16. Г.И. Мишин, А.П. Бедин, Н.И. Ющенко, Г.Е.Скворцов, А.П.Рязин. Аномальная релаксация и неустойчивость ударных волн в газах. ЖТФ т.51, в.11,1981, стр. 2315-2324.
17. В.Е.Гордеев. Предельная скорость пересжатой детонации и устойчивость скачков в детонационном спине. ДАН СССР.1976.Т. 226,№3. Стр.619-622.
18. Yu.L. Serov. Interaction of shock waves with plasma: detonation of explosives on the basis of nitro-compounds (nitroglycerine, nitroglycol, trotyl). 8th International Workshop on Magneto-Plasma Aerodynamics. Moscow, Russia, March 31- April 2, 2009.

ON DD SYNTHESIS AT VERY INITIAL AND FURTHER STAGES OF NANOSECOND VACUUM DISCHARGE WITH DEUTERIUM-LOADED PD ANODE

Yu. K. Kurilenkov, V.P. Taranov, V.T.Karpukhin and G.E.Valyano

Joint Institute for High Temperatures of Russian Academy of Sciences, 13/19 Izhorskaya Str., 125412 Moscow, Russia (yukurilenkov@rambler.ru)

Abstract. The energetic ions and DD neutrons from microfusion at the interelectrode space of a low energy nanosecond vacuum discharge with deuterium-loaded Pd anode has been demonstrated recently. To understand better the physics of fusion processes the detailed PIC simulation of the discharge experimental conditions have been developed using a fully electrodynamic code KARAT. The dynamics of main charge particle species was reconstructed in time and interelectrode space. The principal role of a virtual cathode (VC) and the corresponding single and double potential well formed in the interelectrode space are recognised. The calculated depth ϕ of the quasistationary potential well (PW) of the VC is about 50-60 kV, and the D^+ ions being trapped by this well accelerate up to energy values needed to provide collisional DD nuclear synthesis. Both experiment and PIC simulations illustrate very favourable scaling of the fusion power density at decreasing of VC radius ($\sim \phi^2/r_{VC}^4$) for the chosen inertial electrostatic confinement fusion scheme based on nanosecond vacuum discharge. Meanwhile, the initial stage of discharge is understood still poorly. When voltage is applied, the electron beam extracted from cathode starts to interact with the surface of deuterium-loaded Pd anode. This early stage of discharge manifests sometime the peaks registered by photomultipliers which are similar to neutron ones from time-of-flight measure under the study of collisional DD synthesis at the further stages of discharge. The detailed study of Pd anode surface morphology have been performed and recognized, in particular, the number of various pores and craters of different sizes. We remark that besides of rather usual craters (due to electron beams – anode interaction) some of the craters on the Pd anode surface may correspond to anode ectons (explosive centres) and consider their possible nature. The data obtained are compared with recent results on initiation of DD reactions by electron beams at deuterium-loaded Pd foils and correspondent data on their surface morphology.

1. Introduction.

Being by definition on the boundary between condensed matter physics and plasma physics, warm dense matter (WDM) is expected in any systems with high local concentration of energy that start as solid and are heated to become plasmas. Laser-target interactions, particle beam-target interactions, shock waves, high pressure and other studies of WDM at large and medium scale facilities (see, for instance, [1,2]) are supplemented successfully by small-scale experiments. For example, table-top experiments using femtosecond laser irradiation of clouds of clusters [3] have demonstrated how x-rays, fast ions, and even DD synthesis neutrons can be generated. Also, different states of matter in unusual conditions have been realized and under the study at vacuum discharges, where an extensive experience has been accumulated [4,5]. In fact, solid density electrodes, vacuum environment, fast and local energy deposition provides the framework to create and study WDM also. For example, there are many ways to concentrate energy up to 10^4 J/g in microscopic volumes of a cathode. These concentrations of energy result in microscopic explosions accompanied by emission of electrons, creating a plasma, liquid droplets of metal, and metal vapor. This effect has been called “ecton” (explosive center) effect [6,7]. Ectons, thus, arise because of high power density concentrated at a metal surface, and one of the most common

methods to create this specific state of WDM is Joule overheating of micro volumes of cathode. Related anode phenomena are still poorly investigated.

The energetic ions and DD neutrons from microfusion at the interelectrode space of a low energy nanosecond vacuum discharge has been demonstrated recently [8,9]. The efficiency of hard X-rays and fast ions generation by nanosecond vacuum discharge, as well as the neutron generation, is at least two orders of magnitude higher than for experiments on DD fusion driven by Coulomb explosion of laser irradiated deuterium clusters [3]. To understand better the physics of fusion processes the detailed PIC simulation of the discharge experimental conditions have been developed using a fully electrodynamic code [10]. The dynamics of main charge particle species was reconstructed in time at anode - cathode (AC) space. The principal role of a virtual cathode (VC) and the corresponding single and double potential well formed in the interelectrode space were recognised. The calculated depth of the quasistationary potential well (PW) of the VC is about 50-60 kV, and the D^+ ions being trapped by this well are accelerating there. Correspondingly, head-on collisions of D^+ ions with energies of a few tens of keV is followed by DD nuclear fusion, transforming the interelectrode space into something like a reactor chamber. PIC modeling allows the identification of the small-scale experiment [8-10] with a rather old branch of

plasma physics, as inertial electrostatic confinement fusion (IECF) system (see [11-14] and refs therein). Pioneers of IECF were O. Lavrent'ev in the USSR and F. Farnsworth in the USA, but due to different reasons, including a rather low value for $Q = E_{\text{fusion}}/E_{\text{input}} \sim 10^{-6}$ or even less, this concept for fusion was almost forgotten. Just during last couple of decades interest in IECF was renewed at US and Japan mainly as a simple source of neutrons [12-14]. Furthermore, some modern experimental set-ups under study and construction at LANL provide new expectations to get efficiency $Q > 1$ [13c,14] (as a minimum in theory).

Underline, that the source of D^+ ions for DD synthesis at PW is the erosion anode plasma or, more accurately, WDM of deuterium-loaded Pd anode, created by electron beams in discharge at the anode within 10-20 nsec when the voltage applied. The physics of DD synthesis at this and further stages of discharge was clarified, in particular, due to PIC simulations. Very initial stage of discharge (1-3 nsec), when electron beam extracted from cathode just coming to anode and starts to interact with deuterium-loaded Pd is still not investigated properly.

Meanwhile, palladium- hydrogen (deuterium) systems themselves are interesting both from fundamental and applied points of view, in particular, as systems which could be utilized for energy storage (surfaces, nanocrystals, vacancy- and dislocation-rich materials, thin films, multilayers, and clusters as systems of major interest are addressed in review [15]). Small angle neutron scattering measurements of deuterium dislocation trapping in Pd have recognized rod-like

trapping geometry [16], as well as that dislocations in H(D)-cycled Pd can absorb large amount of hydrogen (deuterium) [17]. Anomalies in the electron transport and magnetic properties in a deformed loaded Pd foil were interpreted in terms of filamentary superconductivity attributed with the condensation of the trapped hydrogen (deuterium) into a metallic-like phase ($\sim 10^{24} \text{ cm}^{-3}$) within the dislocation core [18]. (This metallic phase have been predicted theoretically also [19]). Spectra of collective excitations at deuterium – loaded Pd were considered in [20], and have been shown that excitation of the hydrogen subsystem as a result of the electron bombardment is specified by the generation of plasmons in the crystalline lattice, which are localized in the vicinity of hydrogen (deuterium) atoms. Further, very recent studies of dense hydrogen shown that even more dense phase may exist, called ultra-dense deuterium (with the bound DD distance is 2.3 pm, corresponding to $\sim 8 \times 10^{28} \text{ cm}^{-3}$, which was estimated directly from experiment [21]). The possibility of DD fusion under relatively weak laser beam irradiation of ultra-dense deuterium was investigated, and time-of-flight (TOF) particles detection recognized all particles expected from DD synthesis [21]. Thus, we may assume that latter few examples imply that WDM physics are also might be relevant to possible nuclear microexplosions on deuterium-loaded Pd surface at initial stage of vacuum discharge (under possible triggering of DD reactions by internal electron beams), and this stage also have to be the subject of experimental study and analysis.

The paper is organized as follows. The

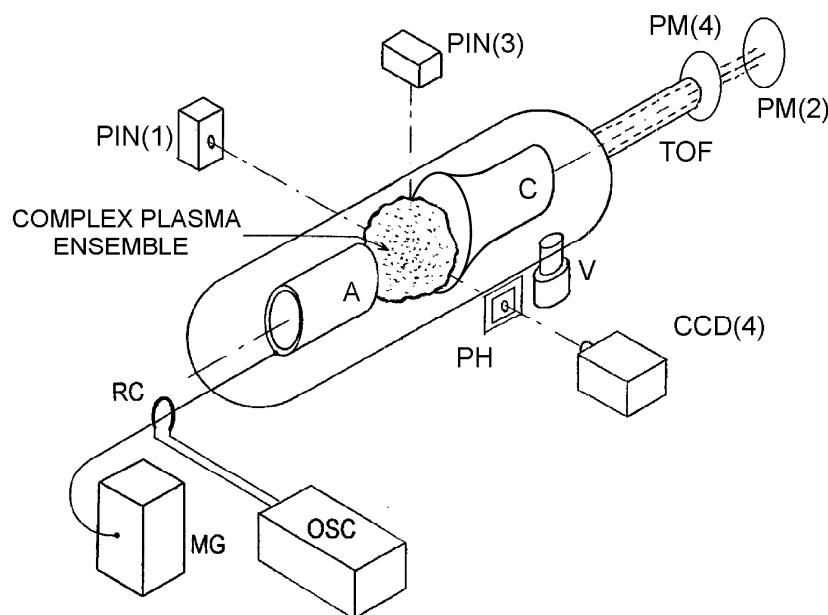


Fig.1. Schematic of the experiment for generating interelectrode complex plasma ensembles with multiple DD fusion events : MG – Marx generator, R – Rogovskii coil, A and C – anode and cathode, PIN – instant PIN diodes, CCD – camera, PH – pinhole, PM2 and PM4 – photomultipliers, OSC – oscilloscope, TOF- time of flight tube, V - vacuum pump

experiment on DD synthesis at nanosecond vacuum discharge of low energy is described briefly at Section 2. The main physical results of PIC modeling of experimental conditions are given at Section 3. The features of fusion events observed in experiment are discussed at Section 4. The specifics of neutron yield and DD fusion power density of IECF based on nanosecond discharge are considered at Section 5. Observations of DD synthesis at initial stage of discharge and surface morphology of Pd anode are presented and discussed at Section 6. Section 7 concerns discussion and some concluding remarks.

2. Experimental set-up. DD microfusion and neutron yield.

The source (Fig.1) is based on an electrical

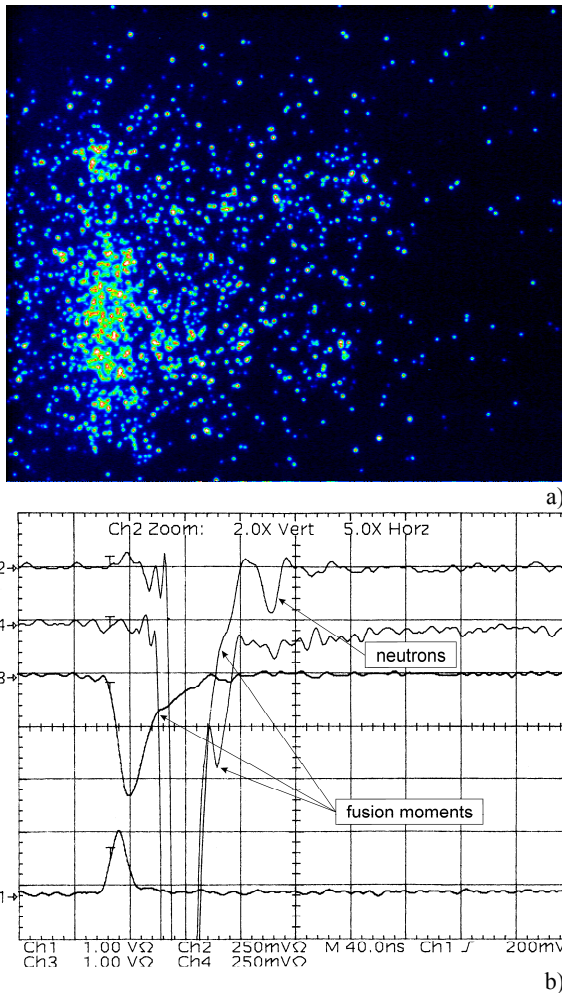


Fig.2. X-ray dynamics in regime 1: (a) X-ray CCD image for a transparent low density interelectrode ensemble with DD fusion accompanied by a moderate neutron yield, (b) extra X-ray spark in Ch. 4—manifestation of the beginning of nuclear reactions (sensitivity of channel 2 is 250 mV; time scale is 40 ns/div). The delay of the neutron peak in channel 2 corresponds to ≈ 46.6 ns/m (or 2.45 MeV neutrons due to DD fusion).

discharge having a rise time of about 10 nsec [8,9]. Set-up consists of a cylindrical vacuum chamber (diameter 50mm) having three windows closed by Mylar films 70 μm thick. This cylinder is connected to a vacuum pump able to reach 10^{-6} to 10^{-7} mbar and working in a continuous regime throughout the series of discharge shots. Two electrodes are included on the cylinder axis: a hollow anode can be displaced by means of a screw and a hollow cathode is fixed. The distance between the electrodes can vary by 0.1 mm steps up to 6-7 mm maximum. The source is included in a coaxial high voltage cable having 50 Ω impedance, which is connected to a four-stage Marx generator (≈ 1 J) delivering a 50 ns pulse of maximum voltage 70 kV in a 50 Ω load. The value of the current is usually 1 kA. Three Mylar windows allow the x-ray intensity measurement in three perpendicular directions

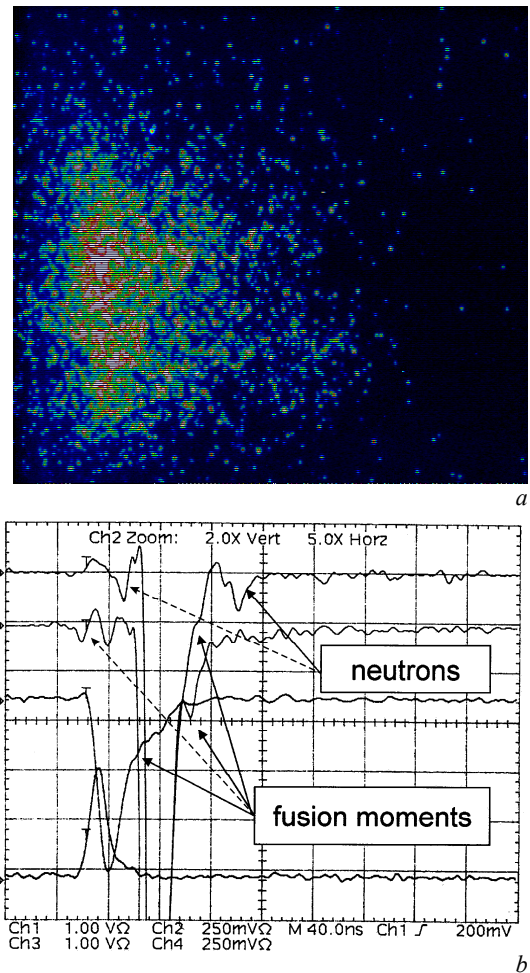


Fig.3. X-ray dynamics in regime 2: (a) X-ray CCD image for low density interelectrode ensemble with DD fusion accompanied by neutron yield, (b) extra X-ray spark in Ch. 4—manifestation of the beginning of nuclear reaction (sensitivity of channel 2 is 250 mV; time scale is 40 ns/div). The delay of the neutron peak in channel 2 corresponds to ≈ 46.6 ns/m (or 2.45 MeV neutrons due to DD fusion). Dotted lines correspond to initial stage of discharge (see Section 6).

(side-on right, left and upper ones) in the plane corresponding to the anode edge. Another Mylar window and/or TOF tube allows the end-on measurement through the hollow cathode. Calibrated PIN diodes having a 1 to 2 ns rise-time are used to measure the x-ray output. The x - rays CCD image of sources is obtained by means of a pinhole with diameter 0.1 mm bored in a 1mm thick lead screen covered by 100 μm thick Al foil.

Neutron generation in x-ray ensembles (like in Fig.2a and Fig.3a below) due to DD reactions of nuclear synthesis has been registered using a slightly modified experimental set-up in comparison with earlier x-ray and fast ions studies [8]. The new cylindrical Cu anodes ($\varnothing = 0.6 \text{ cm}$) have a set (3 or 12) of thin hollow Pd deuterated tubes ($\varnothing = 0.1 \text{ cm}$) attached to anode end-on, and the hollow cathode was constructed from Al. The standard electrolysis in heavy water for about 6 hours at a current of 100 mA has been used for regular partial saturation of Pd elements of the anode by deuterium. Note that channels 1 and 3 (Fig.1) represent the x-ray intensity from instant PIN diodes which have a maximum sensitivity at $\approx 10 \text{ keV}$. Harder x-rays (with energy $> 60 \text{ keV}$) are registered by PM2 covered usually by 2 mm Cu absorber (the signal at ch.2 is delayed due to electronic scheme of PM2 for $\approx 35 \text{ nsec}$ in comparison with the instant PIN diodes signals for all oscillograms presented below). TOF measurements have been performed with photomultipliers PM4 and PM2 (Fig.1), located along the electrode axes at the distances of $L=40\text{-}50 \text{ cm}$ and $L=50\text{-}90 \text{ cm}$, correspondingly (channels 4 and 2 on oscillograms like on Fig.2b; photomultipliers were screened and covered by scintillators). Beyond the usual hard x-rays (first strong peak at channel 2), PM2 may indicate the well reproducible signal (second small peak) with delay about 46.6 nsec/m, typical “signature” for 2.45 MeV neutrons from DD synthesis reactions. Meanwhile, PM4 ($L= 40 \text{ cm}$) is located usually between the source and PM2 ($L=80 \text{ cm}$), and have to register especially the moment of time when fusion events may take place (if the main x-ray peak itself will not be too broad to avoid the screening of this natural “reference point” due to extra X-rays as illustrated by Fig.2b, Fig.3b). The second small peak from PM2 corresponds to the neutron yield due to $\text{D}+\text{D} = \text{n} + \text{He}^3$ reaction (like on Figs 2b, 3b). The changing of the distances between dusty hard x-ray source and PM2 is followed by the corresponding displacement of the second (neutron) peak. The plates CR39 and PN3 have been used simultaneously with the TOF scheme to detect neutrons. Their development shows the variable number of tracks which have to be attributed to neutrons also. The minimal energy of deuterons, E_D , estimated from the spread of arrival times $\Delta t \approx 778 d_{SD} (E_D)^{1/2}$ of neutrons at a

detector is about 20 keV (d_{SD} is the distance from source to detector in meters, E_D is ion energy in keV) [14].

In fact, a typical example from the x-rays data base of images of interelectrodes dusty matter with lower neutron yield $\sim 10^5/4\pi$ (and low total x-ray ones) is shown in Fig.2a. Namely, rather low x-ray yield allows us to register more accurately the moment of microfusion events. The next example of interelectrode ensemble with slightly more dense x-ray images is shown on Fig.3 (specifics of initial stage of this regime is discussed at Section 6). The value of the neutron yield from random interelectrode media is variable, and turns out to be about $10^5/4\pi$ per shot for “transparent” ensembles (like presented on Figs.2a,3a) and, looking forward, up to $\sim 10^7/4\pi$ for dense interelectrode ensembles (like on Fig. 11 below, Section 4) under $\approx 1 \text{ J}$ of total energy deposited to create all the discharge processes at the single shot (assuming isotropic yield).

3. PIC simulations. Virtual cathode and potential well formation.

The complex physics of nanosecond discharge processes and the mechanisms of microfusion were poorly understood, and motivated the interest in complementary PIC (particle-in-cell) KARAT simulations [24]. In addition to representing the key points of general physical picture, computer modelling allows clarification of the details of the experimental data. To explain the nature of fusion at experiments with nanosecond vacuum discharge [8,9], just the limited number of PIC 2D calculations results are presented and discussed below. First, discharge geometry and particle dynamics is shown on Fig.4. Next, Fig.5 represents a phase diagram, and demonstrates the appearance

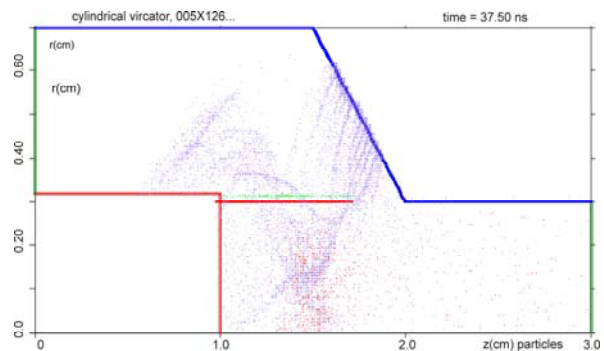


Fig. 4. Virtual cathode formation and discharge geometry and particle dynamics at 25 ns of calculations (the “erosion anode plasma” (green line) is adjacent perpendicular to the anode (A-left) base near the semitransparent “foil,” which simulates thin hollow Pd tubes filled with deuterium in the actual experiment; the blue dots show quasirelativistic beam electrons pulled by the field from the cathode (C- right), and the red dots show fast ions filling the space inside the anode ($r = 0\text{-}0.3 \text{ cm}$).

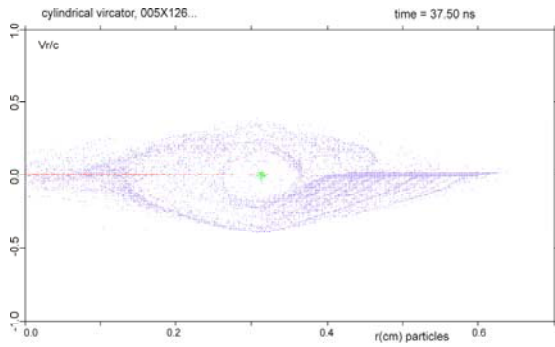


Fig.5 Phase portrait of particles in the case of the formed virtual cathode for $r \approx 0.3-0.4$ cm (the dots show electrons accelerated as approaching the Pd tubes to V_r^e max $\approx 0.3-0.4$ c ($r = 0.32$ cm), and the horizontal line $V_r/c \approx 0$ (in the interval $r = 0-0.32$ cm) shows accelerated ions (c - light velocity); the erosion "anode plasma" is the small spherical region at the center, where $V_r/c = 0$ and $r \approx 0.32$ cm);

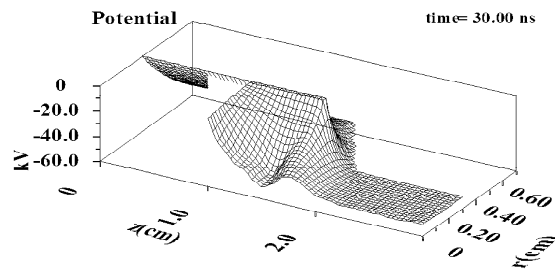


Fig. 6. Typical single (with respect to Z) potential well at 30 ns of calculations (the minimum of the potential well is at $Z \approx 1.5$).

of the VC. Related with the VC, examples of PW is shown in Fig. 6. For the PIC calculations anode Pd tubes were modeled by a semitransparent "foil". Some anode "erosion plasmas" were added also (the small green sphere at the centre of the "void" in Fig.5, where $V_r/c \approx 0$ and $r \approx 0.3$ cm). When voltage is applied, electron beams are extracted from the internal surface of cathode ($r \approx 0.4-0.6$ cm) and accelerated up to $v_{e-max} \approx 0.3c - 0.4c$ near Pd tubes ($r = 0.3$). Interaction of electron beams with tubes provides erosion of system (Pd+D₂) and ejection (implosion) of deuterium and palladium vapors into the near anode axis area (accompanied by their partial nucleation at real experiment). Further, since the experimental current I_A exceeds the limiting Langmuir value $I_A > I_L$ [25], cumulative convergence of head-on e-beams at the axis (inside the space restricted by Pd tubes) provides total deceleration of electrons (as well as partial reflection of electrons outside, $V_r/c > 0$), and VC appears (at $r \approx 0.1$ cm).

Due to VC, a negative potential about a few tens of keV will appear at the axis (at $Z \approx 1.4-1.6$ cm), and the internal part of the near anode area will be filled by accelerated ions (Fig.5, red

horizontal line $V_r/c \approx 0$ at $r = 0 - 0.3$ cm interval; this line will be split, in the ion scale of velocities, at $r = 0$ (on the Z axis) into two head-on converged branches of ions with velocities $V_r^i/c = \pm 0.5 \times 10^{-2}$). The well depth oscillates around of the applied voltage with amplitude up to 20%. Ions being accelerated from different edges of the PW to the Z axis, represent head-on fluxes at $r \rightarrow 0$ with ion energies of 20-50 keV. Evidently, this explains the collisional DD fusion observed in the real experiments (in that case we also have to take into account collisions with neutrals, deuterium clusters and the deuterated anode itself) [10]. The area of Z and R at the half-width of the PW contains an almost isotropic distribution of fast ions (volume of the "reactor", Fig7; picture for V_r/c has similar shape being 20% broader by velocity) with mean energy about 25 keV. System of Pd tubes is open and allows to run away from PW for some of ions along axis Z (Fig.7) . PIC simulations allow provide the optimization of the electrodes geometry, as well as the testing new geometries. Calculated energy of electrons and ions as function of their radii positions are shown at Fig.8. In whole, we may underline that A-C geometry chosen in experiment is efficient way to transform the energy of electron beams into energy of fast ions of the same value,

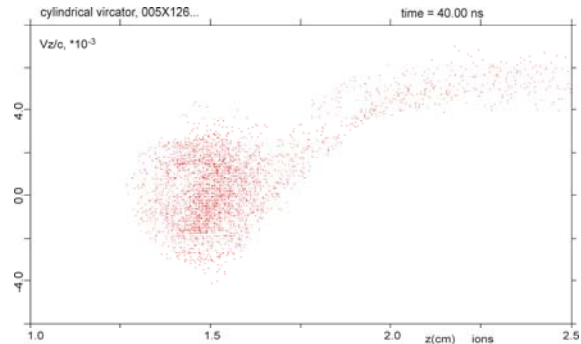


Fig.7. Axial velocities of ions at potential well on 30 ns of calculations.

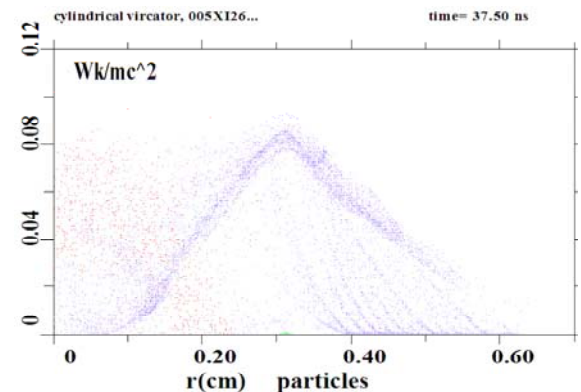


Fig.8. Energy of electrons (blue dots) and ions (red dots) as function of their radial position.

but in another part of interelectrode space.

PIC simulations have assisted in understanding some effects observed in the experiments earlier [9]. For example, the shapes of some PIC non-Maxwellian distribution functions are in correlation with a “plateau” in histograms for fast ions tracks observed in the experiments (see Fig.8 at [9]). Another example, well reproducing experiments by simulations, are the double potential wells in the first stage of discharge. It looks very probable that the appearance of double wells might explain the double neutron peak observed sometimes in experiment (as in Fig.5 [10]). We can see that the PW lifetime in experiment is about $T_{PW} \approx 20\text{-}25$ nsec, and after that the VC has to be neutralized ($T_{PW} \gg \omega_{pi}^{-1}$) by the flux of ions. Since the total pulse T_{pulse} of voltage is about 50 nsec, there are sufficient conditions for the VC appearing in the experiments again ($I_A > I_L$), and a new double PW will appear. Ion collisions at this PW will be manifested by a second double neutron peak like have been registered earlier (see Fig. 5 in [10]). Note that the appearance of single-, double-, and multiple PWs and non-Maxwellian distributions of ions are typical features of systems with IECF.

The model of collective ion acceleration [26] at a vacuum discharge, based on the concept of *nonstationary* potential wells (PW) before the front of the cathode flare in the regimes of non-stable current carrying, was developed earlier [27]. On the basis of this model the explanations were given for the early experimental data of A.A. Plutto [28] on occasional anomalous ions acceleration. Our results of PIC simulations for real electrodes geometry and vacuum discharge conditions of experiment [8,9] using electrodynamic code KARAT [10,29] have recognizing that the concept of PW is more universal and represents the basis for IEC fusion reactor: namely, a *quasistationary* PW at interelectrode space with depth up to $\sim 80\%$ of the applied voltage provides radial electrostatic acceleration of ions up to the same energies. Correspondingly, head-on collisions of ions at the axis with energies of a few tens of keV is followed by DD nuclear synthesis, transforming the interelectrode space into a reactor chamber. Specifics of IECF based on nanosecond vacuum discharge and comparison with available advanced IECF systems [13,14] is discussed at Sections 5 and 7.

4. Inerelectrode ensembles with multiple fusion events and trapped fast ions.

Next possible feature of neutron yield is illustrated by the shot presented in Fig.9a,b. The CCD image in Fig.9a shows the ensemble of an intermediate density of clusters, but the oscillograms (channel 2, PM2, L= 50 cm,

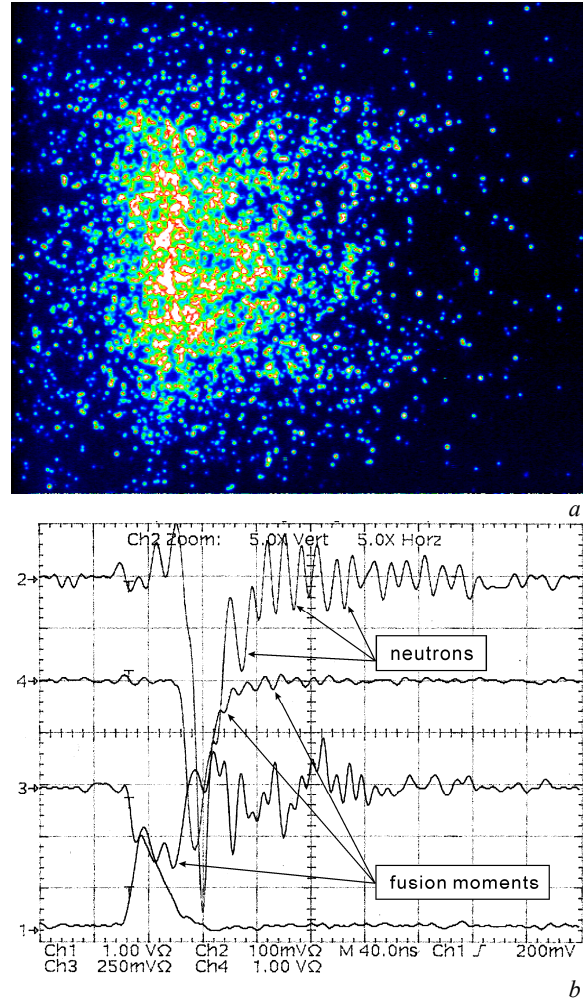


Fig. 9. X-rays dynamics in regime 3: (a) X-ray CCD image for a rarefied transparent ensemble with multiple DD fusion; (b) pulsating neutron yield, Ch 2, several X-rays peaks in Ch 4 show the sequential instants of DD reactions.

sensitivity of 100mV) manifest an essential *pulsating neutron yield* (Fig.9b). Correspondent extra x-rays due to each DD fusion event are registered as fractures both at the PIN diode (channel 3) and PM4 signals of hard x-rays intensity (the right parts of these x-ray intensity curves are modulated by the same moments of fusion with delay ≈ 35 nsec in comparison with instant diods signals, chs 1,3). The intensity of the neutron peaks registered is weakened partially due to a possible reflection from the 2 mm Pb absorber located in front of PM2. Remind, that typical hierarchy of related times at multiple fusion events (MFE) [9] for particular fusion moment contains usually the instant signal from ch.1 or ch.3 at the moment t_f , next, electronically delayed signal at ch.4, $t_f + 35$ nsec, and time of flight delayed neutron signal at ch.2, $t_f + 35$ nsec + t_{TOF} , correspondingly.

Another effect may appear if the concentration of grains is increased essentially but their mean

sizes decreased (we have $\sim 10^{-3} - 1\mu\text{m}$). We may regulate partially the level of x-ray absorption and multiple scattering inside the ensemble of clusters by varying the interelectrode volume within an order of magnitude (by changing of A-C distance, 0.5 - 0.1 cm) under approximately the same value of mass transfer from anode and under smooth variation of the pressure at the range $10^{-6} - 10^{-2}$ mbar (that influences the processes of nucleation also). In the diffuse regime, $\lambda \ll l_{sc} \ll R$, light being trapped in a disordered system may make a long random walk before it leaves the medium from the nearby surface area [30-32] ($l_{sc} = 1/N_0 Q_S$ - mean free path of photons due to scattering, R - ensemble dimension and λ - the wavelength; Q_S - scattering cross section, N_0 - volume density of scattering particles, $N_0^{-1/3} \gg \lambda$). Dense interelectrode ensemble seems manifest the ability to “trap” partially even x-rays. The dynamics of x-ray radiation at the regime close to x-ray diffusion is very differ from ordinary (transparent or disordered) x-ray ensembles (as in Figs. 2,3): the diffused lower energy x-ray photons (energy ~ 3 -10 keV) are delayed to appear from ensemble interior in comparison with very hard x-ray emission (ch.2, photon energy ≥ 60 keV) which is not trapped. Usually PIN diode signals are decreasing in intensity also in the diffuse regime if density of ensemble grows. For dense self-organized ensembles, if intensity on ch.1 turns out less than triggering value $U_{\text{trig}} = 100\text{mV}$, oscillograms are not registering and we may observe just CCD picture. Example CCD image of ensemble with “trapped” x-rays for this particular case is shown on Fig.10. Other “ball”-like ensembles with very low x-rays yield but bright images are shown elsewhere [9,33].

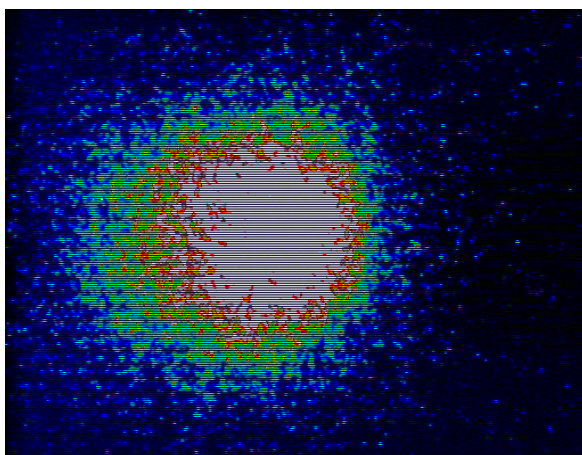


Fig.10. CCD image of dense self-organized interelectrode clusters ensemble with diffused X-rays photons (few keV) inside .

It appears reasonable to try to combine the advantages of interelectrode cluster ensembles with

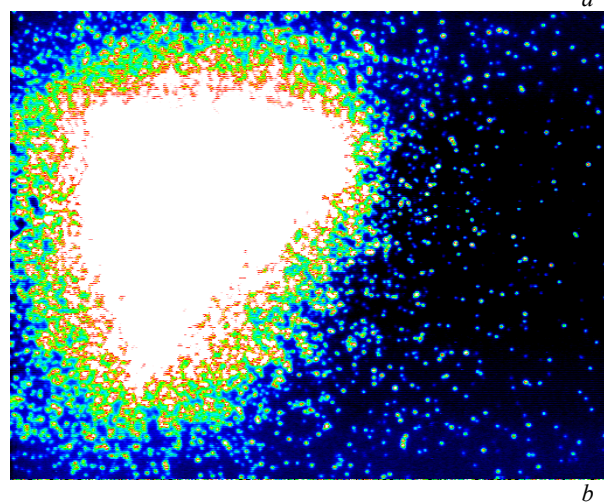
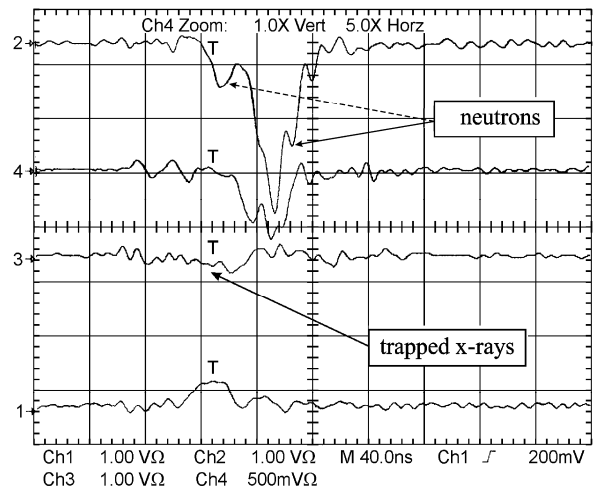


Fig.11. X-rays dynamics in regime 4 : (a) Oscillograms of x-rays yield (channels 1 and 3) and neutron yields (channel 2) for specific interelectrode ensemble with trapped fast ions and x-rays (“triple” anode, see text for details of experiment). (b) CCD image of corresponding self-organized cluster ensemble (complex plasma microreactor).

multiple fusion events (Fig.9) and with *diffused x-rays under total trapping of fast ions* (Fig.10) Namely, particular example of cluster ensemble with similar combined features is shown in Fig. 11 as prototype of a table-top *complex plasma microreactor* (see also Fig.6 in [10]). We observe a bright image of cluster ensemble, but with very low hard x-ray yield under their partial diffusion (channels 1,3). The growing (left) part of intensity curve from PM4 (channel 4) represents mainly the extra x-rays due to fusion events with few corresponding peaks. The main part of intensity registered by PM2 (channel 2) represents the strong pulsating neutron yield as a manifestation of “waves” of DD microfusion due to periodic deuterium ions collapse, but on the essential background of fast deuterium ion – deuterium clusters target DD synthesis ($L= 90$ cm, 0.5 mm thick Cu absorber, channel 2 sensitivity is 1V). The

sensitivity of channel 4 ($L = 45$ cm) is higher than for channel 2. This means that mainly the process of neutrons coming were registered by PM2. Thus, the ensembles with more saturated x-ray images correspond to higher neutron yields due to essential stopping of deuterium ions on clusters (some neutron yield at very initial stage, Fig.11a, is discussed below, section 6).

The efficiency of neutron production at our low-energy discharge (as well as hard x-rays) may be two orders of magnitude higher than for fusion events driven by laser irradiated clusters explosions (10^4 neutrons for 120 mJ of laser energy [3]), while the total estimated number of deuterons in the laser focal area and ejected from anode into interelectrode space at our single shot is of the same order ($\sim 10^{13} - 10^{14}$). This efficiency has been realised due to several reasons [8,9] and, in particular, due to the fact that for experiments [3] with fusion driven by Coulomb explosion of clusters the collisional free path l_D for ions D^+ is much longer than the plasma dimension (which is about laser focal diameter $d_{focal} = 200\mu\text{m}$), $l_D \gg d_{focal}$. In our vacuum discharge, the smooth variation of the relation between l_D and cluster ensemble radius, R_{ball} , is possible. As a result, it may include even the trapping of all the deuterium fast ions (see Fig.5 in [9]) generated inside the ensemble of cold grains, $l_D < R_{ball}$ ("dusty" stopping). Thus, it looks rather naturally that the neutron yields, in fact, will be essentially higher for ensembles with brighter CCD images, which have a lower transparency for x-rays and fast ions, meanwhile, just neutrons are leaving it (like on Fig.11).

5. Single and pulsating regimes of neutron yield.

Earlier, the study of correlations between PW structures and neutron yields have recognized that not only well depth, but namely potential instability in time defines the neutron yield in ion beams interactions [34]. In our experiments also, not only the PW structure but also the dynamics of potential will define the character of the neutron yield. As a result, three types of observed neutron yield could be recognized in the experiments [10]:

1) single peaks (as in Fig.2,3), 2) multiple intermittent neutron yield (two and more neutron peaks, Fig.5 in [10]), 3) oscillatory or pulsating neutron yield (as on Fig.9).

Let us consider the first two types of neutron yields. As shown in [27], the time taken to form the VC (or the decay time of potential) is about $T_v \approx C_d U / I_L$, where C_d is the diode gap capacitance and U is the potential. Since $I_L \sim U^{3/2} / d_{eff}^2$, then variation of d_{eff} in our experiment [9] changes I_L and, correspondingly, the value T_v (d_{eff} is the effective interelectrode distance for non-planar electrodes) [25]. Thus, at rather large d_{eff} we have $T_v \approx T_{pulse}$,

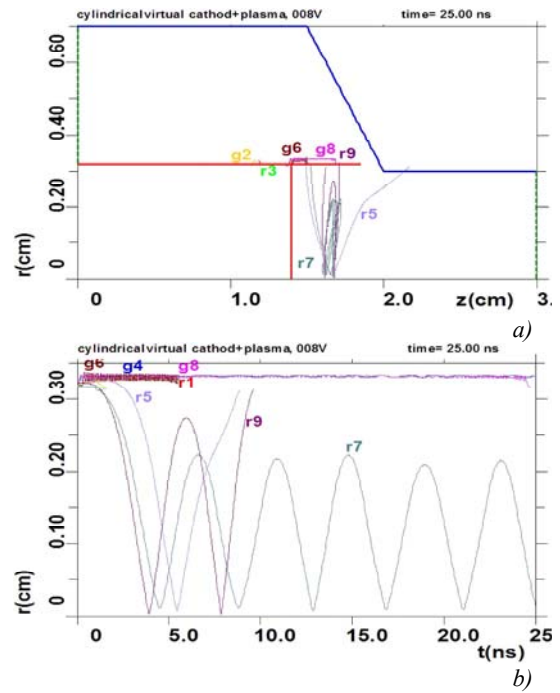


Fig.12 (a) Trajectories of the few chosen deuterons moving at R-Z plane for particular A-C distance (b) The function of different ions position by radius of time.

and just a single peak will be observed in experiments (first type). Decreasing d_{eff} increases I_L and lowers T_v , and step by step at decreasing of $T_v < T_{pulse}$ we get double, and multiple neutron yields (second type). At $U = 50$ kV, $I_A / I_L \approx 1.5$, $C_d \approx 300\text{pF}$ [9] giving $T_v \approx 28$ nsec. This is not far from the time taken to form the VC for the experimental case were two double neutron peaks were registered (Fig.5 in [10]).

The third type of neutron yield is of special interest. At $I_L \rightarrow I_A$, if the electron distribution in the VC would be close to uniform and the well would still be present, then ion oscillations at the PW will be approximately harmonic. At the moments of maximum periodic compression of the ionic subsystem, the DD reaction will take place and the neutron yield will be a pulsating one (Fig.9). The period of oscillations of the neutron yield is about 12-13 nsec in the experiments [9] ($T_v \ll T_{pulse}$), and it represents now mainly the frequency of harmonic oscillations D^+ in the PW (Fig.9) instead of T_v (as for the first type of neutron yield). In fact, the pulsating neutron yield is appearing in experiment just as d_{eff} is decreasing. PIC modeling of this (Fig.9) particular experimental regime (Fig.12a, compare with geometry presented on Fig.4) gives ion trajectories (Fig.12b) and energies (not shown here) which are corresponding namely to their periodic oscillations (ions acceleration – deceleration) at PW. In summary, neutron yield as a single peak is the result of a single collapse of ions at the well bottom at neutralization of VC in regime

$T_v \approx T_{\text{pulse}}$, (Figs.2,3) and pulsating (oscillatory) yield corresponds to ions harmonic oscillations at PW ($T_v \ll T_{\text{pulse}}$) accompanied by periodic collapses at the axis (PW bottom). The second type of neutron yield is an intermediate between single and oscillatory ones.

The pulsating neutron yield regime (Fig.9) is suggestive of the interesting and stimulating conception of periodically oscillating plasma spheres (POPS), developed during the last decade in theory and in experiment [13,14]. There it was suggested to abandon the standard scheme of IECF, where particular ion beams interact with each other, and use in addition the injection of electrons into grids (in order to get a uniform electron background inside the cathode grids). Ions then will undergo radial harmonic oscillations with any amplitude at the potential well formed, and at the moments of maximal compression high fusion power density will be provided $P_{\text{fusion}} \approx 3\varphi^2 \theta^2 f^2 \langle \sigma v \rangle / 2\pi e^2 r_{VC}$, where φ is the well depth, θ the radial ion plasma compression ratio $r_{\text{max}} / r_{\text{min}}$, $f = n_i / n_e$, r_{VC} the radius VC, and $\langle \sigma v \rangle$ the averaged cross-section (here P_{fusion} is the total power integrated over a single period [13]). A typical POPS frequency is $\nu_{\text{POPS}} \sim (2\varphi/m_i)^{1/2} / r_{VC}$ (m_i –ion mass). Analysis of POPS physics has shown that a potential well depth of about 60% of the applied voltage is enough for realization of the concept of a reactor in oscillating systems. At the present moment in spite of POPS attractiveness and demonstration ones in principle, the PW depth reported is still ≤ 1 keV, and POPS frequency $\nu_{\text{POPS}} \leq 1$ MHz (applications, economy, limitations are discussed in detail at [14]).

Generally speaking, POPS are particular and well-defined cases or analog of the *multiple fusion events* (MFI) [9] at vacuum discharge at regime $T_v \ll T_{\text{pulse}}$ discussed above. In fact, instead of special injections of electrons into a spherical device to produce a VC as in [14], nanosecond vacuum discharge with hollow cathode provides itself (after voltage is applied) automatic extraction of electron beams from the cathode and their further acceleration and converging injection into anode area on the axis to form a VC (Figs.4,5). By analogy with POPS expressions we may estimate the fusion power density $P_{\text{fusion}} \sim \varphi^2 \theta^2 f^2 \langle \sigma v \rangle l / 2\pi e^2 r_{VC}^2$ at the volume of nuclear burning for reactor with cylindrical geometry (l is the length of the cylinder) [9]. Assuming $\varphi \approx 60$ keV and $r_{VC} \approx 0.1$ cm, as well as $f^2 \sim 1$, $\theta \leq 10^3$, $l \approx 0.5$ cm, we get the yield $\sim 10^5$ neutrons for a single collapse of D^+ ions at the discharge axis or for one period of ions oscillations. Thus, a specific advantage of IECF systems like POPS [14] or MFI [10] is the favorable scaling of fusion power density (with decreasing set-up size) which is increased with decreasing of r_{VC} and increasing of PW depth. As discussed above, during the total time of the voltage pulse applied we may get from single to 4-5

moments of deuterium ions collapses at the axis (depending of relation between T_v and T_{pulse}). It will be accompanied by the correspondent number of neutron peaks in real experiments (like on Figs.9,11 above), but the total neutron yield will depend of role of channel D^+ - cluster in reactions of DD synthesis (compare CCD and yields of shots presented on Fig.9 and Fig.11).

6. On DD synthesis at very initial stage of discharge.

PIC modeling of particle dynamics and processes in vacuum discharge shows qualitatively, in particular, what is going during first 1-2 nsec after voltage applied. During this time the electron beam extracted from cathode is reaching the deuterium- loaded anode and starting to interact with the Pd surface. This relatively fast initial stage of discharge in our experiment is understood still poorly, in comparison with more late processes of virtual cathode and potential well formation. At this section we would like at first to pay attention and to discuss some specifics of possible particle emission at initial stage of discharge, registered at experiment earlier [9], as well as to consider some features of Pd anode surface morphology.

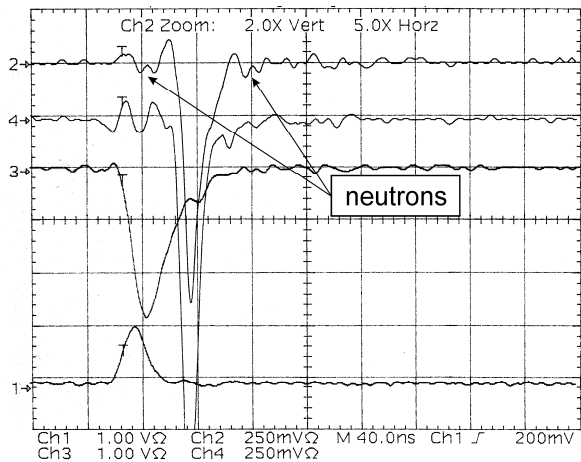


Fig.13. X-rays dynamics in regime 5, where the piece of paraffin have been located between plasma source and photomultipliers 4 and 2.

At very initial stage of discharge the oscillograms sometime manifest the peaks which are reminding to observer the neutron peaks from collisional DD synthesis registered by TOF manner on the late stage of discharge [8-10]. Let us come back to shot presented above on Fig.3 and discuss in more detail the oscillograms, where the neutron peak (ch.2, to the right side from the main strong X-rays maximum) as well as the moments of collisional DD fusion have been registered by different manner also (channels 1,3 and 4). In fact, on the left side from the strong X-rays maximum some peak on ch.2 have been registered also

(indicated by dotted line). Intensities registered on ch.4 contain some specifics also. Let us consider the first in time peak at ch.4 as possible extra X-rays from the moment of electron beam coming on Pd anode surface. If to move further in time (to the right on Fig.3) we see that some next peaks are appearing, at first on ch.4 and after that on ch.2 also. Since PM4 located exactly between plasma source and PM2, we may conclude (from the relative positions of this peaks in time) that the delays of their consequent appearing in channels 4,2 corresponds to TOF for DD neutrons (46,6 nsec/m). In other words, neutrons are coming first on PM4 (and partially are registered there), and later on neutrons are registering by PM2 (the possible synthesis moment and neutrons coming are shown on Fig.3b by dotted lines).

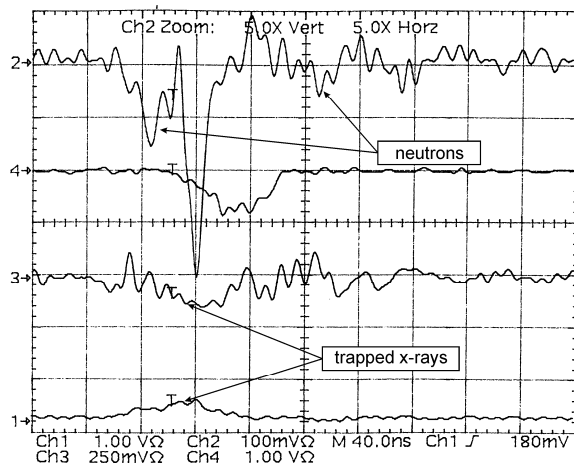


Fig.14. X-rays dynamics in regime 6 for anode with 12 Pd tubes ("coronal" anode),

The implicit assumption that this peaks belong namely to neutrons is supported partially by the next experimental shot (Fig. 13) where the massive piece of paraffin (material with light nucleus for strong neutron scattering) was located between plasma source and PM4, PM2. We observe that namely both peaks on ch.2, located almost symmetrically relative to the main X-rays peak, turn out to be suppressed as a possible result of neutron scattering (also, both main X-rays peaks on chs 4,2 became more narrow). Meanwhile, the neutrons on ch.4 (if to suppose that it is a neutrons) are registered almost by the same manner (as on the oscillogramms for previous shot, Fig.3) by PM4 located very close to paraffin. Next number of shots when paraffin was put in between PM4 and PM2 (and put out after) gave completely the same qualitative picture in the behavior of both maximums. Remark also, that if we have used Pb absorbers (thickness from 3 mm to 5 cm) before PM2, just initial neutron peaks and peaks of neutrons at the end of discharge have been

registered by PM2, meanwhile hard x-rays were absorbed completely.

In whole, the essential part of oscillogramms from the database accumulated contain the specific and correlated in time peaks yet before the strong X-rays burst. Thus, seems that the beginning of interaction of electron beams with Pd anode loaded by deuterium is possible to connect with appearing of some indicators of DD synthesis. As we can conclude from detail TOF analysis the most probably that these peaks are neutron ones, although there is still no obvious answer to the question about mechanism of DD synthesis.

Remark, the neutron peaks of variable intensity due to collisional synthesis at potential well at the stationary stage of discharge are registering practically at each shot, meanwhile, the peaks at initial stage do appear rather often but in more chaotic manner and sometime are not recognizing definitely on the background of other processes. Relation of intensities of first and second peaks presented on Fig.3 above corresponds to the first week of experiments with new anode with three Pd tubes attached to Cu end-on (anode "triple", this anode have been used in the shots presented on Figs.2,3,9,11 discussed above). Modified anode with twelve Pd tubes attached end-on along perimeter of Cu cylindrical basis (anode "coronal") have been used in experiment also (see for example Figs.10,14,15). After some time of work (about 300 shots) we may remark the tendency presented on the Fig.14 (this shot corresponds to the end of the total one year period of experiments, but this is the first shot after the next regular loading of Pd anode by deuterium). We can see that neutron signal from initial stage of discharge is essentially stronger than analogous signal at the end. One more example of the same tendency is given on the next shot with the same anode (Fig.15a). CCD image of correspondent interelectrode space is shown on Fig.15b, where the bright X-rays from Pd anode surface sites are represented also (note, that similar bright anode surface sites at CCD image do appear under transition from regime 1, Fig.2, to regime 2, Fig.3, and followed by appearing of neutron peak at very initial stage of discharge, Fig.3, ch.2). Remind that Pd surface will be four time larger for "coronal" anode, and correspondingly, the transparency for e-beams passage through Pd tubes will be essentially lower than for "triple" anode (Fig.4). Thus, there will be worse conditions for "coronal" anode to form VC and PW similar to ones presented on Figs. 4-6.

In the summing up, we may conclude from the analysis of available experimental data that initial stage of discharge may accompanied also by certain neutron yield which is changing by more random manner from shot to shot in comparison with the yield from synthesis at PW at the second stage of

discharge. The larger Pd surface of “coronal” anode have to provide more essential interaction with electron beam and higher neutron yield at initial stage, correspondently. The latter tendency have been observed at experiment (compare yields on Figs. 2,3 and on Figs.14,15). From the other side, when the “triple” anode interior (see Fig.4) will be fulfilled by deuterium clusters, the neutron yield on second stage will be enhanced in comparison with the yield at initial stage due to periodical collisions of fast ions with clusters inside of correspondent PW (Fig.11).

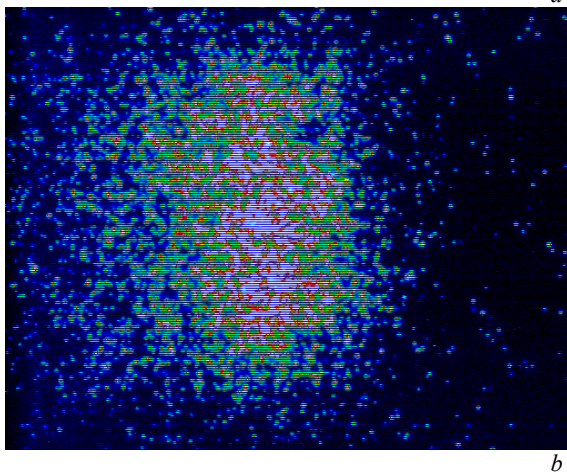
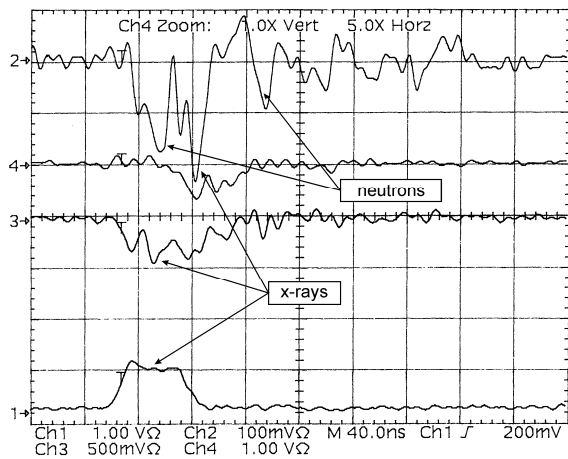


Fig.15. X-rays dynamics in regime 7: (a) Oscillograms of x-rays yield (channels 1 and 3) and neutron yields (channel 2) for next shot with anode with 12 Pd tubes (b) CCD image of corresponding cluster ensemble with random and overlapped “islands” of WDM at Pd anode surface.

At present section we have emphasized namely the experimental TOF results for initial stage. The mechanism of possible DD synthesis under interactions in the system “electron beam – deuterated Pd” is not clear and represents the subject of separate work, nevertheless, we may just to discuss here some hypothetical assumptions. In particular, concerning the possible qualitative

explanations, we may remark that both experiment and PIC simulations illustrate very favourable scaling of the fusion power density $\sim \varphi^2/r_{VC}^4$ (at decreasing of radius r_{VC}) for the chosen IECF scheme [9,10] based on nanosecond vacuum discharge (small plasma volume keeps the total fusion power for cylindrical geometry as $\sim 1/r^2$, approximately). Extrapolation of fusion power density for very small r_{VC} gives that under $r_{VC} \rightarrow 0$ the value of fusion efficiency formally becomes $Q > 1$ at $r_{VC} < 1 \mu m$ (if to include oscillations of ions also) [35]. Thus, the role of micropores or microcracks on loaded Pd anode surface as potential natural microchannels for number of microfusions near the surface at initial stage of discharge has to be the subject of special interest and further analysis. Deuterium loaded anodes surfaces after the big number of shorts at the end of experimental cycle becoming more perturbed and developed, and this effect have to be more pronounced for larger surface values. In a result, seems reasonable that oscillograms related and discussed above (Figs.14,15) are recognising the increased role of the first (in time) neutron peak for “coronal” anode.

Let us discuss some changes in surface morphology of Pd anode tubes along the shots to supplement the information from oscillograms of intensities. In fact, the more detailed study of our Pd anode surface under electronic microscope has recognized the number of various micropores and craters of different sizes as a result of periodic bombardment by electron beams. Energy deposition from e-beam is unevenly along particular Pd tube (see scheme on Fig.4 for illustration), and different parts of anode tubes will be perturbed by different manner. In whole, character of surface is changing essentially from strongly perturbed and melted zones (on the free end of tube which is close to cathode) up to weakly perturbed areas with some separate microcraters (on opposite end of Pd tube near the head-end of Cu part of anode). Even deeply melted and strongly perturbed end of Pd tubes contains a lot of pores of micron sizes (with densities $\sim 10^6 - 10^7 cm^{-2}$). The middle part of tubes is melted more homogeneously, meanwhile, the weakly perturbed part close to Cu head-end is abounded by separate and overlapped craters, and even by well-defined linear chains of craters (general view of particular parts of weakly perturbed Pd surface presented on Figs.16 for different scales). This area contains also micro pores, micro cracks and Pd surface itself is covered by micro particles of different sizes and densities. The total volume of information from scanning electron microscope (SEM) study is rather large and will be discussed in more detail elsewhere. Nevertheless, as an additional illustration, SEM photos with better resolution for couple fragments of surface from the middle part of Pd tube and from



a



b

Fig.16. Surface morphology integrated over experimental activity with deuterium-loaded Pd anode (fragment 1, “coronal” anode; particular part of Pd tube, which is close to Cu head-end of anode, scale 60 μm).

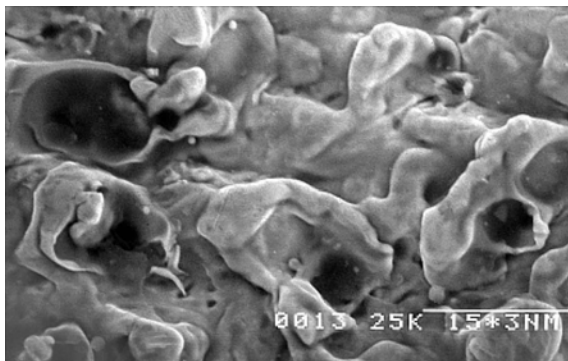


Fig.17. Deuterium-loaded Pd anode surface morphology at the end of vacuum discharge experiments (fragment 2, “coronal” anode, middle part of Pd tube, scale 15 μm).

near Cu head-end area are given on Fig.17 and Fig.18, correspondingly (these are integral pictures over all shots also). At present, we would like to pay attention just on relatively large craters (with the sizes about ~10 μm) at the upper left parts of each last two Figures. The shape and character of

both these craters are differ from other typical traces of interactions of e-beams with Pd anode surface (Fig.16) in vacuum discharge [4,7].

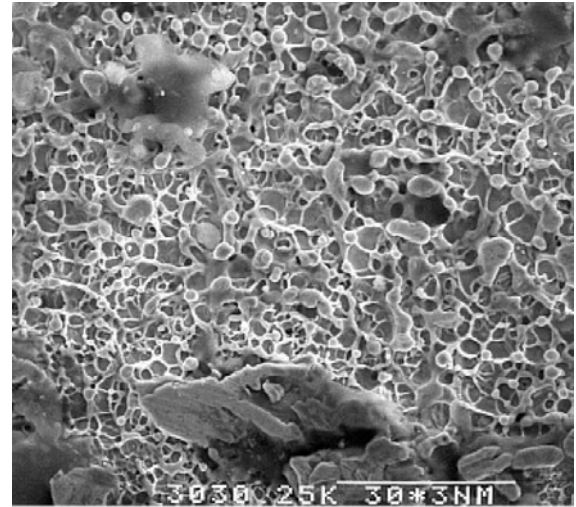


Fig.18. Deuterium-loaded Pd anode surface morphology integrated over all experimental shots of vacuum discharge (fragment 3, “triple” anode; part of Pd tube, which is close to Cu head-end of anode, scale 30 μm).

7. Discussion and concluding remarks.

Generally speaking, DD synthesis discussed above have been realized on the framework of WDM created under interactions of electron beams coming from cathode with deuterium - loaded Pd anode. In one case (on the second stage of discharge), anode erosion and ionization of part of deuterium atoms provides appearing of D^+ at the edge of deep potential well. Their further acceleration and head-on collisions at PW followed by DD synthesis and neutron yield related. Simultaneously, anode erosion partially provides the fulfillment of PW by deuterium clusters (dense interelectrode ensembles). Thus, in addition to particle-particle syntheses, the channel of DD synthesis like D^+ - deuterium cluster have to be considered since VC is located sometimes inside of a “cloud” of burning “dust” nucleated (or ejected) from anode material (this effect still has not been included in PIC modeling). The total trapping of fast ions observed in experiment [9] would increase the neutron yield essentially. A related example of a self-organized cluster ensemble was shown in Fig.11. This shot and ensemble registered by CCD is similar to ensemble presented on Figure 6 in [9] and manifests a high level of pulsating neutron yield also ($\sim 10^7/4\pi$). Fast ions and even few keV hard x-rays are trapped there, and just neutrons are leaving these sorts of interelectrode ensembles (prototype of complex plasma microreactor). Note, that appearing of collisions of fast ions with deuterium clusters target inside of PW will increase

efficiency at the beginning, but further growing of the role of this channel of DD reaction will restrict efficiency on the level of $Q_{lim} \sim 0.1 - 0.02$.

We remark that the frequency of neutron yield oscillations in vacuum discharge [9] is about $\approx 77-83$ MHz, and coincides with extrapolation of POPS expressions [14] to A-C geometry and PW depth. It seems that this agreement is not accidental and confirms the similarity to POPS physics during some MFI regimes of nanoseconds vacuum discharge. Last one might provide at the collapse moments the ion densities $n_{i\ max} \sim 10^{21} - 10^{23}$ cm^{-3} and compression of ion subsystem up to $\sim 1-10$ μm (for similar POPS conditions the calculated value is $n_{i\ max} \sim 10^{19}$ cm^{-3} , and r_{min} at the compression moment is ~ 60 microns [13]). The miniature size ($r_{VC} \sim 0.1$ cm) as well as rather deep PW (like $\varphi \approx 50-55$ keV) correspond to the extremely high fusion power densities ($\sim \varphi^2/r_{VC}^4$) demonstrated at the present moment by our system of table-top IECF [8-10]. On the other hand, rather small absolute “reactor” volume, nanosecond scale of T_{pulse} , and losses restrict the total neutron yield, but keep is acceptable for some modern applications. In whole, the trapping of fast ions by interelectrode ensembles of clusters, especially noticeable under effects of ensemble self-organizations represents additional opportunities as well as some complexity for “reactor” optimization. Since for IECF systems $P_{fusion} \sim I^2$ and $Q_{fusion} \sim I$, scaling by current and changing the values of Q for different regimes of discharge need additional analysis also.

The physics of initial stage, when WDM created under beginning of e-beam interaction with Pd loaded anode, and mechanism of DD synthesis observed (Figs.3,14,15) are not so clear as for the stage of VC and PW formation, described in detail by PIC simulations. Meanwhile, namely during recent few years the special interest to the systems like “electron beam – deuterium loaded Pd” have increased and some experimental data and related models have appeared. In particular, the model of stimulation of DD reaction by electron beams at loaded Pd surface have been developed [20]. This is one of the number of models which are developing to explain the possible so-called low energy nuclear reactions (LENR) at deuterium- loaded Pd (see review [36]). Recent theoretical study [37] and calculations [20] have shown that the excitation of the hydrogen subsystem (which leads to desorption of H,D) as a result of the electron bombardment is stipulated by the generation of plasma oscillations in the crystalline lattice, which are localized preferentially in the vicinity of hydrogen (deuterium) atoms. This process results in the electron-density oscillations and in the appearance of strong electric fields ($\sim 10^8$ V/cm) in the volume and on the plane of the hydride. The oscillation scales are being commensurable with the lattice parameter (typically, $\sim 0.3-0.4$ nm). As a result, as

authors supposed, the correspondent acceleration of D^+ could lead to enhance of DD-reaction yield even for a low energy deuteride excitation.

Any LENR models are still under the questions, but well-defined experiments related represent the great interest. In particular, statistically significant emissions of DD-reaction products (3 MeV protons and 1 MeV tritons), as well as high energy alpha particles have been registered under electron beam stimulation of the D-desorption from Pd/PdO:Dx targets [38]. Electron beam (energy 30 keV, current < 1 μA) bombardment is accompanied by formation of numerical pores (from Pd through the PdO) with diameters in the range of 100–2000 nm while the surface which has not been subjected to the e-beam bombardment shows smooth PdO structure. Underline, the larger pores (> 350 nm) have not been found in the reference Pd/PdO:Hx samples after electron beam. Large craters ($\sim 10-12$ μm) are also have appeared only at the Pd/PdO:Dx surface after electron beam treatment. Authors of [38] conclude, that formation of large craters at the deuterium loaded target indicates to high energy density (energy concentration) at some specific sites of the Pd/PdO surface through which the energy release is occurred, and these sites can show enhanced nuclear emission.

Coming back to our surface morphology data obtained after discharge, underline, that craters presented on Fig. 17 are very similar to large craters ($\sim 10-12$ μm) from recent experiments mentioned above [38]. We might assume that besides of rather usual craters (due to interaction of electron micro beams with anode under typical energy introduced $\sim 10^4$ J/g, Fig.16) some of the craters on the Pd anode surface created at vacuum discharge (Figs.17,18) have to be interpreted as manifestation of specific *anode ectons of nuclear origin* (just cathode ectons [6,7] are especially well-known and studied at present time). It is not excluded, that not only the usual anode erosion, but mass ejection assisted by anode ectons which is originated from surface DD microsynthesis provides also the creation of namely dense interelectrode ensembles. However, the available stage of study does not allow us to share properly the possible standard explosive evaporation of anode material by electron beam [7] (or any superheating effects under fast energy deposition [39]) from more exciting scenario of triggering any nuclear reactions on deuterium- loaded Pd anode surface by electron beams at the process of vacuum discharge. But if these kind of anode ectons do exist, in fact, their nature could be related with effects of electron beam – loaded Pd surface micro pores interactions at initial stage of discharge (“classical” physics like micro-scale system of IECF at $r_{VC} \rightarrow 0$ [35]) or could be related with some LENR effects stimulated by electron beam like discussed at

[20,37,38]. The overlapping of both mechanisms is not excluded also, and have to be a subject of further study as well as analysis and verification of other mechanisms, like recognizing now the opportunity of laser-driven (or beam-driven) microfusion in ultra-dense deuterium clusters as dislocation cores at host lattice [21,22]. Interesting, that LENR effects were mentioned by Rick Nebel recently [40] as a part of spinoffs and applications of IECF also.

Remark, that “rechargeable” (periodically loaded by deuterium) Pd anode is specific and complex target for electron beams along discharge, so anode surface morphology, different features of micro sites and nature of craters have to be studied further in more detail. Note, that related craters (like on Fig.18) sometime can appear and spontaneously also (without any electron beam stimulation), for example, the microcraters which have been observed under Pd/D electrolysis co-deposition process [41] or at ultrasonically-excited electrolysis experiments [42]. Meanwhile, the possible induced number of craters at the presence of electron beams might be essentially higher. From the other side, we have to keep in mind that the foreign inclusions (phase insertions) with the mass density different from the basic target material are able to initiate cratering as well as the geometrical perturbations of the irradiated surface relief [43]. The craters induced by foreign inclusions are almost indistinguishable in form and size from the induced by surface perturbations craters [43,44]. Thus, reliable analysis of crater formation mechanisms of deuterium-loaded Pd anode surface represents rather complex and non-trivial task.

At the present moment, we may conclude that 2,45 MeV neutrons have been observed at the time-of-flight study from DD synthesis which is realizing probably by different manner at initial and stationary stages of vacuum discharge within just 50 nsec [8-10]. The physics of collisional DD synthesis at small-scale low energy vacuum discharge with deuterium-loaded Pd anodes have been clarified definitely, but the number of questions which are answered do produce a new ones. Thus, further experimental study as well as theoretical analysis and computer modelling of new effects, especially provided by e-beam interaction with deuterium-loaded Pd anode at initial stage of discharge are reasonable.

Acknowledgments.

We would like to thank G.A. Mesyats, A. A. Rukhadze, V. E. Fortov, N.A. Ratakhin and S.Barengolts for interest and partial support of the work as well as for stimulating discussions on different stages. One of us (Yu.K) appreciates greatly the long-time collaboration and scientific exchange with M.Skowronek, G.Maynard, Y.Vitel

and J.Dufty, and their essential participating especially at the beginning of the work presented. We express gratitude to E.Bocharova for technical assistance under manuscript preparation.

References:

1. M Koenig A Benuzzi-Mounaix¹, A Ravasio et al Plasma Phys. Control. Fusion **47**, B441 (2005)
2. R.W.Lee.Warm Dense Matter: a Perspective. Int. Workshop on Warm Dense Matter, Porquerolles, France (2007) <http://www.luli.polytechnique.fr/wdm07/program.html>
3. T. Ditmire, J. Zweiback, V.P.Yanovsky, T.E.Cowan, G.Hays, and K.B.Warton. Nature (London) **398**, 489 (1999); J.Zweiback, R.A.Smith, T.E.Cowan et al Phys. Rev.Lett. **84**, 634 (2000).
4. G.A.Mesyats, D.I.Proskurovsky. Pulsed Electrical Discharge in Vacuum (Springer-Verlag, Berlin Heidelberg,1989).
5. R.L.Boxman, S.Goldman and A.Greenwood. IEEE Trans.Plasma Sciences. **25**, 1174 (1997).
6. G.A.Mesyats. JETPh Lett. **57**, n.2, 88(1993).
7. G.A.Mesyats. Cathode Phenomena in a Vacuum Discharge: The breakdown, the spark, and the arc (Nauka,Moscow, 2000).
8. Yu.K. Kurilenkov, M. Skowronek, G.Louvet, A.A. Rukhadze, J.Dufty. Journal de Physique IV **10**, Pr5-409 (2000); Yu.K. Kurilenkov, M. Skowronek. Journal of Physics (Pramana, Indian Acad.Sci.) **61**, 1188 (2003).
9. Yu.K. Kurilenkov, M.Skowronek and J. Dufty.J.Phys. A: Math & General (IOP) **39**, 4375 (2006); Yu.K. Kurilenkov. Int. Workshop on Warm Dense Matter, Porquerolles, France (2007) <http://www.luli.polytechnique.fr/wdm07/program.html>
10. Yu. K. Kurilenkov, M.Skowronek, V.P.Tarakahov et al. *J.Phys. A: Math &Theor* **42**, 214041 (2009).
11. O.Lavrent'ev. Ukrainian Phys. Journ. **8** 440 (1963; B.D.Bondarenko. Uspekhi Phys.Nauk **171**, 886 (2001).
12. W.C. Elmore et al. Phys. Fluids **2** 239 (1959); R.L.Hirsch J.Appl. Phys. **38**, 4522 (1967).
12. R.A. Nebel and D.C. Barnes Fusion Technology **38**, 28 (1998); R. A. Nebel and D. C. Barnes Phys. Plasmas **5**, 2498 (1998). D C. Barnes, M. M. Schauer et a. Phys. Plasmas **7**, 1693 (2000).
13. R. A. Nebel et al Phys. Plasmas **12**, 012701 (2005); J.Park, R.Nebel et al Phys. Plasmas **12** 056315 (2005);
14. J. Park, R. A. Nebel, R. Aragonéz, et al. Innovative Confinement Concepts Workshop

- (USA, Texas, Austin, February 13-16, 2006) Proceedings
<http://icc2006.ph.utexas.edu/proceedings.php>
15. A. Pundt and R. Kirchheim. Annual Review of Materials Research **36**, 555-608 (2006)
 16. B.J.Heuser and J.King. J.Alloys and Compounds **261**, 225 (1997)
 17. B.J. Heuser and S.J. King Met. & Material Transaction **A29**, 1594 (1998).
 18. A. Lipson, B.J.Heuser, C.Castano et al. Phys.Rev. B **72**, 212507 (2005).
 19. N.W.Aschroft. Journal of Low Temperature Physics, **139**, Nos. 5/6 711 (2005).
 20. I. P. Chernov, Yu.M.Koroteev et al. Doklady Akademii Nauk, **420**, 758 (2008); A. Lipson et al, Proceedings of the 8th International Workshop on Anomalies in Hydrogen/Deuterium Loaded Metals, Sicily, Italy (ISCMNS, 2008) pp. 182-203.
 21. S.Badei, P.U.Andersson, L.Holmlid. Int.J.Hydrogen Energy **34**, 487 (2009).
 22. S.Badei, P.U.Andersson, L.Holmlid. Laser&ParticleBeams **28**, 313 (2010).
 23. R.A.Lerche, D.W.Phillion, and G.L.Tietbohl. Rev.Sci.Instrum **66**, 933 (1995).
 24. V.P.Tarakanov. User's Manual for Code KARAT (BRA Inc., Va, USA, 1992).
 25. Yu.K.Bobrov, V.P.Bistrov and A.A.Rukhadze. Short Communications (Physics), Lebedev Phys.Inst N7 23 (2005).
 26. A.E.Dubinov, I.Yu.Kornilova and V.D.Selemer. *Uspekhi Phys.Nauk* **172**, 1225 (2002).
 27. S.A.Barengol'ts, G.A.Mesyats E.A. Perel'shtein. *JETPh* **91**,1176 (2000).
 28. A.A.Plyutto. *JETPh* **12**, 1106 (1960); *Journ.Techn.Physics* **40**, 2534 (1970).
 29. Yu. K. Kurilenkov, V.P.Tarakanov and S.Yu.Gus'kov. Plasma Physics Reports **36**, No.13, 1227 (2010).
 30. V. S. Letokhov. *Sov. Phys. JETP* **26** no 4, 835 (1968).
 31. D. Wiersma and A. Lagendijk. *Phys. Rev.E*, **54** no. 4, 4256 (1996); *Physics World* **10** no.1, 33 (1997).
 32. M. P.van Albada, B.A. van Tiggen, Ad Lagendijk, and A.Tip. *Phys. Rev. Lett*, **66**, 3132 (1991).
 33. Yu.K. Kurilenkov and M.Skowronek *Plasma Physics Reports*, **36**, No.13 1219 (2010).
 34. M.Onishi, K.H.Sato et al. *Nuclear Fusion* **37**, 611 (1997).
 35. S.Yu.Gus'kov and Yu.K.Kurilenkov. *JETPh Lett*., to be submitted (2010)
 36. B.Barnhart et al. Defense Analysis Report DIA -08-0911-003, November 2009.
 37. V. Silikin, I.Chernov et al, Phys.Rev.B, **76**, 245105 (2007).
 38. A. G. Lipson, I. P. Chernov et al. Doklady RAN **425** № 5 621 (2009); A. G. Lipson et al. 15th Int.Conf. on Condense Matter Nuclear Physics, Rome, 2009.
 39. G. E. Norman, V. V. Stegailov,, and A. A. Valuev. *Contrib. Plasma Phys.* **43**, No. 5-6, 384 (2003)
 40. R.Nebel. 11th United States/Japan Workshop on Inertial Electrostatic Fusion (USA, Wisconsin, Madison, October 12-13, 2009) Summary.
 41. P.A. Mosier-Boss, S. Szpak, F. E. Gordon and L.P.G. Forsley. *Naturwissenschaften* **96**, 135 (2009); S. Szpak et al 14th Int. Conf. on Condensed Matter Nuclear Science, Washington, DC (2008).
 42. I. Dardik, T. Zilov, H. Branover et al. 14th International Conference on Condensed Matter Nuclear Science, Proceedings (USA, Washington DC, 2008) p.17.
 43. A.Y. Leyvi, A.E. Mayer, V.A. Shulov, and A.P. Yalovets // 9th Conf on Material Modification with Particle Beams and Plasma Flows, Proceedings (Russia, Tomsk 2008) p.113.
 44. N.B.Volkov, K.A.Talala, A.E. Mayer and A.P. Yalovets. *Technical Physics Letters* **32**, 434 (2006).

PLASMA-ASSISTED REACTION OF HETEROGENEOUS AL-H₂O MIXTURE IN HIGH-SPEED SWIRL FLOW

*Klimov A., Bityurin V., Grigorenko A., Efimov A.V., Kutuzov D.S.,
Tolkunov B.N., Tsymbal A.A., Polyakov L.B.*

Joint Institute of High Temperature RAS
Izhorskaya 13/19, Moscow, 127415, Russia

Abstract. There is considerable interest to creation of new alternative power sources today [1]. The present work is devoted to consideration of design and operation of a high-effective hydrogen generator based on Al-H₂O chemical reaction assisted by a non-equilibrium plasmoid. This work is the continuation of the previous one [2]. The rate of this reaction may be increased up to factor 10³ by non-equilibrium plasma. Active excited particles, radicals and ions are created by a non-equilibrium electrical discharge in swirl flow in the plasma-chemical reactor (PCR). It is well-known that these particles can accelerate a creation of the chains in a reaction zone. High gas temperature in a plasma zone accelerates this reaction rate also. The main goal of this work is a design, manufacture and testing of the demo- PCR with hydrogen mass flow about of 0.1- 1G/s. The following tasks are studied in these experiments:

1. Study of the optimal parameters of a swirl flow in the PCR (component mass flow rates, flow velocity distribution, gas temperature distribution and so on).
2. Study of a stable electric discharge regimes in swirl gas flow. Optimization of power supply electric parameters.
3. Measurement of plasma parameters in the PCR.
4. Chemical analysis of the final species in this PCR.

The parameters and characteristics of electric discharge, plasma and swirl flow are measured in this work. Minimal energy balance of hydrogen molecule creation will be measured in this PCR namely.

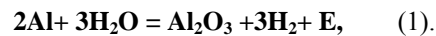
Nomenclature

PCR	= plasma-chemical reactor
I	= electric discharge current
V	= electric discharge voltage
F	= HF frequency
N _d	= power input in plasma
N _e	=electron concentration
M	=Mach number
V _{af}	= airflow velocity
P _{st}	=static pressure
T _g	= gas temperature
T _R	=rotation temperature
T _V	=vibration temperature
T*	=electron excitation temperature
T _b	=black body temperature
E/P	=relative electric field
j ² /P ²	=relative current density
N/V	=specific power input in plasma
Q	=mass flow rate

Introduction

Today there are many discussions about a low-coast aluminum fuel for electric power production [1-3]. This method is named aluminum-

hydrogen power production and based on the following chemical reaction:



where E~15MJ/kg Al- energy release

However the characteristic rate of this heterogeneous reaction (aluminum powder + water steam) is rather small. So, it is important to study *a plasma-assisted oxidation* of Al powder in water steam in detail to accelerate this reaction. *This is a main task of this work.* The rate of this reaction may be increased up to factor 10³ by non-equilibrium plasma. Active excited particles, radicals and ions are created by a non-equilibrium electrical discharge in swirl flow inside plasma-chemical reactor (PCR). It is well-known that these particles can accelerate of additional chain creation in a reaction zone. High gas temperature in a plasma zone accelerates this reaction rate also. Note that there are active dusty (cluster) charged particles in a reaction zone of this PCR. Non- ideal plasma is created in this reactor (parameter

$$\gamma = Ze^2 / (N_d)^{-1/3} kT_g > 1).$$

High amplitude local electric field is created near a surface of this charged dusty (cluster) particle. So, traditional chemical kinetics may be wrong (uncorrected) near surfaces of these particles. So, measurement of a local electric potential in this heterogeneous plasma is very important task also.

The second important task of this work is to study of the properties and parameters of a

heterogeneous plasma created by pulsed repetitive HF discharge (or DC discharge) in swirl flow. Hot ionized hydrogen flow ($T_g \sim 3000\text{K}$, $N_e/N_a \sim 10^{-2}$) obtained in this PCR will be used in MHD power generator in future. Design of this power generator and its operation are discussed in the work [9].

I. Experimental Setup

Scheme of the experimental setup is shown in the fig.1. The general view of this setup is shown in the fig.2. The PCR is made of quartz tube diameter

60-80 mm. Tube's thickness is about 3-5 mm. Swirl gas flow (or non-swirl one) is created by tangential injector (4) and axial injector (3) in this reactor. Aluminum powder is injected through tube electrode (2). This powder is pushed by argon jet in a mixer-container. Swirl argon flow is created in this reactor by swirl generator (3). It is possible to control of a vortex parameter $S = Q_\tau/Q_z$, (where Q_τ – tangential flow mass rate, Q_z – axial mass flow rate) in this experiment. Note, that this reactor design is optimal one for a separation of hydrogen and Al_2O_3 by inertial body force. Hydrogen is evacuated from

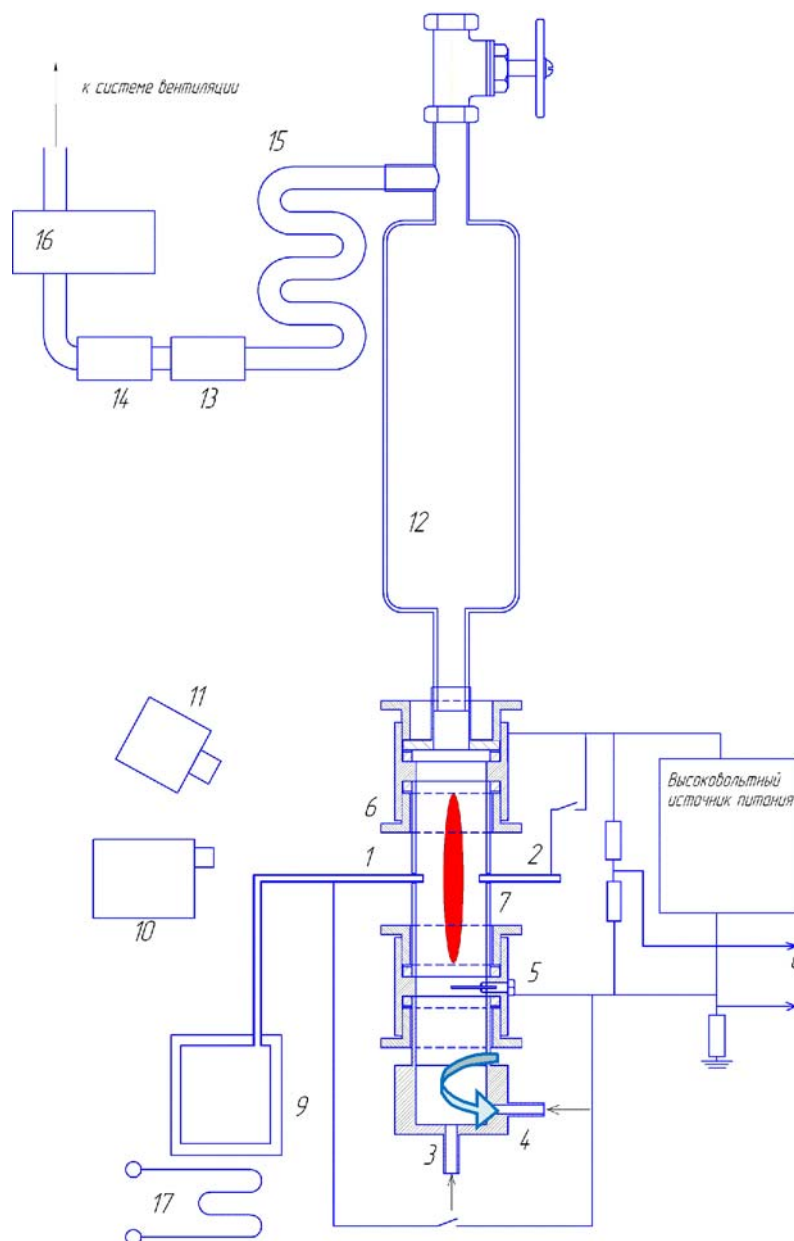


Figure 1. Scheme of the PCR. 1,2- tube electrodes - injectors for $\text{H}_2\text{O}+\text{Al}$, 3,4- nozzles – injectors for argon flow, 5- tungsten electrode; 6- reactor chamber; 7- quartz tube; 8-oscilloscope; 9- H_2O steam generator; 10- spectrometer AvaSpec 2048; 11-CCD camera Citius; 12- gas silencing chamber; 13- gas filter; 14-chemical sensor; 15- water cooling tube; 16-pump; 17-electric heater



Figure 2. General view of the experimental set up. 1,2- tube electrodes - injectors for H_2O+Al , 3,4- nozzles – injectors for argon flow, 5-reactor chamber; 6- quartz tube; 7-water steam generator; 8- gas silence chamber; 9- water cooling tube; 10- electric heater

reactor by thin quartz tube (chemical probe) arranged near axis. Both a vertical electric discharge and horizontal electric discharge are created in this set up. Hydrogen mass flow rate is measured by the gas analyzer AVP-01G. Water steam is generated by an electric heater (9, 17). Parameters of an electric discharge is measured by the voltage probe Tektronix P-6015, current probe Tektronix and oscilloscope. Optical spectra of a plasma formation are recorded by the spectrometer AvaSpec 2048($\lambda=200-800nm$)

A heterogeneous plasmoid in gas flow is recorded by the high- speed camera Citius. The following power supplies are used in this work: DC power supply (8kV, 2Amp) and Tesla's coil HF generator ($F= 450\text{ kHz}$, $N_{HF}=1-10\text{ kW}$, pulse duration- $10 \div 10000\mu s$, pulse repetitive frequency- $10-10^4\text{ Hz}$). Parameters of an electric discharge is measured by voltage probe Tektronix P-6082, current probe Tektronix and oscilloscope.

II. Main Experimental Results

The physical processes, plasma and discharge parameters in a heterogeneous plasma are studied in this work. The composition of output gas flow and the final species concentrations are measured in this PCR.

The typical picture of a longitudinal plasmoid in swirl flow is shown in fig.3, 4. One can see the different locations of hydroxyl- hydrogen molecules (red-violet kernel near vortex axis) and AlO molecules (thin blue halo around this axis) in this plasmoid, fig.4.

The typical optical spectrum of heterogeneous plasma is shown in the fig.5. One can see that there are the atomic optical lines (Al , H , Ar , electrode's metal atoms), the molecular bands (OH , AlO , O) and the continuous spectrum in this figure. Note that a continuous spectrum is connected with a hot dusty particle radiation. The obtained spectra are processed. The measured rotation temperature in



Figure 3. Plasma chemical reactor with pulsed repetitive HF discharge in H₂O-Al mixture

plasma is about of $T_R \sim 2000-3000K$, atom excitation temperature $T^* \sim 3000K$, black body temperature $T_b \sim 3500K$.

The value N_e is estimated by a measured plasma conductivity σ in our experiment. The value σ is estimated by voltage V_d and current I_d measured between the electrodes. The diameter D and the length L of plasma formation are measured from the obtained high-speed frames. The typical value σ is about $20 \text{ Ohm}^{-1}\text{m}^{-1}$. The typical electron concentration in plasma is about of $N_e = 10^{14} \text{ cm}^{-3}$.

The analysis of the final species of output gas flow in PCR is fulfilled. It is obtained that the main dusty particles are the fine-dispersed Al_2O_3 particles and fine-dispersed Al particles (non-reacted powder). The typical average diameter of this dusty particle is about 1μ or less. Note that the typical average diameter of the initial aluminum particles is about of 100μ .

Hydrogen is evacuated from this reactor by tube chemical probe (15, fig.1). This gas sample is analyzed by a chromatograph. The maximal H₂ concentration measured in this experiment is about

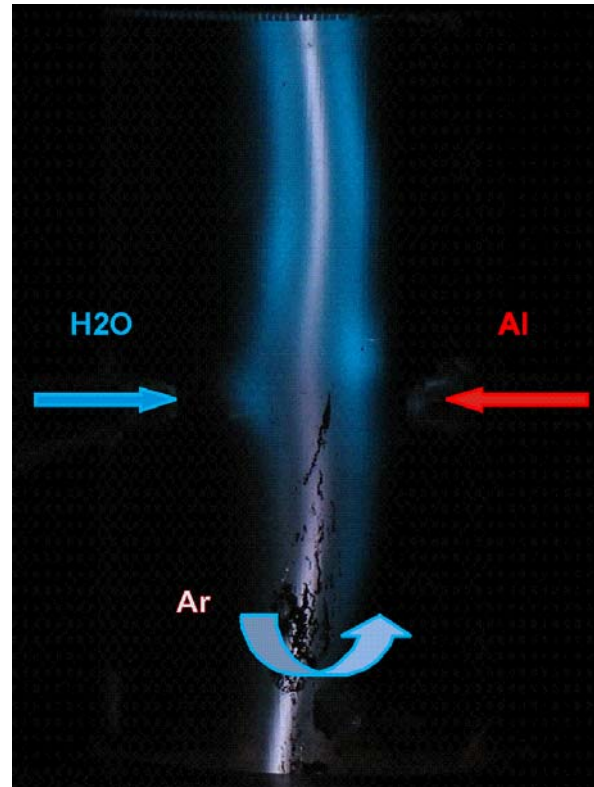


Figure 4. The typical heterogeneous plasma formation created by vertical electric discharge in swirl flow. DC current-1Amp, DC voltage -200V, $V_f \sim 10\text{m/s}$, $P_{st} \sim 1 \text{ Bar}$, $Q_{AL} \sim 0.05\text{G/s}$, $Q_{H2O} \sim 0.3\text{G/s}$

20-50%. The hydrogen mass flow rate measured by a gas analyzer in this demo- reactor is about of $0,1\text{G/sec}$. Plasma parameters such as electron concentration, conductivity, power input are measured in this work.

It is revealed that there are positive charged dusty ions AlO and Al_2O_3 in cylindrical plasma formation, fig.3.

There is considerable sedimentation of these ions in the cathode electrode namely. So, one can conclude that there is localization of the negative charged ions OH^- near vortex axis in the PCR. The positive ions Al_2O_3^+ (AlO^+) are concentrated in plasma halo around plasma kernel. In a result it a double electric layer is created in this plasma formation. High positive potential about several kV is measured near external boundary of this plasmoid. This double electric layer stabilizes this plasmoid considerably. Note that this radial gradient electric field can change the plasma-chemical kinetics considerably also. This question will be studied in detail in future experiments.

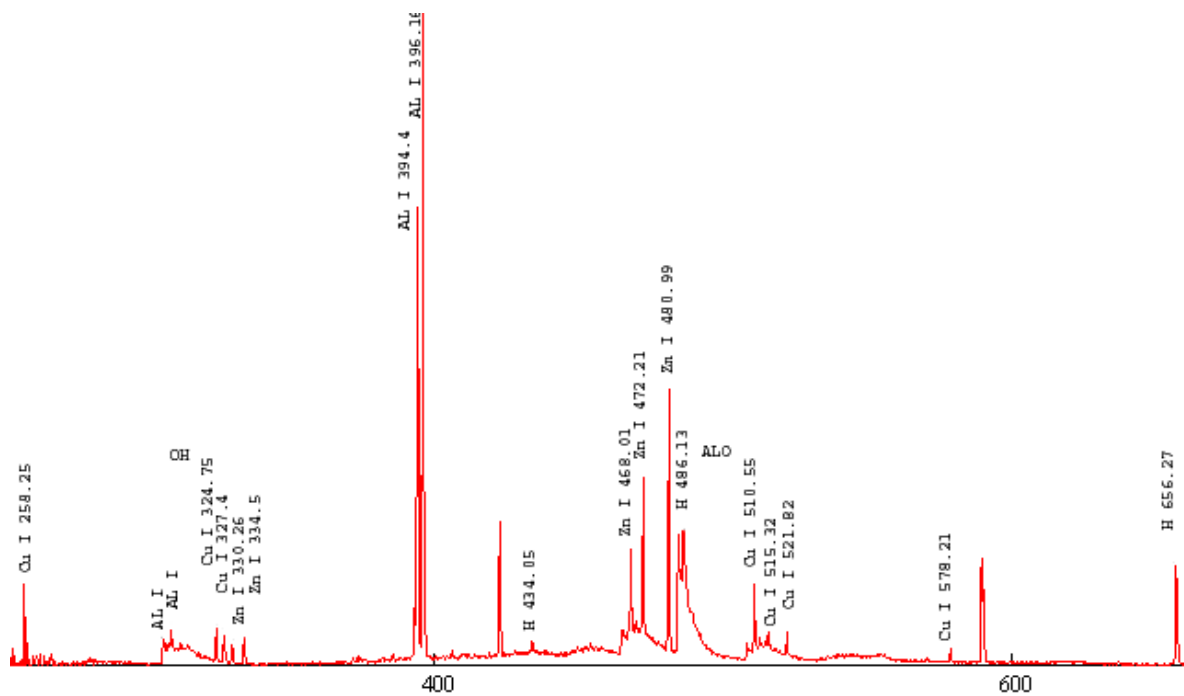


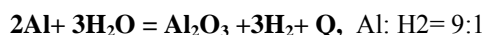
Figure 5. The typical optical spectrum of a plasma formation created by HF discharge in the PCR

III. Completeness of plasma assisted aluminium oxidation

It is revealed that completeness of a reaction in this PCR is very high about of 90-95%. Really the typical experimental conditions are the following:

- Electrode arrangement vertical
- Electrode material Al
- Water steam injection through electrode
- Al powder injection through electrode
- Testing gas for swirl flow Ar
 - DC voltage 800 V
 - DC current 2 Amp
 - Gas temperature $T_g \sim 3500K$
 - Electron concentration $N_e \sim 10^{14} \text{ cm}^{-3}$
 - Al mass flow rate 0.3 G/sec
 - H₂O mass flow rate 0.3 G/sec
 - Hydrogen mass flow rate ~0.04 G/sec

The hydrogen mass flow rate may be estimated by the following relations:



So, theoretical value Al: H₂ = 0.3G/s: 0.033G/s is obtained from measured Al flow mass rate. Experimental value of hydrogen mass flow rate is about Al: H₂ = 0.3G/s: 0.04G/s. Note that measured hydrogen mass flow rate by water steam dissociation in plasma is about of ~0,01G/s. So,

completeness of the oxidation reaction is very high about 95%

Some remarks about acceleration of this reaction by plasma. Note that the typical residence time of reagents in the PCR is about

$$t_r \sim L/V_{af} = 0.1\text{m}/(30\text{m/s}) \sim 300\mu\text{s},$$

where V_{af} - typical velocity of gas mixture flow in PCR, L- reaction zone dimension.

The typical chemical reaction time is about $t_{ch} \sim 10 \text{ ms}$ at the experimental conditions closed to our ones [10]. So, there is considerable acceleration of this reaction by plasma $t_{ch}/t_r \sim 30$.

IV. Conclusion

1. Stable plasma-assisted reaction of Al-H₂O mixture is obtained in our experiment.
2. High completeness of Al oxidation in water steam at plasma assistance is realized in this experiment
3. High electron concentration $N_e \sim 10^{14} \text{ cm}^{-3}$ is obtained in Al plume in H₂O-Ar flow at plasma assistance
4. High temperature $T_g \sim 3000K$ is measured in Al-H₂O plume in the PCR
5. Al-H₂O chemical reaction assisted by HF plasma is studied in this work. Considerable acceleration of this chemical reaction is obtained in this experiment.
6. Heterogeneous plasmoid with strong double electric layer is created in H₂O-Armixture in

swirl flow. The typical value of charged plasmoid's electric potential is about several kV.

References

1. Sheindlin A.E., Zhuk A.Z., et.al., Using of Low-Coast Aluminium in Electric Energy production, J. Power Sources, 2006
2. Sheyndlin A. E., Al-H₂ power stations, JIHT RAS, M., 2007, P.139
3. Klimov A., Bityurin V., Grigorenko A., Kutlaliyev V., Moralev I., Tolkunov B, 47th AIAA Aerospace Sciences Meeting Including The New Horizons Forum and Aerospace Exposition, Plasma Assisted Combustion of Heterogeneous Fuel in High-Speed Airflow, AIAA Paper AIAA-2009-1411-250, P.11
4. Klimov A., Bityurin V., Chinnov V., Non-Premixed Plasma-Assisted Combustion of Hydrocarbon Fuel in High-Speed Airflow, Paper 2006-0670. Proc. 44th AIAA Aerospace Sciences Meeting & Exhibit, 9-13 January 2006, Reno, NV, P.10
5. Potapkin B., Rusanov V., Plasma Catalysis, Low Temperature Plasma. Encyclopaedia. M.RAS., 2006, P.4-36
6. Combustion Laws, 2006, Moscow, RAS IVTAN, P.352
7. Klimov A., Moralev I., et.al., Non-Premixed Plasma-Assisted Combustion, AIAA Paper, Proc. 45th AIAA Conf. Reno NV, 7-11 Jan 2007, P.11
8. Miller T.F., Herr J.D., Green Rocket Propulsion by Reaction Al and Mg and Water, AIAA Paper 2004-4037, P.10
9. Bityurin V., Ivanov V., et.all., Assessment of Characteristics of MHD Generators on Aluminum Oxidation Products, AIAA Paper 2011-1074, P.12

INFLUENCE OF GASDYNAMIC PROCESSES ON STRUCTURE AND BREAKDOWN LEVELS OF MW DISCHARGE INITIATED BY LASER SPARK

*S. Afanas'ev, V. Brovkin, Yu. Kolesnichenko, and I. Mashek**

Joint Institute for High Temperatures RAS, Moscow

*Saint-Petersburg State University, Saint-Petersburg

Abstract. Experimental results on initiation of MW discharge by means of laser spark in free space are presented. Ignition thresholds of laser initiated MW discharge under different air pressure and wide diapason of time delays of MW pulse relative laser one are measured. Peculiarities of MW discharge structure formation on laser spark itself and on gasdynamic disturbances created by laser spark at later stages are investigated. Under the reduced air pressure the possibility of MW discharge ignition by application of low-power laser beam is demonstrated. Also presented are some results of MW beam – laser spark interaction modeling.

Microwave (MW) discharge in the free space is a phenomenon of considerable interest, which can be used in numerous practical applications [1, 2]. However, the MW discharge initiation in air at pressures close to atmospheric requires a rather high level of electric field strength, which is not provided by the existing devices. For this reason, experiments are usually carried out using various initiators in the pathway of MW propagation [3]. One possible means of initiating MW discharge employs laser radiation [4]. This is a promising method for the distant initiation of MW discharge, which allows the zone of energy deposition to be localized (under certain conditions), the discharge to be redirected, and the gas breakdown threshold to be significantly reduced.

This work reports the results of an experimental investigation of the initial stage of formation and threshold characteristics of MW discharge initiated by laser spark in air at atmospheric pressure. We also present data on attempts at the MW discharge initiation at reduced pressures by laser radiation without spark generation.

The experiments were performed using a linearly polarized MW in the centimeter wavelength range ($\lambda_{MW} = 2.3$ cm) with an electric field amplitude of $E \geq 5$ kV/cm, which was emitted via a horn into a vacuum chamber and focused by a metal mirror to a region with dimensions on the order of $(\lambda_{MW}/2)$. The duration of MW pulses τ_{MW} did not exceed $4\mu\text{s}$ and their repetition rate was 1 Hz. The beam of second harmonic radiation of a Nd:YAG laser ($\lambda = 532$ nm) with a pulse duration of $\tau_{las} = 10$ ns was oriented along the electric field vector in the MW and introduced into the chamber with the aid of a mirror via a quartz window. The laser pulse energy could be varied from 50 to 320 mJ, which was sufficient to generate laser spark (LS) in air at atmospheric

pressure. The laser beam was focused by a lens with a focal distance of $f = 45$ mm into a region of the main lobe of the MW directivity pattern. The axes and central zones of the focused laser and MW beams spatially coincided to within 2 mm. The time T_{del} of the MW pulse delay with respect to the laser pulse could be varied within broad limits.

The appearance of discharge was detected visually and with the aid of a photoelectron multiplier and a high speed camera (PCO.Sensicam) with exposure times within 0.5–1000 μs . The MW discharge in air at atmospheric pressure was stably initiated, being either directly induced by LS or formed in the excited gas medium (strongly perturbed by LS) for a rather long time after termination of the laser pulse. Figure 1 presents typical photographs of the LS initiated MW discharge, which were obtained at various delays of the MW pulse relative to the laser pulse. The bright vertical band on these images results from the action of LS flashing on the CCD matrix.

The LS size was about 6×3 mm and the glow time (at a 0.5 maximum level) did not exceed 500 ns. At small times of the MW pulse delay relative to the laser pulse, the MW discharge channel developed directly from the LS region, predominantly from its top or bottom part. As the delay time increased, the MW discharge region exhibited considerable growth. For a delay time within several dozen microseconds, concentric discharge channels were frequently formed. With a further increase in the delay, the discharge region shifted toward the MW source, and sinusoidal channels were observed [5]. For the given level of field strength, the LS initiation of discharge took place for delays up to ~ 1 ms. The average velocity of discharge channels under these conditions was $\sim (1-5) \times 10^5$ cm/s..

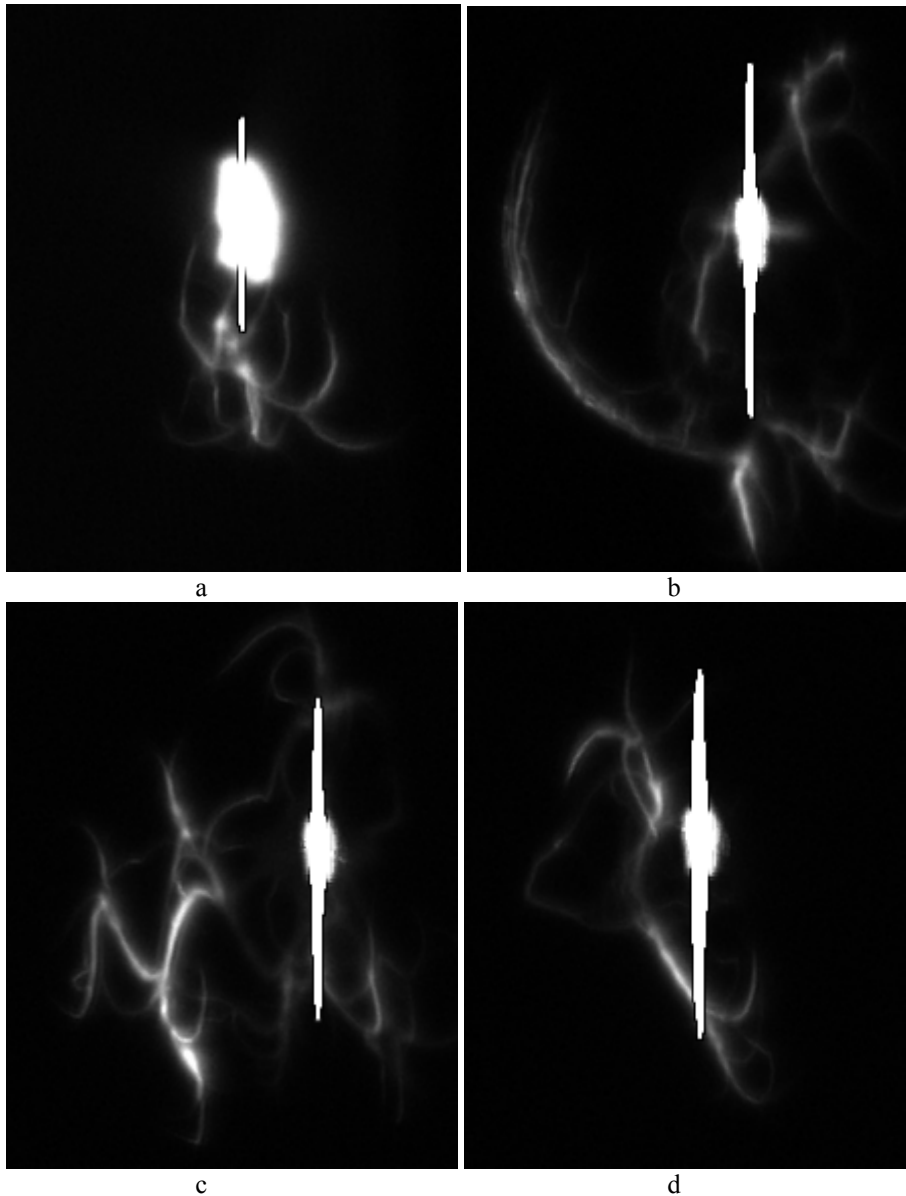


Fig.1. Photographs (obtained with a $2\mu\text{s}$ exposure) of LS initiated MW discharge for various delays between the MW and laser pulses (T_{del} , μs): (a) 0; (b) 12; (c) 20; (d) 700. MW beam propagates left to right ($E = 5 \text{ kV/cm}$, $\tau_{\text{MW}} = 4 \mu\text{s}$). Laser beam propagates top to bottom (320 mJ , $\tau_{\text{las}} = 10 \text{ ns}$).

Variation of the MW pulse delay time relative to the laser pulse was accompanied by significant changes in the threshold for MW discharge formation. For this reason, a special series of measurements was devoted to determining the breakdown characteristics in air at atmospheric pressure. At every fixed delay of the MW pulse relative to the laser pulse, the level of incident MW power was increased until the onset of the MW discharge channel formation. The MW pulse duration was $4\mu\text{s}$ and the LS was generated at a laser intensity of 320 mJ . The results of these experiments are presented in Fig. 2. As can be seen from these data, there is a sharp drop in the breakdown field (E_{break}) at

small delay times ($T_{\text{del}} < 15 \mu\text{s}$), followed by a rather stable stage and a gradual increase in the E_{break} value up to maximum at $T_{\text{del}} \sim 500\text{--}1000 \mu\text{s}$.

Apparently, the LS at small delay times is surrounded by a photoionization generated plasma coat, in which the MW discharge channel is developed that starts directly from the LS. The presence of a seeding electron density and the field enhancement near the extended spark (the size of which is close to λ_{MW}) provide conditions for effective initiation of the MW discharge immediately outside the LS poles (inside LS, the electron density at this time is above the critical level that hinders penetration of the microwave field). These

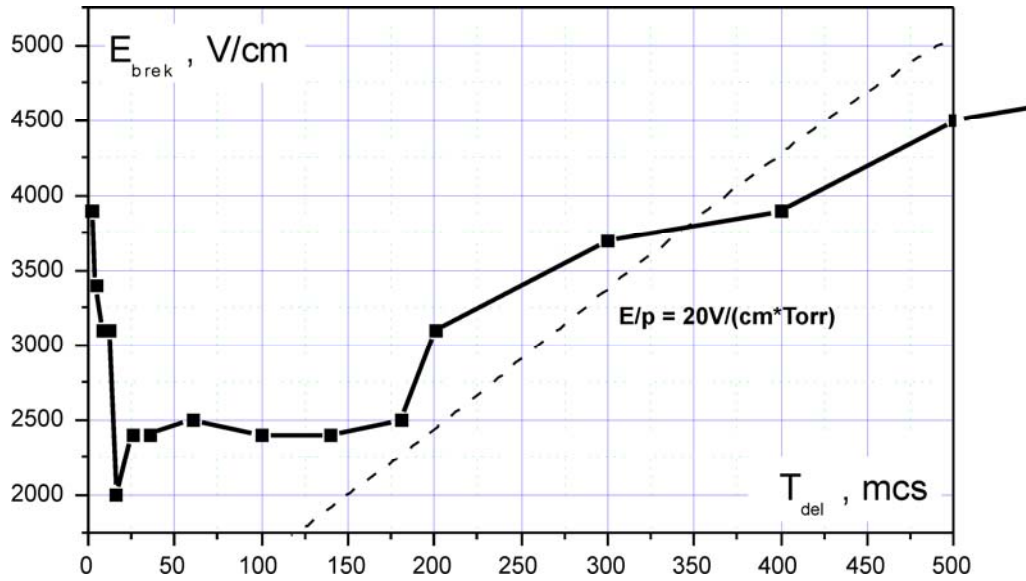


Fig.2. Plot of the MW breakdown threshold field E_{break} versus MW pulse delay time T_{del} relative to the initiating laser pulse in air at atmospheric pressure.

experiments (like many other) show that the MW discharge is highly sensitive to the presence of gasdynamic fronts and readily develops along them. Indeed, a shock wave that runs away from the LS front is already well developed at 15 μ s (with a spherical front clearly visualized by the MW discharge in Fig. 1b). Estimations of the shock wave velocity at this stage, based on the glow front monitoring at various moments of time, give $\sim 5 \times 10^4$ cm/s.

For a delay time in excess of 100 μ s, plasma in the LS region becomes transparent for the microwave field [6], so that the measured values of breakdown fields most probably reflect a change in the gas density inside the LS. Then, the LS region exhibits cooling and the gas density in the region of energy deposition gradually increases (while the gas pressure in the breakdown region is already leveled), which leads to an increase in then breakdown field. Glumac et al. [7] experimentally measured temporal variation of the gas temperature during the LS evolution (decay) for about 1 ms upon generation in air at atmospheric pressure by the Nd:YAG laser second harmonic pulse (under the conditions close to those in our case). Using these results for estimating the temporal variation of the gas density, we have constructed a dashed line in Fig. 2 so as to provide the best fit to our experimental points for $T_{del} > 100$ μ s. It was found that this line corresponds to a reduced electric field of $E/p = 20$ V/(cm Torr), which is much lower than the standard breakdown field in air. This result indicates that the breakdown threshold depends on additional factors rather than entirely on the gas density. Deeper insight into this issue requires additional thorough investigation.

Investigation of gasdynamic processes influence at the discharge structure and the thresholds of its initiation under the various delay time was carried out. Figure 3 illustrates partially these results.

Analysis of the results of Schlieren registration of the process of MW discharge initiation at different stages of its developments shows:

- under the short delays of MW pulse (up to 10-20mcs) the discharge starts right from the domain of LS, developing along the laser beam and gasdynamic front of shock wave, arising as a result of laser breakdown; in a zone of MW discharge a break of shock wave and displacement of its front is observed,
- under defined conditions stimulated MW discharge is formed inside gasdynamic cavity around the LS core up to delays in tens of microseconds;
- at later stages of interaction (210mcs) the vortex zone is forming in the domain of LS, from which MW channels take start;
- analogues scenario is observed during rather long period of time while gasdynamic perturbation exists in the focal region of MW radiation, which definitely favours decreasing of breakdown thresholds and exactly here MW channels are forming and take start.

Another important parameter influencing the MW discharge threshold for various delays of the MW pulse relative to the laser pulse is the laser pulse energy. For a given level of the MW field, the maximum delay time for which the LS is capable of initiating the MW discharge decreases with the laser pulse energy. For small delays, a change in the breakdown field is relatively small. At atmospheric pressure, even very weak LS readily initiated the MW discharge. However, we failed to initiate the MW discharge by laser pulses in a sparkles regime.

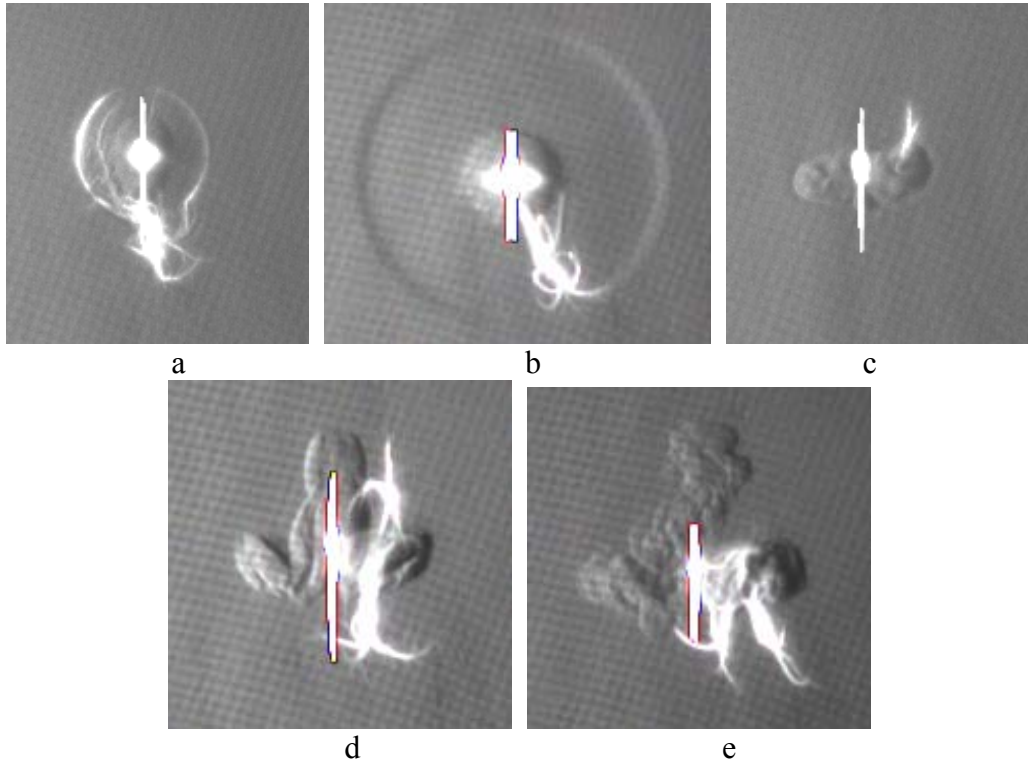


Fig.3. Schlieren photo of MW discharge initiated by LS, exposure time 0.5mcs (a-c) and 3,5mcs (d-e). MW – laser delay (mcs): a) 5, b) 20, c) 210, d) 505, e) 964. MW beam propagates left to right ($E = 5 \text{ kV/cm}$, $\tau_{MW} = 4 \text{ } \mu\text{s}$). Laser beam propagates top to bottom (200mJ (a-c), 500mJ (d-e), $\tau_{las} = 10\text{ns}$).

Unexpected results were obtained at a reduced pressure ($p \leq 130 \text{ Torr}$), where laser beam with an energy of $\sim 50 \text{ mJ}$ ensured the formation of an electrodeless MW discharge and provided a significant (20–30%) decrease in the breakdown threshold with respect to the MW field.

Thus, the results of our investigations showed that the MW discharge in air at atmospheric pressure can be reliably initiated by LS both at the stage of its formation and in the late stages of decaying gasdynamic perturbations, up to a delay time of $\sim 1 \text{ ms}$. The experiments also demonstrate that the MW discharge in air at reduced pressures can be reliably initiated by light, at a significant decrease in the breakdown threshold.

This study was supported in part by EOARD (ISTC grant no. 3058) and the Presidium of the Russian Academy of Sciences (Program no. 11).

References

1. Yu. Kolesnichenko, V. Brovkin, O. Azarova, V. Grudnitsky, V. Lashkov, I. Mashek, Proceedings of

the 41st AIAA Aerospace Sciences Meeting & Exhibit

(January 6–9, 2003, Reno, NV), AIAA Paper 2003-0361.

2. *MW Discharge: Fundamentals and Applications*, Ed. By Yu. A. Lebedev (Yanus_K, Moscow 2006).

3. V. G. Brovkin and Yu. F. Kolesnichenko, Zh. Tekh. Fiz. **64** (2), 194 (1994) [Tech. Phys. **39**, (1990)].

4. V. G. Brovkin, D. F. Bykov, S. K. Golubev, S. I. Gritsinin, G. G. Gumberidze, I. A. Kossyi, and M. I. Taktakishvili, Zh. Tekh. Fiz. **61** (2), 153 (1991) [Sov. Phys. Tech. Phys. **36**, (1991)].

5. V. G. Brovkin and Yu. F. Kolesnichenko, Pis'ma Zh. Tekh. Fiz. **16** (3), 55 (1990) [Tech. Phys. Lett. **16**, (1990)].

6. Yu. Kolesnichenko, D. Khmara, V. Brovkin, and S. Afanas'ev, Proceedings of the 45th AIAA Aerospace Sciences Meeting & Exhibit (January 8–11, 2007, Reno, NV), AIAA Paper 2007-1228.

7. N. Glumac, G. Elliott, and M. Boguszko, AIAA J. **43**, 1984 (2005).

METHODS OF DEFINITION OF GAS STREAM PARAMETERS AT NOT DESIGNED MODE OF NOZZLE OPERATION

A.A.Karachev, P.V.Kopyl, V.M.Shibkov, L.V.Shibkova

Faculty of Physics, Moscow State University, 119991, Moscow, Russia,

shibkov@phys.msu.ru

Abstract. For studying influence of low temperature plasmas on kinetics of combustion of hydrocarbon fuel at atmospheric pressure of air it is necessary to know the basic characteristics of a stream, including its speed. In work three methods of definition of an air stream speed at atmospheric pressure of air in the discharge chamber are considered. In this case Laval nozzle works in not-designed mode. Speed of an air stream was defined experimentally by three ways: on drift of a flame ignited by a surface microwave discharge; on position of Mach's jump in case of a supersonic stream; with the help of the thermocouple.

I. Introduction

In the process of searching for optimal methods of generating non-equilibrium plasma in a supersonic flow, a microwave discharge of a new type was suggested in [1], namely, a microwave discharge developed by a surface wave on a dielectric body subjected to supersonic flow of air. The main properties of such discharge system is investigated in [1-11].

For employing a surface microwave discharge in various fields of supersonic plasma aerodynamics, one must optimize the conditions of its generation. In particular, experiments at atmospheric air pressure must be performed for investigating the process of ignition and combustion of liquid hydrocarbons. This is due to the fact that volatile liquids with free surface, which are placed in a vacuum chamber, begin to rapidly evaporate with decreasing pressure in the chamber, and this prevents one from performing experiments with hydrocarbons in the liquid phase at an air pressure below one atmosphere.

It was previously [3] experimentally demonstrated that a pulse power of 10-20 kW is required for generating a surface microwave discharge on a Teflon antenna in the air pressure range of 0.1-50 torr, while the power required for initiating a surface microwave discharge at atmospheric pressure is of the order of 250 kW. It was necessary to develop a new system for initiation of a surface microwave discharge for the purpose of reducing the level of pulse power.

It is known [12, 13] that if a discharge is initiated by some method, it will exist for a long time at much lower values of power than those required for initial breakdown of gas. Numerous methods exist for initiating a microwave discharge, for example, by laser spark, by spark discharge, by vacuum ultraviolet irradiation of the region in which it is planned to initiate a discharge, by using various metal wires, dipoles, and so on. However, the metal-dielectric contact is most effective from

the standpoint of initiating a microwave discharge [13].

In studies [1-4], a surface microwave discharge was generated on a Teflon antenna. In so doing, the metal-dielectric contact was structurally removed from the region of strong electric field, which required high values of power input for generating a surface microwave discharge at high pressures of air. Therefore, we changed the unit for delivery of microwave energy to the antenna and replaced the Teflon antenna by a quartz one [8-10]. This made technically possible the contact between the quartz antenna and the wider wall of metal waveguide, where the amplitude of electric field intensity is maximal for a wave of the H_{01} type. We selected the direction of propagation of microwave power as the positive direction of the OX axis; in so doing, the origin of coordinates $x = 0$ is located in the cross section where the metal waveguide ends and the quartz antenna begins, i.e., at the metal-dielectric interface in the zone of delivery of microwave energy to the antenna. The employed system of energy delivery (metal waveguide-quartz antenna) made possible an order of magnitude reduction of the power required for generating a surface microwave discharge at atmospheric pressure. Readily realized in the experiments is a microwave discharge on the surface of a quartz antenna of rectangular cross section $9.5 \times 19 \text{ mm}^2$ and 115 mm long in air at atmospheric pressure $p = 760$ torr.

II. Experimental Installation

Experiments were carried out on the installation consisting of a vacuum chamber, a receiver of a high pressure of air, a receiver of a high pressure of propane, a system for producing a supersonic gas flow, magnetron generator, system for delivering microwave power to the chamber, cylindrical and rectangular aerodynamic channels, sources of high-voltage pulses, a synchronization unit, and a diagnostic system (Fig. 1).

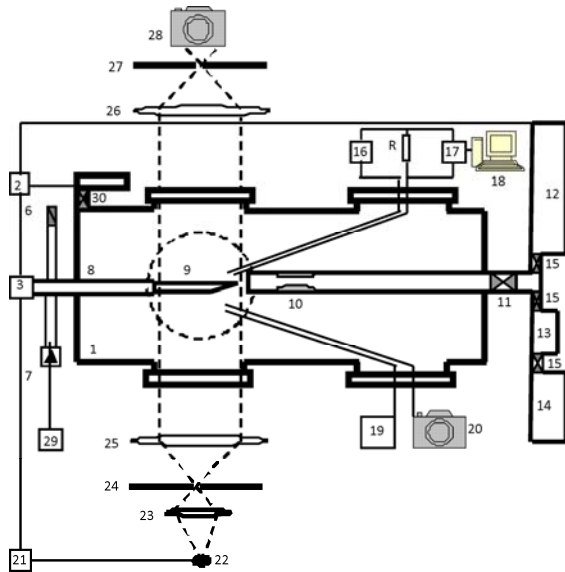


Figure 1. Block diagram of the experimental setup: 1 – vacuum chamber; 2 – synchronization units; 3 – magnetron; 6 – directional coupler; 7 – crystal microwave detector; 8 – waveguide; 9 – antenna; 10 – cylindrical aerodynamic channel with Laval nozzles; 11 – electric hydraulic valve; 12 – air high pressure receiver; 13 – propane high pressure receiver; 14 – high-pressure cylinder with propane; 15 – valves; 16 – block of probe; 17 – power supply; 18 – computers; 19 – monochromator, CCD sensor or photomultiplier tube; 20 – video and photo camera; 21 – pulsed power supply for shadow graphics installation; 22 – pulsed flash-lamp; 23, 25, 26 – lenses; 24, 27 – diaphragms; 28 – photo camera; 29 – digital oscilloscope.

The basic component of the experimental setup is an evacuated metal cylindrical chamber, which serves simultaneously for supersonic flow creation, and as a tank for the expiration of gases or combustion products. The inner diameter of the vacuum chamber is 1 m, and its length is 3 m.

A high-speed flow was produced by filling the vacuum chamber with air through a specially profiled Laval nozzle mounted on the outlet tube of the electromechanical valve and designed for Mach number of $M < 2$.

The microwave source is a pulsed magnetron generator operating in the centimeter wavelength range. The parameters of the magnetron generator are as follows: the wavelength is $\lambda = 2.4$ cm, the pulsed microwave power is $W_p < 100$ kW, the pulse duration is $\tau = 1\text{--}200$ μs , and the period-to-pulse duration ratio is $Q = 1000$. The vacuum system of the chamber allows us to vary the pressure over a wide range from 10^{-3} to 10^3 Torr.

The diagnostic complex included optical refraction sensors, photoelectronic multipliers, pulse shadow installation, system for measurement of flame conductivity, electric probes, a two-wire line, spectrometers, digital oscilloscopes, digital photos and movie cameras, thermocouples.

III. Experimental Results

The used compressor enabled to pump air in a receiver up to pressure of 6 atm that allowed to create high-speed air streams with the desired values of velocity at atmospheric pressure in a chamber. At atmospheric pressure of air in the chamber Laval nozzle worked in not-designed mode. Speed of an air stream was defined experimentally by three ways:

- on drift of a flame ignited by a surface microwave discharge;
- on position of Mach's jump in case of a supersonic stream;
- with the help of the thermocouple.

The first method is based that an oblique jump of density appears on the forward end of the thin pointed plate streamlined by a supersonic stream.

Therefore, instead of the antenna in the chamber the thin pointed plate (chisel) was located so that its axis and an axis of air flow coincided. One of the sides of a chisel is oblique. An oblique jump of density arising on a forward edge of chisel was registered with the help of shadow installation. Value of flow Mach number was defined on the measured corner of an inclination between jump and not oblique surface of a chisel under the formula [14]:

$$M = \frac{1}{\sin \alpha},$$

where α is a corner between jump and not oblique side of a chisel. The sample of a shadow picture in case of a supersonic stream with flow Mach number $M=2$ is submitted on Fig. 2.

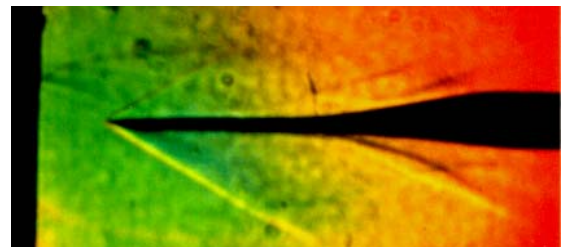


Figure 2. An instant shadow picture of a thin pointed plate streamlined by a supersonic stream. (Flow Mach number $M = 2$, initial air pressure in the chamber $p_0 = 40$ torr).

It is necessary to emphasize, that jump on a forward edge of the pointed plate did not arise, if it is streamlined by a subsonic air stream. Therefore in experiments the shadow picture was fixed only at such values of p/p_0 at which of an oblique jump of density started to arise. The chisel was put for improvement of a shadow picture as she is much more thin than the antenna and has small thickness in comparison with the cross-section size of a stream. Therefore jump on the end of a chisel is

seen precisely as against the antenna. The distance from a chisel up to nozzle changed in limits of $z = 0-10$ cm. Difference of pressure changed in a range of 1-6 atmospheres. Experimentally received dependence of flow Mach number on the ratio of pressure in a receiver to pressure in the chamber is submitted on Fig. 3.

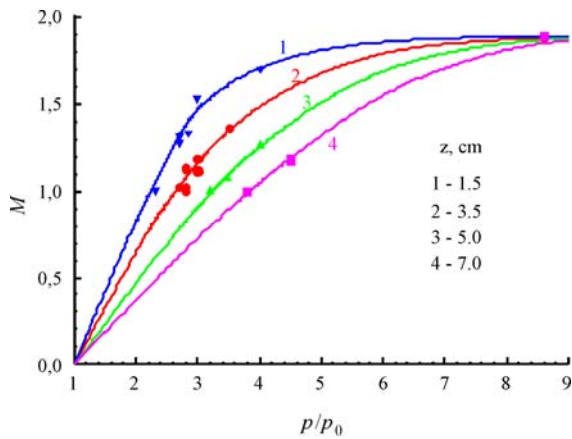


Figure 3. Dependence of a stream Mach number on the ratio of pressure in a receiver to pressure in the chamber (the data received in the first way). Initial pressure in the chamber $p = 760$ torr, for an extreme right point $p_0 = 40$ torr.

Speed of a stream can be determined under the formula [14]:

$$v = a_{cr} \sqrt{\frac{\frac{k+1}{2} M^2}{1 + \frac{k-1}{2} M^2}}$$

где a_{cr} is critical speed.

Speed of a stream grows at increase in the ratio of pressure in a receiver to pressure in the chamber and at value of $p/p_0 = 6-8$ leaves on stationary size. Nozzle passes in a designed mode. In this case nozzle is designed for flow Mach number of $M = 2$.

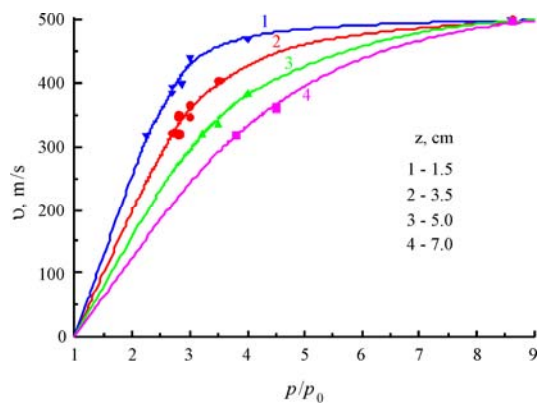


Figure 4. Dependence of a stream velocity on the ratio of pressure in a receiver to pressure in the chamber (the data received in the first way). Initial pressure in the chamber $p = 760$ torr, for an extreme right point $p_0 = 40$ torr.

In Fig. 4 curve of $v(p/p_0)$, received at the big distances from nozzle, are below, i.e. speed of a stream decreases with increase in distance. It is obvious, that at atmospheric pressure because of braking speed of a stream on the big distances from a cut nozzle at the same pressure ratio should decrease, as it is observed in experiment.

The second method of definition of speed of a stream is based on registration of time evolution of drift in an air stream of a flame of burning of a alcohol thin film which is ignited with the help of a surface microwave discharge. Photos of ignition of alcohol in high-speed air streams are submitted in Fig. 5.

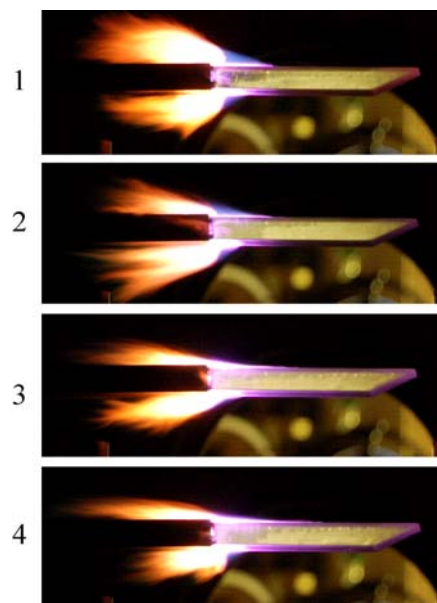


Figure 5. Alcohol ignition under condition of a surface microwave discharge at $\tau = 120 \mu s$, $p_0 = 1$ atm, $W = 65$ kW and different air flow velocity v , m/s: 1 – 190, 2 – 260, 3 – 390; 4 – 440.

Experiments have shown, that a surface microwave discharge results in ignition of a thin film of alcohol both in subsonic (look Fig. 5, the frames 1 and 2), and in supersonic (3 and 4) air streams. Thus in photos at a surface of the antenna it is distinctly seen thin (thickness about 1 mm), brightly luminous layer representing plasma of a surface microwave discharge. Ignition occurs in the field of existence of a surface microwave discharge in a zone of a supply of microwave energy. At a pulsed microwave power of 65 kW ignition is initiated already at microwave pulse duration of $10 \mu s$. The period of an induction decreases from 100 up to $5 \mu s$ at increase in a microwave pulse power from 20 up to 75 kW. In a subsonic stream (see Fig. 5, a frame 1) ignition of a thin film of alcohol at pulsed power of 65 kW occurs already on distance of 0.5 cm from forward front of a surface microwave discharge. On an angle of an inclination

of combustion border to a direction of an air stream it is possible to determine transversal speed of ignition front propagation. With increase in speed of a stream (see Fig. 5) an angle of an inclination of combustion border decreases, however in experimental conditions of transversal speed of alcohol ignition front propagation does not depend on speed of a stream and at a microwave pulsed power of 65 kW is equal 80 m/s.

Experimentally dependence of speed of a stream on a ratio of pressure in a receiver and in the chamber on different distances from nozzle along flow axis was determined. With help of a high-speed video camera process of burning of a liquid film of kerosene in an air stream (look Fig. 6) was registered. The video camera frame frequency is known. On images we know displacement of area of combustion in pixels and in centimeters.

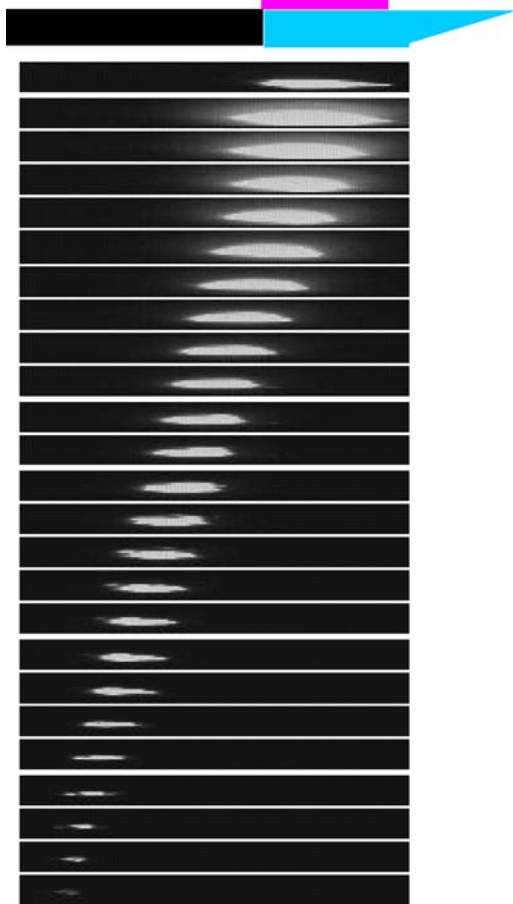


Figure 6. Dynamics of the flame drift initiated by a surface microwave discharge under condition of subsonic air stream. Frequency of the frames $f = 31250$ Hz, $z = 10$ cm, $p/p_0 = 1.1$.

The received experimental dependence of speed of a stream on the ratio of pressure in a receiver to pressure in the chamber is submitted in Fig. 7. At increase in the ratio of pressure p/p_0 speed of a stream grows.

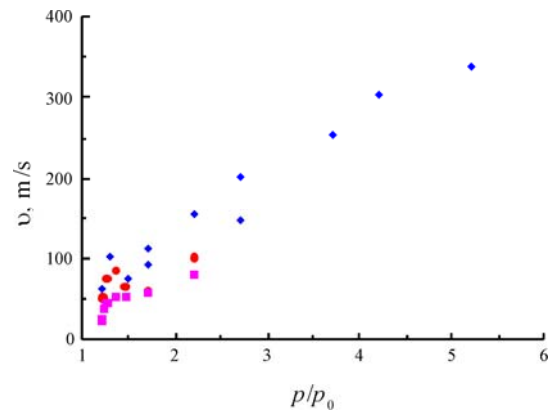


Figure 7. Dependences of speed of a stream on the ratio of pressure in a receiver to pressure in the chamber (the data received in the second way).

We compare the data resulted in Fig. 4 and Fig. 7. In Fig. 8 results of comparison are submitted.

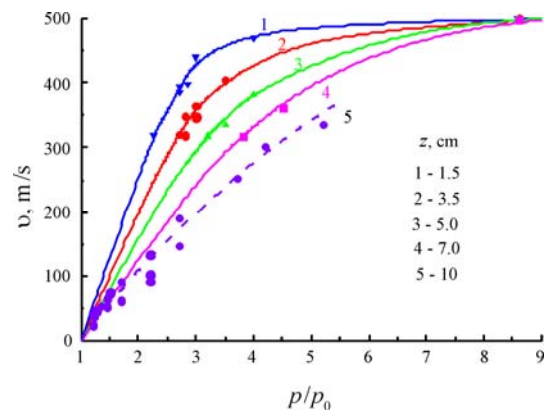


Figure 8. Dependences of speed of a stream on the ratio of pressure in a receiver to pressure in the chamber. The results received in the first and second ways.

Points of dependence of $v(p/p_0)$, determined with the help of the high-speed chamber have lain below curves $v(p/p_0)$, obtained with the help of jumps in a shadow picture. It is connected with the fact that these points are received on distance from nozzle $z = 10$ cm. And the further from nozzle speed of a stream is measured, the lower its speed can be because of its braking in air of atmospheric pressure. Therefore the data received by these two ways, is well coordinated.

The new method of measurement of transition of a subsonic stream in a supersonic condition with use of the standard free thermocouple has also been offered and approved. In the beginning graduation of the thermocouple was made. For this purpose the thermocouple was located in a free stream with flow Mach number $M = 1$. At this value of the flow Mach number temperature in a stream $T = 250$ K. Then the temperature in conditions of subsonic and supersonic flows created at the different ratio p/p_0 of pressure p in a receiver to pressure p_0 in the

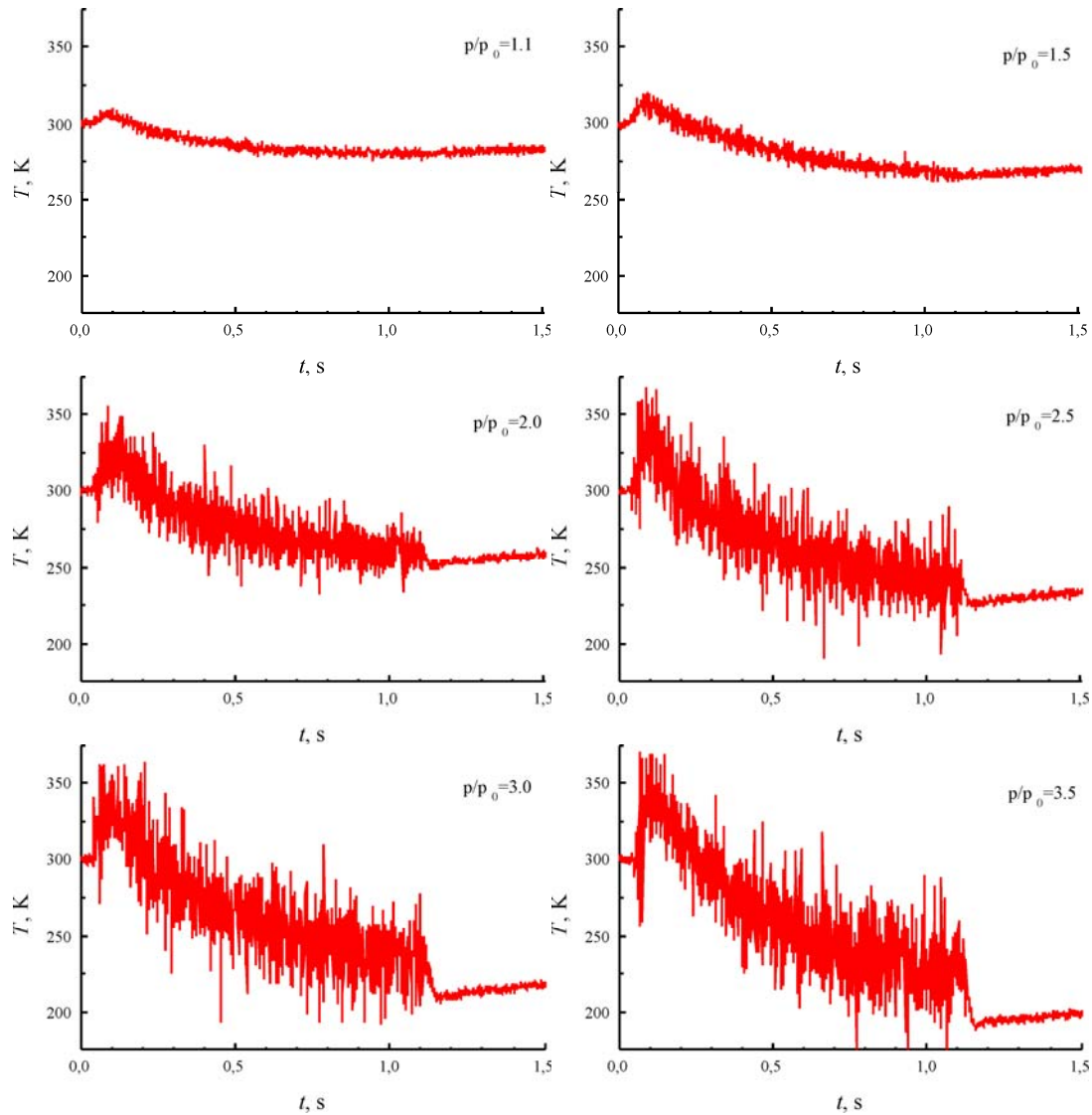


Figure 9. Dependences of a stream temperature on time. ($z = 1$ cm).

chamber can be defined on amplitude of the signal from the thermocouple registered by an oscilloscope.

The time dependences of a signal from the thermocouple in subsonic and supersonic streams are submitted in Fig. 9. Experiments show, that at switching off of a subsonic stream the signal from the thermocouple does not undergo any sharp changes, and within several seconds in process of the thermocouple heating slowly relaxed to the value corresponding to room temperature.

In conditions of a supersonic stream there is a jump in front of the free thermocouple. It results in change of a thermal stream on a surface of the free thermocouple. Thus the thermocouple temperature remains above, than temperature of air in a supersonic stream. When supersonic stream is switching off the temperature registered by the thermocouple, placed in a free stream, sharply falls

within the limits of 5-50 K depending on speed of a stream up to the values corresponding to true temperature of gas in a supersonic stream. Besides, noise registered by the thermocouple sharply grow at transition from a subsonic stream through $M = 1$ to a supersonic one, that also is the indicator showing, that the stream becomes supersonic.

Results of the given experiment well correlate with the data of a shadow method which allows to define of a stream velocity on position of the jump, arising on the thin pointed plate, and also by definition of speed on drift of a flame ignited by a pulse surface microwave discharge.

IV. Acknowledgments

This work was partially supported by the Russian Foundation for Basic Research (grant # 08-02-01251-a and grant # 11-02-01091-a).

V. References

1. Shibkov, V.M., Vinogradov, D.A., Voskanyan, A.V. et al., *Vestn. Mosk. Univ. Ser. 3 Fiz. Astron.*, 2000, vol. 41, no. 6, p. 64.
2. Shibkov, V.M., Aleksandrov, A.F., Ershov, A.P. et al., *Vestn. Mosk. Univ., Ser. 3 Fiz. Astron.*, 2004, vol. 45, no 5, p. 67.
3. Shibkov, V.M., Ershov, A.P., Chernikov, V.A., and Shibkova, L.V., *Zh. Tekh. Fiz.*, 2005, vol. 75, no 4, p.67.
4. Shibkov, V.M., Dvinin, S.A., Ershov, A.R, and Shibkova, L.V., *Zh. Tekh. Fiz.*, 2005, vol. 75, no.4, p.74.
5. Shibkov, V.M., Aleksandrov, A.F., Ershov, A.P. et al., *Fiz. Plazmy*, 2005, vol. 31, no. 9, p. 857.
6. Dvinin, S.A., Shibkov, V.M., and Mikheev, V.V., *Fiz. Plazmy*, 2006, vol. 32, no. 7, p. 654.
7. Shibkov, V.M., Dvinin, S.A., Ershov, A.P. et al., *Fiz. Plazmy*, 2007, vol. 33, no. 1, p. 77.
8. Shibkova, L.V., *Vestn. Mosk. Univ., Ser. 3 Fiz. Astron.*, 2007, vol. 48, no. 5, p. 62.
9. Shibkova, L.V., Ignition of Alcohol under Conditions of Surface Microwave Discharge in Air, *Preprint of Dept. of Physics, Moscow State Univ.*, M.: 2007, no.4.
10. Shibkova, L.V., Physical Processes in Moving Plasma of Multicomponent Inert and Chemically Active Mixtures, *Extended Abstract of Doctoral (Phys.-Math.) Dissertation*, Moscow: Joint Inst. for High Temperatures, Russ. Acad. Sci., 2007.
11. Shibkov, V. M., Alexandrov, A. F., Chernikov, A.V. et al., Influence of Surface Microwave Discharge on the Characteristics of Supersonic Flow Near Streamlined Body, *AIAA-2005-0779*.
12. Zarin, A.S., Kuzovnikov, A.A., and Shibkov, V.M., *Svobodno lokalizovannyi SVCh-razryad v vozdukh* (Free-Localized Microwave Discharge in Air), Moscow: Neft' i Gaz, 1996.
13. Batanov, G.M., Gritsinin, S.I., Kossyi, I.A. et al., *Tr. Fiz. Inst. Akad. Nauk SSSR*, 1985, vol. 160, p. 174.
14. Abramovich, G.N. *Applied Gas Dynamics* (Nauka, Moscow, 1991) [in Russian].

EVALUATION OF RADIATION LOSSES IN AL-H₂ MHD GENERATOR PATH

Bityurin V.A., Galaktionov A.V., Kolpakov A.V.

Joint Institute for High Temperatures RAS, 125412, Moscow, Russia
andrei.v.galaktionov@gmail.com

1. Introduction

Recent studies [1-3] have demonstrated that rapid development of Al-H₂ technology creates very favorable conditions for developing innovative high-performance MHD generators. In such generators working fluid is hydrogen, which is heated to a temperature ~ 3000-3500K, and which is derived from the oxidation of aluminum with water.

The oxidation of aluminum with water in the combustion chamber of reactor of such generator and the subsequent installation path contains water vapor, particles and drops of aluminum, alumina and intermediate reaction products, which are numerous combinations of aluminum, oxygen and hydrogen. All these components, when heated to ~3500K, are actively involved in the radiative heat transfer. Simple estimations show that radiative losses to reactor walls are of the same order as the generator power, so that the possibility of generator practical implementation is not evident. However, radiative heat transfer in a multicomponent chemically reacting mixture in reactor is an important mechanism of heat transfer.

Unfortunately, optical properties of numerous compounds of aluminum, oxygen and hydrogen at high temperatures are often unknown. There exist data for the optical properties of water and steam, as well as for aluminum, alumina and their melts, but for even relatively well-studied alumina at high temperatures optical properties reported in papers by different investigators differ by several orders of magnitude [4,5]. In addition, the construction Al-H₂ MHD generators are still under development and so that parameters of generator are not fixed. So to evaluate radiative losses from gas mixture to reactor walls we consider in our investigation only melt alumina drops. As an example we consider experimental setup with Al flow rate 100 grams per second.

There are three known ways to reduce radiation losses from gas mixture to the walls in the reactor:

- to use effectively reflecting high-temperature coating for reactor walls;
- to achieve large optical thickness of the gas mixture to “trap” thermal radiation inside gas mixture, so that radiative losses will be small

because they will be determined by a thin wall layer with temperatures close to the wall temperature;

- to achieve small absorption optical thickness of the mixture on the absorption, in this case radiative losses will be small due to “transparency” of gas mixture.

The latter mode is interesting in any cases, since particles and drops of alumina should be removed from the hydrogen before it reaches MHD channel.

Unfortunately, the three ways badly work together and generate many conditions of radiative heat transfer. Though we derive rigorous and adequate estimations of radiative losses which is useful for engineering approach.

2. Flow optical properties evaluation

It is known that for MHD generator conditions hydrogen is a transparent gas for radiative heat transfer waveband. At the same time steam and relatively cold unburned aluminum particles and drops intensively absorb thermal radiation emitted by hot alumina drops and screen reactor walls. Optical properties of other chemical compounds are unknown. Thus for upper estimation of radiative losses it is rationally to calculate radiation from alumina drops assuming local thermodynamic equilibrium for the gas particles mixture.

Alumina has anomalous optical properties. Its absorption coefficient abruptly increases at melting point by several orders of magnitude [4,5] (Fig. 1). Characteristic size of alumina drops in gas mixture varies from several nanometers to tens of microns. Drops with nanometer radii are formed in the reaction of aluminum vapor with water vapor, and drops with microns radii are the result of aluminum particles burning.

Using Mie theory [6] one can calculate absorption and scattering efficiencies for alumina drops of arbitrary sizes. We assumed characteristic temperature of the drops to be about 3000K. Thus wavelength for maximum of the Plank distribution for thermal radiation is about 1 micron. At the Fig. 2 absorption Q_{abs} and transport scattering Q_{tr} efficiencies are shown, and it can be seen that:

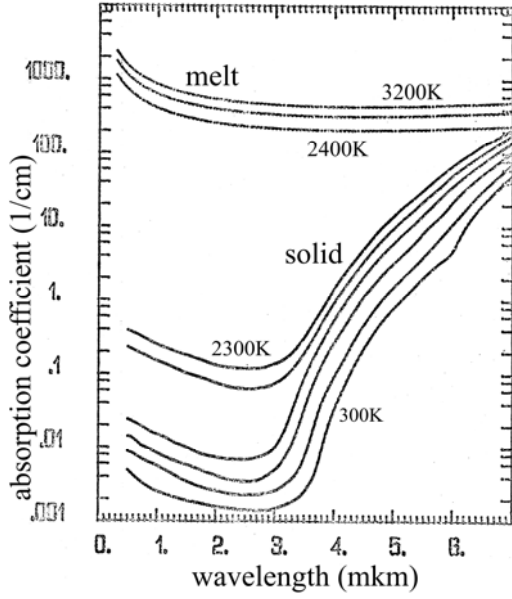


Figure 1. Alumina absorption coefficient

- the scattering is greater than absorption for drops with radii between 30 nanometers and 5 microns, scattering can exceed the absorption by several orders of magnitude.
- for drops smaller than 30 nanometers scattering is insignificant and Rayleigh approximation is applicable.

In Rayleigh case we have following expressions for efficiencies:

$$Q_{\text{abs}} = \frac{4\pi d}{\lambda} \text{Im} \left(\frac{\varepsilon - 1}{\varepsilon + 2} \right), \quad (1)$$

$$Q_{\text{tr}} = \frac{8}{3} \left(\frac{\pi d}{\lambda} \right)^4 \left| \frac{\varepsilon - 1}{\varepsilon + 2} \right|^2, \quad (2)$$

where d - is the drops diameter, $\varepsilon = N^2 = (n - ik)^2$ - permittivity of melted alumina, λ - thermal radiation wavelength.

Using absorption and transport scattering efficiencies for the drops and calculating their concentration on the basis of alumina volumetric rate R (m^3/c), canal cross-section S (m^2) and flow velocity v (m/c), one can calculate optical properties of the flow:

absorption coefficient :

$$\alpha = \frac{3Q_{\text{abs}}R}{2Svd}, \quad (3)$$

transport scattering coefficient

$$\beta_{\text{tr}} = \frac{3Q_{\text{tr}}R}{2Svd}, \quad (4)$$

and radiation diffusion coefficient

$$D = 1/3(\alpha + \beta_{\text{tr}}).$$

It is important to point out that for small ($d < 60 \text{ nm}$) drops and fixed alumina volumetric rate the absorption coefficient of the flow does not depend on the drops diameter

$$\alpha = \frac{6\pi R}{\lambda S v} \text{Im} \left(\frac{\varepsilon - 1}{\varepsilon + 2} \right).$$

Of course real flows contain some mixtures of drops with different diameters. In this case one can simply average optical properties over known drops diameters distribution because absorption and scattering of different drops are independent and additive.

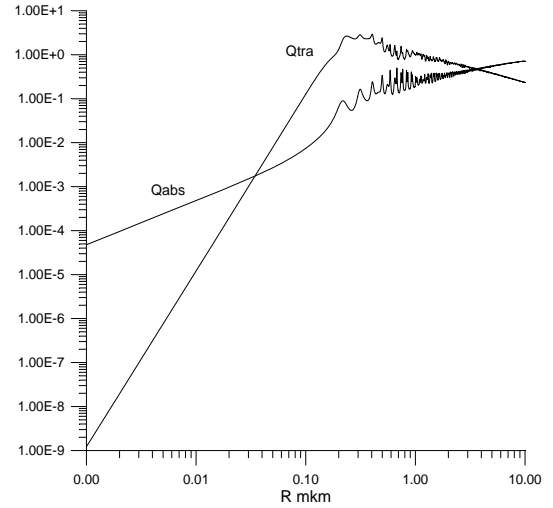


Figure 2. Dimensionless absorption Q_{abs} and transport scattering Q_{tr} cross-section of alumina drops at wavelength 1 micron.

3. Estimations of radiation losses

We start from rigorous radiation transfer equation for selective absorbing, emitting and scattering media

$$\begin{aligned} \Omega \nabla I_{\nu}(\mathbf{r}, \Omega) + (\alpha_{\nu} + \beta_{\nu}) I_{\nu}(\mathbf{r}, \Omega) = \\ \beta_{\nu} \int S_{\nu}(\Omega \cdot \Omega') I_{\nu}(\mathbf{r}, \Omega') d\Omega' + \alpha_{\nu} n_{\nu}^2 I_{p\nu}(T(\mathbf{r})), \end{aligned} \quad (5)$$

where Ω is the radiation propagation direction, $I_{\nu}(\mathbf{r}, \Omega)$ is the radiation intensity, α_{ν} and β_{ν} is

the absorption and scattering coefficients, $S_\nu(\Omega \cdot \Omega')$ is the scattering phase function, n_ν is the effective refractive index of the flow (below $n_\nu = 1$), $I_{p\nu}$ is the equilibrium radiation intensity in vacuum, $T(\mathbf{r})$ is the flow temperature. In the above expressions index ν denote spectral dependence of a quantity.

Solving equation (5) with sufficient boundary conditions [7] and known from the hydrodynamics part of the problem temperature distribution $T(\mathbf{r})$, one can find divergence of radiant flux density for energy balance equation to close the problem:

$$\frac{\partial H}{\partial t} = \int_{\Sigma} \alpha_\nu \{U_{p\nu}(T(\mathbf{r})) - U_\nu(\mathbf{r})\} dV + \dots \quad (6)$$

Here H is the enthalpy, $U_\nu(\mathbf{r}) = \int_{4\pi} I_\nu(\mathbf{r}, \Omega) d\Omega$ is the spectral energy density of thermal radiation, $U_{p\nu} = \int_{4\pi} I_{p\nu} d\Omega$. Integration is fulfilled over waveband Σ which is significant for thermal radiation transfer.

For engineering analysis we shall consider MHD generator setup consisting of several parts with volumes V_i (combustion chamber, nozzle throat etc.). Integrating equation (5) over angle, spectrum and each volume V_i we obtain:

$$\int_{V_i} \int_{\Sigma} \nabla \mathbf{q}_\nu dV = \int_{V_i} \int_{\Sigma} \alpha_\nu (U_{p\nu}(T(\mathbf{r})) - U_\nu(\mathbf{r})) dV dV \quad (7)$$

where \mathbf{q}_ν is the spectral radiant flux density. Using well-known mathematical analysis theorem one can replace in the left side of the equation (7) volumetric integral with the surface one: $\int_{V_i} \int_{\Sigma} \nabla \mathbf{q}_\nu dV = \int_{S_i} \mathbf{q}_\nu dV d\mathbf{S}$. It is obvious

that the surface integral is approximately equal to the radiation losses. We neglect here radiant fluxes through imaginable boundaries between setup parts, which are mutually compensating. Therefore, we have derived useful and rigorous expression for radiant losses:

$$Q_i \cong \int_{V_i} \bar{\alpha} (4\sigma T^4(\mathbf{r}) - U(\mathbf{r})) dV, \quad (8)$$

where $U = \int U_\nu d\nu$, $\bar{\alpha}$ is the averaged over Plank distribution absorption coefficient. Thus, we have shown that directly from radiation transfer equation follows that radiation losses to the setup walls is

equal to volumetric integrals from radiation sources/drains in the full energy balance equation.

Expression (8) is useful for derivation of desired radiative losses estimations. Both quantities in the integral are positive and, it is obvious that $T(\mathbf{r}) \leq T_{\max}$ and $U(\mathbf{r}) \geq 4\sigma T_w^4$, where T_w is the walls temperature. Thus, we have

$$Q \leq 4\sigma \bar{\alpha} V (T_{\max}^4 - T_w^4). \quad (9)$$

Here and below we omit MHD generator setup parts index i . The rigorous estimation (9) is always true. However, it is useful only for optically thin ($\bar{\alpha}l \ll 1$) setup sections, where characteristic dimension is l . The estimation (9) does not take into account wall reflection and optically thin section is sufficiently rare case. Nevertheless, it is very profitable. The fact of the matter is that it is necessary to remove alumina drops from the hydrogen flow to make efficient MHD generator. Therefore, the flow optical thickness somewhere is to be small.

It can be easily seen from the estimation (9), that radiative losses are proportional to the average absorption coefficient and to the section volume. So, using expression (3) for given alumina volumetric rate R (m^3/c) we have:

$$Q \leq 6R \bar{\alpha} \bar{Q}_{abs} \sigma (T_{\max}^4 - T_w^4) / d, \quad (10)$$

where τ is the drops in section residence time, d is the drop diameter and \bar{Q}_{abs} is the middle dimensionless absorption cross-section. As was mentioned above for small drops (in comparison with maximum of Plank distribution wavelength) the absorption coefficient of the flow and therefore radiative losses does not depend on the drops diameter. This means that radiative losses do not depend on setup geometry. The only way to reduce the losses is to increasing flow velocity to shrink the drops in section residence time τ .

Unfortunately, the hydrogen flow with alumina drops is rarely optically thin. Moreover, as mentioned above (see Fig. 2) the scattering is greater than absorption for drops with radii between 30 nanometers and 5 microns and can exceed absorption by several orders of magnitude. In this case radiative heat transfer is characterized by multiple scattering and the estimations (9, 10) over evaluate radiative losses. To find more realistic estimations we assume that the flow is isothermal ($T(\mathbf{r}) \equiv T_{\max}$) in each section but we calculate energy density of thermal radiation in expression (8) by radiation diffusion approach. The approach assumes that radiant flux density is proportional to gradient of the radiation energy density. Radiation diffusion approach is equivalent to P_1

approximation [7] of the spherical harmonics method for solution of the radiation transfer equation (5). It is well known [9], that radiation diffusion approach is at least qualitatively correct in any case. Using operator technique [10] one can show that at least in unbounded media inaccuracy of diffusion approach is equivalent to optical properties imprecision with several tens percent magnitude. Absorption coefficient of melted alumina is known with much worse accuracy.

Here we consider only cylindrical geometry and one-dimensional radiation diffusion along the radius of section:

$$-\frac{1}{r} \frac{\partial}{\partial r} r D \frac{\partial}{\partial r} U + \alpha U = \alpha 4 \sigma T(r)^4 \quad (11)$$

with boundary conditions

$$q = -D \frac{\partial}{\partial r} U = 0 \quad \text{when } r = 0 \quad (12)$$

$$-D \frac{\partial}{\partial r} U = \frac{1}{2} \frac{\varepsilon_w}{2 - \varepsilon_w} (U - 4 \sigma T_w^4) \quad \text{when} \\ r = r_0, \quad (13)$$

where ε_w is the boundary emissivity, $T(r) \equiv T_{\max}$, T_w is the wall temperature, r_0 is the setup section radius.

Using equations (11-13) one can find effective emissivity of the flow

$$Q \leq \varepsilon_{eff} S_w \sigma (T_{\max}^4 - T_w^4), \\ \varepsilon_{eff} = \frac{2 \varepsilon_w D \xi I_1(\xi r_0) / (2 - \varepsilon_w)}{D \xi I_1(\xi r_0) + \varepsilon_w I_0(\xi r_0) / 2(2 - \varepsilon_w)}, \quad (14)$$

where S_w is the section wall area, $\xi = \sqrt{\alpha/D}$, I_0, I_1 is the modified Bessel functions.

For optically thick flow boundary layer, the solution for isothermal flow gives overrated radiation flux. So we propose new approximative temperature distribution of the flow where δ is the thickness [7] of the boundary layer:

$$T(r) = (A - B I_0(r/\delta))^{1/4} \quad (15)$$

where

$$A = (T_{\max}^4 I_0(r_0/\delta) - T_w^4) / (I_0(r_0/\delta) - 1) \approx T_{\max}^4, \\ B = (T_{\max}^4 - T_w^4) / (I_0(r_0/\delta) - 1).$$

The expression (15) gives $T(0) = T_{\max}$ and $T(r_0) = T_w$.

The temperature distribution allow us to find in close analytical form the energy density of thermal radiation and the radiation flux from the diffusion equation (11):

$$U(r) = 4 \sigma (A - B b I_0(r/\delta) - C I_0(\xi r)), \quad (16)$$

$$q(r_0) = 4 \sigma (B b D I_1(r_0/\delta) / \delta + C D \xi I_1(\xi r_0)), \quad (17)$$

$$Q \cong q(r_0) S_w \quad (18)$$

where $b = (\xi \delta)^2 / ((\xi \delta)^2 - 1)$ and the constant C is to be found from the boundary condition (14)

$$C = \frac{\varepsilon_w (A - B b I_0(r_0/\delta) - T_w^4) / 2(2 - \varepsilon_w) - B b D I_1(r_0/\delta) / \delta}{D \xi I_1(\xi r_0) + \varepsilon_w I_0(\xi r_0) / 2(2 - \varepsilon_w)}$$

Unfortunately, the estimations above do not take into account influence of radiation on the temperature distribution in the flow. So, next step of improving the radiation losses estimation accuracy is a direct numerical simulation of the whole problem.

4. Radiation losses in experimental setup

As an example, we consider estimation of radiation losses in experimental setup with aluminum mass rate $R_{Al} = 100 \text{ g/s}$ (Fig. 3). The setup is under designing now.

A mixture of steam and aluminum powder (with characteristic particle size 0.1-10 micron) is injected into combustor. Its reacts with hydrogen and alumina drops generation. The table below shows temperatures and flow velocities in several setup sections that are calculated by MHD generator mathematical model [8]. The table also shows effective emissivity of the flow for three alumina drops sizes calculated by expression (14) with the boundary emissivity $\varepsilon_w = 0.5$.

It can be easily seen that the slow flow may emit 25-44% of black body radiation. But fast flow in the nozzle emits up to 3-6% of black body radiation due to optical thickness of the flow is low. Unfortunately, in the majority of cases the radiation losses are too high and we have to seek new ways to reduce their.

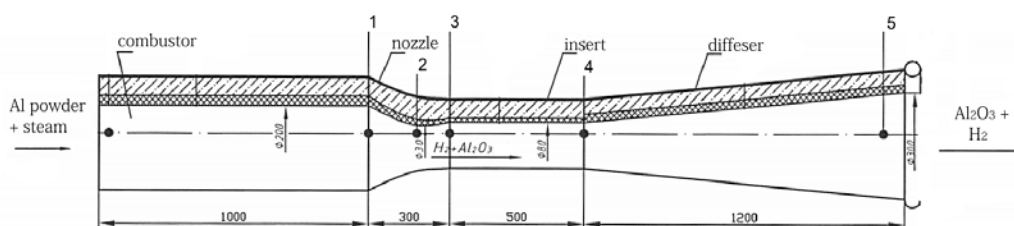


Figure 3. Experimental setup

Table. Effective emissivity of the flow

Point	end of	T_{mix} K	Flow velocity (m/c)	ϵ_{eff} d=0.1 mkm	ϵ_{eff} d=1 mkm	ϵ_{eff} d=10 mkm
1	combustor	3026	36,4	0,2536	0,3699	0,3654
2	nozzle throat	2888	861,4	0,0963	0,3445	0,1728
3	nozzle	2440	1722,6	0,0343	0,2469	0,0676
4	insert	2712	971,2	0,0584	0,3086	0,1110
5	diffuser	2882	10	0,3591	0,3741	0,4473

5. Conclusions

We proposed a set of simple rigorous analytical estimations of radiation losses to walls in Al-H₂ MHD generator path. We found that for small ($d < 60$ mkm) alumina drops and optically thin flow radiation losses do not depend on drop size and on the geometry of the reactor parts. For arbitrary flow optical thickness the estimations are based on radiation diffusion approximation. We also take into account temperature distribution in the flow, which is important for optically thick flow boundary layer.

Our calculations show that for alumina drops with diameter about one micron multiple scattering of thermal radiation plays important role; and the scattering helps to reduce radiation losses.

We estimated that in designing experimental setup with aluminum flow rate 100 gram per second radiation losses might be significantly (3-30 times) less than black body radiations. Nevertheless, in the majority of cases the radiation losses are too high and we have to seek new ways for their reducing.

References

1. Aluminum-hydrogen energy. Ed. Sheindlin E.M.: High Temperatures RAS, 2007. - 278 p.
2. A.E. Sheindlin, V.A. Bityurin, A.Z. Zhuk, V.I. Zalkind, P.P. Ivanov, V.I. Miroshnichenko Aluminum-hydrogen MHD electrical power

generators. DAN, Energy, 2009, Vol.425, No.4, pp.1-3

3. A.E. Sheindlin, V.A. Bityurin, A.N. Bocharov, P.P. Ivanov, A.I. Klimov, V.I. Miroshnichenko, V.I. Zalkind, A.Z. Zhuk, Perspectives of MHD electrical power generation on Aluminum Oxidation by Water Products, In: 44th Plasmadynamics and Laser Conference, June 22 – June 25, San Antonio, Texas.
4. Linhart J.K. and others, Optical properties of leucosapphire at high temperatures. TVT 1982 V. 20 № 5, p. 872 and № 6, p. 1085.
5. Sarou-Kanian V., Rifflet J.C., Millot F. IR radiative properties of solid and liquid alumina: Effects of temperature and gaseous environment. Int. J. Thermophys., 2005, v.26, No.4, p.1263-1275.
6. Bohren K. Haffman D. Absorption and scattering of light by small particles. Wiley, New York, 1983.
7. Otsisik M. N. Complex heat transfer. Wiley, New York, 1976.
8. E.M. Shelkov, P.P. Ivanov, G.M. Korjagina, G. P. Malujonok, S. A. Medin Mathematical model of MHD power station. 8-ep Int. Conf. On MHD energy conversion. Moscow 12-18 September 1983 V. 1, pp. 22-30.
9. Zel'dovich, Ya. B. and Raizer, Yu. P. Physics of Shock Waves and High-Temperature Hydrodynamic Phenomena. Mineola, NY: Dover Publications, 2002.
10. Galaktionov A.V. Using operator technique in analysis of nonsteady radiative heat transfer problems. TVT 1992. V. 30. No 4. pp. 803 - 810

FLOW CONTROL AROUND WING MODEL BY HF DBD DISCHARGE

Moralev I., Bityurin V., Kasansky P., Klimov A., Chertov D.

¹ Joint Institute for High Temperatures RAS,
Izhorskaya 13, bld..2, Moscow, 125412, Russia

E-mail: ivmoralev@gmail.com

Abstract. In the current work, airflow around a wing model controlled by pulse-periodic HF discharge with typical frequency 350kHz at flow velocity up to 20m/s and $Re < 2 \times 10^4$. Transversal HF discharge on a wing model surface near its leading edge is created. It is shown that HF discharge operation, starting from some power input, leads to the shift of the flow separation line on the wing surface at the large attack angles. Wing drag reduce is revealed at attack angles $\alpha > \alpha^* = 11^\circ$ at plasma on. Pressure distribution in the wake of this model is obtained at the different Strouchal's numbers. Shadow pictures of the airflow around the wing model are presented. Mean discharge power input doesn't exceed 10W/cm at the peak HF power about of ~1 kW.

Nomenclature

HF	= high frequency
DBD	= dielectric barrier discharge
SHFD	= surface HF discharge
f_{HF}	= HF frequency
F_M	= modulation frequency
τ_i	= pulse duration
I_{HF}	= HF electric discharge current
U_{HF}	= HF electric discharge voltage
N_{HF}	= pulse power input in plasma
M	=Mach number
V_{af}	= airflow velocity
P_0	= stagnation pressure
P_{st}	= static pressure
Sh	= Strouchal's number
α	=attack angle

I. Introduction

Boundary layer control by means of different surface electric discharges is intensively studied today [1-3]. It is well known that efficiency of flow control near a body by a chord-wise dielectric barrier discharge (DBD) is decreased considerably at high airflow velocity ($V_{af} > 10\text{m/s}$). The reason is physical limitations on the DBD induced momentum, while pressure gradients in the external flow increases with velocity increase [4,5].

However, attempts are recently made to use the surface discharges for boundary layer control, referring to other mechanisms of discharge –flow interaction.

Airflow separation control near the wing model by nanosecond electric discharge was studied at flow velocity up to 100m/s [2]. The reattachment of the boundary layer was obtained at pulse repetition frequencies $Sh \sim 1$.

The problem of a boundary layer flow turbulization and generation of a longitudinal vorticity by means of DBD was studied in [6].

Surface high frequency discharge was proposed in [7,8] for separation control on a flat plate and cone drag reduction. It was shown, that at definite angles of attack and discharge regimes, significant change in pressure distribution behind the plate can be achieved.

Since the flow separation control around a wing is of significant practical importance, it was widely studied up to date. However, most authors, both working with conventional and with nanosecond DBD at velocities up to tens meters per second, report an effective stall control at large attack angles at discharge positioned near the leading edge of the model. Several studies, concerning flap aerodynamics improvement by conventional DBD can be found in [3,9,10]. It is also known, that at $Re < 10^5$, leading-edge stall mainly takes place due to laminar boundary layer separation. Boundary layer turbulization leads to separation delay due to a higher stability of the turbulent boundary layer. It is shown, that nanosecond discharge operation near the leading edge leads to significant (up to $2-4^\circ$) stall delay at high attack angles.

Unsteady forcing seems to be an essential feature of any DBD, therefore several studies were focused on forcing frequency optimization. Starikovskii et.al. [2] reported a maximum efficiency of nanosecond discharge at $Sh \sim 1$, Samimi et.al. [3] found frequency ranges for conventional discharge forcing. Furthermore, in vortex street formation along the shear layer behind the flap was obtained, synchronized to the actuator forcing.

Main goal of our current work is a parametric study of the flow behind the wing with transversal surface high frequency discharge, at relatively low velocity $V_{af} \sim 20\text{m/s}$. SHFD was already shown to affect the separation process and drag of the round-edged flat plate [7,8].

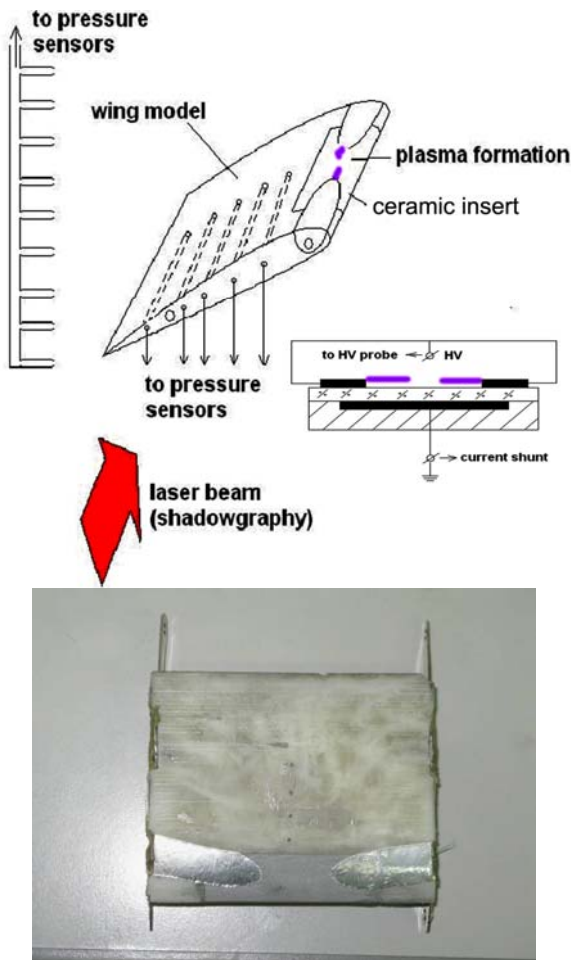


Fig.1. Airfoil model. a) model scheme, b) model photograph.

II. Experimental setup

Low-velocity (<20m/s) experiments were carried in the aerodynamic channel with 100x100x300 test section, operating in a continuous regime. Flow velocity can be changed by controlling the blower motor. Large-scale flow turbulence after the blower was quenched by honeycomb. However, turbulence level remained high enough (~several percents).

NACA 23012 airfoil model 8cm x 10cm (chord x span) was manufactured from Nylon-6. Model was positioned in the test section at a desirable attack angle using rotating windows. The electrodes were arranged near the model's leading edge (fig.1), with wiring connected to the mounting points of the model.

Flow blockage was up to 30% at 20° attack angle and 10% at 0° attack angle.

Discharge was created by "RF switch" generator, loaded with the model through the air-core resonant transformer with resonance frequency ~350 kHz. Output voltage measured was up to 14 kV, the peak discharge power- 200 W. The generator was operating in the pulse-periodic regime, creating RF pulses with 30-100 us duration and repetition frequency up to 10 kHz. Typical RF

pulse is shown on fig.2. Rise time was about 5 - 10 us. Pulse shape changed with discharge power due to resonant frequency shift during the pulse. These changes weren't controlled in the experiments.

Discharge voltage was measured with Tektronix P6014A HV probe, discharge current was measured in the ground lead with Tektronix AC current shunt. Stray current was negligible due to significant discharge capacity. Electrical power input was calculated by digital multiplication of current and voltage signals via TDS 2014B oscilloscope with ~10% error.

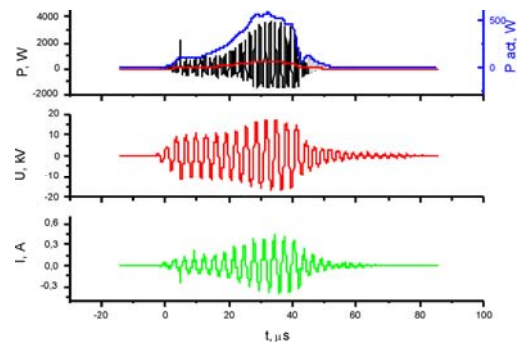


Fig.2. Typical voltage, current and power oscillograms during the pulse.

Wake structure was studied by an array of 14 0.7mm Pitot tubes, positioned 0.5-5 diameters downstream from the model, in the middle of its span. Alternatively, tube was transferred across the wake by a DC motor driver. Static pressure distribution along the model chord was measured at 5 positions, separated by 8 mm, with the first one at $x/d \sim 0.4$. The pressure was measured by a 16-channel pressure scanner Esterline 9116 with 500 Hz time resolution. Pressure values were then averaged on the ~1-2s period.

Shadow pictures of the flow were taken by excimer KrF laser (248nm) with 20ns pulse length. Direct shadow method with a divergent beam was used. Pictures were acquired by digital camera from the white-sheet paper used as wavelength convertor (UV to blue). The system was synchronized with the discharge pulses through the frequency divider and delay generator, allowing phase-locked acquisition of shadow images.

III. Results and discussion

A. Pressure measurements.

Parametric study.

It was revealed, that discharge SHFD ignition near the leading edge of the model can significantly reduce the model's drag.

Pressure distributions across the model wake at different attack angles are shown on fig.3. Drag reduction was obtained for attack angles

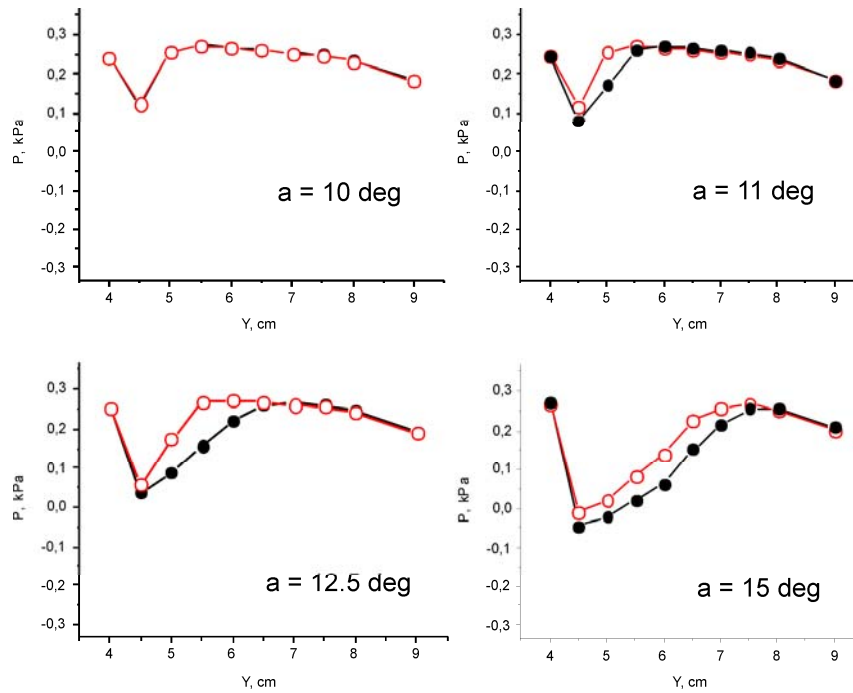


Fig.3. Total pressure distributions in the wake at different model's attack angles. Open symbols' – discharge on, closed – discharge off. $V=20\text{m/s}$, $P=1\text{ atm}$, $N_p\sim 200\text{W}$, $Sh\sim 2$.

$20^\circ > \alpha > 11^\circ$. At higher attack angles, experiments were not carried. One can see, that at discharge on, wake diameter and pressure losses are significantly reduced. At several experiments, drag decreases to the level of 60% of initial value. At attack angles $< 11^\circ$, no effect was obtained at any discharge power. At attack angle of 11° a significant increase of the model drag is obtained, indicating the stall at the leading edge.

Frequency dependency of the total pressure change at two different stations is shown on fig.4, total pressure distributions across the wake at different modulation frequency – on fig.5. Two frequency ranges where discharge affects the wake

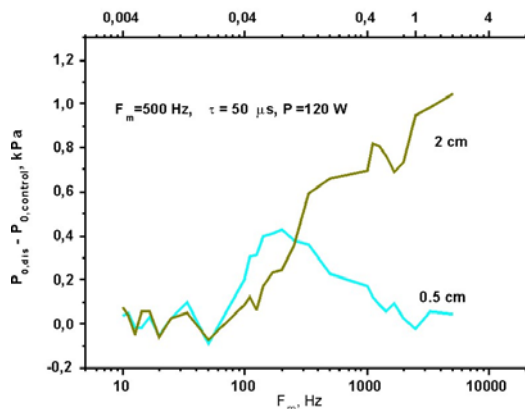


Fig.4. Total pressure at two positions vs excitation frequency.

properties for $V=20\text{ m/s}$ are obtained: $Sh\sim 1$ and $Sh>1$. It was revealed, that wake changes differently at this two frequency ranges: for $Sh\sim 1$, pressure is increased near the model surface, while at higher frequencies, separation bubble boundary is mainly disturbed. These differences can mean that different mechanisms are responsible for flow momentum transport in these two cases. Possibly, forcing at $Sh\sim 1$ interacts with the vortex shedding frequency from the wing's leading edge, while in the case of $Sh\gg 1$ turbulization of the shear layer takes place.

Actuator position significantly influences it's efficiency. It was revealed, that slight variations

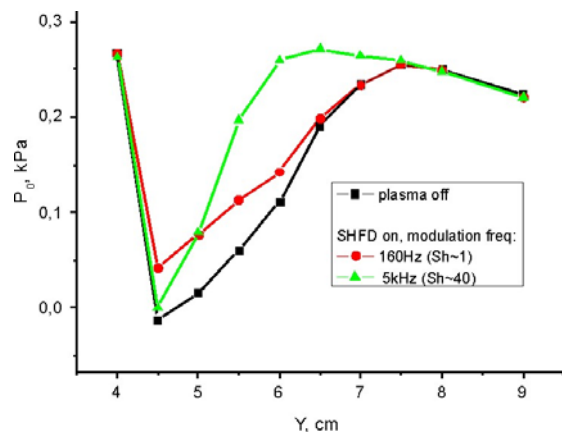


Fig.5. Total pressure distributions across the wake at different modulation frequency. $\alpha=15^\circ$, $P_t=120\text{W}$

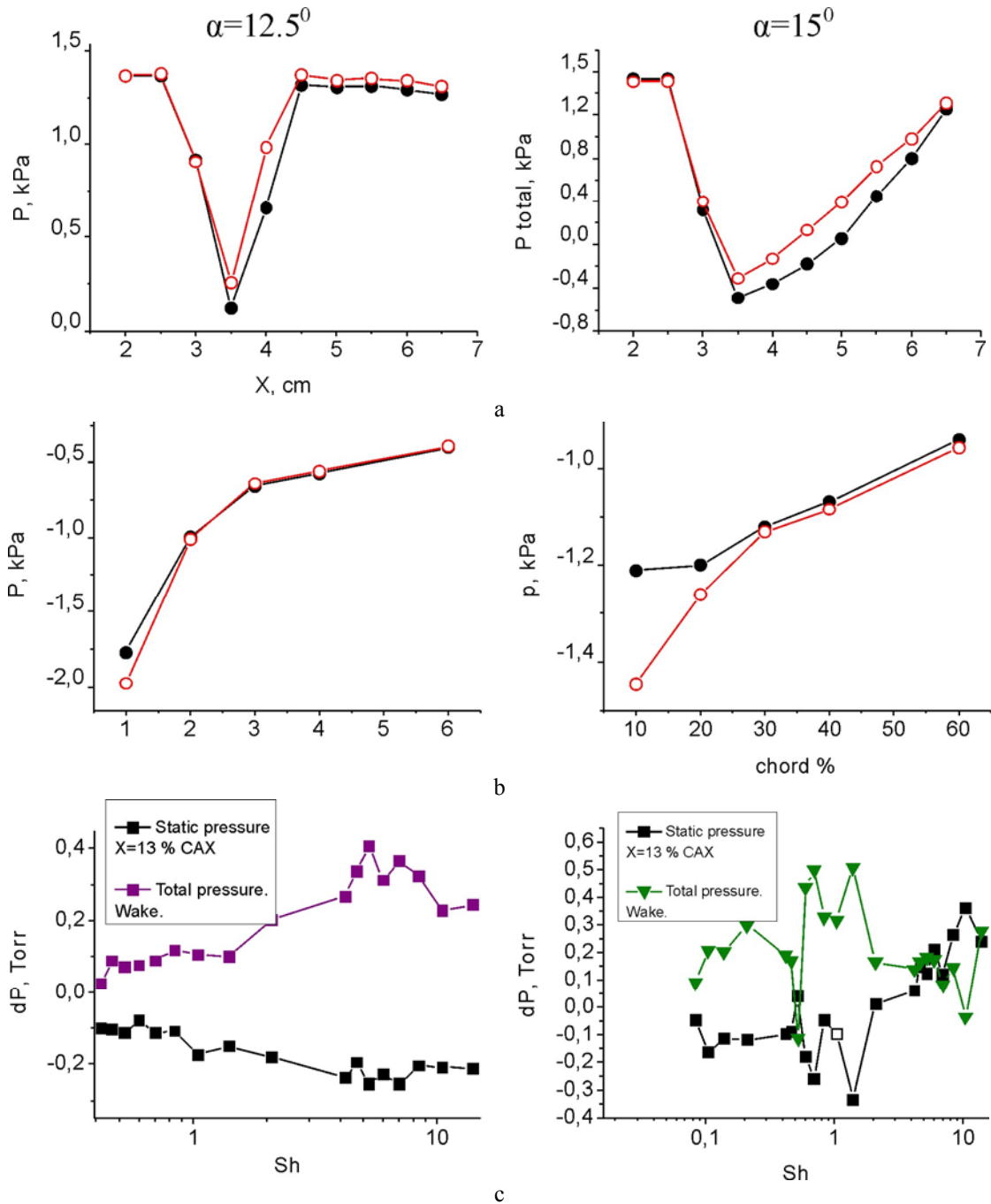


Fig.6. Total pressure distributions across the wake (a), static pressure distribution along the model's chord (b) and pressure change vs frequency for two stations: one on the model surface and one in the wake behind the wing (c). For a,b: open symbols-plasma on, closed ones – plasma off. Left column -- $\alpha=12.5^\circ$, right -- $\alpha=15^\circ$.

of the actuator position from model to model significantly influence the discharge effectiveness.

Frequency dependencies were also studied at different attack angles of the model. Fig.6. represents total pressure distributions across the wake (a), static pressure distribution along the model's chord (b) and pressure change vs frequency for two stations: one on the model surface and one in the wake behind the wing (c). It is clearly seen that at angles $\sim 11-12^\circ$ no peak for $Sh \sim 1$ is obtained, while it is clearly seen for higher angles of attack.

Static pressure distributions along the chord clearly shows pressure decrease on suction side right past the discharge, that means that flow velocity increases near the wall in this region.

B. Flow visualization

Phase-locked shadow images of the flow at the suction side of the wing is shown on fig. 7. Since flow gradients at 20 m/s are below the sensitivity limit of our system, 1 mm helium jet was injected 5mm before the model. Special precautions

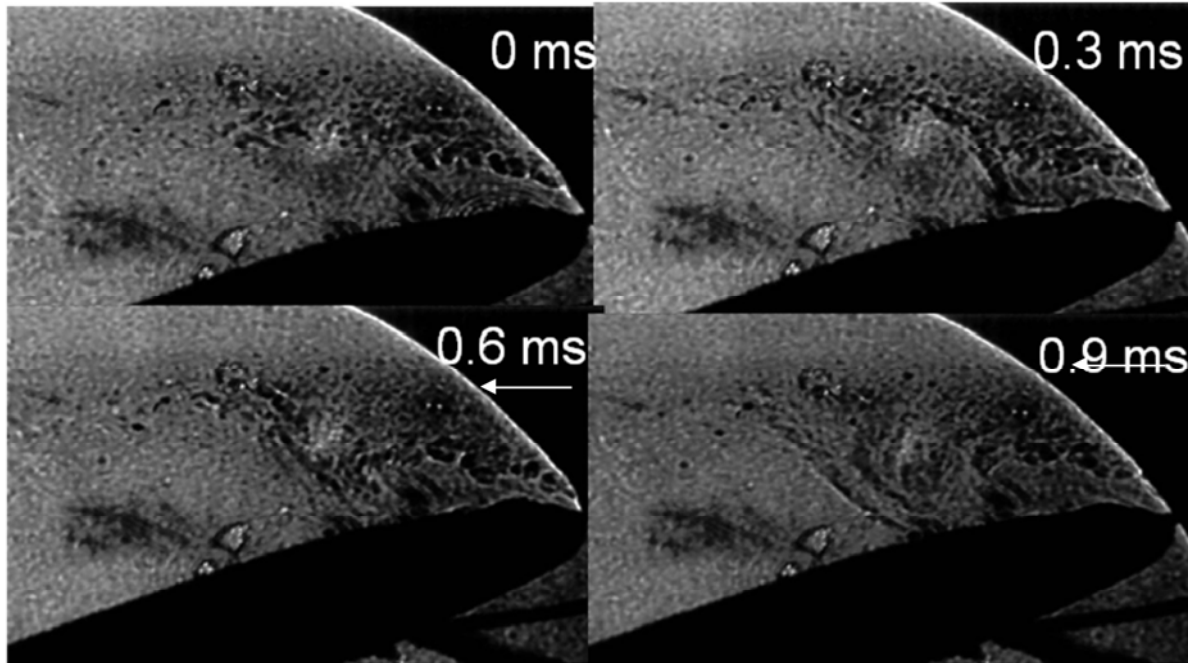


Fig.7. Shadow pictures of the flow at discharge on at different delays. $F_m=200$ Hz, $P_i=120$ W, $V_{af}=19$ m/s.

were taken to check the influence of the He supply tube on the model's drag. At zero delay, one can see an undisturbed flow, separating from the model surface. Ultrasonic waves, created by discharge can be seen at the electrodes region. Discharge initiation is followed by a vortex formation near the leading edge of the model. Vortex is typically formed 0.2 ms after the discharge pulse and appears as a jet deformation towards the model surface. One should note that 200 μ s is a typical time that 20m/s flow needs to pass a distance between leading edge and discharge position. During the further pulses, vortex is convected downstream along the model surface. The primary reason of vortex formation seems to be a temporal (pulse-correlated) reattachment of the flow at some region near the leading edge.

IV. Conclusions

- Flow control by SHFD around the wing model was studied at $V_{af}=20$ m/s, $Re=10^4$ at different Strouhal numbers.
- Discharge is revealed to decrease model's drag at attack angles $20^\circ > \alpha > 11^\circ$.
- Two frequency ranges are found: $Sh \sim 1$ and $Sh \gg 1$. Different changes in the wake are obtained at these two range: for $Sh \sim 1$, pressure is increased near the model surface, while at higher frequencies, separation bubble boundary is mainly disturbed.
- At just-after-stall attack angles, high frequency forcing appears to be most effective, while at

higher attack angle, resonance at $Sh \sim 1$ appears.

- Separation bubble deformation appears as vortex formation due to temporally local shift of the separation point during discharge operation.

References

1. J. Huang, T.C. Corke, and F.O. Thomas, "Unsteady Plasma Actuators for Separation Control of Low-Pressure Turbine Blades," *AIAA Journal*, vol. 44, Jul. 2006, pp. 1477-1487.
2. D.V. Roupasov, a a Nikipelov, M.M. Nudnova, and a Y. Starikovskii, "Flow Separation Control by Plasma Actuator with Nanosecond Pulsed-Periodic Discharge," *47th AIAA Aerospace Sciences Meeting Including The New Horizons Forum and Aerospace Exposition 5 - 8 January 2009, Orlando, Florida, 2009*, pp. 168-185.
3. J. Little and M. Samimy, "High-Lift Airfoil Separation with Dielectric Barrier Discharge Plasma Actuation," *AIAA Journal*, vol. 48, Dec. 2010, pp. 2884-2898.
4. A.V. Likhanskii, M.N. Shneider, D.F. Opaits, R.B. Miles, and S.O. Macheret, "Limitations of the DBD effects on the external flow," *48th AIAA Aerospace Sciences Meeting Including the New Horizons Forum and Aerospace Exposition 4 - 7 January 2010, Orlando, Florida, 2010*.
5. D.F. Opaits, M.R. Edwards, S.H. Zaidi, M.N. Shneider, R.B. Miles, and S.O. Macheret,

- “Surface plasma induced wall jets,” *48th AIAA Aerospace Sciences Meeting Including the New Horizons Forum and Aerospace Exposition 4 - 7 January 2010, Orlando, Florida*, 2010.
6. R.E. Hanson, P. Lavoie, and A.M. Naguib, “Effect of Plasma Actuator Excitation for Controlling Bypass Transition in Boundary Layers,” *48th AIAA Aerospace Sciences Meeting Including the New Horizons Forum and Aerospace Exposition 4 - 7 January 2010, Orlando, Florida*, 2010, pp. AIAA 2010-1091.
 7. V.A. Bityurin, A.N. Bocharov, A.I. Klimov, I.A. Moralev, and B.N. Tolkunov, “Surface HF Plasma Actuator in Airflow,” *40th AIAA Plasmadynamics and Lasers Conference 22 - 25 June 2009, San Antonio, Texas*, 2009, pp. AIAA 2009-4073.
 8. A.I. Klimov, V.A. Bityurin, I.A. Moralev, B.N. Tolkunov, K. Zhirnov, and V. Kutlaliyev, “Surface HF Plasma Aerodynamic Actuator,” *46th AIAA Aerospace Sciences Meeting and Exhibit 7 - 10 January 2008, Reno, Nevada*, 2008, pp. AIAA 2008-1411.
 9. J. Little and M. Samimy, “Control of Separation from the Flap of a High-Lift Airfoil with DBD Plasma Actuation,” *48th AIAA Aerospace Sciences Meeting Including the New Horizons Forum and Aerospace Exposition 4 - 7 January 2010, Orlando, Florida*, 2010, pp. AIAA 2010-1088.
 10. J. Little and M. Samimy, “Control of Separation from the Flap of a High-Lift Airfoil with DBD Plasma Actuation,” *48th AIAA Aerospace Sciences Meeting Including the New Horizons Forum and Aerospace Exposition 4 - 7 January 2010, Orlando, Florida*, 2010, pp. AIAA 2010-1088.

FLOW CONTROL AROUND CYLINDER BY HF DBD DISCHARGE

Moralev I., Bityurin V., Kasansky P., Klimov A., Chertov D.

¹ Joint Institute for High Temperatures RAS,
Izhorskaya 13, bld..2, Moscow, 125412, Russia
E-mail: *ivmoralev@gmail.com*

Abstract. Control of airflow around a cylindrical model by pulse-repetitive HF discharge ($F_{HF} \sim 350\text{kHz}$) is studied at airflow velocity up to 120 m/s and Reynolds number $Re = 2 \times 10^4 \div 2 \times 10^5$. It is obtained that HF pumping higher than the critical one changes airflow around cylindrical model and decreases wake's diameter. Pressure distribution in a model's wake and on the model surface are obtained at different HF discharge power, different duty cycle and different pulse repetitive frequency. Shadow pictures of airflow around a cylinder are obtained. Creation of a secondary large-scaled vortex in the cylinder's wake is recorded in these pictures. Mean discharge power input doesn't exceed 10 W/cm, peak HF power doesn't exceed 1 kW. Main parameters of a surface HF discharge are obtained measured. The possible physical mechanism of the surface discharge interaction with airflow in a separation region is discussed in this work

Nomenclature

HF	= high frequency
DBD	= dielectric barrier discharge
SHFD	= surface HF discharge
f_{HF}	= HF frequency
F_M	= modulation frequency
T_i	= pulse duration
I_{HF}	= HF electric discharge current
U_{HF}	= HF electric discharge voltage
N_{HF}	= pulse power input in plasma
M	= Mach number
V_{af}	= airflow velocity
P_0	= stagnation pressure
P_{st}	= static pressure
T_g	= gas temperature
T_R	= rotation temperature
Sh	= Strouhal's number
α	= attack angle of actuator

I. Introduction

Boundary layer control by means of different surface electric discharges is intensively studied today [1-3]. It is well known that efficiency of flow control near a body by a chord-wise dielectric barrier discharge (DBD) is decreased considerably at high airflow velocity ($V_{af} > 10\text{m/s}$). The reason is physical limitations on the DBD induced momentum, while pressure gradients in the external flow increases with velocity increase [4,5].

However, attempts are recently made to use the surface discharges for boundary layer control, referring to other mechanisms of discharge – flow interaction.

Airflow separation control near the wing model by nanosecond electric discharge was studied at flow velocity up to 100m/s [2,3]. The reattachment of the boundary layer was obtained at pulse repetition frequencies $Sh \sim 1$.

The problem of a boundary layer flow turbulization and generation of a longitudinal vorticity by means of DBD was studied in [6].

Surface high frequency discharge was proposed in [7,8] for separation control on a flat plate and cone drag reduction. It was shown, that at definite angles of attack and discharge regimes, significant change in pressure distribution behind the plate can be achieved.

Main goal of our current work is to study the separation process and wake structure behind the circular cylinder with transversal SHFD, operating on it's surface.

Cylinder was chosen for this study as an aerodynamic body with well-known flow structure. Low-speed flow around the cylinder with the DBD discharge actuators was studied in [9-11]. Wake structure at pulse-periodic discharge operation was studied in [9], actuator orientation effects – in [10]. In [11], vortex shedding was synchronized along the length by means of co-flow DBD. However, all authors implies that it is ionic wind, induced by the discharge, that leads to effects obtained.

II. Experimental setup

Low-velocity ($< 20\text{m/s}$) experiments were cared in the aerodynamic channel with 100x100x300 test section, operating in a continuous regime. Flow velocity can be changed by controlling the blower motor. Large-scale flow turbulence after the blower was quenched by honeycomb. However, turbulence level remained high enough (\sim several percents).

High-speed experiments ($< 300\text{m/s}$) were cared in the 50mm diameter open jet. Flow was organized at the exit of conical nozzle with a contraction ratio ~ 2 . In this case, aerodynamic system was supplied from 0.8 m³ high pressure tanks. Experiment duration was about 0.5 - 1s, depending on the airflow velocity.

Model (fig.1) was manufactured of a 40mm diameter quartz tube. Dielectric thickness was $\sim 2\text{mm}$. Discharge was organized in a spanwise direction. Electrodes were manufactured of

aluminum foil 200 μm thickness, the inner one was covered by epoxy or silicon resin to avoid arcing in the discharge gap.

Discharge was created by “RF switch” generator, loaded with the model through the air-core resonant transformer with resonance frequency ~ 350 kHz. Output voltage measured was up to 20 kV, the peak discharge power- 1 kW. The generator was operating in the pulse-periodic regime, creating RF pulses with 30-100 μs duration and repetition frequency up to 10 kHz. Typical RF pulse is shown on fig.2. Rise time was about 5 - 10 μs . Pulse shape changed with discharge power due to resonant frequency shift during the pulse. These changes weren't controlled in the experiments.

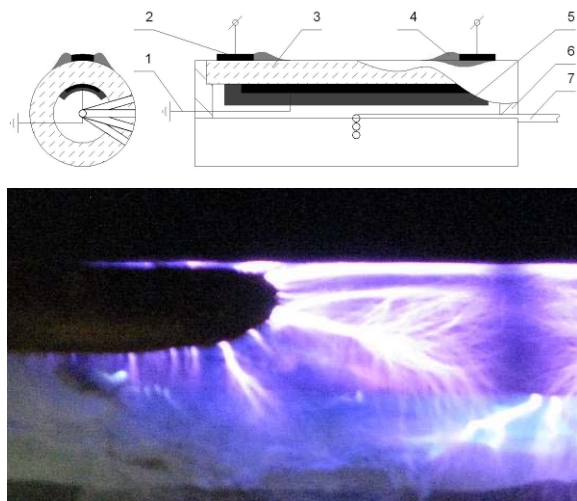


Fig.1. Model scheme and discharge photo. 1-ground lead, 2-exposed electrode, 3- quartz body, 4-discharge, 5- epoxy layer, 6-pressure tubes, 7- fastening bolt.

Discharge voltage was measured with Tektronix P6014A HV probe, discharge current was measured in the ground lead with Tektronix AC current shunt. Stray current was negligible due to significant discharge capacity. Electrical power input was calculated by digital multiplication of current and voltage signals via TDS 2014B oscilloscope with $\sim 10\%$ error.

Wake structure was studied by an array of 14 0.7mm Pitot tubes, positioned 0.5-5 diameters downstream from the cylinder, in the middle of its span. Alternatively, tube was transferred across the wake by a DC motor driver. The pressure was measured by a 16-channel pressure scanner Esterline 9116 with 500 Hz time resolution.

Shadow pictures of the flow were taken by excimer KrF laser (248nm) with 20ns pulse length. Direct shadow method with a divergent beam was used. Pictures were acquired by digital camera from the white-sheet paper used as wavelength convertor (UV to blue). The system was synchronized with the discharge pulses through the frequency divider

and delay generator, allowing phase-locked acquisition of shadow images.

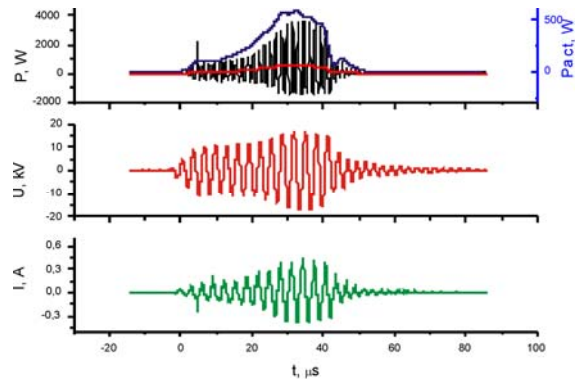


Fig.2. Typical voltage, current and power oscillograms during the pulse.

Flow smoke visualization was also performed. Ammoniac smoke was injected in the rear point of the cylinder, tangentially to model's surface.

III. Results and discussion

A. Pressure measurements.

Parametric study.

It was revealed, that discharge SHFD ignition on the cylinder surface can impact the separation process on the cylinder surface, change the properties of the flow in the wake and reduce aerodynamic drag. Typical signal for one of the dynamic pressure sensors in a wake is shown on fig.3. It is clearly seen, that at the discharge on, the wake diameter decreases.

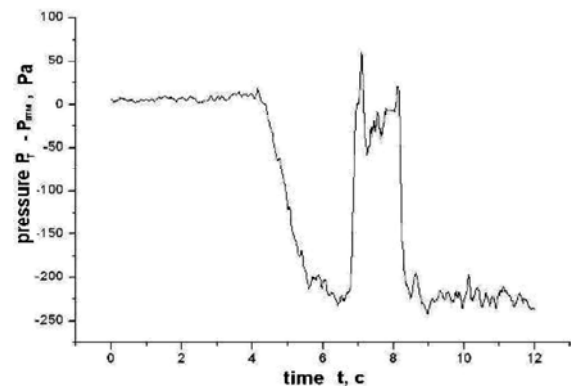


Fig 3. Rise of dynamic pressure when discharge is on.

Frequency dependence of the total pressure losses decrease is shown on fig.4. Two frequency ranges where discharge affects the wake properties for $V=20$ m/s are obtained: $Sh \sim 0.25$ and $Sh > 1$. One should note that value $Sh \sim 0.3$ corresponds to typical vortex shedding frequency for a circular

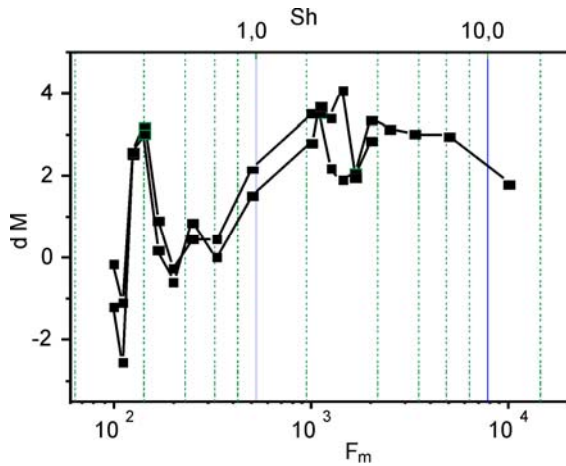


Fig.4. Total pressure losses vs excitation frequency.

cylinder at Re numbers considered.

Pulse energy effect on the wake was studied at oncoming flow velocity 20 m/s. To focus the study on the unsteady energy release effects, duty cycle (and pulse energy) was varied at constant mean discharge power. It is obtained

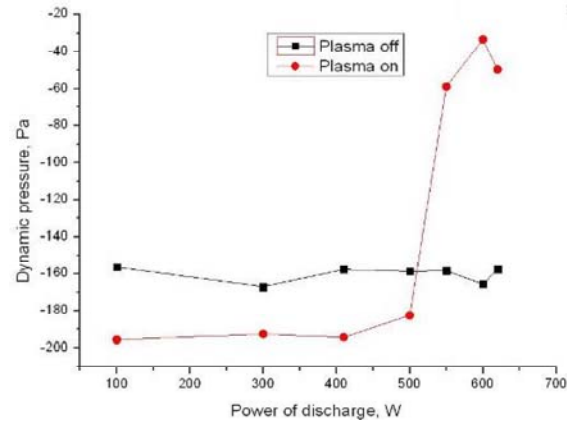


Fig 5. Dynamic pressure in the airflow behind the cylinder at different pulse power. $F_m=200$ Hz, mean power is constant $PHF=20$ W, $x=1$ cm.

(fig.5), that at Strouhal number $Sh=2$, wake collapse is not obtained up to the energy ~ 20 mJ. At $Sh\sim 0.3$, this critical value is ~ 5 mJ. Quasi-stationary energy release (at low pulse power) can even lead to the increase of the wake diameter. This means

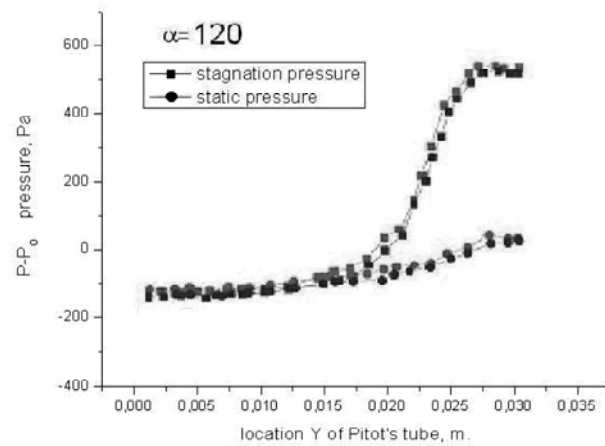
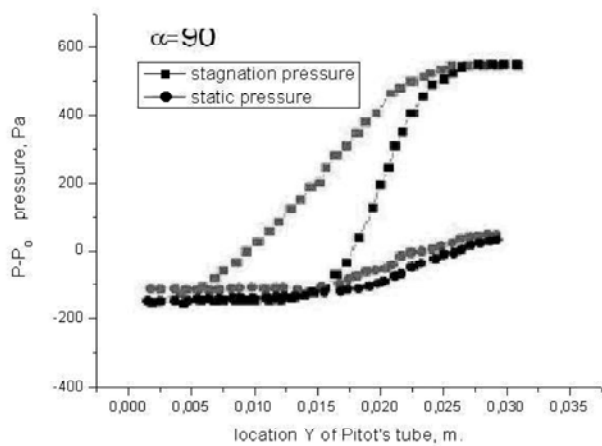
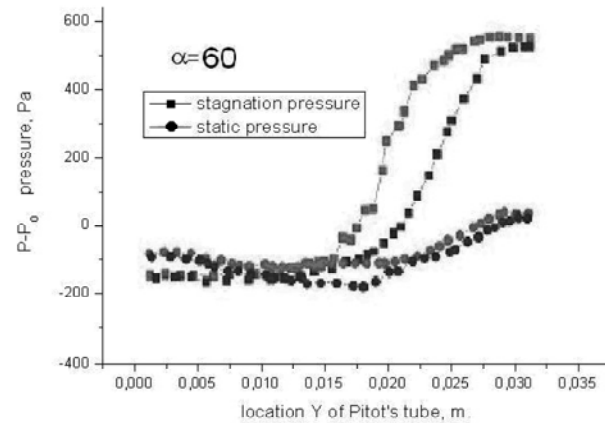
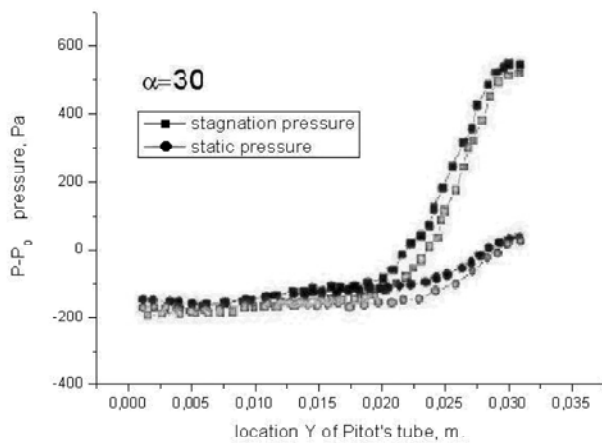


Fig.6. Dependence of stagnation pressure distribution and static pressure distribution across the wake on attack angle α of HF plasma actuator (black-with discharge, grey without discharge).

that steady heating of the boundary layer can not be the mechanism responsible for drag reduction effects effect described here.

A. Higher velocities

Discharge power should be obviously increased with oncoming velocity to obtain separation control.

Total pressure distributions across the cylinder wake at oncoming velocity ~ 100 m/s and cylinder diameter ~ 20 mm is shown on fig.5. It is clearly seen, that at discharge on, the wake diameter decreases. At flow velocity >100 m/s discharge effectiveness decreases. This can happen due to change of separation regime to turbulent one. However, detailed study of Re influence on the effectiveness of the discharge can't be made on this experimental setup due to a high turbulence level of the oncoming flow.

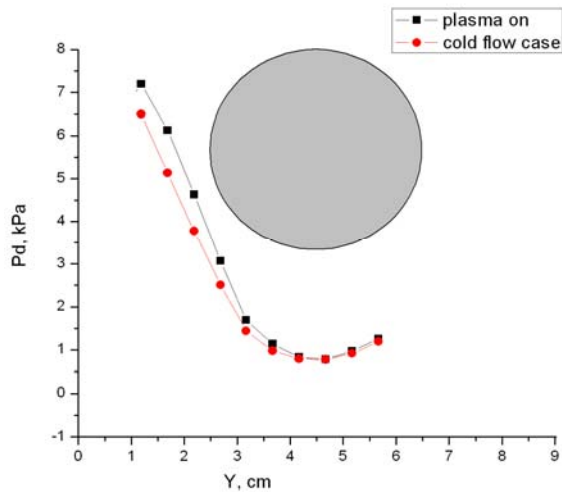


Fig7. Total pressure distributions in the cylinder wake. $V=100$ m/s, $P_p=500$ W.

B. Flow visualization

It is also revealed (fig.6) that actuator position significantly influences it's efficiency. The actuator, for this Reynolds number, is most efficient at angles $\sim 80-90$ deg (0 corresponds to forward stagnation point). It stays efficient up to the angles $\sim 40-60$ deg. Actuator, placed in the separation region (120 deg) doesn't significantly affect the wake properties. One should note, that laminar boundary layer separates from the cylinder surface at $\alpha \sim 87^\circ$ [12]. Hence, optimal actuator performance is achieved near the separation line.

Flow visualization images are shown on fig.8. One can see large-scale vortices creation in the wake, phase-locked to the discharge pulse.

Pressure disturbances, created by SHFD were visualized by shadow method. On fig.9. one can see compression or acoustic waves packages,

propagating from the discharge channels. Distance between waves and number of oscillations in a package exactly corresponds to the frequency and form of HF pulse.

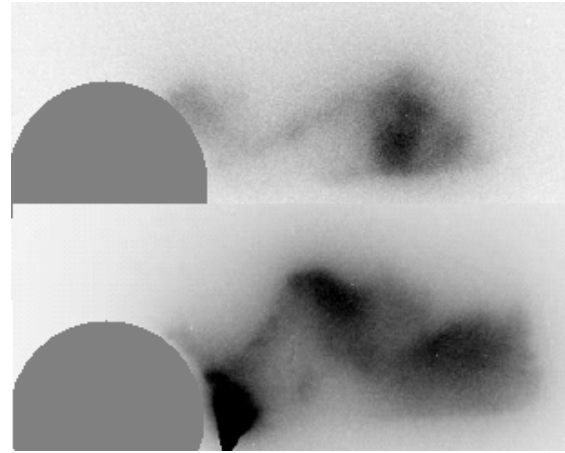


Fig8. Flow patterns at different delays after the discharge pulse 1-300us, 2-600us. $V=20$ m/c, $F_m=1$ kHz (Sh-2).

From fig.9, discharge propagation velocity can be determined to be 2×10^3 m/s. Wave structure is significantly nonhomogenous. Cylindrical waves, corresponding to the positions of discharge channels can be obtained. Further interference leads to plain wavefront formation

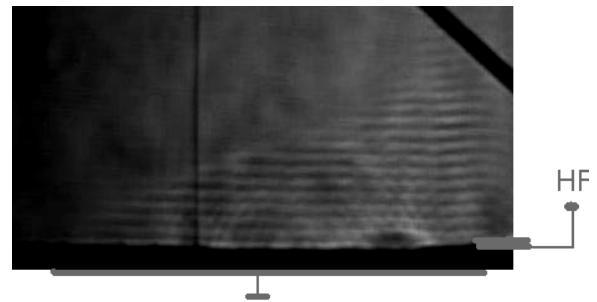


Fig.9. Discharge propagation shadow picture. Delay from power pulse edge ~ 6 us., $N_{HF} \sim 1$ kW, $U_{HFa} \sim 20$ kV, underlay- 4mm PMA.

C. Discussion

Results obtained can't be explained from the position of ionic wind generation in the discharge ([9-11]) or time-average heating of some regions in a boundary layer (e.g. [13,14]).

Instead, we can assume the main mechanism of the discharge- boundary layer interaction to be the pressure disturbances by abrupt heat release in discharge channels [2]. Disturbances created can themselves induce normal momentum transfer or can lead to the boundary layer turbulization. Both effects lead to separation point movement towards the rear point of the body. Induced large-scale vortices shedding can lead to

the resonances with low Strouhal numbers and should be obtained for any impact mechanism.

Typical energy input to the discharge during the pulse is about 2×10^{-4} J. specific energy input to the discharge channels is about $0.1-1$ J/cm³. Peak temperature in the filaments measured from N₂⁺ band emission appears to be ~ 1500 K.

IV. Conclusions

- Flow control by SHFD was studied at $V_{ar} < 120$ m/s, $Re = 10^4 - 10^5$ at different Strouhal numbers and actuator positions. Discharge appeared to be most effective for $Sh \sim 0.3$ and $\alpha \sim 90^\circ$.
- There is a threshold value of RF pulse energy required for flow separation control.
- Large-scale vortex shedding, phase locked with discharge operation, was obtained at $Re \sim 10^4$.
- Mechanism of actuation by SHFD seems to be connected with compression waves, generated in a boundary layer in each half-period of RF pulse due to abrupt heat release.

V. References

1. J. Huang, T.C. Corke, and F.O. Thomas, "Unsteady Plasma Actuators for Separation Control of Low-Pressure Turbine Blades," *AIAA Journal*, vol. 44, Jul. 2006, pp. 1477-1487.
2. D.V. Roupasov, a a Nikipelov, M.M. Nudnova, and a Y. Starikovskii, "Flow Separation Control by Plasma Actuator with Nanosecond Pulsed-Periodic Discharge," *AIAA Journal*, vol. 47, Jan. 2009, pp. 168-185.
3. J. Little and M. Samimy, "High-Lift Airfoil Separation with Dielectric Barrier Discharge Plasma Actuation," *AIAA Journal*, vol. 48, Dec. 2010, pp. 2884-2898.
4. A.V. Likhanskii, M.N. Shneider, D.F. Opaitis, R.B. Miles, and S.O. Macheret, "Limitations of the DBD effects on the external flow," *48th AIAA Aerospace Sciences Meeting Including the New Horizons Forum and Aerospace Exposition 4 - 7 January 2010, Orlando, Florida*, 2010.
5. D.F. Opaitis, M.R. Edwards, S.H. Zaidi, M.N. Shneider, R.B. Miles, and S.O. Macheret, "Surface plasma induced wall jets," *48th AIAA Aerospace Sciences Meeting Including the New Horizons Forum and Aerospace Exposition 4 - 7 January 2010, Orlando, Florida*, 2010.
6. R.E. Hanson, P. Lavoie, and A.M. Naguib, "Effect of Plasma Actuator Excitation for Controlling Bypass Transition in Boundary Layers," *48th AIAA Aerospace Sciences Meeting Including the New Horizons Forum and Aerospace Exposition 4 - 7 January 2010, Orlando, Florida*, 2010, pp. AIAA 2010-1091.
7. V.A. Bitururin, A.N. Bocharov, A.I. Klimov, I.A. Moralev, and B.N. Tolkunov, "Surface HF Plasma Actuator in Airflow," *40th AIAA Plasmadynamics and Lasers Conference 22 - 25 June 2009, San Antonio, Texas*, 2009, pp. AIAA 2009-4073.
8. A.I. Klimov, V.A. Bitururin, I.A. Moralev, B.N. Tolkunov, K. Zhirnov, and V. Kutlaliev, "Surface HF Plasma Aerodynamic Actuator," *46th AIAA Aerospace Sciences Meeting and Exhibit 7 - 10 January 2008, Reno, Nevada*, 2008, pp. AIAA 2008-1411.
9. F.O. Thomas, A. Kozlov, and T.C. Corke, "Plasma Actuators for Cylinder Flow Control and Noise Reduction," *AIAA Journal*, vol. 46, Aug. 2008, pp. 1921-1931.
10. S. Yamada, S. Kouji, I. Hitoshi, H. Shinji, and M. Motosuke, "Flow Behavior behind a Circular Cylinder by DBD Plasma Actuators in Low Reynolds Number," *48th AIAA Aerospace Sciences Meeting Including the New Horizons Forum and Aerospace Exposition 4 - 7 January 2010, Orlando, Florida*, 2010, pp. AIAA 2010-549.
11. T. McLaughlin, M. Munska, J. Vaeth, and T. Dauwalte, "Plasma-Based Actuators for Cylinder Wake Vortex Control," *2nd AIAA Flow Control Conference, Portland, Oregon, June 28-1, 2004*, 2004, pp. AIAA-2004-2129.
12. P.K. Chang, *Separation of Flow*, Pergamon Press, 1970.
13. A.V. Kazakov, M.N. Kogan, and A.P. Kuryachii, "Reduction of turbulent friction under local surface heating," *Journal of Applied Mechanics and Technical Physics*, vol. 37, Nov. 1996, pp. 832-838.
14. A.V. Kazakov and A.P. Kuryachii, "Effect of nonisothermality of the surface of a thin profile on the stability of a laminar boundary layer," *Fluid Dynamics*, vol. 21, 1987, pp. 706-711.

MHD POWER EXTRACTION IN RE-ENTRY FLIGHT

V.A. Bityurin, A.N. Bocharov

Joint Institute of High Temperatures of Russian Academy of Sciences, Russia, Moscow
e-mail: bocharov@ihed.ras.ru

Abstract. An idea is proposed to utilize the high-speed high-enthalpy flow in on-board magnetohydrodynamic generator while re-entry flight. Numerical estimations of MHD power extraction are presented for one of the trajectory point of the Stardust re-entry capsule flight path. It is shown that up to 5% of the total enthalpy flux could be converted to electrical power which constitutes about 3MWt.

Idea to extract electric power from the high-speed flow during the vehicle re-entry flight has been first considered in early 1990th [1]. The idea was motivated by the interest in aerospace community to the methods for quick generation of electric power while aerospace vehicle flight. The first assessments of the extraction of power of order of 1MWt during re-entry flight path have shown the principal feasibility of the idea. Later, the experimental hypersonic surface MHD generator has been demonstrated in [2, 3], in which electric power 60W/cm² has been achieved. In those studies a new potential for appropriate organization of MHD interaction in hypersonic flow was recognized. One could expect that rather low ionization degree is achieved over a lengthy surface under real flight conditions (see, for example, [4]). High ionization degree, and, as consequence, high electrical conductivity is expected to be realized only in the shock layer bulk near the critical point of the vehicle. At the same time, the flow over an extensive surface downstream the critical point is chemically frozen, in which the ionization may be not sufficient to maintain sufficient MHD interaction level. Therefore, in the current paper modification to surface MHD generator (like those proposed in [1 – 3]) is considered. The feature of the proposal is to organize re-entry flight MHD generation in the configuration similar to air-breathing unit.

Schematic of the re-entry flight MHD generator is presented in Fig.1. The flow between two thick plates is considered. The flow is assumed to be uniform in the direction perpendicular to the main flow plane, which, in turn, is the direction of the magnetic field. To avoid possible stagnation of the flow due to MHD interaction in the duct the bottom part of the duct is taken as diverging one. Thus, classic linear MHD generator is considered, in which electrical conductivity is provided by “natural” thermal ionization of air behind a shock.

The power extraction is estimated under the following free-stream conditions corresponding to 60 km altitude trajectory point of the Stardust return capsule flight path.

$$\rho = 2.34 \cdot 10^{-4} \text{ kg/m}^3, p = 16.6 \text{ Pa}, V = 11137 \text{ m/s}, T = 238.5 \text{ K}, M = 36, T_{wall} = 2500 \text{ K}.$$

Here ρ is density, p is pressure, V is velocity, T is temperature, M is Mach number.

At this stage we consider a flow in the duct to be in local thermodynamic equilibrium. The air LTE model is taken from paper [5]. Electrical commutation scheme is also shown in Fig.1. So called frame channel is analyzed. The electrodes of frames F_i ($i=1, \dots, 7$) are assumed to hold at the same potential (different for every frame) and the same current passes through electrodes of the frame. The leftmost electrodes on the upper wall and the rightmost electrodes on the bottom one represent the load circuit, which also has a resistance to be found from the condition of maximum extracted power. It is assumed that magnetic field is created by two coils such that the coil plane is parallel to free-stream one. Thus, the direction of the magnetic field is perpendicular to the plane in which the MHD flow is considered. That is, $\mathbf{B} = B(x,y)\mathbf{e}_z$, \mathbf{B} is magnetic flux density and \mathbf{e}_z is unit vector in z-direction. Example of the distribution of magnetic induction $B_z(x,y)$ is shown in Fig.1.

Electric potential lines and electric current stream lines are shown in Fig.2. These distributions are obtained for the MHD generator operation mode corresponding to the maximal extracted electric power. At this operation mode, the load current is about 184 kAmps, and the load voltage is about 16 Volts. The total electric power is approximately 3MW, which is about 5% of the total enthalpy flux.

The change in the flow structure due to MHD interaction in the duct can be seen in Fig.3. Here, the static pressure field is shown for two flow cases, without magnetic field (upper) and with magnetic field (bottom). It should be noticed that short-term MHD device is currently considered, which life-time is strongly restricted by the presence of high temperature plasma in the duct and, hence, by very high heat fluxes to the wall.

References

1. *Bityurin V.A., Bocharov A.N., and Ivanov V.A.* MHD control of space vehicle // IVTAN-ANRA Technical Rep. 94/3, IVTAN-ANRA, Moscow, 1994, p.37 (in Russian).
2. *Bityurin V., Bocharov A., Baranov D. and Bychkov S.* Power Extraction Experiment with a Surface MHD Generator in Hypersonic Airflow // 38th AIAA Plasmadynamics and Lasers Conference In conjunction with the 16th International Conference on MHD Energy Conversion. 2007. Miami, FL. June 25-28. AIAA Paper 2007-3882.
3. *Bityurin V.A., and Bocharov A.N., and Popov N.A.* Experimental and Numerical Studies of MHD Interaction in Hypersonic Flows // High Temperatures, 2010, Vol. 48, No.1 (additional), p.44 (in Russian).
4. *Bityurin V.A., Bocharov A.N., and Popov N.A.* Study of MHD deceleration in the Earth Atmosphere // High Temperatures, 2010, Vol. 48, No.1 (additional), p.113 (in Russian).
5. *Kraiko, A.N., and Makarov, V.E.* Explicit Formulas for Calculation of Equilibrium Composition and Thermodynamic Functions of Air in the Range of 200K – 20000K // High Temperatures, 1996, Vol. 34, No. 2, p.208 (in Russian).

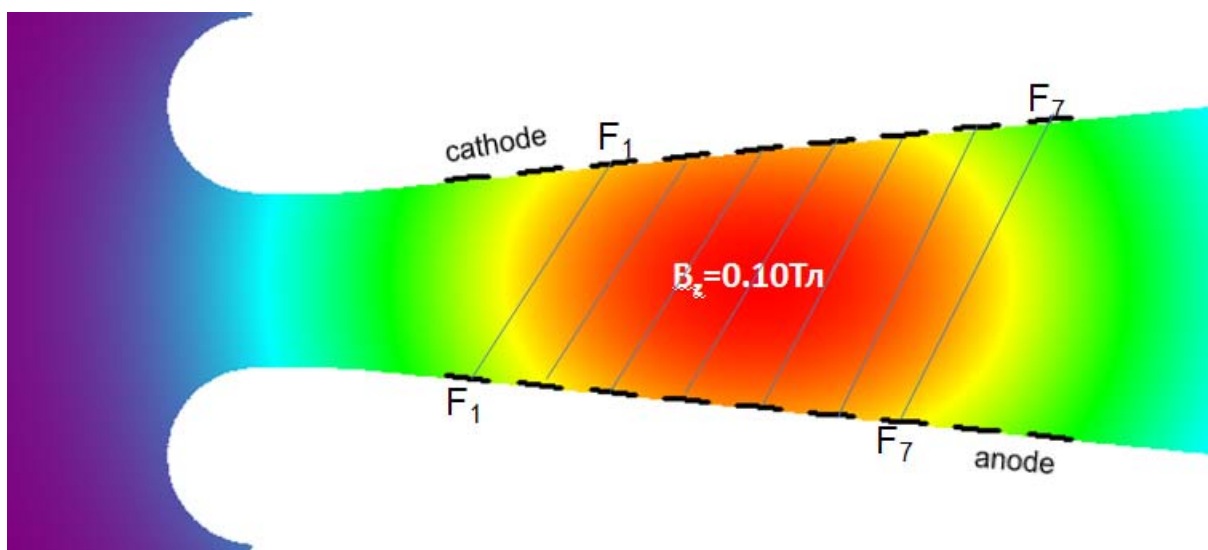


Fig.1. Schematic of the MHD flow in the duct, electric circuit configuration, and distribution of magnetic induction B_z .

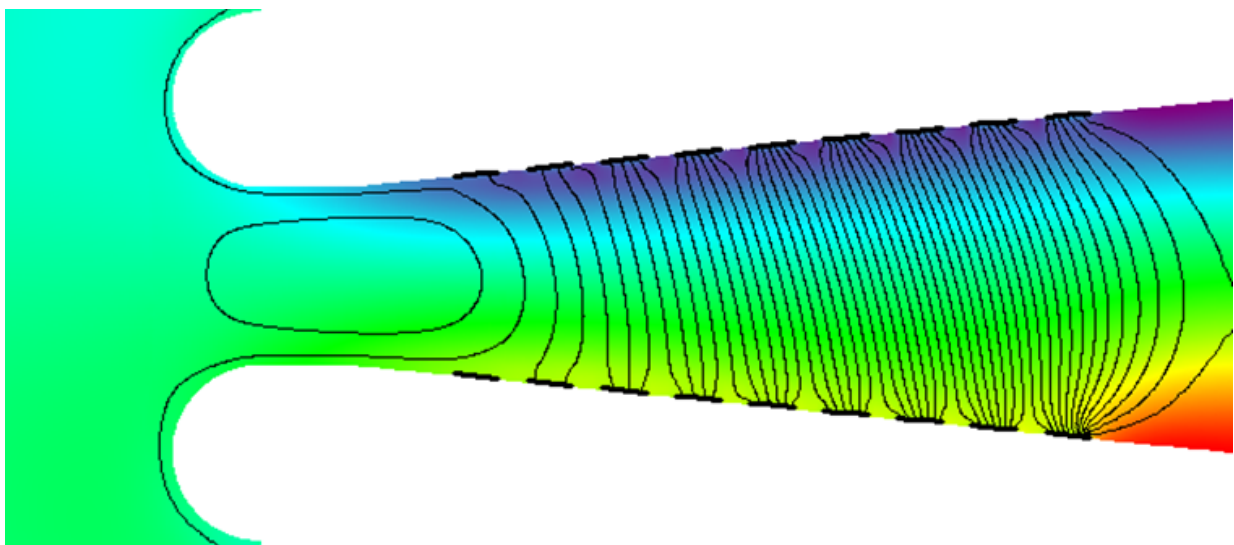


Fig.2. Electric potential (filled, colored) and electric current stream lines (black) for the 3MW operation mode. Load voltage is 16V, load current is 184kAmps, total power is 2.9 MW.

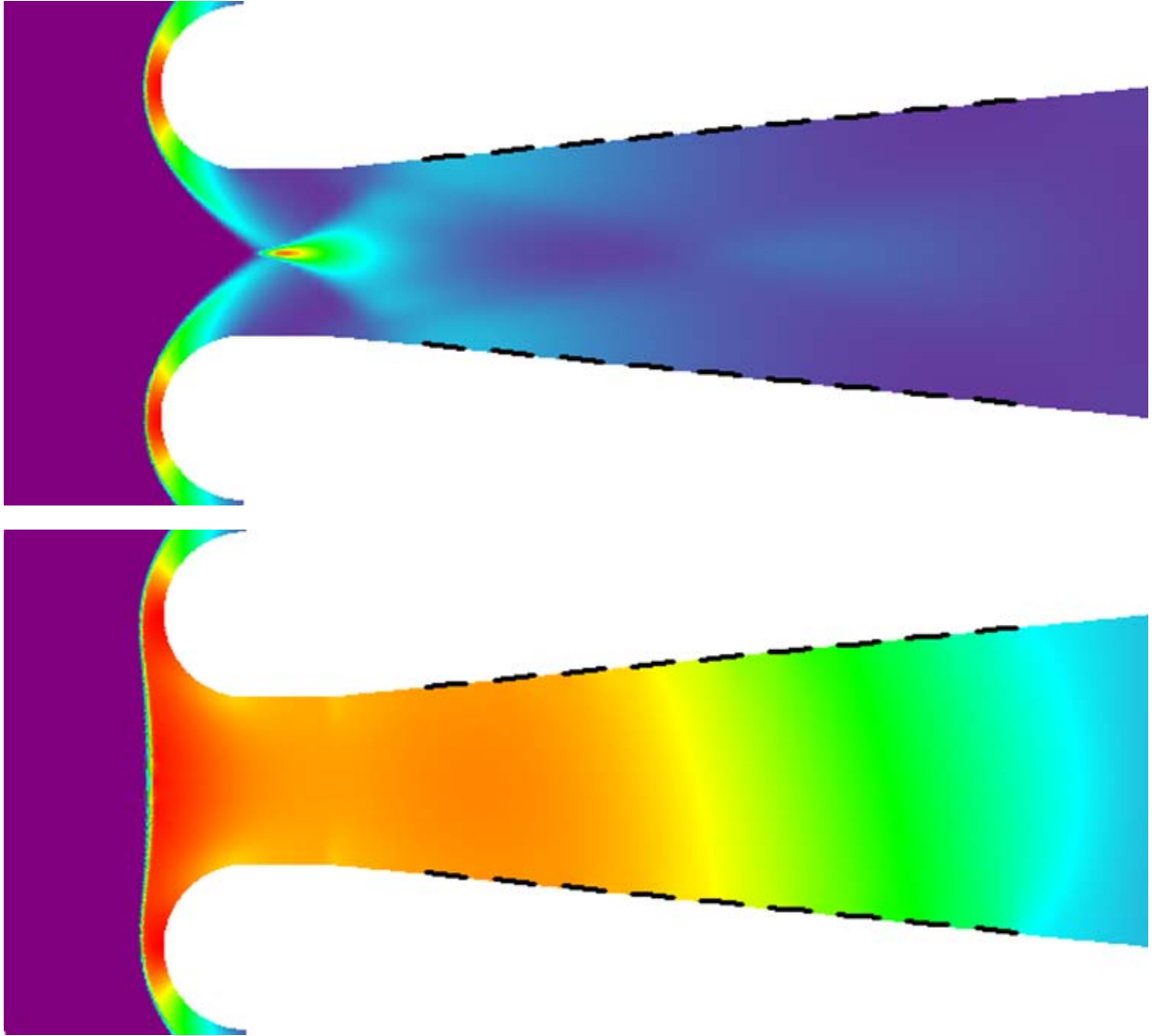


Fig.3. Pressure field for two flow cases: MHD off (upper) and MHD on ($B_{max}=0.1Tl$, bottom).

PHYSICAL-CHEMICAL KINETICS OF ALUMINIUM OXIDATION BY STEAM.

A.S. Dobrovolskaya (MIPT)

Motivation to this work was experimental research in plasma-assisted combustion of aluminum powder in a steam. Physical-chemical kinetics mechanism of aluminum oxidation by steam is analyzed in the paper with computer simulation. The products of these reactions are condensed corundum and gaseous hydrogen. Full simulation requires solving equations of hydrodynamic in combination with gas-phase chemical kinetics and heterogeneous processes. Therefore zero-dimensional chemical kinetics with simple corundum condensation is sufficient for qualitative understanding of processes in this system.

Twenty eight chemical reactions occurring in gaseous phase were considered along with the condensation of corundum (Al_2O_3). The constants of rate for these reactions are

$$K_i = k_i \cdot T^n \cdot \exp\left(-\frac{E_a}{RT}\right), \quad (1)$$

where k_i , E_a and n are shown in table 1. Reactions 1-18 are from [1], 19-28 are from [2].

The condensation model is based on the simplified micro kinetic scheme of liquid-state growth from the supersaturated vapor phase [3]. In this model condensation takes into account when partial pressure of corundum exceeds its saturation pressure. In this simulation the dusty particles adding from outside were considered because the condensation on the macro-particles is faster than the formation of nucleation centers. So, mass flow of the condense corundum depends on average radius of particles, their number and difference between partial pressure of corundum and its saturated pressure. In the expressions below r is average radius of particles, T – gas temperature,

$$J = \frac{u}{4}(n(t) - n_{sat}(r, T))4\pi r^2 \left[\frac{\text{mole}}{\text{s} \cdot \text{particle}} \right]$$

is a flow of condensed corundum to particle, V_l – mole volume of liquid Al_2O_3 , N_z – Al_2O_3 -particle concentration, C – heat capacity of gaseous mixture, q_{vap} – vaporization heat of corundum, n – concentration of gaseous Al_2O_3 , n_{sat} – saturation concentration of Al_2O_3 , u – thermal velocity of Al_2O_3 . Therefore one can add the equations 2-4 to equations of chemical kinetics with rate constants (1).

$$\frac{dn}{dt} = W_{chem} - \frac{u}{4}(n(t) - n_{sat}(r, T))4\pi r^2 \cdot N_z, \quad (2)$$

$$\frac{dr}{dt} = V_l \frac{u}{4}(n - n_{sat}(r, T)), \quad (3)$$

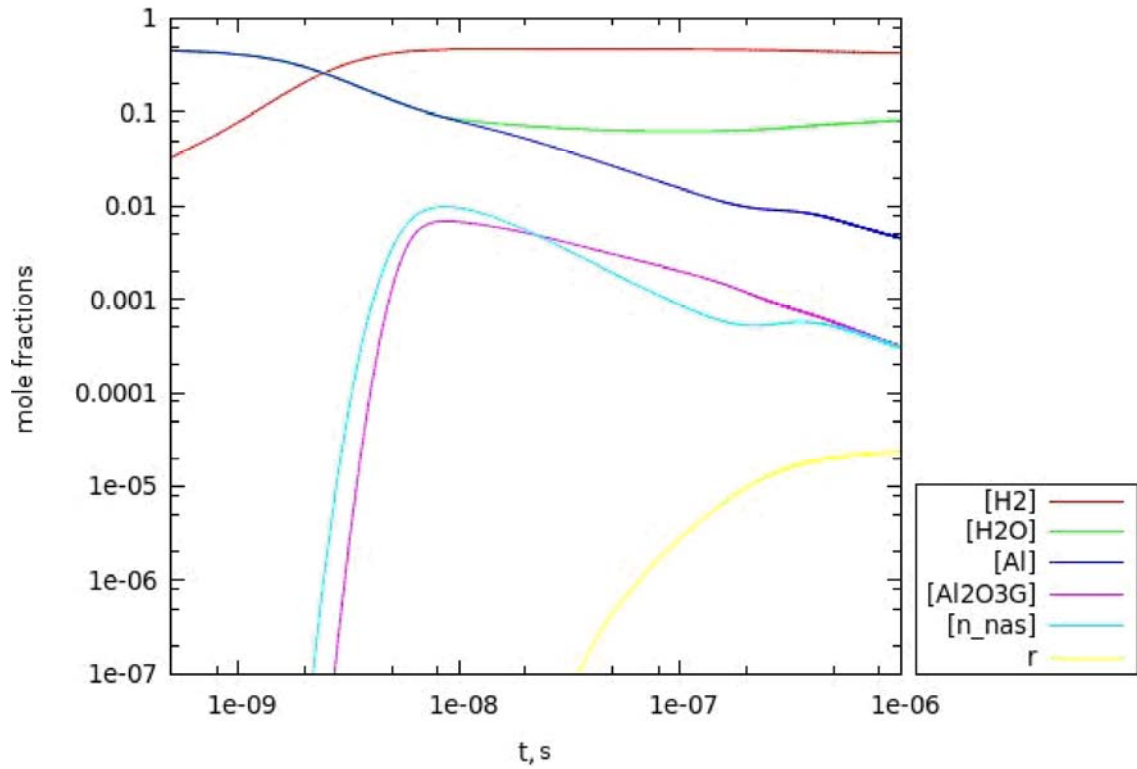
$$\frac{dT}{dt} = \left(\frac{dT}{dt} \right)_{chem} + \frac{1}{C_v} \frac{u}{4}(n - n_{sat}(r, T))4\pi r^2 \cdot q_{vap} \cdot N_z \quad (4)$$

It was found that condensation of corundum effects on chemical composition of mixture and energy balance. If we take into account condensation the temperature of the gaseous mixture increases slightly. Nevertheless the differences between simulation and experimental results were significant. In experimental there was a huge amount of hydrogen, the temperature was about 3000 K and there wasn't a gaseous corundum at all. But simulation shows us temperature about 2500 K (and it continue to decrease) and a lot of gaseous corundum after termination of condensation because of the saturation pressure of Al_2O_3 already became to exceed the partial one at 2500. One can take into account that there is no mention of gaseous Al_2O_3 in numerous experimental papers about aluminum oxidation with water and there is lack of theoretical information about its thermo-dynamical properties. So it's naturally to suppose that such model is incorrect.

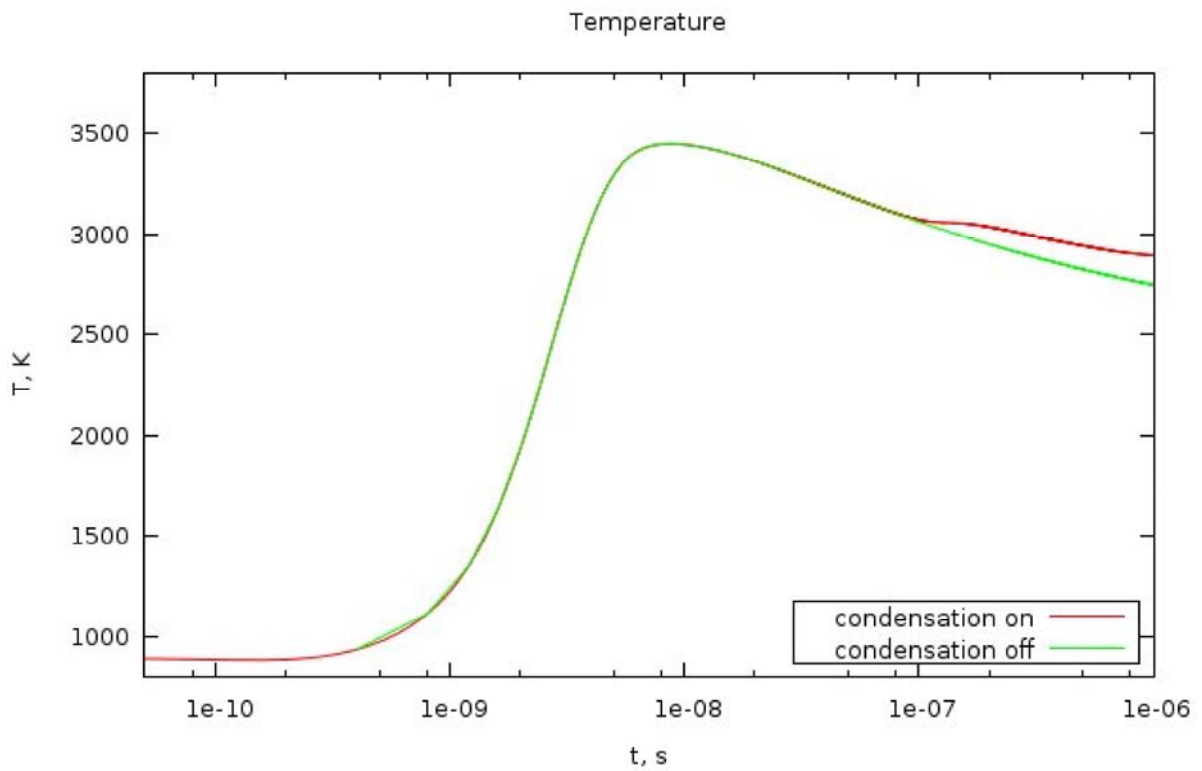
In this work was shown that heat emission during pure chemical oxidation was insufficient for heating up to experimental temperatures, and one need to take into account the condensation process. But model where condensation results from supersaturation of gaseous Al_2O_3 is incorrect and we need to continue investigations.

References

1. E. B. Washburn, J. N. Trivedi, L. Catoire and M. W. Beckstead, The simulation of the combustion of micrometer-sized aluminum particles with steam, *Combust. Sci. and Tech.*, 180: 1502-1517, 2008.
2. Biturin V, Bocharov A, Filimonova E. Effect of nitrogen oxide on ignition of non-premixed



Picture 1. Major species mole fraction.



Picture 2. Temperature of gaseous mixture.

Table 1.

№	Reaction	$k, \text{sm}^3 \text{s}^{-1} \text{mole}^{-1}$	k, s^{-1}	$n, (\text{T})^n$	E_a/R	E_a, cal
1	$\text{Al} + \text{H}_2\text{O} = \text{AlO} + \text{H}_2$	9.60E+013			2868.6	5700.4819
2	$\text{AlO} + \text{H}_2 = \text{Al} + \text{H}_2\text{O}$	2.61E+013			2868.6	5700.4819
3	$\text{Al} + \text{H}_2\text{O} = \text{AlOH} + \text{H}$	1.14E+012			442.8	879.93216
4	$\text{AlOH} + \text{H} = \text{Al} + \text{H}_2\text{O}$	1.00E+011			442.8	879.93216
5	$\text{Al}_2\text{O}_3(\text{gas}) = \text{Al}_2\text{O}_2 + \text{O}$		3.00E+015		49144.4	97659.752
6	$\text{Al}_2\text{O}_2 + \text{O} = \text{Al}_2\text{O}_3(\text{gas})$	5.68E+010		1	2944.5	5851.3104
7	$\text{Al}_2\text{O}_3(\text{gas}) = \text{AlO} + \text{AlO}_2$		3.00E+015		63915.4	127012.68
8	$\text{AlO} + \text{AlO}_2 = \text{Al}_2\text{O}_3(\text{gas})$	2.10E+009		1	-3296	-6549.811
9	$\text{Al}_2\text{O}_2 = 2\text{AlO}$		1.00E+015		59335.7	117911.9
10	$2 \text{AlO} = \text{Al}_2\text{O}_2$	5.12E+009		1	-5062	-10059.21
11	$\text{Al}_2\text{O}_2 = \text{Al}_2\text{O} + \text{O}$		1.00E+015		52466	104260.44
12	$\text{Al}_2\text{O} + \text{O} = \text{Al}_2\text{O}_2$	2.83E+010		1	-7288	-14482.71
13	$\text{AlO}_2 = \text{AlO} + \text{O}$		1.00E+015		44564.6	88558.773
14	$\text{AlO} + \text{O} = \text{AlO}_2$	1.40E+011		1	1230	2444.256
15	$\text{AlOH} = \text{AlO} + \text{H}$		1.00E+015		57725.2	114711.52
16	$\text{AlO} + \text{H} = \text{AlOH}$	2.65E+010		1	-1930	-3835.296
17	$\text{AlOH} = \text{Al} + \text{OH}$		1.00E+015		66431.8	132013.27
18	$\text{Al} + \text{OH} = \text{AlOH}$	2.65E+010		1	-580	-1152.576
19	$\text{H} + \text{H} + \text{M} = \text{H}_2 + \text{M}$	6.40E+017		-1	0	0
20	$\text{H}_2 + \text{M} = \text{H} + \text{H} + \text{M}$	5.88E+018		-1.1	52462.3	104253.08
21	$\text{OH} + \text{OH} = \text{H}_2\text{O} + \text{O}$	6.00E+018		1.3		0
22	$\text{H}_2\text{O} + \text{O} = \text{OH} + \text{OH}$	6.30E+009		1.3	8542.7	16976.053
23	$\text{H} + \text{H}_2\text{O} = \text{H}_2 + \text{OH}$	1.00E+009		1.5	9346.7	18573.762
24	$\text{H}_2 + \text{OH} = \text{H} + \text{H}_2\text{O}$	2.20E+008		1.5	1758.8	3495.0874
25	$\text{O} + \text{OH} = \text{H} + \text{O}_2$	2.80E+015		-0.8	-50.3	-99.95616
26	$\text{H} + \text{O}_2 = \text{O} + \text{OH}$	1.90E+014			8241.2	16376.913
27	$\text{O} + \text{H}_2 = \text{OH} + \text{H}$	1.50E+013			4472.4	8887.5533
28	$\text{OH} + \text{H} = \text{O} + \text{H}_2$	6.90E+012			3517.6	6990.1747

ELECTRICAL DISCHARGE INTERACTION WITH GAS MEDIUM IN EXTERNAL MAGNETIC FIELD AND ITS INFLUENCE ON FLOW STRUCTURE AND MIXING

Klementyeva I.B., Bityurin V.A., Bocharov A.N.

Joint Institute for High Temperatures of RAS

ira.klementyeva@mail.ru

Abstract. Electrical discharge interaction with gas medium in external magnetic field, in task of investigation of MHD-method of mixing and combustion intensification, is discussed in the paper. Phenomenological explanation of mechanisms of that interaction influence on flow structure and mixing is given. Earlier obtained numerical and experimental results that demonstrate features of the influence are summarized. Overall picture of flow field under investigation is discussed. Three types of flows comprising the complex observed flow field are described: vortical flow, caused by non-potential electromotive body force, in cross section plane of discharge channel; swirling flow of medium near central electrode and gas movement in radial direction taking place in longitudinal section plane of the discharge channel.

Introduction

Investigation of electrical discharge interaction with gas medium in external magnetic field and investigation of that interaction influence on flow structure and mixing are connected with technical task of fuel and oxidizer mixing and combustion intensification in high-speed chambers of chemical reactors using MHD-method. Effective and stable mixing and combustion of non-premixed gas fuel and oxidizer is an essential issue at high-speed combustion chambers designing. The problem is that speed of fuel and oxidizer streams is too high to allow them to create a combustible mixture during short residence times. And it is actual to apply mechanisms for mixing and hence combustion intensification. A possible way to intensify mixing and combustion of non-premixed gas fuel and oxidizer is to use the MHD-method. The MHD-method is described in [1, 2], its point is

to use electrical discharge current with magnetic field interaction for secondary vertical flows generation in gas medium.

The MHD-method is based on a 'reaction volume' concept. Combustion as an elementary chemical reaction between fuel and oxidant molecules can occur only in the region where direct contact of these molecules takes place. That region is called the 'reaction volume' and it is formed due to diffusion across a contact surface of fuel and oxidizer streams, i.e.:

$$V(t) = S(t) \cdot \delta(t),$$

$V(t)$ is the 'reaction volume', $S(t)$ is a contact surface area of streams, $\delta(t) \approx \sqrt{Dt}$ is a diffusion layer thickness, D and t are diffusivity and time correspondingly. Molecular diffusion is a slow process on scales of available for mixing times that are limited by fuel and oxidizer residence in combustion chamber.

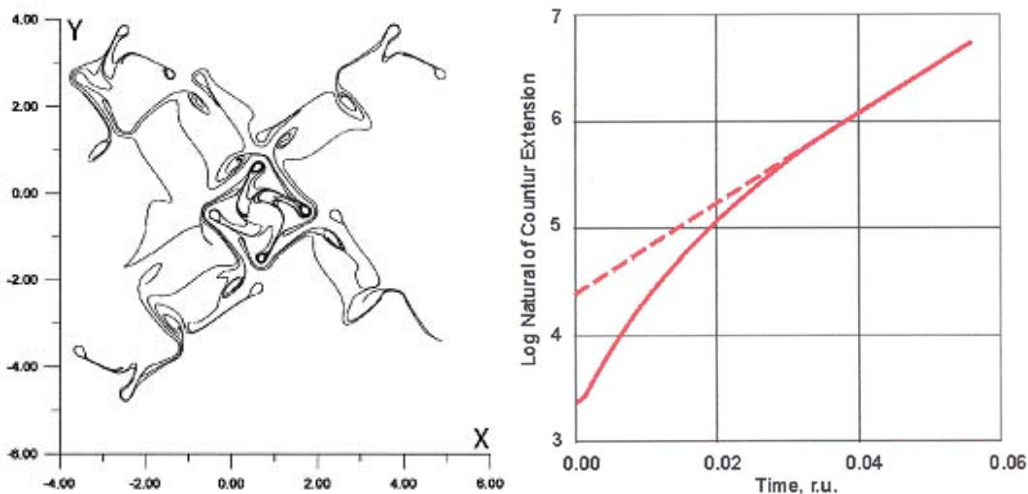


Fig. 1. Circle contour deformation. Contour length increase.

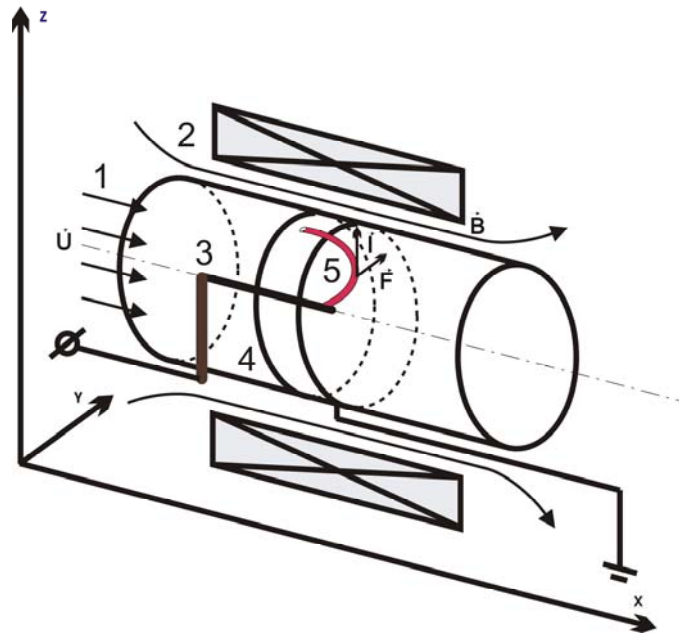


Fig. 2. Principle scheme of investigations. 1 – gas flow, 2 – magnetic field, 3 – central wire electrode, 4 – annular electrode, 5 – electrical discharge.

But it is possible to enhance ‘reaction volume’ formation through contact surface increase that can be done by secondary vortex motion organization in flows (kinematical mixing), using MHD-method.

It is shown in [3 – 5] that in disturbed turbulence flow material lines lengths and material surface areas (that is the contact surface area of two streams in task of mixing) grows exponentially versus time, i.e:

$$S \sim S_0 \exp \{t\Omega\},$$

S_0 is an initial contact surface area value, Ω is a typical scale of vortical flow non-uniformity.

Exponential growth of contour length is also demonstrated in [6], where disturbed flow is defined by random velocity field that is direct solution of Euler equations for incompressible medium for 2D task setup. Being placed in medium with such velocity field initially circle contour starts to deform, while its length increases in time according to exponential law (Fig.1).

Generated due to electrical discharge current with magnetic field interaction secondary vortical flows lead to ‘reaction volume’ increase through contact surface deformation of two streams and therefore intensify fuel and oxidizer mixing process. At the same time discharge localization on the contact surface of two reagents provides induction time reduction and mixing intensification due to diffusivity increase at high temperatures.

MHD-method scheme, that is at the same time is a scheme of experimental and numerical investigations of electrical discharge with gas medium interaction in external magnetic field and

of that interaction influence on flow structure and mixing, is depicted in Fig. 2.

Representing oxidizer main stream 1 comes into experimental section from left to right. Representing fuel gas can be injected co/counter to the main stream through located on aerodynamical duct axis injection system. Initiated between wire 3 and annular 4 electrodes in magnetic field 2 the electrical discharge 5 under electromotive body force \mathbf{F} action deforms, moves and represents a source of disturbances in flow, that are intensifying factor for mixing.

Processes and phenomena caused by the MHD-method of mixing and combustion intensification are complex. To study them a set of physical and numerical models of different range of description were worked out and physical experiments were organized.

Influence of electrical discharge interaction with gas medium in external magnetic field on flow structure

Theoretical, numerical and experimental investigations allowed revealing mechanisms of the influence on flow structure and mixing.

Flow structure in the configuration under consideration is complicated and it is possible to see three components in it: vortical flows generated in cross section plane of the discharge channel due to non-potentiality of the electromotive body force; swirling gas flow forced by discharge rotation near the central electrode; gas medium movement due to electrical discharge spiral evolution in radial direction towards the annular electrode in longitudinal section plane of the discharge.

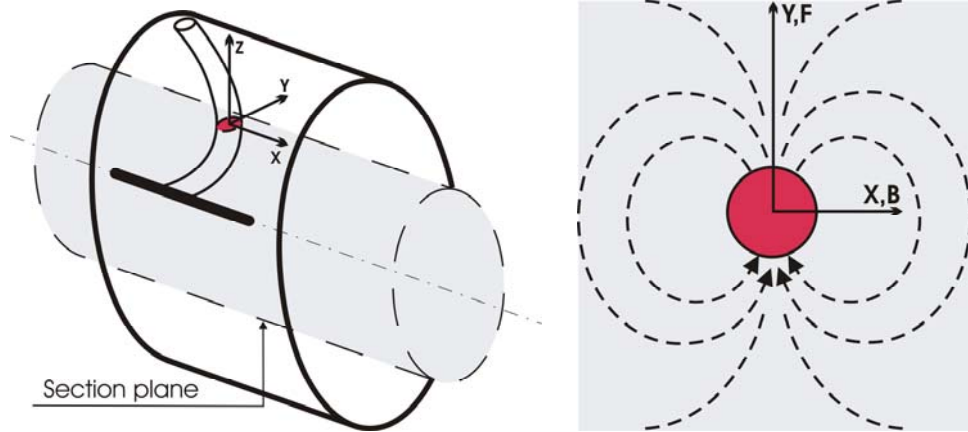


Fig. 3. Vortical flow generated in cross section plane of the discharge channel.

Fig. 3. is considering vortical flow that takes place in cross section plane of the discharge channel. Domain of interest in the case is a rectangular plane that is an unrolled cylindrical surface crossing a gap between the central wire and the annular electrodes.

In external magnetic field in medium with non-uniform conductivity, that is the gas flow with the constricted electrical discharge, the non-potential electromotive body force $\mathbf{I} \times \mathbf{B}$ cannot be stabilized by pressure gradient for two-dimensional case.

$$\rho \frac{d\mathbf{v}}{dt} = \rho \mathbf{F} - \text{grad } p,$$

$$\text{rot} \mathbf{F} = B_x \frac{dj_z}{dx},$$

ρ is gas medium density, \mathbf{v} is velocity, \mathbf{F} is the electromagnetic body force, p is pressure, B_x is x component of magnetic induction vector, j is z component of current density vector.

The force uncompensation leads to secondary flow generation that is revealed in electrical discharge movement and vortices presence around it. Flow structure under consideration corresponds to pressure distribution, which is linear inside conducting zone and dipole-like outside it. Pressure on border of the discharge channel with non-conducting gas is uninterrupted in continuum approach. That is why in cross section

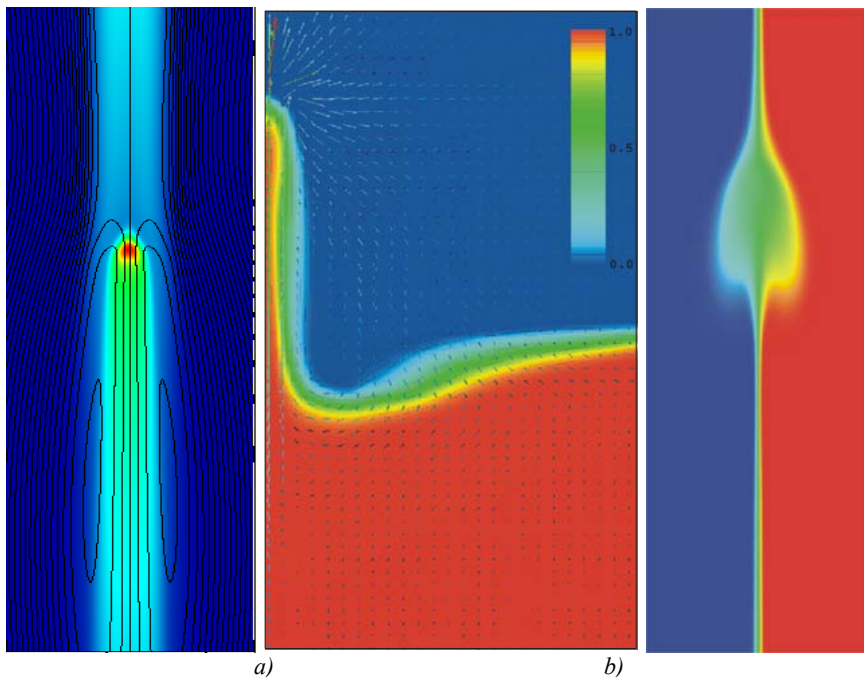


Fig. 4. a) Shape of the discharge in cross section plane, vortical flow structure b) contact surface deformation at perpendicular and longitudinal discharge channel movement correspondingly.

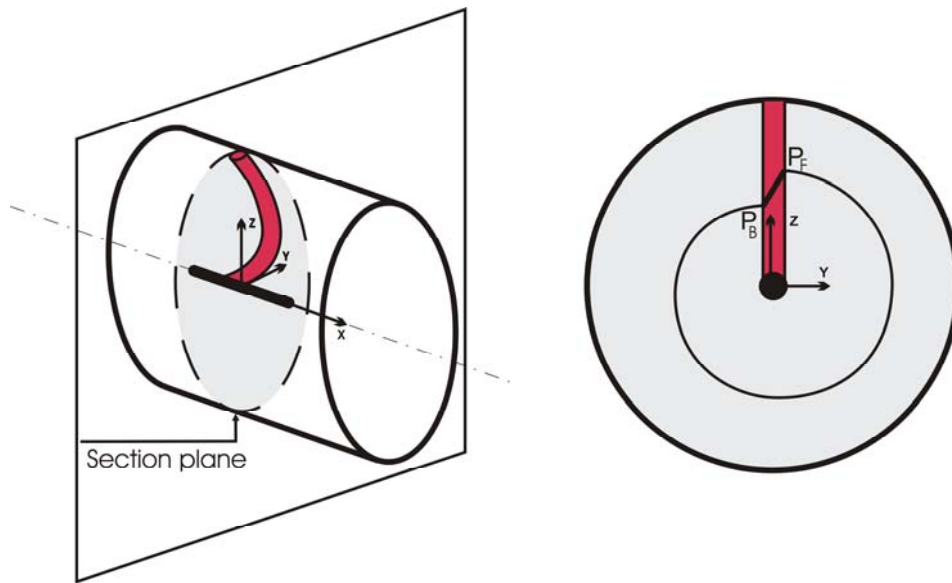


Fig. 5. Swirling flow of gas medium around the central electrode.

plane discharge shape sets according to condition of pressure continuity and looks like in Fig. 4., where one can see results of numerical simulation described in [7].

Discharge region in Fig. 4. a) is a dark asymmetrical spot. Current quasi-lines reflect vortical structure of secondary flow generated around the discharge channel. Light region in front of the discharge is a thermal wake left during its previous passing.

Contact surface deformation of two gases demonstrates influence of the described above vortical flow on mixing. Fig. 4. b) represents results for two cases of mutual position of the contact surface and discharge channel movement trajectory – perpendicular [8] and longitudinal [9] ones correspondingly. Here light zone is the ‘reaction volume’, formed on the contact surface of two media.

If to consider whole volume of investigation now and summarize the vortical flows of cross section plane throughout the discharge channel, rate of medium disturbances in the system is an integral of micro disturbances (taking place in cross section plain of the discharge due to non-potentiality of the electromotive force) over discharge channel length.

Other flow structure is observed in longitudinal section plane of the discharge channel, where swirling flow of medium around the central electrode takes place (Fig. 5).

For initial time moment in external magnetic field pressure difference sets inside the conducting discharge channel. Pressure difference magnitude is the same for each section of the discharge all along its length. Since pressure distribution is uninterrupted on borders of

conducting area, pressure gradient is created in the medium around the discharge and gas starts to move. Pressure gradient value increases towards the central electrode and hence velocity of gas rotation increases towards center of considered area too:

$$\nabla p = \frac{p_F - p_B}{r},$$

$$v \sim \nabla p,$$

p_F , p_B are maximum and minimum pressure values on the border of discharge zone and cold gas, r is discharge gap radius, v is medium movement velocity.

In longitudinal section plane flow structure through velocity field (marked with arrows) and current channel shape are demonstrated by results of numerical simulation (Fig. 6. a) [4, 5] and experiments (Fig. 6. b) [4 – 6]. It is seen that the discharge untwists around the central electrode; observed discharge channel shape is a result of gas medium movement caused by the pressure distribution in the gap that in its turn is determined by the electromotive body force acting transversally to the discharge current. In the considered configuration contact surface deformation of two media, represented as result of numerical simulation, approves existence of the swirling flow around in the central part of the system (Fig. 6. c).

Speed of discharge channel elements sharply increases from the annular electrode towards the central one. With time the discharge under considered conditions takes a shape of spiral untwisting around the wire electrode. Outer part of the discharge spiral, where the electromotive body force acts in radial direction of the discharge gap,

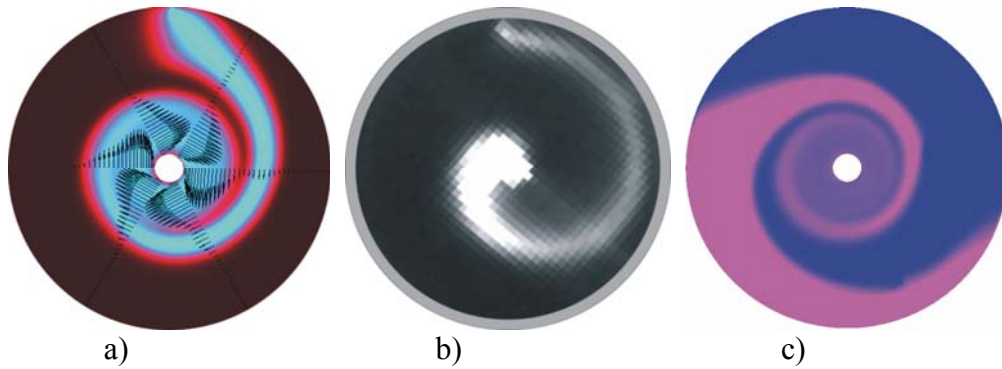


Fig. 6. a) Velocity field and discharge shape (results of numerical simulation); b) discharge shape (experiment); c) contact surface deformation of two media (numerical simulation).

moves towards the annular electrode, forcing gas media to flow at the same direction. Near the central part of the discharge gap the electromotive body force acts on the discharge mainly in azimuth direction because current is normal to the wire electrode. Here swirling flow of gas takes place as usual. Fig. 7 depicts discharge spiral evolution scheme (Fig. 7. a), results of numerical simulation (Fig. 7. b) [2, 4] and experiments (Fig. 7. c) [2, 4, 5] that demonstrates flow structure and discharge shape for the case under consideration.

Conclusions

Flow structure under conditions of electrical discharge with magnetic field interaction in coaxial electrodes configuration is complex and it is defined by a number of factors. One can see at least three mechanisms that form the investigated flow and define mixing. Observed flow structure is a compound of vertical micro flows generated in cross section plane of the discharge due to non-potentiality of the electromotive body force; gas medium swirling forced by discharge rotation around the central electrode; and gas movement in radial direction owing to discharge spiral evolution.

In secondary vortical flows field, that is result of electrical discharge current with magnetic field interaction, contact surface area of two media increases. Contact surface area increase leads to 'reaction volume' rise and hence provides fuel and oxidizer mixing process intensification.

References

1. *Bityurin V.A., Bocharov A.N.* Advanced MHD assisted Mixing of Reacting Streams // In: 39th AIAA Aerospace Sciences Meeting & Exhibit. Reno, NV, 2001. AIAA Paper 2001-0793.
2. *Bocharov A.N., Leonov S.B., Baranov D.S., Klement'eva I.B., Bityurin V.A.* MHD Enhanced Mixing and Combustion in Cocurrent Streams // In: 4th Workshop on Magnetoplasma Aerodynamics in Aerospace Applications. Moscow, Russia, 2002. P. 220 – 230.
3. *Ottino J.M.* The kinematics of mixing: stretching, chaos, and transport. Cambridge University Press, 1997.
4. *Monin A.S., Yaglom A.M.* Statistical hydromechanics, mechanics of turbulence. P. 1. M.: Nauka, 1966. P. 505 – 529.
5. *Monin A.S., Yaglom A.M.* Statistical

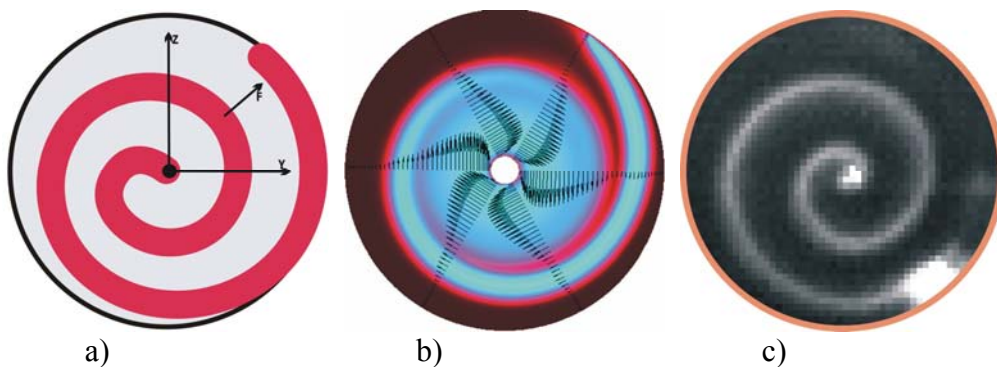


Fig. 7. Discharge spiral evolution scheme, velocity field and discharge shape (results of numerical simulation and experiments correspondingly).

- hydromechanics, mechanics of turbulence. P. 1. M.: Nauka, 1967. P. 513 – 517.
6. *Bityurin V., Potebnya V., Tseskis A.* Evolution of a Current Plasma Clot in Turbulent Flow // In: 33rd SEAM Conference. Tennessee, 1995. P. IV. 7.
 7. *Klement'eva I., Bocharov A., Bityurin V., Klimov A.* Experimental and Numerical Study of MHD Assisted Mixing // In: 15th International Conference on MHD Energy Conversion and 6 International Workshop on Magnetoplasma Aerodynamics. Moscow, Russia, 2005. P. 365 – 374.
 8. *Bocharov A.N., Leonov S.B., Baranov D.S., Klement'eva I.B., Bityurin V.A.* MHD Enhanced Mixing and Combustion in Cocurrent Streams // In: 4th Workshop on Magnetoplasma Aerodynamics for Aerospace Applications. Moscow, Russia, 2002. P. 220 – 230.
 9. *Bityurin V.A., Klementyeva I.B., Bocharov A.N., Klimov A.I.* Magnetically Driven Electrical Discharges in High Speed Reacting Flows for the MHD Assisted Mixing and Combustion // In: 45th AIAA Aerospace Sciences Meeting & Exhibit. Reno, NV, 2007. AIAA Paper 2007-1024.
 10. *Bityurin V., Bocharov A., Klement'eva I., Klimov A.* Numerical and Experimental Study of MHD Assisted Mixing and Combustion // In: 44th Aerospace Sciences Meeting and Exhibit. Reno, NV, 2006. AIAA Paper 2006-1009.
 11. *Klement'eva I., Bityurin V.* Electrical Discharge – Gas Flows Media Interaction in External Magnetic Field // In: 46th Aerospace Sciences Meeting and Exhibit. Reno, NV, 2008. AIAA Paper 2008-1393.

ON THE SCALING FOR A MICROFUSION FLYING MACHINES (MFFM) AND THE VARIETY MOBILE SYSTEMS

Valentine A. Belokogne

Oceanology Institute RAS, Academia Cosmonautica, RANS, International Academy of Futures Research,
Moscow, Russia

kancelariya@ocean.ru

The Inertial Confinement Fusion, applicable to the variety of the unique mobile systems rather than to the industrial energetics.

The very important point here consists in the necessity to reach superhigh density of the fusion fuel (max ρ), as soon as the fusion energy Y (Joules) of the microexplosion is $Y \approx 10^7/\rho^2$, i.e. $Y = 10^{8-10}$ Joules corresponds to $\rho_{\max} = 100 \div 1000 \text{ g/cm}^3$ at $Z \approx 14$ for DT fuel, and $Z \approx 16$ for DD and D^3He (both $\approx 10^{11}$ J/g) fuel [1, 2, 3].

Since the very first (1960-1974) papers by John Hopkins Nuckolls, and his colleagues [5], the perspectives of MFFM, and the variety of mobile systems based on the ICF Power are discussed hotly.

As soon as the mass M of the system depends on the character dimension by $M \sim l^a$, and the ICF reactor size

$$r \sim l,$$

then at the microexplosion energy (at proper repetition rate) $Y \sim r^{1/b}$ with $Y \sim 1/\rho^c$ (where $\rho = \rho_{\max}$ of the fusion fuel superdensity at the initial one $\approx 0.2 \text{ g/cc}$) $\rightarrow M \sim \rho^{abc}$

For the instance:

$$a = 3, b = 2/5 \text{ and } M \sim 1/\rho^{2.4}$$

The illustrations of [5, 7, 8] are important for the understanding the recent progress to MFFM first realization since 2017-2022 years.

References

1. John H. Nuckolls: ICF papers, LLL 1960-1962; Preprint UCRL-JC-131075, (1999).
2. Ray Kidder: ICF papers, LLL 1962-1964.
3. John H. Nuckolls et al: ICF aerospace applications, LLL 1972-1979.
4. D.Kuchemann: AERODYNAMIC DESIGN OF AIRCRAFT, Pergamon Press 1978.
5. Laser Program Annual Reports, LLL-LLNL, 1972-1994; John Lindl: INERTIAL CONFINEMENT FUSION, Springer (and refs in it), N-Y, 1998.
6. V.A. Belokogne: PROGRESS IN FUSION POWERED FLYING MACHINE DESIGN (and refs in it), 15th International Conference on MHD Energy Conversion and 6th Workshop on Magnetoplasma Aerodynamics for Aerospace Applications, Moscow, Russia, May 24-27, 2005. Proceed., v.3.
7. Orth Ch.: VISTA, Final Report, LLNL 2003.
8. Storm Erik: On National Ignition Facility (NIF), and National Ignition Campaign (NIC) advances, LLNL, September 2010.

Index of Autors

<i>Afanas'ev S.</i> (St. Petersburg State University, Russia)	266
<i>Aleksandrov N.L.</i> (Moscow Institute of Physics and Technology, Dolgoprudny, Moscow Region, Russia)	164
<i>Anokhin E.M.</i> (Moscow Institute of Physics and Technology, Dolgoprudny, Moscow Region, Russia)	164
<i>Ashurbekov N.A.</i> (Dagestan State University, Makhachkala, Russia)	193
<i>Azarova Olga</i> (Dorodnicyn Computing Center of RAS, Moscow, Russia)	70
<i>Barkhudarov E.M.</i> (Institute of Mechanics, Moscow State University, Moscow, Russia)	125
<i>Baryshnikov A.S.</i> (Ioffe Physical Technical Institute of the Russian Academy of Sciences, St.Petersburg, Russia)	232
<i>Basargin I.V.</i> (Ioffe Physical Technical Institute of the Russian Academy of Sciences, St.Petersburg, Russia)	232
<i>Belyaev I.</i> (TsAGI, Zhukovsky, Moscow region, Russia)	21
<i>Belokogne Valentine A.</i> (Academia Cosmonautica, RANS, ICAD RAS, Academy of Futures Research), Moscow, Russia)	304
<i>Berezhetskaya N.K.</i> (A.M.Prokhorov General Physics Institute of RAS, Moscow, Russia)	125
<i>Bityurin V.A.</i> (Joint Institute for High Temperatures RAS, Moscow, Russia)	21, 112, 156, 195, 260, 276, 281, 287, 292,
<i>Bocharov A.N.</i> (Joint Institute for High Temperatures RAS, Moscow, Russia)	195, 292
<i>Boytsov A.Yu</i> (Joint Institute for High Temperatures RAS, Moscow, Russia)	40
<i>Brovkin V.</i> (Joint Institute of High Temperatures, RAS, Moscow)	266
<i>Bychkov V.L.</i> (M.V.Lomonosov Moscow state university, Moscow, Russia)	93
<i>Chertov D.</i> (Joint Institute for High Temperatures RAS, Moscow, Russia)	281, 287
<i>Chistyakova M.V.</i> (Ioffe Physical Technical Institute of the Russian Academy of Sciences, St.Petersburg, Russia)	232
<i>Correale Giuseppe</i> (NEQLab Research BV, The Hague, 2521 AL, The Netherlands)	134
<i>Deminsky M.A.</i> (State Research Center of Russia "Kurchatov Institute", Moscow, Russia)	115, 172
<i>Dobrovol'skaya A.S.</i> (Joint Institute for High Temperatures RAS, Moscow, Russia)	295
<i>Dvinin S.A.</i> (M.V.Lomonosov Moscow state university, Moscow, Russia))	93
<i>Efimov A.V.</i> (Joint Institute for High Temperatures RAS, Moscow, Russia)	260
<i>Enenko A.A.</i> (Institute of High Current Electronics RAS, Tomsk, Russia)	103
<i>Erofeev A.V.</i> (Ioffe Physical Technical Institute of the Russian Academy of Sciences, St.Petersburg, Russia)	208

<i>Filimonova E.A.</i> (Joint Institute for High Temperatures RAS, Moscow, Russia)	112
<i>Firsov A.A.</i> (Joint Institute for High Temperatures RAS, Moscow, Russia)	100, 186
<i>Fokeev V.P.</i> (Institute of Mechanics, Lomonosov Moscow State University, Moscow, Russia)	224
<i>Fomichev V.P.</i> (Khristianovich Institute of Theoretical and Applied Mechanics SB RAS, Novosibirsk, Russia)	205
<i>Fomin V.M.</i> (Khristianovich Institute of Theoretical and Applied Mechanics SB RAS)	84
<i>Fortov V.E.</i> (Joint Institute for High Temperatures RAS, Moscow, Russia)	227
<i>Frants O.B.</i> (Institute of High Current Electronics RAS, Tomsk, Russia)	103
<i>Galaktionov A.V.</i> (Joint Institute for High Temperatures RAS, Moscow, Russia)	276
<i>Georgievsky P.Yu.</i> (Institute for Mechanics of Moscow State University, Russia)	54
<i>Geyman V.G.</i> (Institute of High Current Electronics RAS, Tomsk, Russia).	103
<i>Godin S.</i> (Joint Institute for High Temperatures RAS, Moscow, Russia)	21
<i>Golub V.V.</i> (Joint Institute for High Temperatures RAS, Moscow, Russia)	88
<i>Grigorenko A.V.</i> (Joint Institute for High Temperatures RAS, Moscow, Russia)	260
<i>Grin Yu.I.</i> (Institute of Mechanics, Lomonosov Moscow State University, Moscow, Russia)	224
<i>Iminov K.O.</i> (Dagestan State University, Makhachkala, Russia)	193
<i>Isaenkov Yu.I.</i> (Joint Institute for High Temperatures RAS, Moscow, Russia)	186
<i>Karachev A.A.</i> (Faculty of Physics, Moscow State University, Moscow, Russian)	156, 270
<i>Karpukhin V.T.</i> (Joint Institute for High Temperatures RAS, Moscow, Russia)	245
<i>Kasansky P.</i> (Joint Institute for High Temperatures RAS, Moscow, Russia)	281, 287
<i>Klement'eva I.B.</i> (Joint Institute for High Temperatures RAS, Moscow, Russia)	298
<i>Klimov A.I.</i> (Joint Institute for High Temperatures RAS, Moscow, Russia)	13, 21, 40, 260, 281, 287
<i>Kobzev O.V.</i> (Dagestan State University, Makhachkala, Russia)	193
<i>Kobzeva V.S.</i> (Dagestan State University, Makhachkala, Russia)	193
<i>Kochetov I.V.</i> (M.V.Lomonosov Moscow state university, Moscow, Russia)	115
<i>Kochetov I.V.</i> (SRC RF Troitsk Institute for Innovation and Thermonuclear Research, Troitsk, Moscow region, Russia)	172
<i>Kogan M.N.</i> (TsAGI, n.a. N.E. Zhukovsky Zhukovsky, Moscow region, Russia)	59
<i>Kolesnichenko Y.</i> (Joint Institute of High Temperatures, RAS, Moscow)	70
<i>Kolesnichenko Yu.</i> (Joint Institute of High Temperatures, RAS, Moscow)	266
<i>Kolpakov A.V.</i> (Joint Institute for High Temperatures RAS, Moscow, Russia)	276
<i>Konstantinovskij R.S.</i> (Faculty of Physics, Moscow State University, Moscow, Russian)	156
<i>Konyukhov A.V.</i> (Joint Institute for High Temperatures RAS, Moscow, Russia)	227
<i>Kop'ev V.A.</i> (A.M.Prokhorov General Physics Institute of RAS, Moscow, Russia)	125
<i>Kopiev V.F.</i> (TsAGI, Zhukovsky, Moscow region, Russia)	21

<i>Kopyl P.V.</i> (Faculty of Physics, Moscow State University, Moscow, Russian)	156, 270
<i>Korolev Yu.D.</i> (Institute of High Current Electronics RAS, Tomsk, Russia)	103
<i>Kossyi I.A.</i> (A.M.Prokhorov General Physics Institute of RAS, Moscow, Russia)	125
<i>Kozlov A.N.</i> (Keldysh Institute of Applied Mathematics, RAS, Russia)	216
<i>Kucherov A.N.</i> (TsAGI, n.a. N.E. Zhukovsky Zhukovsky, Moscow region, Russia)	59
<i>Kurilenkov Yu. K.</i> (Joint Institute for High Temperatures RAS, Moscow, Russia)	245
<i>Kutuzov D.S.</i> (Joint Institute for High Temperatures RAS, Moscow, Russia)	260
<i>Kwing-So Choi</i> (University of Nottingham, UK)	23
<i>Landl N.V.</i> (Institute of High Current Electronics RAS, Tomsk, Russia)	103
<i>Lapushkina T.A.</i> (<i>Ioffe Physical Technical Institute of the Russian Academy of Sciences, St.Petersburg, Russia</i>)	208
<i>Leonov S.B.</i> (Joint Institute for High Temperatures RAS, Moscow, Russia)	100, 115, 186
<i>Levin V.A.</i> (Institute for Automation and Control Processes of RAS, Russia)	54, 125
<i>Likhachev A.P.</i> (Joint Institute for High Temperatures RAS, Moscow, Russia)	227
<i>Lomanovich K.A.</i> (Khristianovich Institute of Theoretical and Applied Mechanics SB RAS, Russia)	84
<i>Manuilovich I.S.</i> (Institute of Mechanics, Moscow State University, Moscow, Russia)	125
<i>Markov V.V.</i> (Institute of Mechanics, Moscow State University, Moscow, Russia)	125
<i>Mashek I.</i> (St. Petersburg State University, Russia)	266
<i>Miller A.B.</i> (TsAGI, Zhukovsky, Moscow region, Russia)	100
<i>Moralev I.</i> (Joint Institute for High Temperatures RAS, Moscow, Russia)	21, 40, 281, 287
<i>Mursenkova I.V.</i> (Lomonosov Moscow State University, Physical dep., Moscow, Russia)	51
<i>Napartovich A.P.</i> (SRC RF Troitsk Institute for Innovation and Thermonuclear Research, Troitsk, Moscow region, Russia)	115
<i>Nikipelov Andrei</i> (Moscow institute of physics and technology, Dolgoprudny, Russia)	134
<i>Nikolaeva V.I.</i> (Joint Stock Company “Scientific Research Institute of Radio Device Instruments”, Moscow, Russia)	105
<i>Ostrikov N.N.</i> (TsAGI, Zhukovsky, Moscow region, Russia)	21
<i>Pashchina A.S.</i> (Joint Stock Company “Scientific Research Institute of Radio Device Instruments”, Moscow, Russia)	105
<i>Petrova T.A.</i> (M.V.Lomonosov Moscow state university, Moscow, Russia)	35
<i>Podzin V.E.</i> (Khristianovich Institute of Theoretical and Applied Mechanics SB RAS, Novosibirsk, Russia)	205
<i>Polyakov L.B.</i> (Joint Institute for High Temperatures RAS, Moscow, Russia)	260
<i>Poniaev S.A.</i> (Ioffe Physical Technical Institute of the Russian Academy of Sciences, St.Petersburg, Russia)	208

<i>Popov Iliia</i> (NEQLab Research BV, The Hague, 2521 AL, The Netherlands)	134
<i>Popov N.A.</i> (D.V.Skobel'tsyn Institute of Nuclear Physics, Moscow State University, Moscow, Russia)	125, 141, 195
<i>Postnikov B.V.</i> (Khristianovich Institute of Theoretical and Applied Mechanics SB RAS, Russia)	84
<i>Prudchenko V.A.</i> (Joint Stock Company "Scientific Research Institute of Radio Device Instruments", Moscow, Russia)	105
<i>Rakitin A.</i> (NEQLab Research BV, The Hague, 2521 AL, The Netherlands)	134, 179
<i>Richard Whalley</i> (University of Nottingham, UK)	23
<i>Saveliev A.S.</i> (Moscow Institute of Physics and Technology, Russia)	88
<i>Schweigert I.V.</i> (ITAM SB RAS, Novosibirsk, Russia)	46
<i>Serov Yu.L.</i> (Ioffe Institute RAS, St.-Petersburg, Russia)	238
<i>Shevchenko A.B.</i> (Khristianovich Institute of Theoretical and Applied Mechanics SB RAS, Novosibirsk, Russia)	205
<i>Shibkov V.M.</i> (Faculty of Physics, Moscow State University, Moscow, Russian)	156, 270
<i>Shibkova L.V.</i> (Faculty of Physics, Moscow State University, Moscow, Russian)	156, 270
<i>Shugaev F.V.</i> (M.V.Lomonosov Moscow state university, Moscow, Russia)	35
<i>Shurupov M.A.</i> (Joint Institute for High Temperatures RAS, Moscow, Russia)	186
<i>Sidorenko M.K.</i> (Joint Stock Company "Scientific Research Institute of Radio Device Instruments", Moscow, Russia)	105
<i>Son E.E.</i> (Joint Institute for High Temperatures RAS, Moscow, Russia)	88
<i>Starikovskii A.Yu.</i> (Drexel University, Philadelphia, PA, USA), (NEQLab Research BV, The Hague, 2521 AL, The Netherlands)	134, 179
<i>Tarakanov V.P.</i> (Joint Institute for High Temperatures RAS, Moscow, Russia)	245
<i>Tolkunov B.N.</i> (Joint Institute for High Temperatures RAS, Moscow, Russia)	260
<i>Trushkin A.N.</i> (SRC RF Troitsk Institute for Innovation and Thermonuclear Research, Troitsk, Moscow region, Russia)	172
<i>Tsybal A.A.</i> (Joint Institute for High Temperatures RAS, Moscow, Russia)	260
<i>Umanskii S.Ya.</i> (Institute of Chemical Physics RAS, Moscow, Russia)	172
<i>Valyano G.E.</i> (Joint Institute for High Temperatures RAS, Moscow, Russia)	245
<i>Yarantsev D.A.</i> (Joint Institute for High Temperatures RAS, Moscow, Russia)	186
<i>Yadrenkin M.A.</i> (Khristianovich Institute of Theoretical and Applied Mechanics SB RAS, Novosibirsk, Russia)	205
<i>Zaitsev M.Yu.</i> (TsAGI, Zhukovsky, Moscow region, Russia)	21
<i>Znamenskaya I.A.</i> (Lomonosov Moscow State University, Physical dep., Moscow, Russia)	51

НАУЧНЫЕ ТРУДЫ
Девятое Международное Собрание по Магнитоплазменной Аэродинамике

Подписано к печати 17.12.2010
Печать офсетная
Тираж 100 экз.

Заказ № _____

Формат 60×84/8
Усл.печ.л. 38,5

ООО «Печатный Салон «Шанс»». 125412, Москва, Ижорская ул., 13, стр.2
Материал отпечатан по оригиналам-макетам